

ACS SYMPOSIUM SERIES **730**

Spectroscopy of Superconducting Materials

Eric Faulques, EDITOR
Institut des Matériaux

September 13, 2012 | <http://pubs.acs.org>
Publication Date: September 2, 1999 | doi: 10.1021/bk-1999-0730.fw001



American Chemical Society, Washington, DC

In Spectroscopy of Superconducting Materials; Faulques, E.;
ACS Symposium Series; American Chemical Society: Washington, DC, 1999.



Spectroscopy of superconducting materials

Library of Congress Cataloging-in-Publication Data

Spectroscopy of superconducting materials / Eric Faulques, editor.

p. cm.—(ACS symposium series ; 730)

Proceedings of the Symposium on Applications of Spectroscopy to Superconductors, held 1998 in Dallas.

Includes bibliographical references and index.

ISBN 0-8412-3609-7

1. Superconductors—Spectra Congresses.

I. Faulques, Eric. II. Symposium on Applications of Spectroscopy to Superconductors (1998 : Dallas, Tex.) III. Series.

QC611.97.S64S65 1999
537.6'23'0287—dc21

99-14283
CIP

The paper used in this publication meets the minimum requirements of American National Standard for Information Sciences—Permanence of Paper for Printed Library Materials, ANSI Z39.48-1984.

Copyright © 1999 American Chemical Society

Distributed by Oxford University Press

All Rights Reserved. Reprographic copying beyond that permitted by Sections 107 or 108 of the U.S. Copyright Act is allowed for internal use only, provided that a per-chapter fee of \$20.00 plus \$0.50 per page is paid to the Copyright Clearance Center, Inc., 222 Rosewood Drive, Danvers, MA 01923, USA. Republication or reproduction for sale of pages in this book is permitted only under license from ACS. Direct these and other permission requests to ACS Copyright Office, Publications Division, 1155 16th St., N.W., Washington, DC 20036.

The citation of trade names and/or names of manufacturers in this publication is not to be construed as an endorsement or as approval by ACS of the commercial products or services referenced herein; nor should the mere reference herein to any drawing, specification, chemical process, or other data be regarded as a license or as a conveyance of any right or permission to the holder, reader, or any other person or corporation, to manufacture, reproduce, use, or sell any patented invention or copyrighted work that may in any way be related thereto. Registered names, trademarks, etc., used in this publication, even without specific indication thereof, are not to be considered unprotected by law.

PRINTED IN THE UNITED STATES OF AMERICA

American Chemical Society
Library
1155 16th St., N.W.
Washington, D.C. 20036

Advisory Board

ACS Symposium Series

Mary E. Castellion
ChemEdit Company

Arthur B. Ellis
University of Wisconsin at Madison

Jeffrey S. Gaffney
Argonne National Laboratory

Gunda I. Georg
University of Kansas

Lawrence P. Klemann
Nabisco Foods Group

Richard N. Loepky
University of Missouri

Cynthia A. Maryanoff
R. W. Johnson Pharmaceutical
Research Institute

Roger A. Minear
University of Illinois
at Urbana-Champaign

Omkaram Nalamasu
AT&T Bell Laboratories

Kinam Park
Purdue University

Katherine R. Porter
Duke University

Douglas A. Smith
The DAS Group, Inc.

Martin R. Tant
Eastman Chemical Co.

Michael D. Taylor
Parke-Davis Pharmaceutical
Research

Leroy B. Townsend
University of Michigan

William C. Walker
DuPont Company

Foreword

THE ACS SYMPOSIUM SERIES was first published in 1974 to provide a mechanism for publishing symposia quickly in book form. The purpose of the series is to publish timely, comprehensive books developed from ACS sponsored symposia based on current scientific research. Occasionally, books are developed from symposia sponsored by other organizations when the topic is of keen interest to the chemistry audience.

Before agreeing to publish a book, the proposed table of contents is reviewed for appropriate and comprehensive coverage and for interest to the audience. Some papers may be excluded in order to better focus the book; others may be added to provide comprehensiveness. When appropriate, overview or introductory chapters are added. Drafts of chapters are peer-reviewed prior to final acceptance or rejection, and manuscripts are prepared in camera-ready format.

As a rule, only original research papers and original review papers are included in the volumes. Verbatim reproductions of previously published papers are not accepted.

ACS BOOKS DEPARTMENT

Preface

The need for energy storage, energy saving, acceleration of information, development of communications, and the growing worldwide interest in environmental problems, has led researchers to find new materials that can contribute to these vital priorities of the 21st century. Among these materials, superconductors are those which occupy the largest place, because the frame of their applications is enormous. The gain brought by a possible discovery of applicable room temperature superconductors would be one of the greatest achievements of the hard sciences. In this context, the recent discovery of novel superconductors of which several are effective well above the liquid nitrogen temperature and their first applications to industry have resulted in an increasing number of chemists and physicists working in this field. In this area of science, physics and chemistry appear to be extremely entangled: no research in physics and no application of these materials can be achieved without the savoir-faire and the knowledge of solid-state chemists. As a feedback, any progress in the understanding of their solid-state properties leads to the synthesis of new structures.

One important scientific area shared by chemists and physicists is *spectroscopy*. The goal of the Symposium on Applications of Spectroscopy to Superconducting Materials, held in Dallas in 1998, was to combine the strengths and experience of solid-state chemists and physicists from several countries. This book is a detailed account of the talks which were given for this purpose. Because spectroscopy covers the X-ray, microwave, high-energy, and optical ranges, it offers a great variety of tools to investigate the intimate structures of superconductors and the mechanisms governing their properties.

This book gives an up-to-date overview of relevant aspects of spectroscopy applied to superconducting materials. Important techniques have been selected like Raman scattering, infrared absorption, X-ray photoelectron and Auger spectroscopy, time-resolved spectroscopy, microwave plasma resonance, Mössbauer spectroscopy, photoconductivity, and point-contact spectroscopy. Some theoretical papers are also included as well as general papers concerning new materials, magnetotransport phenomena, and structures. I hope the book will be useful to researchers and engineers not necessarily in the field. They will find in it many tools and methods that can be used for studying other classes of materials. I thank the authors who have taken time from their busy activities to present their research at the symposium and to prepare the papers published in this volume.

Acknowledgment

Acknowledgment is made to the Donors of The petroleum Research Fund, administered by the American Chemical Society, for support of the Symposium on Applications of Spectroscopy to Superconducting Materials.

ERIC FAULQUES
Institut des Matériaux Jean Rouxel
Laboratoire de Physique Cristalline
University of Nantes
2 rue de la Houssinière, BP 32229
F-44322 Nantes Cedex, France

Chapter 1

Introduction to the Spectroscopy of Exotic Superconductors

Eric Faulques

**Institut des Matériaux de Nantes Jean Rouxel, Laboratoire de Physique
Cristalline, University of Nantes, 2 rue de la Houssinière, BP 32229,
F-44322 Nantes Cedex, France**

Advances in the comprehension of novel superconductors have been promoted by the advent of new instrumentation in spectroscopy. In this introductory chapter, some aspects of energy spectra are described with the intention to outline concepts used in the following chapters. Interplay between atomic and electronic structures and interference phenomena between vibrational and electronic excitations are ultimately decisive in deciphering the puzzle of exotic superconductivity. An application to optical devices is briefly introduced.

Until now much of progress has occurred in the understanding of the structural, electronic, and magnetic properties of superconductors, and research in the field is becoming more and more vivid. This volume is almost entirely targeted at studies of unconventional high temperature superconductors except for chapters 2, 10 (in part) and 14. Indeed, possible applications of high- T_c superconductivity to the public domain and everyday life are numerous and concern the most important aspects of industry and technology. Examples are superconducting quantum interference devices for measurements of very weak magnetic fields, Josephson junction devices, circuitry connections, transducers, sensors and levitated vehicles. Intensive research concerning the fundamental properties and the applications of novel superconductivity is conducted in all the fields of science and technology. In this context spectroscopy plays a still unsurpassed role. The great variety of spectroscopies and the increasing number of late-discovered superconductors would make a thorough presentation embodying all the aspects of this intriguing field an enormous task beyond the scope of this book. That is why, for example, nuclear magnetic resonance (NMR), tunneling, electron energy loss (EELS), far infrared reflectivity, angle resolved photoelectron spectroscopy (ARPES), x-ray absorption (XAFS), photothermal deflection are not treated here. As a matter of fact, they have been more widely used by physicists than by chemists. However, in the present volume, the applications of microprobe spectroscopy are particularly well represented as well as other spectroscopy techniques hardly discussed in other books like microwave plasma resonance, point-contact spectra (related to tunneling), ultrafast optical spectra, photoconductivity, Mössbauer, Auger, x-ray photoelectron spectroscopy and Rutherford backscattering spectrometry. Theoretical aspects in lattice dynamics and electronic light

scattering are not omitted. Two chapters are specially aimed at optical devices. Also, one of our main concerns was to review the successful application of Raman spectroscopy to exotic superconductivity which we believe is appropriate to the present stage of development of the field. As specified in the Preface, this book is the outcome of mixed contributions of physicists and chemists. Chapters 6, 9, 13, 14, 16, 17 contain more fundamental physics, but they can be read by solid-state chemists. All other chapters encompass attractive areas of spectroscopy applicable to chemistry. At the end of the volume we have placed a breakthrough paper, chapter 18. The reader may like to consult it immediately, since it is a captivating example of masterful application. As a result, a number of spectroscopy techniques applied to high- T_c superconductors are well represented in this book. In the present introductory chapter, the editor tries to clarify some relevant conceptual ideas perhaps not familiar to solid-state-chemistry spectroscopists. It should be stressed that all these techniques are easily transferable to the inspection of other inorganic or organic compounds.

The exotic superconductors. Superconductivity is one of the most attractive properties of matter and occurs for several classes of materials. This macroscopic effect is consequential to pure microscopic quantum events taking place when the material is cooled below a critical temperature T_c . In the superconducting regime, the resistance drops to absolutely zero. Subsequently, there is no heat dissipation, and the material has the peculiarity, called the Meissner effect, to expel from its interior external magnetic fields. Superconducting materials may be classified as conventional and unconventional superconductors. Conventional materials are pure metals and alloys, and their physical properties are described by the Bardeen-Cooper-Schrieffer (BCS) theory. The temperature T_c at which they become superconducting does not exceed 23 K (Nb₃Ge), close to the theoretical limit. Unconventional (or exotic) superconductors go well beyond this frontier and do not enter the BCS frame. The BCS mechanism of superconductivity involves phonon-assisted pairing of the electrons responsible for the conducting properties. The electrons at the Fermi level condense as bosons (electron-pair quasi-particles) in the lowest energy state, obeying the Bose statistics. Consequently, the pairs are singlets with spin zero, and an energy gap 2Δ opens up at the Fermi level which is much smaller than the gaps of semi-conductors (a few meV). In ordinary BCS superconductors, the orbital part of the total pair wavefunction $\psi(\mathbf{r})$ (\mathbf{r} = space coordinate) is isotropic and has an s -symmetry. In some of the heavy fermion systems (CeCu₂Si₂, UPt₃, UBe₁₃, URu₂Si₂, UNi₂Al₃, UPd₂Al₃) which have strong localized or itinerant antiferromagnetic order, the wavefunction has d -state orbital angular momentum. In high T_c or organic superconductors, the wavefunction is not completely determined. Recent works show that in cuprate superconductors there could be d - or *extended-s-wave* ($s+id$) pairing, inferring that these materials are not conventional BCS superconductors. In the organic superconductors, the issue remains open. The electron pair wavefunction may be pictured by the macroscopic order parameter $\Delta(\mathbf{r})$ or the superconducting gap at the Fermi surface proportional to $\psi(\mathbf{r}) = \exp(i\mathbf{p}_s \cdot \mathbf{r}/\hbar)$, where \mathbf{p}_s is the momentum of a pair. For an s -state, the superconducting gap 2Δ should be isotropic in \mathbf{k} -space (reciprocal lattice), namely $\Delta(\mathbf{k}) = \Delta_0$. If the order parameter is d -type, the superconducting gap is anisotropic with nodes in the energy dispersion such as $\Delta(\mathbf{k}) = \Delta_0 \cos 2\varphi$, where $\varphi = \tan^{-1} k_y/k_x$.

Since 1980 a number of novel/unconventional superconductors have been discovered. The first important class is the organic superconductors pioneered by Jérôme (*1,2*). They are exemplified by the well-known TMTSF and BEDT-TTF radical cation salts: the Bechgaard quasi-1D salts like (TMTSF)₂PF₆ ($T_c = 0.9\text{K}$, 12 kbars), (TMTSF)₂ClO₄ ($T_c = 1.4\text{K}$), and the quasi-2D salts like $\beta_{\text{H}}(\alpha_{\text{t}})$ -(BEDT-TTF)₂I₃ ($T_c =$

8K), κ -(BEDT-TTF)₂Cu(NCS)₂ ($T_c = 10.4$ K), and κ -(BEDT-TTF)₂Cu[N(CN)₂]Cl ($T_c = 12.8$ K, see Ref.2 for examples of the crystal structures). Organic donors like TMTSF (tetramethyltetraselenafulvalene), BEDT-TTF (bis(ethylenedithio)tetrathiafulvalene = (C₅S₄H₄)₂) and derived molecules like BEDO-TTF, BEDT-TSeF, DMET, DMET-TSF yield numerous organic conductors owing to an almost limitless variety of anionic acceptors. These salts have stacking structures labeled α , β , τ , θ , κ , ϵ , ξ , η ... strongly affecting their conducting properties. A number of them are superconductors. Organic conductors constitute an attractive field in solid state physics and chemistry and are mostly explored, because they exhibit an extraordinary array of interrelated phenomena (charge and spin density waves, antiferromagnetism, superconductivity, quantized Hall effect, giant magnetoresistance). Their physical properties are remarkably stable with respect to physical aging and are not affected by oxygen and moisture. The second and perhaps most amenable and applicable materials are the copper oxides compounds or high temperature (high- T_c) cuprates discovered by *Bednorz, Müller, and Chu* (3,4) which have been extensively discussed in the media, because most of them superconduct well above the boiling temperature of liquid nitrogen. These include compounds like Tl₂Ba₂CuO_{6+ δ} ($T_c = 78$ K), YBa₂Cu₃O₇ ($T_c = 92$ K), Bi₂Sr₂CaCu₂O_{8+ δ} ($T_c = 85$ K), Bi₂Sr₂Ca₂Cu₃O₁₀ ($T_c = 110$ K), HgBa₂Ca₂Cu₃O_{8+ δ} ($T_c = 164$ K). When not sufficiently protected, these materials are, however, somewhat instable to aging, depletion of oxygen atoms and alteration of their structure by environmental conditions like moisture that may result in relatively short times in a loss of superconductivity. The third important novel materials are the alkali salts of the C₆₀ (fullerene) molecule. Examples are K₃C₆₀ ($T_c = 19.3$ K), Rb₃C₆₀ ($T_c=30.7$ K), and Cs₂RbC₆₀ ($T_c = 33$ K). The last discovered novel superconductors are the borocarbides like LuNi₂B₂C ($T_c = 16.6$ K) and their derivatives.

Examples of physics and chemistry of conventional superconductors should be the starting point of a volume aimed at spectroscopic features of exotic superconductors. Different physical properties of lamellar metallic dichalcogenides (like 2Ha- NbSe₂, $T_c = 7.2$ K; 2Ha-TaSe₂, $T_c = 0.15$ K; 1T-VSe₂) and A-15 phases (like Nb₃Sn, $T_c = 18.5$ K; V₃Ga, $T_c = 16$ K) are recalled in chapter 2 by *Molinié et al.* In fact it is compulsory to emphasize that these conventional superconductors were used recently to build new insertion forms leading to *new selenides* presenting *exotic superconductivity* or *ferromagnetism*. The new phases exemplified in chapter 2 are the superconductors SnNb₅Se₉ ($T_c = 17.5$ K), Sn(Ta,Nb)₅Se₉ ($T_c = 17.1$ K) and the ferromagnet GaV₃Se₉ ($T_{CURIE} = 25$ K) obtained respectively from the mixture of Nb₃Sn/NbSe₂, Nb₃Sn/TaSe₂, and V₃Ga/VSe₂. The unit cells of the novel phases are multiple of those of the pristine diselenides as shown by powder x-ray diffraction and x-ray Buerger precession. There is an important disorder along the c axis. This also confirms that the new phases are not simply intergrowth phases of the starting compounds. Raman spectroscopy and Mössbauer spectrometry strongly corroborate this fact. As illustrated in Figure 1, Raman spectra of the starting products (upper panel) do not show coincidences with those of the final products (lower panel). The Mössbauer studies of SnNb₅Se₉ ruled out the possibility of an insertion of tin atoms in 2Ha-NbSe₂, since two kinds of Sn-sites exist. The first one belongs to the Nb₃Sn-type site, the second one to that observed in the "misfit compounds". SnNb₅Se₉ exhibits a very specific superconductivity (an exotic one, because we are not able to define it) with a significant anisotropy of the critical field compared to that of NbSe₂. This constitutes a further proof that this phase is not an intergrowth phase, but is formed by dissolution of the A-15 phase in the diselenide. Depending on the physical properties of the pristine MSe₂ phases, superconductors (from NbSe₂ and TaSe₂), or a ferromagnet (from VSe₂) were synthesized.

High- T_c cuprates: structures, analysis, and electronic states. Optical spectroscopic studies of high- T_c materials demand preliminary chemical and physical characterizations of the samples concerning transport properties, crystal quality, stoichiometry, epitaxial film quality, film thickness, and elemental analysis in the bulk and at the surface. In this volume several powerful analytic techniques are thoroughly described: ion backscattering spectrometry (chapter 3: *Chu et al.*), Auger and x-ray photoelectron spectroscopy (PES) (chapter 4: *Perry*), x-ray diffraction and transport properties (chapter 5: *Browning et al.*).

The elucidation of the electronic structures in superconducting materials can be carried out using Auger and PES (chapter 4: *Perry*). Parent modern techniques like scanning Auger microprobe and PES implemented on synchrotron beam lines have already been applied to the study of these materials. The fact that oxidation states, electronic states and mixed metal species are easily studied with these techniques is extremely relevant to the determination of the structures and the bonding of these mixed-valence compounds. These spectroscopies are both useful for the study of the metallic (Cu $2p$, Pb $4f$, Ba $3d$, Cr $2p$), oxygen O $1s$, and other states in superconductors but may be employed also to look at heterogeneous surfaces at the micron scale. The synchrotron beam deliver an x-ray radiation brightness much higher than that of conventional x-ray generators and allows the detection of chemical species in low concentration. Due to the high-resolution attainable with the synchrotron it is possible to obtain very good images of the elements on a surface and then to investigate the chemical heterogeneity, an issue which is particularly important in the case of composite wire and tape processing. Chapter 4 is an interesting overview of what kind of informations can be gained by applying these techniques to the high-temperature superconductors $YBa_2Cu_3O_7$, $Bi_2Sr_2CaCu_2O_8$, $Pb_2Sr_2YCu_3O_8$, $Hg_{1-x}Cr_xSr_2CuO_{4+y}$, $La_{2-x}Ca_xCuO_4$, $Tl_2Ba_2CaCu_2O_8$ and should be extremely valuable for researchers and chemists not necessarily involved in the field of high- T_c superconductivity.

The problem of structural defects affecting superconductivity in high- T_c cuprates is particularly critical (see chapter 5 by *Browning et al.* and the following discussion). This issue is closely related to chapters 7-10 and 15 dealing with oxygen ordering in $YBa_2Cu_3O_7$. Hereby, investigations are carried out using magnetotransport and detailed x-ray structural studies. For the crystal structure of orthorhombic $YBa_2Cu_3O_{7-\delta}$, the reader may refer to Figure 15 in chapter 3 by *Chu et al.* which shows the notation of different atoms.

Dynamical spectra and interference effects. Several chapters are focused at the detailed description of micro-Raman spectra in high- T_c superconductors. The reader will feel that a lack of data exists for the organic superconductors which are not covered here except in chapter 14 by *Kamarchuk et al.* concerning the point contact spectroscopy technique. In this introductory chapter, the editor will try to fill this gap by giving some data taken from the recent literature. Overviews of the vibrational spectra of organic superconductors were published before (5).

The identification of atomic motions and phonons in high- T_c superconductors is meaningless if one relies only upon experimental spectra and comparison with similar perovskite compound spectra. Therefore, lattice dynamical calculations are of prime importance to unravel the assignment of vibrational bands and have been applied by researchers to develop coherent interpretations of the spectra. There are several shell-model methods to calculate in a general frame the whole spectrum of vibrational frequencies (phonons) in cuprate superconductors (chapter 6: *De Wette* and 6). In this case, application of lattice dynamics allows the determination of phonon specific heat and

resistivity. Of course, the calculation may be restricted to specific phonon dynamics and thus can be performed analytically (like the important apical oxygen mode at 500 cm^{-1} of $\text{YBa}_2\text{Cu}_3\text{O}_{7-\delta}$, see chapter 9 : *Rumyantsev and Yampolskii*).

The determination of the different phases and the elucidation of the reordering process of oxygen atoms in oxygen-deficient $\text{YBa}_2\text{Cu}_3\text{O}_{6+\delta}$ and overdoped $\text{YSr}_2\text{Cu}_3\text{O}_{7.7}$ compounds which are relevant to their conducting properties is detailed in chapter 7 by *Iliev*. After a presentation of the various phases encountered in the $\text{YBa}_2\text{Cu}_3\text{O}_{6+\delta}$ system due to variations of the oxygen sublattice in CuO chains, the author establishes that, at a microscopic level, tetragonal and orthorhombic microdomains can be found in these materials complementing x-ray diffraction studies of chapter 5.

The investigation of the intimate structure of one of these phases, $\text{YBa}_2\text{Cu}_3\text{O}_{6.5}$, the so-called orthorhombic-II, may be carried out using the Raman band of the O4 apical oxygen atom of the structure belonging to BaO planes (see chapter 8 by *Ivanov*). The ortho-II phase is characterized by alternating oxygen-full and oxygen-empty CuO chains in the reservoir layer of the superconductor. *Ivanov* develops an original model to evaluate the scattering efficiency of the apical oxygen vibrations from experimental data.

A complementary approach for the treatment of the oscillations of the apical O4 oxygen atom in $\text{YBa}_2\text{Cu}_3\text{O}_{7-\delta}$ is possible by deriving the solutions of the dynamical equations for the corresponding Raman- and infrared-active vibrations in perfect/defective crystals and thin films. The Raman scattering intensities are calculated (chapter 9: *Rumyantsev and Yampolskii*). The evaluation of light scattering in films with oxygen vacancies in the O4-Cu1-O4 bridge linking the conducting CuO_2 plane, the BaO plane (in which O4 sits), and the reservoir plane formed by CuO chains may be used to determine theoretically the O4 oxygen-vacancy concentration C^v which is relevant to superconducting properties.

Another probe of the oxygen sublattice in $\text{YBa}_2\text{Cu}_3\text{O}_{7-\delta}$ using emission Mössbauer spectroscopy is described by *Nath et al.* in chapter 10. $\text{Nd}_{2-x}\text{Ce}_x\text{CuO}_4$ ($T_{\text{cmax}} = 25\text{K}$), and $\text{HoNi}_2\text{B}_2\text{C}$ ($T_c = 8\text{K}$) are also investigated. The principle of this spectroscopy is based on the substitution of slight amounts of Cu by ^{57}Co which decays in ^{57}Fe isotope emitting γ -rays. In this chapter the authors use a different notation to label the oxygen atoms. Whilst the O(4) and O(5) atoms are in the basal plane containing the CuO chains, the O(1) atom is in fact the apical oxygen. The dynamics of the CuO chains in $\text{YBa}_2\text{Cu}_3\text{O}_{7-\delta}$ may be studied with this technique as well as spin clusters with magnetic order. Oscillations of the chain oxygen ions between two potential wells are evidenced.

In the case of composite materials of high- T_c superconductors ($(\text{Bi,Pb})\text{Sr}_2\text{Ca}_2\text{Cu}_3\text{O}_y$, $\text{TlBa}_2\text{Ca}_2\text{Cu}_3\text{O}_x$) and metals (Ag) used to fabricate wires or tapes for industrial purposes, there is a strong necessity to also employ Raman microspectroscopy. Indeed, during the fabrication of these devices, a number of impurity or parasitic phases which are not superconducting may form and dissipate. This technique can identify these phases, but it is also opportune in investigating their microscopic spatial distribution in the composite matrix, since it is possible to perform imaging Raman spectroscopy (chapter 11: *Maroni et al.*).

In the same spirit, infrared spectroscopy of hybrid materials formed by organic monolayers adsorbed on surfaces of $\text{YBa}_2\text{Cu}_3\text{O}_{7-\delta}$ smooth films (or ceramics) deposited on various substrates ends up being an efficient technique of control (chapter 12: *Ritchie et al.*). The monolayers are organic substances like $\text{CH}_3(\text{CH}_2)_{17}\text{SH}$, $\text{CH}_3(\text{CH}_2)_{17}\text{NH}_2$, $(\text{CH}_3(\text{CH}_2)_7)_2\text{NH}$. The roughness of $\text{YBa}_2\text{Cu}_3\text{O}_{7-\delta}$ surfaces is crucial to the monolayer ordering, and is characterized using atomic force microscopy and x-ray diffraction. The molecular orientation, the degree of crystallinity and the thermal stability of the organic monolayers are evaluated by the lineshapes and peak positions of the -CH, -CH₂ and -

CH₃ vibrations recorded in grazing incidence infrared Fourier-transform spectroscopy. This work is particularly important for possible applications of adsorbed monolayers on cuprates like corrosion protection, chemical sensing, and high density memory devices.

Some aspects of renormalization (or self-energy) effects in Raman spectra of exotic superconductors were reviewed (7). Since then there has been additional interesting data in the literature which are worth mentioning here. An important issue concerns the Fano interference effect which has been observed in the Raman spectra of high- T_c cuprates (8). In semiconducting phases like YBa₂Cu₃O₆ and PrBa₂Cu₃O₇, the lineshape of all the phonons is a well symmetric Lorentzian. In high- T_c phases, the lineshapes become extremely asymmetric at temperatures below T_c and can be reproduced in a first approximation by an asymmetric Lorentzian, the Fano function. On the one hand, the antisymmetric B_{1g} phonon at $\omega_a = 340 \text{ cm}^{-1}$, assigned to the vibrations of the CuO₂-plane O2 oxygen atom, is particularly representative of this effect. On cooling, this phonon broadens and shifts in frequency towards lower values ($\delta\omega_a/\omega_a = -2.3\%$) as shown in Figure 2. On the other hand, the CuO₂-plane-oxygen symmetric A_g phonon at $\omega_b = 450 \text{ cm}^{-1}$ hardens below T_c , i.e., its energy increases ($\delta\omega_b/\omega_b = +0.9\%$). Other examples of Fano shape are given by the Raman band at 162 cm^{-1} of the superconductor SnNb₅Se₉ (see Figure 1), or by that of V₃Ge ($T_c = 6.3\text{K}$) peaking around 280 cm^{-1} at 50K (9) when recorded below T_c . According to the pioneering works of Fano (10), Balkanski (11) and Cardona (12) these phenomena indicate that a coherent coupling between the vibrational states and a background spectrum of electronic excitations should occur which generates a renormalization of the phonon energies in the superconducting state (SC). Furthermore, they suggest that superconductivity is phonon-mediated as in classical superconductors.

Hadjiev *et al.* in chapter 13 are reviewing the basic theory of this interference effect and give the method used to evaluate the Raman intensities in the SC state and the electron-phonon coupling constant. They apply successfully this theory to the strongly renormalized phonons of the new compound (Cu,C)Ba₂Ca₃Cu₄O_x ($T_c = 117\text{K}$).

In YBa₂Cu₃O₇, the interference effect is particularly strong in the case of the Ba mode lying at 115 cm^{-1} and needs to be carefully examined in order to identify the intrinsic nature of this coupling. Indeed, a remarkable fact is that the Ba mode is strongly mixed with the Cu vibrations around 150 cm^{-1} as shown by the deep spectral valley occurring in between them (Figure 2). This low frequency spectrum, lying between $80\text{-}180 \text{ cm}^{-1}$, cannot be adequately reproduced using a simple combination of Fano and Lorentzian functions. A more elaborate calculation of the spectrum is necessary to address the issue of the strong lineshape variations observed at low temperatures. If one assumes that Ba and Cu modes interact coherently with a common continuum of electronic excitations, it is found that satisfactory fits of the experimental spectra are achieved (see Faulques and Ivanov, 13). The method used was to derive the spectral calculation in a nonanalytical way considering the Green's function of the two phonons in interaction with the continuum. By itself the Green's function method is well known of Raman spectroscopists and has been successfully applied to reproduce Raman spectra of various substances. The point was to choose a proper Hamiltonian describing the nonadiabatic interaction between the vibrational states and the electronic excitations. This has been done by Ivanov in his Ph.D. thesis (14).

This calculation has been the basis of a more proper identification of the electronic scattering continuum which seems to stem from low-energy electronic interband transitions. In considering the ΓXY section of the Fermi surface of YBa₂Cu₃O₇ in Figure 3, one sees that it consists of four sheets labeled S1, S2, S3, and S4 (15). S1 originates from electronic states of the electronic "reservoir" layer, i.e., the infinite CuO chains. S2 and S3 are the conducting bands of the two conducting CuO₂ planes of the structure.

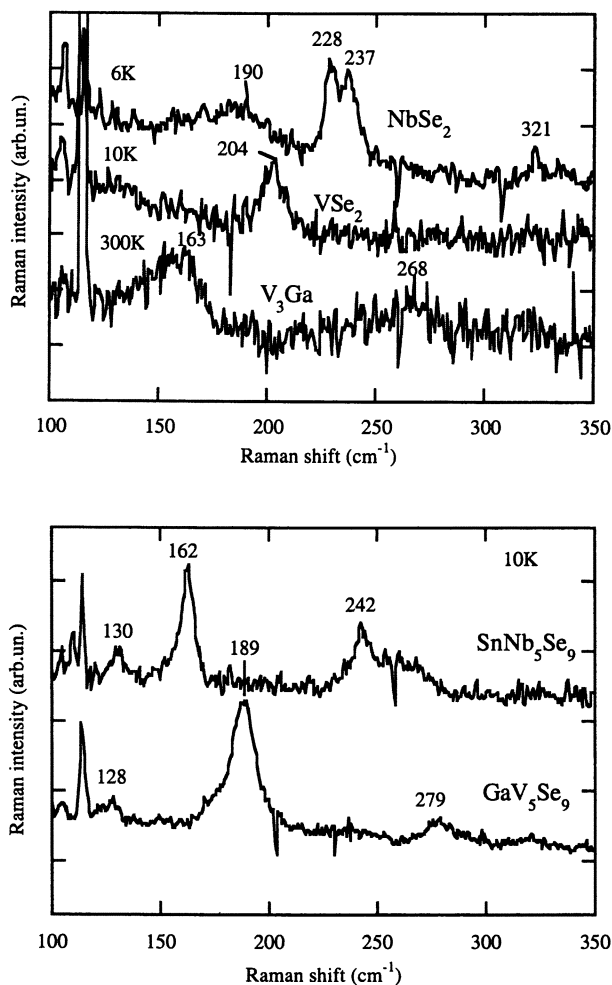


Figure 1. Top: Micro-Raman spectra of NbSe₂, VSe₂, V₃Ga, taken at 6K (below T_C), 10K and 300K respectively. Bottom: Micro-Raman spectra of the new selenides SnNb₅Se₉ and GaV₅Se₉ taken at 10K (below T_C and T_N). The 300K Raman spectrum of the superconductor Nb₃Sn not shown here exhibits two very weak bands peaking at 151 and 173 cm⁻¹. Excitation line 514.5 nm.

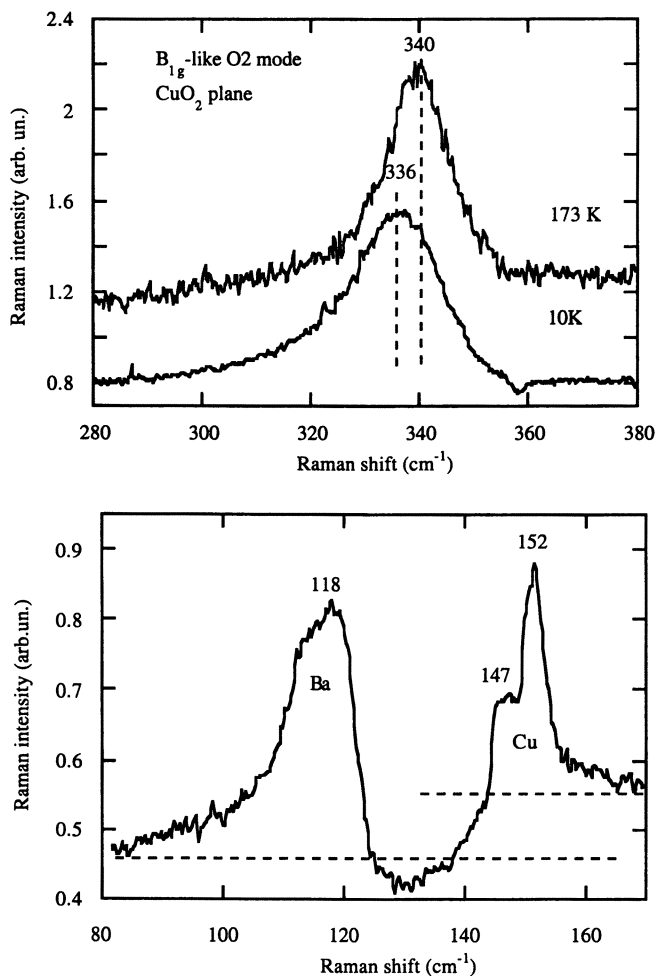


Figure 2. Raman spectra of a thin $\text{YBa}_2\text{Cu}_3\text{O}_7$ superconducting film. Top: Self-energy effects on the O2 phonon (CuO_2 plane). The phonon line at 10 K is strongly asymmetric (Fano-interference shape). The shift $\delta\omega$ in frequency is related to the real part of the self-energy, and the broadening to the imaginary part. Bottom: Low frequency spectrum and fine structure of the Ba and Cu2 modes (CuO_2 plane). Excitation line 676.4 nm. Adapted with permission from *Faulques and Ivanov*, Ref. (13).

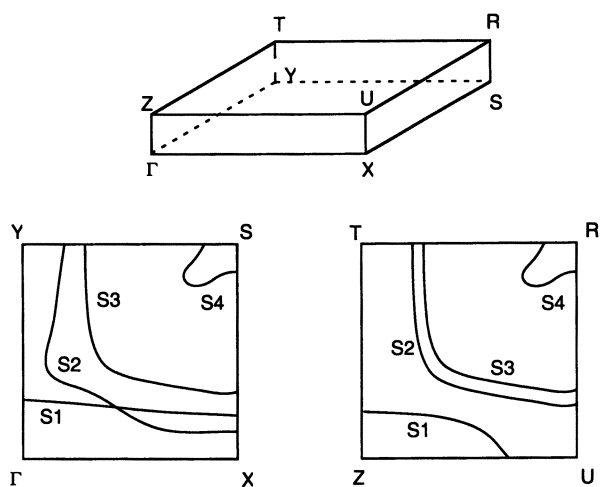


Figure 3. Brillouin zone of $\text{YBa}_2\text{Cu}_3\text{O}_7$, with high-symmetry points and sections of the Fermi surface. Origin of the bands: S1 CuO chain; S2 and S3 conducting CuO_2 planes, S4 BaO plane. (Modified and adapted from reference 15. Copyright 1992.)

Finally, S4 comes from the electronic states of the BaO plane. It is formed by mixing the Ba $p(x)$ and apical-oxygen O4 $p(y)$ orbitals. A similar band S4' should also exist but is shifted by about 320 cm^{-1} ($\approx 40\text{ meV}$) below the Fermi level and involves Ba $p(y)$ and O4 $p(x)$ mixed orbitals. Therefore, two pictures may be drawn for the origin of the interband transitions. The first one is, since the Ba mode at 115 cm^{-1} appears to interfere strongly with electronic excitations, these transitions may occur between S4 and S4'. The second one is that if the superconducting gap is anisotropic, as suggested by the experiments described in the next section, the low-energy electronic interband transitions may just be the transitions between the S1 and S2/S3 sheets of the Fermi surface, i.e. between the CuO chain band and one of the CuO₂ plane band. In summary, the data obtained by a number of groups concerning these self-energy effects in the phonon spectra of high- T_c superconductors substantiate relatively strong electron-phonon coupling in these materials.

Research in the field of vibrational spectroscopy of organic superconductors has been directed recently towards three areas. The first one is the clarification of the origin of the vibrations in these structures with the help of isotope markers. The second one focuses on the geometry and environment of the anionic species which remained not clearly established, for instance, the trihalide ions in (BEDT-TTF)₂X where X=I₃, I₂Br, IBr₂. The third direction seeks clues for behaviors similar to those found in high- T_c cuprates when the sample is cooled below T_c : phonons shifts, and electron-phonon interactions, i.e., in other words self-energy effects. In the latter case, data at hand will be presented in the forthcoming paragraphs.

In organic superconductors, β and κ -phases have a quasi-two-dimensional electronic character as in layered high- T_c cuprates and, therefore, comparisons between these two kinds of materials may be drawn. It is noteworthy that the vibrational spectrum of the anionic and BEDT-TTF molecular sublattices in organic superconductors is particularly sensitive to the stacking, the immediate surroundings, and the conformation of-CH₂ groups in BEDT-TTF. Thus, discrimination of these structures is possible. As a typical case, Raman spectra of normal and inter-ring-¹³C-labeled β -(BEDT-TTF)₂I₃ ($T_c = 1.5\text{ K}$) single crystals prepared by the group of *Batail* (16) have been studied at low temperature (17). Spectra of the triiodide region taken at 8 K revealed the appearance of a line at 108 cm^{-1} characterizing a phase transition of the anionic sublattice in which, in agreement with x-ray data, I₃⁻ anions adopt an asymmetric geometry. The strong degree of mixing of the C=C ring and C=C central bond vibrations (respectively at 1493 and 1467 cm^{-1}) was also evaluated using the frequencies of the isotopic compound (respectively at 1488 and 1420 cm^{-1}). In related studies, *Wojciechowski et al.* (18) have recently looked at the low-temperature Raman spectra (20 K) of the isostructural organic superconductors β -(BEDT-TTF)₂X (X = I₃, (I₃)_{0.85}(I₂Br)_{0.15}, IBr₂, (I₃)_{0.3}(IBr₂)_{0.7}) grown by chemical oxidation. From these data a preliminary assignment has been made. The band at 120 cm^{-1} stems from I₃⁻ anions, and the one at 139 cm^{-1} in the X=(I₃)_{0.85}(I₂Br)_{0.15} crystal from I₂Br⁻ anions, whereas the Raman spectrum of the mixed X=(I₃)_{0.3}(IBr₂)_{0.7} crystal proves that IBr₂⁻ and I₂Br⁻ anions dominate in the structure. In the X=IBr₂ crystal small amounts of I₃⁻ and I₂Br⁻ are also present. In this study, Raman spectroscopy comes out to be a more sensitive tool than x-ray diffraction. The same authors also investigated phase transitions in the 80 K Raman spectra of reticulate doped polymer composites of (BEDT-TTF)₂I₃ embedded in polycarbonate films. Results showed that in non-annealed composites the organic conductor was α -(BEDT-TTF)₂I₃ whereas in 150°C -annealed composites β - (BEDT-TTF)₂I₃ moieties were found (19).

The keen efforts made in the comprehension of self-energy effects in cuprates has boosted the research for similar phenomena in organic superconductors to unveil the mechanisms of superconductivity (20). As an illustration, *Pedron et al.* have reported

recently careful Raman measurements in κ -(BEDT-TTF)₂Cu(NCS)₂ and κ -(BEDT-TTF)₂Cu[N(CN)₂]Br ($T_c = 11.6$ K) pristine systems and substituted with ¹⁴C, ³⁸S and ²H isotopes (21,22) in the temperature range 1.5 K-100 K. These works are exemplary due to the extreme difficulty to measure precisely phonon shifts on low frequency bands in these compounds. Stray light and Rayleigh light are also difficult to eliminate. For both materials, they found a hardening (increase in frequency) below T_c of all the low-energy phonons lying above the BCS gap. The average relative frequency shift $\delta\omega/\omega$ is about +1% for κ -(BEDT-TTF)₂Cu[N(CN)₂]Br (+3% for the 27.4 cm⁻¹ phonon) and +3% for κ -(BEDT-TTF)₂Cu(NCS)₂. For the above mentioned reasons, the authors could not look for changes of the phonons below 25 cm⁻¹ which are expected to be closer in energy to the superconducting gap. Thus, the upper limit on the BCS energy gap would be about 25-28 cm⁻¹. From these data, *Pedron et al.* claimed that the gap is rather *s*-wave than *d*-wave. One must, however, keep in mind that anharmonic effects and phase transitions at very low-temperature may contribute to the hardening of the phonons. This has been exemplified in the work of *Eldridge et al.* (23) concerning the 892 cm⁻¹ B_{3g} mode of κ -(BEDT-TTF)₂Cu[N(CN)₂]Br which exhibits an increase below T_c of +2.2 cm⁻¹. The superconducting transition was supposed to involve a change of the geometry or the arrangement of BEDT-TTF molecules. The electron-phonon interaction could not be accounted for satisfactorily for this hardening. Moreover, in studying gap anisotropy, electronic and phononic Raman scattering cannot be placed on an equal footing as sketched in the following section. The symmetry of the order parameter has to be determined from polarized electronic Raman spectra rather than from phonon change measurements. Figure 4 is an example of low temperature spectra (5.5 K) of κ -(BEDT-TTF)₂Cu[N(CN)₂]Br and κ -(BEDT-TTF)₂Cu(NCS)₂ single crystals recorded in Nantes. The crystals were synthesized by *Plouvier-Meziere* and *Batail*. Low and high frequency spectra characterize the vibrations of the acceptor anion and those of C=C bonds in the BEDT-TTF radical cation donor, respectively. The relatively satisfactory fits of the spectra with a many-phonon model adapted from Ref. (13) show that substantial electron-phonon coupling may occur with low-energy excitations. A slight hardening (+2.5 cm⁻¹) of the low-frequency bands was observed on cooling below T_c , possibly indicating a correlation between low-energy phonons and the superconducting mechanism. For β -(BEDT-TTF)₂I₃ attempts were made to find self-energy effects using Fano lineshapes for the Raman band at 1420 cm⁻¹ in a ¹³C-partially -substituted crystal (inter-ring C=C vibration). The half-width-at-half-maximum of the band was found to decrease on lowering the temperature, but no significant variation of the frequency could be established (17).

Perhaps the most convincing data evidencing self-energy effects in organic superconductors are in the work of *Pintschovius et al.* (24) reporting inelastic neutron scattering experiments in κ -(BEDT-TTF)₂Cu(NCS)₂. The energy of the transverse acoustic phonons was ascertained to increase dramatically just below T_c and was especially well revealed in the case of the phonon with wave vector $q = (-0.225, 0, 0.45)$ at 2.4 meV (19 cm⁻¹, $\delta\omega/\omega = +7.4\%$). This hardening is possibly connected with the opening of a superconducting gap 2Δ at 2.4 meV corresponding to $2\Delta/k_B T_c \approx 3.1$, close to the BCS parameter 3.52 predicted for conventional superconductivity. These experiments would be in favor of a BCS phonon-mediated interaction.

Nature of the pairing interaction. Electronic Raman spectra may be used to assess the intrinsic nature of the pairing mechanism of the Cooper pairs in high- T_c superconductors. The nature of the electron pair wavefunction is one of the most debated issues concerning the superconducting mechanism of novel superconductors. Indeed, within the great body of experience, there has emerged surprisingly few techniques

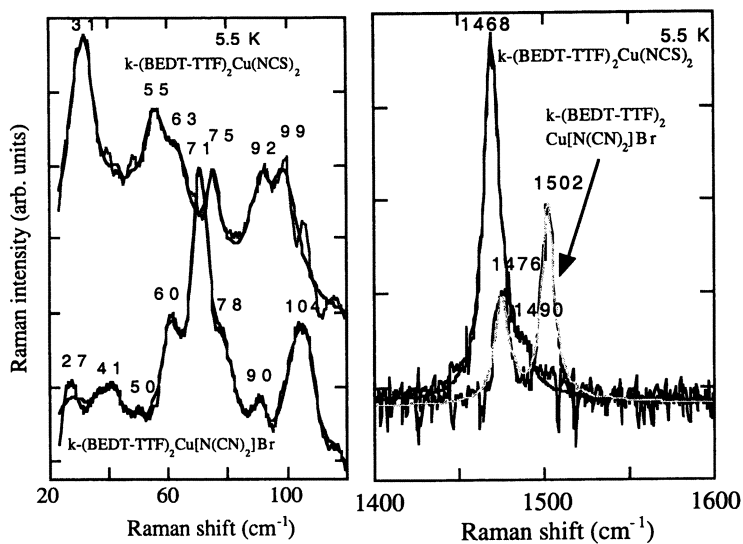


Figure 4. Micro-Raman spectra of κ -(ET) $_2$ Cu(NCS) $_2$ and κ -(ET) $_2$ Cu[N(CN) $_2$]Br single crystals in the superconducting state (ET = BEDT-TTF) using a X 50 objective. The incident and scattered electric fields are parallel to the most developed facet of the crystals. Solid lines are spectral fits obtained using a many-phonon model adapted from Ref. (13). Excitation line 514.5 nm. Crystals provided by *Plouvier-Meziere* and *Batail*, Nantes.

capable of exploring the true nature of the superconducting gap. Among them are ARPES, tunneling, and electronic Raman spectroscopy.

We will not develop here the rudiments of the electronic Raman scattering theory for exotic superconductors which proves to be an efficient, direct and simple tool for studying gaps and pseudo-gaps in these materials, since this may be found in chapter 13: *Hadjiev et al.* We just pay attention to the point that electronic Raman scattering in superconductors is dominated by two terms: γ_k and λ (Eqs.[4], [7] and [8] of chapter 13). The first term γ_k is the Raman vertex, which is dependent of the curvature of the energy dispersion $\varepsilon(\mathbf{k})$. In the simplest model, $\varepsilon(\mathbf{k}) = \hbar^2 \mathbf{k}^2 / 2m^*$ is a parabolic band, with m^* being the effective electron mass; different expressions for $\varepsilon(\mathbf{k})$ have to be derived from the superconductor symmetry. The second term is the imaginary part λ of the complex Tsuneto function in the superconducting state (25) which depends on the superconducting gap $\Delta(\mathbf{k})$:

$$\lambda = 4|\Delta(\mathbf{k})|^2 \left(\omega^2 - 4|\Delta(\mathbf{k})|^2 \right)^{-1/2} \quad [1.1]$$

Thus, it can be seen that electronic Raman scattering (ERS) probes different parts of the Fermi surface and then yields informations about the gap anisotropy and the symmetry of the order parameter Δ . Most of the cuprates have D_{2h} (or D_{4h}) point groups. The *gerade* irreducible representations are A_g (A_{1g}), B_{1g} (B_{2g}), B_{2g} . The symmetry dependence of ERS spectra over different symmetry channels follows the symmetry of the hybridized orbitals involved in the scattering process: x^2, y^2, z^2 for A_g ; $x^2 + y^2, z^2$ for A_{1g} ; xy or $x^2 - y^2$ for B_{1g} and B_{2g} . In ERS, the scattering in the superconducting state should therefore be dependent on the pairing symmetry. For instance, $\gamma_k = \cos k_x + \cos k_y, \cos k_x - \cos k_y$, and $\sin k_x \sin k_y$ for channels A_{1g}, B_{1g} , and B_{2g} , respectively. In recording ERS spectra for different polarization geometries allowing these symmetries, one may determine if the gap is anisotropic or not looking at the position and lineshape of the broad scattering continuum peak characteristic of the electronic scattering. The gap may be isotropic when the ERS maximum does not vary in the different polarizations. When the spectral shape of this continuum shows substantial variation over different symmetry channels, one can conclude that the gap is likely of anisotropic nature. For example, in nominally pure crystals of $\text{Bi}_2\text{Sr}_2\text{CaCu}_2\text{O}_{8+\delta}$ ($T_c = 90\text{K}$), the A_{1g} ($x^2 + y^2$) ERS spectrum is obtained for the XX polarization in which the electric fields are parallel to one of the Cu-O bonds of the CuO_2 plane. The ERS is peaking at about $2\Delta/k_B T_c = 6$ (375 cm^{-1}). For the XY polarization in which incident and scattered electric fields are crossed, the ERS is B_{1g} (xy or $x^2 - y^2$) and is peaking at $2\Delta/k_B T_c = 8.6$ (538 cm^{-1}). That being so, one may infer the gap of this system is d -wave (25), since calculations well reproduce the spectral shape for both polarizations.

Theoreticians have predicted that for a d -wave pairing, the low frequency part of the electronic Raman spectrum in D_{4h} superconductors obeys an ω^3 dependency for the B_{1g} channel ($x^2 - y^2$) and varies linearly in ω for other symmetries (26). Further experimental work confirmed that such a behavior could be extracted from the spectra of pure high- T_c superconductor like $\text{Ti}_2\text{Ba}_2\text{CuO}_{6+\delta}$, $\text{Bi}_2\text{Sr}_2\text{CaCu}_2\text{O}_{8+\delta}$. A way to check the theory is the study of overdoped or underdoped superconducting systems with a range of definite impurity concentrations in which metallic atoms are partially replaced. Precisely, theory predicted that impurity scattering should give clues to distinguish anisotropic s and d -wave gaps. These systems have a lower T_c than corresponding nominally doped materials due to i) the introduction of impurities, ii) and the removal or addition of oxygen atoms in their structure. Accordingly, researchers have studied systems like overdoped $\text{Bi}_2\text{Sr}_2\text{CaCu}_2\text{O}_8$

($T_c = 55\text{K}$), $\text{YBa}_2\text{Cu}_3\text{O}_{6.5}$ ($T_c = 60\text{K}$), $\text{Bi}_2\text{Sr}_2\text{Ca}_{0.62}\text{Y}_{0.38}\text{Cu}_2\text{O}_{8+\delta}$ ($T_c = 57\text{K}$) (27). The B_{2g} ERS spectra of these compounds below T_c are consistent with the opening of a superconducting d -wave gap $2\Delta_0 \approx 8k_B T_c = 320\text{ cm}^{-1}$. Moreover, for $T^* \leq 200\text{ K}$ a pseudo-gap opens up at $15k_B T_c \approx 700\text{ cm}^{-1}$, an energy close to that of the antiferromagnetic exchange J which would be in accord with a magnetic mechanism.

Hadjiev et al. in chapter 13 give additional data for these experiments by studying the ERS response of $(\text{Cu,C})\text{Ba}_2\text{Ca}_3\text{Cu}_4\text{O}_x$ ($T_c = 117\text{K}$). They set forth that a strong anisotropy occurs between different polarization conditions with broad ERS peaking at 650 cm^{-1} and 490 cm^{-1} in the B_{1g} and $A_{1g} + B_{2g}$ channels, respectively. This system follows the ω -linear behavior in the A_{1g} channel.

The nature of the pairing is of course not limited to the study of Raman spectra and may be explored with other techniques like tunneling and quantum flux measurements (28). Chapter 14 is an abridgment of the point-contact spectroscopy (PCS) technique invented by Yanson in 1974 and applied to normal metals and superconductors. This technique has similarities with tunneling spectroscopy but is much easier to carry out since no stringent constraints are necessary for the measurements. Indeed, tunneling measurements of dI/dV (I : current, V : voltage) are made using either normal-insulator-superconductor or superconductor-insulator-superconductor junctions and thus necessitate a thin insulating oxide layer. In PCS one needs only normal-superconductor or superconductor-superconductor structures. Thin films and crystals can easily be measured. A point contact spectrum is the low-temperature voltage dependence $S(V)$ of the second derivative of point-contact current-voltage characteristics $d^2V/dI^2(V)$. Point contacts can be made with displacement technique, needle-anvil contacts, or break junctions. Surfaces of samples have to be chemically or electrochemically cleaned before the operation. *Kamarchuk et al.* demonstrate that this technique goes along with the determination of very important parameters in metals and superconductors like the electron-phonon interaction, the Josephson critical current and the energy gap of superconductors. Examples of point-contact spectra taken at low temperature on β -(BEDT-TTF) $_2\text{I}_3$ and $[(\text{C}_2\text{H}_5)_4\text{N}]_{0.5}[\text{Ni}(\text{dmit})_2]$ ($\text{Ni}(\text{dmit})_2 = \text{Ni}(\text{C}_3\text{S}_5)_2$) are given. The reader may be surprised that the peaks of the spectra are given in meV units, whereas the spectra are plotted against mV units. In fact these two units are equivalent and therefore point-contact spectra are just energy spectra as in absorption or Raman spectroscopy. For β -(BEDT-TTF) $_2\text{I}_3$, two types of point contact spectra come forth using two different contact technique orientations. The first type spectra show features of the intramolecular vibrational spectrum of the organic metal at 55, 103, 134 and 145 meV (443, 830, 1080, 1170 cm^{-1}). The second type spectra have maxima at 4 and 15 meV, well correlated with the Raman-active vibrations of the I_3^- anions at 30 and 120 cm^{-1} . Among other important experimental results, the authors proposed that the energy gap 2Δ of β -H-(BEDT-TTF) $_2\text{I}_3$ would be near 3 meV (24 cm^{-1}) with $2\Delta/k_B T_c = 4.1$, a value close to that predicted by the BCS theory for an electron-phonon mediated interaction ($2\Delta = 2.43\text{ meV} = 19.6\text{ cm}^{-1}$, $2\Delta/k_B T_c = 3.52$). *Ernst et al.* (29) found previously a $\delta^{(1)}$ structure at 5 meV ($T = 1.6\text{ K}$), i.e., twice the energy of the 2Δ BCS gap, decreasing strongly with applied magnetic fields of 1-2 T.

An already confused situation still remains in the nature of the pairing interaction in organic superconductors that is still debated and not yet ascertained. Since these materials have a strong structural anisotropy, it is possible that they have also an anisotropic superconducting gap and that the pairing would be d -wave. Moreover, as pointed out recently by *Friedel* (30), it appears that both cuprates and organic superconductors exhibit antiferromagnetic phases and van Hove anomalies (VHA) near the Fermi level. VHA can

explain low T_c values in organic superconductors and high T_c in cuprates, although they are insensitive to the nature of the pairing interaction.

Photoexcited carriers and relaxation dynamics. Evolution and relaxation of photogenerated charge carriers in solids presenting an electronic gap, and therefore in cuprates, may be investigated with photoconductivity. Quite generally the sample is illuminated with white or monochromatic light and the evolution of the photocurrent before and after illumination cut-off is studied vs. the temperature T , the time t , and the wavelength λ . In the latter case, excitation spectra may follow the general shape of the optical absorption. An interesting property common to several semi-conductors like GaAs or hydrogenated amorphous silicon is persistent photoconductivity (PPC, 31,32). Let us first introduce shortly studies in compounds like the layered perovskite $\text{Nd}_2\text{Ti}_3\text{O}_9$ and the conducting polymer polyparaphenylenevinylene (PPV) carried out under air traces and revealing PPC extending over long times after illumination cutoff (33,34). PPC is driven by the instantaneous lifetime $\tau_{\text{inst}}(t)$ of the photocarriers after illumination cut-off defined as

$$\tau_{\text{inst}}(t) = i_p(t) \times \left| \frac{di_p(t)}{dt} \right|^{-1} \quad [1.2]$$

In both $\text{Nd}_2\text{Ti}_3\text{O}_9$ and PPV one can show that $\tau_{\text{inst}}(t) \propto t^\alpha$. Therefore, the variation of photoconductivity vs. time is given by the stretched-exponential Kohlrausch's law

$$i_p(t) = i_p(0) \exp(-t/\tau)^\beta \text{ with } \beta = 1 - \alpha. \quad [1.3]$$

This law is the signature of dispersive scattering of the charge carriers. In PPV, the long-lived contribution is extrinsic and due to dissociation of polaron pairs assisted by electronegative defects. Oxygen vacancies and adsorption of oxygen atoms at the surface are found to play a crucial role in $\text{Nd}_2\text{Ti}_3\text{O}_9$ and to act on the thermal activation of $\tau_{\text{inst}} = \tau_0 \exp(E^*/kT)$. Additionally, $\tau_{\text{inst}}(t)$ in $\text{Nd}_2\text{Ti}_3\text{O}_9$ is proportional to the density of chemisorbed oxygen atoms moving into vacancies, and $\beta(T)$ is characteristic of localized states below the conduction band edge.

It is well-known that the semi-conducting state of the $\text{YBa}_2\text{Cu}_3\text{O}_{6+x}$ system ($x \approx 0.4$) may be converted to a metallic state with superconducting properties when the sample is exposed to cumulative photon doses Q (photodoping). For a thin film sample illuminated at $T = 100$ K, the transition begins at $Q = 3.6 \times 10^{22}$ photons/cm² and is completed for $Q = 5 \times 10^{23}$ photons/cm². Photodoping is explained by photogeneration of electron-hole pairs. Photoexcited holes increase the total concentration of free holes in the conducting CuO_2 planes, while photoexcited electrons may get trapped at unoccupied $O^- p$ levels of the CuO -reservoir chains. Moreover, PPC is observed at low temperatures in this system (for $0.15 < x < 0.4$). Relaxation of PPC occurs at room temperature and can be described with Kohlrausch's laws (Kudinov *et al.*, 35,36). PPC relaxation is possible since thermal activation releases trapped electrons which recombine with holes. PPC under white light illumination on partially oxygen depleted $\text{YBa}_2\text{Cu}_3\text{O}_{6.5}$ thin films ($T_c = 52$ K) was also reported by Stockinger *et al.* (37). Time-dependence of the resistivity and Hall resistivity/mobility were well described by Kohlrausch's laws with time constants τ following the anticipated exponential thermal activation. The main conclusion was that photoassisted oxygen-ordering and charge transfer from CuO_2 planes to CuO chains contribute to PPC. Oxygen ordering changes the carrier mobility while charge transfer modifies the photogenerated carrier concentration. An alternative model is the electron

trapping at oxygen vacancies in the CuO chains inducing a local distortion that acts like a barrier hampering recombination with holes. Very similar effects in the optical response of various cuprate thin films grown by magnetron sputtering on MgO and SrTiO₃ substrates are discussed in chapter 15 by *Hoffmann et al.* Three types of cuprates are investigated: RBa₂Cu₃O_{6+δ} (I) (R = Gd, Y) which have CuO chains in the structure, TlBa₂CuO_{6+δ} (II), and Bi₂Sr₂Ca_{1-x}Y_xCu₂O_{8+δ} (III) without CuO chains. This is a study of electron-hole pairs dissociation under white and monochromatic light illumination. The common physical property for all these compounds is PPC which is therefore *not limited to cuprates with CuO chains*. After white light illumination at 95 K for 8 hours, (I) exhibits a decrease in resistance and an increase of T_c by about 10 K due to a carrier density increase. The photoinduced change persists with long lifetime and relaxes thermally at high temperature. Doping and spectral dependence studies in (I) and (II) show that PPC is not due to assisted oxygen ordering but rather due to an electron trapping mechanism. The electrons from the photogenerated pairs get trapped at a localized state, while the holes are transferred to the conduction CuO₂ layer. Hence, it would be interesting to study in the future the time dependence of the photocurrent decay in other cuprates than YBa₂Cu₃O_{6+x} in order to see if it follows Kohlrausch's laws. Evolution of β(T), τ(T) and τ(t) in cuprates, which are structurally related to perovskites, could be of major interest. Photoinduced oxygen reordering in cuprates has also been recently probed with Raman spectroscopy by *Fainstein et al* (38) and *Panfilov et al.* (39). These papers consider in detail the behavior of the so-called Raman forbidden lines occurring at 230/248 and 596 cm⁻¹ in YBa₂Cu₃O_{6+x} and GdBa₂Cu₃O_{6+x} under laser light illumination (see also 13 for a very detailed description of these Raman modes in various oxygen-depleted and optimally doped thin films). These modes are Raman-forbidden for infinite CuO_x chains but become active for short chain fragments (in a parallel theme a theoretical treatment of the apical oxygen vacancy modes is also given in chapter 9: *Rumyantsev and Yampolskii*). The study of their intensity (or relative intensity) vs. time, temperature, excitation energy and oxygen content shows a reordering or a redistribution of the oxygen sublattice due to photoinduced hopping of oxygen atoms. Consequently, the dynamical changes in the CuO_x chains explain definitely PPC and photoinduced superconductivity in these cuprates.

It is then obvious that more information on the dynamics of charge carriers in these materials is of the utmost importance. The advent of ultrashort laser pulses and the availability of reliable femtosecond laser equipment in the market have given researchers the possibility to explore the fascinating area of temporal physics and to seek for non-equilibrium phenomena not visible with other optical spectroscopy tools. The general principles and spectroscopic applications of femtosecond laser pulses have been summarized in a recent textbook (40). It was therefore requisite to include in this book a contribution to this field depicting time-resolved photoinduced absorption spectroscopy in high-T_c superconductors (chapter 16: *Mihailovic and Demsar*). This technique probes in real times the recombination dynamics of quasiparticles and completes steady-state measurements of photocarrier generation. Let us remember that from the classical time-frequency Fourier analysis, one can derive a general inequality linking the spectral width Δν and the duration Δt of a pulse: ΔνΔt ≥ K, where K is a constant depending on the shape of the pulse (K = 0.441 for a Gaussian function). Therefore, the shorter the pulse, the broader its spectral bandwidth. For a Ti³⁺:Sapphire laser generating 100 femtosecond pulses at the wavelength λ₀ = 800 nm (i.e. ν₀ = 12500 cm⁻¹ = 375 THz), the spectral bandwidth of the pulses is 4.41 THz (in spectroscopist units Δν = 147 cm⁻¹). Therefore Δλ/λ₀ = Δν/ν₀ = 0.012 and Δλ = 0.012 × 800 = 9.6 nm. This means that the pulses cover about 3% of the visible spectrum. In particular, this can affect spectral resolution of time-resolved Raman spectra.

Transient absorption (or transmission) measurements are performed with the pump-probe method. As illustrated in Figure 1 of chapter 16, the ultrashort beam is separated into two components: the pump pulse which perturbs the sample at time $t_0=0$, and the optical-delayed probe beam analyzing the sample response at time $t_0+\Delta t$. The detected intensity of the probe beam is $I(\nu_0)$ before perturbation and $I(\nu,\Delta t)$ after excitation. Application of the Beer-Lambert law yields the optical density D (spectral analysis) and the population dynamics of the excited states (temporal analysis):

$$D(\nu,\Delta t)=\alpha_\nu N_e(\Delta t)\ell \quad [1.4]$$

$$\ln D(\Delta t) = \ln N_e(0)\alpha_\nu - \Delta t/\tau, \quad [1.5]$$

where α_ν is the absorption coefficient at frequency ν , ℓ is the sample thickness, τ is the time of decay, $N_e(\Delta t)$ is the population of excited states at time Δt and absorbing at frequency ν .

It follows that when a sample is excited with a pulse the population decay of the excited states must satisfy the rate equation

$$\partial N_e/\partial t = -N_e/\tau \quad [1.6]$$

where τ is the relaxation time of non radiative and radiative decays. As soon as bimolecular exciton annihilation processes take place, a second term $-\gamma N_e^2$ should enter on the right hand side of Eq. [1.6].

Several issues are addressed in chapter 16. The experimental constraints of pump-probe experiments are summarized. The photogeneration of carriers under ultrashort pulses and their relaxation in superconductors are thoroughly explained as well as a model for evaluating the heating effects in the samples. The authors stress that carrier relaxation in superconductors occurs at much longer times τ_R than in normal metals (about 10 fs-100 fs) due to the presence of the superconducting gap. Fast (0.5 ps) and slow decays (extending to more than 13 ns) in the photoinduced absorption measurements are observed. One has typically $\tau_R = 0.5$ -3 ps in optimally doped $\text{YBa}_2\text{Cu}_3\text{O}_{7-\delta}$. The photoinduced transmission amplitude $-|\Delta T/T|$ is basically a function of the superconducting gap which depends on the temperature according to Eqs. [4,5]. $-|\Delta T/T|(T)$ is also strongly dependent on the gap anisotropy as shown in Fig. 7.

Microwave resonance spectra. The chemist reader will find in chapter 17, *Kadowaki et al.*, useful relationships concerning the basic physics of superconductors. The paper is intended to provide an overview of the application of microwave techniques to the determination of important physical parameters of superconductors. For this purpose the authors recall the classical Maxwell theory applied to transverse and longitudinal electromagnetic waves (EMW). The equations of the Josephson effect are also recalled. In the microwave range (typically 1-96 GHz), EMW penetrating in a superconductor induce collective superconducting electron excitations known as Josephson plasma excitations. EMW can be either transversal or longitudinal, and therefore will generate transverse or longitudinal plasma waves in the material. The plasma frequencies ω_p for these oscillations are rather low, since they amount to about 100 GHz, and their energy lies below the superconducting gap (70 meV). The authors describe the model used to calculate the plasma resonance absorption lines vs. the applied magnetic field H . The experimental set-up which is very similar to the electron spin resonance apparatus based on the "magic tee" and the resonator cavity are sketched. They

insist on the fact that the size L of the sample is critical for the detection of the transverse plasma resonances. Examples of longitudinal and transverse plasma oscillations in the compound $\text{Bi}_2\text{Sr}_2\text{CaCu}_2\text{O}_8$ are finally reviewed with their dependence vs. L , the field H , and the temperature T . Softening of the plasma frequency near the transition temperature T_c is found. These observations lead the authors to propose that the longitudinal plasma mode is the Nambu-Goldstone mode in the superconducting state which consequently arises from spontaneously broken gauge symmetry in close analogy to the Weinberg-Salam theory.

Optical devices. Chapter 18 by *Eames et al.* is an application of dye/superconductor assemblies to the selective detection of different wavelengths of visible light. This contribution prepared by the *McDevitt's* group is one of the best examples combining synthesis, chemistry, and spectroscopy to achieve a finalized optical sensor. The design of the device is based on the antenna effect provided by molecular substances, in this case dyes which can be rhodamine 6G, oxazine 1 perchlorate, or a squarylium-pyrylium dye. Antenna effects are observed, for instance, in compounds where rare earths on oxide surfaces are complexed by organic molecules. If suitable ligands are used for complexation there is an increase of the energy transfer from the ligand to the metal resulting in high luminescence efficiency of the rare earth. Examples are Eu^{3+} supported on silica gels functionalized with imidazole, acetylacetone, or benzoyltrifluoroacetone (41). In chapter 18, dyes are deposited onto a $\text{YBa}_2\text{Cu}_3\text{O}_7$ superconductor bridge to make an assembly. The superconducting microbridge acts as a transducer, i.e., the optical signal is converted into variable electrical signals which are a function of the input. In this case the resistivity response is enhanced at the maximum absorption energies of the dye. The superconductor acts also as a bolometer, since its electrical resistance varies upon the temperature change caused by the absorption process. Therefore, a proper choice of dyes absorbing selectively at desired visible wavelengths is crucial. A polymer matrix is used in which the dyes are incorporated in order to narrow the optical absorption bands and to ameliorate the selectivity. The optical characterization of the assemblies is carried out using techniques such as optical absorption, steady-state and transient photoconductivity, in function of temperature and layer thickness. The resulting devices are optical sensors responding at wavelengths 450, 535, 750 nm (three-color sensor) and wavelengths 501, 535, 655, 715 nm (four-color sensor).

Conclusions. The contributions to this volume exemplify the quest for theories and physical characterization techniques of spectroscopy that adequately forecast and shed light on phenomena responsible for electron-phonon interactions, pairing, dynamical rearrangement processes, quasi-particle excitations, and magnetism in unconventional superconductors. The general pattern of these processes is inherent to atomic, electronic, spin, and excitonic dynamics. On the one hand, it is clear that the oxygen-sublattice ordering and the carrier dynamics in cuprates govern the interplay between conducting phenomena and structures. Vibrational Raman spectra, photoconductivity measurements and time-resolved spectroscopy have yielded so far essential data to elucidate these questions. Oxygen defects and vacancies in the structure are now better understood with vibrational spectra. On the other hand, the fundamental point in question is the true nature of the superconducting mechanism. For high- T_c and organic superconductors, fermiology is the backbone of this quest. The experimental investigations of the Fermi surfaces, photocarrier generation, and electronic states, probed with modern spectroscopies like electronic Raman scattering, tunneling or photoelectron spectroscopy, have given by this time a great body of evidence toward d -wave or *extended* s -wave pairing in cuprates.

They should convey in the near future more information for a coherent description of the inner mechanisms of superconductivity. The following chapters in this book express the views of the authors in this maturing field and help to clear up the matter. Beside the fundamental studies, engineers and researchers in applied physics and chemistry have already endeavored to develop promising applications of these materials in which optical/chemical sensors and electric/electronic devices may play a great role.

Acknowledgements

The editor would like to thank Dr. Batail and Dr. Plouvier-Meziere for providing large single crystals used in this introduction to exemplify Raman spectroscopy on organic superconductors.

Literature cited

*Unité Mixte de Recherche n° 6502 - Centre National de la Recherche Scientifique / Université de Nantes.

1. Jérôme D., Mazaud A., Ribault M. and Bechgaard K., *J.Phys.Lett.*, **1980**, *41*, L95.
Jérôme D. and Schultz H.J., *Adv. Phys.*, **1982**, *31*, 299.
2. Jérôme D., *Science*, **1991**, *252*, pp. 1509-1514.
3. Bednorz J.G. and Müller K.A., *Z.Phys.B*, **1986**, *64*, 189.
4. Chu C.W., Hor P.H., Meng R.L., Gao L., Huang Z.J., Wang Y.O., *Phys.Rev.Lett*, **1987**, *58*, 405.
5. Williams J.M., Ferraro J.R., Thorn R.J., Carlson K.D., Geiser U., Wang H.H., Kini A.M., and Whangbo M.H., *Organic Superconductors*, Prentice-Hall: Englewoods Cliffs, New Jersey, **1992**; Faulques E., in *Materials Synthesis and Characterization*, Dale L. Perry Ed., Plenum Publishing Corp.: New-York, **1997**, pp 61-102.
6. Chaplot S.L., Reichardt W., Pintschovius L., Pyka N., *Phys. Rev. B*, **1995**, *52*, pp 7230-7242.
7. Thomsen C., in *Light Scattering in High Tc Superconductors*, *Topics in Applied Physics*, M. Cardona and G. Güntherodt Eds., Springer-Verlag:Berlin, **1991**, 68.
8. Limonov M.F., Rykov A.I., Tajima S., Yamanaka A., *Phys. Rev. Lett.*, **1998**, *80*, 825 and references therein.
9. Dierker S.B., Merlin R., Klein M.V., Webb G.W., Fisk Z., *Phys. Rev.B*, **1983**, *27*, 3577.
10. Fano U., *Phys. Rev.*, **1961**, *124*, 1866
11. Balkanski M., Jain K.P., Beserman R., Jouanne M., *Phys.Rev.B*, **1975**, *12*, 4328.
12. Cerdeira F., Fjedly T.A., Cardona M., *Phys.Rev.B*, **1973**, *8*, 4734.
13. Faulques E., Ivanov V.G., *Phys. Rev.B*, **1997**, *55*, 3974.
14. V.G. Ivanov, *Ph.D. Thesis*, Nantes, 22 apr. **1998**.
15. Mazin I.I., Rashkeev S.N., Liechtenstein A.I., Andersen O.K., *Phys. Rev. Lett.*, **1992**, *46*, 11232.
16. Auban-Senzier P., Bourbonnais C., Jérôme D., Lenoir C., Batail P., Canadell E., Buisson J.P. and Lefrant S., *J. Phys. I France*, **1993**, *3*, pp 3871-885 and references therein.
17. Faulques E., Girault C., Lefrant S., Lenoir C., Batail P., Molinié P., Buisson J.P., *Condensed Matter and Materials Communications*, **1997**, *4*, 111.
Faulques E., Girault C., Lefrant S., Batail P., Lenoir C., Buisson J.P., *Synthetic Metals*, **1997**, *86*, 1985.

18. Wojciechowski R., Ulanski J., Lefrant S., Faulques E., Laukhina E., *Synthetic Metals*, **1999**, to be published.
19. Wojciechowski R., Ulanski J., Kryszewski M., Tracz A., Jeszka J.K., Müller H., Lefrant S., Faulques E., *Synthetic Metals*, **1998**, *94*, 27.
20. Pokhodnia K.I., Graja A., Weger M., Schweitzer D., *Z.Phys.B*, **1993**, *90*, 127.
21. Pedron D., Visentini G., Cecchetto E., Bozio R., Williams J.M., Schlueter J.A., *Synthetic Metals*, **1997**, *85*, 1509 and Pedron D., Visentini G., Bozio R., Williams J.M., Schlueter J.A., *Physica C*, **1997**, *276*, 1.
22. Pedron D., Bozio R., Schlueter J.A., Kelly M.A., Kini A.M., Williams J.M., *Synthetic Metals*, **1999**, to be published.
23. Eldridge J.E., Lin Y., Wang H.H., Williams J.M., Kini A.M., *Phys. Rev.B*, **1998**, *57*, 597.
24. Pintschovius L., Rietschel H., Sasaki T., Mori H., Tanaka S., Toyota N., Lang M., Steglich F., *Europhys. Lett.*, **1997**, *37(9)*, 627.
25. Kendziora C., Kelley R.J., Onellion M., *Phys. Rev. Lett.*, **1996**, *77*, 727.
26. Devereaux T.P., Einzel D., Stadlober B., Hackl R., Leach D.H., Neumeier J.J., *Phys. Rev. Lett.*, **1994**, *72*, 396.
27. Nemetschek R., Opel M., Müller P.F., Hackl R., Berger H., Forro L., Erb A., Walker E., *Phys. Rev. Lett.* **1997**, *78*, 4837.
28. Burns G., *High Temperature Superconductivity, an Introduction*, Academic Press Inc.: San Diego, **1992**.
29. Ernst G., Nowak A., Weger M., Schweitzer D., *Europhys. Lett.*, **1994**, *25*, pp 303-309.
30. Friedel J., *Eur. Phys. J. B*, **1998**, *4*, pp 409-411 and references therein.
31. Queisser H.J., *Phys. Rev. Lett*, **1985**, *54*, 234.
32. Hamed A.J., *Phys. Rev.B*, **1991**, *44*, 5585.
33. Dulieu B., Bullo J., Wéry J., Richard M., Brohan L., *Phys. Rev.B*, **1996**, *53*, 10461.
34. Dulieu B., Wéry J., Lefrant S., Bullo J., *Phys. Rev.B*, **1998**, *57*, 1.
35. Kudinov V.I., Kirilyuk A.I., and Kreines N.M., *JETP Lett.*, **1992**, *56*, 102.
36. Kudinov V.I., Chaplygin I.L., Kirilyuk A.I., Kreines N.M., Laiho R., Lahderanta E., and Ayache C., *Phys. Rev. B*, **1993**, *47*, 9017.
37. Stockinger C., Markowitsch W., Lang W., Kula W., Sobolewski, *Eur. Phys. J. B*, **1998**, *2*, pp 301-311.
38. Fainstein A. et. al., *Phys. Rev. B*, **1998**, *58*, pp 9433.
39. Panfilov A. G. et. al., *Phys. Rev. B*, **1998**, *58*, pp 12 459.
40. *Femtosecond Laser Pulses, Principles and Experiments*, C.Rullière Ed., Springer-Verlag: Berlin-Heidelberg-New York, **1998**.
41. Nassar E.J., Serra O.A., Viana Rosa I.L., *J.Alloys and Compounds*, **1997**, *250*, pp 380-382 and references therein.

Chapter 2

Dissolution of A-15 in Metallic Dichalcogenides: A Route to New Superconductors and Ferromagnets

Philippe Molinié¹, Annie Leblanc¹, Eric Faulques¹, Zeineddine Ouili²,
Jean-Claude Jumas³, and Claude Ayache⁴

¹Institut des Matériaux de Nantes Jean Rouxel, Laboratoire de Physique Cristalline, University of Nantes, 2 rue de la Houssinière, BP 32229, F-44322 Nantes Cedex, France

²URPMA, Route Ain El Bey, 25000 Constantine, Algérie

³LPMS Université II, 34095 Montpellier cedex, France

⁴DRECAM/SPEC Saclay, 91191 Gif/Yvette cedex, France

Dichalcogenides of transition metals (chemical formula : MX_2 , where M = metals of column IV, V, VI and $\text{X} = \text{S, Se}$) present a rich variety of lamellar structures. Here we focus on the metallic dichalcogenides MX_2 with 2H stacking for NbSe_2 , TaSe_2 and 1T stacking for VSe_2 , which are considered as members of a model family. We review different properties and their thermal evolution : transport, specific heat, spectroscopy, magnetic susceptibility, superconductivity and soft phonon dynamics. In addition we briefly present the superconducting properties and spectroscopy data of the A15 intermetallic compounds. After a sketch of the intercalated phases $(\text{Int})_x(\text{MX}_2)_y$ and "misfits" compounds $(\text{BX})_n(\text{MX}_2)_y$, we present a new family of ternary compounds BM_3Se_9 ($\text{B} = \text{Sn, Ga}$ and $\text{M} = \text{Nb, Ta, V}$) which are superconductors or ferromagnets.

The superconductivity in the low-dimensional synthetic metals (1-3) presents a challenge for the solid state sciences. Organic or inorganic conductors, possibly intercalated layer or chain compounds offer a remarkable chemical flexibility for trying to optimize the superconducting parameters, to increase the critical temperatures (T_c) or critical fields (H_c). However, the low-dimensional character of these materials makes other ground states enter in competition with superconductivity. A condensation of conduction electrons in charge-density-waves (CDW) or spin density-waves (SDW) decreases considerably the critical temperature or even inhibits superconductivity in most one-dimensional systems.

The knowledge obtained by the study of the high temperature T_c superconductors (4) shows the necessity to have compounds whose structure is built with :

- lamellar sheets (the CuO_2 layers) where the superconductivity starts ;
- and with electron "reservoir" layers which make possible the optimization of physical properties and superconductivity. These reservoirs structurally situated between the (CuO_2) layers are often composed of chains.

Besides a great chemical flexibility of these phases is necessary (cationic substitution, possible intercalation, variable oxygen content...) to allow us "to ring the compositional changes". On the other hand, a general interest for the diverse multilayers (5-6) has emerged, associating magnetic or superconducting metals and semi-conductors. The most

striking example of this is : the giant magnetoresistant layer systems which lead to an active research into various electronic applications. It is therefore most important to go on researching into new systems. The dichalcogenides of transition metals (7-8) fit this kind of prospect, due to the existence of Van der Waals gap in which can be inserted varied chemical species, ions or molecules or even complete planes as in the components of the "misfit" type. This work fits into such studies with the ambition of examining if it is possible by chemical means to realize chain-shaped insertions, as it is done in most high T_c cuprates.

We think we may have reached such a solution by proving the dissolution of A15 phases (9-10) with characteristic M-M chains, as the guest, between the layers, of a crystalline host lattice of metallic diselenides ($NbSe_2$, $TaSe_2$, VSe_2). As an example, the dissolution of some Nb_3Sn in $2H_a-NbSe_2$ produces a new phase whose superconducting characteristics make it utterly different from its parents ($T_c = 17K$, $H_{c2}(0) = 2.3T$). We have also synthesized by dissolution of some V_3Ga in $1T-VSe_2$ a new derivative which is ferromagnetic as well as anisotropic and metallic. This is remarkable if we compare it to the dichalcogenides which are magnetic only when they are in an isolating state.

Before coming to the description of the synthesis, of the structure and properties of these derivatives, we think it is useful to recall quickly the characteristic properties of the A15 and of the dichalcogenides, in order to place this present work in a better light.

A-15 PHASES AND DICHALCOGENIDES : TWO RICH FAMILIES RULED BY LOW DIMENSIONALITY AND ELECTRON-PHONON INTERACTION.

General Properties of a-15 Phases

Superconducting A15 compounds were discovered in 1954. Since this early work, several thousand original publications have appeared on this growing subject (9-12). The real story of these phases began with the discovery of high superconducting transition temperatures for V_3Si and Nb_3Sn (13-14). One important aspect of the A15 is apparent coincidence of optimum superconducting properties and marginal structural stability. Both phenomena certainly derive from the same cause : electronic structure.

The stoichiometric formula of A15 is A_3B . The A atom is always a transition element (Ti, V, Cr, Zr, Nb, Mo, Ta, W); the B atom can be either a non-transition metal (Al, Si, P, Ga, Ge, As, In, Sn, Sb, Pb, Bi) or a transition element (Co, Ni, Ru, Rh, Pd, Re, Os, Ir, Pt, Au). The B atoms form a body-centred cubic lattice. On each face there are equidistant A atoms which form continuous chains through the system. The three chains do not intersect (Figure 1).

In 1986, Bednorz and Muller discovered a superconducting critical temperature T_c 30K in the system $La_{(2-x)}Ba_xCuO_4$ (1). Before that the A15 phases were considered as High- T_c superconductors. In fact by 1980 it appeared that the upper limit for the superconducting transition temperature T_c had essentially been reached. The majority of the binary A15 phases are superconducting, and about 15 of them exhibit a critical temperature exceeding 10K. The superconducting properties are strongly influenced by the composition and the degree of atomic order (19-20). The best A15 compound is Nb_3Ge with $T_c=23.3K$ and the industrial phase is Nb_3Sn ($T_c=18K$) with which we build superconducting coils for high fields.

Since all known A15 compounds are extreme type II superconductors, the upper critical field H_{c2} , and particularly its zero temperature value $H_{c2}(0)$ is one of the basic parameters characterizing these materials (21). Experimental upper critical field curves are usually determined by resistivity measurements for Nb_3Sn and V_3Ga (22) (Table I). The experiments lead to the general conclusion that actually little or no paramagnetic limitation seems to be present in the Nb-based A15 compounds, whereas H_{c2} of V_3Ga is strongly depressed at low temperature indicating a strong paramagnetic limitation. The anisotropy of H_{c2} in single crystals of Nb_3Sn has been studied over a large temperature range (23). However the anisotropy found is surprisingly small.

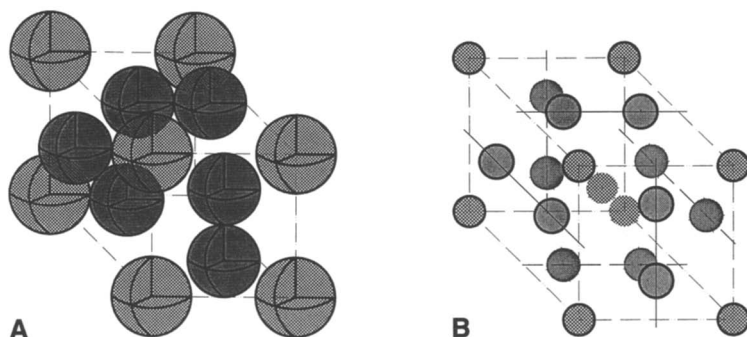


Figure 1 : The A15 type structure at 300K (15-18) A_3B space group $Pm\bar{3}m$, A atoms (shaded) are in 6c position and B atoms (cross-hatched) in 2a.

Table I. Crystallographic and Superconducting Parameters of Nb_3Sn and V_3Ga Phases.

<i>phases</i>	<i>Nb₃Sn</i>	<i>V₃Ga</i>
a (nm)	0.5291	0.4815
d (g/cm ³)	8.913	6.234
Space group	$Pm\bar{3}m$	$Pm\bar{3}m$
T_c onset	18.3	14.9
$\partial H_{C2}/\partial T$ (T/K)	2.0	2.7
$H_{C2}(0)$ (T)	24	22

Undoubtedly, the detection of low temperature structural transition in V_3Si and Nb_3Sn (24) has added a new important aspect to the puzzle of the A15 compounds. We use the term "martensitic" in the sense of a diffusion-less transformation occurring in Nb_3Sn near 45K (25). One was able to establish that the transition is indeed of the first order, as characterized by a significant spontaneous strain at T_m (26). However, according to combined neutron diffraction and specific heat measurements (27) the 18.3K superconducting transition clearly corresponds to the tetragonal phase. The structural transition may be pictured as a crystal Jahn-Teller effect according to the Labbé-Friedel model (28) or a Peierls gap instability (29-31).

The limits of stability of V_3Ga phase are now well known (18) and the Nb_3Sn phase is stable at low temperature. The properties of V and Nb A15 compounds with high T_c are truly structure-characteristic and unparalleled in different atomic arrangements with similar stoichiometry. Many experimental evidences have established that for all typical A15 superconductors, a decrease in long range atomic order causes a usually important decrease of the transition temperatures. The essential physical origin of this reduction undoubtedly lies in the variation of the electronic density of states. In V_3Ga , the variation of T_c on thermal treatment should reflect the temperature dependence of the equilibrium order parameter in the absence of any compositional changes. Nb_3Sn and V_3Ga exhibit a large and roughly comparable decrease of T_c with radiation dose, due to an anti-site disorder (19-20).

General Properties of Dichalcogenides

Dichalcogenides of transition metals(32) have the chemical formula, MX_2 , where M stands for a metal of column IV,V,VI and X represents one of the chalcogen elements(33-34). Their lamellar structures consist of sandwiches that are three atom-sheets thick. The bonding within each sandwich is covalent, while that between them is weak Van der Waals type. The top and the bottom sheets are of hexagonally packed chalcogen atoms, while the middle sheet is of metal atoms. These X-M-X sandwiches can show either octahedral (AbC) or trigonal prismatic (AbA) coordination of the metal atoms. The sandwiches stack in a variety of ways, giving either pure octahedral (1T-VSe₂), pure trigonal prismatic (2H_a-NbSe₂, 2H_a-TaSe₂) or mixed coordination polytypes (Figure 2).

Metals of the group IV adopt preferentially the 1T structure while those of group VI are rather of the 2H type. All compounds of these groups are semi-conductors excepting the case of the semi-metallic TiSe₂ and possibly of TiS₂. On the contrary, metals of group V may adopt both crystalline forms or can be also found in mixed stacking sequences. All the corresponding structures are metallic at high enough temperature. The 2H-MX₂ family (M= V,Nb, Ta; X= S,Se) merits special attention since it offers the possibility of studying the coexistence between superconductivity and charge-density-waves(CDW). The band structure is rather wellknown. The states close to the Fermi level have a marked d_{z^2} character(34-36). The Fermi surface possesses two different types of hole pockets: the first one is elongated along the Γ A direction in the hexagonal Brillouin zone while two other quasicylinders are located around the HKH end H'K'H' edges. The lattice dynamics look also quite similar provided mass difference between element is considered.

Metallic diselenides MSe₂ (M= V,Nb,Ta) are well-known for undergoing charge-density-wave (CDW) transition linked to their two-dimensional character (9,37-38). The CDW transition temperatures, T_d , are 112K, 122.3K, 33.5K for 1T-VSe₂, 2H_a-TaSe₂ and 2H_a-NbSe₂, respectively. The accompanying incommensurate lattice distortion (ILD) which also develops below T_d is however close to the commensurate modulation wave $Q=(a^*/3,0,0)$. The commensurate state is reached at a lock-in temperature, T_L , 62K for 1T-VSe₂, and 90K for 2H_a-TaSe₂, while 2H_a-NbSe₂ undergoes no lock-in transition.

Direct evidence for the existence of CDW/ILD on the metallic transition metal diselenides has been obtained by electron diffraction(39), and neutron scattering(40-42). Beside these diffraction techniques the CDW/ILD state has been studied at microscopic scale by various techniques like Raman scattering(43-45), ESCA (46-47), Mössbauer effect(48) and nuclear magnetic resonance (NMR)(49-50). The NMR study was made on one single crystal of 2H_a-NbSe₂ weighing 98mg, on pulsed NMR spectrometer. The corresponding lineshape of the observed lines is characteristic of the symmetry of the CDW/ILD state and of its incommensurate (or commensurate) character. The observed lineshape indicates the local coexistence of three incommensurate CDW, confirming the results obtained from neutron scattering(40), and eliminates the possibility of equivalent domains with single q vectors. This triple CDW remains incommensurate at 2.1 GPa, with $T_d=26$ K. The amplitude of the broadening gives a measure of the amplitude of the CDW, and the maximum redistribution of conduction electrons within an atomic cell was found equal to 9% at 4.2K in 2H_a-NbSe₂. The amplitude of the CDW/ILD was also found proportional to T_d as expected in mean field theory.

Before the discovery of the CDW phenomena, the superconductivity of 2H_a-NbSe₂ was widely reported(51) and it was strongly enhanced by pressure (0.5 K/GPa)(51-52). The dependence of T_c on lattice instabilities has been of constant interest in the past especially in the A15 compounds in which a martensitic transformation occurs at temperature T_m above T_c . A correlation between pressure dependence of T_m or T_d (CDW) and T_c is suggested by experiments in V₃Si, Nb₃Sn(53-54) and 2H_a-TaS₂(55). In the case of 2H_a NbSe₂, under 2GPa, we observe the linear decrease of T_d with pressure and above 2GPa, T_d decreases much more strongly and must cross the variation of T_c with the pressure around 3.6GPa. These results give the first clear evidence that the pressure enhancement of superconductivity in the MX₂ compounds is due to a progressive removal of the CDW(38) (Table II).

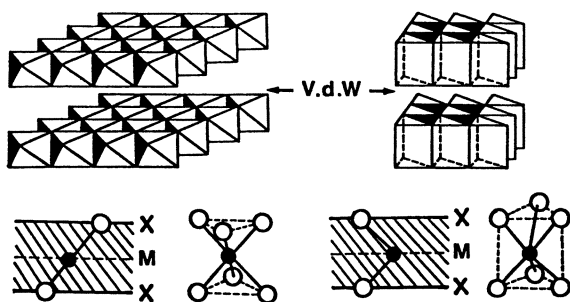


Figure 2 : General form for the Se-M-Se slabs.

Table II. Structural and superconducting parameters of 1T-VSe₂, 2H_a-NbSe₂ and 2H_a-TaSe₂.

<i>phases</i>	<i>1T-VSe₂</i>	<i>2H_a-NbSe₂</i>	<i>2H_a-TaSe₂</i>
T synthesis (K)	1078	1053	1123
T growing (K)	1078	1053	1098
a (nm)	0.3442(1)	0.3436(1)	0.3356(1)
c (nm)	0.6104(1)	1.2546(1)	1.2696(1)
symmetry	P $\bar{3}$ /m1	P6 ₃ /mmc	P6 ₃ /mmc
d (g/cm ³)	5.856(1)	6.454(1)	8.727(1)
$\partial \ln T_d / \partial P$ (%/hMPa)	0.33(1)	-1.0(1)	-0.15(1)
T _c onset (K)	-	7.12(1)	0.15(1)
$\partial \ln T_c / \partial P$ (%/hMPa)	-	0.70(1)	5.0(1)
P limit (hMPa)	-	36.(1)	38.(1)
T _c limit (K)	-	8.2(1)	4.5(2)
$\partial H_{c2} / \partial T$ (T/K)	-	0.81(6)	-
ϵ anisotropy	-	3.6(3)	-

In these compounds the superconductivity competes and coexists with CDW of different strength. Following results on electron irradiated 2H_a-TaS₂, 2H_a-TaSe₂ and 2H_a-NbSe₂ demonstrate that a considerable variation of T_c and inhomogeneous superconductivity can be associated with a low concentration, of the order of 10⁻³-10⁻² atomic fraction, of irradiation induced defects(56). The superconducting transitions(57) of irradiated samples are observed at temperatures clearly separated from the T_c-values typical of pristine materials, in the case of TaS₂-2H and TaSe₂-2H well above ! These studies(58) have also shown that the irradiation induced defects perturb the CDW, the phase transitions become smeared and are displaced to lower temperatures(59). As mentioned above the pressure experiments have supplied evidence on the negative correlation between the CDW onset temperature and T_c(38). So it is not surprising to see T_c increase with increasing concentration of irradiation induced defects. However the inhomogeneous character of the superconductivity requires that the remaining CDW-amplitude should be subjected to spatial modulation on a scale exceeding the superconducting coherence length.

More generally the irradiation induced defects seem to be comparable with the strongest substitutional defects studied, i.e. group VIII_B metals. Such substitution suppresses the CDW phase transition more rapidly and the transport properties follow quite closely those irradiation defects. This is especially true for the localization effects in TaS₂-1T(59,60) or for the approach to localization in VSe₂. On the other hand the substitution with IV_B or V_B transition metals(61-63) as well as substitution in the chalcogen sublattice(62) is more subtle and can often be regarded as a gradual change from one compound to another.

The mechanism of the transition is thought to result mainly from electron-phonon interaction in presence of quasi-2D "nesting" conditions. A Van Hove anomaly resulting

from the connection between the zone center isoenergy surfaces and the edge ones is also possible; but its distance from the Fermi level, E_F , is still uncertain. The total width of the predominantly d_z^2 character band near E_F is more than 2eV. A detailed theoretical investigation of the electron-phonon interaction in those systems shows the importance of both the nesting conditions and the q -dependent electron-phonon coupling coefficient to cause the lattice instability(7). This approach, a weak coupling one in essence, obtained good success in particular by predicting the right symmetry for the soft phonon mode. However it failed to provide a satisfactory evaluation of the different observed T_d 's. As stressed by McMillan, the problem of entropy appears to be a central issue for a complete understanding of the CDW mechanism.

Atomic, Molecular and Misfit Insertion in Dichalcogenides

As shown in the Figure 3a the particular disposition of the sheets in the dichalcogenides of transition metal allows an intercalation process in these phases of organic molecules, alkali and transition metal atoms(2,8,64). Large inorganic species (pillars) may be introduced between the layers as an alternative to organic molecules. Here we describe the "misfit" compounds $(BX)_n(MX_2)_m(I,2)$, with $(B = Sn, Pb, Ln)$, $(M = V, Nb, Ta)$ and $(X = S, Se)$, which can be considered as intercalated forms of pure dichalcogenides MX_2 by an isolant or magnetic layer BX species(65)(Figure 3b). The anisotropy of the physical properties is expected for these compounds because they have a 2D structural type. The electrical characteristics of the misfit phases have been attributed to the MX_2 part, similar properties are observed for the parent binary chalcogenes (66). In the system $(PbS)_{1.14}(NbSe_2)_m$ ($m=1,2,3$) Oosawa et al (67) observe that the superconductivity is related to the number(m) of MX_2 layers ($T_c = 3.4K$ for $m = 2$ and $T_c = 4.8K$ for $m = 3$).

A Route to New Insertion Forms

In 1986, Bednorz and Muller discovered a superconducting critical temperature $T_c = 30K$ in the system $La_{(2-x)}Ba_xCuO_4$, this was therefore a major event in the study of superconductivity (4) and a great surprise. As it is frequently the case, it did not take long before other workers reproduced their data and began to "ring the compositional changes" leading to the discovery of a T_c of 90K in $YBa_2Cu_3O_{(7-\delta)}$ ($\delta = 0.1$). We can write the formula of this ceramics as : $(Y, Ba_2CuO_3)(CuO_2)_2$ then we can define two types of sheets : one is " the electron reservoir layer" (Y, Ba_2CuO_3) , the other "the superconducting layer" (CuO_2) . This description shows the strong structural anisotropy of these phases. The systems, like di- or tri-chalcogenides, organic conductors, intercalated compounds of graphite, etc., can be structurally described as built up with chains or layers subunits, and they are thus well named as low dimensional synthetic metals.

Our purpose was to include superconducting chains in bad metallic samples to form a multilayer system(5-6). For this goal, first we chose well defined dichalcogenide $2H_a-NbSe_2$, and the industrial A15 Nb_3Sn . In fact it was possible to intercalate Nb and Sn atoms into $NbSe_2$ without damaging the structure. Moreover, the cubic cell of a A15 phase is isotropic at first sight and can be compared to a sphere like an atom of transition metal, while the a parameter is compatible with the product $a\sqrt{3}$ of the host network cell (Figure 4). In the case of $NbSe_2$, the inclusion of some Nb_3Sn along the c axis could have given two multilayer systems : one for $T < 7.5K$ made with two superconducting phases and the other for $T > 7.5K$ as Metal:Superconductor:Metal arrangement. With a paramagnetic phase VSe_2 , we could have expected a Paramagnetic:Superconductor:Paramagnetic multilayer system.

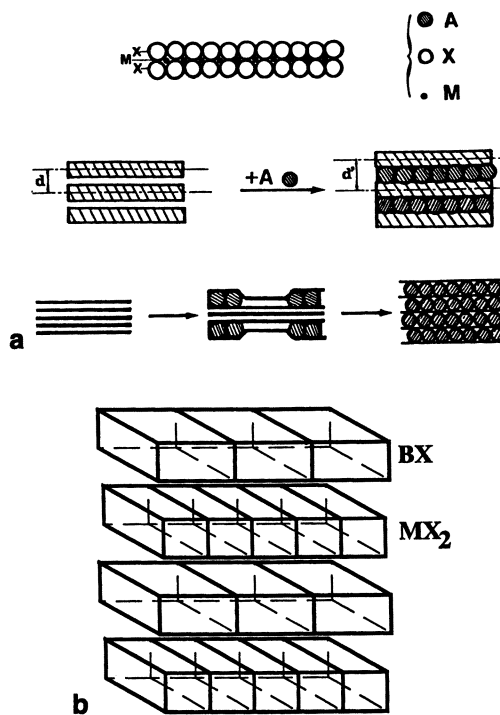


Figure 3 : -a- Intercalation process in MX_2 phases; A can be organic molecules such as amine, alkali and metal atoms as Li, Na, Fe, Mn, Sn, or semi-conductor layers as SnSe, PbSe. -b- Schematic representation of "misfit" compounds.

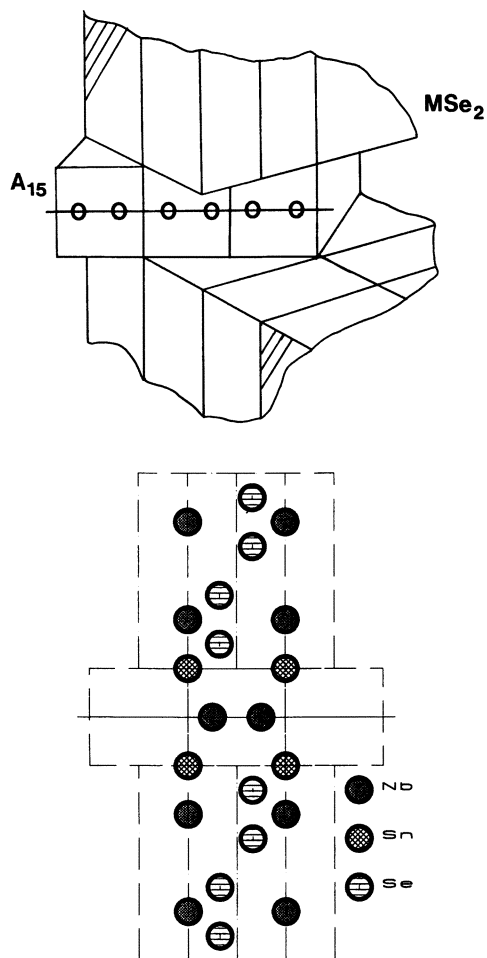


Figure 4 : Schematic inclusion of A15 chains in a $2H_2$ - MSe_2 with $2a \times 2a$ superstructure

THE NEW STRUCTURES OBTAINED THROUGH THE DISSOLUTION PROCESS

Synthesis of Powders and Crystals

For the synthesis of the pure MSe_2 we used starting metals (Nb,V,Ta) 99.95% pure and Selenium 99.9995% pure. Stoichiometric amounts of these elements, with a small excess of selenium $0.1\text{mg}/\text{cm}^3$, were placed in evacuated (10^{-3}mbar) quartz tubes and reacted at 1053K for $NbSe_2$, 1123K for $TaSe_2$ and 1078K for VSe_2 for at least three weeks. A special program of warming up the temperature was used to guarantee the stoichiometry and the crystallinity of the powder samples. The $2H_a-NbSe_2$ and $2H_a-TaSe_2$ crystals were grown by vapour phase transport in a 50K gradient of temperature around 1053K and 1098K respectively with iodine transport agent (68). The polytype of these phases was confirmed by X-rays (Table II)(69-70). The stoichiometry for $1T-V_{1+x}Se_2$ was confirmed by susceptibility measurements(71-72) and by a new refined crystal structure ; the value x of the excess of V atoms, lying in the Van der Waals sheet, is, in both cases, 0.005. For $2H-NbSe_2$ the value 7.1K of T_C indicates a good stoichiometry of the powders and crystals used (73). In the present work five A15 phases, purchased at CERAC Incorporated (purity 99.9%), Nb_3Sn , Nb_3Ge , V_3Ga , V_3Si and V_3Sn were used.

New selenides phases have been synthesized from a mixture of 5% in mass of A15 in a pure MSe_2 placed in evacuated (10^{-3}mbar) quartz tubes and heated at 873K for two months at least. Only three mixtures give homogeneous samples. They were checked first by the metallographic method on small crystalline samples. The metallic compounds are hardly absorbent and very often non transparent in thin strips. The polished section can be studied in a reflected light in metallographic microscope. Each phase of a non-homogeneous synthesis has a chromatic response so we can determine the number of the present phases and after we can proceed to an elemental analysis of each phase by using a scanning electron microscope equipped with an EDX system. For $Nb_3Sn/NbSe_2$ and V_3Ga/VSe_2 mixtures the syntheses are very homogeneous, even in millimetric crystals we have a good stoichiometry in all the volume. For the $Nb_3Sn/TaSe_2$ mixture the situation is more complicated: the ratio Ta/Nb is not always well defined.

Structural Characterization

The crystallized powders were characterized by density measurements, and X-ray powder diffraction. The observed density does not agree with those calculated from the initial mixtures (Table IV). All spectra obtained differ from those of the pristine phase ; see for example the case of the new phase synthesized with the $Nb_3Sn/NbSe_2$ mixture (74) (Table III).

The general feature observed for the X-ray pattern indicates we do not have an interlaccation or an intergrowth process. The structural studies on a single crystal taken in $Nb_3Sb/NbSe_2$ system cannot allow us to determine the crystallographic structure. In fact we observe a strong disorder along the c axis.

Raman and Mössbauer Characterization

We characterized our samples by Raman and Mössbauer spectroscopies. The Raman studies were extensively made on the $Nb_3Sn/NbSe_2$ phase(75). The observed spectrum at 5.5K for this phase is somewhat different of those observed for $2H_a-NbSe_2$ and Nb_3Sn , despite some resemblance. It confirms that the new phase is not simply an intergrowth

Table III. X-ray powder diffraction of $2H_a$ - $NbSe_2$, Nb_3Sn and the new phase $Nb_3Sn/NbSe_2$

<i>Nb₃Sn /NbSe₂</i>		<i>2H_a-NbSe₂</i>				<i>Nb₃Sn</i>					
<i>d (obs)</i>	<i>I%</i>	<i>d (obs)</i>	<i>h</i>	<i>k</i>	<i>l</i>	<i>I%</i>	<i>d (obs)</i>	<i>h</i>	<i>k</i>	<i>l</i>	<i>I%</i>
6.876	14										
6.711	2										
6.393	5										
		6.281	0	0	2	58					
		3.139	0	0	4	10					
3.002	7										
2.976	13	2.990	1	0	0	5					
2.937	69										
		2.905	1	0	1	90					
2.834	14										
2.775	4										
2.755	7										
		2.695	1	0	2	80	2.645	2	0	0	20
2.534	12										
2.520	5										
2.510	8										
2.490	8										
		2.431	1	0	3	62					
2.408	2										
2.370	2						2.366	2	1	0	52
2.335	26										
2.310	4										
2.299	8										
2.284	19										
2.267	11										
		2.163	1	0	4	100	2.160	2	1	1	67
2.069	1	2.092	0	0	6	18					
2.054	7										
2.005	5										
1.992	2										
		1.921	1	0	5	9					
1.733	100	1.723	1	1	0	42					
		1.712	1	0	6	4					
1.682	4										
		1.662	1	1	2	7					
		1.569	0	0	8	22					
1.550	15										
1.541	1										
1.517	1	1.537	1	0	7	14	1.527	2	2	2	11

phase of $2\text{H}_a\text{-NbSe}_2$ and Nb_3Sn , otherwise we would obtain a superimposition of the spectra of the pristine (43-45). If the Raman spectra are mainly sensitive to the Se-Nb-Se layers, our results show that the new superconductors have almost the same selenium stacking as $2\text{H}_a\text{-NbSe}_2$.

The Mössbauer studies, in temperature range 4-295K, made essentially on $\text{Nb}_3\text{Sn}/\text{NbSe}_2$ samples with different thermal treatments confirm the results of the Raman study. All the spectra indicate that we have two kinds of Sn atoms in the structure, one (I) representing 8% of the Sn atoms belongs to those observed in Nb_3Sn (76) with the following parameters at 295K ($\langle\delta\rangle = 1.6\text{mm/s}$; $\langle\Gamma\rangle = 0.9\text{mm/s}$) and the second (II) part of Sn atoms (93%) belongs to the environment type SnSe(77) with the following parameters at 295K ($\langle\delta\rangle = 3.5\text{mm/s}$; $\langle\Gamma\rangle = 0.9\text{mm/s}$). This last site (II) may be wholly isotropic or split in isotropic and anisotropic halves ($\langle\Delta\rangle = 0.7\text{mm/s}$) depending on the temperature variation or on the thermal treatment. The same Sn sites will be observed in "misfit compounds" (78). We can eliminate the possibility of an insertion of tin atoms in $2\text{H}_a\text{-NbSe}_2$ (79). The variation of the population of the isotropic part of the site II may indicate that some structural transformation can happen near 80K (80).

A New General Emerging Structure

An elemental analysis of powder and crystals was systematically carried out using a scanning electron microscope JEOL 35c equipped with a TRACOR EDX system. The results are summarized in the table IV, the corresponding formula is BM_5Se_9 with $\text{B} = \text{Ga, Sn}$ and $\text{M} = \text{V, Nb, Ta}$. The cell parameters are in all cases derived from those of pristine phases by the following relation: $a \sim 4a''$; $b \sim 4a''\sqrt{3}$; $c \sim 9/2c''$; where a'' and c'' are the cell parameters of the pristine diselenides (Table IV). All the obtained cells can be described as a superstructure of the pristine diselenide's orthohexagonal cell, with an important disorder along c axis. However three new selenides SnNb_5Se_9 (74-76), $\text{Sn}(\text{Ta, Nb})_5\text{Se}_9$ and GaV_5Se_9 have been synthesized.

OCCURENCE OF SUPERCONDUCTIVITY OR MAGNETISM IN THE NEW PHASES

For all new phases the magnetic properties of crystal and powder samples were carried out in the temperature interval from 2 to 300K using a commercial SQUID magnetometer "MPMS-5" from Quantum Design. The powder samples are placed in medical caps. The measurements are also made on millimetric crystal samples weighing 200-300 μg , oriented according to the applied field. The parallelepipedic sample has square or hexagonal faces, we expect that these faces contain the a and b crystallographic axis and the vertical edge could be the c axis like in dichalcogenides crystals. We performed two sets of experiments: one where the face is parallel to the applied field ($H_0 \perp c$) and the second where it is perpendicular to the applied field ($H_0 \parallel c$).

Specific Superconductivity of SnNb_5Se_9

The susceptibility curves shown in Figure 5 reveal a superconducting behaviour observed for different powder samples of SnNb_5Se_9 obtained from different compositional mixtures and thermal treatments. The empty squares (\square) curve is observed for powder samples synthesized by the normal procedure seen chapter 3.1. The best superconducting phase seems to be synthesized with 6% in mass of Nb_3Sn in $2\text{H}_a\text{-NbSe}_2$ (\blacksquare). The thermal treatment of the first mixture is also important and the speed of the quench influences the

Table IV. Structural and compositional parameters of the three new phases (d_o and d_c stand for measured and calculated density).

<i>Phases</i>	<i>SnNb₅Se₉</i>	<i>Sn(Ta,Nb)₅Se₉</i>	<i>GaV₅Se₉</i>
Sn%at	6.6(1)	2.8(1)	-
Nb%at	33.0(2)	0.9(1)	-
Ta%at	-	33.5(2)	-
Ga%at	-	-	6.5(1)
V %at	-	-	33.4(2)
Se%at	60.4(2)	62.6(2)	60.1(2)
a (nm)	1.3579(1)	1.3500(1)	1.3439(1)
b (nm)	2.3530(1)	2.3530(2)	2.3499(1)
c (nm)	5.5205(3)	5.4999(3)	2.7590(2)
symmetry	Pmmm	Pmmm	Pmmm
d_o (g/cm ³)	6.524(1)	8.680(2)	5.667(2)
4a"(nm)	1.3744	1.3424	1.3768
4a"√3(nm)	2.3805	2.3250	2.3846
9/2c"(nm)	5.6457	5.7132	2.7468
d_c (g/cm ³)	6.548	8.736	5.872

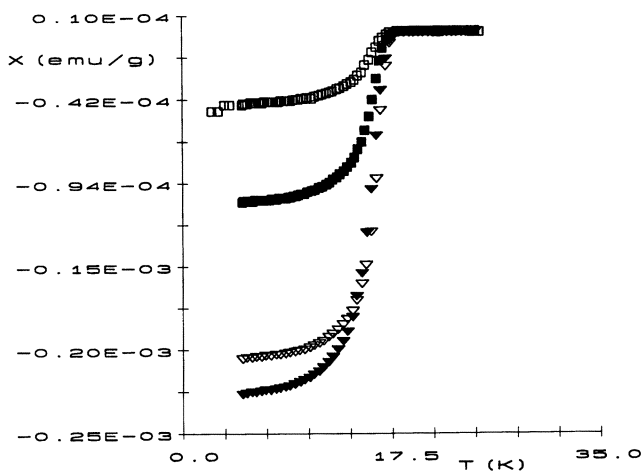


Figure 5 : Susceptibility of powder samples versus temperature for SnNb_5Se_9 in zero field cooling under a field strength of 0.01T. \square synthesized with 5% in mass of Nb_3Sn . \blacksquare synthesized with 6% in mass. ∇ and \blacktriangledown Powder samples, synthesized with 5% in mass, quenched with two different speeds.

superconducting volume which is multiplied by ~ 5 for the quenched phases (∇ and \blacktriangledown). The critical temperature found for SnNb_5Se_9 was 17.5K for all powder samples and in all cases we did not see any transition at 7.1K, where $2\text{H}_a\text{-NbSe}_2$ usually undergoes a superconducting transition. The behaviour of the superconducting properties of SnNb_5Se_9 crystal (Figure 6) and its comparison with the pristine crystal phases are given in table V. The major result of this crystal study was the discovery of a significant anisotropy ($\epsilon = (\partial H_{C_i \perp c} / \partial T) / (\partial H_{C_i} // c / \partial T)$ with $i = 1, 2$) when the applied field is $\perp c$ or $// c$. This anisotropy is smaller than the one observed in a pure $2\text{H}_a\text{-NbSe}_2$ but much bigger than that of Nb_3Sn . This fact is a new proof that SnNb_5Se_9 is not an intergrowth phase.

Table V. Comparison of superconducting parameters measured in crystal samples

Phases	$2\text{H}_a\text{-NbSe}_2$	Nb_3Sn	SnNb_5Se_9
T_c onset(K)	7.12(1) 3	18.3	17.5(2)
$\partial H_{C_1} // c / \partial T$ (T/K)	0.0100(1)	-	0.0061(1)
ϵ anisotropy	2.4	-	1.3(1)
$\partial H_{C_2} // c / \partial T$ (T/K)	0.81(6)	2.0	0.10(3)
ϵ anisotropy	3.6(3)	1.	1.5(1)
$\chi(5\text{K})\text{emu cm}^{-3}$	-0.07	-0.12	-0.0009
el/at	5.66	4.75	5.53

Anisotropic Ferromagnetism in Metallic GaV_5Se_9

As in 1T-VSe_2 which is not a superconductor, the new phase GaV_5Se_9 undergoes a ferromagnetic transition at 21K (Figure 7). The magnetization measurements performed at 4.5K on oriented crystal (Figure 8) show two behaviours : one when $H_0 // c$ the full magnetization appears at 0.70T and an hysteresis loop is observed with a coercive field of 0.01T; the second when $H_0 \perp c$ the full magnetization is reached at 0.25T and we do not observe an hysteresis loop. The easy magnetization axis lies in the hexagonal face of the crystal, but we do not know exactly the relative position of the a and b axis. The anisotropic characters of this new phase can be the origin of the difference observed in the values of the susceptibility measured in zero field cooling (ZFC) (\blacksquare) and those obtained in field cooling (FC) (\square) at low temperature (Figure 7).

CONCLUSIONS

By reference to the carbon chemistry and especially to the intercalated graphite with alkali metal atoms, our purpose at the beginning was to include superconducting chains (intermetallic A15 superconductors) in a metallic dichalcogenides of transition metal to form a multilayer system like in "misfit compounds". The three synthesized phases with a general formula BM_5Se_9 ($B = \text{Sn, Ga}$ and $M = \text{V, Ta, Nb}$) cannot be seen as intercalated compounds. Each of them can be described as a stacking of eight slabs Se-M-Se and one layer Sn-Nb-Sn . All the investigations made on these compounds such as metallographic or chemical studies and Raman or Mössbauer spectroscopies confirm the dissolution of the

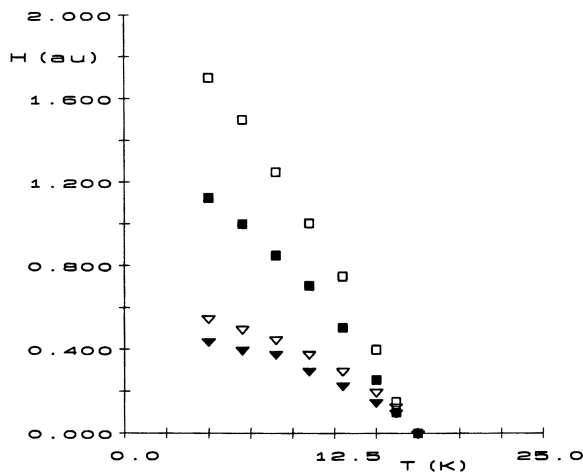


Figure 6 : Variation of critical fields H_{C1} and H_{C2} versus temperature for oriented SnNb_5Se_9 crystal. \square $H_{C2} \perp c$ in T ; \blacksquare $H_{C2} // c$ in T ; ∇ $H_{C1} \perp c$ in dT ; \blacktriangledown $H_{C1} // c$ in dT.

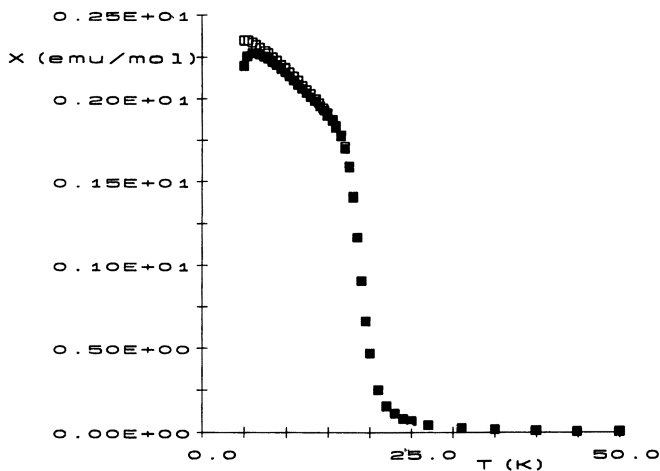


Figure 7 : Susceptibility versus temperature for GaV_5Se_9 for powder sample. \blacksquare ZFC ; \square FC.

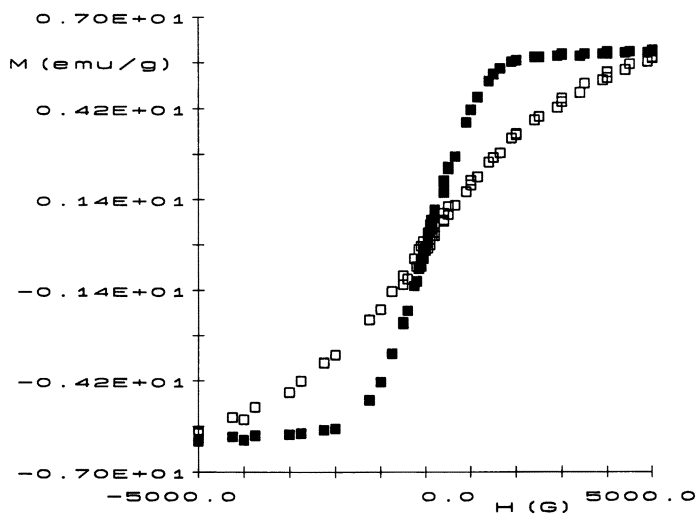


Figure 8 : Magnetization measurements at 4.5K on oriented GaV₅Se₉ crystals. ■ H₀-L_c ; □ H₀//c.

A15 phase in a diselenide matrix. Depending on the physical properties of the pristine MX_2 we synthesized superconducting or ferromagnetic phases. The anisotropy of the magnetic properties observed when the applied field is parallel to the face ($\perp c$) or perpendicular ($\parallel c$) like in the dichalcogenides MX_2 , confirms that these phases cannot be regarded as intergrowing phases. The critical temperature value of 17.5K obtained in SnNb_5Se_9 must be an intrinsic property, because, in NbSe_2 and in Nb_3Sn , the T_C are strongly depressed by the atomic disorder. The ferromagnetic properties observed in GaV_5Se_9 corroborate this trend.

LITERATURE CITED

- 1 - Keller, H.J. In *Chemistry and Physics of one dimensional metals*, Ed.; Plenum Press New York, 1977.
- 2 - Cheetman, A.; Day, P. In *Solid State Chemistry Compounds*, Eds.; Clarendon Press Oxford, 1992.
- 3 - Jérôme, D.; Schulz, H.J. *Adv. Phys.* **1982**, *31*(4), 299-490.
- 4 - Bernodz, J.G.; Muller, K.A. In *Earlier and Recent Aspect of Super Conductivity*, Eds.; Springer-Verlag, 1990.
- 5 - Kawaguchi, K.; Sohma, M. *Phys. Rev. B* **1992**, *46*, 14722.
- 6 - Mühge, Th.; Westerholdt, K.; Zabel, H.; Garif'yanov, N.N.; Gorynov, Yu.V.; Garifullin, I.A.; Khaliullin, G.G. *Phys. Rev. B* **1997**, *55*(14), 8945-8954.
- 7 - Motisuki, K. In *Structural phase transitions in layered transition metal compounds* Ed.; Publied by D. Reidel, Dordrecht, Holland, 1986.
- 8 - Kotami, A.; Suzuki, N. In *Recent advances in magnetism of transition compounds* Eds., World Scientific Publishing Co. Pte. Ltd., 1993.
- 9 - Muller, J. *Reports Prog. Phys.* **1980**, *43*, 41-687.
- 10 - Wiesinger, H.D. *Phys. Status Solidi(a)* **1977**, *41*, 465.
- 11 - Gregory, E.; Gulka, E.A.; Pyon, T. *IEEE Trans. Applied Superconductivity*, **1997**, *2*(7), 1498.
- 12 - Buzek, C.E.; Sulten, P.; Sirot, E.; Kohler, C.; Mocařir, P.; Peltier, F.; Grumbalt, G.; *IEEE Trans. Applied Superconductivity*, **1997**, *2*(7), 1041.
- 13 - Hardy, G.F.; Hulm, J.D. *Phys. Rev.* **1954**, *93*, 104.
- 14 - Mathias, B.T.; Geballe, T.H.; Geller, S.; Corenzwit, E. *Phys. Rev.* **1954**, *95*, 1953.
- 15 - Staudenmann, J.L. *Solid State Comm.* **1978**, *26*, 461.
- 16 - Waterstrot, R.M. Thesis n° 1871, University of Geneva, 1978.
- 17 - Staudenmann, J.L. Thesis N=F81735, University of Geneva, 1976.
- 18 - Flükiger, R.; Staudenmann, J.L.; Fischer, P. *J. Less-Common Metals* **1976**, *50*, 253.
- 19 - Flükiger, R.; Jorda, J.L. *Solid State Comm.* **1974**, *14*, 443.
- 20 - Testardi, L.R. *Cryogenics* **1977**, *17*, 67.
- 21 - Goldman, B.B. *Reports Prog. Phys.* **1966**, *29*, 445.
- 22 - Hechler, K.; Horn, G.; Otto, G.; Saur, E. *J. Low Temp. Phys.* **1969**, *1*, 29.
- 23 - Foner, S.; McNiff, E.J. *Physica* **1976**, *58A*, 318.
- 24 - Batterman, B.W.; Barrett, C.S. *Phys. Rev. Letters* **1964**, *13*, 310.
- 25 - Shirane, G.; Axe, J.D.; Bugeneun, R.J. *Solid State Comm.* **1971**, *9*, 397.
- 26 - Vieland, L.J.; Cohen, R.W.; Rehwold, W. *Phys. Rev. Letters* **1971**, *26*, 373.
- 27 - Junod, A.; Muller, J.; Rietschel, H.; Schneider, E. *J. Phys. and Chem. Solids* **1978**, *39*, 317.
- 28 - Labbé, J.; Friedel, J. *J. Phys.* **1966**, *27*, 153-303.
- 29 - Gor'kov, L.P. *Soviet Phys. Cryst. JETP* **1974**, *38*, 380.
- 30 - Khoder, A.F.; Labbé, J.; Couach, M. *Ann. Chim. Fr.* **1984**, *9*, 851.
- 31 - Khoder, A.F.; Labbé, J.; Couach, M.; Sénateur, J.P. *J. Phys.* **1986**, *47*, 1233.

- 32 - Levy, F. In *Physics and Chemistry of Materials with Layered Structures*, Ed.; D. Reidel, Dordrecht, Holland, 1976-1979, vol 1-6.
- 33 - Wilson, J.A.; Yoffe, A.D. *Adv. Phys.* **1969**, *18*, 193.
- 34 - Wilson, J.A.; DiSalvo, F.J.; Mahajan, S. *Adv. Phys.* **1975**, *24*, 117.
- 35 - Friend, R.H.; Jérôme, D. *J. Phys. C12* **1979**, 1141.
- 36 - Sugai, S. *Phys Status Solidi B* **1985**, *129*, 13.
- 37 - Jérôme, D.; Berthier, C.; Molinié P.; Rouxel, J. *J. Phys.* **1976**, *37*, C4-125.
- 38 - Berthier, C.; Molinié, P.; Jérôme, D. *Solid State Comm.* **1976**, *18*, 1393.
- 39 - Williams, P.M.; Parry, G.S.; Srcuby, C.B. *Phil. Mag.* **1974**, *29*, 695.
- 40 - Moncton, D.E.; Axe, J.D.; DiSalvo, F.J. *Phys. Rev. B* **1977**, *16*, 801.
- 41 - Ayache, C.; Currat, R.; Molinié, P. *Physica B* **1992**, *180-181*, 333.
- 42 - Ayache, C.; Currat, R.; Hennion, B.; Molinié, P. *J. Phys. IV* **1993**, *3(C2)*, 125.
- 43 - Tsang, J.; Smith, J.E.; Shafer, M.W. *Phys. Rev. Letters* **1976**, *37*, 1407.
- 44 - Steigmeyer, E.F.; Harbeke, G.; Andersset, H.; DiSalvo, F.J. *Solid State Comm.* **1976**, *20*, 667.
- 45 - Holly, J.A.; Klein, M.V.; McMillan, W.L.; Meyer, S.F. *Phys. Rev. Letters* **1976**, *37*, 1145.
- 46 - Wertheim, G.K.; DiSalvo, F.J.; Chiang, S. *Phys. Rev. B* **1976**, *13*, 5476.
- 47 - Hugues, H.B.; Pollak, R.A. *Comm. Phys.* **1976**, *1*, 61.
- 48 - Burtz, T.; Vasquez, A.; Ernst, H.; Lerf, A. *Phys. Rev. Lett.* **1976**, *58A*, 51.
- 49 - Molinié, P.; Rouxel, J.; Berthier, C.; Jérôme, D. *Solid State Comm.* **1976**, *19*, 131.
- 50 - Berthier, C.; Jérôme, D.; Molinié, P. *J. Phys. C*, (Solid State Phys.) **1978**, *11*, 787.
- 51 - Molinié, P.; Jérôme, D.; Grant, A.J. *Phil. Mag.* **1974**, *30*, 1091.
- 52 - Smith, T.F.; Delong, L.E.; Mosdembough, A.R.; Geballe, T.H.; Schwall, R.E. *J. Phys. C* **1972**, *5*, L230.
- 53 - Mattheis, L.F. *Phys. Rev. B* **1973**, *8*, 3719.
- 54 - Woolley, A.M.; Wexler, B. *J. Phys. C*, **1977**, *C10*, 2601.
- 55 - Delaplace, R.; Jérôme, D.; Molinié, P. *J. Phys. Lett.* **1976**, *37*, L13.
- 56 - Corbett, J.W.; Bourgouin, J.C. In *Points Defect in Solids*; Grawford, J.H., Slifkin L.M., Ed.; Plenum, New York, **1975**.
- 57 - Mutka, H. Ph D Thesis, University of Orsay.
- 58 - Nabutovokii, V.M.; Shapiro, B.Y. *Solid State Comm.* **1981**, *40*, 303.
- 59 - Mutka, H.; Zuppiroli, L.; Molinié, P.; Bourgouin, J.C. *Phys. Rev.* **1981**, *B23*, 503.
- 60 - DiSalvo, F.J.; Wilson, J.A.; Waszczak, J.V. *Phys. Rev. Lett.* **1976**, *36*, 885.
- 61 - Gras, J.P.; Haen, P.; Monceau, P.; Waysand, G.; Molinié, P.; Rouxel, J. *Il Nuivo Cimento* **1977**, *1(3)*, 519.
- 62 - *Intercalation chemistry*; Whittingham, M.S.; Jacobson, A.J., Eds.; Academic Press: New York, **1982**.
- 63 - Schneemeyer, L.F.; Sienko, M.J. *J. Less-Common Metals* **1978**, *62*, 343.
- 64 - Levy, F.; Froidevaux, Y. *J. Phys. C* (Solid State Phys.) **1979**, *12*, 473.
- 65 - Wieggers, G.A.; Meerschaut, A. *J. Alloys and Compounds* **1992**, *178*, 351.
- 66 - Auriel, C.; Roesky, R.; Meerschaut, A.; Rouxel, J. *Mater. Research Bull.* **1993**, *28*, 247-254.
- 67 - Oosawa, Y.; Gotoh, Y.; Akimoto, J.; Tsunoda, T.; Sohma, M.; Onoda, M. *Japan J. Appl. Phys.* **1992**, *31*, L1096.
- 68 - Molinié, P. Ph D thesis, University of Nantes, **1977**.
- 69 - Brown, B.E.; Beersten, D.J. *Acta Cryst.* **1965**, *18*, 31.
- 70 - Rignault, J.; Morosini, G.; Tomas, A.; Molinié, P. *Acta Cryst.* **1982**, *B38*, 1557-1559.
- 71 - Friend, R.H.; Jérôme, D.; Schleich, D.M.; Molinié, P. *Solid State Comm.* **1978**, *27*, 169-173.
- 72 - Mutka, H.; Molinié, P. *J. Phys. C* (Solid State Phys.) **1982**, *15*, 6365-6319.
- 73 - Garoche, P.; Veyssié, J.J.; Manuel, P.; Molinié, P. *Solid State Comm.* **1976**, *19*, 455-460.

- 74 - Leblanc, A.; Molinié, P.; Bouaoud, S.E.; Ouli, Z. *Condensed Matter and Materials Comm.* **1997**, *4(2/3)*, 151-158.
- 75 - Soreau-Leblanc, A.; Molinié, P.; Faulques, E. *Physica C* **1997**, *282-287*, 1937.
- 76 - Soreau-Leblanc, A.; Molinié, P.; Jumas, J.C. *Physica C* **1997**, *282-287*, 741.
- 77 - Shier, J.S.; Taylor, R.D. *Phys. Rev.* **1968**, *174*, 346.
- 78 - Jumas, J.C.; Olivier-Fourcade, J.; Lavela, P.; Morales, J.; Tirado, J.L. *Chem. Mater.* **1995**, *7*, 1193.
- 79 - Gentile, P.S.; Driscoll, D.A.; Hockman, J. *Inorg. Chim. Acta* **1979**, *35*, 249.
- 80 - Chechersky, V.; Gal, M.; Homonnay, Z.; Vanko, Gy.; Kuzmann, E.; Tyagi, S. Greene, R.L.; Vertes, A.; Nath, A. *Physica C* **1997**, *C277*, 36-42.

Chapter 3

Application of Rutherford Backscattering Spectrometry to Cuprate Superconductors

Wei-Kan Chu, Jiarui Liu, and Zuhua Zhang

Texas Center of Superconductivity, University of Houston,
Houston, TX 77204

New developments in ion beam analysis were stimulated by the discovery of high temperature superconductors (HTS) in 1986. During the last decade, the range of ion beam energy and ion species were expanded mainly for ion beam analysis of cuprate superconductors. In this review paper, basic applications of ion backscattering spectrometry in cuprate superconductors will be summarized. For instance, stoichiometry measurement by RBS, film thickness and uniformity characterization, crystal and epitaxial film quality characterization by RBS/Channeling, radiation damage and regrowth of HTS superconductors and substrates will be discussed. The difficulties and possible solutions will be discussed. Some advanced applications of RBS and channeling in cuprate superconductors will be presented. For instance, study of atomic displacement/thermal vibration anomaly across T_c by RBS-Channeling, selective labeling by ^{18}O and NRA/channeling study of anomalies in selective sites of oxygen atoms, strain measurement between HTS films and substrates, buffer layer characterization and interdiffusion study will be discussed.

Rutherford backscattering spectrometry (RBS) is probably the most frequently used ion beam analytical technique among surface analysis tools. [1,2] Elastic scattering between energetic incident ions and atomic nuclei in a sample is the basis of the RBS technique, which was first investigated by Rutherford in 1911. When the incident ion energy is not too high (a fraction of MeV to a few MeV), the short-range nuclear force is screened by the Coulomb force between the nuclei. The interaction is classical and the process can be accurately described by the simple Coulomb potential. This technique is absolute quantitative due to its classical, accurately predictable cross section. The technique is also independent of chemical or physical states of the materials because the information comes only from the interaction between nuclei. The other advantages of RBS are high elemental

or isotopic sensitivity, high depth resolution and non-destructibility. Since the mid-70s RBS has evolved from an obscure nuclear technique into a mature analytical tool for surface and near-surface layer analysis. The principal application field of RBS was related to semiconductor materials, such as doping by ion implantation, annealing and crystal regrowth, thin film characterization, interface reaction and interdiffusion measurements. In 1986, many years of searching for high Tc superconductors led to the discovery of Cu-O based compounds $\text{LaBa}_2\text{Cu}_3\text{O}_{7.8}$ with Tc of 37 K and then $\text{YBa}_2\text{Cu}_3\text{O}_{7.8}$ with Tc of 93 K in 1987.[3,4] RBS can be a simple and reliable method for stoichiometry measurement in new material searching. A decisive improvement of the critical current density in high Tc materials has been achieved with thin films.[5] RBS, as a well-known analysis technique for thin films, has successfully been applied in routine analysis in order to optimize the procedure of film preparation. Variation of compositions at interfaces due to reactions can be analyzed nondestructively, together with the crystal quality of the film as a function of depth. Lattice mismatch and the associated strain can be determined as well as the extent of mosaic spread. In more than 10 years of high Tc superconductor research, RBS has been further developed to fulfil the materials research requirements.

In this paper we discuss the basic problems of RBS application in HTS materials characterization and some advanced topics of HTS research by using RBS-channeling analysis. Readers who want to know the details of RBS technique may find some basics of RBS in refs. 1 and 2.

HTS characterization by RBS

RBS can be successfully applied in basic characterization of both bulk and thin film HTS samples in composition, elements concentration, depth profiling, film thickness determination, diffusion and/or interface reaction between HTS film, buffer-layer and substrate.

HTS thin films preparation and characterization are important material issues for both basic research and application. HTS thin films with excellent superconducting properties in Tc and Jc are important materials for electronic devices. High quality HTS films with different orientations are also important for basic research in superconductivity. Various thin film preparation techniques have been applied and a large number of substrate materials with and without buffer layers have been tested in HTS thin film preparation. RBS has been routinely used in optimization of HTS films providing simple, fast and reliable information on the film thickness, elemental composition and the depth profiles, crystalline quality, degree of homogeneity and the possible diffusion and interfacial reaction.

Different ions, from p, α -particle to Li, C, O or even heavier ions in a energy range from keV to hundreds MeV can be used for RBS analysis depending on the mass resolution, depth resolution and elements sensitivity required. MeV α -particle beam is most often used due to its more accurate stopping power. Li and other heavy ions with higher energy are used to get better mass resolution for heavy elements and better depth resolution. 2 MeV proton and 3.05 MeV or up to 6-8.8 MeV α -particle beams are used for non-Rutherford backscattering to get enhanced sensitivity for light elements such as oxygen, carbon and others. Computer simulation is necessary to get accurate results. There are many good software packages for RBS simulations, such as RUMP,[6] RBX [7] and GISA.[8]

Film thickness measurement: RBS is a unique tool to determine the film thickness. The main advantage of RBS in this application is that it can carry out a non-destructive measurement on unpatterned film and provide the thickness of individual layers of multilayer samples. One example shown in Fig.1 is a $\text{YBa}_2\text{Cu}_3\text{O}_{7.8}$ film of 190 nm on MgO substrate with 100 SrTiO_3 buffer layer. The thickness in atomic density can be obtained within 5% uncertainty. The geometrical thickness of the film can be calculated from the energy difference ΔE between the front and back edges of an element spectrum, knowing the $\text{YBa}_2\text{Cu}_3\text{O}_{7.8}$ density and the stopping cross section. Unfortunately, according to our experience and reports from other laboratories, the thickness from RBS is always less by 15-20% than the geometrical thickness by other measurements. Borgesen et al. re-measured the stopping cross section for elemental Y, Cu and Ba at energies between 0.6 and 5.14 MeV. [9] The only problem they found is that the stopping cross section of Ba at 1.5 MeV is 7% less than Ziegler's prediction. The stopping cross section of $\text{YBa}_2\text{Cu}_3\text{O}_{7.8}$ based on Borgesen's data and Bragg's rule can not explain the 15-20% problem in RBS thickness determination. Cheang-Wong et al. and then Quan et al. measured the stopping cross section of amorphous $\text{YBa}_2\text{Cu}_3\text{O}_{7.8}$ films and epitaxial $\text{YBa}_2\text{Cu}_3\text{O}_{7.8}$ films respectively. [10,11] The discrepancies between these measurements and Ziegler's prediction are 12% and 15% respectively. The reason for these discrepancies may be 1) violation of Bragg's rule; 2) effect of solid oxygen; 3) structure effect and 4) density difference due to light elements impurities. While the explanation is still not clear, we suggest using a correction factor of 0.88 for the predicted stopping cross section of $\text{YBa}_2\text{Cu}_3\text{O}_{7.8}$ to get geometrical thickness.

Elements composition and stoichiometry: The elemental composition can be determined in area density, $(\text{Nt})_i$, in atoms/cm² for the element i :

$$(\text{Nt})_i = A_i / (\Omega \sigma_i)$$

where t is the geometric film thickness, N is the atomic density, Q is the number of incident ions, Ω is the detector solid angle and σ_i is the scattering cross section. In material study, very often the average elements ratio stoichiometry is more important than the absolute atomic density N . The average ratio of element X and Y can be determined simply from $N_x/N_y = A_x \sigma_y / A_y \sigma_x$. When the peaks for different elements are well separated, as shown in Fig.1, A_x and A_y can be taken from the total counts under the separate peaks, so the accuracy is mainly determined by the statistic error. If all correction factors for the cross section (nuclear interaction and electron screening factor) are considered accurately, better than 1% uncertainty of the stoichiometry can be reached. The area density can be uncertain by about 3% from the absolute measurements. In $\text{YBa}_2\text{Cu}_3\text{O}_{7.8}$ thin film analysis in the case shown in Fig.1, the stoichiometry of Y, Ba and Cu can be obtained with the error better than 1%. In a thicker film, different element peaks can be separated by incident ions with higher energy. Martin et. al showed that with an 8.8 MeV α -particle beam elements peaks can be separated in a 770 nm thick film. [12] In bulk and thick film samples, when the elements peaks are overlapped as in Fig. 2, the number of counts A_i has to be taken from the plateau heights with less accuracy due to subtraction. The stoichiometry uncertainty again is determined mainly by the statistics. Quan et al. estimated the sensitivity limit for the detection of Y, Ba and Cu in $\text{YBa}_2\text{Cu}_3\text{O}_{7.8}$ samples by 2 MeV α -particles. [11] Fig. 3 shows this estimate is based on commonly used experimental parameters: $Q = 10\text{-}15 \mu\text{C}$, $\Omega = 3\text{-}5 \text{msr}$ and the channel width ΔE_{chan} is 1-4 keV. From Fig. 3 we can see that the sensitivity limits under these reasonable experimental parameters are 3.5%, 2% and 3% for Y, Ba and Cu in $\text{YBa}_2\text{Cu}_3\text{O}_{7.8}$ respectively. If the plateau height count can be increased by a factor of 10, the sensitivity

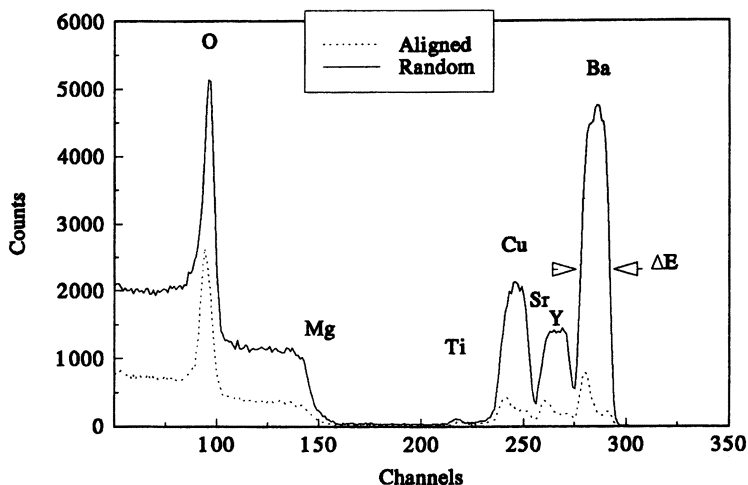
YBCO/SrTiO₃/MgO

Figure 1: RBS spectrum of YBa₂Cu₃O_{7.8} thin film (190 nm) on MgO substrate with a 10 nm SrTiO₃ buffer layer. The incident α -particle energy is 3.05 MeV for resonance scattering on ¹⁶O.

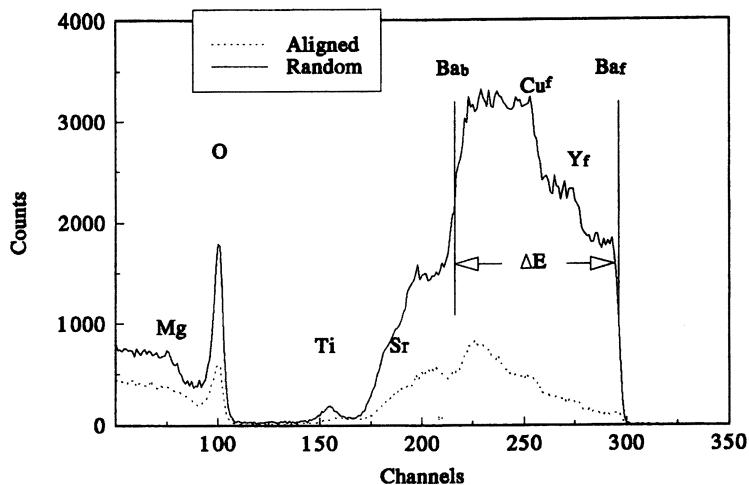
YBCO/SrTiO₃/MgO

Figure 2: RBS spectrum of YBa₂Cu₃O_{7.8} thick film (1000 nm) on MgO substrate with a 40 nm SrTiO₃ buffer layer. The incident α -particle energy is 3.05 MeV for resonance scattering on ¹⁶O. The Mg signal is shifted below the ¹⁶O resonance peak from the YBa₂Cu₃O_{7.8} film, and the ¹⁶O signal can be measured accurately without heavy elements background.

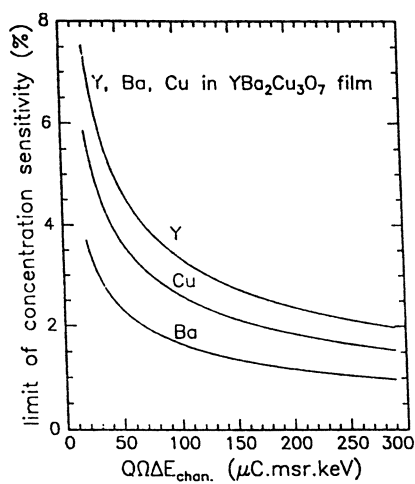
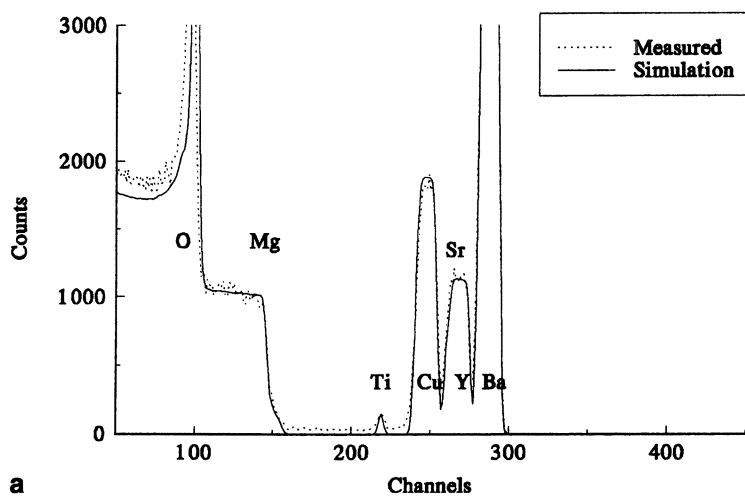


Figure 3: Sensitivity limit of 2 MeV α -RBS for Y, Ba and Cu in a film of $\text{YBa}_2\text{Cu}_3\text{O}_{7-\delta}$, where $Q\Omega\Delta E_{\text{chan}}$ is a product of beam dose, detector solid angle and energy width per channel. Typical experimental parameters are: $Q=10-15 \mu\text{C}$, $\Omega=3-5 \text{ msr}$ and $\Delta E_{\text{chan}} = 1-4 \text{ keV}$.

limit will be better than 1% for all three elements. A difficult problem in $\text{YBa}_2\text{Cu}_3\text{O}_{7.8}$ characterization by standard RBS is the oxygen ration determination. Since the superconductivity of HTS materials is very sensitive to the oxygen concentration, the measurement of oxygen concentration is of particular interest. The sensitivity of oxygen determination is low due to the overlapping of oxygen signals on the signals from substrates and heavy elements in the sample, if the sample is thick. Quan et al. estimated the oxygen sensitivity in $\text{YBa}_2\text{Cu}_3\text{O}_{7.8}$ film at different substrates and got a sensitivity of 9% for silicon substrate to 12% for SrTiO_3 substrate. [11] To overcome this difficulty, different techniques have been used such as 3.05 MeV resonance on oxygen in (α, α) backscattering, [13-16] non-Rutherford scattering at higher α -particle energies up to 8.8 MeV, [12,17,18] non-Rutherford scattering by protons [19-22] and so on. A very popular method is the resonance (α, α) backscattering on oxygen at 3.05 MeV, where oxygen can be detected with enhanced sensitivity by a factor of 22, while the cross section of heavy elements are classical, as shown in Figs. 1 and 2. The oxygen sensitivity limit in this resonance method is from 3% to 5% depending on the atomic number of substrate elements and the optimization of other parameters. Fig.2 shows a well designed sample of $\text{YBa}_2\text{Cu}_3\text{O}_{7.8}$ film on MgO with a thin SrTiO_3 buffer layer. The oxygen peak is separated from the Mg signal due to the 1 μm $\text{YBa}_2\text{Cu}_3\text{O}_{7.8}$ film, so the resonance oxygen peak can be measured as a background-free element, similar to the Y, Ba and Cu peaks in Fig.1. In this case, the sensitivity for oxygen measurement is better than 3%. Chernenko et al. even claimed an accuracy of 1% for oxygen measurement by this resonance, obtained by 1) improved simulation with least square fitting; 2) using the oxygen ratio in substrate oxide as a standard, and 3) taking into account a double scattering process.[16] In non-Rutherford backscattering on oxygen by higher energy α -particle from 4-8.8 MeV, the cross section for oxygen can be enhanced by a factor of 10-150, so a sensitivity limit of 1-3% also can be realized, if careful simulation is performed. Jiang et al. performed non-Rutherford backscattering by 1.5-2.5 MeV proton for oxygen ratio measurement in $\text{YBa}_2\text{Cu}_3\text{O}_{7.8}$ film. Normalizing with the substrate oxygen in SrTiO_3 , an uncertainty of better than 5% has been achieved [22].

Depth profiling: HTS films are deposited on different substrates and sometimes with different buffer layers. The high temperature deposition and annealing for HTS film deposition may cause strong diffusion and/or interface reaction between HTS film, buffer layer and substrate. Depth profiling in the multilayer system is needed to clearly and quickly explore all kinds of problems in film deposition. RBS is the only method which can clearly and quickly provide non-destructive depth profiling in a multilayer system. It has been observed that deposition of $\text{YBa}_2\text{Cu}_3\text{O}_{7.8}$ films on some important electronic materials such as Si and sapphire is hopeless without a buffer layer, and different layers have been investigated by RBS. [23]. Fig. 4 shows RBS spectra of $\text{YBa}_2\text{Cu}_3\text{O}_{7.8}$ film on MgO with a buffer layer (a) and without a SrTiO_3 buffer layer (b). To get the depth profile near the interface, a multilayer simulation has to be performed. Qualitatively we can see from the differences between measured spectra and the simulated spectra without diffusion is that the back edges of the Cu in the sample without a buffer layer are smeared towards the substrate. In the spectrum without a buffer layer, the Cu back edge is smeared more than Y and Ba, so Cu is more active in the interface diffusion. RBS in combination with channeling effect can provide information of interface mismatch and defects depth profiles at the surface and interface, as described in the next paragraph.

RBS spectra of YBCO/SrTiO₃/MgO film
 $E\alpha = 3.05 \text{ MeV}, 165^\circ$



RBS spectra of YBCO/MgO film
 $E\alpha = 3.05 \text{ MeV}, 165^\circ$

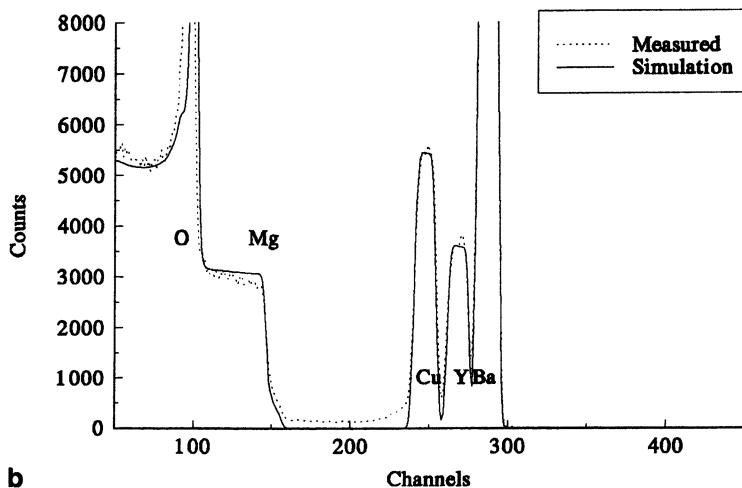


Figure 4 : YBa₂Cu₃O_{7- δ} film on MgO with a buffer layer (a) and without a buffer layer (b).

American Chemical Society
 Library
 1155 16th St., N.W.
 Washington, D.C. 20036

RBS-channeling characterization of HTS

RBS in combination with channeling effect is a powerful tool for crystal characterization in real space. RBS-channeling has been successfully used in routine measurement of HTS films in film preparation optimization. This technique also has been used in studies of film growth mechanism, radiation damage/regrowth and strain relaxation investigation in HTS films. The study of atomic displacement/thermal vibration anomalies by RBS-channeling will be introduced in the next paragraph.

High resolution RBS-channeling study of initial growth stage of YBCO films: The example presented here is especially interesting. It clearly demonstrates the power of depth profiling of the RBS-channeling technique. In normal RBS-channeling configuration using 2 MeV He ions and a Si detector set at a large angle to the He beam, the typical depth resolution is about 20 - 30 nm. Using glancing incidence geometry, the depth resolution can be increased to about 3 nm. However, by lowering the energy of the He ions and using an electrostatic analyzer detection system to replace the ordinary Si detector, the depth resolution of the RBS-channeling analysis can be further reduced to sub-monolayers. With such high depth resolution, P.D. Huttner et al. have successfully characterized the initial growth stage of YBCO epi-films on SrTiO₃ and MgO substrates [24]. The detailed description of the detection system is given in [25]. Fig. 5 is the backscattering spectra of ultrathin YBCO epi-film on a SrTiO₃ substrate (Fig. 5(a)) and on a MgO substrate (Fig. 5(b)) with thickness between 0.8 nm and 3.6 nm [24]. Only the RBS signals from the Ba atoms are shown in Fig. 5. For the films grown on the SrTiO₃ substrate (Fig. 5(a)), since the Ba signals for the 3.6 nm thick film show a rectangular shape, the authors concluded that the deposition of three unit cells of YBCO leads to a full and homogeneous coverage. For films with a thickness larger than 1.2 nm, since the RBS signals have the same maximum as that of a 3.6 nm thick film the authors further concluded that substrate coverage close to 100% is reached. However, the shape of the lower energy portion of the spectra, which corresponds to the backside of the films, is quite different. The spectra of the films which have a thickness equal to integral times of the unit cells, such as 1.2 nm (one unit cell), 2.4 nm or 3.6 nm, have a rather sharp backside indicating a smooth and planar back surface. Those films, which have a thickness equal to a fraction of unit cells (2.0 nm and 3.0 nm) are broadened with a step-like behavior. Based on the above RBS observations, the authors claimed that the initial growth stage of YBCO epi-film on SrTiO₃ substrate follows a layer-by-layer growth mode with one unit cell block as a growth layer. After one such layer covers the substrate, the growth of the next layer is initiated. The authors pointed out that the layer-by-layer growth in blocks of one unit cell on SrTiO₃ substrate agreed with observations of RHEED oscillations by Terashima et al. [26]

On the other hand, for film grown on MgO substrate, the authors observed quite a different growth mode. The RBS spectra for these films are shown in Fig. 5(b). While the spectrum of the 3.6 nm film on MgO is similar to that of the 3.6 nm film on SrTiO₃, the spectra for the 3.0 nm and 2.5 nm films are completely different. The lower energy edges of their spectra have a step-like shape with step widths corresponding to a thickness of unit cell. From the step height, the authors estimated the coverage. The conclusion is that for the 3.0 nm film the first unit cell layer is nearly completed while the coverage of the second and third layer is incomplete. For the thinner films (1.5 nm and 2.0 nm films), the first unit cell coverage is not completed but the shapes of the low energy tails indicate the presence of further unit cell blocks in the film height. Thus the authors concluded that the growth of YBCO film on MgO substrate follows the island growth mode. This conclusion is confirmed by Pennycook et al. with electron microscopy [27].

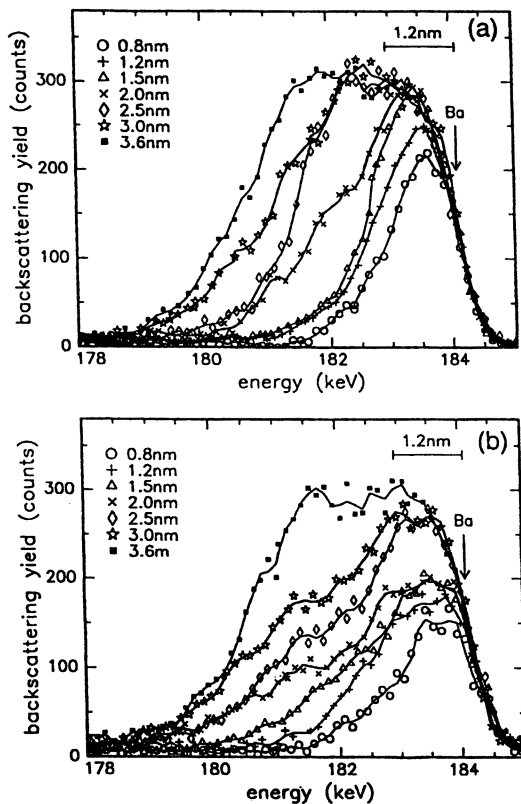


Figure 5: Backscattering spectra of ultra thin YBCO films with thickness between 0.8 nm and 3.6 nm on SrTiO₃ (a) and MgO (b) substrates. Only the signals from Ba atoms are shown. (Reproduced with permission from reference 24. Copyright 1996).

Radiation damage and regrowth: Structural defects play an important role in the electrical properties of high T_c superconductors. There are many ways to introduce structural defects into superconductors. In this paper, the emphasis will be on the radiation induced defects. For example, using high-energy light ion irradiation to create point defects or using low energy ion implantation to introduce impurities. In the former case, the concentration, the depth distribution and the annealing behaviors of these radiation created point defects are important parameters for interpreting the electrical behaviors of the superconductors. In the latter case, very often the sample will be amorphized and the recrystallization process needs to be carried out to recover the crystalline structure as well as the superconductivity. In general, X-ray diffraction can tell how good is the crystallinity of the superconductor. But it does not quantitatively provide detailed information on the concentration, the depth distribution of the point defects, or on the regrowth of the amorphized layers. TEM analysis is able to reveal the details of the microstructure of samples, but the sample preparation is time consuming and destructive. On the other hand, RBS-channeling can quantitatively provide such essential information in a fast and non-destructive way.

Several authors [28, 29] have studied the regrowth of amorphized YBCO thin films. The example presented here is from X.D. Wu et al. [28] on the regrowth study of an oxygen ion amorphized YBCO epi-film grown on LAO substrate. The RBS-channeling ψ_{\min} values for Ba are 3-5% for as-deposited films indicating high quality of the films. Fig. 6(a) is the RBS-channeling random and aligned spectra for an as-implanted sample. The Ba signals of the damaged layer in the aligned spectrum have reached random level indicating that the channeling effect has been lost due to disorder in the damaged layer. The thickness of the damaged layer is about 80 nm. Fig. 6(b) is the aligned spectra for the as-implanted, 650 °C/1hr. and 700 °C/1hr. annealed samples. It can be seen from these spectra that the solid epitaxial regrowth started from the interface, then proceeded towards the surface. Detailed RBS-channeling analysis on samples annealed at temperatures ranging from 650 °C to 1000 °C resulted an Arrhenius plot (Fig.6(c)) which shows single activation energy of 0.46 eV. However, the solid phase epitaxial regrowth process (SPE) does not always dominate the regrowth of the damaged YBCO epi-film. Several factors will affect the regrowth, such as the microstructure of the damaged layer, the annealing temperature, and the structure of the substrate [28-30]. Y. Li et al. studied the regrowth of Ar ion damaged YBCO epi-film on (100) SrTiO₃ substrate using X-ray diffraction and RBS-channeling analysis [30]. Fig. 7 displays the RBS-channeling spectra for YBCO film implanted with 100 keV $1 \times 10^{16}/\text{cm}^2$ Ar ions after annealing at different temperatures [30]. As can be seen in Fig. 7, the RBS yield in the aligned spectra reduces with the annealing temperatures, indicating the occurrence of the recrystallization. However, as compared with Fig. 6(b), the reduction of the RBS yield in Fig. 7 does not start at the interface. Instead, it starts all over the whole film. This indicates that in this case, homogeneous nucleation and reorientation, rather than the SPE process, dominated the regrowth.

Strain relaxation in YBCO epi-film observed by RBS-channeling: The most commonly used substrates for grown YBCO epi-films are MgO, SrTiO₃ and LaAlO₃. Due to the lattice mismatch between these substrates and the YBCO films, lattice strains can be expected in the initial stage of growth. However, as the thickness of the film increases beyond the critical thickness, the film relaxes. In the case of c-oriented film, such relaxation can be observed by the channeling angular-yield profile (channeling dip) measurement along the inclined axis. [31,32] The upper part of Fig.8 schematically shows an unstrained (relaxed) YBCO film on top of a (100) oriented MgO substrate. [32] The lower part of Fig.8 shows the channeling dip measured along the $\langle 100 \rangle$ (a) and the

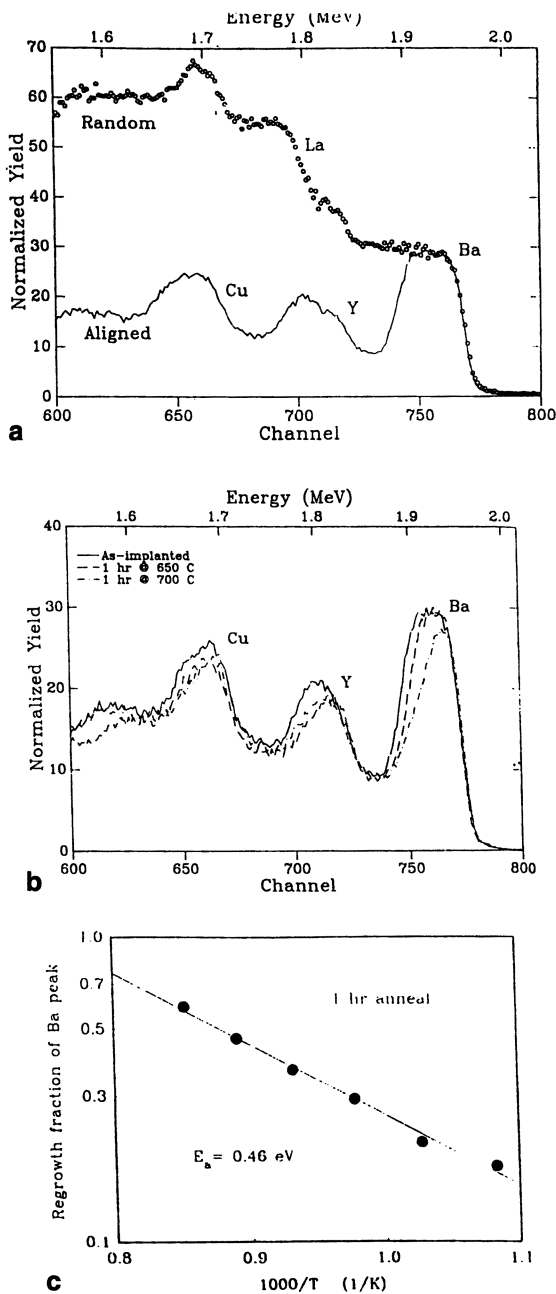


Figure 6: (a) 2.2 MeV He ions RBS-channeling random and aligned spectra of oxygen ions ($1 \times 10^{16}/\text{cm}^2$) as-damaged YBCO epi-films on LaAlO_3 substrate. (b) RBS-channeling aligned spectra for damaged films after annealing in oxygen for 1 hour at 650 °C and 700 °C. (c) Arrhenius plot of the regrowth. Single activation energy of 0.46 eV was obtained (Reproduced with permission from reference 28. Copyright 1993.)

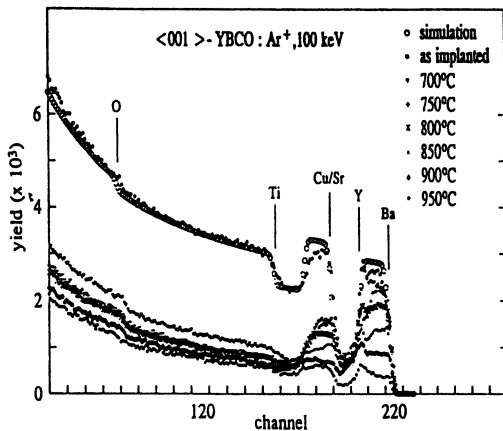


Figure 7: RBS-channeling spectra for YBCO film on SrTiO₃ implanted with 100 keV $1 \times 10^{16}/\text{cm}^2$ Ar ions after annealing at various temperatures ranging from 700 °C to 950 °C. (Reproduced with permission from reference 30. Copyright 1995.)

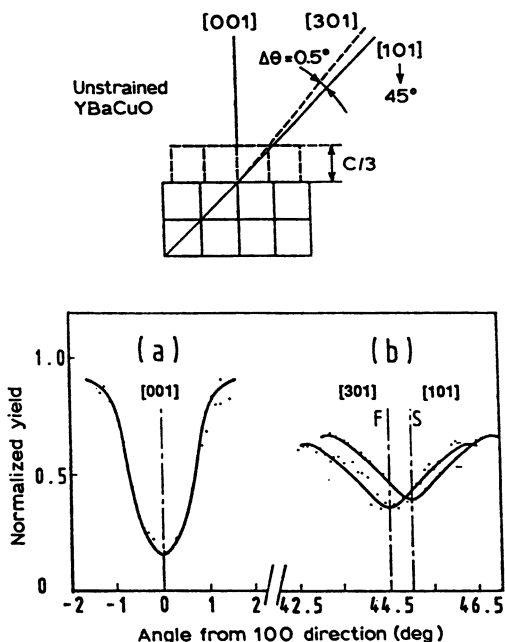


Figure 8: Upper portion: Schematic drawing of unstrained (relaxed) YBCO film on the top of a MgO substrate; Lower portion: Channeling dip of 1.8 MeV He ions through [001] (a) and [301] (b) directions of a YBCO epi-film on MgO. In (b) the angular difference between the [301] of the film and [001] directions of the substrate is clearly shown. (Reproduced with permission from reference 32. Copyright 1993.)

inclined $\langle 301 \rangle$ and $\langle 101 \rangle$ directions (b) on an 81 nm thick YBCO film on $\langle 100 \rangle$ MgO. The measured angular difference between the $\langle 301 \rangle$ axis of the film and the $\langle 101 \rangle$ axis of the MgO is 0.5° , which is in agreement with the calculated value for an unstrained film (Fig.8, upper part). This result indicates that the 81 nm thick YBCO film is relaxed. A similar result has been reported by H. Jhans et al. [31]

In the case of $\langle 110 \rangle$ oriented YBCO film, strain relaxation has been observed by J. Qu et al. [33] The YBCO films were deposited on $\langle 110 \rangle$ oriented SrTiO_3 substrate in Ar and O_2 mixture (~2:1) using an inverted cylindrical magnetron sputtering system. The substrate temperature during the deposition was 575°C , 745°C , and 785°C with a total gas pressure of 80, 280, and 320 mtorr respectively. The thickness of the films was between 300 nm and 400 nm. In the process of characterizing the quality of the $\langle 110 \rangle$ oriented YBCO film, it was observed that the center of the channeling dip of the films was not always aligned with that of the SrTiO_3 substrate (Fig.9). The angular deviation depends on the conditions employed in the deposition (substrate temperature and gas pressure). Since the substrate temperature and gas pressure control the oxygen content of the film, the angular deviation observed is related to the oxygen content. For the film deposited at $745^\circ\text{C}/280$ mtorr which is the optimal condition and offers high oxygen content, the observed deviation is 1° , while for the film deposited at $575^\circ\text{C}/80$ mtorr which offers low oxygen content, the observed deviation is zero. In YBCO crystal, an increase of oxygen content leads to a decrease in lattice constant in the c- and a- direction but an increase in the b-direction. So the more oxygen in the YBCO, the larger the difference in lattice constant between its a- and b- directions. Fig. 10 shows the schematics of the lattice of a $\langle 110 \rangle$ oriented YBCO lattice grown on a $\langle 110 \rangle$ oriented SrTiO_3 substrate [33]. For low oxygen content, the a- and b- directions have nearly equal lattice constant. Thus it is clear from Fig.10 that the $\langle 110 \rangle$ direction of the YBCO film should be well aligned with the substrate. However, for high oxygen content, the a- and b- directions have large differences, therefore the $\langle 110 \rangle$ direction of the film deviates from that of the substrate.

Atomic displacement/thermal vibration anomaly in HTS

The probability for a channeled probing particle to have close-encounter events (Backscattering, Nuclear reaction, or Particle Induced X-rays Emission etc.) with atoms in a crystal is very sensitive to the displacement of the atoms off the normal atomic axis or plane. A small displacement could cause significant reduction of the angular width of a channeling dip or an increase of the width if the displacement makes a rough atomic row smoother. A displacement as small as 1 picometer can be detected.

For high T_c superconductors, the association of the phonons and other structural changes with the superconducting phase transition has been considered as vital for the interpretation of its superconductivity since the discovery of this new class of materials [3, 4]. Ion channeling technique provides a very sensitive direct real space probe for studying the displacement of atoms or distortion of the lattice in high T_c superconductors. By measuring the width of the channeling dip around the transition temperature T_c , the change of the displacement of the atoms in high T_c superconductors can be analyzed.

Several groups have used RBS-channeling techniques to study the structural displacement of atoms in high T_c superconductors [34-39]. Fig. 11 [34] shows a set of channeling dips measured at temperatures of 100 K, 80 K, and 33 K on a $[001]$ oriented YBCO single crystal ($T_c = 92$ K). It can be seen that while cooling down from 100 K (above T_c) to 80 K (below T_c), the FWHM of the channeling dip increased 5-6%. This abrupt 5-6%

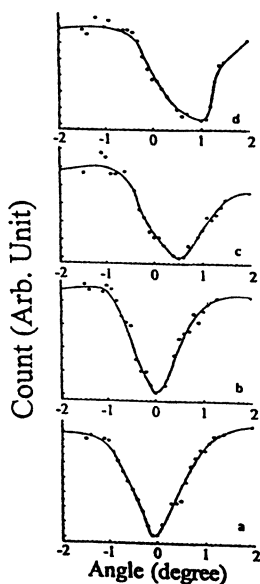


Figure 9: Channeling dips of $\{110\}$ oriented YBCO film prepared with different parameters (temperature/total pressure of argon and oxygen gas). (a) substrate, (b) film grown at 575 °C/80 mtorr; (c) film grown at 785 °C/320 mtorr; (d) film grown at 745 °C/280 mtorr. (Reproduced with permission from reference 33. Copyright 1996.)

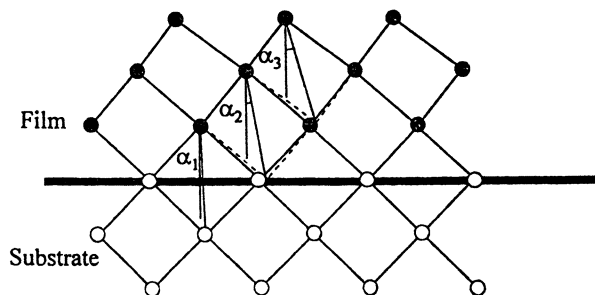


Figure 10: Schematics for the $\{110\}$ direction misorientation between YBCO film and SrTiO_3 substrate. (Reproduced with permission from reference 33. Copyright 1996.)

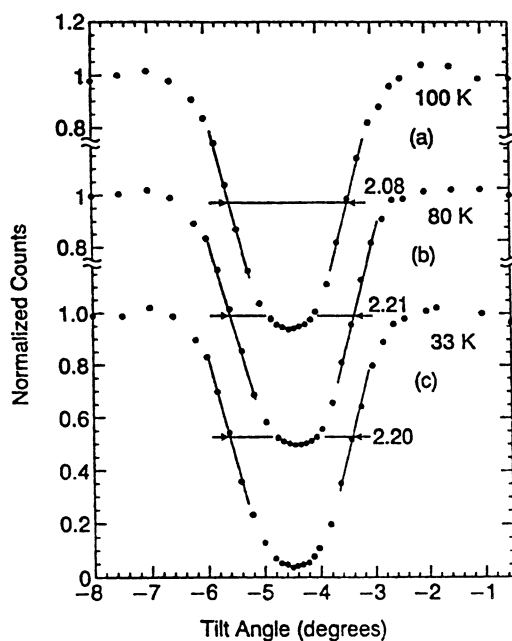


Figure 11: The [001] channeling dips (angular scans) taken at temperatures above T_c , 100 K (a) and below T_c , 80 K (b) and 33 K (c) in YBCO single crystal ($T_c = 92.5$ K). A 5–6% increase in the FWHM is seen across T_c between 100 K and 80 K, with practically no change between 80 K and 33 K. (Reproduced with permission from reference 36. Copyright 1989.)

increase across T_c is about two times the value if the atomic displacement follows the normal Debye behavior. From 80 K to 33 K, no appreciable change occurred. However, a similar measurement on a non-superconducting YBCO single crystal showed that no abrupt change is seen in the FWHM from 100 K to 80 K (Fig. 12(ref. 34)). The observed variation of FWHM follows the normal Debye behavior. Channeling analysis further reveals that such abrupt jump in the FWHM of the channeling dip is associated with the T_c . Fig. 13 [37] shows several channeling dips measured on the oxygen deficient YBCO crystal with T_c only 54 K[37]. For this sample, the abrupt change only occurred across 54 K.

It should be mentioned here that the channeling dips shown in Fig. 11, Fig. 12, and Fig. 13 were made using the combined RBS signals from Cu, Ba and Y sublattices. It has been shown that channeling dips made using only the RBS signals from Ba and Y sublattices have no abrupt changes across T_c . This indicates that the abnormal structural change across T_c is associated with Cu sublattices. What about the oxygen sublattices? Due to the low sensitivity to oxygen, conventional RBS is not suitable to analyze the oxygen atoms when they are in a heavy matrix. To overcome this difficulty, J.U. Andersen et al [35] used 7.6 MeV He ion $^{16}\text{O}(\alpha,\alpha)^{16}\text{O}$ non-Rutherford elastic resonance scattering. This resonance enhances the oxygen signal to 120 times the conventional RBS signal making the accurate measurement of the displacement of oxygen atoms possible. Fig. 14 shows the energy spectrum taken on a YBCO sample using a He ion beam of resonance scattering energy 7.62 MeV at random incidence [35]. The number of the He ions scattered from oxygen atoms is much more than that from the Cu, Ba and Y atoms. Several channeling dips around T_c were made with the enhanced oxygen signals. In order to extract the displacement of the oxygen atoms from the channeling dips, a sophisticated computer simulation program was developed. A small increase between 70 K and 100 K in oxygen displacement/vibration has been established. But no evidence has been observed for the larger increase in O4 atoms (apical oxygen) as seen in Ref.40. Further experiments are needed to clarify the discrepancy.

Selective labeling by ^{18}O and NRA/Channeling analysis

Oxygen is a key element in high temperature oxide superconductors. The physical properties of HTS materials, such as $\text{YBa}_2\text{Cu}_3\text{O}_{7-\delta}$, depend on both the oxygen stoichiometry and the ordering of oxygen atoms. For $\text{YBa}_2\text{Cu}_3\text{O}_{7-\delta}$, the critical temperature T_c reaches a maximum of 93 K for $0 < \delta < 0.2$ and decreases to 60 K for $0.3 < \delta < 0.5$. At $\delta > 0.6$ the phase transition from orthorhombic to tetragonal occurs and $\text{YBa}_2\text{Cu}_3\text{O}_{7-\delta}$ becomes a transparent insulator. The phase transition is manipulated by the oxygen loss at a specific crystallographic site, oxygen atoms in Cu-O chain or O(1), as shown in Fig.15. Selective study of the concentration and ordering of the oxygen atoms O(1) is of particular interest for both the basic research of superconductivity and the application of $\text{YBa}_2\text{Cu}_3\text{O}_{7-\delta}$ films. Investigations of the thermodynamic stability of $\text{YBa}_2\text{Cu}_3\text{O}_{7-\delta}$ as a function of temperature and oxygen pressure indicates the possibility for selective labeling of O(1) with different isotopes. Cheang Wong et al. and Garcia Lopez et al. have successfully labeled O(1) with ^{18}O in c- $\text{YBa}_2\text{Cu}_3\text{O}_{7-\delta}$ and α - $\text{YBa}_2\text{Cu}_3\text{O}_{7-\delta}$ film, respectively. [41, 42] The selective labeling can be performed at different levels: 1). Selective labeling in the CuO chain O(1); 2). Partial labeling of oxygen in the CuO₂ planes O(2), O(3) and of bridging oxygen O(4); 3). total oxygen exchange. Fig. 16 shows a RBS/Channeling spectra at 3.045 MeV performed at room temperature for a 540 nm thick $\text{YBa}_2\text{Cu}_3^{16}\text{O}_6^{18}\text{O}_1$ film. Once the selective labeling has been done, oxygen atoms at different crystallographic sites can be measured or depth profiled by resonance BS on ^{16}O

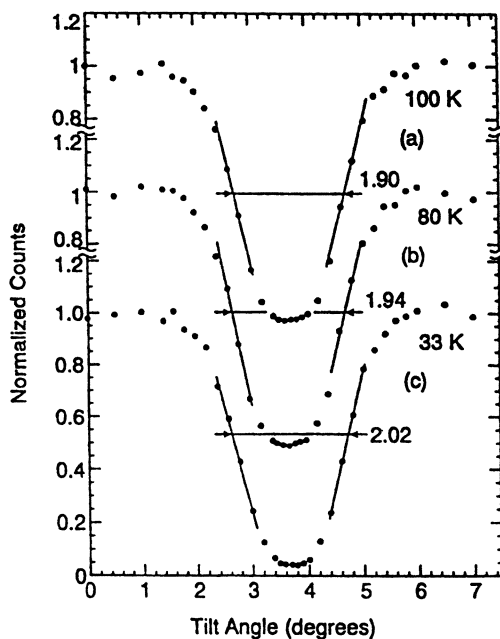


Figure 12: Same as in Fig. D except the sample is non-superconducting. No abrupt change in FWHM is seen, instead there is a small increase throughout the temperature range as expected from a normal Debye-like behavior. (Reproduced with permission from reference 36. Copyright 1989.)

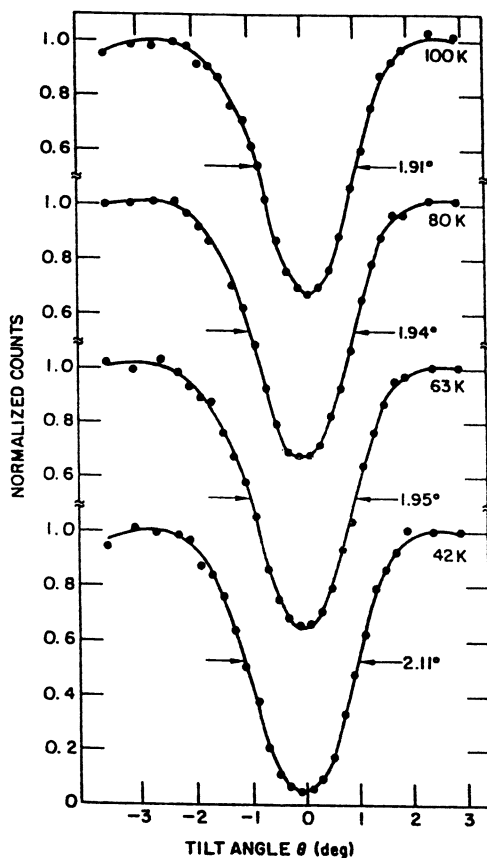


Figure 13: 1.5 MeV He ions RBS-channeling angular scans along the [001] of a YBCO single crystal with $T_c = 54$ K. Scans were made at temperatures above T_c : 100 K, 80 K, 63 K and below T_c : 42 K. Sudden increase of FWHM occurred between 63 K and 42 K. (Reproduced with permission from reference 39. Copyright 1991.)

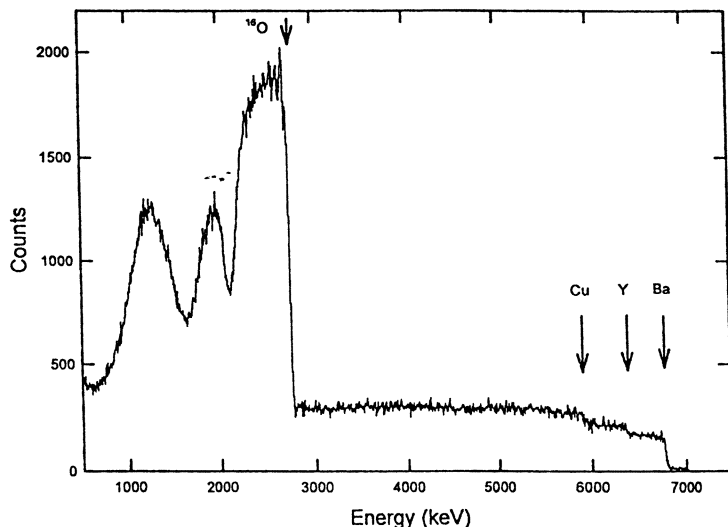


Figure 14: Non-Rutherford elastic scattering energy spectrum of 7.62 MeV He ions on a YBCO single crystal at random incidence with a scattering angle of $173^\circ - 176^\circ$ to the incidence direction. Upper edges of the Ba, Y, Cu and O are marked. The oxygen signals have been tremendously enhanced. (Reproduced with permission from reference 37. Copyright 1989.)

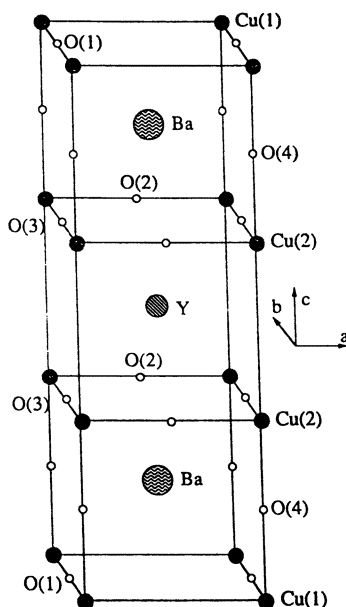


Figure 15. Crystal structures of orthorhombic $\text{YBa}_2\text{Cu}_3\text{O}_{7.8}$ which shows the notation of different atoms.

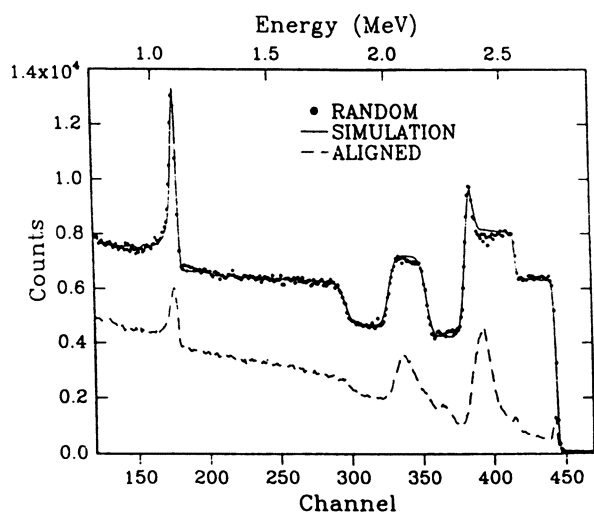


Figure 16. RBS/Channeling spectra at 3.045 MeV performed at room temperature for a 540 nm thick $\text{YBa}_2\text{Cu}_3^{16}\text{O}_6^{18}\text{O}_1$ film. (Reproduced with permission from reference 42. Copyright 1994.)

or by nuclear reaction on ^{18}O . We introduce a nuclear reaction technique for ^{18}O analysis as a useful extension of the ion beam analysis technique for HTS research.

^{18}O is a minor isotope of 0.204% natural abundance relative to the 99.76% abundance of the major isotope ^{16}O . In an ^{18}O labeling in a reasonable level the natural ^{18}O of 0.204% can be considered as a low background. The large difference in mass between ^{18}O and ^{16}O (12.5%) can provide evident isotope effect in the materials studied. ^{18}O is an excellent tracer, and has been successfully applied in isotope effect of Tc in $\text{YBa}_2\text{Cu}_3\text{O}_{7-\delta}$ [43] in the study of lattice vibration modes [44] in the anisotropy measurement of the diffusion coefficient along a/b and c-axes, [45] in the physics of defects in the oxygen sublattice, [42] and the oxygen diffusion in ^{18}O -implanted YBCO films.[46] The $^{18}\text{O}(p,\alpha)^{15}\text{N}$ reaction shows high Q-value and large cross section, in contrast to p-induced reactions on ^{16}O which all have negative reaction energy, and thus make no interference with the major isotope ^{16}O at low incident proton energy. There are two methods in NRA: (1) method of reaction resonance and (2) method of energy analysis of the reaction product charged particles. The widely used resonance at 629 keV is useful for profiling the near surface layer of a few thousand Å with depth resolution of 200 Å to 500 Å. [42] The depth resolution in the case of energy analysis depends on the energy resolution. After a careful optimization, we suggest using energy analysis of the α -particles to get better depth resolution than the resonance method, as shown in Fig. 17. [47] The depth resolution is 170 Å near the surface and to 250 Å at the 0.5 μm depth. The energy analysis method is faster, simpler, and has a good depth resolution for thick samples, which is very similar to RBS. As an example, Fig. 18 shows depth profiles of ^{18}O in 200 keV ^{18}O -implanted SrTiO_3 substrate single crystal for at RT. The measured profile is in good agreement with TRIM simulation.

Combining selective labeling with 3.05 MeV resonance scattering on ^{16}O and nuclear reaction analysis of ^{18}O , a series of important investigations can be performed. The most important topic is the lattice thermal vibration study by channeling as mentioned in paragraph 4. The thermal vibration of O(1) is most interesting for superconductivity mechanism studies, but unfortunately it is not active in Raman spectrometry. When O(1) is selectively labeled by ^{18}O , NRA/channeling with α -particle from (p, α) reaction can be selectively applied for the measurement of O(1) thermal vibration and all the rest of the oxygen atoms can be measured by 3.05 MeV resonance BS/channeling. Another topic is to study the defects on Cu-O chains and their correlation with the defects in the rest of the oxygen sublattice and the defects in the cation sublattice. The oxygen loss or disordering due to ion irradiation from Cu-O chains and other oxygen sublattice is also interesting for the Tc degradation mechanism.

Summary

During the past decade the RBS technique, and ion beam analysis in general, have been further developed mainly for HTS material research and development. Routine RBS provides quick answers to many HTS materials issues. As mentioned in paragraphs 2 and 3, the basic characterization with RBS/channeling was applied for the measurement of stoichiometry, thin film thickness, elements depth profiling, interface diffusion and/or interface reaction, crystal quality investigation of HTS single crystals and epitaxial films, radiation damage and crystal regrowth and strain measurement in thin films. An advanced RBS/channeling measurement yields more specific information depending on the material issues it is designed for. Two advanced applications, the study of thermal vibration anomaly across Tc by RBS/Channeling and the selective labeling by ^{18}O and NRA/channeling study of anomaly in selective oxygen sublattice, were discussed in some

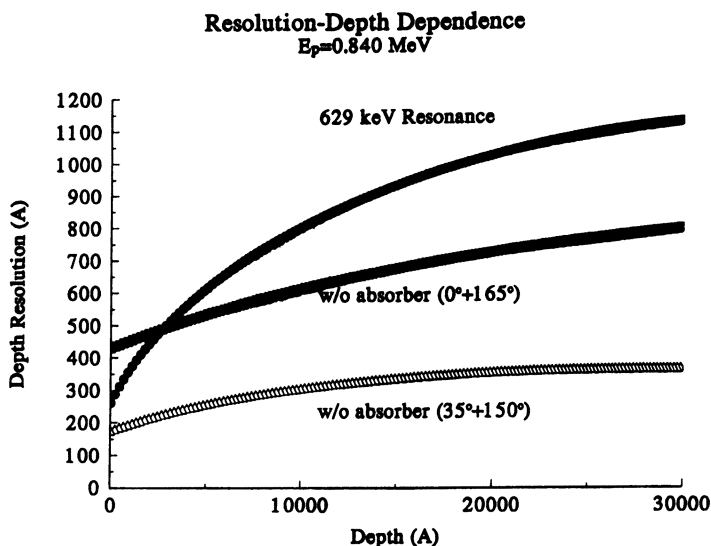


Figure 17. Depth resolution-depth dependence in YSZ crystal for 629 keV resonance method and method of energy analysis for different geometries without absorber. The $(0^\circ+165^\circ)$ geometry is for normal incident beam and the detector at 165° . The $(35^\circ+150^\circ)$ geometry is for the detector at 150° and the sample is tilted by 35° .

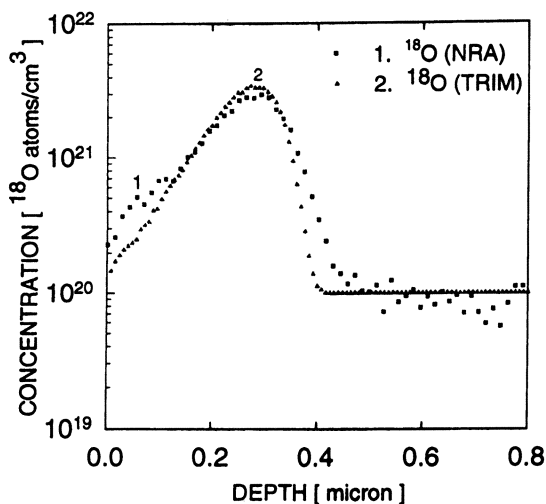


Figure 18. Depth profile of ^{18}O in ^{18}O -implanted SrTiO_3 substrate single crystal for 200 keV at RT. The measured profile is in good agreement with TRIM simulation.

detail. The RBS technique is only as significant as the material issue, such as the HTS superconductivity mechanism and the HTS physical and technological problems. RBS will become more powerful when combined with other characterization techniques, such as NRA, PIXE, ERD in ion beam analysis, and other material characterization techniques such as XRD, TEM, SEM, SIMS and Raman spectroscopy.

Acknowledgment

ARPA MDA 972-90-J-1001 and the State of Texas through the Texas Center for Superconductivity at the University of Houston. This work is supported in part by the MRSEC Program of the National Science Foundation under Award Number DMR-9632667.

References

1. Chu, W. K., Mayer, J. W., Nicolet, M. -A. Backscattering Spectrometry, Academic Press, New York, 1978.
2. Chu, W. K., Liu, J. R., Zhang, Z. H., Ma, K. B. in: Characterization of Materials, Part II, ed. Eric Lifshinin in the series Material Science and Technology: A Comprehensive Treatment, Vol. 2B. eds. R. W. Cahn, P. Haasen and E. J. Kramer (VCH, Weinheim, Germany, 1994).
3. Bednorz, J. G., Muller, K. A., Z. Phys. 1986, B64, 189.
4. Wu, M. K., Ashburn, J. R., Torng, C. J., Hor, P. H., Meng, R. L., Gao, L., Huang, Z. J., Wang, Y. Q., and Chu, C. W. Phys. Rev. Lett. 1987, 58, 908.
5. Chaudhari, P., Koch, R. H., Laibowitz, R. B., McGuire, T. R., and Gambino, R. J. Phys. Rev. Lett. 1987, 58, 2684.
6. Doolittle, L. R. Nucl. Instr. & Meth. 1986, B15, 227.
7. Kotai, E. Nucl. Instr. & Meth. 1994, B85, 588.
8. Saarialhti, J. and Rauhala, E. Nucl. Instr. & Meth. 1992, B64, 734.
9. Borgesen, P. Lilienfeld, D. A. Nucl. Instr. & Meth. 1989, B36, 1.
10. Cheang-Wong, J. C., Li, J., Ortega, C., Siejka, J., Vizkelethy, G., and Lemaire, Y. Nucl. Instr. & Meth. 1992, B64, 169.
11. Quan, Z., Schurig, Th., Menkel, S., Knappe, S., Beyer, J., Koch, H. Physica C 1995, 249, 309.
12. Martin, J. A., Nastasi, M., Tesmer, J. R., and Maggiore, C. J. Appl. Phys. Lett. 1988, 52, 2177.
13. Bplanpain, B., Revesz, P., Doolittle, L. R., Purser, K. H., and Mayer, J. W. Nucl. Instr. & Meth. 1988, B34, 459.
14. Berling, P., Benenson, R. E., Nucl. Instr. & Meth. 1989, B36, 335.
15. Tesmer, J. R., Nastasi, M. Nucl. Instr. & Meth. 1990, B45, 476.
16. Chernenko, I. P., Kobzev, A. P., Korneev, D. A. and Shirokov, D. M. Surface and Interface Analysis 1992, 18, 585.
17. Leavitt, J. A., McIntyre, L. C. Nucl. Instr. & Meth. 1989, B40/41, 797.
18. Brabour, J. C., Doyle, B. L. and Myers, S. M. Phys. Rev 1988, B38, 7005.
19. Ruahala, E., Keinonen, J., Jarvinen, R., Appl. Phys. Lett. 1988, 52, 1520.

20. Xie, T., Ryan, S. R., Fischbeck, H. J. *Nucl. Instr. & Meth.* 1989, B40/41, 766.
21. Rauhala, E., Saarilahti, J. and Nath, N. *Nucl. Instr. & Meth.* 1991, B61, 83.
22. Jiang, W., Zhu, P., Yin, S., Xu, T., Ren, M. and Zhou, J. *Nucl. Instr. & Meth.* 1993, B83, 552.
23. Lubig, A., Buchal, Ch., Frohlingdorf, J., Zander, W. and Stritzker, B. *Nucl. Instr. & Meth.* 1990, B50, 114.
24. Huttner, D., Meyer, O., Reiner, J., Linker, G. *Nucl. Instr. & Methods*, 1996, B118, 578.
25. Smeenk, R.G., Tromp, R.M., Kersten, H.H., Boerboom, A.J.H. and F.W. Saris, *Nucl. Instr. & Methods*, 1982, 195, 581.
26. Terashima, T., Bando, Y., Iijima, K., Yamamoto, K., Hirata, K., Hayashi, K., Kamigaki, K. and Terauchi, H. *Phys. Rev. Letters* 1990, 65, 2684.
27. Pennycook, S.J., Chisholm, M.F., Jesson, D.E., Feenstra, R., Zhu, S., Zheng, X.Y. and Lowndes, D.J. *Physica C*, 1992, 202, 1.
28. Wu, X.D., Luo, L., Muenchausen R.E. and Foltyn, S.R. *J. Mater. Res.* 1993,7, 531.
29. Martinez, J.A., Wilkens, B., Stoffel, N.G., Hart, D., Nazar, L., Venkatesan, T., Inam, A. and X.D. Wu, *Appl. Phys. Letters*, 1990,57, 189.
30. Li, Y., Linzen, S., Machalett, F., Schmidtl, F., Seidel, P. *Physica C* 1995, 243, 294.
31. Jhans, H., Earwaker, L.G., Chew, N.G., Edwards J.A. and Cullis, A.G. *Nucl. Instr. & Methods*, 1991, B56/57, 768.
32. Kechouane, V., L. Haridon, H., Salvi, M., Favenned, P.N., Gauneau, M. and Guilloux Viry, M., Karkut, M.G., Thivet, C., Perrin, A. *J. Materials Science* 1993, 28, 4934.
33. Qu, J.Z., Liu, J.R., Chen, Q.Y., Cui, X.T. and Chu, W.K. *Nucl. Instr. & Methods*, 1996, B118, 684.
34. Sharma, R.P., Venkatesan, T., Zhang, Z.H., Liu, J.R., Chu, R. and Chu, W.K. *Physical Review Letters* 1996, 77, 4624.
35. Andersen, J.U., Ball, G.C., Davies, J.A., Forster, J.S., Geiger, J.S., Haakenaasen, R., Hecker, N.E., Rehn, L.E., Sharma, R.P., Uguzzoni, A. *Nucl. Instr. & Methods*, 1996, B118, 190.
36. Sharma, R.P., Rehn, L.E., Baldo, P.M. and Liu, J.Z. *Phys. Rev.* 1988, B38, 9287.
37. Sharma, R.P., Rehn, L.E., Baldo, P.M. and Liu, J.Z. *Phys. Rev.* 1989, B40, 11396.
38. Sharma, R.P., Rehn, L.E., Baldo, P.M. and Liu, J.Z. *Phys. Rev. letters* 1989, 62, 2869.
39. Sharma, R.P., Rotella, F.J., Jorgensen J.D. and Rehn, L.E. *Physica C* 1991, 174, 409.
40. Rimmel, J., Meyer, O., Geerck, J., Reiner, J., Linker, A., Erb G. and Muller- Vogt, G. *Phys. Rev.* 1993, B48, 16168.
41. Cheang Wong, J. C., Ortega, C., Siejka, J. and Trimaile, I. *Nucl. Instr. & Meth.* 1992, B64, 179.
42. Garcia Lopez, J. Cheang-Wong, J. C., Ortega, C., Siejka, J., Trimaille, I., Sacuto, A., Linker, G. and Meyer, O. *Nucl. Instr. & Meth.* 1994, B85, 462.
43. Combescot, R. *Phys. Rev. Lett.* 68(1992)1089.

44. Irvin, J. C., Chrzanowski, J., Altendorf, E., Frank, J. F. and Jung, J. J. *Mater. Res.* 1990, 5, 2780.
45. Bredikhin, S. I., Emelchenko, G. A., Shechtman, V. Sh., Zhokhov, A. A., Carter, S., Chater, R. J., Kilner, J. A. and Steele, B. C. H. *Physica C* 1991, 179, 286.
46. Li, Y. P., Liu, J. R., Chu, W. K., Kilier, J. A. Tate, T. and Chater, R. J. *Proceedings of the 14th International Conference on Applications of Accelerator in Research and Industry*, Nov. 6-9, 1996 Denton, Texas. American Institute of Physics 1997, p. 692.
47. Liu, J. R., Li, Y. L., Chen, Q. Y., Cui, X. T., Christoffersen, R., Jacobson, A. and Chu, W. K. *Depth Resolution and Dynamic Range of ¹⁸O(p, α) ¹⁵N Depth Profiling*, will be published in *Nucl. Instr. & Meth. B* 1998.

Chapter 4

Applications of X-ray Photoelectron and Auger Spectroscopy to Superconducting Materials

Dale L. Perry

Lawrence Berkeley National Laboratory, University of California,
Berkeley, CA 94720

X-ray photoelectron and Auger spectroscopy are extremely effective for the study of the bonding and chemistry of ceramic high-temperature superconducting metal oxides. The two types of spectroscopy are useful for studying both the analytical aspects of the materials and the details of the chemical bonding of the elements involved, details which include oxidation state, diamagnetism/paramagnetism, and electronic spin state. When x-ray sources are used to generate both spectra, the combined spectrum can be used to give even more chemical information, one approach being the use of Auger parameters. The use of synchrotron-generated x-ray-induced x-ray photoelectron and Auger spectroscopy, coupled with microscopy, can be used to obtain x-ray photoelectron and Auger-based spectra that yield chemical and bonding information with high lateral resolution on a micron (or submicron) scale.

Since the report of the synthesis and properties of the first ceramic, high-temperature superconducting metal oxide by Chu and his associates at the University of Houston in 1987 (1), there has been immense interest in both the synthesis and characterization of this new class of superconductors. A detailed knowledge of the chemistry of the elements that comprise the superconductors is useful from both a guide on synthetic approaches and as a very important tool for gaining an understanding of the mechanisms of the superconducting process. Spectroscopic and microscopic techniques are extremely important in determining the chemical states and other aspects of the chemical bonding in these materials.

X-ray photoelectron and Auger spectroscopy serve a very strong two-fold purpose, that of acting as analytical techniques and as probes for studying the bonding and chemistry of the particular elemental species components of the reactions of the superconducting materials. With x-ray photoelectron and Auger spectroscopy, a wide variety of electronic and bonding phenomena related to the materials can be studied; among these are

oxidation states, electronic states (such as electronic spin states and paramagnetism vs diamagnetism), and mixed metal species. These two spectroscopies also can be used in tandem with one another and with other complementary techniques such as spectroscopic microprobes to provide even more information about both the chemical bonding of the elements and their distribution in the materials. The techniques also can be used in conjunction with microscopic techniques to give laterally-resolved data concerning the surface/bulk properties of superconducting materials.

The present work is focused on the use of combined x-ray-induced photoelectron/Auger spectroscopy and the use of the combined spectra in tandem with one another to study basic and applied chemical aspects of superconducting materials and the use of the two techniques combined with microscopic approaches. It describes some of the research reported to date, covering several of the different types of applications of x-ray photoelectron and Auger spectroscopy. The treatise here is not intended to be exhaustive, but rather as a guide to the scope of past applications of the techniques to superconducting materials as well as a guide to other future investigations predicated on new experimental techniques such as the micro-ESCA synchrotron techniques described below.

X-Ray Photoelectron and Auger Spectroscopy

A. General Considerations

X-ray photoelectron (also sometimes called Electron Spectroscopy for Chemical Analysis, or ESCA) and Auger spectroscopy have been used to perform many studies on a wide variety of materials. Spectral studies involving metal oxides, sulfides, semiconductors, and other solid-state materials have been investigated extensively, while other systems such as ceramics, films, and ferroelectrics have also been reported. In general x-ray photoelectron and Auger spectroscopy can be used to derive much useful information concerning not only solid samples of interest but also reaction interfaces, with the major requirement being that the systems be amenable to ultra-high vacuums. Auger spectroscopy that uses electron beams to generate the spectra has been extremely useful in the elemental point analyses of heterogeneous materials, interfaces, and composites on both qualitative and quantitative bases. Reactions such as corrosion, grain boundaries changes, elemental segregation in alloys, and gas reactions with surfaces are all chemical systems that are readily studied by Auger spectroscopy. High-purity elemental standards and sensitivity factors coupled with ion-sputtering to obtain depth profiles can give a very detailed picture of a material. It combines a high sensitivity for the top 5-20 Angstrom surface region of a material for elements above helium in the Periodic Table with a very quick accumulation of spectral data. Auger electron spectra can also be used to determine chemical states of elements present in the material.

X-ray photoelectron spectroscopy, also an ultra-high vacuum technique, is a very effective complementary surface technique to Auger spectroscopy. Like Auger spectroscopy, it can be used very effectively as both an analytical and research tool to study electronic, magnetic, and oxidation states of elements. Spectroscopic parameters such as binding energies (2), satellite structure associated with main photoelectron lines (3-5), and spin-orbit and multiplet splitting (6,7) studied collectively, provide invaluable details about the elements' chemistries.

For extensive, detailed introductions to the principles of the two types of spectroscopy, the reader should consult treatises on x-ray photoelectron [8-11] and Auger spectroscopy [12-14].

Application of X-Ray Photoelectron and Auger Spectroscopy to Superconducting Materials

Several investigations of high-temperature superconducting metal oxides using x-ray photoelectron and Auger spectroscopy have been reported in the literature. Meyer *et al* (15) have reported extensive x-ray photoelectron results of studies of lanthanum-strontium, yttrium-barium, and bismuth-calcium-strontium cuprates. Figure 1 shows spectra that reveal features indicative of the chemical states of the copper and oxygen. The binding energies of the copper $2p_{3/2}$ photoelectron lines indicate the divalent nature of the copper species; additionally, the satellite structure found to the high binding energy side of the main line agrees with an assignment of paramagnetic copper (16-18). Satellites exhibiting this intensity relative to the main line are a result of a paramagnetic copper species. In the case of copper(I), however, the copper electronic state, reflecting an electronic configuration of $[Ar] d^{10}$, has all d shells filled and is thus diamagnetic. In such cases, the satellite structure for the copper is much less intense in the spectrum or not observed at all. One should also note the difference in the satellite structure in the top spectrum is due to the overlapping bismuth $4s$ photoelectron line at ~ 938 eV. A detailed analysis of the oxygen $1s$ line shows that it can be de-convoluted into various inequivalent chemical states of the oxygen in the metal oxide, including oxygens that comprise copper-oxygen planes, bismuth-oxygen planes, chains, and off-plane environments.

These same researchers also used x-ray photoelectron spectroscopy in a rigorous study of yet another area of great interest in the field of high-temperature superconducting metal oxides, that of films and interfaces involving the superconductors. Figure 2 shows again the copper $2p_{3/2}$ photoelectron line and its associated satellites of a series of overlayers of elemental and calcium fluoride films that have been deposited on $YBa_2Cu_3O_{6.9}$ substrates, using the satellite/main photoelectron peak ratio as an indicator of the reactivity of the metal and calcium fluoride films with the superconducting substrate. In the top spectrum, for example, representing the reaction of a copper film with the substrate, the copper is reduced from its original copper(II) state, as shown by the loss of the satellite intensity relative to the main photoelectron line. Conversely, the overlayers of films of bismuth, gold, and calcium fluoride showed minimal alteration of the chemical state of the divalent copper involving the interface with the superconducting substrate. Many other researchers have also reported the use of x-ray photoelectron spectroscopy to study high-temperature superconducting metal oxides, with many of the studies discussed in a number of reviews [19-22].

Auger spectroscopy also has been used to study high-temperature superconducting metal oxides, many of the studies including microscopic imaging that has been available on commercial instruments known as scanning Auger microprobes, or SAM's. Electron beam-induced Auger spectroscopy is very useful for examining surfaces for heterogeneity, with the sample spot size under study being less than a micron. It is thus very useful for looking at defects on surfaces of superconductors. Larger areas of a fraction of a millimeter also can be examined by looking at averaged areas. Two major drawbacks are

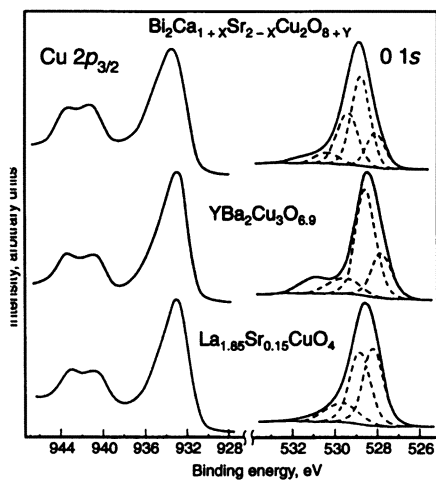


Figure 1. X-ray photoelectron spectra of metal cuprate high-temperature superconductors. Adapted from Ref. 15.

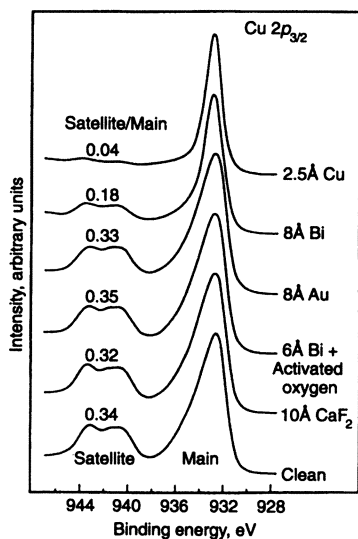


Figure 2. Overlayer thin films on $\text{YBa}_2\text{Cu}_3\text{O}_{6.9}$. Adapted from Ref. 15.

sample “charging” and surface damage due to the effects of the electron beam used to generate the Auger spectrum. These problems can be alleviated to some extent by taking x-ray-generated Auger spectra as discussed below. Several reviews [22, 23-25] can be found in the literature.

Auger Parameters of Elements in Superconducting Oxides

Over the last three decades, there has been a steady increase in the combined use of x-ray photoelectron and x-ray-generated Auger spectroscopy to study solid state materials. By combining the x-ray photoelectron binding energies of an element with the Auger kinetic energy lines that are obtained in the same x-ray-induced spectrum, one obtains what is referred to as the *Auger parameter*. The combination of both photoelectron and Auger lines for this parameter has several advantages for gaining information about the chemical states of the elements in a material. First, the two spectra are co-generated in a combined spectrum, thus canceling “charging” effects and creating an internal calibration between the two sets of lines. Second, the magnitude of the shift of core level Auger lines in an x-ray-excited spectrum are greater than the shift of the core level x-ray photoelectron lines for the same element. Because of this, a modified Auger parameter, α' , as defined in Equation 1, is simply the sum of the binding energy of the photoelectron line and the kinetic energy of the Auger line. The kinetic energy of the Auger line is derived by subtracting the value of the Auger line in terms of its binding energy in the x-ray-generated spectrum from the energy of the x-ray source. Figure 3 shows a diagram for the Auger parameter for copper, an element common to many of the high-temperature metal oxide superconductors.

$$\alpha' = BE_{\text{photo}} + KE_{\text{Auger}} \quad (1)$$

The combined x-ray generated photoelectron and Auger spectrum was taken on a commercial spectrometer using a Mg $K\alpha$ 1253.6 eV x-ray source. The binding energy of the most intense core copper $2p_{3/2}$ photoelectron line is at 932.4 eV, while the copper LMM Auger line is at 335.0 eV on the binding energy scale. By subtracting 335.0 eV from the photon energy of 1253.6 eV of the magnesium $K\alpha$ x-ray source, one obtains 918.6 eV as the kinetic energy of the copper LMM line. Upon substituting these values into Equation 1, the modified Auger parameter of 1851.0 eV is obtained for copper metal. Copper and its compounds exhibit Auger parameters [2] that range over several electron volts and can be used to distinguish between different chemical compounds and chemical states of an element. Table 1 shows some typical combinations of x-ray photoelectron/Auger lines that can be used to study high-temperature superconductors. Several reviews of Auger parameters and their applications have been published [26-32], including one review of oxygen Auger parameters and their use in studying high-temperature superconductors [33].

X-Ray Photoelectron Spectromicroscopy

Traditional applications of x-ray photoelectron spectroscopy have been ones that generate spectra of samples such as powders, films, and crystals. These spectra represent a rather large sampling area of the material, typically several millimeters. If, however, one

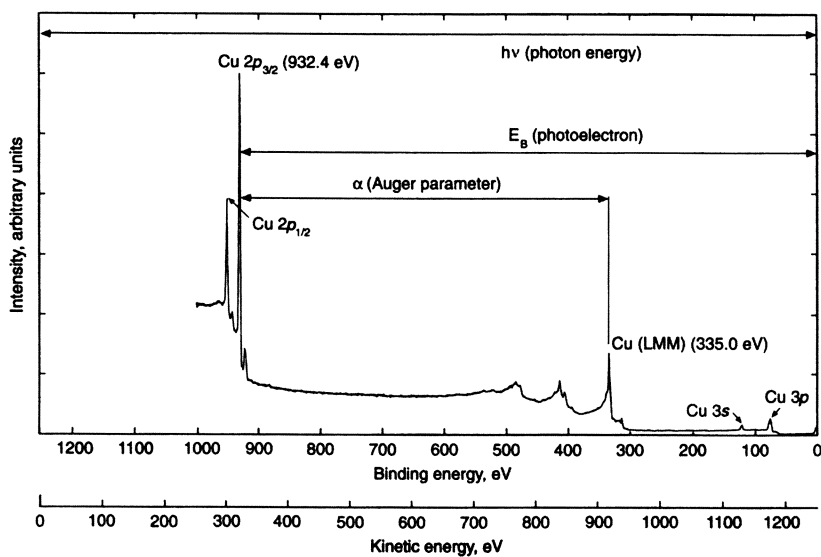


Figure 3. Auger parameter for copper metal.

Table I. X-Ray Photoelectron/Auger Lines for Use in the Study of Representative Superconducting Metal Oxides Using Auger Parameters

<i>Superconducting Metal Oxide System</i>	<i>Applicable Photoelectron/(Auger) Lines</i>
1. $\text{YBa}_2\text{Cu}_3\text{O}_{7-x}$	Cu $2p_{3/2}$ (LMM), Ba $3d_{5/2}$ (MNN)
2. $\text{Pb}_2\text{Sr}_2\text{YCu}_3\text{O}_8$	Cu $2p_{3/2}$ (LMM), Pb $4f_{7/2}$ (NOO)
3. $\text{Hg}_{1-x}\text{Cr}_x\text{Sr}_2\text{CuO}_{4+y}$	Cu $2p_{3/2}$ (LMM), Cr $2p_{3/2}$ (LMM) Hg $4f_{7/2}$ (NOO)
4. $\text{La}_{2-x}\text{Ca}_x\text{CuO}_4$	Cu $2p_{3/2}$ (LMM), Ca $2p_{3/2}$ (LMM) La $3d_{5/2}$ (MNN)
5. $\text{Tl}_2\text{Ba}_2\text{CaCu}_2\text{O}_8$	Cu $2p_{3/2}$ (LMM), Ba $3d_{5/2}$ (MNN) Ca $2p_{3/2}$ (LMM)
6. $\text{BiSr}_2\text{CaCu}_2\text{O}_8$	Cu $2p_{3/2}$ (LMM), Ca $2p_{3/2}$ (LMM) Bi $4f_{7/2}$ (NOO)

wishes to look at much smaller domains involving inhomogeneities on the surface of a material—domains on the order of several microns—he must resort to techniques that afford much better lateral resolution on the surface. One very powerful technique is the combination of x-ray photoelectron spectroscopy with microscopy to give x-ray photoelectron spectromicroscopy. A wide variety of different chemical phenomena related to surface heterogeneities can be studied, including different oxidation, electronic spin, and diamagnetic/paramagnetic states, among others. A few commercial instruments are available for performing laterally resolved and mapped x-ray photoelectron experiments. One, the PHI Quantum 2000, is marketed by Physical Electronics, Inc., of Eden Prairie, Minnesota, as a scanning ESCA microprobe. X-rays in this system are generated by impinging an electron beam onto an aluminum anode, with an ellipsoidally shaped crystal monochromator focusing the x-rays onto the sample being studied. An investigator can change the diameter of the x-ray probe from 10 to 200 μ by changing the diameter of the electron beam on the anode. As is the case for x-ray-generated photoelectron spectra discussed above, this instrument also can be used to collect Auger spectra. Several good reviews discussing x-ray photoelectron spectromicroscopy and its practice can be found in the literature [34].

Synchrotron-Based X-Ray Photoelectron and Auger Microscopy

In the last several years, yet still another tool has become available to look at bulk and surface chemical and electronic states of elements that are part of high-temperature superconducting metal oxides. Synchrotron radiation facilities that have come online afford an extremely powerful approach to the study of these materials. These sources generate x-ray beams that far exceed those that are available to researchers as part of

traditional x-ray spectrometers. At these facilities, beamlines are dedicated to a variety of types of spectroscopies, each having the ability to be used for performing detailed studies on chemical and material systems. Using these radiation sources, however, allows researchers to both study samples containing species at detection levels far below those attainable by normal instruments and to obtain extremely high-resolution lateral images of elements. Several good treatises on the many applications of synchrotron radiation have been published [35-37].

Figure 4 shows the configuration [38] of one such beamline, X1-SPEM-II, at the National Synchrotron Light Source (NSLS) at Brookhaven National Laboratory. The schematic of the beamline is one that describes the beamline configuration for x-ray photoelectron spectroscopy. The beamline consists of a focused, monochromatized x-ray beam from an undulator (devices which are in place to generate the necessary radiation with enhanced characteristics and consisting of arrays of permanent magnets), the beam directed to a microprobe. The electrons that are emitted are analyzed by a hemispherical analyzer, which provides the x-ray photoelectron spectrum. By centering on various aspects of the spectrum, images of the sample surface can be obtained. Figure 5 shows an image of strontium in a sample of $\text{Bi}_2\text{Ca}_2\text{SrCu}_2\text{O}_x$ (BCSCO) taken at a photon energy of 270 eV Synchrotron Radiation Research Center (SRRC) in Hsinchu, Taiwan [39]. By imaging the sample using the strontium $3p$ line, one can see that the region marked A is enriched with strontium due to chemical inhomogeneity. Another image of a square-patterned YBaCuO thin film (200 Angstroms) deposited on a PrBaCu substrate [40] can be seen in Figure 6, with the image being obtained using the copper $2p$ photoelectron line.

Similar synchrotron beamlines for Auger imaging have been developed. A photon-induced scanning Auger microscope at the BESSY synchrotron facility in Berlin has been designed that also can be used to take x-ray photoelectron spectra [41]. This microscope is capable of achieving lateral spatial resolution ranging from 3-4 microns in one Auger configuration to submicron resolution by using another.

Acknowledgments

This work was supported by the U. S. Department of Energy under Contract Number DE-AC03-76SF00098. The author also wishes to thank Dr. Eric Faulques for his invitation to participate in the symposium.

Literature Cited

1. Wu, M.K.; Ashburn, J.R.; Torng, C.J.; Hor, P.H.; Meng, R.L.; Gao, L.; Huang, Z.J.; Wang, Y.Q.; Chu, C. W. *Phys. Rev. Lett.* **1987**, *58*, 908.
2. Wagner, C.D.; Riggs, W. M.; Davis, L. E.; Moulder, J. F. In *Handbook of X-Ray Photoelectron Spectroscopy*; Mullenberg, G.E., Ed; Perkin-Elmer, Physical Electronics Division: Eden Prairie, Minnesota, 1979.
3. Aarons, L. J.; Guest, M.F.; Hillier, I. H.; *J. Chem. Soc., Faraday Transactions. II* **1972**, *68*, 1866.
4. Brisk, M. A.; Baker, A.D. *J. Electron. Spectrosc. Related Phenom.* **1975**, *7*, 197.
5. Vernon, G. A.; Stucky, G.; Carlson, T. A. *Inorg. Chem.* **1976**, *15*, 278.

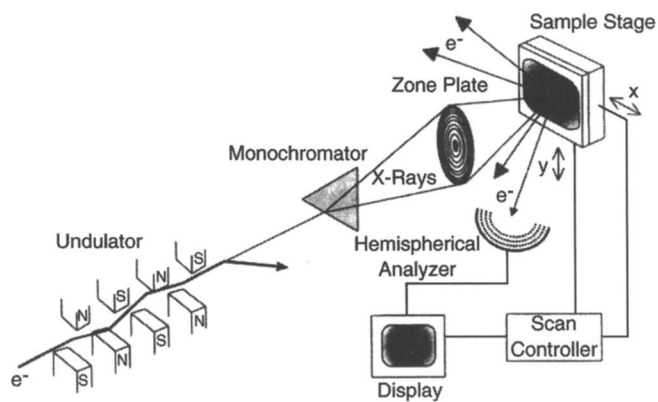


Figure 4. Schematic of the X1-SPEM-II at the National Synchrotron Light Source, Brookhaven National Laboratory. Adapted from Ref. 38.

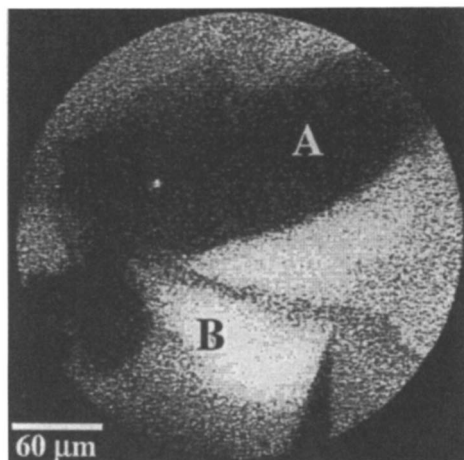


Figure 5. Strontium image from a sample of $\text{Bi}_2\text{Ca}_2\text{SrCu}_2\text{O}_x$. Adapted from Ref. 39.

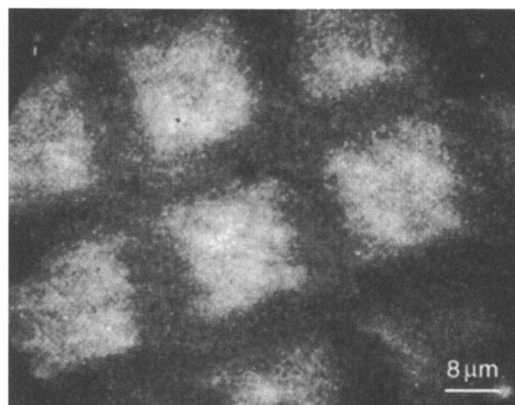


Figure 6. Copper image from a sample of YBaCuO deposited on PrBaCuO . Adapted from Ref. 40.

6. Siegbahn, K.; Nordling, C.N.; Fahlman, A.; Nordberg, R.; Hamrin, K.; Hedman, J.; Johansson, G.; Bergmark, T.; Karlsson, S.E.; Lindgren, I.; Lindberg, B. *ESCA, Atomic, Molecular, and Solid State Structure Studied by Means of Electron Spectroscopy*; Almquist and Wiksell: Upsala, 1967.
7. Siegbahn, K.; Nordling, C.; Johansson, G.; Hedman, J.; Heden, P.F.; Hamrin, K.; Gelius, U.; Bergmark, T.; Werme, L.O.; Manne, R.; Baer, Y. *ESCA Applied to Free Molecules*; North-Holland: Amsterdam, 1969.
8. Riggs, W. M.; Parker, M. J. In *Methods of Surface Analysis*; Czanderna, A. W., Ed.; Elsevier Publishing: New York, 1975.
9. *Electron Spectroscopy: Theory, Techniques, and Applications*; Brundle, C.R.; Baker, A.D., Eds.; Academic Press, London, 1978.
10. *Handbook of X-Ray and Ultraviolet Photoelectron Spectroscopy*; Briggs, D., Ed.; Heyden Press, London, 1972.
11. Barr, T.L. *The Principles and Practice of X-Ray Photoelectron Spectroscopy*, CRC Press: Boca Raton, FL, 1994.
12. Carlson, T. A. *Photoelectron and Auger Spectroscopy*; Plenum Press: New York, NY, 1975.
13. Thompson, M.; Baker, M.D.; Cristie, A.; Tyson, J.F. *Auger Electron Spectroscopy*; Wiley-Interscience: New York, NY, 1985.
14. *Practical Surface Analysis by Auger and X-Ray Photoelectron Spectroscopy*; Briggs, D.; Seah, M. P., Eds.; John Wiley & Sons, New York, NY, 1983.
15. Meyer, H. M.; Hill, D. M.; Weaver, J. H.; Nelson, D. L. In *Chemistry of the High-Temperature Superconductors II*; Nelson, D.L.; George, T. F., Eds.; ACS Symposium Series 377, American Chemical Society: Washington, DC, 1988; pp. 280-290.
16. Frost, D. C.; Ishitani, A.; McDowell, C.A. *Molec. Phys.* **1972**, *24*, 861.
17. Scrocco, M. *Chem. Phys. Lett.* **1979**, *63*, 52.
18. Brisk, M. A.; Baker, A.D. *J. Electron Spectrosc. Relat. Phenom.* **1975**, *7*, 197.
19. Veal, B.W.; Gu, C. *J. Electron Spectrosc. Relat. Phenom.* **1994**, *66*, 321.
20. Kotani, A.; Okada, K. *Prog. Theor. Phys. Suppl.* **1994**, *101*, 329.
21. Padalia, B.D.; Mehta, P.K. *Stud. High Temp Supercond.* **1989**, *1*, 283.
22. Fink, J.; Nuecker, N.; Romberg, H.A.; Fuggle, J.C. *IBM J. Res.Dev.* **1989**, *33*, 372.
23. Ramaker, D.E. *AIP Conf. Proc. (Thin Film Process. Charact. High-Temp. Supercond.)* **1988**, *165*, 284.
24. Chang, C.C.; Venkatesen, T.; Hegde, M.S.; Hwang, D.M.; Ramesh, R.; Rogers, C.T.; Frenkel, A.; Chase, E. W.; Nazar, L. *Proc. SPIE-Int. Soc. Opt. Eng. (Process. Films High Tc Supercond. Electron.)* **1990**, *1187*, 216.
25. Wendin, G. *J. Phys., Colloq., High-Energy Spectroscopies and High-Tc Superconductors: An Overview* **1987**, *C9(Vol. 2)*, C9-1157.
26. Wagner, C.D.; Passoja, D.E.; Hillery, H.F.; Kinisky, T.G.; Six, H.A.; Jansen, W.T.; Taylor, J.A. *J. Vac. Sci. Techno.* **1982**, *21*, 933.
27. Wagner, C.D.; Gale, L.H.; Raymond, R. H. *Anal. Chem.* **1979**, *51*, 466.
28. Wagner, C.D. In *Practical Surface Analysis by Auger and X-Ray Photoelectron Spectroscopy*; Briggs, D.; Seah, M. P., Eds.; John Wiley & Sons, New York, NY, 1983, Appendix 4, p. 477.
29. Perry, D.L. In *Applications of Analytical Techniques to the Characterization of Materials*, Perry, D.L., Ed; Plenum Press, New York, NY, 1991, p. 1.

30. Lozzi, L.; Passacantando, M.; Picozzi, P.; Santucci, S.; Tomassi, G.; Alfonsetti, R.; Borghesi, A. *Surf. Interface Anal.* **1994**, *22*, 190.
31. Berrie, C. L.; Langell, M. A.; *Surf. Interface Anal.* **1994**, *21*, 245.
32. Peisert, H.; Chasse, T.; Streubel, P.; Meisel, A.; Szargan, R. *J. Electron Spectrosc. Relat. Phenom.* **1994**, 321.
33. Moretti, G. *J. Electron Spectrosc. Relat. Phenom.* **1992**, *58*, 105.
34. Coluzza, C.; Moberg, R. *J. Electron Spectrosc. Relat. Phenom.* **1997**, *84*, 109.
35. *Synchrotron Radiation Research*; Winick, H.; Doniach, S., Eds.; Plenum Press, New York, NY, 1980.
36. *Applications of Synchrotron Radiation*; Catlow, C.R.A.; Greaves, G.N., Eds.; Chapman and Hall, New York, NY, 1990.
37. *Photoemission and Absorption Spectroscopy of Solids and Interfaces with Synchrotron Radiation*; Campagna, M.; Rosei, R., Eds.; North-Holland, Amsterdam, 1990.
38. Ade, H.; Smith, A.P.; Zhang, H.; Zhuang, G.R.; Kirz, J.; Rightor, E.; Hitchcock, A. *J. Electron Spectrosc. Relat. Phenom.* **1997**, *84*, 53.
39. Hwu, Y.; Tung, C.Y.; Pieh, J.Y.; Lee, S. D.; Almeras, P.; Gozzo, F.; Berger, H.; Margaritondo, G.; De Stasio, G.; Mercanti, D.; Ciotti, M.T. *Nucl. Instr. Meth. Phys. Res. A*, **1995**, *361*, 349.
40. Hwu, Y. *J. Electron Spectrosc. Relat. Phenom.* **1997**, *84*, 149.
41. Weiss, M.R.; Wustenhagen, V.; Fink, R.; Umbach, E. *J. Electron Spectrosc. Relat. Phenom.* **1997**, *84*, 9.

Chapter 5

Magnetotransport and Structural Studies of the High Temperature Superconductor $\text{YBa}_2\text{Cu}_3\text{O}_{7-\delta}$

V. M. Browning¹, E. F. Skelton¹, S. B. Qadri¹, M. S. Osofsky¹, J. Z. Hu²,
L. W. Finger², M. Raphael³, L. Thilly¹, and K. R. Meyers¹

¹Naval Research Laboratory, Code 6344, Washington, DC 20375

²Geophysical Laboratory and Center for High Pressure Research,
Carnegie Institution of Washington, Washington, DC 20015

³George Washington University, Washington, DC 20052

The high temperature superconductor $\text{YBa}_2\text{Cu}_3\text{O}_{7-\delta}$ exhibits a variety of unusual features in both the normal-state and superconducting transport properties. Determining the intrinsic nature of these properties is crucial. Transport studies of crystal samples of $\text{YBa}_2\text{Cu}_3\text{O}_{7-\delta}$ exhibit many of the features attributed to fully oxygenated, homogeneous samples. However, extensive structural studies have revealed the presence of structural inhomogeneities. These results question whether transport measurements alone are a reliable indicator of sample quality and whether any of the properties measured in crystals should be attributed to intrinsic effects.

The discovery of high temperature superconductivity (HTS) in the mid-1980's precipitated a renewed interest in device applications which could potentially exploit the many advantages afforded by the ability to carry current with zero losses. Cellular communications, rf microwave electronics and power generation are all technologies which could see great improvement in performance by incorporating superconducting elements in the circuit design. Unfortunately, the HTS have found limited success in finding their "niche" in any technology. This is largely due to their failure to meet initial expectations with regards to their power handling capabilities. For this reason, an enormous amount of research effort has been expended in order to better understand the physics and materials issues which govern the HTS.

Early on in the history of HTS research, it was realized that these materials were extraordinarily sensitive to processing conditions. Their layered, perovskite structure together with their chemical complexity presented a challenge to material scientists to optimize processing and growth techniques. These efforts were further complicated by the realizations that the physics of the HTS was quite different than that of their conventional low T_c counterparts. In particular, many of the observable

transport properties exhibited by the HTS were not readily understood, therefore it was difficult to guide a material synthesis approach since it was not clear which properties were important to optimize.

After several years of intensive research, phase diagrams were eventually reported (1-4) and a consensus was reached as to what properties could be used to judge sample "quality". It soon became generally accepted that certain transport properties could be used to determine the oxygen stoichiometry and homogeneity in single crystal samples. Low resistivity values and a linear temperature dependent resistivity were normal state properties that indicated homogeneity and optimal doping, while a high T_c and sharp superconducting transition were desirable superconducting properties (5,6). In terms of these parameters, single crystal samples far surpassed thin films; therefore, crystals were considered more desirable for many experiments since it was believed that they would be more representative of the intrinsic properties.

Once it was established that high quality single crystals could be reproducibly grown in abundant quantities, there were a host of new experiments which revealed several interesting features in the transport properties, particularly in the so-called "mixed-state" in which vortex dynamics dominate many of the observed transport phenomenon. The HTS are type II superconductors which means that for fields larger than a critical field, H_{c1} , and for temperatures less than the superconducting transition temperature, T_c , magnetic flux lines can penetrate the material and coexist with superconductivity. This is accomplished by the formation of vortices in which supercurrents flow around "normal" or non-superconducting cores. These vortices can move under the influence of applied electric current and be a source of dissipative losses. Since H_{c1} is quite small for the HTS (~10 Oe), most magnetotransport measurements (Hall effect, magnetoresistance, etc.) are necessarily performed in the mixed state. Examples of unusual mixed state properties observed in many of the HTS include a vortex lattice "melting" transition (7-10) and a negative Hall anomaly (11-15). These will be discussed in more detail and representative data from crystal samples of $YBa_2Cu_3O_{7-\delta}$ (YBCO), will be presented. Since many of these features are generally only seen in what are considered to be the highest quality single crystal samples, it has been believed that they were intrinsic in nature. These results have led to extensive efforts on the part of the theoretical community to provide explanations.

Recent results, however, have questioned the validity of the assumption of an intrinsic origin of many of the properties associated with the HTS. In particular, several studies have suggested the presence of inhomogeneities in crystal samples which would normally have been considered "high quality" based on their transport properties (16,17). Considering the robust nature of many of the observed transport properties, one can easily appreciate the challenge facing theorists to either account for the presence of inhomogeneities in the HTS or explain why they may be ignored.

In this chapter, the various transport properties of the most widely studied HTS, $YBa_2Cu_3O_{7-\delta}$, will be reviewed together with the present understanding(s) of their origins. Highlights of a recent study (17) which provides the most thorough investigation to date of the transport and structural properties of crystal samples of YBCO will be presented. These results have demonstrated, for the first time, that

structural defects exist even in crystals which exhibit many of the features attributed to optimally doped, homogeneous samples.

Magnetotransport Properties of $\text{YBa}_2\text{Cu}_3\text{O}_{7-\delta}$

Although the mechanism of superconductivity in the HTS is still unresolved, considerable progress has been reported in characterizing the transport properties. Determining the intrinsic behavior of these materials is crucial. Based upon the assumed high quality of the samples under consideration, many of the more well-studied transport properties have generally been accepted as representative of intrinsic behavior. These studies, which have explored the nature of both vortex dynamics and the mechanism of superconductivity have revealed unusual behaviors and have spawned new theories.

It is now well known that both the superconducting and the normal state properties of YBCO are strongly affected by the oxygen content. In general oxygen deficiency leads to a deviation from linear $\rho(T)$ above T_c as well as an increase in the magnitude of the resistivity values (18). In addition the superconducting transition temperature decreases with oxygen content and is suppressed completely for $7-\delta < 6.4$ (19,20).

The determination of sample quality is often based upon the transport properties rather than on any structural examinations, despite the results of several studies which have suggested the presence of structural defects in polycrystalline samples, crystals and films, of YBCO. We shall now examine the magnetotransport properties of crystal samples of YBCO which exhibit many of the features generally attributed only to the "highest quality" samples.

Normal State Properties. As mentioned previously, low resistivity, high T_c , and sharp superconducting transition are generally associated with high-quality samples. Based on these criteria, many experiments have focused on single-crystal samples since they are presumed most likely to be defect free and representative of the intrinsic nature of the materials. The crystals reported on in this study were grown in a zirconia crucible using a self-decanted flux method (21). Crystals grown using this method are generally heavily twinned. De-twinned crystals may be prepared by applying pressure along one axis of a sample while annealing in a flowing oxygen atmosphere (22). The degree of twinning in a crystal sample can be assessed by visual inspection using polarized light and/or x-ray diffraction. Electrical contacts were made by sputtering 200 nm gold stripes along the edges of the crystal to which 25 μm diameter gold wires were attached using silver epoxy. A short, high temperature anneal in flowing oxygen resulted in contact resistances $< 1 \Omega$. Magnetotransport measurements were taken in a superconducting magnet capable of producing a 13 T persistent dc field. The orientation of the sample in field was determined using a Hall sensor and was adjusted using a goniometer which allowed sample rotation.

One of the normal-state properties of the HTS which has been widely studied is the linear temperature dependence of the resistivity observed in nominally fully-

oxygenated samples. This behavior is considered somewhat of a puzzle since in some of the HTS, the linear temperature dependence is observed over a very large temperature range (23,24). This suggests that electron-phonon coupling is small in these materials and also implies an unusually low Debye temperature. Both of these statements are hard to reconcile with the observed high temperature superconducting transition temperatures in terms of electron-phonon interactions, suggesting another mechanism as the origin of the T-linear behavior.

The temperature dependent resistivity has been well studied in both twinned and untwinned samples. The presence of Cu-O chains along the *b*-axis in untwinned samples leads to an anisotropy in the measured resistivities (5). This anisotropy has been shown by Welp *et al.* (6) to be highly sensitive to the oxygen content with the anisotropy decreasing with increasing oxygen deficiency. Figure 1 shows the resistivity versus temperature data obtained from a twinned YBCO crystal, while the inset shows the resistivities obtained along the *a* and *b* axes of a de-twinned single crystal sample. Both samples exhibit high (>93 K), sharp (<300 mK) superconducting transitions. The room temperature resistivity and the residual resistivity (extrapolated from the data just above T_c) are within the range of values reported in the literature for high-quality samples. These data reveal the linear temperature dependence of the resistivity seen in both the twinned sample and for the *a* and *b* axes separately.

Halbritter has proposed a model which relates the slope, α , and zero-temperature intercept, $\rho(0)$, to sample inhomogeneities (25). In his model, sample inhomogeneities can locally distort the current density and act as scattering centers. The distortion of the current density can result in the formation of "weak links" which affect the superconducting properties while the additional scattering centers affect the measured normal state resistivities. The observed temperature dependence of the resistivities for the twinned and detwinned sample are consistent with the literature values reported for high quality samples.

In addition to a linear temperature dependent resistivity, the HTS are known to exhibit a temperature dependent Hall coefficient that varies approximately as $1/T$. Unlike the resistivity, the Hall effect is predicted by Onsager's relation to be isotropic. Harris *et al.* (26) have verified this indirectly by measuring the Hall effect along the *a*- and *b*- axes of two different crystals prepared under identical processing conditions. In order to confirm this directly, the Hall effect was measured in a single detwinned crystal using an unconventional contact geometry. In this configuration, point contacts were applied along the perimeter of the sample. In order to measure transport in a particular direction, contacts along the edge perpendicular to that direction were shorted together to form current leads. The remaining leads were used to measure the appropriate transverse (ρ_{xy}) or longitudinal (ρ_{xx}) resistivities. Figure 2 shows the isotropic temperature dependence of the resistivities for this sample.

The observed $1/T$ temperature dependence of the Hall resistivity (ρ_{xy}) together with the linear dependence of the normal state resistivity (ρ_{xx}) seen in many samples has provided considerable evidence which suggests that the temperature dependence of $\cot(\theta_H) = \rho_{xx}/\rho_{xy}$ obeys a strict T^2 dependence (27,28). Several models have been proposed to account for these observations. Anderson suggests

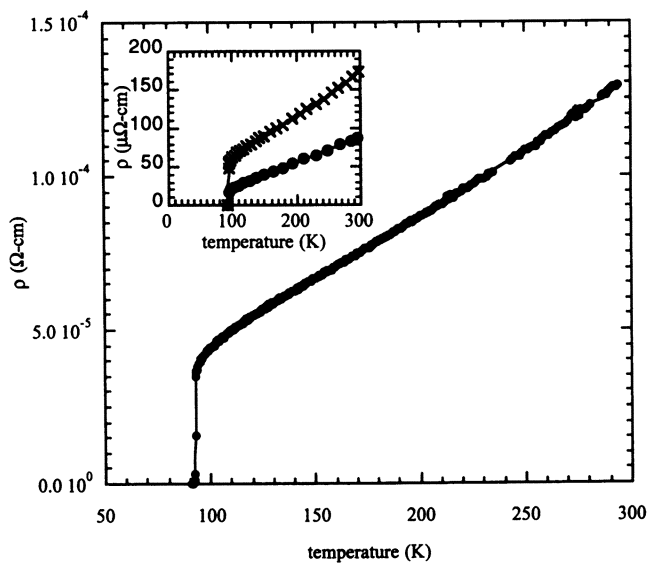


Figure 1. Resistivity versus temperature for a twinned YBCO crystal. The inset shows data for the *a*- (x) and *b*- (●) axes resistivities taken on a detwinned YBCO crystal.

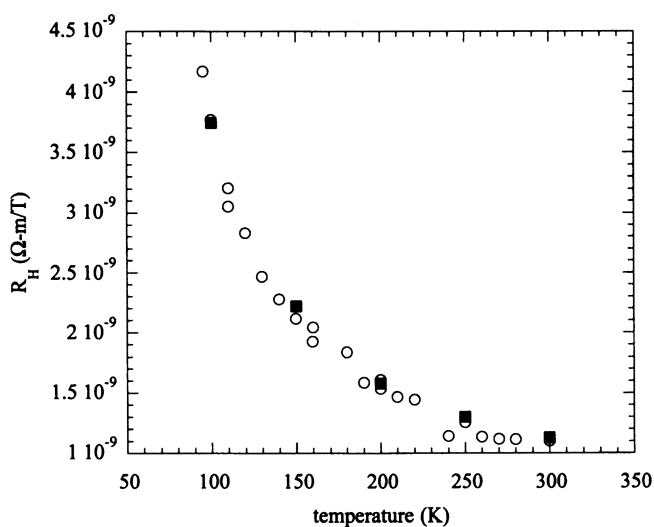


Figure 2. Temperature dependence of the Hall coefficient as measured along the *a*- (O) and *b*- (■) axes of a detwinned YBCO crystal.

that the observed behavior of $\cot(\theta_H)$ is due to different relaxation rates for charge and spin carriers (29). Carrington *et al.* (30) propose that the observed temperature dependences can be explained in terms of variations of the mean free path around the Fermi surface, while other models suggest that the temperature dependence reflects an actual change in carrier concentration (31,32). All of these models assume that the observed T^2 dependence is intrinsic in nature based on the high quality of the samples measured.

Mixed State Properties. Due to the short coherence length in the a - b plane ($\xi_{ab} \sim 20$ - 30\AA), the superconducting order parameter is highly sensitive to structural inhomogeneities on similar length scales. We will now examine several features of the superconducting state which are generally attributed to intrinsic effects and which are often observed in only the highest-quality samples.

The Hall effect in a detwinned YBCO crystal has been measured by Rice *et al.* (15) below T_c . The crystal measured in their study exhibited a very high, sharp superconducting transition and low resistivity. Their results are similar to those reported in twinned YBCO films (33,34) and crystals (35) and in $\text{Bi}_2\text{Sr}_2\text{CaCu}_2\text{O}_{8+y}$ and $\text{Tl}_2\text{Ba}_2\text{CaCu}_2\text{O}_8$ films (11,36) in that the Hall resistivity undergoes a sign change in a range of magnetic fields and temperatures below T_c . This effect has been seen in many of the HTS materials and, in fact, a second sign reversal exists in some of the materials which are more weakly coupled along the axis perpendicular to the CuO planes (37-39). This increased anisotropy results in a reduced ability of the crystal to "pin" vortices which, in turn, causes more dissipation due to vortex motion.

Further study by Harris *et al.* (26) of the angular dependence of the Hall resistivity in the mixed state have suggested a scaling relationship of the Hall conductivity with the angle between the c -axis and applied field. A model by Geshkenbein and Larkin (40) argues that the sign change arises in a two-component system in which the quasiparticle and vortex Hall currents have opposite sign. Implicit in the analysis of Harris *et al.*'s data (with respect to the Geshkenbein and Larkin model) is the assumption of fully oxygenated, homogeneous samples. The negative Hall anomaly as observed along the a -axis of a detwinned crystal is shown for various applied fields in Figure 3. The isotropic nature of this effect is shown in the Figure 3 inset.

Another example of an experiment that has revealed unusual mixed state behavior is the temperature dependent magnetoresistivity of detwinned crystals of YBCO. "Clean" YBCO crystals in the presence of an applied magnetic field have exhibited a sharp drop in resistivity at temperatures below T_c where the resistivity has reached approximately 10% of its extrapolated normal state value (7-10). This drop is approximately 100-200 mK wide in low fields. This result has been attributed to a vortex lattice "melting" transition. It has further been shown by Kwok *et al.* (8) that this drop can be suppressed by pinning at twin boundaries which suggests the effect is intrinsic. The observation of this effect is, therefore, considered a signature of high quality samples. Kwok *et al.* (41) have also reported the observation of a peak in the critical current density of a twinned sample which

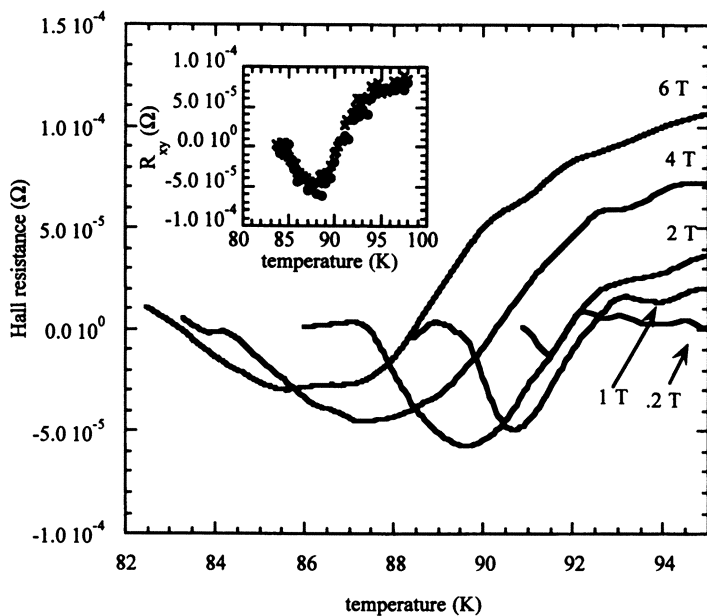


Figure 3. Field dependence of ρ_{xy} along the a -axis of a detwinned YBCO crystal below T_C as a function of applied field. The inset compares data taken along the a - (x) and b (●)- axes.

immediately precedes the "melting" transition. They attribute this effect to the enhanced pinning afforded at the twin boundaries.

The magnetoresistance along the *a*- and *b*- axes for a detwinned crystal in the mixed state is shown in Figure 4. The Figure 4 inset shows similar data taken on a twinned sample for various applied fields. The angular dependence of the twinned sample (not shown) is in agreement with Kwok *et al.*'s results which were interpreted as suggesting pinning at twin boundaries as a mechanism for suppressing the effect. However, the results of extensive structural studies, which we will now discuss, indicate the presence of various defects in crystals which exhibit this effect which preclude ruling out an extrinsic origin.

Structural Studies of $\text{YBa}_2\text{Cu}_3\text{O}_{7-\delta}$

One of the earliest hints that inhomogeneities might be affecting the sample properties came from magnetization studies. Anomalous features were observed in the constant-temperature magnetization curves obtained from crystal $\text{YBa}_2\text{Cu}_3\text{O}_{7-\delta}$ samples (42-46). It was shown that samples greater than several hundred micrometers in size generally showed evidence of granular behavior (44). These results demonstrated the pervasive nature of inhomogeneities in many YBCO crystals. In particular, Osofsky *et al.* (47) demonstrated a correlation between the observation of a low field minimum in the field dependent magnetization and the onset of "granular" behavior which they attributed to locally oxygen depleted regions.

Parks *et al.* (48) have shown that the *c*-axis lattice parameter of the orthorhombic unit cell is a reliable measure of the oxygen composition for bulk samples with disordered oxygen chains. Skelton *et al.* (49,50), using energy dispersive x-ray-diffraction techniques with synchrotron radiation, studied the variation of the *c*-lattice parameter of single crystals of YBCO and found evidence that the oxygen content diminishes near the sample surface. In addition, Qadri *et al.* (16), reported the detection of variations in the *c*-axis lattice parameter near the surfaces of YBCO crystals based on high resolution x-ray-diffraction studies. In order to determine whether structural inhomogeneities may exist in samples which exhibit "optimal" transport properties, extensive structural studies were used to examine the crystallinity of several samples with well characterized transport properties. As will be discussed, these results revealed the presence of inhomogeneities which question whether any of the observed transport properties are representative of intrinsic behavior.

High-resolution x-ray-diffraction measurements are performed on a Huber four-circle diffractometer using triple-crystal arrangement in which the monochromating and analyzing crystals are both Ge(111). Cu $K\alpha$ radiation from a rotating-anode x-ray tube is used. The $K\alpha_2$ peak is eliminated by adjusting the aperture slits between the monochromating crystal and the sample. The x-ray absorption length ($1/\mu$), for Cu $K\alpha$ radiation in YBCO is 9.1 μm . The reciprocal of the attenuation coefficient for the (006) reflection, also for Cu $K\alpha$ radiation, is 1.7 μm (51). These values bracket the upper and lower absorption limits between mosaic

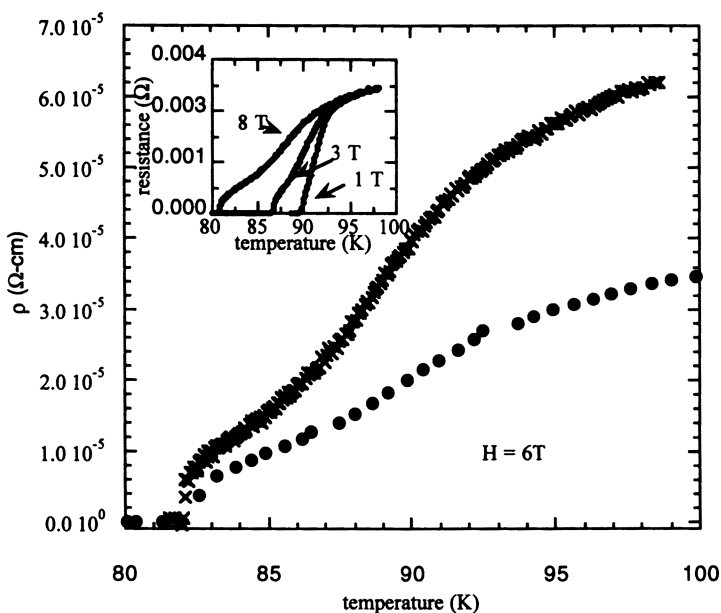


Figure 4. Magnetoconductance vs. temperature for a detwinned YBCO crystal along the a - (\times) and b - (\bullet) axes taken in an applied field of 6 Tesla. The inset shows similar data taken for a twinned sample in various applied fields.

and perfect crystals. They are representative of the depth of material being sampled in the high resolution measurements.

A representative scan along the $[0,0,l]$ reciprocal lattice vector of the $(0,0,6)$ reflection, $(\theta-2\theta)$ scan, is shown for a twinned YBCO crystal in Figure 5. Note that when examined using a conventional single-crystal diffractometer with a graphite analyzer, only a single broad peak is seen. The angular resolution of a typical conventional diffractometer is about 7 arc minutes, whereas that afforded by the high-resolution diffractometer is about 9 arc seconds.

The c -axis lattice parameter of the YBCO unit cell is a reliable indicator of the oxygen content in crystals. A simple relationship between oxygen content and the c -axis length has been established:

$$7-\delta = 74.49 - 5.787c,$$

where c is in angstroms (21). Based on this equation, the values of $(7-\delta)$ obtained from the data shown in Fig. 5 range from 6.84-6.99 based on the 3 observable peak positions. The weighted average yields a value of $(7-\delta)$ of 6.87 +/- .04.

To obtain information about the quality of individual grains or domains, rocking curves are also measured. The (006) reflection of a crystal sample is centered in ω and χ with 2θ set at a value corresponding to a particular peak. A rocking curve corresponding to the $\theta-2\theta$ scan shown in Figure 5 is shown in Figure 6 for the same sample. The measured data can be deconvoluted into multiple peaks which may be due to different oxygen concentrations and small-angle grain boundaries between crystallites.

In order to probe the interior of the crystal, the very high-energy x-rays available at the National Synchrotron Light Source (NSLS) at Brookhaven National Laboratory were used. Details of the energy dispersive diffraction facility on Beamline X17C used for this work have been described elsewhere (50).

The cross section of the impinging beam is defined by four tungsten blocks. These are controlled by computer-driven micropositioners and were set to define a beam approximately 10 μm wide and 10 μm high. Measurement of the actual cross section was accomplished by stepping a knife edge through the beam at 1 μm intervals and monitoring the transmitted intensity I_0 .

For this measurement, crystals are bonded to a glass fiber which is mounted on a four-circle $(2\theta, \omega, \chi, \phi)$ diffractometer with its $[0,0,l]$ reciprocal lattice vector approximately in the horizontal plane at $\chi \sim 0$ and normal to the incident beam at $\omega = 0$. The angle ϕ is held constant during these experiments.

A crystal is positioned so that the beam passes through its geometric center. The intensity of the $(0,0,l)$ diffraction spectra is optimized by adjusting ω and χ , and the angular positions are calibrated using the diffraction pattern from a gold foil. To avoid saturation of the Ge detector an Al plate approximately 10 mm thick is placed in the incident beam.

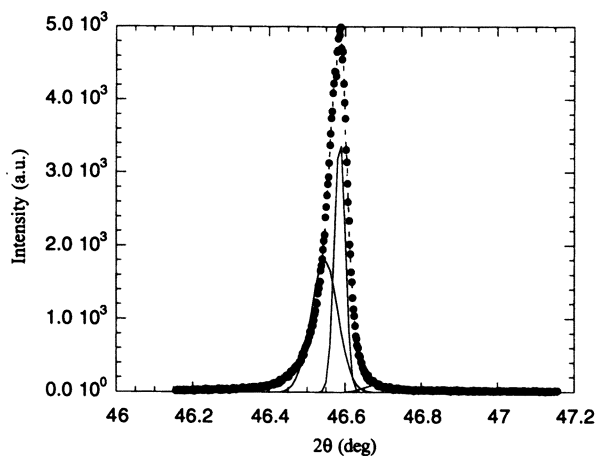


Figure 5. High-resolution specula scan of the (006) reflection for a crystal sample of YBCO taken using a triple-crystal diffractometer with $\text{Cu } K\alpha_1$ radiation. (Adapted from ref. 17)

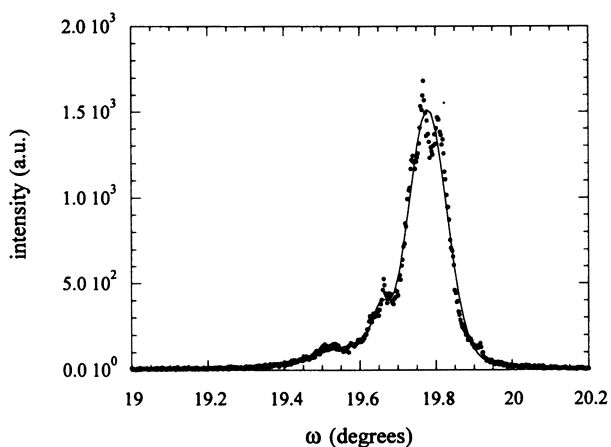


Figure 6. The rocking curve of the (006) diffraction peak shown in Figure 5. (Adapted from ref. 17).

Typically, the strongest peak in the measured spectrum, is selected for determining the length of the c -axis. This energy is chosen so that it is sufficient to allow collection of data from anywhere in the crystal interior. The intensity around the selected diffraction peak, $E_{0,0,l}$ is measured as the crystal is stepped through a series of (y,z) coordinates.

Typically several scans are made for each crystal measured and the resulting data is analyzed to yield data for the oxygen content ($7-\delta$) as a function of sample position (y,z) . Figure 7 shows a three dimensional plot of $(7-\delta)$ as a function of (y,z) for a twinned YBCO crystal which exhibits transport properties consistent with "high quality" samples. These results show clearly the large variations in c -axis which are interpreted as variations in oxygen content in the interior of the crystal.

Conclusion

Quite recently, there have been a number of experimental results which underscore the need for further understanding of the role inhomogeneities play in the transport properties of the HTS. One new technique described by Raphael *et al.* (52) may prove useful for further study of the effects of inhomogeneities, particularly in the mixed state of the HTS. They have demonstrated that the third harmonic of the a.c. susceptibility, V_{3f} , provides a sensitive measure of oxygen inhomogeneities in type II superconductors including the HTS. Peaks in V_{3f} occur at temperatures at which hysteresis in the motion of the vortices causes a nonlinear response to the applied ac field. In zero dc magnetic field, a homogeneous sample will show a single peak at the critical temperature, T_c . Figure 8a shows the multiple peaks that occur at T_c in an inhomogeneous Tl 2201 single crystal. A comparison with the more conventional first harmonic measurement, shown in Figure 8b, demonstrates the ability of the third harmonic technique to reveal structure within the transition. Evidence that this structure is due to oxygen disorder comes from annealing studies. Figure 9 shows a different Tl 2201 crystal before and after annealing at 400 °C in helium gas. The sharper transition at a higher T_c indicates that the sample is now reduced and more homogeneous with respect to oxygen content. Further confirmation of this interpretation awaits study via high resolution x-ray diffraction.

In addition to the crystal studies already discussed, Raman spectroscopy studies have demonstrated the pervasive nature of structural defects in thin films (53). Understanding how these defects might form "weak links" which can limit power handling capability and ultimate device performance provides the motivation for further study. In particular since thin films are known to be prone to even higher defect concentrations than found in crystals, the need for an understanding of their limitations becomes even more urgent since many potential applications of HTS will require thin films. The structural techniques used in this study can and have been used to look at thin films. The ability to scan various regions of a sample is particularly useful for thin films and provides a means of "quality control" for predicting device performance.

Although the robust nature of the transport properties reported here as well as those reported in the wide body of literature available on the HTS suggest an

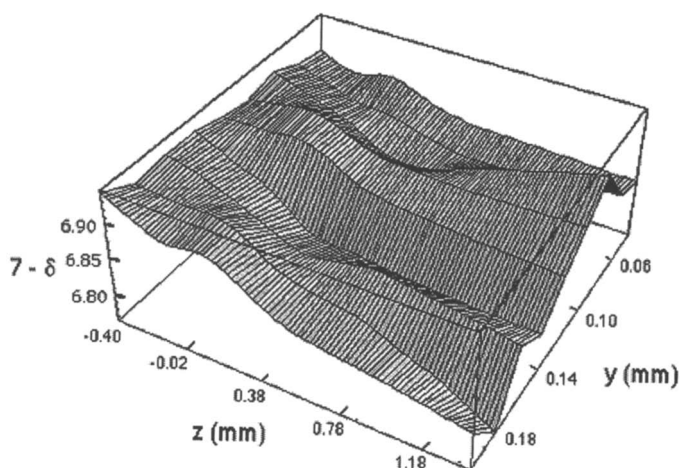


Figure 7. Three-dimensional plot of $(7-\delta)$ vs. y and z for a twinned YBCO crystal showing variations in oxygen content within the sample interior. (Reproduced with permission from ref. 17. Copyright 1997 The American Physical Society.)

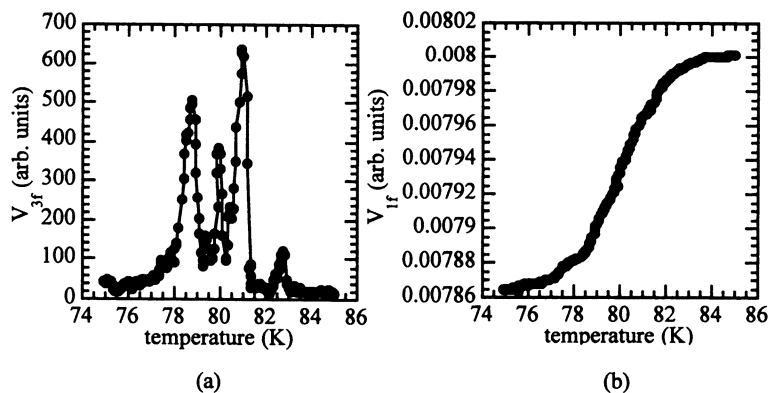


Figure 8. Third harmonic (a) and first harmonic (b) ac susceptibility measurements of a Tl 2201 crystal sample.

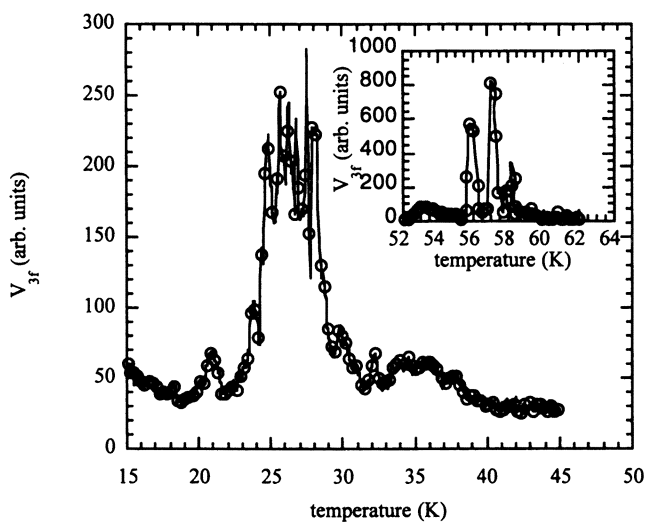


Figure 9. Third harmonic ac susceptibility measurements of an over-doped Tl 2201 single crystal sample. The inset shows the results obtained after annealing to reduce oxygen content.

intrinsic origin for many of the observed properties, one must be cognizant of the pervasive nature of structural inhomogeneities. The transport studies together with the structural studies reported by Browning *et al.* (17), which have been highlighted in this chapter, represent the most thorough characterization of HTS samples reported to date. The results have significant implications for current theories and indicate that despite exhibiting all of the transport properties that are generally associated with high-quality crystals, this sample contains oxygen defects. This brings into question the assumption that samples can be determined to be optimally doped, homogeneous crystals based on transport properties alone. These results present a challenge to theorists to either explain why the presence of inhomogeneities can be ignored or to predict how experimental results may be affected by them.

Literature Cited

- 1: Oka, K.; Unoki, J. *J. Crystal Growth* **1990**, *99*, 922.
- 2: Zhang, W.; Osamura, K.; Ochiai, S. *J. Am. Ceram. Soc.* **1990**, *73*, 1958.
- 3: Roth, R. S.; Dennis, J. R.; Davis, K. L. *Advan. Ceram. Mater.* **1987**, *2*, 303.
- 4: Lee, B.-J.; Lee, D. N. *J. Am. Ceram. Soc.* **1991**, *74*, 78.
- 5: Friedmann, T. A.; Rabin, M. W.; Giapintzakis, J.; Rice, J. P.; Ginsberg, D. M. *Phys. Rev. B* **1990**, *42*, 6217.
- 6: Welp, U.; Fleshler, S.; Kwok, W. K.; Downey, J.; Fang, Y.; Crabtree, G. W.; Liu, J. Z. *Phys. Rev. B* **1990**, *42*, 10189.
- 7: Safar H.; Gammel, P. L.; Huse, D. A.; Bishop, D. J.; Rice, J. P.; Ginsberg, D. M. *Phys. Rev. Lett.* **1992**, *69*, 824.
- 8: Kwok, W. K.; Fleshler, S.; Welp, U.; Vinokur, V. M.; Downey, J.; Crabtree, G. W.; Miller, M. M. *Phys. Rev. Lett.* **1992**, *69*, 3370.
- 9: Charalambous, M.; Chaussy, J.; Lejay, P.; Vinokur, V. *Phys. Rev. Lett.* **1993**, *71*, 436.
- 10: Kwok, W. K.; Fendrich, J.; Fleshler, S.; Welp, U.; Downey, J.; Crabtree, G. W. *Phys. Rev. Lett.* **1994**, *72*, 1092.
- 11: Iye, Y.; Nakamura, S.; Tamegai, T. *Physica C* **1989**, *159*, 616.
- 12: Galffy, M.; Zirngiebl, E. *Solid State Commun.*, **1988**, *68*, 929.
- 13: Chien, T. R.; Jing, T. W.; Ong, N. P.; Wang, Z. Z. *Phys. Rev. Lett.* **1991**, *66*, 3075.
- 14: Hagen, S. J.; Lobb, c. J.; Greene, R. L.; Forrester, M. G.; Kang, J. H. *Phys. Rev. B* **1990**, *41*, 11630.
- 15: Rice, J. P.; Rigakis, N.; Ginsberg, D. M.; Mochel, J. M. *Phys. Rev. B* **1992**, *46*, 11050.
- 16: Qadri, S. B.; Osofsky, M. S.; Browning, V. M.; Skelton, E. F.; Vanderah, T. A. *Appl. Phys. Lett.* **1996**, *68*, 2729.
- 17: Browning, V. M.; Skelton, E. F.; Osofsky, M. S.; Qadri, S. B.; Hu, J. Z.; Finger, L. W.; Caubet, P. *Phys. Rev. B* **1997**, *56*, 2860.
- 18: Ito, T.; Takenaks, K.; Uchida, S. *Phys. Rev. Lett.* **1993**, *70*, 3995.
- 19: Hauff, R.; Breit, V.; Claus, H.; Herrmann, D.; Knierim, A.; Schweis, P.; Wuhl, H.; Erb, A.; Muller-Vogt, G. *Physica C* **1994**, *235-240*, 1953.

- 20: Janod, E.; Junod, A.; Graf, T.; Wang, K.-Q.; Triscone, G.; Muller, J. *Physica C* **1993**, *216*, 129.
- 21: Vanderah, T. A.; Lowe-Ma, C. K.; Bliss, D. E.; Decker, M. W.; Osofsky, M. S.; Skelton, E. F.; Miller, M. M. *J. Cryst. Growth* **1992**, *118*, 385; Osofsky, M. S., Cohn, J. L.; Skelton, E. F.; Miller, M. M.; Soulen, R. J., Jr.; Wolf, S. A.; Vanderah, T. A. *Phys. Rev. B* **1992**, *45*, 4916.
- 22: Giapintzakis, J.; Ginsberg, D. M.; Han, P. D. *J. Low Temp. Phys.* **1989**, *77*, 155.
- 23: Gurvitch, M.; Fiory, A. T. *Phys. Rev. Lett.* **1987**, *59*, 1337.
- 24: Martin, S. *et al. Phys. Rev. B* **1990**, *41*, 846.
- 25: Halbritter, J. *Phys. Rev. B* **1993**, *48*, 9735.
- 26: Harris, J. M.; Ong, N. P.; Yan, Y. F. *Phys. Rev. Lett.* **1994**, *73*, 610; Harris, J.M.; Ong, N. P.; Matl, P.; Gagnon, R.; Taillefer, L.; Kimura, T.; Kitazawa, K. *Phys. Rev. B* **1995**, *51*, 12053.
- 27: Chien, T. R.; Wang, Z. Z.; Ong, N. P. *Phys. Rev. Lett.* **1991**, *67*, 2088.
- 28: Carrington, A.; Walker, D. J. C.; Mackenzie, A. P.; Cooper, J. R. *Phys. Rev. B* **1993**, *48*, 13051.
- 29: Anderson, P. W. *Phys. Rev. Lett.* **1991**, *67*, 2092.
- 30: Carrington, A.; Mackenzie, A. P.; Lin, C. T.; Cooper, J. R. *Phys. Rev. Lett.* **1992**, *69*, 2855.
- 31: Manako, T.; Kubo, Y.; Shimakawa, Y. *Phys. Rev. B* **1992**, *46*, 11019.
- 32: Alexandrov, A. S.; Bratkovsky, A. M.; Mott, N. F. *Phys. Rev. Lett.* **1994**, *71*, 1734.
- 33: Luo, J.; Orland, T. P.; Graybeal, J. M.; Wu, X. D.; Muenchausen, R. *Phys. Rev. Lett.* **1992**, *68*, 690.
- 34: Colino, J.; Gonzalez, M. A.; Martín, J. I.; Velez, M.; Oyola, D.; Prieto, P.; Vicent, J. L. *Phys. Rev. B* **1994**, *49*, 3496.
- 35: Harris, J. M.; Ong, N.P.; Yan, Y. F. *Phys. Rev. Lett.* **1993**, *71*, 1242.
- 36: Hagen, S. J.; Lobb, C. J.; Greene, R. L.; Eddy, M. *Phys. Rev. B* **1991**, *43*, 6246.
- 37: Zavaritsky, N. V.; Samoilov, A. V; Yurgens, A. A. *Physica C* **1991**, *180*, 417.
- 38: Samoilov, A. V.; Ivanov, Z. G.; Johansson, L.-G. *Phys. Rev.* **1994**, *49*, 3667.
- 39: Dascoulidou, A.; Galffy, M.; Hohn, C.; Knauf, N.; Freimuth, A. *Physica C* **1992**, *201*, 202.
- 40: Geshkenbein, V. B.; Larkin, A. K. *Phys. Rev. Lett.* **1994**, *73*, 609.
- 41: Kwok, W. K.; Fendrich, J. A.; van der Beek, C. J.; Crabtree, G. W. *Phys. Rev. Lett.* **1994**, *73*, 2614.
- 42: Kupfer, H.; Apfelstedt, I.; Flukiger, R.; Keller, C.; Meier-Hirmer, R.; Runtsch, B.; Turowski, A; Wiehc, U.; Wolf, T. *Cryogenics* **1989**, *29*, 268.
- 43: Sulpice, A.; Lejay, P.; Tournier, R.; Chaussy, J. *Europhys. Lett.* **1988**, *7*, 365.
- 44: Yeshurun, Y.; McElfresh, M. W.; Malozemoff, A. P.; Hagerhorst-Trewhella, J.; Mannhart, J.; Holtzberg, F.; Chandrashekar, G. V. *Phys. Rev B* **1990**, *42*, 6322.
- 45: Daeumling, M.; Seuntjens, J. M.; Larbalestier, D. C. *Nature* **1990**, *346*, 332.
- 46: Welp, U.; Kwok, W. K.; Crabtree, G. W.; Vandervoort, K. G.; Liu, J. Z. *Appl. Phys. Lett.* **1990**, *57*, 84.
- 47: Osofsky, M. S.; Cohn, J. L.; Skelton, E. F.; Miller, M. M.; Soulen, R. J., Jr.; Wolf, S. A.; Vanderah, T. A. *Phys. Rev. B* **1992**, *45*, 4916.

- 48: Parks, M. E.; Navrotsky, A.; Mocala, K.; Takayama-Muromachi, E.; Jacobson, A.; Davies, P. K. *J. Solid State Chm.* **1989**, *79*, 53.
- 49: Skelton, E. F.; Drews, A. R.; Osofsky, M. S.; Qadri, JS. B.; Hu, J. Z.; Vanderah, T. A.; Peng, J. L.; Greene, R. L. *Science* **1994**, *263*, 1416.
- 50: Skelton, E. F.; Qadri, S. B.; Osofsky, M. S.; Drews, A. R.; Broussard, P. R.; Hu, J. Z.; Finger, L. W.; Vanderah, T. A.; Kaiser, D.; Peng, J. L.; Anlage, S. A.; Greene, R. L.; Giapintzakis, J. *Proc. SPIE* **1995**, *2516*, 160.
- 51: Warren, B. E.; *X-Ray Diffraction Procedures*; Addison-Wesley: Reading, MA, 1969; pp. 328-329.
- 52: Raphael, M. P.; Reeves, M. E.; Skelton, E. F. *Rev. Sci. Inst.* **1998**, *69*, 1.
- 53: Gibson, G.; MacManus-Driscoll, J. L.; Cohen, L. F. *IEEE Trans. Appl. Supercond.* **1997**, *7*, 2130.

Chapter 6

Lattice Dynamical Calculations of High- T_c Superconducting Compounds

F. W. de Wette

Department of Physics, University of Texas at Austin, Austin, TX 78712

The experimental information about the lattice dynamics of most high-temperature superconducting compounds (HTSC) consists mainly of measurements of the optical modes and the phonon densities of states. This lack of information hampers the development of lattice dynamical models. To overcome this difficulty one can treat the lattice dynamics of the HTSC in analogy with that of the oxidic perovskites, namely with shell models which employ Coulomb potentials, ionic polarizabilities and short-range repulsive pair potentials which are obtained from well-studied compounds. With such models one can calculate all the phonons, and the phonon-related properties. Of the former we discuss phonon dispersion and phonon densities of states; of the latter we discuss phonon specific heat and comment on the role of phonons in the electrical resistivity.

The basic mechanism of high temperature superconductivity is still unknown. While many new or exotic mechanisms have been proposed, the electron-phonon interaction has not been ruled out, and certainly could provide a contributing mechanism. As a result, the lattice dynamical (phonon) properties of high-temperature superconducting compounds (HTSC), both in their superconducting and normal states have been extensively studied through Raman (1,2) and infrared (ir) scattering (3,4), as well as inelastic neutron scattering (5); the phonon density of states has also been studied in tunneling experiments (6). Furthermore, phonons play their customary role in the specific heat of the HTSC (7), and are of importance for the transport properties (8).

This general interest and importance of phonons in the HTSC was the motivation for our theoretical studies of the lattice dynamics and the phonon-related properties of these compounds in their semiconducting (nonsuperconducting) state (9-16). So far we have treated ten compounds, namely $\text{YBa}_2\text{Cu}_3\text{O}_7$ (10), $\text{Bi}_2\text{CaSr}_2\text{Cu}_2\text{O}_8$ (11), six thallium compounds (12,14), $\text{Pb}_2\text{Sr}_2\text{YCu}_3\text{O}_8$ (13), and $\text{Nd}_{2-x}\text{Ce}_x\text{CuO}_4$ (15) on a common basis, i.e. using a model employing a consistent set of interaction potentials and other model parameters (La_2CuO_4 (9)), the first compound that we considered, was not treated

on this same basis). Our approach enabled us to treat the lattice dynamics of these compounds with the knowledge of the experimental structures as the only input and then to predict for most of the compounds (without much prior knowledge of the experimental results) the optical modes with sufficient accuracy (in the average of 10%) to correctly determine their sequence of polarization assignments. This predictive capability and overall agreement with the results of optical experiments has certainly justified and validated our general approach.

After a description of our lattice dynamical method, a number of results for phonon related properties of the HTSC are briefly discussed: optical phonons, phonon dispersion curves, phonon densities of state, lattice specific heat, and resistivity.

Lattice Dynamical Model

A customary lattice dynamical calculation requires knowledge of the crystal structure and of the particle (ionic) interactions. The structure is determined by x-ray or neutron diffraction. For the ionic interactions one customarily uses models, which are supposed to represent the characteristics of the underlying electronic structure and its effects on the ionic interactions in a reasonable fashion (17-19). In the dynamical matrix the ionic interactions are expressed in terms of force constants, which are usually determined from least-squared fits of calculated to experimental phonon dispersion curves. In the case of the HTSC, a number of difficulties are encountered with this approach. First, because of the large number of particles in the unit cell and the relatively low symmetry of the HTSC, a large number of model parameters are needed. In most cases the number of measured phonon frequencies is insufficient to determine these parameters, and moreover, little or no experimental information is available about the vibrational eigenvectors. Since only eigenvalues in combination with eigenvectors determine the dynamical problem uniquely (20), the dynamical matrix constructed in this fashion is poorly determined; this in turn means that calculated eigenvectors may not have the proper physical meaning. Because of these unusual circumstances, a different approach to the lattice dynamics of the HTSC had to be followed. This approach is based on the following considerations: (1) The HTSC are closely related to their parent compounds, the oxidic perovskites, and the latter are, in their undoped form, predominantly ionic materials; some of them exhibit incipient or real lattice instabilities (e.g. as a function of doping). (2) The primary interactions in the perovskites are long-range Coulomb interactions and short-range overlap interactions resulting from the predominantly closed-shell electronic configurations. These interactions can be properly represented in the framework of shell models, including dynamic deformations of the electronic charge distribution in the form of ionic polarizabilities. (3) The short-range interactions of the ion pairs can be represented by Born-Mayer potentials, which are quite independent of the crystal environment of the ion pair. As a result these pair potentials can, to a good approximation, be transferred from well-studied compounds (such as the perovskites, and metal oxides) to related but little known compounds (such as the HTSC) for which no direct experimental phonon information is available. (4) A dynamical matrix based on potentials rather than on mere force constants, has the advantage that the underlying physics is transparent, and the eigenvalues and eigenvectors are obtained in the same approximation; this results in a reasonably accurate and internally consistent dynamical description. On the basis of these principles we have been able to treat the lattice dynamics of the HTSC (in the harmonic approximation) with the models using the *same* short-range potentials for the ionic pair interactions (such as Cu-O, Ba-O, Sr-O, etc.) which are common to all the compounds.

A very important additional condition which we require of our calculations with these models is that they lead to complete *dynamic stability* (i.e., real phonon energies for all wave vectors in the Brillouin zone) for all compounds treated. Because of the delicate stability of the HTSC this is an extremely stringent condition, particularly in combination with the requirement of common potentials. Therefore, the fact that these requirements could be fulfilled for this entire series of compounds means that we have succeeded in developing a strongly coherent lattice dynamical approach, which requires for its implementation, in essence, only a knowledge of the structures of the HTSC. This should be contrasted with force constant approaches; not only do they require for the determination of the model parameters, for each compound a substantial number of dynamical input data, but these force constants themselves are not transferable from one compound to another. A particularly serious shortcoming of some force constant calculations is the absence of Coulomb interactions and ionic polarizabilities. In the perovskites and the HTSC the competition between the Coulomb and the short-range forces can result in mode softening which, in turn, can be the cause of structural phase transitions, such as the tetragonal to orthorhombic transitions occurring in $\text{La}_{2-x}\text{M}_x\text{CuO}_4$ and $\text{YBa}_2\text{Cu}_3\text{O}_{7-\delta}$ as functions of doping (21).

Results

Optical Phonons. One of the early goals of our work was to assist in the characterization of the optical phonons, measured by Raman and ir spectroscopy. For instance, our calculations on $\text{YBa}_2\text{Cu}_3\text{O}_7$ (10,16) helped settle some controversies in the mode assignments of this compound. As an illustration we display in Figure 1 the energies and polarizations of the Raman A_{1g} modes of (orthorhombic) $\text{YBa}_2\text{Cu}_2\text{O}_7$, calculated with our "common" model (unpublished). In these calculations no attempt has been made to fit any particular measured phonon energy. The calculated phonon energies agree well within 10% with the measurements (except for the 380 cm^{-1} mode; the average for all optical modes, however, is 5.4%). This kind of agreement is typical for what is obtained for all the compounds calculated with our common model (10,11,13-15). In view of the very general considerations and input data from which the potentials for this common model were obtained, one certainly cannot expect any better agreement. This also means that the model for any particular compound should be modified or extended only if accurate and detailed inelastic neutron scattering measurements of phonon dispersion curves present compelling reasons for such modifications.

Phonon Dispersion Curves. Measurements of the phonon energy $\hbar\omega(\mathbf{q})$ as functions of the wave vector provide the most complete experimental information about the phonons, particularly if polarization vector information is also available. Phonon dispersion curves are measured with coherent inelastic neutron scattering; this requires single crystals of the order of 1 cm^3 . Since HTSC crystals of this size were initially not available, the phonon dispersion studies were slow to get started, and to date, have been performed for only a handful of compounds.

Our lattice dynamical calculations were initiated prior to these measurements and cover a much broader group of compounds. Due to these circumstances, experimental phonon dispersion information has not directly been taken into account in most of our calculations. An exception is the case of Nd_2CuO_4 (24) for which inelastic neutron scattering measurements were made (25) prior to the calculations. The latter were performed with two interaction models: 1. the *generic model*, in which the interaction potentials of given ion pairs (e.g. Cu-O, O-O) are the same for all compounds in which they are used, and 2. the *fitted model*

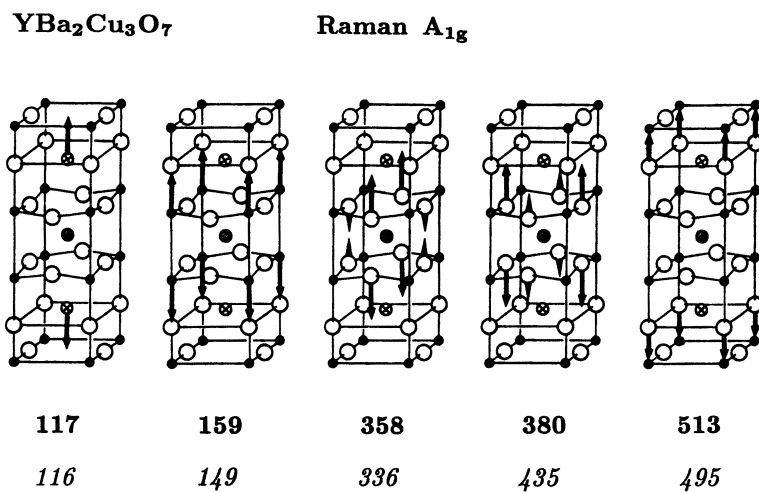


Figure 1. Polarization diagrams of the Raman A_{1g} modes of YBa₂Cu₃O₇. The phonon frequencies are in cm⁻¹; the experimental values (*italics*) are from ref. 23. (Reproduced with permission from ref. 22. Copyright 1991 Gordon and Breach.)

in which the measured phonon dispersion data were used to refine the model. Figure 2 (top) shows the Brillouin zone of the body centered tetragonal structure with symmetry directions indicated. In Figure 2 (bottom) we present the calculated phonon dispersion curves (left and right panels) and the measurements (middle panel), for wave vectors along the main symmetry directions. The calculated curves are drawn according to their representation (full, broken, dashed, dotted lines) in agreement with the experimental designations (in the middle panel the lines connect points of the same representation, as a guide to the eye).

Comparing the left and middle panels we see reasonable overall resemblance of these sets of curves and the ordering of the branches according to the various representations is given correctly by the calculations. This is rather striking, because the generic model was developed without experimental dispersion data. However, it is not surprising that there are discrepancies, such as the lower acoustic modes along ΓX . Nevertheless the overall agreement just noted provides a rather powerful justification for our general approach to the lattice dynamics of these complex compounds.

The dispersion results of the fitted model (r.h. panel) are of course in better agreement with experiment; in particular the acoustic modes are improved substantially.

Phonon Densities of State (PDOS). While dispersion curves contain the most detailed lattice dynamical information, PDOS can often reveal important features of the phonon spectra. PDOS are measured by incoherent inelastic neutron scattering (c.f. 5) and by tunneling experiments (c.f. 6).

The PDOS function $F(\omega)$ is needed in the calculation of the thermodynamic properties (e.g., specific heat), but is also a key ingredient in calculations of the transition temperature T_c (e.g., Eliashberg theory) and the isotope effect. The effects of isotope substitution are very clearly revealed in the calculated PDOS functions. In Figure 3 we show the calculated PDOS for $YBa_2Cu_3O_7$ (26). The solid line curves are for the compounds with all oxygens being the ^{16}O isotope, the dashed line with the ^{18}O isotope. It is interesting to observe that the frequency shift is not limited to a few sharp peaks representing the oxygen vibrations, but that it has a significant effect on the entire spectrum. This has important consequences for the evaluation of the isotope shift in T_c ; the entire PDOS function is needed.

The PDOS for typical HTSC's extend to 600-800 cm^{-1} (24,26,30). If one uses such a PDOS in McMillan's equation for T_c in strong-coupling BCS superconductors (27) one finds a value for T_c in the range 30-50 K (26). This means that for $L_{2-x}M_xCuO$, the measured T_c (34-37K) can be obtained with McMillan's equation; moreover the $^{16}O \rightarrow ^{18}O$ isotope shift ΔT_c is also found to be of the right order of magnitude. These results would support the conclusion that $L_{2-x}M_xCuO_4$ is a strong-coupling BCS superconductor. In contrast, for $YBa_2Cu_3O_7$ and the thallium compounds, the T_c values lie outside the validity range of McMillan's equation. This, together with the apparent absence of the isotope effect in these compounds, has been taken to mean that an alternative microscopic mechanism underlies the high- T_c phenomenon. However, if this new mechanism would also underlie the T_c of $L_{2-x}M_xCuO_4$, rather than the electron-phonon (el-ph) interaction, one would have to explain why the isotope effect is nevertheless present. This, and recent tunneling experiments (28), seem to indicate that the el-ph interaction must play a strong supportive role in the high- T_c phenomenon.

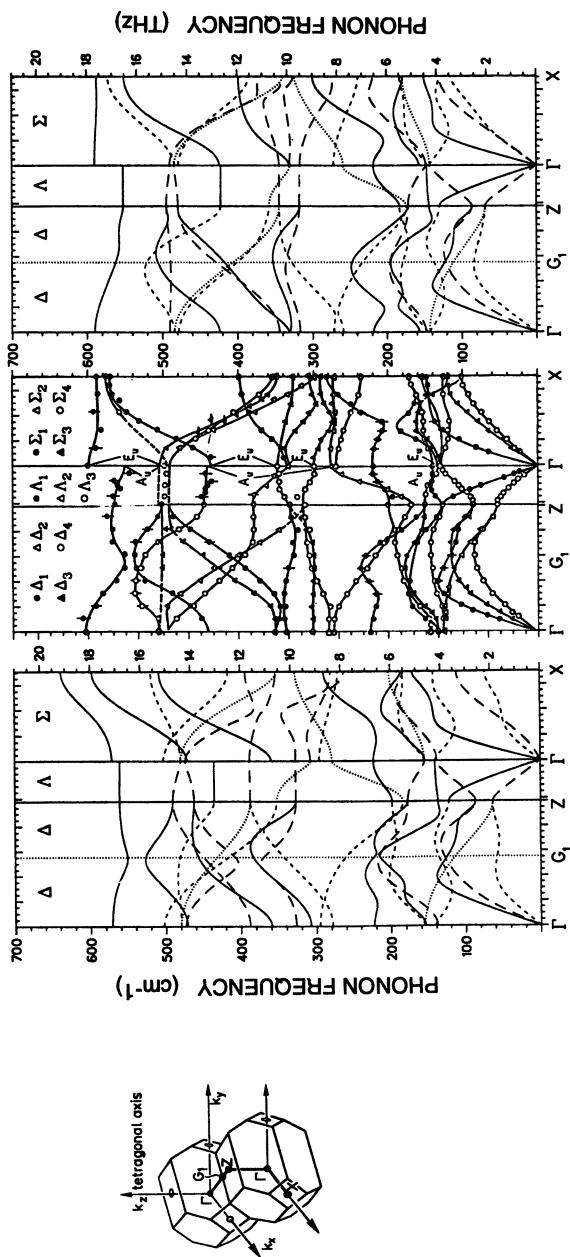


Figure 2. (Left) Brillouin zone (BZ) of the body centered tetragonal structure, with symmetry directions indicated. (Right) Phonon dispersion curves of Nd₂CuO₄ along symmetry directions in the BZ. For explanation see text. (Reproduced with permission from reference 24. Copyright 1993 American Physical Society.)

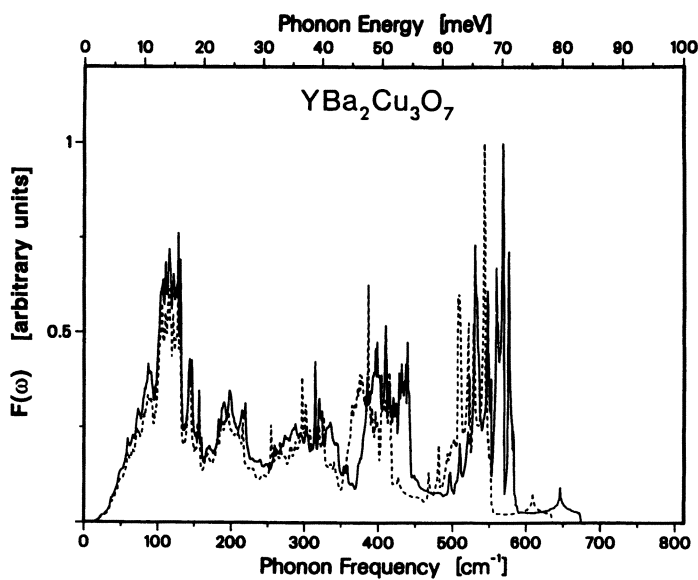


Figure 3. Calculated PDOS of YBa₂Cu₃O₇. Solid line for ¹⁶O, dashed line for ¹⁸O. (Reproduced with permission from ref. 26. Copyright 1988 American Physical Society.)

Lattice Specific Heat. Specific heat measurements have traditionally been an important tool in the study of superconductors; they reveal the value of T_c and allow the investigation of the electronic, vibrational, and magnetic excitation spectra. HTSC pose a special problem because the lattice (phonon) specific heat is unusually large, and there are also contributions from extrinsic effects (defects, structural instabilities) which complicate the disentanglement of the various intrinsic contributions (cf. 7). In order to separate the latter, it is therefore very important to be able to evaluate the phonon specific heat as accurately as possible. This, of course, is particularly important below T_c where the other intrinsic contributions are of greatest interest.

Given the PDOS $F(\omega)$ of a particular HTSC, the lattice (phonon) specific heat $c_v^{\text{ph}}(T)$ is given by the customary expression

$$c_v^{\text{ph}}(T) = \frac{k_B^2 T}{\hbar} \int_0^\infty \frac{x^2 e^x}{(e^x - 1)^2} F\left(x \frac{k_B T}{\hbar}\right) dx,$$

where $x = \hbar\omega/k_B T$. It turns out that the so-called *Debye region* where $c_v^{\text{ph}} = \beta T^3$ extends to only very low temperatures (~ 4 K or less) for most HTSC; this has to do with the very small region around the origin in wave vector space, where the acoustic modes $\omega(\mathbf{q})$ are linear functions of \mathbf{q} : $\omega(\mathbf{q}) = v_{\text{sound}} \mathbf{q}$. The extent of the Debye region is best judged by considering the function $c_v(T)/T^3$. In Figure 4 we have plotted the function $c_v^{\text{ph}}(T)/T^3$ as calculated for $\text{YBa}_2\text{Cu}_3\text{O}_7$ (29) in the temperature ranges 0 - 100 K and 0 - 10 K, respectively. From Figure 4b it is evident that the Debye region, where $c_v^{\text{ph}}(T)/T^3 = \beta$ does not extend beyond 3K.

Furthermore, we see from Figure 4a that in the range 5 - 12 K, $c_v^{\text{ph}}(T)/T^3$ is linear in T , *i.e.* $c_v^{\text{ph}}(T) \approx \beta T^3 + \delta T^4$, while for $T > 12$ K $c_v^{\text{ph}}(T)/T^3$ is no longer linear in T . It is thus clear that even at low temperatures (> 3 K) where most solids exhibit Debye behavior, for the HTSC $c_v^{\text{ph}}(T)$ is a quite complicated function of T (cf. also 30). This behavior is a direct consequence of the non-linear character (curvature) of the acoustic modes in the low frequency regime, combined with the hybridization of the acoustic and optical modes at low energies (≈ 2 THz), which gives rise to Einstein-like modes at these energies (cf. 31).

Electrical resistivity. A final comment concerns the electrical resistivity. For many HTSCs the normal-state electrical resistivity parallel to the Cu-O planes has been found to be a surprisingly linear function of T over a wide range of temperatures. This has been regarded as a very characteristic property of the HTSCs, and a number of investigators (cf. 8) have considered this as a strong indication that a microscopic mechanism different from the electron-phonon (el-ph) interaction must be underlying the high- T_c phenomenon in these compounds. However, other investigators (cf. 8, 32) have shown that the occurrence of linear resistivity over a broad range of temperatures is compatible with the Bloch-Grüneisen (BG) theory of resistivity in metals. Thus, the linear resistivity does, in itself, not rule out the el-ph interaction as a possible (important) underlying mechanism of high-temperature superconductivity. A calculation of the normal-state electrical resistivity $\rho(T)$ of a metal employs the PDOS of the compound (cf.

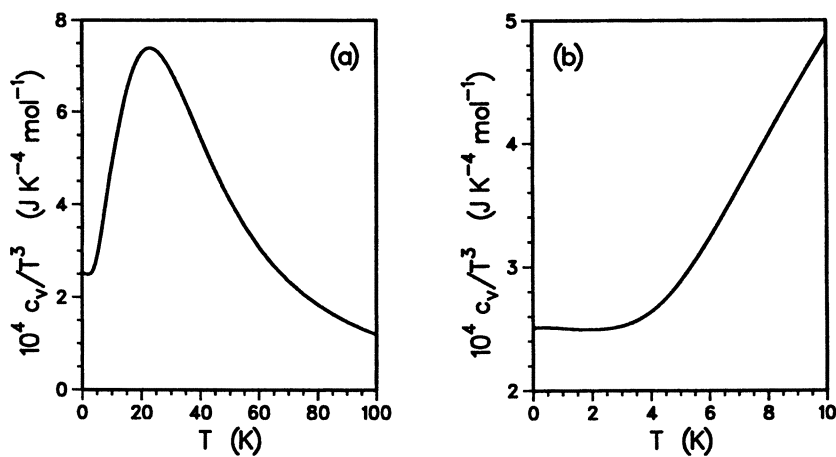


Figure 4. $c_v^{\text{ph}}(T)/T^3$ for YBa₂Cu₃O₇ in the ranges 0 - 100 K and 0 - 10 K (Reproduced with permission from ref. 29. Copyright 1990 American Physical Society.)

32). In such a calculation for $\text{YBa}_2\text{Cu}_3\text{O}_7$ (33), it was found that $\rho(T)$ is linear in T for $T \geq 90$ K, and in general, that a typical PDOS of HTSCs leads to phonon-induced electrical resistivities which are pseudo-linear functions of T down to temperatures of the order of typical transition temperatures of the HTSCs.

These resistivity calculations do not take into account Umklapp scattering. However, in $\text{YBa}_2\text{Cu}_3\text{O}_7$ and other HTSCs, Umklapp scattering is likely to be important at low temperatures of the order of T_c , because the low-lying optical branches, extending over the entire Brillouin zone, make low frequency phonons with large wave-vectors available for Umklapp scattering at these lower temperatures. Therefore, it stands to reason that the presence of low-frequency phonons with large wave-vectors will restrict the BG regime of the resistivity to lower temperatures than follows from the BG theory ($\rho \propto T^5$), according to which only acoustical phonons contribute to $\rho(T)$ at low temperatures. This effect of an extension of the linear (classical) regime to lower temperatures may be one of the reasons why the $\rho(T)$ for some HTSCs seems to extrapolate to zero for $T \rightarrow 0$ (8).

Summary

The lattice dynamics of the high- T_c superconducting compounds can be treated with shell models based on interaction potentials between pairs of ions. The potentials are separated in long-range Coulomb and short-range overlap parts for which we assume Born-Mayer potentials. These potentials are independent of the spatial arrangement of the interacting ion pair as long as the ions in the crystal have approximately closed shell configurations. As a result, to a large extent, these potentials can be transferred from one compound to another, and also between structures. In addition to the pair potentials we take into account displacement induced deformations of the electronic charge densities in the form of polarizabilities. These potentials and polarizabilities are determined from reliable measurements of the phonon dispersion curves of related compounds (perovskites, metal oxides). The requirements of common pair potentials for different compounds, and of phonon stability for all compounds treated, restricts the available space of the potential parameters to a very narrow range, and allows only minor parameter variations. In our calculations this procedure yielded for all allowed sets of parameters Raman and ir modes of the various compounds which are close to the experimental data. This allowed us to determine the Bi-O and Tl-O interaction potentials in going from $\text{YBa}_2\text{Cu}_3\text{O}_7$ (10) to $\text{Bi}_2\text{CaSr}_2\text{Cu}_2\text{O}_8$ (11) and $\text{Tl}_2\text{CaBa}_2\text{Cu}_2\text{O}_8$ (12). With these lattice dynamical models one can calculate the complete phonon spectra and the phonon related properties of the HTSC. This should be of particular importance for the study of these compounds, because it will allow the (in many instances large) phonon contributions to be subtracted from the measured quantities so that contributions of non-phonon mechanisms can be better isolated.

Acknowledgement. The author acknowledges support by the Robert A. Welch Foundation (Grant F-433) during the entire period in which the research described here was carried out.

Literature Cited

1. Thomsen, C., and Cardona, M. *Physical Properties of High Temperature Superconductors I*, Ginsberg, D.M., Ed. (World Scientific, Singapore 1989), pp. 409-507.
2. Timusk, T., and Tanner, D.B. in *Physical Properties of High Temperature Superconductors I*, Ginsberg, D.M., Ed. (World Scientific, Singapore 1989), pp. 339-408.
3. Tanner, D.B., and Timusk, T. in *Physical Properties of High Temperature Superconductors III*, Ginsberg, D.M., Ed. (World Scientific, Singapore 1992), pp. 363-470.
4. Litvinchuk, A.P., Thomsen, C., and Cardona, M. in *Physical Properties of High Temperature Superconductors IV*, Ginsberg, G.M., Ed. (World Scientific, Singapore 1994), pp. 375-470.
5. Pintschovius, L., and Reichardt, W. in *Physical Properties of High-Temperature Superconductors IV*, Ginsberg, G.M., Ed. (World Scientific, Singapore 1994), pp. 295-374.
6. Hasegawa, T., Ikuta, H., and Kitazawa, K., in *Physical Properties of High Temperature Superconductors III*, Ginsberg, G.M., Ed. (World Scientific, Singapore 1994), pp. 525-622.
7. Junod, A., in *Physical Properties of High Temperature Superconductors II*, Ginsberg, D.M., Ed. (World Scientific, Singapore 1990), pp. 13-120.
8. Iye, Y., in *Physical Properties of High Temperature Superconductors III*, Ginsberg, D.M., Ed. (World Scientific, Singapore 1992), pp. 285-362.
9. Prade, J., Kulkarni, A.D., de Wette, F.W., Kress, W., Cardona, M., Reiger, R., and Schröder, U., *Solid State Commun.* **1987**, *64*, 1267-1271.
10. Kress, W., Schröder, U., Prade, J., Kulkarni, A.D., and de Wette, F.W., *Phys. Rev.* **1988**, *B 38*, pp. 2906-2909.
11. Prade, J., Kulkarni, A.D., de Wette, F.W., Schröder, U., and Kress, *Phys. Rev.* **1989**, *B 39*, 2771-2774. zzt
12. Kulkarni, A.D., Prade, J., de Wette, F.W., Kress, W., and Schröder, U., *Phys. Rev.* **1989**, *B 40*, 2642-2645.
13. Kress, W., Prade, J., Schröder, U., Kulkarni, A.D., and de Wette, F.W., *Physica* **1989**, *C162-164*, pp. 1345-1346.
14. Kulkarni, A.D., de Wette, F.W., Prade, J., Schröder, U., and Kress, W., *Phys. Rev.* **1990**, *B 41*, 6409-6417.
15. Heyen, E.T., Kliche, G., Kress, W., König, W., Cardona, M., Rampf, E., Prade, J., Schröder, U., Kulkarni, A.D., de Wette, F.W., Pinol, S., Paul, D. McK., Morán, E., and Alario-Franco, M.A., *Solid State Commun.* **1990**, *74*, 1299-1304.
16. Liu, R., Thomsen, C., Kress, W., Cardona, M., Gegenheimer, B., de Wette, F.W., Prade, J., Kulkarni, A.D., and Schröder, U., *Phys. Rev.* **1988**, *B 37*, 7971-7974.
17. Only in a first-principles calculation are the particle interactions obtained from complete solutions of the electronic problem. Such an approach involves large-scale calculations which are at present unpractical for the HTSC. They have only been carried out for La_2CuO_4 (18) and $\text{YBa}_2\text{Cu}_3\text{O}_7$ (19); they still require parametrizations of the interactions for the calculation of phonons for general wave vectors.
18. Cohen, R.E., Pickett, W.E., and Krakauer, H., *Phys. Rev. Lett.* **1989**, *62*, 831-834.
19. *Ibid*, **1990**, *64*, 2575-2578.

20. Leigh, R.S., Szigeti, B., and Tewari, V.K., Proc. Roy. Soc. London **1971**, Ser. A *320*, 505-526.
21. In our calculation of $\text{La}_{2-x}\text{M}_x\text{CuO}_4$ (Ref. 9) a 20% reduction in the La charge, representing the effect of doping, gives rise to mode-softening at the X point of the Brillouin zone, which ultimately leads to the tetragonal to orthorhombic transition.
22. de Wette, F.W., Comments Cond. Mat. Phys. **1991**, *15*, 225-240.
23. McCarty, K.F., Lin, J.Z., Shelton, R.N., and Radousky, H.B., Phys. Rev. **1990**, B *41*, 8792-8797.
24. Rampf., E., Schröder, U., de Wette, F.W., Kulkarni, A.D., and Kress, W., Phys. Rev. **1993**, B *48*, 10143-10152.
25. Pintschovius, L., et al., Physica **1991**, B *174*, 323-329.
26. de Wette, F.W., Prade, J., Kulkarni, A.D., Schröder, U., and Kress, W., Phys. Rev. **1988**, B *38*, 6583-6587.
27. McMillan, W.L., Phys. Rev. **1968**, *167*, 331-334.
28. Shimada, D., Tsuda, N., Paltzer, U., and de Wette, F.W., Physica **1998**, C (in press).
29. de Wette, F.W., Kulkarni, A.D., Prade, J., Schröder, U., and Kress, W., Phys. Rev. **1990**, B *42*, 6707-6710.
30. Kulkarni, A.D., de Wette, F.W., Prade J., Schröder, U. and Kress, W., Phys. Rev. **1991**, B *43*, 5451-5458.
31. de Wette, F.W., and Kulkarni, A.D., Phys. Rev. **1992**, B*46*, 14922-14925.
32. Allen, P.B., Comments Condens. Matter Phys. **1992**, *15*, 327-353.
33. de Wette, F.W., and Kulkarni, A.D., Phil. Mag. B **1994**, *70*, 637-642.

Chapter 7

Raman Spectroscopy of Phase Separation and Reordering Processes in YBCO-Type Compounds

Milko N. Iliev

Texas Center for Superconductivity, University of Houston,
Houston, TX 77204-5932

At a microscopic level the local structure of oxygen-deficient $\text{YBa}_2\text{Cu}_3\text{O}_x$ -type compounds ($0 < x < 1$) is characterized by the coexistence of different types of arrangements of the oxygen atoms in the 'basal' Cu1-O planes. As a rule, the size of ordered domains is below the detection limit of standard X-ray and neutron diffraction techniques which average the lattice parameters and interatomic distances over all coexisting local structures. In contrast, Raman spectroscopy allows one to detect coexisting microdomains due to the fact that the Raman-active vibrations are sensitive mainly to the nearest surroundings of the vibrating atom and the superimposed Raman signals coming from domains of different atomic ordering (OI, OII, T) differ significantly in frequency and resonant properties. The existence of domains of partial oxygen disorder (T'-phase) results in the appearance of additional Raman lines. The relative weight of OI, OII, T and T' domains is determined mainly by the averaged oxygen content x and the temperature. This allows one to monitor the reordering processes during annealing in different atmospheres or in vacuum. In the overdoped case ($x > 7$) the oxygen arrangement is more complicated and still not well established. The Raman spectra of overdoped $\text{YSr}_2\text{Cu}_3\text{O}_{7.7}$ ($T_c = 60$ K), which are substantially different from those of $\text{YBa}_2\text{Cu}_3\text{O}_x$ are also discussed.

Long after their discovery the $\text{RBA}_2\text{Cu}_3\text{O}_x$ compounds (R = Y, Rare Earth) were treated exclusively as single-phase materials. Within a picture based on results of X-ray (XRD) and neutron diffraction (NRD) analysis, for $x = 7$ the materials are orthorhombic (space group $Pmmm$). The withdrawal of oxygen from the basal planes decreases the orthorhombicity (represented by the a/b ratio) and at $x < 6.4$ - 6.5 the structure becomes tetragonal ($I4/mmm$). While for the limit values of $x = 7$ (full chains) and $x = 6$ (empty chains) it is reasonable to accept that the averaged structure determined by XRD or NRD coincides with the local structure of the smallest-size

domains, this *a priori* cannot be true for the intermediate values of x . What one expects in that case is either statistical distribution of the oxygen atom in the basal planes over all available "chain" (O1) and "vacancy"(O5) sites (like in the high temperature tetragonal T' phase), or coexistence of ordered domains of different oxygen content.

The existence in $\text{YBa}_2\text{Cu}_3\text{O}_x$ (YBCO) of several types of stable and metastable ordered phases has been predicted on the basis of Monte Carlo simulations and has intensively been discussed in a number of theoretical works (1-3). Although experimental indications for formation of some of these phases (OII, OIII) at x equal to some rational numbers have also been reported (4-6), the diffraction pattern in most of the numerous XRD and NRD experiments have been found to correspond to a single-phase rather than a multi-phase structure in the whole $6 < x < 7$ range. These results are not controversial. They only imply that the average size of ordered domains (if present) is below the detection limit of conventional diffraction techniques (typically > 100 lattice constants). Indeed, studies of local-structure-dependent parameters such as the number and energies of Raman phonons (7-9) or of transitions between the crystal-field-split 4f levels of the rare earth elements (10,11) have shown that the phase separation in poorly oxygenated $\text{RBa}_2\text{Cu}_3\text{O}_x$ does take place at a microscopic level. Moreover, such a phase separation seems to be the rule rather than a result of occasional fulfillment of special conditions concerning temperature, oxygen stoichiometry and history of the sample.

Further, we motivate the effectiveness of Raman spectroscopy for analysis of phase separation in the YBCO-type materials. It will be shown that except for characterization of a sample with respect to the existence of microdomains of different oxygen ordering, Raman technique can successfully be applied in studies of reordering processes during different treatments, such as thermal annealing, ion cluster bombardment, application of an electric field, *etc.* Raman spectroscopy of materials of excess oxygen content (overdoped case) will also be discussed.

Raman Spectra of the Four Stable Phases in $\text{YBa}_2\text{Cu}_3\text{O}_x$

The four stable phases firmly established for $\text{RBa}_2\text{Cu}_3\text{O}_x$ are Ortho-I (OI, $x = 7$), Ortho-II (OII, $x = 6.5$), Tetragonal (T, $x = 6$), and high-temperature Tetragonal (T', $6 < x \leq 7$). As shown in Figure 1 they differ by mainly oxygen arrangement in the basal planes. Except for small changes in interatomic distances, the rest of the structure remains the same for all phases. It is worth noting, however, that for the OI and T phases the atomic sites in the basal plane are centers of symmetry and hence the vibrations of Cu1 and O1 atoms are Raman-inactive. This is not true for the OII and T' structures.

The application of Raman spectroscopy for study of phase separation in $\text{RBa}_2\text{Cu}_3\text{O}_x$ ($6 < x < 7$) is based on the experimental finding that the Raman spectrum of $\text{RBa}_2\text{Cu}_3\text{O}_x$ is a superposition of spectra of several coexisting microphases with their relative weight determined by their abundance and Raman cross sections. Given the Raman spectra of the separate microphases, one can select "markers" for the presence of a particular phase. Such markers are specific Raman lines of definite polarization properties and resonant behavior. The variations of the relative intensity of a marker upon different treatments could be used as a measure for variations of the

relative weight of the corresponding microphase. On the basis of our knowledge of the Raman spectra of the stable microphases in $\text{YBa}_2\text{Cu}_3\text{O}_x$ we will propose spectral features which are most suitable for markers of particular microphases in a given scattering configuration.

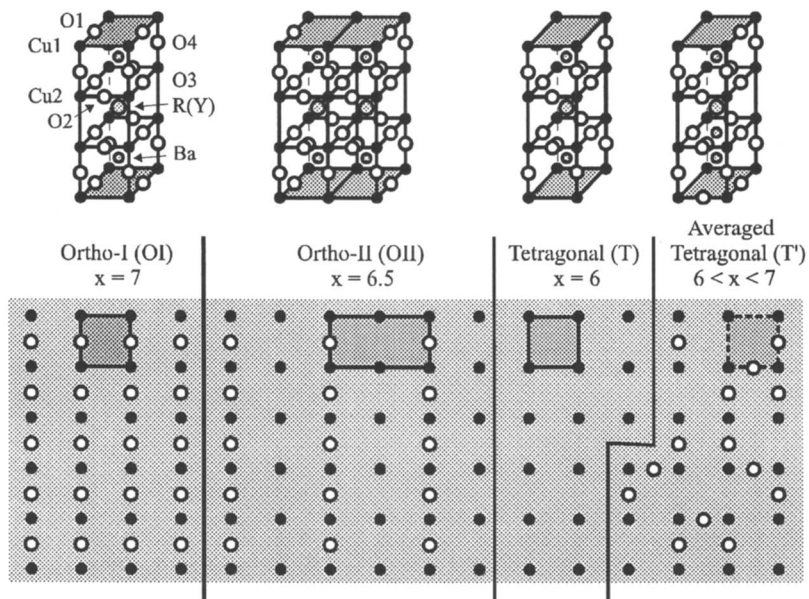


Figure 1. Atomic arrangements in the "basal" Cu1-O plane for the four stable phases of $\text{RBa}_2\text{Cu}_3\text{O}_x$. The corresponding unit cells of OI, OII, T and T' structures are also shown.

Ortho-I and T Phases: The Raman spectra of the $\text{RBa}_2\text{Cu}_3\text{O}_x$ in the limit cases $x = 7$ (Ortho-I) and $x = 6$ (T) are well known. The corresponding phonon modes differ significantly in frequencies, polarization properties and resonant behavior (dependence of phonon line intensity on the excitation laser photon energy) (7-9, 13). The frequency and polarization differences are illustrated in Figure 2 showing the zz and xx/yy polarized spectra as obtained from the same single crystal ($T_c = 89$ K) before ($x \approx 7$, OI phase dominates) and after thermal annealing in vacuum ($x \approx 6.1-6.2$, T phase dominates). With these parallel scattering geometries one expects for both materials five Raman lines: $5A_g$ or $4A_{1g} + B_{1g}$ for OI and T phases, respectively. As follows from Figure 2, the appearance in the xx/yy spectra of Raman lines near 140 cm^{-1} and 450 cm^{-1} is an ambiguous indication for the presence of T-type domains whereas the observation with the same scattering geometry of a peak near 500 cm^{-1} indicates domains of OI-type ordering. The coexistence of OI and T domains could be evidenced by observation of a shift of the Cu2 mode ($140-150 \text{ cm}^{-1}$) if the zz and xx/yy spectra are compared. Indeed, in the zz spectra the T-component is of negligible intensity for laser excitations in the visible range and therefore only the higher frequency OI component and possibly the OII component are pronounced. In contrast, in the xx/yy spectra the

line appears at lower wavenumber as the T component dominates, whereas the OI component is of negligible intensity. Similar xx - zz shift is expected for the apex oxygen band near 500 cm^{-1} , in particular at lower exciting photon energies. Due to appearance of the T component of the apex oxygen band with only zz scattering geometry, the complex apex oxygen band will be shifted towards lower wavenumbers in this polarization.

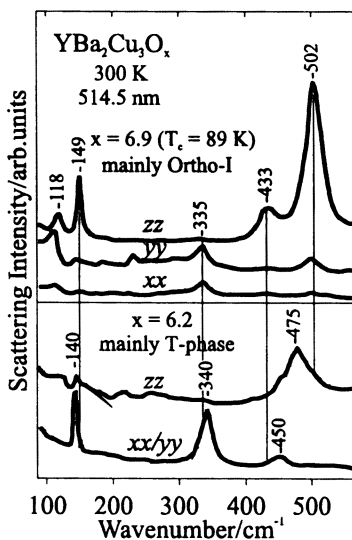


Figure 2

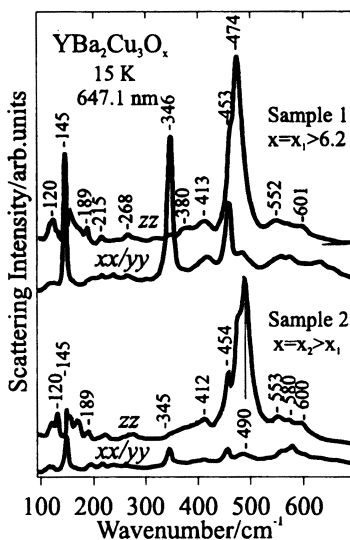


Figure 3

Figure 2. Polarized Raman spectra a single crystal of $\text{YBa}_2\text{Cu}_3\text{O}_x$ measured before ($x \approx 6.9$, mainly Ortho-I phase) and after ($x \approx 6.2$, mainly T-phase) annealing in vacuum. (Reproduced with permission from ref. 8. Copyright 1996 John Wiley and Sons.)

Figure 3. Polarized Raman spectra of two different oxygen-deficient crystals of $\text{YBa}_2\text{Cu}_3\text{O}_x$. (Reproduced with permission from ref. 8. Copyright 1996 John Wiley and Sons.)

Ortho-II Phase: The Ortho-II phase ($x = 6.5$) cannot be isolated as a separate sample, i.e. it coexists with other stable phases. Due to doubling of its unit cell, however, the number of Raman allowed modes is also doubled. Additional Raman lines could be used as "markers" for the presence of the Ortho-II phase. For example, the weak lines near 190 and 410 cm^{-1} (Fig.3) have been assigned to the Ortho-II phase on the basis of lattice dynamical calculations (8). The apex oxygen peak for the Ortho-II phase is at $488\text{--}490\text{ cm}^{-1}$. The resonant behaviour of the Ortho-II Raman lines is still not established.

Averaged Tetragonal (T') Phase: The Raman spectrum of averaged tetragonal (T') phase for some excitation photon energies and for some x -values is known from high-temperature measurements. In Figs. 4a and 4b are shown, respectively, the zz and

xx/yy -polarized Raman spectra of $YBa_2Cu_3O_x$ ($x \approx 7$, $T_c = 90$ K) *before*, *during* and *after* two subsequent laser annealings in air. Using the method of Ref.(14) the annealing temperatures were estimated to 275°C (548 K) for the zz - and 390°C (663 K) for the xx/yy -oriented samples. Except for the spectral features at wavenumbers close to the known O1 and T modes, one observes new strong bands near 590 cm^{-1} (zz) and 226 cm^{-1} (xx). Strictly speaking, the point symmetry is lost in T' phase and all atomic vibrations should be Raman allowed. The breaking of local symmetry however, is most strongly pronounced for Cu1 and O1 sites, which are otherwise centers of symmetry. The new features in the high-temperature spectra have been assigned to vibrations of O1 (590 cm^{-1}) and Cu2 (226 cm^{-1}). As seen in Fig 4, these bands with lower intensity are also observed at low temperatures indicating the presence of Cu2 and O1 at non-centrosymmetric sites (most reasonably at the ends of broken Cu-O chains). It worth noting that the band near 230 cm^{-1} is strongly resonant and has maximum intensity for photon excitation near 2 eV (15). In another approach, the T' domains and related Raman lines could be treated as regions of local distortions and local ("defect") modes, respectively.

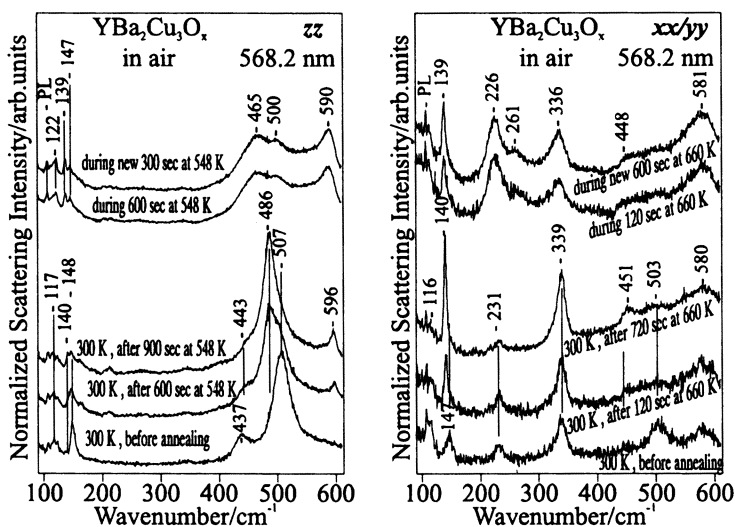


Figure 4. zz (left) and xx/yy (right) polarized spectra of $YBa_2Cu_3O_x$ *before*, *during* and *after* two subsequent annealing steps in air. The starting oxygen content was close to 7. (Reproduced with permission from ref. 9. Copyright 1997 Elsevier Science.)

Raman Evidences for Phase Separation in $YBa_2Cu_3O_x$

There are various Raman evidences for coexistence of microdomains of different oxygen arrangement in nominally single phase samples. Fig.5 illustrates that the apex oxygen band in an oxygen deficient $YBa_2Cu_3O_x$ sample shifts significantly toward lower wavenumbers with increasing wavelength of the excitation laser light. Such a behavior could be explained by the complex structure of the band with the zz scattering geometry and different resonant behavior of the three components centered near 475

cm^{-1} (T), 490 cm^{-1} (Ortho-II) and 502 cm^{-1} (Ortho-I). While the T-component increases with excitation laser wavelength, the OI component decreases (16,17). The result is a shift of the complex band toward lower wavenumbers. Additional evidence for microphase separation is the previously discussed zz - xx shift of certain Raman lines. The type of coexisting microphases could directly be identified by their “markers”, in particular at low temperatures as illustrated in Fig.6 on the example of two (001)-oriented $\text{YBa}_2\text{Cu}_3\text{O}_x$ thin films with nominal oxygen content close to $x = 7$.

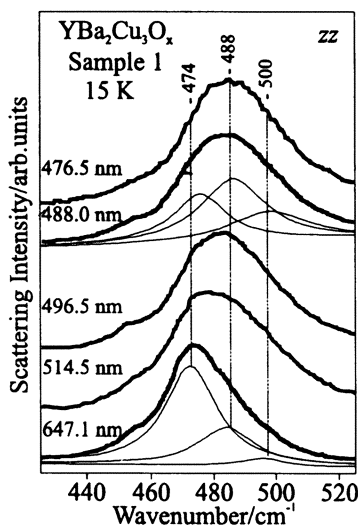


Figure 5

Figure 5. Variations of the line shape and position of apex oxygen band (zz) with excitation phonon energy. The complex band profile can be fitted for each photon energy by three Lorentzians centered near 474 cm^{-1} (T), 488 cm^{-1} (Ortho-II) and 500 cm^{-1} (Ortho-I). (Reproduced with permission from ref. 8. Copyright 1996 John Wiley and Sons.)

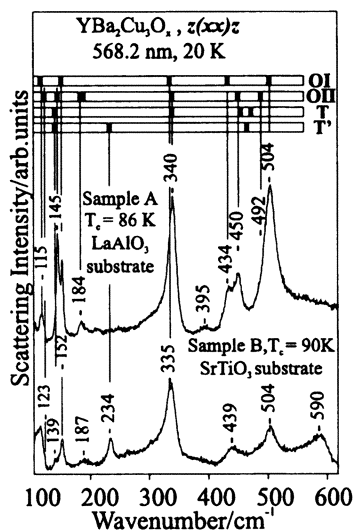


Figure 6

Figure 6. xx/yy Raman spectra of two different YBCO thin films at low temperature. For Sample A the phase separation is evidenced by the complex lineshape of the Cu_2 , O_2 , O_3 -in phase and O_4 bands. The lines at 234 and 590 cm^{-1} in the spectrum of Sample B indicate a significant number of broken chains. (Reproduced with permission from M.N. Iliev et al., *Journal of Alloys and Compounds* **1997**, 251, 99. Copyright 1997 Elsevier Science.)

Monitoring of Oxygen Reordering Processes during Laser Annealing

Fig.4 illustrates how Raman spectroscopy could be applied for monitoring the oxygen reordering processes during annealing in air. Prior to laser annealing the zz and xx/yy spectra are the typical ones for an $\text{YBa}_2\text{Cu}_3\text{O}_7$ (Ortho-I) sample, although the weak structure at 231 cm^{-1} indicates the presence of free chain ends or isolated O_1 atoms. During laser heating in air the oxygen content slightly decreases (the oxygen out-diffusion prevails oxygen in-diffusion) and most of the O_1 atoms are no longer strongly bonded to their chain sites. The structure becomes a mixture of undisturbed Ortho-I

domains and domains of oxygen disorder (T'). This is in particular true for the zz sample (annealed at 548 K) where both Ortho-I and T' lines are observed, e.g. the Cu_2 lines at 147 and 139 cm^{-1} . For the xx samples (annealed at 663 K) no traces of the OI phase are detectable. After annealing, the OI atoms relax rapidly in arrangements corresponding to Ortho-I, Ortho-II, T and some remaining T' structures. The presence of Ortho-II is evidenced by the 486 cm^{-1} component of the apex oxygen band. The Raman lines at 140 cm^{-1} and 450 cm^{-1} can be assigned equally well to either T or T' arrangements.

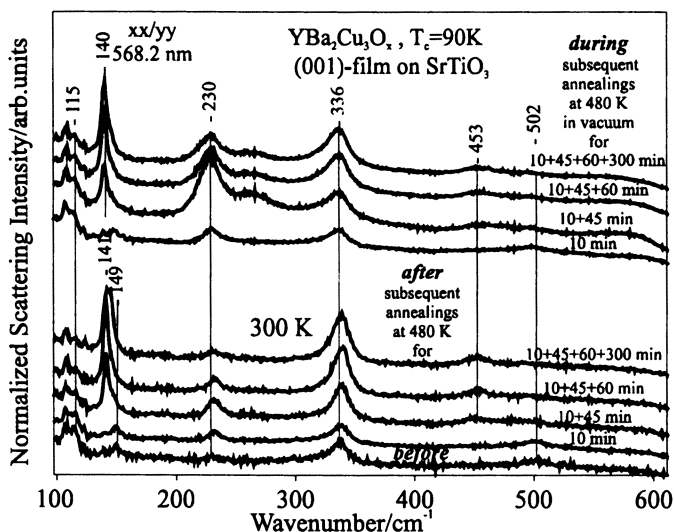


Figure 7. Variations of the lineshape of the xx/yy Raman spectra of an YBCO thin film ($T_c = 90$ K) during and after subsequent annealing steps in vacuum. (Reproduced with permission from ref. 9. Copyright 1997 Elsevier Science.)

Due to in-diffusion of oxygen the decrease of total oxygen content during annealing in air is restricted to $x = 6.6-6.7$ (14,18). This range can be extended towards lower values of x by performing similar experiments in vacuum. In Fig. 7 are shown the variations of the xx/yy - polarized Raman spectra of a $YBa_2Cu_3O_7$ thin film ($T_c = 90$ K) before, during and after several consecutive annealing steps with $P_{laser} = 25$ mW. The most remarkable results is that the intensity of the 231-265 cm^{-1} spectral feature goes through a well-pronounced maximum. Assuming that the vibrational Raman intensity of the chain-end atoms depends mainly on their concentration, a natural explanation can be given in the following scheme: (1) breaking the perfect chains at high temperature; (2) increasing the number of chain fragments with out-diffusion of O1; (3) reaching a maximum of chain fragments (and the end chain atoms, basically responsible for the 231 cm^{-1} mode); (4) decreasing the number of chain fragments when the total oxygen content approaches the value of 6.

The examples given above demonstrate the efficiency of Raman spectroscopy to monitor oxygen rearrangement during out-diffusion of oxygen. In a similar manner one can study the reordering processes during oxygen in-diffusion. This can be done by (laser) annealing of oxygen-deficient samples in air (14) or oxygen atmosphere (19).

The Raman spectra in this case are modified in a reverse order. Provided the isotopic mass of oxygen in the atmosphere differs from that of the oxygen atoms in the sample, one can also obtain an additional information on the processes of isotopic substitution. Fig.8 shows schematically the idea and the results of a Raman study of isotopic substitution during laser annealing of $\text{YBa}_2\text{Cu}_3^{18}\text{O}_{6.2}$ in air. In these experiments the surface of a microcrystal was first annealed in air by intensive laser radiation (laser power of 15 mW at the focus spot of 1.5 μm Gaussian radius). The radial temperature distribution calculated using the method of Ivanov et al.(14) is shown in the right part of Fig. 8.

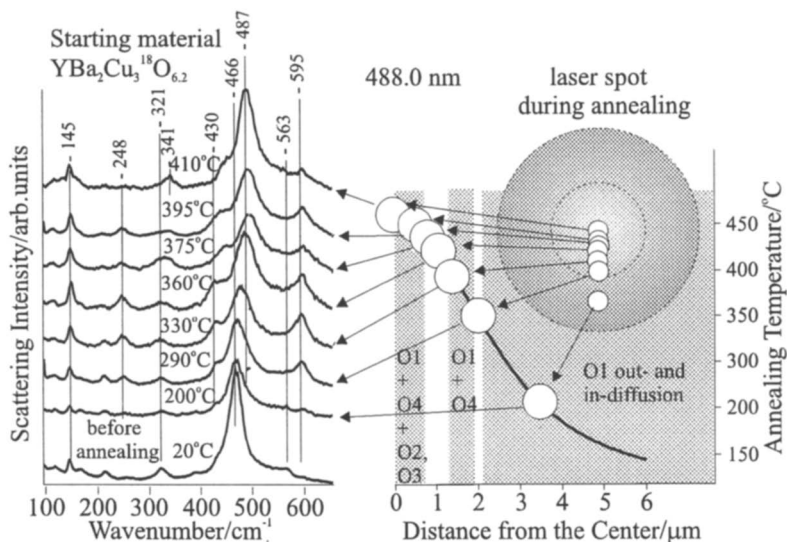


Figure 8. Raman spectra of $\text{YBa}_2\text{Cu}_3^{18}\text{O}_{6.2}$ at points corresponding to different annealing temperatures in air. The variation of temperature with distance from the center of irradiated spot is also shown. (Adapted with permission from ref. 14. Copyright 1995 American Physical Society.)

At the center of the irradiated spot the annealing temperature is high enough to activate $^{16}\text{O} \rightarrow ^{18}\text{O}$ isotopic exchange at all oxygen sites (O2,O3,O4,O1). At distances 1-2 μm from the center the exchange takes place over only O4 (apex) and O1 (chain) sites. At the lowest annealing temperatures ($> 3 \mu\text{m}$ from the center) the exchange is only over the O1 sites. On the left part of Fig.8 are shown the Raman spectra measured with much lower power before laser annealing and at several points at different distance from the center of the irradiated spot, i.e. at points corresponding to different annealing temperatures. Before annealing all peaks related to oxygen vibrations are observed at lower wave number if compared to standard $\text{YBa}_2\text{Cu}_3^{16}\text{O}_x$ samples. In the spectrum obtained from the point annealed at 200 $^{\circ}\text{C}$ two new weak lines appear at 248 cm^{-1} and 595 cm^{-1} , while the weak line at 563 cm^{-1} disappears. Note that the ratio of wavenumbers $563/595 \approx (16/18)^{-1/2}$ is exactly what one would expect for an oxygen vibration provided natural ^{16}O substitutes for ^{18}O . When at $T_{\text{anneal}} < 300 \text{ }^{\circ}\text{C}$ oxygen diffusion and isotopic exchange take place only in the basal planes, the increase in intensity of the 595 cm^{-1} line in favor of that at 563 cm^{-1} unambiguously indicate that

they correspond, respectively, to vibrations of ^{18}O and ^{16}O atoms at O1 sites. This conclusion is also supported by the fact that in the spectra obtained from spots annealed at 200°C and 290°C one does not establish any upward shift of the frequencies of the apex and plane-oxygen modes, which would result from ^{16}O for ^{18}O substitution at these sites. The increase, gradual saturation and the decrease of the 595 cm^{-1} peak with increasing annealing temperature find explanation in a similar way. The intense absorption of atmospheric oxygen leads to formation of new, relatively short chain fragments. At higher oxygen content (moving to the center of the irradiated spot) the additional oxygen may connect already existing chain fragments, which results in the decrease and the almost total suppression of the 595 cm^{-1} band. In this case the total oxygen content is near 6.5. Therefore, one may conclude that the relatively long and well oriented copper-oxygen chains are formed.

Other Processes of Oxygen Rearrangement Probed by Raman Spectroscopy

Raman spectroscopy has successfully been applied to monitor other processes such as **electromigration** (20,21) and **ion cluster beam bombardment** (22) that result in oxygen rearrangement in YBCO. It has been shown in electromigration experiments that by applying a current density of $1\text{--}2\text{ MA/cm}^2$ to thin film microbridges at room temperature, a long-range migration of the positively charged chain oxygen vacancies takes place (20). Due to aggregation of oxygen vacancies near the cathode, the *xx/yy* Raman spectra in this region exhibit strong enhancement of the “tetragonal” features in favor of the “Ortho-I” features. Similar changes in the Raman spectra of YBCO thin films were observed after applying the ion cluster beam bombardment technology (22) for smoothing of thin film surface (Figure 9).

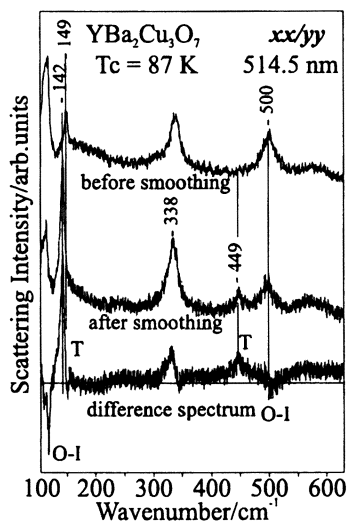


Figure 9. Raman spectra of (001)-YBCO thin film *before* and *after* surface smoothing by Ar-ion-cluster bombardment. The difference spectrum (at the bottom) clearly demonstrates the increase of T-phase components in favor of Ortho-I ones.

Within this technology clusters of 1000-5000 Ar atoms remove a thin layer on the film surface, the surface damage being restricted to 10-15 nm in depth. Although the signal from the damaged upper layer should be only a small part of the integrated response from the whole scattering volume (the penetration depth for the laser excitation light is 500-1000 nm), it follows from Fig.9 that there is a significant evolution of the Raman spectrum after ion cluster bombardment. The intensity of the Ortho-I peak at 500 cm^{-1} decreases almost twice and relatively strong markers of oxygen deficient domains appear at 142 and 449 cm^{-1} . This indicates that a significant part of the scattering volume has become oxygen deficient. An additional annealing in oxygen atmosphere restores the pure Ortho-I type spectrum.

Raman spectroscopy of Overdoped YBCO-Type Materials

While the Raman spectra of optimally doped and underdoped $\text{YBa}_2\text{Cu}_3\text{O}_z$ ($6 < x < 7$) are well established and the variations of the spectral lineshapes with x may reasonably be explained, there are relatively few Raman studies on 123-type materials of higher oxygen content ($x > 7$). Typical representatives of such materials are $\text{YSr}_2\text{Cu}_3\text{O}_{7+\delta}$ compounds, in which part of the chain Cu atoms are replaced by small higher-oxidation state ions, as well as $\text{YSr}_2\text{Cu}_3\text{O}_{7+\delta}$ and $\text{YBa}_2\text{Cu}_2\text{AuO}_{7+\delta}$, prepared under high pressure in the excess oxygen. Although the averaged structure as derived from the diffraction pattern is a tetragonal one, the arrangement of oxygen atoms in the "basal" planes may differ significantly from the known Ortho-I or Ortho-II type orderings. In particular, it has been shown that the chain oxygens in $\text{YSr}_2\text{Cu}_{3-y}\text{M}_y\text{O}_{7+\delta}$ ($\text{M}=\text{Mo}, \text{W}, \text{Re}$) are displaced from their $(0, 1/2, 0)$ positions in $\text{YBa}_2\text{Cu}_3\text{O}_7$ ($Pmmm$) to $(\pm x, 1/2, 0)$ on either side of the mirror plane (23). Such a displacement (see Figure 10), which allows

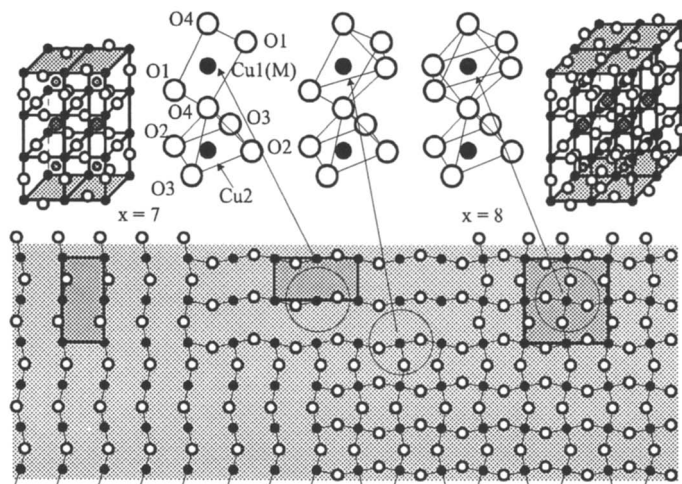


Figure 10. Local oxygen arrangements in the basal planes of overdoped 123-type materials. The shift of O1 atoms from their centrosymmetric sites results in "zig-zag" chains. The possible atomic coordination of apex oxygen atoms are also shown.

elongation of Cu1-O (M-O) bonds to more reasonable values in otherwise compressed unit cell, is expected for $\text{YSr}_2\text{Cu}_3\text{O}_{7.8}$ as well. The possible oxygen orderings corresponding to oxygen content $x = 7$ and $x = 8$ are shown, respectively, in the left and right part of Fig.10. It is plausible to expect that for materials of oxygen content between 7 and 8, domains of these two types of oxygen arrangement will coexist and the Raman spectrum will be a superposition of contributions from these two phases and from the phase boundary region. In Fig.10 are shown the different local coordination of an "apex" oxygen atom. An important consequence of the replacement of "linear" Cu1-O chains by "zig-zag" chains in overdoped materials is that the O1 and Cu1 sites are no longer centers of symmetry and the corresponding vibrations are also Raman allowed. This should result in additional enrichment of Raman spectra.

Figure 11 shows the Raman spectra of $\text{YSr}_2\text{Cu}_3\text{O}_{7.7}$ as obtained at room temperature in several (nearly-) exact scattering configurations. The wavenumbers of the lines at 158 cm^{-1} (A_{1g}), 324 cm^{-1} (B_{1g}) and 436 cm^{-1} (A_{1g}) are very close to the ones of the same symmetry in $\text{YBa}_2\text{Cu}_3\text{O}_x$ and can unambiguously be assigned to the well known modes involving vibrations along c of Cu2, O2,O3 (out-of-phase) and O2,O3 (in phase). At least five superimposed Raman bands are present in the region between 450 and 600 cm^{-1} ($483, 532, 549, 570$ and 584 cm^{-1}). As a rule the substitution of Sr for Ba and the increase of oxygen content stiffen the $A_g(A_{1g})$ mode of apical oxygen (O4) in 123 compounds and, intuitively, the predominantly zz -polarized lines at 549 and 584 cm^{-1} can be assigned to O4 vibrations along c in the pure $\text{YSr}_2\text{Cu}_3\text{O}_7$ and $\text{YSr}_2\text{Cu}_3\text{O}_8$ structures, respectively. No definite assignment of all Raman lines could be performed at this stage.

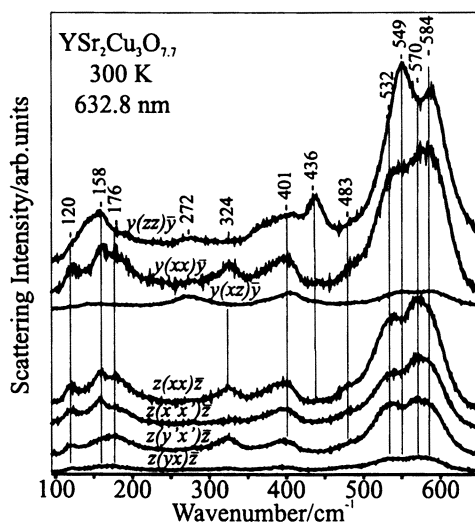


Figure 11. Polarized Raman spectra of $\text{YSr}_2\text{Cu}_3\text{O}_{7.7}$ in several exact scattering configurations.

Conclusion

Raman spectroscopy provides clear evidences that at a microscopic level the structure of $\text{YBa}_2\text{Cu}_3\text{O}_x$ -type compounds ($6 < x < 7$) consists of coexisting domains of Ortho-I, Ortho-II, T, and T'-type oxygen ordering. The variations of x change the relative weight of these domains and their contribution to the complex Raman spectra. The Raman spectroscopy be used as an analytical technique for characterization of YBCO materials with respect to the phase separation as well as for monitoring the changes in the microstructure due to different treatments.

In the overdoped case ($7 < x < 8$) the microstructure changes significantly as the O1 atoms are shifted from their centrosymmetrical sites and the coexisting structures with $x = 7$ and $x = 8$ have "zig-zag" instead of "linear" chains. The Raman measurements confirm the expected enrichment of the spectra. The assignment of all observed Raman lines to definite atomic vibrations requires additional information on their variations upon changes of oxygen content and excitation photon energy.

Acknowledgments

The close collaboration with V. Ivanov, V. Hadjiev, M. Cardona, C. Thomsen, H.-U. Habermeier, M. Abrashev, V. Popov, S. H. Hu, H.-G. Lee, and A. P. Litvinchuk is greatly acknowledged. This work has been supported by the State of Texas through the Texas Center of Superconductivity at the University of Houston (TCSUH), by NSF through the Materials Research Science and Engineering Center at the University of Houston (MRSEC-UH), by the Bulgarian National Fund for Science (F410/94), the Commission of EU (CIPA-CT93-0032) and the Alexander von Humboldt Foundation (Bonn, Germany).

References

1. Wille L. T.; Berera A. and De Fontain D. *Phys. Rev. Lett.* **1988**, *60*, 1965.
2. Zubkus V. E.; Lapinskas S. and Tornau E. E. *Physica C* **1989**, *159*, 501.
3. Semenovskaya S. and Khachatryan A. G. *Philos. Mag. Lett.* **1992**, *66*, 105.
4. Cava R. J.; Batlogg B. Chen C. H., Reitman E., Zahurak S. and Werder D. *Nature* **1987**, *329*, 423.
5. Alario-Franco M. A., Chaillout C., Capponi J. J. and Chenavas J. *Mat. Res. Bull.* **1987**, *22*, 1685.
6. Sonntag R., Hohlwein D., Bruckel T. and Collin G. *Phys. Rev. Lett.* **1991**, *66*, 1497.
7. Iliev M.; Thomsen C., Hadjiev V. and Cardona M. *Phys. Rev. B* **1993**, *47*, 12341.
8. Iliev M. N.; Hadjiev V. G. and Ivanov V. G. *J. Raman Spectroscopy* **1996**, *27*, 333.
9. Iliev M. N.; Habermeier H.-U., Cardona M., Hadjiev V. G. and Gajic R. *Physica C* **1997**, *279*, 63.
10. Mesot J.; Allenspach P., Staub U., Furrer A. and Muttko H., *Phys. Rev. Lett.* **1993**, *70*, 865.
11. Bakharev O. N.; Dooglav A. V., Egorov A. V., Navrin O. V., Naletov V. V., Teplov M. A., Volodin A. G. and Wagener D. in: *Phase Separation in Cuprate Superconductors*, Springer-Verlag, Berlin, 1994.
12. Ivanov V. G. and Iliev M. N. *Physica C* **1995**, *244*, 293.
13. Iliev M. and Hadjiev V. *J. Phys.: Condens. Matter* **1990**, *2*, 3135.

14. Ivanov V. G.; Iliev M. N., Thomsen C. *Phys. Rev. B* **1995**, *52*, 13652.
15. Wake D.R.; Slakey F., Klein M. V., Rice J. P., Ginsberg D. M. *Phys. Rev. Lett.* **1991**, *67*, 3728.
16. Heyen E. T.; Kircher J., Cardona M. *Phys. Rev. B* **1992**, *45*, 3037.
17. Misochko O. V.; Sherman E. Ya., Timofeev V. B. *Physica C* **1991**, 185-189, 1025.
18. Conder K.; Karpinski J., Kaldis E., Rusiecki S., Jilek E. *Physica C* **1992**, 196, 164.
19. Li Y. B.; Shelley C., Cohen L. F., Caplin A. D., Stradling R. A., Kula W., Sobolewski R., MacManus-Driscoll J. L. *J. Appl. Phys.* **1996**, *80*, 2929.
20. Moeckly B. H.; Buhrman R. A., Sulewski P. E. *Appl. Phys. Lett.* **1994**, *64*, 1427.
21. Chamberlain D.; Sydow J. P., Buhrman R. A., Moeckly B. H., Kookrin Char *IEEE Trans. Appl. Superconductivity* **1997**, *7*, 3658.
22. Chu W. K.; Li P. Y., Liu J. R., Wu J. Z., Tidrow S. C., Toyoda N., Matsuo J., Yamada I. *Appl. Phys. Lett.* **1998**, *72*, 246.
23. Harlow R. L.; Kwei G. H., Suryanarayanan R., Subramanian M. A. *Physica C* **1996**, *257*, 125.

Chapter 8

Interference Effects in the Resonant Raman Scattering from the Apical Oxygen Vibrations in the Ortho-II Phase of $\text{YBa}_2\text{Cu}_3\text{O}_x$

Victor G. Ivanov

Faculty of Physics, Sofia University, 5 James Bourchier Boulevard,
BG 1126 Sofia, Bulgaria

We propose a simple interference model for calculation of the Raman efficiency in the ZZ scattering configuration for the apical oxygen vibrations in the Ortho-II phase of $\text{YBa}_2\text{Cu}_3\text{O}_x$, provided the scattering efficiencies of the same mode in the tetragonal and Ortho-I phases of the compound are known. Based on the existing experimental works, the scattering efficiency of the apical mode in the Ortho-II phase is estimated at different frequencies of the exciting light. Possible implications of the model are discussed.

The normal-state and the superconducting properties of the $\text{YBa}_2\text{Cu}_3\text{O}_x$ compound depend strongly on the total oxygen content x of the material. They range from an insulating antiferromagnet at $6 < x < 6.4$ to a normal metal at $6.4 < x < 7$ which displays a superconducting transition at low temperatures. On its side, the critical temperature of the superconducting transition also varies with x , being optimal at oxygen content of approximately 6.95 and exhibiting a well pronounced plateau of 60 K between 6.5 and 6.7 (1). It was shown in several works (2,3) that the existence of the 60 K plateau is due to the formation of a specific, so called Ortho-II phase which is an oxygen superstructure of period of 2 along the orthorhombic a direction.

Figure 1 (a) and (b) shows the oxygen arrangement in the variable oxygen content layers (basal planes) at the limiting values of the oxygen content of the material. The small black circles denote the copper atoms, the bigger open circles stay for the oxygen atoms. The oxygen-deficient structure ($x \approx 6$) is tetragonal and is usually referred to as Tetra phase. The optimally-oxygenated, orthorhombic, Ortho-I phase ($x \approx 7$) consists of long Cu-O chains running along the orthorhombic b

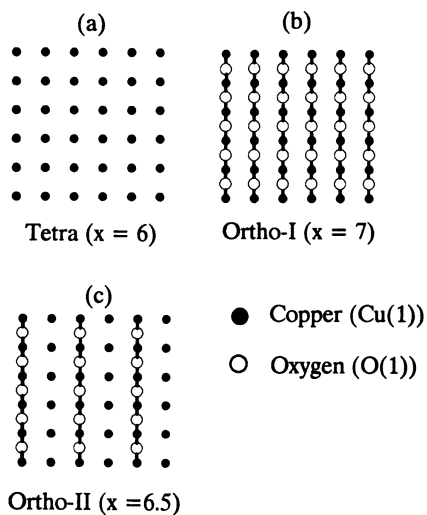


Figure 1. Different types of arrangement of the oxygen atoms in the basal planes of $\text{YBa}_2\text{Cu}_3\text{O}_x$.

direction. The orthorhombic Ortho-II phase (c) is formed at $x \approx 6.5$ and is characterized by alternating full Cu-O chains, like in the Ortho-I, and empty rows of copper atoms, like in the Tetra phase. At high temperatures and off-stoichiometric conditions these structures possess different kinds of oxygen defects, preserving however, on the macroscopic level, the symmetry of the corresponding idealized atomic arrangements.

The physics of the Ortho-II phase is an intriguing problem due to the proximity of the phase in the T - x space to the insulator-to-metal and tetragonal-to-orthorhombic transition lines. The lattice gas model (4) predicts a large temperature and stoichiometry domain of stability of the phase, between $x = 6.3 - 6.7$ and $0 < T < 500$ K. The doubling of the lattice period along a has been confirmed in a number of diffraction experiments, however the corresponding Bragg reflections which occur at the superstructure positions are broad compared to the experimental resolution and indicate a small degree of spatial correlation of the structure (5-7). *Therefore it is difficult to obtain macrosamples exhibiting a well defined Ortho-II ordering of the oxygen, and the direct experimental study of the transport and optical properties of this phase is still missing.*

The Raman spectroscopy has been proven to be a powerful tool for study of the oxygen arrangement in $\text{YBa}_2\text{Cu}_3\text{O}_x$ compounds. It is due to the fact that the intensities and the frequencies of the Raman-active vibrations in the compound depend strongly on the oxygen content of the material (8-10). This dependence is best pronounced for the Ag mode of vibration of the apical oxygen atoms (denoted here by O(4)), frequency of which varies from ≈ 470 cm^{-1} at $x \approx 6$, to ≈ 500 cm^{-1} at $x \approx 7$. This fact allows of a rough estimate for the oxygen content of the material which was shown however to be quite unsatisfactory for samples near to the border of the insulator-to-metal transition. It turns out that the spectral form and the maximum position of the apical band vary with the wavelength of the exciting light (11) and depends on the thermal prehistory of the material (12). It was demonstrated that the shift of the spectral maximum stems from the redistribution of the intensity between three Lorentzian lines with fixed frequencies of ≈ 470 , 486-490 and 500 cm^{-1} which display different resonant properties with respect to the wavelength of the exciting light. These findings were attributed to the coexistence of domains (size of 10-100 lattice constants) of three different phases (the so called structural phase separation): Tetra, Ortho-II, and Ortho-I which give rise to the three constituent lines. Later on, this conclusion was confirmed for different oxygen stoichiometries and thermal treatments of the material, as well as for rare-earth substitution for the Y atom (13,14). It was established however that the apical-mode decomposition into lines at ≈ 470 , 486, and 500 cm^{-1} is not an universal phenomenon and depending on the sample preparation the triplet may appear at shifted positions ≈ 486 , 493, and 500 cm^{-1} (15,16). Therefore, other oxygen-ordered phases may be stabilized under certain conditions and the assignment of the spectral components to definite types of oxygen arrangement should be carried out with great care.

Based on the experimental observations, it follows that a more relevant description of $\text{YBa}_2\text{Cu}_3\text{O}_x$ would be based not solely on the total oxygen content, but on the relative abundance of the different phases which coexist in the material. Provided the

constituent Lorentzian components of the apical band are assigned to definite phases, the volume fraction of the i -th phase can be determined via the relation:

$$(1) \quad P_i = \frac{I_i(\omega) / S_i(\omega)}{\sum_j I_j(\omega) / S_j(\omega)}$$

The quantities I_i are the integrated intensities of the corresponding Lorentzian lines, obtained after a decomposition of the apical band and $S_i(\omega)$ are the corresponding absolute scattering efficiencies for the apical vibrations in these phases. It is assumed in equation (1) that the volume is closely packed by domains of those phases which are abundant in the Raman spectrum:

$$(2) \quad \sum_i P_i = 1$$

Scattering efficiencies for the monophase, oxygen-deficient ($x \approx 6$, Tetra phase) and optimally-oxygenated materials ($x \approx 7$, Ortho-I phase) have been studied thoroughly in previous works (8,9). Thus the missing element for a quantitative phase analysis of $\text{YBa}_2\text{Cu}_3\text{O}_x$ at intermediate oxygen contents is the scattering efficiency of the apical vibrations in the Ortho-II phase as well as in the other phases (e.g. Ortho-III) which may coexist in the volume of the material. Since the direct measurement of the scattering efficiency in these phases is currently inaccessible one may proceed in an alternative way: to compare the relative scattering efficiencies of the different phases abundant in a given sample, provided an *a priori* information on the absolute Raman efficiencies in the Tetra and Ortho-I phases is available. In the present work we develop a model which relates the absolute scattering efficiency for the apical oxygen vibrations in the Ortho-II phase to those in the Tetra and the Ortho-I phases. The model contains also a free variables which are extracted by fitting to experimental data on oxygen-deficient $\text{YBa}_2\text{Cu}_3\text{O}_x$ samples.

Development of the Model

The (absolute) efficiency of the Raman scattering may be defined according to the equation:

$$(3) \quad S(\omega) = \frac{1}{I} \left(- \frac{d^2 I}{dx d\Omega} \right) \frac{1}{(\hbar\omega)^4}$$

where ω and I are the frequency and the intensity of the exciting light, and $(-d^2 I / dx d\Omega)$ is equal to the decrease of the light intensity per unit propagation path due to the Raman scattering within an unit solid angle. The last multiplier accounts for the universal $\propto \omega^4$ dependence of the scattering intensity, thus making $S(\omega)$ essentially material-dependent quantity. It is fairly well satisfied for the Raman scattering from optical phonons that

$$(4) \quad S(\omega) \propto \left| \mathbf{e}_s \cdot \frac{\partial \tilde{\chi}}{\partial Q} \cdot \mathbf{e}_i \right|^2$$

where \mathbf{e}_i and \mathbf{e}_s are the polarization vectors of the incident and scattered photons, and $\partial\chi/\partial Q$ is the derivative of the polarizability of the material with respect to the normal coordinate Q of the vibration. Thus the frequency-dependent function $S(\omega)$ reflects not only the existence of dipole-allowed transitions which contribute to χ but also the orbital character of the involved electronic wave functions. This is due to the fact that the Raman-active vibrations modulate predominantly the on-site electronic energies and the overlap of the orbitals centered on the vibrating atoms and their neighbors.

The Ag apical oxygen vibration in $\text{YBa}_2\text{Cu}_3\text{O}_x$ is best pronounced in the ZZ scattering configuration, the axis Z being parallel to the tetragonal (or orthorhombic) c -direction. The detailed study of the scattering efficiency for this mode in a broad interval of frequencies of the exciting light has proved that in the oxygen deficient compound the main contribution to the ZZ Raman response comes from the hybridized apical oxygen $p(z)$ and the basal-plane copper (Cu(1)) $d(z^2-r^2)$ orbitals (8). From the other hand, it has been shown that in the optimally-oxygenated compound the details of the resonant behavior of $S(\omega)$ can be explained quite satisfactory on the basis of mixing of the $p(z)$ orbitals of the apical oxygen atoms, $d(z^2-y^2)$ orbital of the Cu(1) and the $p(y)$ orbitals of the chain oxygen atoms (8,17). Therefore, as far as we are interested in the ZZ Raman polarizability, it is reasonable to consider the copper-oxygen chains in the Ortho-I phase as electronically-isolated quasi-molecular units. The same conclusion may be drawn for the O(4)-Cu(1)-O(4) dumbbell groups in the Tetra phase.

Our first assumption is that these quasi-molecular species remain insulated from each other also in the Ortho-II phase, where they alternate in the orthorhombic a -direction. Due to the doubling of the lattice period along a , the Γ -point, Ag vibrations of the apical oxygen atoms in the Ortho-II phase stem from both Γ and X - points of the original Ortho-I structure. Based on the assignment of Misochko (18), the line at $\approx 488 - 490 \text{ cm}^{-1}$ stems from the in-phase vibrations along the Z-axis of the apical oxygen atoms from neighboring full and empty chains in the Ortho-II unit cell. In this case we can write for the derivative of the ZZ polarizability the following relation:

$$(5) \quad (\partial\chi^{zz} / \partial Q)_{\text{OrthoII}} = \frac{1}{2} \left\{ (\partial\chi^{zz} / \partial Q)_{\text{dumbbell}} + (\partial\chi^{zz} / \partial Q)_{\text{chain}} \right\}$$

All the polarizabilities which enter the last equation are assumed to refer to the volume of a formula unit containing one Y atom.

The second, and more disputable assumption is that the polarizability of the copper-oxygen chains in the Ortho-II phase is almost the same like, in the Ortho-I phase, and this of the O(4)-Cu(1)-O(4) groups, like in the Tetra phase. This statement may be argued on the basis of the existing *ab initio* calculations of the electronic structure of the Ortho-II phase. It is shown in (19) that the effective charges on the apical oxygen atoms and copper atoms belonging to the empty chains in the Ortho-II phase are to a great accuracy the same, like in the Tetra phase. The situation is found to be the same for the charge distribution in the full chains which resembles this in the Ortho-I phase. Thus one may write:

$$(\partial\chi^{zz} / \partial Q)_{\text{dumbbell}} = (\partial\chi^{zz} / \partial Q)_{\text{Tetra}} \quad \text{and} \quad (\partial\chi^{zz} / \partial Q)_{\text{chain}} = (\partial\chi^{zz} / \partial Q)_{\text{OrthoI}}$$

For obtaining the scattering efficiency one has to rise Equation (5) to the second power making use of (4):

$$(6) \quad S_{Orthol}^{zz} = \frac{1}{4} \left\{ S_{Orthol}^{zz} + S_{Tetra}^{zz} + 2\sqrt{S_{Orthol}^{zz} \times S_{Tetra}^{zz}} \cos \varphi \right\}$$

Deriving the last formula we kept in mind that the derivatives of the polarizability are complex valued functions introducing their relative phase shift φ . Thus we consider the Raman scattering from the apical vibrations in the Ortho-II phase as a result of interference of the partial waves scattered from the Cu-O chains and the isolated O(4)-Cu(1)-O(4) groups. Physically, φ is equal to the phase difference between these waves.

The equation (6) may be experimentally tested on the samples where the domains of the three phases, Tetra, Ortho-II, and Ortho-I are simultaneously present. For this purpose we investigated two sets of Raman spectra in ZZ-scattering configuration from oxygen-deficient $\text{YBa}_2\text{Cu}_3\text{O}_x$ monocrystals, the data set A taken from Ref. (14) and the data set B taken from Ref. (11). Figure 2 shows the series of spectra corresponding to the data set A. The decomposition of the apical band into three components at 478 cm^{-1} , 488 cm^{-1} and 500 cm^{-1} which are shown in the figure is quite satisfactory without including additional Lorentzians in the fit. Thus we may conclude that the investigated sample contains three constituent phases which have to be properly identified. The frequency of 478 cm^{-1} is usually observed in oxygen-depleted samples of oxygen content near to 6 (9,10) and may be ascribed to domains of the Tetra phase. Similarly, the 500 cm^{-1} line is dominant in the well-oxygenated samples and certainly stems from the Ortho-I phase. This assignment is supported also by the fact that the relative intensity of the 500 cm^{-1} component, compared to those of the 478 cm^{-1} line, increases when going from the red (647 nm) to blue exciting light (488 nm) by a factor of 7-8, in good agreement with the resonant Raman data of (8) and (9). We ascribe the line at 488 cm^{-1} to the Ortho-II phase for the following reasons. First, its frequency fits well to the position of the spectral maximum of the apical band in samples of oxygen composition ≈ 6.5 (10,20). Second, the critical temperature for the present sample were found to be 35 K which is a signature of an oxygen content near to 6.4. At this oxygen content the thermodynamical conditions are more favorable for formation of the Ortho-II phase rather than other oxygen superstructures (e. g. the Ortho-III) (3,4). The same assignment were performed for the spectra of the data set B (not presented here).

Figure 3 shows the experimentally observed scattering efficiencies in the Ortho-I and the Tetra phases at different energies of the incoming photons as obtained in (8) and (9). To calculate the scattering efficiency in the Ortho-II phase by means of equation (6), one has to specify $\cos\varphi(\omega)$ which enters the right-hand side. Using the integrated intensities of the components in Figure 2, we adjusted the values of $\cos\varphi$ at any of the exciting wave lengths in such a way that the volume fractions of the three phases calculated by equation (1) display a minimum variation over the whole set of spectra. The free variables in the minimization program were not the cosines but the phase shifts φ , in order to account for the constrain $-1 < \cos\varphi < 1$. The adjusted values of φ and $\cos\varphi$ were found to be independent, within satisfying accuracy, on the starting trial values of φ . We performed this procedure also on the data set B. The as

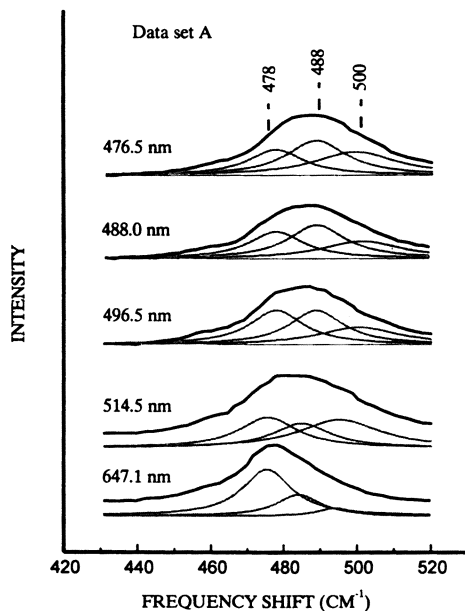


Figure 2. Raman spectra of an oxygen-deficient $\text{YBa}_2\text{Cu}_3\text{O}_x$ monocrystal in ZZ scattering configuration, taken at different wavelengths of the exciting light and their decomposition into three Lorentzian components.

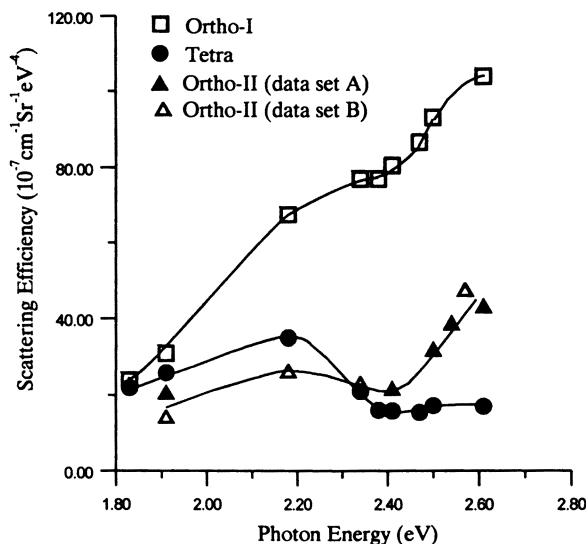


Figure 3. Scattering efficiency of the apical oxygen vibrations in the three phases of $\text{YBa}_2\text{Cu}_3\text{O}_x$. The data for the Tetra and Ortho-I phases are extracted from (8) and (9). The solid lines are only guides for the eye.

obtained values of $\cos\phi(\omega)$ are presented in Figure 4, and the calculated scattering efficiency in the Ortho-II phase at different energies of the exciting photons in Figure 3.

Discussion and conclusions

It is evident from Figure 3 that the calculated efficiencies for the two samples (open and black triangles) define a smooth resonant curve for the Ortho-II phase without large deviation of the individual points. The calculated values of $\cos\phi(\omega)$ display larger scattering at low frequencies of the exciting light, mainly because they are extracted with smaller accuracy, due to the vanishing abundance of the Ortho-I line in the Raman spectra taken at 647 nm. Using calculated efficiencies we determined also the fractions of the three phases in the two investigated samples:

$P_{\text{Tetra}} = 0.58(\pm 0.03)$, $P_{\text{OrthoII}} = 0.316(\pm 0.005)$, $P_{\text{OrthoI}} = 0.10(\pm 0.03)$ for the data set A and

$P_{\text{Tetra}} = 0.45(\pm 0.08)$, $P_{\text{OrthoII}} = 0.360(\pm 0.005)$, $P_{\text{OrthoI}} = 0.19(\pm 0.08)$ for the data set B.

The standard deviations, given in the brackets, are estimated for the whole set of exciting wave lengths.

There is a clearly defined minimum in S_{OrthoII} which correlates well with the shoulder of the scattering efficiency in the Ortho-I phase for the energy of the incoming photons 2.4 eV. According to (17) this shoulder corresponds to the photon energy which is in resonance with the dipole-allowed transition from the crossing point of the chain electronic band with the Fermi level to the nearly dispersionless apical-oxygen band. This implies that at this energy, an onset of the optical absorption takes place leading to singularity in the imaginary part of χ_{chain} . From its side, this singularity results in resonant enhancement of the imaginary part of the polarizability derivative $\partial\chi/\partial Q$ and correspondingly to a phase angle of approximately $\pi/2$. Indeed, an inspect of Figure 4 clearly demonstrates a sharp deep in $\cos\phi$ at this energy, implying a phase shift between the full and the empty chains of nearly $\pi/2$. This fact supports the conclusion that the electronic structure of the copper-oxygen chains in the Ortho-II phase does not differ substantially from this in the Ortho-I phase, in agreement with the *ab initio* electronic-structure calculations (19).

Our procedure for extracting $\cos\phi$ substantially relies on the assumption that the finite-size domains of the Tetra, Ortho-II, and Ortho-I structures which coexist in the multiphase samples under consideration, display the same scattering efficiency profiles, like the corresponding macroscopic, pure, thermodynamic phases. The finite size of the domains may result in two aspects. First, partial mixing of the atomic vibrations between neighboring domains may take part, being accompanied with frequency shift of the Raman bands with respect to their position in the corresponding macroscopic phases (13). Second, the electronic structure of the domains may be modified, e. g. as a result of Cu-O chain breaking, thus leading to different resonant conditions for Raman scattering. In our samples the positions of the constituent Lorentzian lines of the apical band correspond well to the frequencies of the apical vibrations in the monophase samples. According to (13), this is a signature for an

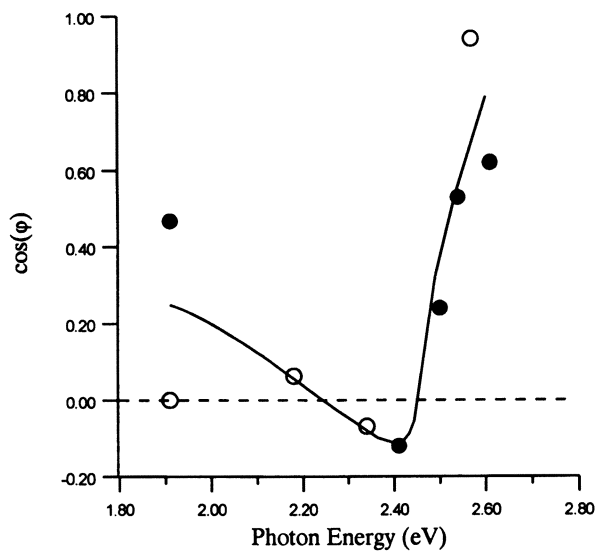


Figure 4. Cosine of the phase shift versus energy of the exciting photons. Filled and opened circles correspond to the data sets A and B respectively. The solid line is a guide for the eye.

average size of the domains exceeding $\approx 100 \text{ \AA}$. Accounting for the small mean free path of the electrons in $\text{YBa}_2\text{Cu}_3\text{O}_x$ ($\propto 10 \text{ \AA}$) one may conclude that the domains are large enough to retain the major features of the electronic structure and the scattering efficiency of the corresponding bulk material.

It is worthy to mention the recent measurements of Liarokapis (16) where the spectral components corresponding to the Tetra and the Ortho-II phases are observed shifted by nearly 8 cm^{-1} with respect to the values reported in the present work. Correspondingly, the relative scattering efficiencies for the three coexisting phases were found approximately frequency independent. By our opinion, this behavior may be attributed to phase separation on smaller space scale where the finite-size effects discussed above take place. Therefore, the applicability of our results to a quantitative phase analysis of oxygen-deficient $\text{YBa}_2\text{Cu}_3\text{O}_x$ samples should be further examined on materials prepared under different technological conditions.

In conclusion, we developed a method for calculation of the scattering efficiency of the apical oxygen vibrations in the Ortho-II phase of $\text{YBa}_2\text{Cu}_3\text{O}_x$. The phase shifts for scattering from the full and the empty chains were determined at different wavelengths of the exciting light. Our results are consistent with the assumption that the full and empty Cu-O chains in the Ortho-II phase retain their native electronic structure presented in the Ortho-I and Tetra phases respectively.

Acknowledgments

This work is supported by the project CIPA-CT93-0032 of the EU, the Bulgarian National Scientific Fund (Grant F410/94) and the foundation "Eureka". The author would like to thank Prof. Iliev for supplying experimental data on the resonant Raman scattering from oxygen-deficient YBCO samples and to acknowledge the instructive discussions with Prof. Liarokapis on the subject of the work.

References

1. Jorgensen, J. D.; Veal, B. W.; Paulicas, A. P.; Nowicki, L. J.; Crabtree, G. W.; Claus, H.; Kwok, W. K., *Phys. Rev. B* **1990**, *41*, 1863.
2. Veal, B. V.; Paulicas A. P., *Physica C* **1991**, *184*, 321.
3. De Fontaine, D.; Ceder, G.; Asta M., *Nature* **1990**, *343*, 544.
4. McCormack, R.; De Fontaine, D.; Ceder, G., *Phys. Rev. B* **1992**, *45*, 12 976.
5. Gerdanian, P.; Picard C., *Physica C* **1993**, *204*, 419.
6. Schwarz, W.; Blashko, O.; Collin, G.; Marucco, F., *Phys. Rev. B* **1993**, *48*, 6513.
7. Schleger, P.; Hadfield, R. A.; Casalta, H.; Andersen, N. H.; Poulsen, H. F.; Von Zimmermann, M.; Schneider, J. R.; Liang, Ruixing; Dosanjh, P.; Hardy, W. N., *Phys. Rev. Lett.* **1995**, *78*, 1446.
8. Heyen, E. T.; Rashkeev, S. N.; Mazin, I. I.; Andersen, O. K.; Liu, R.; Cardona, M.; Jepsen, O., *Phys. Rev. Lett* **1990**, *65*, 3048.
9. Heyen, E. T.; Kircher, J.; Cardona, M., *Phys. Rev. B* **1992**, *45*, 3037.

10. Kirillov, D.; Collman, J. P.; McDevitt, J. T.; Yee, G. T.; Holcomb, M. J.; Bozovic, I., *Phys. Rev. B* **1988**, *37*, 3660.
11. Iliev, M. N.; Thomsen, C.; Hadjiev, V. G.; Cardona, M., *Phys. Rev. B* **1993**, *47*, 12 341.
12. Hadjiev, V. G.; Thomsen, C.; Kircher, J.; Cardona, M., *Phys. Rev. B* **1993**, *47*, 9148.
13. Ivanov, V. G.; Iliev, M. N., *Physica C* **1995**, *244*, 293.
14. Iliev, M. N.; Hadjiev, V. G.; Ivanov, V. G., *Journal of Raman Spectroscopy* **1996**, *27*, 333.
15. Poulakis, N.; Palles, D.; Liarokapis E.; Conder, K.; Kaldis, E.; Müller, K. A., *Phys. Rev. B* **1996**, *53*, R534.
16. Liarokapis, E., *High-Tc Superconductivity 1996: Ten Years after the Discovery*; NATO ASI Series E: Applied Sciences; Kluwer Academic Publishers: Dordrecht / Boston / London, 1997, Vol. 343.; pp 447.
17. Misochko, O. V.; Sherman E. Ya., *ZhETF* **1991**, *99*, 330. Misochko, O. V.; Sherman E. Ya.; Timofeev, V. B., *Physica C* **1991**, *185-189*, 1025.
18. Misochko, O. V.; Tajima, S.; Miyamoto, S.; Koshizuka, N., *Solid State Commun.* **1994**, *92*, 877.
19. Abt, R.; Kouba, R.; Ambrosch-Draxl C., Proceedings of the international workshop on *Anharmonic Properties of High-Tc Cuprates* , Bled, Slovenia 1994; Ed. D. Mihailovich, G. Ruani, E. Kaldis and K. A. Müller; World Scientific: Singapore, 1995, pp. 236.
20. Ivanov, V. G.; Iliev, M. N.; Thomsen C., *Phys. Rev. B* **1995**, *52*, 13 652.

Chapter 9

Spectroscopy of the Apex Oxygen Sublattice in $\text{YBa}_2\text{Cu}_3\text{O}_{7-x}$ Single Crystals

V. V. Rumyantsev and S. V. Yampolskii

Donetsk Physical and Technical Institute, Ukrainian National Academy
of Sciences, R. Luxembourg Street 72, 340114 Donetsk, Ukraine

We have studied the light scattering produced by the oscillations of the apical oxygen O(4) ion along the c-axis of the unit cell in $\text{YBa}_2\text{Cu}_3\text{O}_{7-x}$ -type crystals. This issue is particularly relevant since the superconducting pairing mechanism is due to the fluctuation of O(4) positions. Estimates of the apex oxygen content and a number of consequences resulting from the mixing of the electromagnetic g- and u-modes in a $\text{YBa}_2\text{Cu}_3\text{O}_{7-x}$ near-surface layer have been obtained. When oxygen vacancies are in the O(4)-Cu(1)-O(4) bridges, O(4) vibrations along the c-axis induce a dipole moment simultaneously associated with a Cu(1)-O(4) bond deformation. The latter circumstance causes Raman scattering by dipole-active O(4)-oscillations. This summary presents the calculations of Raman light scattering (spontaneous and stimulated) and second optical harmonic intensities generated by the surface layers of a $\text{YBa}_2\text{Cu}_3\text{O}_{7-x}$ single crystal.

Advances in technology allowing the growth of ultrathin crystalline films and periodic structures with controlled characteristics from molecular beam epitaxy has led to an increased interest in studying similar high-temperature superconducting (HTSC) objects (1). Incidentally, owing to the small coherence length ξ of HTSC, the experimental data are often determined from layers with thickness $d \sim \xi$. Because the oxygen subsystem causes the transport properties of HTSC, the diagnostics of its state as a whole, as well as the apex oxygen sublattice, in particular, are of special interest. The superconducting coupling in $\text{YBa}_2\text{Cu}_3\text{O}_{7-x}$ crystals is connected with the fluctuation of the apex oxygen position (2). It must be noted that in $\text{YBa}_2\text{Cu}_3\text{O}_{7-x}$ single crystals and thin films the oxygen content and the crystal structure of near-surface layers are different from those of the bulk (3). This fact must be taken into account for the interpretation of both electron tunneling and photoemission experiments, as well as for the choice of methods in evaluating the oxygen deficiency content.

Optical methods using different light scattering processes are effective for the study of quasi-two-dimensional and layered structures. At present combination scattering (CS) and infra-red (IR) spectra of $\text{YBa}_2\text{Cu}_3\text{O}_{7-x}$ compounds have been measured repeatedly. In particular, it is known that the 500 cm^{-1} frequency line corresponds to the A_g Raman active mode of c -oscillations involving the O(4) apical oxygen ion (4). This mode softens when x increases (5) and is transformed into a broad peak at $\sim 480\text{ cm}^{-1}$ (4) in $\text{YBa}_2\text{Cu}_3\text{O}_6$. Above the 500 cm^{-1} line a number of additional lines appear with maximum frequencies ranging from 580 to 600 cm^{-1} and 630 - 650 cm^{-1} (4,6,7). The shape and intensity of these bands undergo changes depending on the imperfection of the oxygen sublattice. According to Ref.8, the symmetry of the $\sim 580\text{ cm}^{-1}$ Raman mode is A_g also. On the other hand, the above-mentioned bands have also been found in IR spectra (4,6). The authors of Ref.9 connect the appearance of additional bands with a violation of the selection rules in an imperfect structure or with the arising of superstructures from oxygen vacancy ordering. In Ref.7 the $\sim 590\text{ cm}^{-1}$ band has been ascribed to the valence oscillations of O(4)-Cu(1)-O(4) imperfect groups (i.e. with one oxygen vacancy). In Ref.10 the dependence of the 500 cm^{-1} and $\sim 590\text{ cm}^{-1}$ bands on the oxygen deficiency parameter x under different temperature conditions have been explained by the two-well potential of the O(4) ion.

In this paper the light scattering in quasi-two-dimensional crystalline structures of $\text{YBa}_2\text{Cu}_3\text{O}_{7-x}$ type has been studied by means of an extended phenomenological approach (11). Since the masses of Ba,Y,Cu,O ions relate as 8.6:5.6:4:1 we restrict ourselves to a model in which the heavy ions Y,Ba,Cu form a hard frame and the light oxygen ions oscillate. Incidentally we investigate the role of O(4) oscillations on light scattering in more detail.

Model

In perfect centrosymmetric crystals (which include the $\text{YBa}_2\text{Cu}_3\text{O}_{7-x}$ compounds also) the Raman-active phonons correspond to symmetrical displacements of ions (g -type) and the IR-active ones - to antisymmetrical displacements (u -type). However, in real crystals having defects (vacancies, surfaces, etc.) the selection rules, with respect to parity, are violated. In a $\text{YBa}_2\text{Cu}_3\text{O}_{7-x}$ crystal the displacement of the apex oxygen ion in the O(4)-Cu(1)- ν bridge (i.e. with a vacancy) results, on the one hand, in the appearance of a dipole moment (and, hence, in interaction with the electromagnetic field) but, on the other hand, stretches the chemical bond O(4)-Cu(1) and thereby changes the polarizability \hat{X} . The latter circumstance causes Raman light scattering on the O(4) dipole-active oscillations. A similar phenomenon connected with the mixing of g - and u -modes of O(4) ion oscillations along the c -axis in near-surface layers (but not into the bulk) should be observed on the (110)-surface also because the symmetry of this surface is lower than that of the crystal space group.

At zero approximation, the frequency ω_0 , resulting from O(4) interaction with copper ions Cu(1) and Cu(2) (lying in CuO_2 plane), is doubly degenerated. The accounting of the interaction of the O(4)₁ ion ("over" the Cu(1) ion) with the O(4)₂ one ("under" the Cu(1) ion) removes this degeneracy and leads to the appearance in the potential energy of a term depending on the difference of O(4)₁ and O(4)₂ displacements q_1 and q_2 , respectively: $m(\Delta\omega_1)^2(q_1 - q_2)^2 / 4$. Turning into normal coordinates $q_u = (q_1 + q_2)/\sqrt{2}$, $q_g = (q_1 - q_2)/\sqrt{2}$ we obtain the frequencies of the linear independent oscillations

$$\omega_u = \omega_0, \quad \omega_g = \sqrt{\omega_0^2 + (\Delta\omega_1)^2}. \quad (1)$$

In the case of lattice symmetry distortion (due to vacancies, surfaces, etc.) the symmetrical g and antisymmetrical u combinations of normal coordinates are useless, and a corresponding frequency shift $(\Delta\omega_2)^2$ appears:

$$\Omega_u^2 = \omega_u^2 - (\Delta\omega_2)^2 / 2, \quad \Omega_g^2 = \omega_g^2 - (\Delta\omega_2)^2 / 2. \quad (2)$$

Both normal oscillations, on the one hand, stretch a Cu(1)-O(4) bond (i.e., which reveals itself in the Raman spectra) and, on the other hand, generate a dipole moment (i.e., they are active in IR -absorption). The shares of g - and u - components in the new normal modes q_u , q_g depend essentially on the ratio $\alpha = (\Delta\omega_2)^2 / (2\Delta\omega_1)^2$. In the case $\alpha \gg 1$ both q_u and q_g contain dipole-active displacements and Raman-active ones in approximately equal parts. But if $\alpha \ll 1$, the potential energy U of the oscillations of the O(4) ion pair is:

$$U = m\Omega_u^2 q_u^2 / 2 + m\Omega_g^2 q_g^2 / 2 + \mu q_g q_u, \quad (3)$$

where m is the oxygen ion mass and μ is the coupling parameter of normal coordinates expressed as linear combinations of the even and odd displacements of ions:

$$q_g = q_g + \alpha q_u, \quad q_u = q_u - \alpha q_g. \quad (4)$$

Moreover, the mode of quasi-Raman type has an admixture of dipole-active oscillation. Perhaps, such IR-modes which become active due to the violation of symmetry of the crystalline structure were displayed in the Raman spectra of YBa₂Cu₃O₇ (see Ref.4).

Raman Light Scattering

One of the results of mixing the g - and u - phonon modes in quasi-two-dimensional layers of a YBa₂Cu₃O_{7-x}-type crystal is Raman light scattering on surface polaritons. We investigated the interaction of a TM -polarized electromagnetic field with the crystal surface layer. In Ref.12 the corresponding dispersion laws of polaritons which are localized in this layer were obtained. Their wave length $2\pi/k$ is greater than the layer thickness: $kd \ll 1$. Since the frequencies ω_i of light incident upon a crystal surface are greater than those of O(4) ion oscillations and surface polaritons i.e. $\omega_i \gg \Omega_{u(g)}, \Omega$, the polarizability modulation $\delta\hat{X}$ giving rise to Raman scattering in the adiabatic approximation framework can be written as :

$$\delta X_{ij} = \frac{\partial X_{ij}}{\partial q_g} \delta q_g \exp(-i\Omega t + ik\vec{r}) + c.c. \quad (5)$$

The electric field of light induces a surface density of dipole moments which generates a scattering light flux. The intensity of this flux in zz -polarization is

$$I_s = I_i 4\pi^2 \delta q_{\bar{g}} \left(\frac{\partial \hat{X}_z}{\partial q_{\bar{g}}} \right)^2 \left(\frac{\omega_s d}{c} \right)^2 \tan^2 \theta_s \quad (6)$$

at Stokes and anti-Stokes frequencies $\omega_s = \omega_i \pm \Omega$. Here θ_s is the angle between the z axis ($z \parallel c$) and the direction of scattering, $\delta q_{\bar{g}} \approx \delta q_{\bar{g}} = \alpha q_u$ (to an approximation of α^2) is the u -admixture of the O(4) ion \bar{g} -oscillations under the influence of the electrical field E accompanying the lattice oscillations. The non-linear parameter $\partial \hat{X} / \partial q_{\bar{g}}$ introduced by Placzek (13) is connected with the μ parameter of equation 3.

The dynamical equations for the O(4) ion oscillations in the anharmonic approximation are:

$$\begin{aligned} \ddot{q}_{\bar{u}} + \Gamma_1 \dot{q}_{\bar{u}} + \Omega_u^2 q_{\bar{u}} &= \frac{2e}{m} E - \frac{2\mu}{m} q_{\bar{g}} q_{\bar{u}}, \\ \ddot{q}_{\bar{g}} + \Gamma_2 \dot{q}_{\bar{g}} + \Omega_g^2 q_{\bar{g}} &= -\frac{\mu}{m} q_{\bar{u}}^2 \end{aligned} \quad (7)$$

(we consider that oscillation damping coefficients are approximately equal: $\Gamma_1 \approx \Gamma_2 = \Gamma$). Solving the equation system 7 with the first approximation results in the following:

$$\delta q_{\bar{g}} = \alpha(2eE/m)(\Omega_u^2 - \Omega^2 - i\Omega\Gamma)^{-1}. \quad (8)$$

Let us suppose that the electromagnetic field is $E = \sum_{l=1}^2 E_l \exp(-i\Omega_l t) + c.c.$ (it corresponds to the excitation of bi-harmonical polaritons, for example). Then the solution of the equation system 7 $q_{\bar{u}(\bar{g})} = q_{\bar{u}(\bar{g})}^{(1)} + q_{\bar{u}(\bar{g})}^{(2)}$ in the approximation of terms proportional to the squared field is:

$$\begin{aligned} q_{\bar{u}}^{(1)} &= \frac{(2e/m)E_l \exp(-i\Omega_l t)}{\Omega_u^2 - \Omega_l^2 - i\Omega_l\Gamma} + c.c., \quad q_{\bar{g}}^{(1)} = 0, \quad q_{\bar{u}}^{(2)} = 0, \\ q_{\bar{g}}^{(2)}(\Omega_1 \pm \Omega_2) &= \frac{-(2\mu/m)(2e/m)^2 E_1 E_2}{(\Omega_u^2 - \Omega_1^2 - i\Omega_1\Gamma)(\Omega_u^2 - \Omega_2^2 \mp i\Omega_2\Gamma)} \times \\ &\times \frac{\exp[-i(\Omega_1 \pm \Omega_2)t]}{\Omega_g^2 - (\Omega_1 \pm \Omega_2)^2 - i(\Omega_1 \pm \Omega_2)\Gamma} + c.c. \end{aligned} \quad (9)$$

Moreover,

$$q_{\bar{g}}^{(2)}(2\Omega_1) = \frac{-(2\mu/m)(2e/m)^2 E_1^2}{(\Omega_u^2 - \Omega_1^2 - i\Omega_1\Gamma)^2} \cdot \frac{\exp(-2i\Omega_1 t)}{\Omega_g^2 - 4\Omega_1^2 - 2i\Omega_1\Gamma} + c.c. \quad (10)$$

Let us note that the O(4) ion displacements which produce the surface density of dipole moment and consequently stimulate the scattering field at both Stokes and anti-Stokes frequencies are equal $q_u = q_u^{(1)} + \alpha q_u^{(2)}$.

Taking into account the anharmonic terms in the equations 7 we can study the consequences of u - and g - mode mixing as well as stimulated Raman light scattering and second harmonic generation. In the framework of the anharmonic oscillator model, and using the expanded phenomenological approach (11), we find that the intensity of the second harmonic scattered signal is:

$$I_{2\Omega} = I_i^2 \frac{8\pi^3}{c} \frac{(2e/md)^6 \mu^2 \alpha^2 (\omega d/c)^2 \tan^2 \theta_s}{(\Omega_u^2 - \Omega^2)^4 (\Omega_g^2 - 4\Omega^2)^2} . \quad (11)$$

The mixing of modes with different parity takes place in a small part of the crystal (the volume of a quasi-two-dimensional layer is proportional to its thickness d). That is why the intensity I_s is weaker than that scattered by bulk phonons. But at a frequency Ω near Ω_g , the g -oscillation amplitude of the O(4) ion rapidly increases and the observation of additional scattering of coherent waves at both anti-Stokes and Stokes frequencies can be possible.

Evaluation of the Apex Oxygen Content in YBa₂Cu₃O_{7-x} Films

Raman light scattering can be used in order to estimate the O(4) ion content in the real YBa₂Cu₃O_{7-x} samples also.

In the planar system the dimensionless light scattering characteristic is $W = W_s / W_i$, where W_i , W_s are the energies of incident and scattered light waves, respectively. Then according to Refs.14,15 the differential characteristic of scattering (DCS) $d^2W / d\Omega d\omega_s$ ($d\Omega$ is the solid angle element, ω_s is the scattered wave frequency) is proportional to the Fourier component of the correlation function of the ion displacements $\langle q_i q_k \rangle^{\Omega \vec{k}}$ ($i=1,2$) in the film. The explicit form of this function is determined by the dynamics of elementary excitations modulating the electronic polarizability of the film.

Due to the interaction of phononic and electromagnetic modes there is creation of polaritons in the crystal. The dispersion law of these elementary excitations $\Omega_p = \Omega_p(\vec{k})$ follows from the condition of the existence of a non-trivial solution of the system of linear homogeneous equations with respect to the Fourier components of displacements $q_i^{\Omega, \vec{k}}$ and the field $\vec{E}_m^{\Omega, \vec{k}}$ (from the linearity of Maxwell equation it follows that the relation between the field inside the layer \vec{E}_m and that of the incident wave \vec{E}_i is linear: $\vec{E}_m = \hat{A} \vec{E}_i$, and $\hat{A} \approx \hat{I}$ because the superthin film is practically transparent):

$$\hat{G}(\Omega, \vec{k}) \cdot \begin{bmatrix} \vec{q}_1^{\Omega, \vec{k}} \\ \vec{q}_2^{\Omega, \vec{k}} \\ \vec{E}_m^{\Omega, \vec{k}} \end{bmatrix} = 0 . \quad (12)$$

According to the fluctuation-dissipation theorem (15) the imaginary part of the \hat{G}^{-1} matrix i.e. the response function of the film is proportional to the correlation function $\langle q_i C_i^v q_r C_r^v \rangle$ (thermal and configurational averaging is assumed):

$$\langle q_i C_i^v q_r C_r^v \rangle^{\alpha, \vec{k}} = \frac{i\hbar}{4\pi} \left[G_{ii}^{-1} \right]^* - G_{ii}^{-1} \coth \frac{\hbar\Omega}{2k_B T}, \quad (13)$$

C_i^v is the vacancy concentration, k_B is the Boltzman constant. We consider that $C_i^v = 1$ for the defective bridge and $C_i^v = 0$ for the defect-free one. We suppose that C_1^v and C_2^v are evenly distributed in the film and $\langle C_m^v C_n^v \rangle = C^v \delta_{ij} \delta_{mn}$. In the continuum approximation this equality takes the form:

$$\langle C_i^v(\vec{r}) C_j^v(\vec{r}') \rangle = C^v \delta_{ij} \delta(\vec{r} - \vec{r}') V_0$$

(V_0 is the unit cell volume). The explicit form of the \hat{G} matrix has been obtained in Ref.16 within the Debye model (the corresponding frequencies Ω_R of the vacancy oscillations do not depend on the wave vector \vec{k} in the film plane). In the same paper the expression for the DCS has been also obtained.

In the specific case of Raman light scattering by a thin $\text{YBa}_2\text{Cu}_3\text{O}_{7-x}$ crystalline film with vacancies in O(4)-Cu(1)-O(4) bridges the DCS is

$$\frac{d^2 W}{d\Omega d\omega_s} = \frac{\sin^2 \theta_i \sin^4 \theta_s \omega_s^4}{\cos \theta_i \cos \theta_s c^4} a^2 d^2 (\alpha_{zz}^v)^2 \frac{\hbar}{2\pi m \Omega_p} \frac{4C^v \Gamma \coth(\hbar\Omega/2k_B T)}{[\Omega_p(\vec{k}) - \Omega]^2 + \Gamma^2}. \quad (14)$$

Here θ_i is the angle between the direction of an incident light flux and the c -axis, a is the two-dimensional lattice constant, $\hat{\alpha}^v$ is the Raman tensor (the index v characterizes the given normal oscillation mode). In our approximation we neglect the dependence of the scattering line width Γ on the angle θ_i . From the equation 14 it follows that at $\Omega \rightarrow \Omega_p$ the DCS reaches the maximum value. In Ref.16 the θ_i values for which it is possible to observe the maximum Raman shift have been calculated.

The comparison of the experimentally obtained DCS for the defective film (the corresponding values are labeled with "d") with the DCS expression for the free-defect film near the polariton frequency $\Omega \rightarrow \Omega_p$ yields:

$$C^v = \frac{1}{2} \frac{(\text{DCS})_d (\alpha_{zz}^v)^2 \Omega_p \Gamma_d \coth(\hbar\Omega_R / 2k_B T)}{\text{DCS} (\alpha_{zz}^v)_d^2 \Omega_R \Gamma \coth(\hbar\Omega_p / 2k_B T)}. \quad (15)$$

Within this framework it follows from the equation 15 that the ratio of scattered light intensity in the defective film to that in the perfect film is proportional to the vacancy concentration.

Thus, knowing the population of O(4) ion sites in the perfect lattice and estimating the number of vacancies (by using the DCS obtained experimentally), it is possible to evaluate the apex oxygen content in the $\text{YBa}_2\text{Cu}_3\text{O}_{7-x}$ real lattice.

Conclusion

We have investigated the z-oscillations of the apical oxygen which play an important role in the oxygen sub-system disorder (17). Our model is approximate because it neither takes into account the interaction between the oxygen ions belonging to CuO_2 plane and O(4)-Cu(1)-O(4) bridge (18) nor the oscillation mixing of the CuO_x plane and the bridge group (19). But this model allowed us to clarify the peculiarities of Raman light scattering caused by mixing g- and u- phonon modes. It is suitable for evaluating the scattering differential characteristics and the apex oxygen content in $\text{YBa}_2\text{Cu}_3\text{O}_{7-x}$ thin crystalline films presenting oxygen vacancies.

Finally, we note that there is an increasing interest in the employment of HTSC materials under neutron, ion and electron irradiation, especially as detectors (20-22). The method described in this paper may be useful for the study of particle detection. In Ref.23 it has been used to describe the generation of polaritons in hyperfine $\text{YBa}_2\text{Cu}_3\text{O}_{7-x}$ films by moving β -particles. The measurement of Raman light scattering spectra under β -particle irradiation would allow to obtain the sequence of quasi-instantaneous states of the oxygen sub-system as well as the dynamics of its change.

Literature Cited

1. Jacob, G.; Hahn, Th.; Kluge, Th.; et al. *J.Supercond.* **1991**, *7*, p.197.
2. Ranninger, J. *Z.Phys.* **1991**, *B 84*, p.168.
3. *Physical Properties of High-Temperature Superconductors*; Ginzberg, D.M., Ed.; World Scientific: New Jersey, 1989.
4. Cardona, M.; Genzel, L.; Liu, R.; et al. *Solid State Commun.* **1987**, *64*, p.727.
5. Thomsen, C.; Lin, R.; Bauer, M.; et al., *Solid State Commun.* **1988**, *65*, p.55.
6. Evseev, V.A.; Konopleva, R.F. *Optical Properties of High- T_c Materials in the IR Spectral Region*; Preprint N1585; LIYaF, Leningrad; 1990; 24 p.
7. Belousov, M.V.; Davydov, V.Yu.; Karmanenko, S.V.; et al. *Soviet Journal - Pis'ma v ZhETP*, **1988**, *48*, p.285.
8. Hemley, R.J.; Mao, H.K. *Phys.Rev.Lett.* **1987**, *58*, p.2340.
9. Ponosov, Yu.S.; Bolotin, G.A.; Gurin, O.V.; et al. *Soviet Journal - Pis'ma v ZhETP*, **1988**, *48*, p.380.
10. Gasparov, L.V.; Kulakovskii, V.D.; Timofeev, V.B.; Sherman, E.Ya. *J.Supercond.* **1995**, *8*, p.27.
11. Rumyantsev, V.V.; Shunyakov, V.T. *Sov.Phys.Crystallogr.* **1991**, *36(3)*, p.293.
12. Rumyantsev, V.V.; Shunyakov, V.T. *Sov.Phys.Crystallogr.* **1991**, *36(6)*, p.760.
13. Giordmaire, J.A.; Kaiser, W. *Phys.Rev.* **1966**, *144*, p.676.
14. Agranovich, V.M.; Ginzburg, V.L. *Crystallooptics with the Account of Space Dispersion and Theory of Exitons*; Nauka: Moscow, 1979 (in Russian).
15. Landau, L.D.; Lifshits, E.M. *Statistical Physics*; Nauka: Moscow, 1976 (in Russian).
16. Rumyantsev, V.V.; Shunyakov, V.T. *Superconductivity* **1992**, *5(5)*, p.832.

17. Soldke, E.; Munder, H. *Oxygen Content and Disorder in a-axis Oriented YBa₂Cu₃O_{7-x} Thin Films*; Preprint of the Institute for Thin Film and Technology, Research Center Julich GmbH; 1992; 13 p.
18. Rashba, E.I.; Sherman, E.Ya. *Soviet Journal - SFKht* **1989**, *2*, p.80.
19. Mustre de Leon, J.; Conradson, S.D.; Batistic, I.; Bishop, A.R. *Phys.Rev.Lett.* **1990**, *65*, p.1675.
20. Kirsanov, V.V.; Musin, N.N. *Phys.Lett.* **1990**, *A 143*, p.420.
21. Makletsov, A.A. *Soviet Journal - SFKht* **1990**, *3*, p.900.
22. Zhang, Z.M.; Frenkel, A. *J.Supercond.* **1994**, *7*, p.871.
23. Rumyantsev, V.V. In Abstracts of XXIX Meeting on Low Temperature Physics (Kazan, June 30 - July 4, 1992), Pt.1, Kazan University Publ.House, Kazan, 1992, P.213.

Emission Mössbauer Studies of Some High Temperature Superconductors

Amar Nath¹, Vladimir Chechersky¹, Zoltan Homonnay², and Attila Vertes²

¹Department of Chemistry, Drexel University, Philadelphia, PA 19104

²Department of Nuclear Chemistry, Eotvos Lorand University, P.O. Box 32, H-1518 Budapest, Hungary

Mössbauer spectroscopy provides a very valuable tool for obtaining information on the microscopic level of a local site. Emission Mössbauer spectroscopy is much more sensitive than the regular absorption mode. For emission Mössbauer effect studies, a few tens of parts-per-million of Cu is substituted by ⁵⁷Co with minimal perturbation of the system. ⁵⁷Co faithfully microprobes subtle changes in the electron density, local dynamics, presence of extraneous oxygen and magnetic behavior. A few examples of our studies which led to a better understanding of some superconducting systems will be discussed.

A high resolution neutron powder diffraction study showed that the Cu-O chain in YBa₂Cu₃O_{7- δ} is zig-zag with two potential minima for the O²⁻ ions at about 0.015 nm on either side of the chain. Neutron diffraction cannot tell whether the zig-zag chain configuration is static or dynamic with O²⁻ oscillating between the split-sites. It has been proposed earlier that should the oxygen ions be moving in a double-well potential, that would result in an extraordinary enhancement of the electron-lattice coupling which would explain the high superconducting transition temperature. Our Mössbauer studies show that the oxygen ions are not stationary but oscillate between the two potential wells.

We find that partial substitution of yttrium by praseodymium in the system results in dampening, and finally killing of this oscillation. This correlates well with the deleterious effect of Pr to superconductivity.

The electron-doped material Nd_{2-x}Ce_xCuO₄ becomes superconducting with a Ce⁴⁺ content around 0.16, but only after removal of a minuscule amount of extraneous oxygen. This enigmatic behavior has attracted considerable attention. We find that the presence of a minuscule amount of oxygen results in the localization of the static magnetic order in the Cu-O plane. These microscopic spin clusters have variable size centered around 10 nm. Upon deoxygenation, a major fraction of spin clusters associated with a six

line spectrum vanishes, and converts to a paramagnetically relaxed species with a doublet, which is the signature of the superconducting phase. The Mössbauer parameters also indicate that Nd-Ce-Cu-O is a truly electron-doped superconductor contrary to several reports in the literature.

The Mössbauer studies of $\text{HoNi}({}^{57}\text{Co})\text{B}_2\text{C}$ provide a direct evidence for the electronic phase inhomogeneity in the material.

Introduction

${}^{57}\text{Co}$ decays by Electron-Capture to form the daughter ${}^{57}\text{Fe}$ nucleus in the excited state. The exact energy of the 14.4 keV γ -radiation emitted subsequently is very sensitively dependent on the s -electron density on the nucleus. The latter is largely affected by shielding from d -electrons, i.e., the higher the $3d$ -electron density, the lower will be the s -electron density, and consequently the larger the magnitude of the isomer shift (measured as a doppler-shifted velocity with respect to a standard absorber enriched with ${}^{57}\text{Fe}$). The inverse proportionality between the s -electron density and the isomer shift (δ) is a consequence of the fact that the size of the ${}^{57}\text{Fe}$ nucleus in the excited state is smaller than that in the ground state. The excited ${}^{57}\text{Fe}$ nucleus is cigar-shaped along its spin axis (it has a positive quadrupole moment) and consequently can acquire two orientations with differing interaction energies in the presence of non-zero electric field gradient (i.e. when the surrounding electron cloud deviates from spherical distribution). This results in two quadrupole split lines in the Mössbauer spectra. If the Mossbauer probe senses a local magnetic field, a six-line Mössbauer spectrum is exhibited.

Besides these hyperfine parameters, the probability of the Mossbauer effect itself, which is proportional to the total spectral area, gives information about the local lattice dynamics, because it is directly related to the mean square displacement of the Mössbauer atom at its lattice position.

Mössbauer spectra are recorded by measuring the absorption of the gamma quanta emitted by ${}^{57}\text{Co}$ incorporated in a superconducting material as a function of the velocity of a moving standard absorber. Emission Mössbauer spectroscopy is a few orders of magnitude more sensitive than the absorption mode. For Emission Mössbauer studies, only a couple of tens of parts-per-million of Cu (or Ni) are replaced by ${}^{57}\text{Co}$ with minimal perturbation of the system. Our studies show that ${}^{57}\text{Co}$ faithfully microprobes subtle changes in the electron density, local dynamics, presence of extraneous oxygen, and the magnetic behavior (1-12). Here we discuss a few examples of our studies which hopefully led to a better understanding of some superconducting systems.

Oscillation of O(4) in the Cu-O Chain of $\text{YBa}_2\text{Cu}_3\text{O}_{7-\delta}$.

As the superconductivity in the classic BCS-type low temperature superconductors is based on phonon-electron interaction, lattice vibrations in the YBCO system (and in other high- T_C superconductors) have attracted considerable attention.

The amplitude of vibration of O(4) atoms out of the chain in YBCO has been reported to be large (13-15). A more refined high resolution neutron powder diffraction study (16) showed that the Cu(1)-O(4) chain is zig-zag with two potential minima for O(4) at about 0.015 nm on either side of the chain (Fig. 1). The neutron diffraction studies cannot tell whether the zig-zag chain configuration is static or dynamic with O(4) oscillating between the split-sites. However, the increase of the

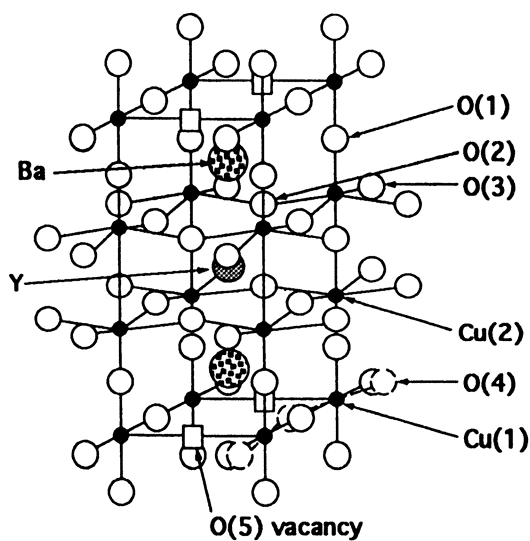


Figure 1. The unit cell of $\text{YBa}_2\text{Cu}_3\text{O}_{7-\delta}$. The dynamic zig-zag structure of the $\text{Cu}(1)\text{-O}(4)$ chain (exaggerated) is illustrated in the bottom-right edge of the cell.

vibrational amplitudes with temperature for the O(4) atoms suggested that the displacement could be partly dynamic (15).

Some researchers proposed that should the oxygen ions be moving in a double-well potential, that would result in an extraordinary enhancement of the electron-lattice coupling (17,18) which would explain the high transition temperatures. Although the BCS theory (weak coupling) anticipates an upper limit of T_C about 30 K, Ginzburg suggested (19) that there is a possibility that anharmonic vibrations may provide a coupling between electrons strong enough to resist temperatures up to 100 K.

We substituted a few tens of parts-per-million of Cu(1) with ^{57}Co to probe the dynamics of the Cu(1)-O(4) chain (2,3). The emission Mössbauer spectra of the fully oxygenated $\text{YBa}_2\text{Cu}_3(^{57}\text{Co})\text{O}_{7-\delta}$ were measured at different temperatures in the range of 80 to 400K (Figs. 2,3). The three major species with quadrupole splittings of 1.98, 1.01, and 1.5 mm/s were assigned to dynamic square planar (species A), static distorted 5-coordinate trigonal-bipyramidal (species B), and 5-coordinate dynamic square-pyramidal (species C) configurations, respectively (Fig. 4). The 5-coordinate species are formed as Co atom has a tendency to attract an additional O^{2-} ion in the vacant O(5) site (Fig. 1). It was observed that above 225K, species B starts converting into species C and the conversion is complete above 350K (Figs 2 and 3). The interconversion is reversible. Our observations were neatly interpreted by assuming oscillation of the oxygen atoms in O(4) sites between the two potential wells, and proposing that this is responsible for triggering the B to C interconversion. In the case of 4-coordinate species A, the two O(4) ions neighboring ^{57}Co participate in the zig-zag motion of the chain (Fig. 4). However, at relatively low temperatures, the preferred configuration of the 5-coordinate species B is the one where the two O(4) ions neighboring ^{57}Co sit in potential wells away from the apical O(5), due to electrostatic repulsion (Fig. 4). This is the static distorted trigonal-bipyramidal species B. In this configuration, the two neighboring O(4) atoms cannot participate in the zig-zag motion of the rest of the chain. At a higher temperature, the repulsion barrier can be overcome and the O(4) ions participate in the zig-zag motion with the rest of the chain. The O(5) ions would also swing about the a-axis to minimize the electrostatic repulsion from the two neighboring O(4) anions. This results in the dynamic square-pyramidal configuration of species C (Fig. 4). Therefore, the zig-zag motion of the chain is responsible for inducing a dynamic equilibrium between species B and C, and the relative amounts vary with the temperature (2,3). The interconversion of species B and C in the temperature range of 200 to 330 K has been confirmed by an independent emission Mössbauer study (20).

Later, there were several reports associating the anharmonicity of chain oxygen motion (21) or that of the O(1) apical oxygen between two potential wells (22-24), with the enhancement of the superconducting transition temperature. The double-well potential for the O(1) apical oxygens was first reported by Mustre de Leon et al. in their EXAFS study of $\text{YBa}_2\text{Cu}_3\text{O}_{7-\delta}$ (22). Subsequent EXAFS work indicates that the splitting of O(1) sites is neither observed for oxygen rich material with $T_C=93\text{K}$ (25) nor for films (26). Moreover, an X-ray single crystal study of $\text{YBa}_2\text{Cu}_3\text{O}_{6.88}$ (27) and a neutron single crystal study of $\text{YBa}_2\text{Cu}_3\text{O}_{6.98}$ (28) did not detect any indication of this splitting. This leaves the anharmonic oscillation of O(4) in the chain as the only candidate for enhancement of the T_C of $\text{YBa}_2\text{Cu}_3\text{O}_{7-\delta}$ (17,18,21).

It was widely believed that the Cu-O chains serve as charge reservoirs only. More recently, it has been shown rather convincingly that the in-plane anisotropy of the penetration depth is due to superconductivity on the Cu-O chains (29,30). In view of this finding and the fact that the existence of potential wells for O(1) apical oxygen is very much in doubt, the dynamics of the chain acquires added importance.

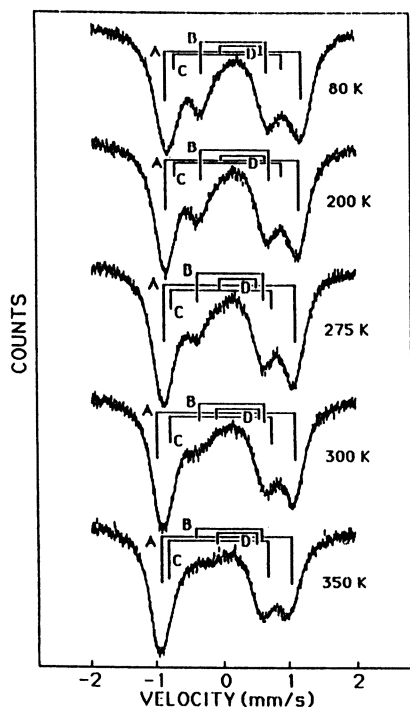


Figure 2. Emission Mössbauer spectra of ^{57}Co -doped $\text{YBa}_2\text{Cu}_3\text{O}_{7-\delta}$ recorded at different temperatures (Reproduced with permission from reference 2. Copyright 1989 Elsevier Science.)

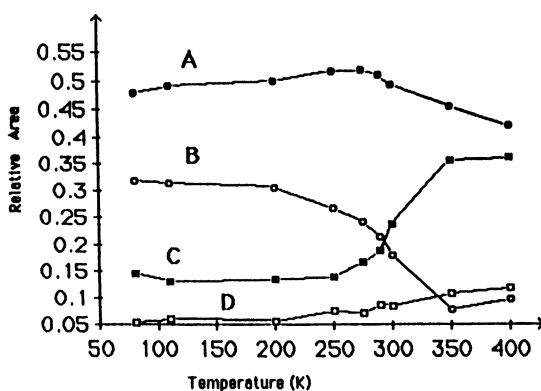


Figure 3. Change of relative areas of doublets A, B, and C in the Mössbauer spectra of $\text{YBa}_2\text{Cu}_3(^{57}\text{Co})\text{O}_{7-\delta}$, as a function of temperature. The Lamb-Mössbauer factors for all species are assumed to be equal. (Reproduced with permission from reference 2. Copyright 1989 Elsevier Science.)

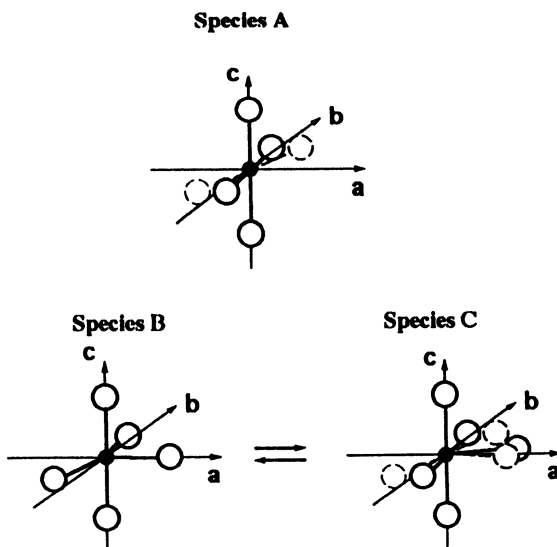


Figure 4. Configurations for ^{57}Co at Cu(1) site: dynamic square-planar, species A, distorted trigonal-bipyramidal, species B, and dynamic square-pyramidal, species C. O(1), O(4) and O(5) atoms are shown along the c, b and a axes, respectively.

In short, we find that the dynamics of the chain is determined by the oscillation of O(4) atoms between the two potential wells on either side of the chain. In addition, the amplitude of the oscillation of O(4) atoms become much larger at about 230 K. The dynamics of the chain is apparently related to the broad peak observed around 220 K by anelastic relaxation as well as by other techniques (31-33). These observations are characteristic of a phase transition, which is however not associated with changes in the lattice parameters (33).

Mössbauer spectroscopy can also provide direct information about lattice vibration by measuring the probability of the Mössbauer effect as a function of temperature as discussed in ref. (12).

Praseodymium Substitution and Metallicity of the Chain in $\text{YBa}_2\text{Cu}_3\text{O}_{7-\delta}$.

The deleterious effect of Pr substitution for Y on the superconductivity has been a major source of controversy. The three major points of view advanced for explaining the effect are hole filling, hybridization of the extended Pr 4f electrons with O 2p states (of the CuO_2 plane), and pair breaking by the magnetic moment of Pr (34-36). If Pr is present as Pr^{4+} while substituting for Y^{3+} , the additional electron in the conduction band will fill up some of the mobile holes in the CuO_2 planes thus vitiating the superconductivity. The hole-filling picture is supported by the fact that the addition of small amounts of Ca to the Pr doped material raises T_C by several degrees indicating partial compensation of Pr^{4+} by Ca^{2+} . Some other measurements like magnetic susceptibility, low temperature transport properties, Cu-NMR, and optical reflectivity also seem to indicate reduction of carriers by hole filling. Hall measurements are not very conclusive. However, a variety of spectroscopic studies like photoemission, XANES, Raman, and EELS have been interpreted as an evidence for Pr in the +3 state. Inelastic neutron scattering, specific heat and susceptibility studies again support the Pr^{3+} state (37). A ^{141}Pr Mössbauer study (38) suggests a formal Pr valence state of 3.4.

We have studied $\text{Y}_{1-x}\text{Pr}_x\text{Ba}_2\text{Cu}_3(^{57}\text{Co})\text{O}_{7-\delta}$ with $x = 0.1, 0.3$ and 0.45 (12, 39). The isomer shifts for species A and C do not show an appreciable change clearly indicating that the hole density on the metallic chains remain unaffected by Pr substitution. These observations would rule out hole filling. However, the dynamics of the chain is affected significantly by Pr substitution. In the previous section, we have discussed that the interconversion of species B and C is triggered by the oscillation of O(4) between the two potential wells on either side of axis b. With increasing Pr-substitution, the B to C conversion diminishes considerably which supports the point of view that the chain dynamics may be involved in superconductivity. Our observations are consistent with localization of holes by hybridization of oxygen in CuO_2 planes with Pr-f electronic states (34, 40, 41).

The Role of Extraneous Oxygen in the Superconductivity of the Nd-Ce-Cu-O System.

Superconductivity has also been discovered in the electron-doped system $\text{Ln}_{2-x}\text{M}_x\text{CuO}_4$ for $\text{M}=\text{Ce}$ and $\text{Ln}=\text{Pr}$ (42), Nd (42), Sm (42), and Eu (43), and for $\text{M}=\text{Th}$ and $\text{Ln}=\text{Pr}$ (43), Nd (44), and Sm (45). Both Ce and Th having a formal oxidation number of +4, donate electrons to the CuO_2 planes resulting in T_C 's as high as ~25 K for $x=0.15$. F^- ions can also be substituted for O^{2-} both within and outside the CuO_2 planes, and the resulting compound $\text{Nd}_2\text{CuO}_{4-y}\text{F}_y$ exhibits superconductivity also (46). Ga^{3+} or In^{3+} ions can also be substituted partially for Cu^{2+} with similar results (47,48).

The electron-doped system differs from its hole-doped analog $\text{La}_{2-x}\text{Sr}_x\text{CuO}_4$ in several respects (49,50). First, in the $\text{T}'\text{-Nd}_2\text{CuO}_4$ structure, the CuO_2 layers contain Cu ions in square planar coordination. On the other hand, in the $\text{T-La}_2\text{CuO}_4$ structure, the Cu ions in the CuO_2 layers are octahedrally coordinated to oxygen. Second, the observation of bulk superconductivity in the electron-doped system is confined to a very narrow range of tetravalent ion (Ce^{4+} or Th^{4+}) concentration centered around $x=0.155$; whereas in its hole-doped counterpart the range is much larger. Third, electron doping is less effective than hole doping in suppressing the long range Cu^{2+} - Cu^{2+} antiferromagnetic ordering in the parent compounds. In the $\text{La}_{2-x}\text{Sr}_x\text{CuO}_4$ system, the holes created by Sr substitution have an appreciable oxygen $2p$ character, resulting in a ferromagnetic interaction of O^- with its immediate Cu^{2+} neighbors, which frustrates the antiferromagnetic ordering (51,52). On the other hand, electron doping in the $\text{Nd}_{2-x}\text{Ce}_x\text{CuO}_4$ system would essentially result in formation of Cu^{1+} ions, which causes nonmagnetic dilution and gradual suppression of antiferromagnetic order (53). Fourth, and most importantly, the as-prepared electron-doped superconducting material exhibits superconductivity only after deoxygenation in an inert ambient above 800°C . Removal of a minuscule amount of extraneous oxygen (~ 0.02 per formula unit) produces a dramatic change in its behavior.

The role of oxygen in the manifestation of superconductivity in $\text{Nd}_{2-x}\text{Ce}_x\text{CuO}_4$ materials has attracted considerable attention. Izumi et al.(54), on the basis of their neutron powder diffraction studies of $\text{Nd}_{1.85}\text{Ce}_{0.15}\text{CuO}_4$, reported a slight deficiency of oxygen on the $\text{O}(2)$ site and full occupancy on the $\text{O}(1)$ site in the CuO_2 plane for the oxygenated material. On deoxygenation, they observed no change on the $\text{O}(2)$ site whereas a slight deficiency was found on the $\text{O}(1)$ site. However, Kwei et al.(55) interpret their own neutron-diffraction observations and that of Izumi et al. differently, and conclude that there are no differences in the oxygen stoichiometry of the oxygenated and deoxygenated samples within the estimated error. Several researchers (56-60), using TGA and/or iodometric technique, have reported that the loss of oxygen during deoxygenation decreases with increase in Ce concentration and is only about 0.02 per unit formula for $x=0.15$. However, for the Ce-free parent compound, Nd_2CuO_4 , a larger loss of oxygen is reported. Marin et al.(61) in a single crystal neutron diffraction study of Nd_2CuO_4 observe oxygen removal of 0.05 from the $\text{O}(1)$ site, whereas the deficiency of 0.06 in the $\text{O}(2)$ oxygen planes remains unaffected during deoxygenation. None of the above-mentioned studies (55,61) could find evidence of the presence of extraneous oxygen in apical positions relative to the Cu atoms (i.e. the $\text{O}(3)$ site) as proposed by Tarascon et al.(56) However, a very recent study of single crystal neutron diffraction of Nd_2CuO_4 by Radaelli et al.(62) reports not only the presence of apical oxygen but its decrease from 0.1 in the as-prepared crystal to 0.04 after deoxygenation.

Here we will discuss some salient features of our work on oxygenated and deoxygenated $\text{Nd}_{2-x}\text{Ce}_x\text{Cu}(^{57}\text{Co})\text{O}_4$ where $x = 0, 0.14, 0.15, 0.16$ and 0.18 . Only compounds with $x = 0.15$ and 0.16 become superconducting on deoxygenation. Oxygenation and deoxygenation were carried out at about 950°C in O_2 and Ar ambients, respectively for 20-30 hours. The microenvironment created by the ^{57}Co microprobe is not necessarily identical to that of its neighboring Cu atoms; nevertheless, the changes in the electron density, the magnetic behavior and the presence of extraneous oxygen can be faithfully sensed by the Mössbauer probe. The presence of extraneous oxygen is detected by the formation of 5- and 6-coordinate (designated as B and C, respectively) species with ^{57}Co . The 4-coordinate species A was not observed.

At higher temperatures (>550 K), the Mössbauer spectrum can be resolved into quadrupole split doublets corresponding to species B and C (Fig. 5). However, at lower temperature the magnetically split sextets for species B and C coexist with their corresponding relaxed quadrupole split doublets. This superparamagnetic behavior is characteristic of variable size spin-clusters as discussed in ref. (8). At any particular temperature, a fraction of the single domain spin clusters with a size lower than a certain limit, would acquire enough thermal energy to overcome the barrier for magnetization reorientation. Consequently, the magnetization flips at a rate faster than the Larmor frequency of excited ^{57}Fe ($\sim 10^8 \text{ s}^{-1}$), and the nuclei experience zero net field during the Mössbauer events as for a paramagnet. For this fraction of relatively small clusters, a superparamagnetically relaxed spectrum consisting of a quadrupole split doublet is observed (Fig. 6). In the case of the large sized spin clusters with slower rate of flipping, the ^{57}Fe nuclei experience an effective magnetic field and a magnetically split six-line Mössbauer spectrum is seen. For the intermediate sized spin clusters, the rate of flipping would be comparable to the Larmor frequency and complex spectra with broadened peaks and unusual line shapes are observed. At low temperatures, larger fractions of species B and C manifest themselves as magnetically split sextets and as the temperature is raised, the superparamagnetically relaxed doublets grow at the expense of the sextets. For instance, in Fig. 6, one can see how the abundance of relaxed doublet C increases with temperature and the sextet area decreases correspondingly. However, for much larger spin clusters, complete relaxation of C does not occur even at 500K, where the central relaxed doublets are associated with a very broad concave hump with asymptotic approach to background.

Species B and C manifest themselves as quadrupole split doublets and/or magnetically split sextets depending on the temperature of the measurement and the size of magnetic clusters. The latter is determined by the presence of extraneous oxygen. We find that the extraneous oxygen situated in apical positions tend to localize electrons donated by Ce^{3+} ions and thereby introduces non-superconducting spin clusters. Our observations (Figs 6-9) show that the 6-coordinate species C is present only in oxygen-rich antiferromagnetically ordered "impurity" regions. The extraneous oxygen in these regions is rather tenaciously held and cannot be removed by conventional deoxygenation procedures. The presence of some additional oxygen, which can be partially removed during deoxygenation, may cause injection of holes, which can bring about magnetic frustration in small regions in the intermediate vicinity. This will enhance superparamagnetism (Fig. 8). However, during deoxygenation partial removal of the excess oxygen eliminates magnetically frustrated pockets and the size of magnetic clusters grows and so superparamagnetism vanishes at 80 K (Fig. 8). Since species C resides in an "impurity region", we can hope to learn about the normal state of the superconducting material $\text{Nd}_{1.84}\text{Ce}_{0.16}\text{Cu}(\text{}^{57}\text{Co})\text{O}_4$ only from species B. It is very interesting to observe that there is no change in the Mössbauer spectrum at temperature 80K on deoxygenation for Ce-rich bulk non-superconducting $\text{Nd}_{1.82}\text{Ce}_{0.18}\text{Cu}(\text{}^{57}\text{Co})\text{O}_4$ (Fig. 9). There is only a small amount of paramagnetically relaxed species B present which is indicative of metallic phase. The rest of the material is oxygen-rich and magnetic which suggests that conventional deoxygenation does not permit desorption of the extraneous oxygen. For the Ce-poor bulk non-superconducting compound, $\text{Nd}_{1.86}\text{Ce}_{0.14}\text{Cu}(\text{}^{57}\text{Co})\text{O}_4$, on deoxygenation, the metallic (and potentially superconducting) fraction as indicated by paramagnetically relaxed B doublet increases from 9 to 14% (Fig. 7). The behavior of the bulk superconductor $\text{Nd}_{1.84}\text{Ce}_{0.16}\text{Cu}(\text{}^{57}\text{Co})\text{O}_4$ is in sharp contrast to the non-superconducting compounds with Ce concentration above or below the optimum value. A large fraction of the magnetically split species B relaxes to a doublet on deoxygenation. The abundance of doublet B increases from 15 to 47% as seen from the Mössbauer

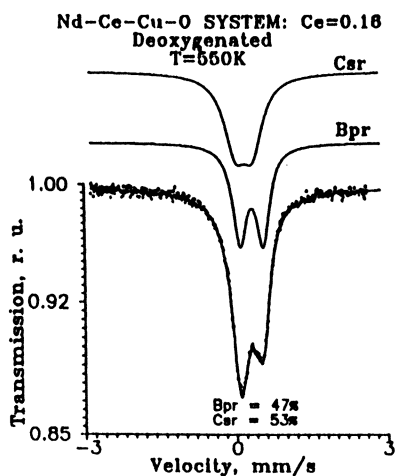


Figure 5. Computer fit of $\text{Nd}_{2-x}\text{Ce}_x\text{Cu}(\text{}^{57}\text{Co})\text{O}_4$ ($x=0.16$) ceramic sample at 550K. Relative abundances of species B and C correspond with those obtained at 80K. "sr" = superparamagnetically relaxed; "pr" = paramagnetically relaxed.

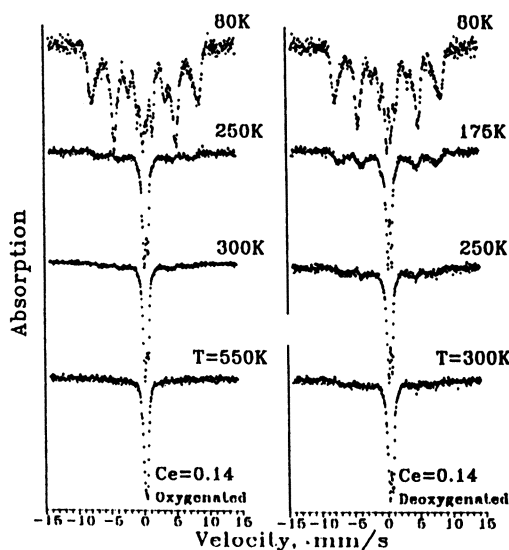


Figure 6. Mössbauer spectra of $\text{Nd}_{2-x}\text{Ce}_x\text{Cu}(\text{}^{57}\text{Co})\text{O}_4$ ($x = 0.14$) ceramic sample at different temperatures. (Reproduced with permission from reference 10. Copyright 1995.)

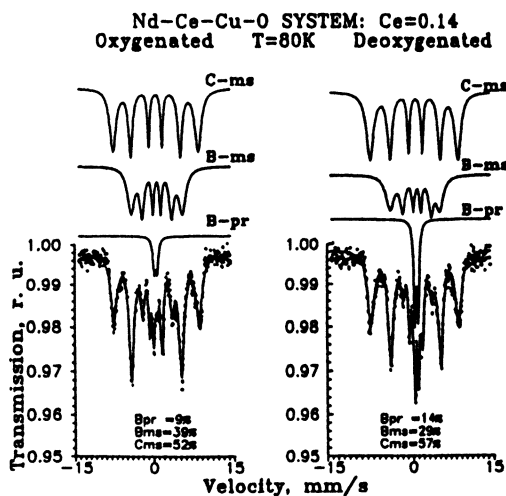


Figure 7. Computer analyzed components of $\text{Nd}_{2-x}\text{Ce}_x\text{Cu}^{(57)\text{Co}}\text{O}_4$ ($x = 0.14$) at 80 K. “ms” = magnetically split; “pr” = paramagnetically relaxed. (Reproduced with permission from reference 10. Copyright 1995.)

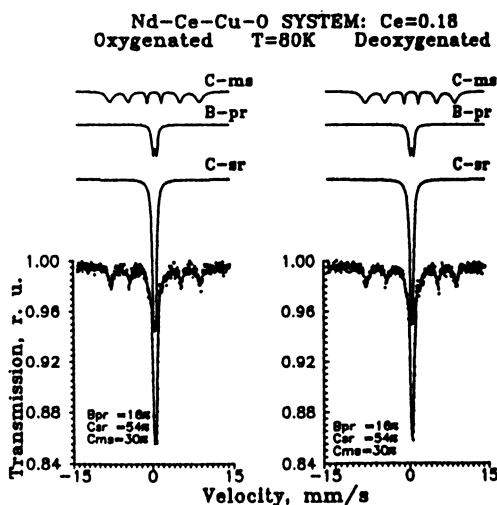


Figure 8. Computer analyzed components of $\text{Nd}_{2-x}\text{Ce}_x\text{Cu}^{(57)\text{Co}}\text{O}_4$ ($x = 0.18$) ceramic sample at 80 K. “sr” = superparamagnetically relaxed; “pr” = paramagnetically relaxed; “ms” = magnetically split. (Reproduced with permission from reference 10. Copyright 1995.)

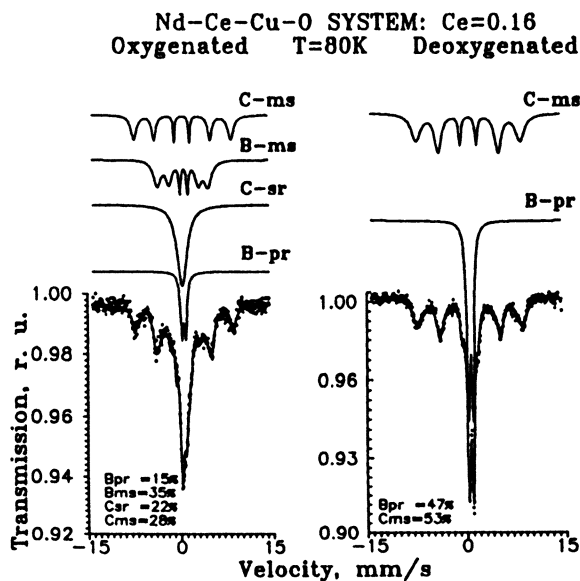


Figure 9. Computer analyzed components of $\text{Nd}_{2-x}\text{Ce}_x\text{Cu}^{(57)\text{Co}}\text{O}_4$ ($x = 0.16$) ceramic sample at 80 K. “sr” = superparamagnetically relaxed; “pr” = paramagnetically relaxed; “ms” = magnetically split. (Reproduced with permission from reference 9. Copyright 1994 American Association for the Advancement of Science.)

spectrum at 80K (Fig. 9). As a matter of fact, the relative abundance of doublet B corresponds to the superconducting volume fraction as estimated by magnetic susceptibility measurements (9). The above observation may be interpreted by assuming that the extraneous oxygen situated in apical positions tend to localize electrons donated by Ce^{3+} ions and thereby introduces non-superconducting spin clusters with quasi-static magnetic order in the Cu-O sheets (8-11). Removal of extraneous oxygen increases considerably the superconducting volume fraction for materials with Ce concentration centered around 0.155.

The question arises as to why extraneous oxygen can be desorbed with relative ease only for Nd-Ce-Cu-O compounds with an optimum cerium content. This apparently anomalous behavior for $Ce=0.16$, where the minuscule amount of apical oxygen dissociates from Cu with ease in the normal state, may be due to some local structural changes of a static or dynamic nature in the puckering of CuO_2 sheets, and/or a change in the electronic behavior.

Mössbauer spectroscopy also sheds some light on the electron density in the $3d$ - band of CuO_2 planes in Nd-Ce-Cu-O system vis-a-vis the CuO chains of the Y-Ba-Cu-O system. The chemical shift of 0.59 mm/s for the five-coordinated species B is significantly larger than those observed for the corresponding five-coordinated species with a static distorted trigonal-bipyramidal configuration, and the one having a dynamic square-pyramidal configuration both formed in the Cu(1)-O chain, viz. 0.11 and -0.03 mm/s at 80K, respectively (2-4). This is indicative of a much lower s - electron density on the ^{57}Co (^{57}Fe) nuclei due to shielding from a much higher density of d - electrons in the Nd-Ce-Cu-O system. This is consistent with the general belief that Nd-Ce-Cu-O material is electron-doped in contrast to Y-Ba-Cu-O compounds which are hole-doped.

In summary, a conventional procedure for deoxygenation brings about little change in the Mössbauer spectra both above and below the optimal superconducting concentration; however, for $x=0.16$, a dramatic change is observed - a major fraction of the magnetically split 5-coordinate species B manifests itself as a paramagnetically relaxed doublet upon deoxygenation, which constitutes a microscopic measure of the superconducting volume fraction. This apparently anomalous behavior at $x=0.16$, where the extraneous oxygen is more readily desorbed, may be related to an electronic and/or local structural change in the CuO_2 plane. It may be mentioned that Brinkman et al. (63) have recently extended the range of Ce concentration over which bulk superconductivity can be observed in the Nd-Ce-Cu-O system by eliminating the oxygen-rich regions.

A special sequence of thermal treatments of $Nd_{1.85}Ce_{0.15}Cu(^{57}Co)O_4$ also allows us to eliminate the impurity phase in which species C resides (11). Then, the spectra are considerably simplified and consist predominantly of species B which resides in the potentially superconducting phase. This permitted us to closely examine the subtle changes in the line shape of species B as a function of temperature in the normal state and allowed us to estimate the rate of magnetic fluctuations as 10^{11} s⁻¹. This might bear on some possible correlation between antiferromagnetic spin fluctuations and superconductivity (11).

The $HoNi_2B_2C$ System

The titled system has attracted a lot of attention due to the interesting interplay of magnetism and superconductivity. It becomes superconducting at about 8K, the superconductivity increases until about 7K as measured by the upper critical field (H_C2), and then it decreases due to the appearance of the incommensurate spiral magnetic states, only to re-enter full fledged superconductivity below 5K co-existing with the commensurate antiferromagnetic structure (64-68). In the approximate temperature range of 4 to 7K, two other incommensurate spiral magnetic states, with

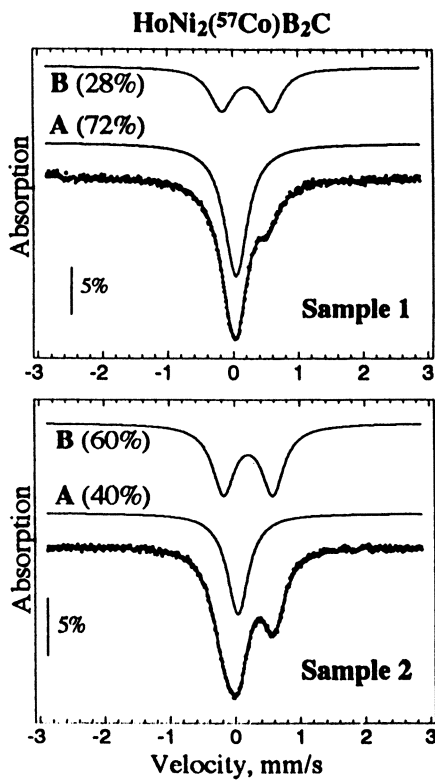


Figure 10. Computer analyzed components in the two samples of $\text{HoNi}_2(^{57}\text{Co})\text{B}_2\text{C}$.

modulation along the a- and c-axes respectively, have been observed. The relative intensities of the three types of co-existing magnetic ordering vary from sample to sample (64, 66, 68, 69). The question arises whether superconductivity and the spiral magnetic states can co-exist or do they occur in different regions of the sample. If so, can borocarbides be electronically inhomogeneous? We substituted a few parts per million of Ni atoms with ^{57}Co with minimal perturbation of the system.

The Mössbauer spectra of two different samples are shown in Fig. 10. There are two species in both samples. Species A has almost zero isomer shift and quadrupole splitting which can be associated with good hybridization of regular NiB_4 tetrahedra; good hybridization will induce delocalization of 3d electrons and impart metallic character and the geometrical configuration results in almost spherical distribution of electron cloud around the probe. The other species have isomer shift of about 0.18 mm/s and a fairly large quadrupole splitting of approximately 0.7 mm/s. It seems that the NiB_4 tetrahedra are slightly distorted in this electronic phase and that the delocalization of 3d electrons is somewhat restricted [70].

In summary, we have evidence of electronic phase inhomogeneity in $\text{HoNi}_2\text{B}_2\text{C}$, one of them is truly metallic with considerable delocalization of 3d electrons. In the other phase, the electrons are delocalized to a lesser extent. The relative ratio of the components varies from sample to sample.

Acknowledgments AN acknowledges partial support from the donors of the Petroleum Research Fund administered by the American Chemical Society. Part of this work was supported by the Hungarian-US Science & Technology Foundation under #4301/96, which is also gratefully acknowledged.

References

- Nath, A.; Nagy, S.; Barsoum, M.; Tyagi, S. D.; Wei, Y. *Solid State Commun.* **1988**, *68*, 181.
- Nath, A.; Homonnay, Z. *Physica C* **1989**, *161*, 205.
- Homonnay, Z.; Nath, A. *J. Supercond.* **1990**, *3*, 433.
- Nath, A.; Homonnay, Z.; Tyagi, S. D.; Wei, Y.; Jang, G-Way; Chan, C-C. *Physica C* **1990**, *171*, 406.
- Homonnay, Z.; Nath, A.; Wei, Y.; Tian, J. *Physica C* **1991**, *174*, 223.
- Kopelev, N.; Chechersky, V.; Tian, J.; Homonnay, Z.; Wei, Y.; Nath, A. *Physica C* **1992**, *193*, 136.
- Chechersky, V.; Kopelev, N.; Tian, J.; Wei, Y.; Nath, A. *Rev. Sci. Instrum.* **1993**, *64*, 1044.
- Chechersky, V.; Kopelev, N.; O, B-h.; Larkin, M. I. Peng; J. L. Markert, J. T.; Greene, R. L. Nath; A. *Phys. Rev. Letters* **1993**, *70*, 3555.
- Nath, A.; Kopelev, N. S.; Chechersky, V.; Peng, J. L.; Greene, R. L.; O, B-h.; Larkin, M. I.; Markert, J. T. *Science* **1994**, *265*, 73.
- Kopelev, N. S.; Chechersky, V.; Nath, A.; O, B-h.; Larkin, M. I.; Markert, J. T.; Peng, J. L.; Greene, R. L. *J. Radioanal. & Nucl. Chem.* **1995**, *190*, 391.
- Chechersky, V.; Kopelev, N. S.; Nath, A.; Peng, J. L.; Greene, R. L.; O, B-h. Larkin, M. I.; Markert, J. T. *Phys. Rev. B* **1996**, *54*, 16254.
- Chechersky, V.; Gal, M.; Homonnay, Z.; Vanko, Gy.; Kuzmann, E.; Tyagi, S.; Greene, R. L.; Vertes, A.; Nath, A. *Physica C* **1997**, *277*, 36.
- You, H. R.; McMullan, K.; Axe, J. D.; Cox, D. E.; Liu, J. Z.; Crabtree, G. W.; Lam, D. J. *Solid State Commun.* **1987**, *64*, 739.
- Marsh, P.; Siegrist, T.; Fleming, R. M.; Schneemeyer, L. F.; Waszczak, V. *Phys. Rev. B* **1988**, *38*, 874.
- Simon, A.; Kohler, J.; Borrmann, H.; Gegenheimer, B.; Kremer, R. *J. Solid State Chem.* **1988**, *77*, 200.

16. Francois, M.; Junod, A.; Yvon, K.; Hewat, A. W.; Capponi, J. J.; Strobel, P.; Marezio, M.; Fischer, P. *Solid State Comm.* **1988**, *66*, 1117.
17. Plakida, N. M.; Aksenov, V. L.; Drechsler, S. L. *Europhys. Lett.* **1987**, *4*, 1309.
18. Hardy, J. R.; Flocken, J. W. *Phys. Rev. Lett.* **1988**, *60*, 2191.
19. Ginzburg, V. L. *Physica C* **1993**, *209*, 1.
20. Andrianov, V. A.; Kozin, M. G.; Romashkina, I. L.; Semenov, S. I.; Rusakov, V. S.; Shlyakhtin, O.A.; Shpinel, V.S. *J.Superconductivity* **1991**, *4*, 1035.
21. Cohen, R. E.; Pickett, W. E.; Krakauer, H. *Phys. Rev. Lett.* **1990**, *64*, 2575.
22. Mustre de Leon, J.; Conradson, S. D.; Batistic, I.; Bishop, A. R. *Phys. Rev. Lett.* **1990**, *65*, 1675.
23. Johnson, K. H.; Clougherty, D. P.; McHenry, M. E. in "*Electronic Structure, Mechanisms for High-T_C Superconductivity*", J. Ashkenzi, G. Vezzoli, eds., Plenum 1991.
24. Egami, T.; Billinge, S. J. L. in "*Progress in Materials Science*", 1994, *38*, p359.
25. Stern, E. A.; Qian, M.; Yacoby, Y.; Heald, S. M.; Maeda, H. *Physica C* **1993**, *209*, 331.
26. Booth, C. H.; Bridges, F.; Boyce, J. B.; Claeson, T.; Lairson, B. M.; Liang, R.; Bonn, D. A. *Phys. Rev. B* **1996**, *54*, 9542.
27. Sullivan, J. D.; Bordet, P.; Marezio, M.; Takenaka, K.; Uchida, S. *Phys.Rev B* **1993**, *48*, 10638.
28. Schweiss, P.; Reichardt, W.; Braden, M.; Collin, G.; Heger, G.; Claus, H.; Erb, A. *Phys. Rev B* **1994**, *49*, 1387.
29. Basov, D. N.; Liang, R.; Bonn, D. A.; Hardy, W. N.; Dabrowski, B.; Quijada, M.; Tanner, D. B.; Rice, J. P.; Ginsberg, D. M.; Timusk, T. *Phys. Rev. Lett.* **1995**, *74*, 598.
30. Tallon, J. L.; Bernhard, C.; Binniger, U.; Hofer, A.; Williams, G. V. M.; Ansaldo, E. J.; Budnick, J. I.; Niedermayer, Ch. *Phys. Rev. Lett.* **1995**, *74*, 1008.
31. Cannelli, G.; Cantelli, R.; Cordero, F.; Trequattrini, F. *Supercond. Sci. Technol.* **1992**, *5*, 247.
32. Chrzanowski, J.; Sujak, B.; Benzar, I. *Mod. Phys. Lett.B* **1990**, *4*, 545.
33. Almond, D.P.; Wang, Q.; Freestone, J.; Lambson, E. F.; Chapman, B.; Saunders, G. A. *J. Phys: Condensed Matter* **1989**, *1*, 6853.
34. Maple, M. B.; Lee, B. W.; Neumeier, J. J.; Nieva, G.; Paulius, L. M.; Seaman, C. L. *J. Alloys Compds.* **1992**, *181*, 135.
35. Radousky, H. B. *J. Mater.Res.* **1992**, *7*, 1917.
36. Genossar, J.; Kuper, C. G. *Proc. Conf. of The Kenya Association of Physicists. Nairobi*, **1992**.
37. Hilscher, G.; Holland-Moritz, E.; Holubar, T.; Jostarndt, H.-D.; Nekvasil, V.; Schaudy, G.; Walter, U.; Fillion, G. *Phys. Rev. B* **1994**, *49*, 535.
38. Moolenaar, A. A.; Gubbens, P. C. M.; van Loef, J. J.; Menken, M. J. V.; Menovsky, A. A. *Physica C* **1996**, *267*, 279.
39. Homonnay, Z.; Klencsar, Z.; Chechersky, V.; Vanko, Gy.; Gal, M.; Kuzmann, E.; Vertes, A.; Tyagi, S.; Greene, R. L.; Nath, A. *unpublished work*
40. Fehrenbacher, R.; Rice, T. M. *Phys. Rev. Lett.* **1993**, *70*, 3471.
41. Merz, M.; Nücker, N.; Pellegrin, E.; Schweiss, P.; Schuppler, S.; Kielwein, M.; Knupfer, M.; Golden, M. S.; Fink, J.; Chen, C. T.; Chakarian, V.; Idzerda, Y. U.; Erb, A. *Phys. Rev. B* **1997**, *55*, 9160.
42. Tokura, Y.; Takagi, H.; Uchida, S. *Nature* **1989**, *337*, 345.
43. Markert, J. T.; Early, E. A.; Bjornholm, T.; Ghamaty, S.; Lee, B. W.; Neumeier, J. J.; Price, R. D.; Seaman, C. L.; Maple, M. B. *Physica C* **1989**, *158*, 178.
44. Markert, J. T.; Maple, M. B. *Solid State Commun.* **1989**, *70*, 145.

45. Early, E. A.; Ayoub, N. Y.; Beille, J.; Markert, J. T.; Maple, M. B. *Physica C* **1989**, *160*, 320.
46. James, A. C. W. P.; Zahurak, S. M.; Murphy, D. W. *Nature* **1989**, *338*, 240.
47. Felner, I.; Yaron, U.; Yeshurun, Y.; Yacoby, E. R.; Wolfus, Y. *Phys. Rev. B* **1989**, *40*, 11366.
48. Ayoub, N. Y.; Almasan, C. C.; Early, E. A.; Markert, J. T.; Seaman, C. L.; Maple, M. B. *Physica C* **1990**, *170*, 211.
49. Almasan, C. C.; Maple, M. B. *Chemistry of High Temperature Superconductors*; ed. by Rao, C. N. R. World Scientific, Singapore, 1991, p205.
50. James, A. C. W. P.; Murphy, D. W. *Chemistry of Superconductor Materials*, ed. by Vanderah; T. A.; Noyes, N. J., 1991, p427
51. Aharony, A.; Birgeneau, R. J.; Coniglio, A.; Kastner, M. A.; Stanley, H. E. *Phys. Rev. Lett.* **1988** *60*, 1330.
52. Luke, G. M. et al. *Nature* **1989**, *338*, 49; Luke, G. M. et al. *Phys. Rev. B* **1990**, *42*, 7981.
53. Oguchi, T.; Obokata, T. *J. Phys. Soc. Jap.* **1969** *27*, 1111.
54. Izumi, F.; Matsui, Y.; Takagi, H.; Uchida, S.; Tokura, Y.; Asano, H. *Physica C* **1989**, *158*, 433.
55. Kwei, G. H.; Cheong, S-W.; Fisk, Z.; Garson, F. H.; Goldstone, J. A.; Thompson, J. D. *Phys. Rev. B* **1989**, *40*, 9370.
56. Tarascon, J. M.; Wang, E.; Greene, L. H.; Ramesh, R.; Bagley, B. G.; Hull, G. W.; Miceli, P. F.; Wang, Z. Z.; Brawner, D.; Ong, N. P. *Physica C* **1989**, *162-164*, 285.
57. Moran, E.; Nazzal, A. I.; Huang, T. C.; Torrance, J. B. *Physica C* **1989**, *160*, 30.
58. Takayama-Muromachi, E.; Izumi, F.; Uchida, Y.; Kato, K.; Asano, H. *Physica C* **1989**, *159*, 634.
59. Markert, J. T.; Ayoub, N. Y.; Bjornholm, T.; Early, E. A.; Seaman, C. L.; Tsai, P. K.; Maple, M. B. *Physica C* **1989**, *162-164*, 957.
60. Klamut, P. W. *J. Alloys Compds.* **1993**, *19*, L5.
61. Marin, C.; Henry, J. Y.; Boucherle, J. X. *Solid State Commun.* **1993** *86*, 425.
62. Radaelli, P. G.; Jorgensen, J. D.; Schultz, A. J.; Peng, J. L.; Greene, R. L. *Phys. Rev. B* **1994**, *49*, 15322.
63. Brinkmann, M.; Rex, T.; Bach, H.; Westerholt, K. *J. Cryst. Growth* **1996**, *163*, 369.
64. Huang, Q.; Santoro, A.; Grigereit, T. E.; Lynn, J. W.; Cava, R. J.; Krajewski, J. J.; Peck, W. F. Jr. *Phys. Rev. B* **1995**, *51*, 3701 ; Grigereit, T. E.; Lynn, J. W.; Cava, R. J.; Krajewski, J. J.; Peck, W. F. Jr. *Physica C* **1995**, *248*, 382.
65. Cho, B. K.; Harmon, B. N.; Johnston, D. C.; Canfield, P. C. *Phys. Rev. B* **1996**, *53*, 2217.
66. Lynn, J.W.; Huang, Q.; Santoro, A.; Cava, R. J.; Krajewski, J. J.; Peck, W. F., Jr. *Phys. Rev. B* **1996**, *53*, 802.
67. Le, L.P.; Heffner, R. H.; Thompson, J. D.; MacLaughlin, D. E.; Nieuwenhuys, G. L.; Amoto, A.; Feyerherm, R.; Gygax, F. N.; Schenck, A.; Canfield, P. C.; Cho, B. K. *Phys. Rev. B* **1996**, *53*, R510.
68. Lynn, J. W.; Huang, Q.; Sinha, S. K.; Hossain, Z.; Gupta, L. C.; Nagarajan, R.; Godart, C. *Phys. Rev. B* **1997**, *55*, 6584.
69. Schmidt, H.; Weber, M.; Braun, H. F. *Physica C* **1995**, *246*, 177 ; *Physica C* **1996**, *256*, 393.
70. Chechersky, V.; Nath, A.; Cava, R.J.; *Physica C* **1998**, *in press*.

Using Imaging Raman Microscopy to Explore Phase Evolution in Composite Ceramic Superconductors

V. A. Maroni¹, A. K. Fischer¹, and K. T. Wu²

¹Chemical Technology Division, Argonne National Laboratory, 9700 South Cass Avenue, Argonne, IL 60439-4837

²State University of New York, Old Westbury Campus, Old Westbury, NY 11568

Raman microspectroscopy and imaging Raman microscopy have proven to be powerful tools for studying the evolution and spatial distribution of chemical phases in the bismuth-based (BSCCO) and thallium-based (TBCCO) families of high-critical-temperature (high-Tc) superconducting ceramics. These techniques have been applied to compressed/sintered powders and silver-clad composite conductors in conjunction with scanning electron microscopy and energy dispersive x-ray spectroscopy. Many important insights have been gained about the identity, size, shape, orientation, and spatial distribution of the various nonsuperconducting secondary phases (NSPs) that form and dissipate during heat treatment of the BSCCO and TBCCO silver-clad composite tapes. The results have allowed us to determine key mechanistic features that influence the formation of the superconducting phases as heat treatment progresses, including the location of lead-rich NSPs and the identification of the constituent phases in certain NSP agglomerations that tend to resist dissipation as high-Tc phase formation proceeds to completion.

The field of high-critical-temperature (high-Tc) superconductivity is maturing at a steady pace (1-3). In the area of systems for electric power applications, the bismuth-based ceramic superconductors prepared in the form of a silver-sheathed composite have been the conductor of choice for practically all applications attempted to date (1,2). The specific composite conductors in the bismuth family that are used in these applications are $(\text{Bi,Pb})_2\text{Sr}_2\text{Ca}_2\text{Cu}_3\text{O}_y$ (Bi-2223) and $\text{Bi}_2\text{Sr}_2\text{Ca}_1\text{Cu}_2\text{O}_z$ (Bi-2212). In addition to these two materials, composite wires containing lead-, bismuth-, and strontium-doped versions of $\text{Tl}_1\text{Ba}_2\text{Ca}_2\text{Cu}_3\text{O}_x$ (Tl-1223) have also exhibited some promise, particularly for high magnetic field applications (2,4). Progress in the development of the metal-clad composite conductor in monofilament and multifilament form has been greatly aided by detailed study of the influence of processing parameters (like oxygen pressure, temperature, and heat treatment time) on phase chemistry and microstructure. In our studies of the processing and properties of high-Tc composites, we have found Raman microspectroscopy and imaging Raman

microscopy to be well suited for the unequivocal identification of most of the important phases that influence conductor performance, as well as for the interrogation of spatial distributions and orientations of troublesome nonsuperconducting phases (5-8). In this contribution we report some recent results for both Ag/Bi-2223 and Ag/Tl-1223 composites that illustrate the utility of the two Raman techniques for such measurements.

Specimen Preparation and Measurement Methods

The procedures used to fabricate and heat treat the Ag/BSCCO and Ag/TBCCO composite conductor specimens investigated in this study have been described in previous publications (6,9-11). The methodology we employ to examine such specimens by Raman microscopy has been covered in detail in two references (5,6) and will be only briefly summarized here. Raman microprobe spectra and Raman spatial images were recorded using a Renishaw System 2000 Raman Imaging Microscope. The excitation source was a 25 mW He-Ne laser (632 nm). The instrument was operated in the grating mode to obtain microprobe spectra and in the filter mode to collect Raman images. To assure that all samples were presented to the laser in a smooth-surface form, each silver-sheathed wire sample was mounted in epoxy, polished until the ceramic core was exposed, washed with toluene, and dried under vacuum prior to examination. Raman imaging studies were conducted by a four step procedure that consisted of obtaining a 40 μm by 40 μm white light image of the region of interest, recording a defocused Raman spectrum within the region of interest (a circular area typically 20 to 30 μm in diameter), collecting a Raman image at each peak frequency and at adjacent background frequencies in the defocused spectrum, and lastly obtaining a spot-focused Raman spectrum in the heart of each phase region revealed by the Raman image. In most cases, the spot-focused spectrum provided an unequivocal identification of the respective phase.

Results and Discussion

The results presented in this paper were chosen to illustrate how Raman microspectroscopy (RMS) and imaging Raman microscopy (IRM) can be used to gain important insights concerning the phase chemistry of silver-sheathed high- T_c composites. In one example, we examine how Tl-Bi-Pb stoichiometry influences phase development in a series of Tl-1223 wires prepared by the oxide-powder-in-tube (OPIT) process. In a second example, we identify a closely spaced array of phases at the silver/BSCCO interface in an Ag/Bi-2223 filament prepared by the wire-in-tube (WIT) method. In a third example, we show how chemically stable multiphase interfaces can cause second phase congestion in OPIT-type Bi-2223 composites

An Investigation of Ag/Tl-1223 Composites with Tl+Bi+Pb=1.1. In a published study employing magnetization and x-ray diffraction methods, Lanagan and coworkers (9) reported some observations concerning the influence of bismuth substitution on liquid formation in heavily-strontium-doped Ag/Tl-1223 composite conductors. An extension of this study that included samples doped with both bismuth and lead

produced an interesting series of samples, which we have investigated by RMS and IRM. For this particular series of samples the ceramic powder stoichiometry was $Tl_aBi_bPb_cBa_{0.4}Sr_{1.6}Ca_{2.0}Cu_{3.0}O_x$, where $a+b+c$ was kept at a value of 1.1. Three composite wires with varied thallium and bismuth contents and two wires with varied thallium, bismuth, and lead contents were heat treated at 840°C for 20 hours in 0.08 atm O_2 . Specimens from all five wires were mounted in epoxy, polished, and examined by the two Raman microscopy techniques to determine phase contents. The remaining segments of the five wires were subjected to a second heat treatment at 870°C for 0.2 hours in 0.08 atm O_2 , and they too were examined by Raman microscopy. The compositions and liquidus onset temperatures (“mp” as determined by differential thermal analysis) for each of the five Ag/Tl-1223 composites are listed in Table I.

Table I. Summary of RMS Results for $(Tl,Bi,Pb)_{1.1}Ba_{0.4}Sr_{1.6}Ca_{2.0}Cu_{3.0}O_x$

Tl/Bi/Pb (mp)	Heat Treatment I (840°C)	Heat Treatment II (870°C)
0.9/0.2/0.0 (863°C)	Tl-1223, Sr-2/1, Ca-2/1, 14/24, Y	Tl-1223, Sr-2/1, Ca-2/1 (minor 14/24, Y, and CuO)
0.7/0.4/0.0 (865°C)	Tl-1223, Sr-2/1, Ca-2/1, 14/24, Y (minor CuO and Z)	Tl-1223, Sr-2/1, Ca-2/1, 14/24, (minor CuO and Z)
0.5/0.6/0.0 (849°C)	Tl-1223, 14/24, Y (minor Ca-2/1)	Tl-1223, Ca-2/1, 14/24, Y (minor CuO)
0.5/0.3/0.3 (847°C)	Tl-1223 (minor Sr-2/1 and Ca-2/1)	Tl-1223, Ca-2/1, 14/24 (minor CuO, Y)
0.3/0.4/0.4 (831°C)	Tl-1223 (minor Ca-2/1)	Tl-1223, Ca-2/1, 14/24

The two heat treatment temperatures, 840 and 870°C, were chosen to be slightly below and slightly above the range of liquidus onset temperatures for the five wires, with recognition that the liquidus onset temperature for the 0.3/0.4/0.4 wire is an exception. Raman spectra of the six phases that were repeatedly observed in the five wires after heat treatments I and II are shown in Fig. 1. The three spectra on the right are known from our prior work (5,6) to be those of calcium-rich $(Ca,Sr)_2CuO_3$ (Ca-2/1), strontium-rich $(Ca,Sr)_2CuO_3$ (Sr-2/1), and $(Ca,Sr)_{14}Cu_{24}O_{41}$ (14/24). The three on the left are those of Tl-1223 (12); a phase we will refer to as the “Y” phase, which contains many of the features found in Raman spectra of monoclinic forms of $BaBiO_3$ and metal-substituted versions thereof (13,14); and an as yet unidentified phase (or collection of phases) observed in minor amounts in two specimens, which we call the “Z” phase. A compilation of the phases we found with regularity in each of the five Ag/Tl-1223 composites after the first and second heat treatments is included in Table I.

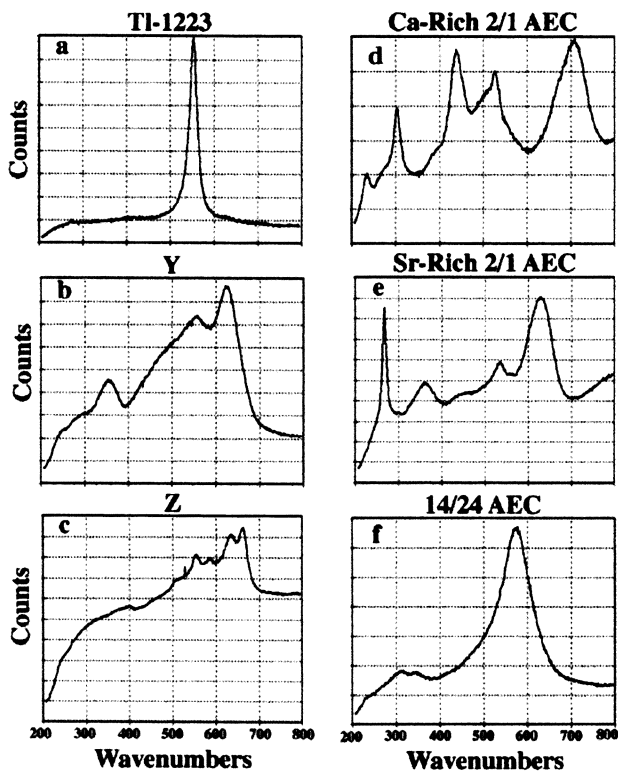


Figure 1. Spot-focused Raman spectra of six phases seen repeatedly in bismuth- and bismuth+lead-doped Ag/Tl-1223 samples after heat treatment at 840 and 870°C in 0.08 atm O₂.

The results in Table I suggest several possible links between Tl/Bi/Pb stoichiometry and phase chemistry and between heat treatment temperature and second phase content. Increasing bismuth (decreasing thallium) in the absence of lead caused an increase in the BaBiO₃-like Y phase and a decrease in the Sr-2/1 phase. The introduction of lead seemed to cause a decrease in the Y and Sr-2/1 phases and a general decrease in the overall second phase content. CuO, although always present in minor amounts, was more prevalent in the samples subjected to the higher heat treatment temperature, i.e., samples that very likely experienced at least partial melting.

Many of the nonsuperconducting second phases observed in this particular series of Tl-1223 wires were 10 μm or larger, and as such they appeared to disrupt the connectivity of the superconducting grains. An example of this is shown in Fig. 2, where we have collected Raman images of a large Ca-2/1 crystallite and adjacent patches of Tl-1223. The defocused Raman spectrum in the upper left of Fig. 2 was obtained from the circled area in the white light image. Bands A, B, C, and E belong to the Ca-2/1 phase (5,6). Background-corrected Raman images of band B (B/B2 in Fig. 2) and band E (E/B5 in Fig. 2) highlight the location of the Ca-2/1 phase. (Bands A and C give images that are similar to B/B2 and E/B5.) Band D in the defocused spectrum belongs to Tl-1223, and its background-corrected Raman image is shown as D/B4 in Fig. 2. The Raman images in Fig. 2 show how the large Ca-2/1 crystallite intrudes on the connectivity of two grains of Tl-1223. Large nonsuperconducting second phase particles are a persistent problem in silver-sheathed composite conductors that is being addressed at many levels in the high-T_c community.

Phase Assemblages in a Fully Processed Ag/Bi-2223 WIT Composite. WIT-type composites are prepared by positioning a thick silver wire along the centerline of a silver billet, packing Bi-2223 precursor powder around the thick wire so that it fills the inside of the billet, capping the billet and drawing it into a fine wire, rolling the wire into a flat filament, and heat treating the filament to form the Bi-2223 phase as described by Lelovic et al. (10). This approach produces a concentric silver/ceramic/silver laminate in which the ceramic ring is only a few microns thick in some places. The impetus for such an embodiment is the mounting evidence that most of the supercurrent in an Ag/Bi-2223 composite wire is carried by a thin well-textured layer of Bi-2223 next to the silver sheath (1,3). According to at least one group of investigators (10), Ag/Bi-2223 composite conductors prepared by the WIT technique exhibit critical current densities that are among the highest reported for BSCCO-based wires at 77 K. The particular specimen reported on in this paper had Bi_{1.8}Pb_{0.35}Sr_{2.0}Ca_{2.0}Cu_{3.0}O_y stoichiometry, was heat treated for 250 hours at 840°C in 0.08 atm O₂ with intermediate pressing after the first 50 hours and the second 100 hours, and was slow cooled at the end of the final 100-hour heat treatment (10°C/hour to 700°C, then 60°C/hour to room temperature). We used Raman microspectroscopy to identify phases near the ceramic/silver interfaces and in regions of the ceramic that were farthest from the silver surfaces.

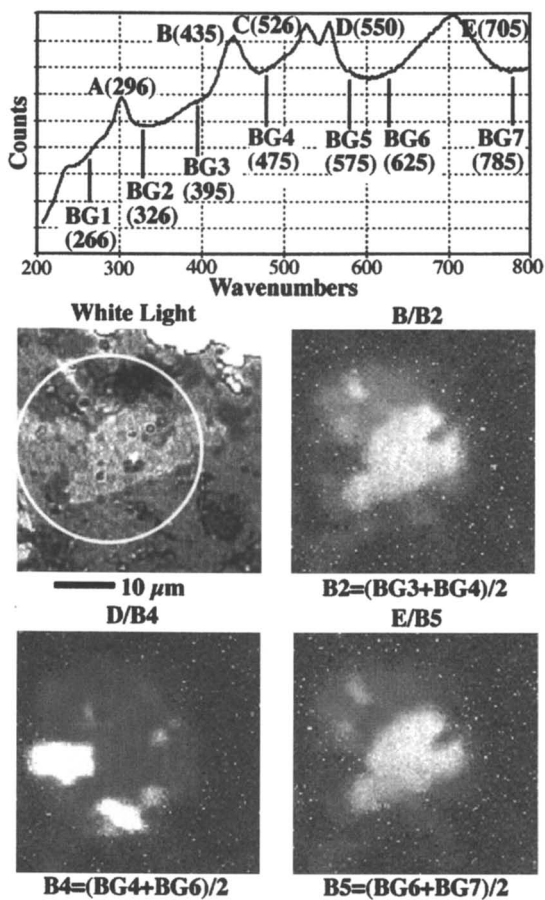


Figure 2. Imaging Raman microscopy analysis of a large calcium-rich 2/1 alkaline earth cuprate crystallite in a bismuth-doped Ag/Tl-1223 specimen heat treated at 870°C in 0.08 atm O₂. (See text for details.)

The white light image in Fig. 3 shows the longitudinal view of a segment of ceramic core running between the silver sheath and the central silver wire (at this point flattened by the rolling process to a narrow elliptical ribbon shape). This particular segment is in the flattened mid-part of the wire where the ceramic layer is the thinnest. Raman spectra taken with the laser spot-focused to 1 to 2 μm diameter reveal a phase mix in this thinned region that consists mostly of Bi-2223/Bi-2212 (each with a band at ca. 625 cm^{-1}), copper oxide (bands at 300 and 350 cm^{-1}), and $(\text{Bi,Pb})_3\text{Sr}_2\text{Ca}_2\text{Cu}_1\text{O}_w$ (also known as the 3221 phase with bands at ca. 620, 555, and 395 cm^{-1}). The indicated band assignments were guided by our prior studies of well characterized standards (5,6).

In transverse views of this same WIT composite, there are regions of the ceramic material in the corners of the filament near the ends of the flattened center wire that are more than 10 μm from any silver surfaces. The white light image of one such region is shown in Fig. 4 together with a defocused Raman spectrum of the circled area in the white light image. Background-corrected Raman images of bands A and B in the defocused spectrum are shown in the middle of Fig. 4. Spot-focused spectra taken in the heart of the band A and band B image emanations (spots X and Y in the white light image) reveal the presence of the Ca-rich 2/1 alkaline earth cuprate and Bi-2223/Bi-2212, respectively. The key finding from the results in Figs. 3 and 4 is that the second phase compositions in regions near to and distant from the silver are different. The 3221 phase, which has been linked to higher critical currents and enhanced flux pinning in Ag/Bi-2223 composites and which is known (15) to be more prevalent in slow-cooled specimens, as is the case for the subject WIT sample, is readily detected in regions of the ceramic that are in close proximity to the silver, but is not detected in ceramic material ten or more microns away from any silver surfaces. This is the first evidence we have uncovered to suggest that 3221 formation may be connected with proximity to silver.

Second Phase Congestion in OPIT-Type Ag/Bi-2223. One of the most informative uses of IRM in our work has occurred during our efforts to elucidate the influences of lead on the formation and stabilization of the Bi-2223 phase in Ag/Bi-2223 composite conductors. One important finding has been that two common second phases in such composites, copper oxide and alkaline earth plumbate, tend to appear in close proximity to one another, and the principal conclusion we have drawn from this observation is that they do not react with one another under the heat treatment conditions normally used to process Ag/Bi-2223 wires. An example of the type of data that support this conclusion is given in Fig. 5.

The defocused Raman spectrum in Fig. 5 (upper right) was obtained from the circled area in the white light image (upper left). From our prior work (5,6) we can preliminarily identify Raman bands A, B, and C in the defocused spectrum as being associated with copper oxide, alkaline earth plumbate, and Bi-2223/Bi-2212. Raman images of each of these bands (shown in the middle of Fig. 5) reveal the locations within the interrogated region (circled area in the white light image) from whence each band is emanating. The intensity of band A relative to its local average background

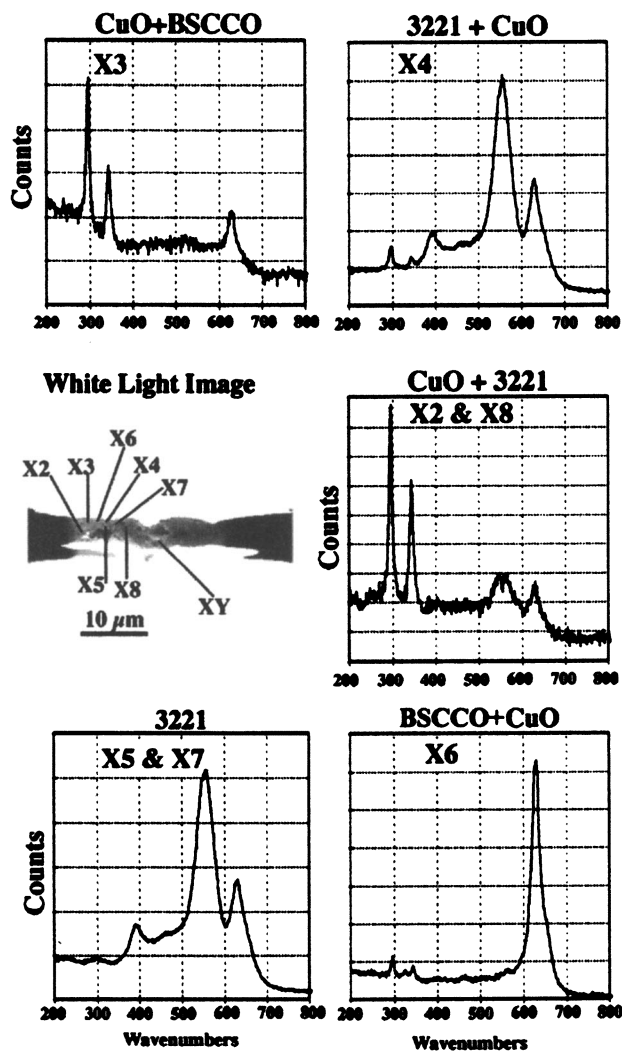


Figure 3. Spot-focused Raman spectra in the vicinity of the ceramic/silver interface in a fully processed wire-in-tube type Bi-2223 composite conductor, showing the occurrence and spatial distribution of CuO, 3221, and Bi-2212/Bi-2223.

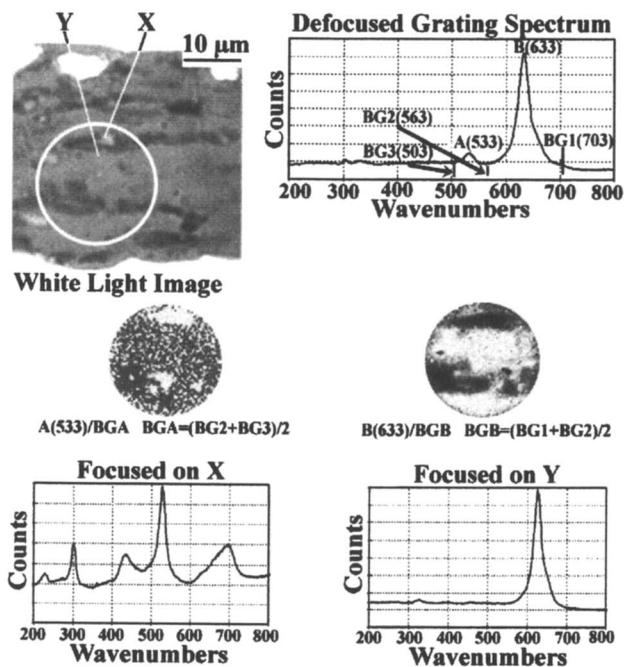


Figure 4. Imaging Raman microscopy analysis of an interior region of the ceramic core in the same full-processed Ag/Bi2223 composite under study in Figure 3. Here, the coexisting phases are the calcium-rich 2/1 alkaline earth cuprate and Bi-2212/Bi-2223. (See text for details.)

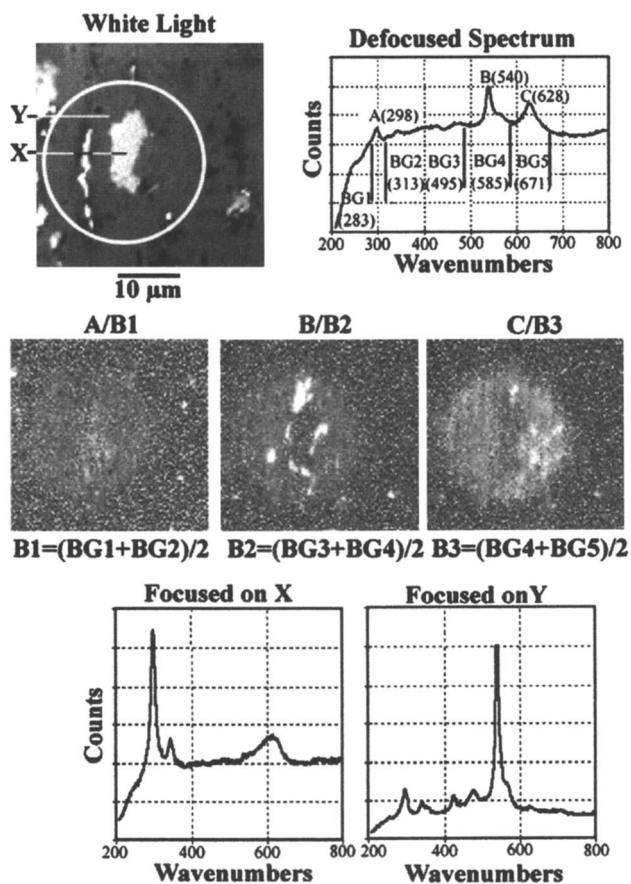


Figure 5. Imaging Raman microscopy analysis of a region of $\text{CuO} + \text{Ca}_2\text{PbO}_4$ congestion in an Ag/Bi-2223 monofilamentary composite conductor. (See text for details.)

(B1) in the defocused spectrum is at the limit of values that allow meaningful imaging, but the band A scattering appears to be coming primarily from the large crystallite in the center of the white light image. We know from energy dispersive x-ray analysis done in a scanning electron microscope that the only metallic element present in this crystallite is copper. The spot-focused Raman spectrum of location "X" in the white light image (lower left in Fig. 5) confirms the presence of copper oxide as the dominant phase, especially considering that we have found copper oxide to be a relatively poor Raman scatterer in the many BSCCO specimens we have examined.

It is also apparent in the B/B2 Raman image in Fig. 5 that the regions of the interrogated area producing band B scattering surround the copper oxide crystallite. The spot-focused Raman spectrum of location Y in the white light image, which is in the heart of the imaged band B emanation, is unequivocally that of Ca_2PbO_4 (5,6). This type of CuO/plumbate congestion is observed with regularity in fully processed versions of slow-cooled and/or lead-rich Ag/Bi-2223 composites, and has given Ag/Bi-2223 wire manufacturers cause to consider modification of stoichiometry and powder preparation specifications to eliminate this congestion problem. Notice also that one can locate the adjacent Bi-2223/Bi-2212 regions by imaging band C in the defocused Raman spectrum of Fig. 5. Image C/B3 shows how the CuO/plumbate congestion could be acting to terminate the superconducting phase grain growth.

Acknowledgments

The authors are grateful to S.E. Dorris and M.T. Lanagan of the Argonne National Laboratory Energy Technology Division for providing the fully processed Tl-1223, WIT, and Ag/Bi-2223 composite wire specimens employed in this research. The work was sponsored by the U.S. Department of Energy, Energy Efficiency and Renewable Energy, as part of a DOE program to develop electric power technology, under Contract W-31-109-Eng-38.

References

1. Balachandran, U.; Iyer, A. N. *Mat. Tech.* **1996**, *11(4)*, 145.
2. Hawsey, R.; Daley, J. *JOM* **1995**, *47*, 56.
3. Batlogg, J. B.; Buhrman, R.; Clem, J. R.; Gubser, D.; Larbalestier, D.; Liebenberg, D.; Rowell, J.; Schwall, R.; Shaw, D. T.; Sleight, A. W. *J. Supercond.* **1997**, *10(6)*, 583.
4. Selvamanickam, V.; Finkle, T.; Pfaffenbach, K.; Haldar, P.; Peterson, E. J.; Salazar, K. V.; Roth, E. P.; Tkaczyk, J. E. *Physica C* **1996**, *260*, 313.
5. Maroni, V. A.; Fischer, A. K.; Wu, K. T. *Spectroscopy* **1997**, *12(7)*, 38.
6. Wu, K. T.; Fischer, A. K.; Maroni, V. A.; Rupich, M. W. *J. Mater. Res.* **1997**, *12(5)*, 1195.
7. Holesinger, T. G.; Bingert, J. F.; Willis, J. O.; Maroni, V. A.; Fischer, A. K.; Wu, K. T. *J. Mater. Res.* **1997**, *12(11)*, 3046.
8. Luo, J. S.; Merchant, N.; Maroni, V. A.; Hash, M.; Rupich, M. In *High Temperature Superconductors: Synthesis, Processing, and Large Scale*

- Applications*; Balachandran, U.; McGinn, P. J.; Abell, J. S., Eds.; 1996 TMS Annual Meeting Proceedings Volume; The Minerals, Metals, and Materials Society: Warrendale, PA, 1996; pp 33-42.
9. Lanagan, M. T.; Hu, J.; Foley, M.; Kostic, P.; Hagen, M. R.; Miller, D. J.; Goretta, K. C. *Physica C* **1996**, *256*, 387.
 10. Lelovic, M.; Krishnaraj, P.; Eror, N. G.; Iyer, A. N.; Balachandran, U. *Supercond. Sci. Technol.* **1996**, *9*, 201.
 11. Dorris, S. E.; Prorok, B. C.; Lanagan, M. T.; Browning, N. B.; Hagen, M. R.; Parrell, J. A.; Feng, Y.; Umezawa, A. Larbalestier, D. C. *Physica C* **1994**, *223*, 163.
 12. McCarty, K. F.; Morosin, B.; Ginley, D. S.; Boehme, D. R. *Physica C* **1989**, *157*, 135.
 13. McCarty, K. F.; Radousky, H. B.; Hinks, D. G.; Zheng, Y.; Mitchell, A. W.; Folkerts, T.; Shelton, R. N. *Phys. Rev. B* **1989**, *40(4)*, 2662.
 14. Sugai, S.; Uchida, S.; Kitazawa, K.; Tanaka, S.; Katsui, A. *Phys. Rev. Lett.* **1985**, *55*, 426.
 15. Parrell, J. A.; Larbalestier, D. C.; Riley, G. N.; Li, Q.; Parrella, R. D.; Teplitzky, M. *Appl. Phys. Lett.* **1966**, *69(19)*, 2915.

Structural Characteristics of Self-Assembled Monolayers on a High- T_c Superconductor Probed by Reflection–Absorption Infrared Spectroscopy

Jason E. Ritchie¹, Cyndi A. Wells¹, David R. Kanis², and John T. McDevitt^{1,3}

¹Department of Chemistry and Biochemistry, The University of Texas at Austin, Austin, TX 78712

²Department of Chemistry and Physics, Chicago State University, Chicago, IL 60628

Methods have been identified that are capable of forming highly organized monolayers on top of $YBa_2Cu_3O_7$ (YBCO), a high- T_c superconductor. The degree of order of these monolayer systems has been assayed using reflection-absorption infrared spectroscopy (RAIRS). Through these investigations, it is found that octadecylamine forms a well ordered, crystalline-like monolayer on the surface of c-axis oriented YBCO thin films, whereas the same reagent adsorbed onto polycrystalline YBCO pellets yields monolayers with disordered, liquid-like structures. A RAIRS comparison of primary, secondary, and tertiary alkylamine reagents has been completed. This paper discusses the adsorption and characterization of organized monolayers supported on YBCO superconductor surfaces. YBCO is the most complex surface yet to be studied that has been shown to support the growth of ordered adsorbate monolayers.

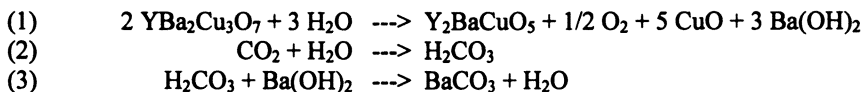
Ever since the discovery of the high temperature superconductors 12 years ago, there has been a tremendous amount of excitement in the scientific and industrial communities in anticipation of the practical utilization of these remarkable materials. Unfortunately, the cuprate compounds possess several degradation pathways including water reactivity, oxygen loss, and oxide ion electromigration. This propensity to degrade has drastically slowed progress in the area of high- T_c research and product development (1-4). The envisioned technological applications and fundamental studies of high- T_c systems depend on a firm understanding of the interfacial properties of these materials. Initial applications using high- T_c materials are beginning to approach the market place, but the true potential

³Corresponding author (mcdevitt@huckel.cm.utexas.edu).

of this area cannot be realized until new processing methods are identified that are capable of controlling the interfacial properties of these reactive cuprate systems (5). Up to this juncture, variations in the local chemical composition of cuprate thin film structures have made it difficult to prepare large arrays of high- T_c junctions suitable for digital applications (6). In spite of the fact that the advantages of high- T_c systems in microelectronics are clearly recognized for superconductor devices relative to conventional semiconductor systems, the high- T_c digital revolution awaits further refinements in the processing of high- T_c systems. Indeed, the identification and optimization of efficient and reproducible processing methods will have a profound influence on the area of high- T_c superconductivity.

Only recently has surface modification chemistry been developed for high- T_c ceramic materials (7). In the other classes of materials (insulators, semiconductors, and metals), spontaneously adsorbed monolayer films have been used to examine fundamental processes involving interfacial electron transfer, adhesion, and surface wetting (8). Furthermore, a variety of interesting practical applications for adsorbed monolayers have been reported in areas such as microcontact printing (9), chemical sensing (10), corrosion protection (11), non-linear optical materials (12), organization of nanoscale particles (13), and high density memory devices (14).

While metal oxide surfaces have been successfully modified previously with alkylsiloxane or alkylcarboxylic acid reagents, the high- T_c superconductors represent a much more complex system than those previously examined. Prior studies have shown that hydrated surfaces can support monolayers. In a number of cases, these hydrated surfaces have been modified with siloxane type reagents. Unfortunately, when exposed to the atmosphere, $YBa_2Cu_3O_7$ rapidly reacts to form non-superconductive corrosion products such as $BaCO_3$, Y_2BaCuO_5 , and CuO (15). Likewise, $YBa_2Cu_3O_7$ is very susceptible to corrosion by water and acids, and so a hydrated surface would only serve to degrade the superconducting material (1,2,16-19).



Reflection-absorption infrared spectroscopy (RAIRS) has been used by many researchers to acquire useful information related to the organization of spontaneously adsorbed monolayers (20-23). The peaks in the carbon-hydrogen stretching region are very diagnostic of the degree of organization of the adsorbed monolayer. Specific frequencies and relative peak intensities of the various carbon-hydrogen vibrations yield useful information regarding the local chemical environment within the SAM layer. In the case of highly ordered, alkylthiol monolayers on gold (111) surfaces, the frequencies observed for d^- (asym. methylene) stretch of 2917 cm^{-1} and d^+ (sym. methylene) stretch of 2850 cm^{-1} agree well with those observed for solid samples of $CH_3(CH_2)_{21}SH$ (20). Molten alkylthiol samples are found to exhibit the analogous methylene stretches at 2924 and 2855 cm^{-1} . These observations suggest that molecules in spontaneously adsorbed alkylthiol monolayers on gold (111) have an

extended linear structure that contains very few *gauche* defects. Interestingly, the intensities of the various methylene and methyl vibrations deviate markedly from those observed for the isotropic samples suggesting a strong organization of the monolayers adsorbed on the surface. From an analysis of the infrared data using the IR transition dipole orientation with respect to the polarization vector of the incident radiation, an estimate for the monolayer tilt angle of $\sim 27^\circ$ has been made. This calculated angle, based on the IR analysis, agrees well with data obtained from other experimental methods such as ellipsometry, He diffraction, and electron diffraction (20,23,24).

In this paper, we describe methods for adsorbing persistent monolayers onto the surface of the high temperature superconductor, $\text{YBa}_2\text{Cu}_3\text{O}_7$ (YBCO). The structural characteristics of these superconductor-localized monolayers are probed using RAIRS. In addition, we report the dependence of the amine substitution pattern and the substrate morphology on the degree of crystallinity of the resulting monolayer. Finally, we explore the thermal stability of these monolayers as well as their suitability for readsorption on heat treated surfaces.

Characterization of Monolayer Order on Smooth YBCO Films

Initially, the infrared evaluation of monolayers on YBCO was complicated by the inherently smaller reflectivities of the YBCO samples. A comparison of the IR reflectivity of YBCO versus gold samples, recorded in the mid-IR, showed important superconductor film thickness and morphology dependencies (Figure 1). At 1600 cm^{-1} , a 1000 \AA YBCO (001) film showed a reflectivity, relative to 2500 \AA gold film, of 41%. A 2500 \AA YBCO (001) film showed a relative reflectivity of 52% to the same thickness of gold under similar circumstances. Under identical conditions, a ceramic pellet of YBCO displayed a relative reflectivity of only 8%. In order to maximize the signal obtained from YBCO samples, it is necessary to maximize the reflectivity and the sample size.

It was known from our prior studies that amine reagents readily adsorb to the surfaces of cuprate superconductors (5,25,26). Likewise, it might be expected that when YBCO surfaces are exposed to hexane solutions of octadecylamine, the amine reagent would spontaneously adsorb to the cuprate surface. Upon examination of the resulting octadecylamine monolayer with the RAIRS method, two peaks are seen in the methylene stretching region (Figure 2) (27). The frequencies of the peaks are 2916 cm^{-1} and 2846 cm^{-1} . In a manner analogous to that described above for the thiol/gold case, these peaks are assigned as the asymmetric and symmetric methylene stretching modes, respectively. Importantly, the frequency of these peaks agrees well with the values for the crystalline monolayers, suggesting that a high degree of conformational order exist within the monolayers on YBCO.

An estimate of the crystallinity of a hydrocarbon monolayer can be made from an examination of the spectral widths of the carbon-hydrogen vibrational modes in conjunction with the peak positions in the RAIR spectra (Table I) (28). Shown in Table I is a compilation of peak positions and full width at half maximum (FWHM) spectral widths for all of the monolayer systems investigated in this report.

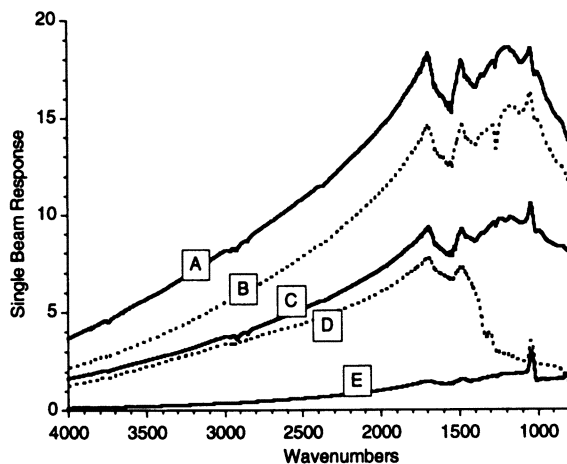


Figure 1. Infrared reflectivities of various substrates examined in this paper. (A) a 2000 Å evaporated gold film on glass, (B) a 100 Å evaporated gold film on glass, (C) a 2500 Å (001) YBCO thin film on MgO, (D) a 1000 Å (001) YBCO thin film on MgO, and (E) a polycrystalline YBCO pellet.

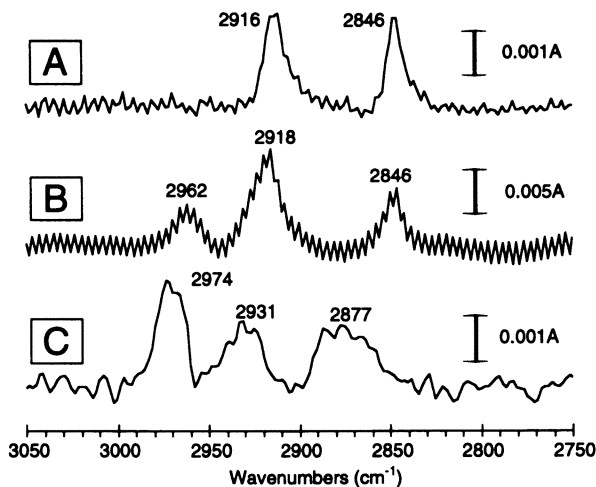


Figure 2. RAIR spectra are shown which were obtained for octadecylamine monolayers supported on various types of YBCO surfaces: (A) a smooth (001) oriented YBCO film prepared by laser ablation, (B) a smooth (100) oriented YBCO film prepared by the same method, and (C) a polycrystalline ceramic pellet of YBCO made by the solid-state method.

Table I: Comparison of the Anti-symmetric Methylene Stretches and Peak Widths for a Variety of Substrates, Monolayers, and Substitution Patterns.

Substrate	Monolayer	Frequency (cm^{-1})	FWHM (cm^{-1})
Gold/Glass	$\text{CH}_3(\text{CH}_2)_{17}\text{SH}$	2918	9
YBCO film (001)	$\text{CH}_3(\text{CH}_2)_{17}\text{NH}_2$	2916	12
YBCO film (001)	$(\text{CH}_3(\text{CH}_2)_7)_2\text{NH}$	2931	14
YBCO film (001)	$(\text{CH}_3(\text{CH}_2)_7)_3\text{N}$	2929	23
YBCO film (100)	$\text{CH}_3(\text{CH}_2)_{17}\text{NH}_2$	2918	20
YBCO pellet	$\text{CH}_3(\text{CH}_2)_{17}\text{NH}_2$	2931	22
YBCO pellet	$(\text{CH}_3(\text{CH}_2)_7)_2\text{NH}$	2929	29
YBCO pellet	$(\text{CH}_3(\text{CH}_2)_7)_3\text{N}$	2933	19
Alumina*	$\text{CH}_3(\text{CH}_2)_{14}\text{COOH}$	2926	34
Neat Solid	$\text{CH}_3(\text{CH}_2)_{17}\text{NH}_2\#$	2917	24
Neat Solid*	$\text{CH}_3(\text{CH}_2)_{14}\text{COOH}\#$	2918	11
Neat Liquid**	$\text{CH}_3(\text{CH}_2)_7\text{SH}\#$	2924	†
Neat Solid**	$\text{CH}_3(\text{CH}_2)_{21}\text{SH}\#$	2918	†

indicates that measurement was made in transmission mode without the use of a substrate

* Adapted from Allara, D.L., et. al., *Langmuir*, 1985, 1, 52-66

** Adapted from Porter, M.D., et. al., *J. Am. Chem. Soc.*, 1987, 109, 3559-3568

† This data was not supplied for these cases

The asymmetric methylene stretch of the superconductor's monolayer has a FWHM of 12 cm^{-1} . Crystalline octadecylthiol monolayers adsorbed to gold (111) surfaces show FWHM of $\sim 10 \text{ cm}^{-1}$, whereas disordered monolayers of hexadecanoic acid adsorbed to Al_2O_3 show FWHM of $\sim 34 \text{ cm}^{-1}$. From these highly reproducible measurements, it can be asserted that octadecylamine monolayers adsorb in a persistent manner onto YBCO methylene vibration of octadecylamine adsorbed to a YBCO (001) oriented thin film (001) films and that such adsorbate layers exhibit a high degree of average chain-conformational order.

The infrared spectrum of octadecylamine on YBCO (001) is very reminiscent of spectra of alkylthiols adsorbed to GaAs (100) (29). Allara and co-workers found that alkylthiols adsorbed on GaAs surfaces exhibit a very large molecular tilt angle of $\sim 57^\circ$ away from surface normal. The similarity of the YBCO and GaAs supported monolayer spectral data suggest a large tilt angle is present also for the cuprate system (*vide infra*).

A RAIR spectrum for octadecylamine adsorbed to a (100), or a-axis, oriented YBCO film is shown in Figure 2B. (Note also that this sample displays periodic features that appear to be present as "background noise." However, more careful analysis of the frequency of such peaks suggests they are caused by an interference phenomenon. Likewise, the frequency dependence of these peaks/troughs corresponds nicely with constructive/destructive wave combinations reflected from exterior and interior surfaces of the high- T_c film. Roughening of the substrate with etching and thermal annealing steps reduces the magnitude of these interference

fringes and can improve the appearance of the spectral features.) These data display similar features seen for the same molecule on (001) oriented YBCO, including the presence of the asymmetric methylene stretch at 2918 cm^{-1} . Interestingly, the in-plane asymmetric methyl stretch is also seen at 2962 cm^{-1} for monolayers on this substrate. This vibrational mode was found to be absent for the monolayer atop (001) YBCO (Figure 2A). The reappearance of the methyl vibration may be caused by a smaller tilt angle in the adsorbate layer fostered by the presence of short Cu-Cu separations for the exposed (100) surface (Figure 3).

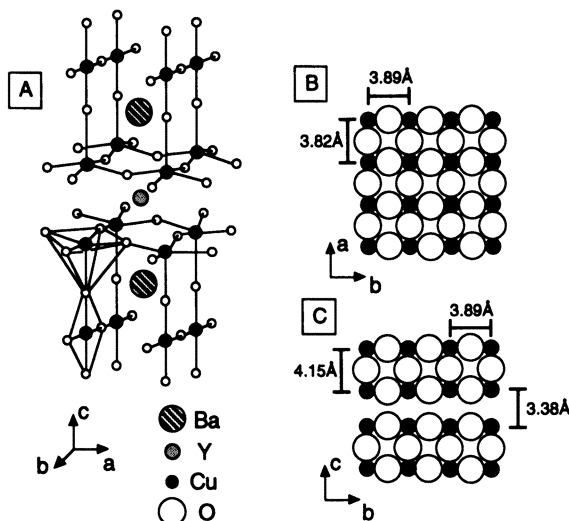


Figure 3. The unit cell of YBCO and the copper containing layers are illustrated. Shown in (A) is the unit cell of YBCO, in (B) the structure of the CuO₂ sheet layer of (001) oriented YBCO, and in (C) the expected copper containing termination for a (100) oriented YBCO sample.

While the asymmetric methylene stretch of octadecylamine adsorbed to YBCO (100) films is observed to be centered at approximately the same place as that obtained for the monolayer on the (001) oriented sample, the spectral width for the YBCO (100) sample is significantly greater than that for the (001) oriented specimen (20 cm^{-1} vs. $8\text{--}12\text{ cm}^{-1}$, see Table I). These observations strongly suggest that the YBCO (100) surface fosters growth of somewhat disordered layers compared to the (001) oriented film samples. The copper-copper distance on the surface of a (100) oriented YBCO film is a constant 3.89 Å in the b-axis, but the same value alternates between 4.15 Å and 3.38 Å along the c-axis (Figure 3). Although the surface copper-copper distances in the a and b lattice directions are nearly the same for (001) oriented YBCO samples, there is a significant difference in the copper-copper spacings for (100) oriented YBCO samples (Figure 3). This difference in spacing

may lead to a decrease in the chemical homogeneity of the resulting monolayer on (100) oriented samples. While the spectral width of the asymmetric methylene stretch of the monolayer atop (100) oriented YBCO is broader than seen in other "ordered" monolayers, the positioning of the peak is good evidence that the monolayer adopts a relatively ordered structure on this substrate. Due to the width of this peak, it is probable that this structure possesses more defects than for the (001) oriented YBCO surface. In addition to the uniformity of the copper-copper adsorbate site spacing issue, it should be noted that sample roughness appears to play an important role in dictating monolayer ordering characteristics (*vide infra*).

Molecular mechanics energy calculations predict a molecular tilt angle (θ_m) value of $\sim 29^\circ$ for alkylthiol on gold (111), in good agreement with experimental data (27). Likewise, a value of $\sim 53^\circ$ has been predicted for θ_m of alkylamine monolayers on YBCO (001) (27). Using this tilt angle, the orientation of the vibrational dipoles has been analyzed. The symmetric methyl vibrational dipole and its angle with respect to the surface normal is shown in Figure 4. Note that only vibrations that have a dipole with a significant component perpendicular to the surface are expected to effectively couple to the infrared radiation. Because of the molecular tilt angle, only $\sim 24\%$ of the total methyl dipole for even numbered carbon chain molecules lies along the surface normal. Thus, these methyl modes are not expected to have a significant signal in the RAIR spectra.

Molecular Ordering Characteristics for Polycrystalline Surfaces

When exposed to octadecylamine, polycrystalline ceramic samples of YBCO are found to support the adsorption of monolayers as shown in Figure 2C. While primary amines form ordered monolayers on (100) and (001) oriented films of YBCO, the same molecule adsorbed on ceramic surfaces is found to exhibit highly disordered assemblies. This lack of crystallinity is evidenced by the asymmetric methylene stretching frequency of 2931 cm^{-1} as well the peak width of 22 cm^{-1} (Table I).

In addition to their polycrystalline nature, ceramic pellet forms of YBCO also possesses enhanced roughness relative to their film counter parts. The roughness issue was explored by Atomic Force Microscopy (AFM). Dramatic differences in the root mean square (RMS) roughness values are noted for evaporated gold on glass (4.4 nm), a (001) oriented YBCO thin film (17 nm), a (100) oriented YBCO thin film (31 nm), and a particularly smooth polycrystalline YBCO pellet (290 nm). AFM images of both YBCO film orientations and an evaporated gold substrate supported on glass are shown in Figure 5. In addition, a typical profilometer trace of a YBCO ceramic pellet is included. The two different YBCO film orientations are of comparable roughness, whereas the gold film is significantly smoother and the ceramic pellet is significantly rougher.

While X-ray diffraction experiments showed that gold evaporated onto glass substrates exhibited nearly exclusive (111) orientation (estimated $>99\%$ aligned), gold that is evaporated onto a rough YBCO ceramic samples adopts rough morphological characteristics and yields polycrystalline orientations. Using this roughened gold as a substrate for monolayer adsorption allows the dependence of the substrate roughness to be studied for the well characterized adsorbate system.

Accordingly, octadecylthiol adsorbed to this roughened gold system shows the typical signature of a disordered monolayer, that is, the asymmetric methylene stretch appears at 2927 cm^{-1} with a spectral width of 33 cm^{-1} (27). These results demonstrate, in a convincing manner, that there is a strong dependence of the surface morphology (surface roughness and crystallographic orientation) on the monolayer ordering characteristics.

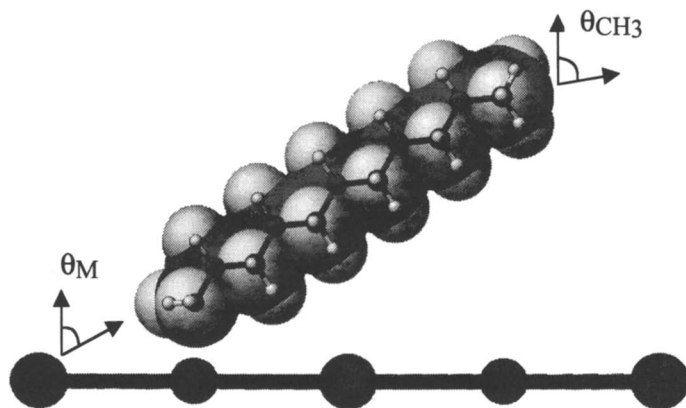


Figure 4. The orientation of the CH_3 (sym) infrared transition dipoles for an extended decyl amine molecule adsorbed atop YBCO is shown. Also shown is the orientation of the molecular tilt axis.

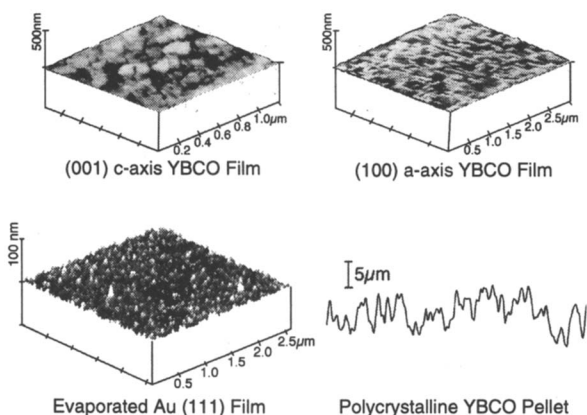


Figure 5. AFM images and a profilometry trace for the four substrates are shown. Included are (A) a typical evaporated gold film on glass, (B) a (001) oriented YBCO film, (C) a (100) oriented YBCO film, and (D) a profilometer trace of a polycrystalline YBCO pellet. For the last case, the profilometry trace length was $2000\text{ }\mu\text{m}$. The large height range for the YBCO pellet prevented an AFM measurement on this surface.

Alkylamine Substitution Pattern Dependence on Monolayer Order

Generally, amines offer the capability of being substituted with different alkyl groups allowing for studies involving the substitution pattern dependence of monolayer ordering characteristics. As will be shown here, the substitution pattern of the monolayer reagent plays a vital role in the crystallinity of the resulting monolayer. While, mono-thiol based reagents can accommodate only one alkyl substituent on the sulfur head group, amines can possess up to three alkyl substituents and retain their ability to adsorb to superconductors (*vide infra*).

Using the RAIRS technique, the adsorption of primary (octadecylamine), secondary (dioctylamine), and tertiary amines (trioctylamine) have all been observed to adsorb spontaneously to YBCO. Quite interestingly, the RAIRS measurement shows that the secondary and tertiary amines do not form crystalline monolayers on YBCO (001) films or pellets (Table I) as do the above described primary amines. Rather, the RAIRS data obtained for these samples are very similar to the primary amine reagents adsorbed on rough substrates. Shown in Figure 6 is a comparison of trioctylamine, dioctylamine, and octadecylamine adsorbed in each case to YBCO (001) oriented thin films. Spectra of these same three amine reagents were taken on rough YBCO ceramic samples (not shown). The results of such studies are summarized in Table I.

It is apparent from the peak position and peak width measurements, that the secondary and tertiary amines form disordered monolayers when adsorbed to both rough and smooth YBCO substrates. This behavior indicates that the crystallinity of the resulting monolayer is strongly dependent on the substitution pattern of the amine monolayer reagent.

Thermal Stability of Monolayers

The RAIRS method has also been used to follow the thermal desorption of alkylamines from YBCO thin films. After desorption of the alkylamine, the YBCO surface can again be modified with an alkylamine monolayer. Initially, a YBCO film was modified with a monolayer of trioctylamine, which yielded an IR signature consistent with a disordered monolayer (Figure 7A). The modified film was then annealed in flowing oxygen at 550°C for 6 hours and the loss of the alkylamine from the surface was noted by the disappearance of methylene vibrational features (Figure 7B). Immediately after annealing and RAIRS characterization, the film was exposed to a 1 mM solution of octadecylamine to reestablish the monolayer (Figure 7C). From an analysis of the peak positions, it is evident that the non-crystalline trioctylamine monolayer was removed by the annealing procedure and replaced by the crystalline octadecylamine monolayer. In addition, it is clear that the surface of the YBCO after monolayer desorption remains receptive to further monolayer adsorption. Thus, thermal desorption appears to be an effective processing procedure that can be exploited to remove the organic layer after its utility is no longer required.

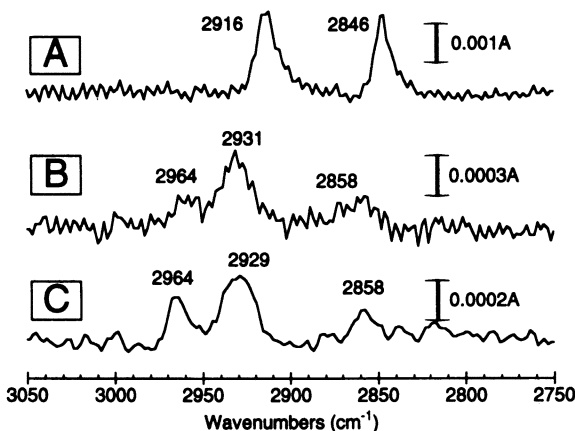


Figure 6. RAIRS data for three different amine reagents adsorbed to YBCO (001) films are provided. Shown here are data for primary, secondary, and tertiary substituted linear alkylamines: (A) octadecylamine, (B) dioctylamine, and (C) trioctylamine. While the dioctylamine and the trioctylamine samples show disordered or liquid like behavior, it is apparent that ordered monolayers are obtained with octadecylamine.

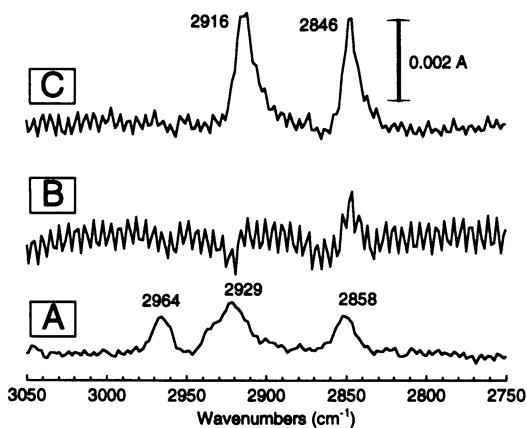


Figure 7. The adsorption and thermal desorption followed by re-adsorption of various amine reagents atop a single YBCO (001) thin film sample are examined by RAIRS measurements. (A) Initially, the high- T_c sample is exposed to trioctylamine resulting in the formation of a disordered monolayer. (B) The same sample is subsequently heated to 550° C in flowing O_2 for 6 hours and shows no infrared signature for adsorbed hydrocarbon. (C) Finally, the same superconductor film specimen is then exposed to octadecylamine and the appearance of an ordered monolayer is observed.

Summary

Infrared methods have been successfully employed in order to evaluate the structural characteristics of YBCO-localized hydrocarbon monolayers. Such measurements have become possible only following the identification of important experimental variables such as superconductor sample thickness, substrate roughness, and monolayer formation procedures. Likewise, a large substrate orientation dependence is noted for this system. Oriented films of YBCO (001) are shown to support crystalline-like monolayers, whereas polycrystalline samples yield disordered adsorbate layers. Furthermore, a substitution pattern dependence for amine reagents is observed. Primary amines form crystalline monolayers, whereas secondary and tertiary amines form disordered monolayers on YBCO (001). Methods for the thermal desorption of the amine reagents from the high- T_c surface have been developed as have strategies for the subsequent readsorption of similar reagents. The reversible adsorption / desorption process noted here suggest that the described "soft chemistry" procedures may be effective for the molecular-level control of superconductor interfacial properties. This behavior may have important implications in the context of developing methods for "chemically benign" processing and packaging high- T_c conductors and devices.

Acknowledgments

JTM and DRK acknowledge the Air Force Office of Scientific Research and the National Science Foundation for support of this work. JTM acknowledges the Office of Naval Research for support of this work. JER acknowledges the support of a University of Texas Continuing Fellowship. DRK acknowledges the Camille and Henry Dreyfus Foundation for support of this work.

Literature Cited

- 1)McDevitt, J. T.; Riley, D. R.; Haupt, S. G. *Anal. Chem.* **1993**, *65*, 535A-545A.
- 2)McDevitt, J. T.; Haupt, S. G.; Jones, C. E. *Electrochemistry of High-T_c Superconductors*; Bard, A. J. and Rubenstein, I., Ed.; Marcel Dekker, 1996; Vol. 19, pp 355-481.
- 3)McDevitt, J. T.; Haupt, S. G.; Clevenger, M. B. *Conductive Polymer / High Temperature Superconductor Assemblies and Devices*; Skotheim, T., Reynolds, J. and Elsenbaumer, R., Ed.; Marcel Dekker: New York, 1996, pp 1029-1058.
- 4)Zhou, J.-P.; Savoy, S. M.; Zhao, J.; Riley, D. R.; Zhu, Y. T.; Manthiram, A.; Lo, R.-K.; Borich, D.; McDevitt, J. T. *J. Am. Chem. Soc.* **1994**, *116*, 9389-9390.
- 5)McDevitt, J. T.; Lo, R.-K.; Zhou, J.; Haupt, S. G.; Zhao, J.; Jurbergs, D. C.; Chen, K.; Mirkin, C. A. *Chem. Mater.* **1996**, *8*, 811-813.
- 6)Zhou, J.; Lo, R.-K.; McDevitt, J. T.; Talvacchio, J.; Forrester, M. G.; Hunt, B. D.; Jia, Q. X.; Reager, D. *J. Mater. Res.* **1997**, *12*, 2958-2975.
- 7)Ulman, A. *An Introduction to Ultrathin Organic Films, From Langmuir-Blodgett to Self-Assembly*; Academic Press: Boston, 1991.

- 8) Bard, A. J.; Abruna, H. D.; Chidsey, C. E. D.; Faulkner, L. R.; Feldberg, S. W.; Itaya, K.; Majda, M.; Melroy, O.; Murray, R. M.; Porter, M. D.; Soriaga, M. D.; White, H. S. *J. Phys. Chem.* **1993**, *97*, 7147-7173.
- 9) Kumar, A.; Whitesides, G. M. *Science* **1994**, *263*, 60-62.
- 10) Dermody, D. L.; Crooks, R. M.; Kim, T. *J. Am. Chem. Soc.* **1996**, *118*, 11912-11917.
- 11) Laibinis, P. E.; Whitesides, G. M. *J. Am. Chem. Soc.* **1992**, *114*, 9022-9028.
- 12) Lin, W.; Lee, T.-L.; Lyman, P. F.; Lee, J.; Bedzyk, M. J.; Marks, T. J. *J. Am. Chem. Soc.* **1997**, *119*, 2205-2211.
- 13) Freeman, R. G.; Grabar, K. C.; Allison, K. J.; Bright, R. M.; Davis, J. A.; Guthrie, A. P.; Hommer, M. B.; Jackson, M. A.; Smith, P. C.; Walter, D. G.; Natan, M. J. *Science* **1995**, *267*, 1629-1632.
- 14) Kawanishi, Y.; Tamaki, T.; Sakuragi, M.; Seki, T.; Suzuki, Y.; Ichimura, K. *Langmuir* **1992**, *8*, 2601.
- 15) Barkatt, A.; Hojaji, H.; Amarakoon, V. R. W.; Fagan, J. G. *MRS Bulletin* **1993**, *18*, 45-52.
- 16) Zhou, J.-P.; Lo, R.-K.; Savoy, S. M.; Arendt, M.; Armstrong, J.; Yang, D.-Y.; Talvacchio, J.; McDevitt, J. T. *Physica C* **1997**, *273*, 223-232.
- 17) Zhou, J.-P.; McDevitt, J. T. *Chem. Mater.* **1992**, *4*, 953-959.
- 18) Riley, D. R.; Jurbergs, D. J.; Zhou, J.-P.; Zhao, J.; Markert, J. T.; McDevitt, J. T. *Solid State Comm.* **1993**, *88*, 431-434.
- 19) Riley, D. R.; McDevitt, J. T. *J. Electroanal. Chem.* **1990**, *295*, 373-384.
- 20) Porter, M. D.; Bright, T. B.; Allara, D. L.; Chidsey, C. E. D. *J. Am. Chem. Soc.* **1987**, *109*, 3559-3568.
- 21) Laibinis, P. E.; Whitesides, G. M.; Allara, D. L.; Tao, Y. T.; Parikh, A. N.; Nuzzo, R. G. *J. Am. Chem. Soc.* **1991**, *113*, 7152-67.
- 22) Allara, D. L.; Nuzzo, R. G. *Langmuir* **1985**, *1*, 52-66.
- 23) Chidsey, C. E. D.; Loiacono, D. N. *Langmuir* **1990**, *6*, 682-691.
- 24) Strong, L.; Whitesides, G. M. *Langmuir* **1988**, *4*, 546-558.
- 25) Chen, K.; Mirkin, C. A.; Lo, R.-K.; Zhao, J.; McDevitt, J. T. *J. Am. Chem. Soc.* **1995**, *117*, 1121-1122.
- 26) Chen, K.; Xu, F.; Mirkin, C. A.; Lo, R.-K.; Nanjundaswamy, K. S.; Zhou, J.-P.; McDevitt, J. T. *Langmuir* **1996**, *12*, 2622-2624.
- 27) Ritchie, J. E.; Wells, C. A.; Zhou, J.-P.; Zhao, J.; McDevitt, J. T.; Ankrum, C. R.; Jean, L.; Kanis, D. R. *J. Am. Chem. Soc.* **1998**, *120*, 2733-2745.
- 28) Byrd, H.; Pike, J. K.; Talham, D. R. *Chem. Mater.* **1993**, *5*, 709-715.
- 29) Sheen, C. W.; Shi, J.-X.; Martensson, J.; Parikh, A. N.; Allara, D. L. *J. Am. Chem. Soc.* **1992**, *114*, 1514-1515.

Raman Scattering from the Superconducting Phase: Electronic Excitations and Phonon Renormalization Effects

V. G. Hadjiev¹, T. Strohm¹, M. Cardona¹, Z. L. Du², Y. Y. Xue²,
and C. W. Chu²

¹Max-Planck-Institut Für Festkörperforschung, Heisenbergstrasse 1,
D-70569 Stuttgart, Germany

²Department of Physics and the Texas Center for Superconductivity,
University of Houston, Houston, TX 77204-5932

The Raman scattering from $(\text{Cu,C})\text{Ba}_2\text{Ca}_3\text{Cu}_4\text{O}_x$ reveals strong superconductivity-related effects. In the Raman spectra of this compound we observed most of the characteristic changes expected in going from the normal to the superconducting state. These are a redistribution of the low frequency electronic excitations, the appearance of a Raman peak due to the scattering via electronic pair breaking, and especially, strong superconductivity-induced phonon self-energy effects. The A_{1g} phonons at 235 cm^{-1} and 360 cm^{-1} , which involve the vibrations of the plane oxygen with some admixture of Ca displacements, exhibit a strong renormalization below T_c . Particularly remarkable is the phonon intensity increase of up to two orders of magnitude when the material becomes superconducting.

Raman spectroscopy is known to be a powerful technique for the characterization and basic studies of high T_c superconductors (HTCS, see, e.g., (1)). The low-energy Raman response of these materials is mainly due to the excitation of electrons occupying states near the Fermi surface (FS) and to the scattering of light by optical phonons which proceeds via electron-phonon interactions. The opening of the superconducting gap results in a redistribution of electronic states and excitations in the immediate vicinity of the FS. This leads to the appearance of an electronic Raman peak below T_c , caused by quasiparticle creation through pair-breaking, and to phonon renormalization by the superconductivity-induced phonon self-energy. Information on the anisotropy of the superconducting order parameter (gap) can be inferred from the electronic peak that develops below T_c (2-4), provided the peak is discernible (5). The asymptotic behavior of this peak for $\omega \rightarrow 0$ also contains symmetry information (3, 4). On the other hand, those phonons that are strongly coupled to electrons

occupying states near the FS can be very sensitive to the opening of the superconducting gap. This results in a change of the phonon renormalization (self-energy) induced by the superconducting transition (6-8). The real part of this self energy represents the contribution of the electron-phonon interaction to the phonon frequency and its imaginary part the contribution to its linewidth. For conventional superconductors this self-energy effect is small and usually gives a change of a few tenths of a wavenumber (9). In HTCS, the phonon self-energy effects below T_c may become sizable ($\sim 10 \text{ cm}^{-1}$) as is well known since the early measurements of $\text{YBa}_2\text{Cu}_3\text{O}_{7.8}$ (10). Coupling of the phonons to the pair breaking excitations leads also to admixture of the corresponding Raman transition amplitudes that results in changes in the phonon intensities when the temperature is lowered below T_c (11,12).

We illustrate here the superconductivity-induced effects in the Raman spectra of HTCS as exemplified by a recent study (13) of $(\text{Cu,C})\text{Ba}_2\text{Ca}_3\text{Cu}_4\text{O}_x$ ((Cu,C)-1234). This compound exhibits a remarkably strong modification of its Raman spectra below T_c (13) similarly to $\text{HgBa}_2\text{Ca}_3\text{Cu}_4\text{O}_x$ (11,12).

Raman scattering from solids (theory)

Electronic Raman scattering efficiency. In a Raman experiment one often measures the scattering intensity I_S , which is given by the energy flux of electromagnetic (light) wave scattered into the solid angle Ω_0 subtended by the spectrometer within a frequency interval $\omega_s + \delta\omega_s$. In cases when a multichannel detector is used, $\delta\omega_s$ is given by the frequency interval dispersed over one or several pixels of the detector. The Raman intensity can also be defined in terms of the number of scattered photons. In this case it is proportional to the scattering cross section $d^2\sigma/d\Omega d\omega_s$ and the generalized dynamic structure factor of the sample $\tilde{S}^T(\mathbf{q}, \omega)$ at a temperature T for a given Raman shift ω and a wavevector transfer \mathbf{q}

$$I_S \propto \frac{d^2\sigma}{d\Omega d\omega_s} = \frac{\omega_s}{\omega_i} r_0^2 \tilde{S}^T(\mathbf{q}, \omega). \quad (1)$$

Here ω_i , ω_s , and $\omega = \omega_i - \omega_s$ are the frequencies of the incident photons, the scattered photons, and the excitations in the solid, respectively, and $r_0 = e^2/mc^2$ is the Thomson radius. The Raman scattering efficiency, given by the scattering cross section determined for a scattering volume equal to unity, $(1/V_{\text{scat}})d^2\sigma/d\Omega d\omega_s$, represents the efficiency per unit pathlength in the sample. Both quantities, the scattering efficiency and the cross section are normalized to the incoming laser flux. When the scattering process is instantaneous, one can define a linear-response function, $\chi_R(\mathbf{q}, t)$, called the Raman susceptibility. The Fourier transform of the Raman susceptibility, $\chi_R(\mathbf{q}, \omega)$, is related to the structure factor $\tilde{S}^T(\mathbf{q}, \omega)$ through the fluctuation-dissipation theorem (2,4):

$$\tilde{S}^T(\mathbf{q}, \omega) = -\frac{\hbar}{\pi} (1 + n_{\omega, T}) \text{Im} \chi_R(\mathbf{q}, \omega), \quad (2)$$

where $n_{\omega,T} = [\exp(\hbar\omega/kT) - 1]^{-1}$ is the Bose-Einstein thermal occupation factor (Stokes scattering is assumed). Thus a Raman response from a given material is related to the imaginary part of the Raman susceptibility of those excitations that take part in the inelastic scattering of light. Theoretical models for the Raman response are usually based on calculations of the Raman susceptibility and related vertices for the scattering processes.

The Raman scattering is a two-photon process. The Hamiltonian of the system (electrons and photons) contains terms that correspond to two types of scattering mechanisms. The “density-like” term, H_{AA} , is quadratic in the vector-potential of the light, $H_{AA} \sim A^2$. It describes non-resonant scattering processes that involve only *intra*band transitions. The second, “current-like”, term H_A , is linear in A , $H_A \sim A \cdot \mathbf{p}$. This term can lead to resonances and it also accounts for virtual *intra*band and *inter*band transitions. In order to describe the Raman scattering amplitude, the H_{AA} has to be treated in first-order and the term H_A in second order perturbation theory. Both terms can be combined in the effective Hamiltonian (2,4):

$$H_{A+A'}^{eff} = r_{gr} \langle A_S^+ A_I \rangle \sum_{n,\mathbf{k}} \gamma_{n,\mathbf{k}}(\mathbf{q}) c_{n,\mathbf{k}+\mathbf{q}}^+ c_{n,\mathbf{k}}, \quad (3)$$

in which the operators A_S^+ and A_I contain the creation operator of the scattered photons and the annihilation operator of the incident photons, respectively. In equation 3, $c_{n,\mathbf{k}+\mathbf{q}}^+$ and $c_{n,\mathbf{k}}$ are the creation and annihilation operators for Bloch electrons in the band n , that is, the sum of their products gives the density of electronic excitations for transitions of electrons from states with a wavevector \mathbf{k} to states with $\mathbf{k} + \mathbf{q}$, where $\mathbf{q} = \mathbf{k}_I - \mathbf{k}_S$ is the wavevector transferred from the light to the sample. The Raman vertex $\gamma_{n,\mathbf{k}}(\mathbf{q})$ is a weighting factor in equation 3. It involves all possible intermediate states and energy denominators and therefore can lead to resonance effects. With some simplifications, which seem to agree with available experimental data, one can apply to the Raman vertex calculations the well known *effective-mass approximation* (see, e.g., (4)). This approximation is valid when (i) the contribution of virtual *intra*band transitions is negligible with respect to that of the *inter*band transition; (ii) the relevant virtual *inter*band transitions have much larger energy than the incoming and scattered photon energies and one can neglect the terms in the denominators of the Raman vertex that contain ω_I and ω_S . In this case the expression for $\gamma_{n,\mathbf{k}}(\mathbf{q})$ becomes identical to that for the inverse effective mass in the $\mathbf{k} \cdot \mathbf{p}$ theory and in the limit $\mathbf{q} \rightarrow 0$, which is relevant for the experiments, we can write:

$$\gamma_{n,\mathbf{k}} = \frac{m}{\hbar^2} \sum_{i,j} e_{S,j} \cdot \frac{\partial^2 \epsilon_{n,\mathbf{k}}}{\partial k_i \partial k_j} \cdot e_{I,j}, \quad (4)$$

that is, the Raman vertex is given by the inverse effective mass tensor contracted with the polarization vectors \mathbf{e}_I and \mathbf{e}_S of the incoming and scattered light, respectively. Equation 4 is particularly useful if the bandstructure is known or can be calculated within *ab initio* local-density approximation (LDA) techniques such as the linear muffin-tin orbital (LMTO) method (14,15).

Once the Raman vertex is determined, the Raman susceptibility is given by a polarization bubble containing two Raman vertices. Taking into account equation 3, we can express the Raman susceptibility as

$$\chi_R(\mathbf{q} \rightarrow 0, \omega) = \left\langle \gamma_{\mathbf{k}}^2 \Pi_{\mathbf{k}}(\omega) \right\rangle_{BZ}, \quad (5)$$

that is, to calculate the scattering efficiency, which is $\sim \text{Im } \chi_R$, the Raman vertex has to be squared, multiplied by the \mathbf{k} dependent electronic polarizability of the system $\Pi_{\mathbf{k}}(\omega)$ and the result averaged over the Brillouin zone. In equation 5 we omitted the band index n for simplicity.

In “clean” metals, that is, in metallic systems with long mean free paths $l. k_F \gg 1$, the normal state electronic scattering is dipole forbidden because final states for vertical transitions ($\mathbf{q} \rightarrow 0$) and small energies are not available in the “clean” limit. Usually, various types of defects in the material can induce the Raman scattering (collision limited regime) (16). We note here that there is no satisfactory *ab initio* theory for the Raman scattering in the normal state of HTCS so far.

In the superconducting state, a gap opens in the quasiparticle spectrum and the *intradband* scattering becomes allowed for $\mathbf{q} \rightarrow 0$ even in the “clean” limit (note that ir-absorption remains forbidden in this limit). The electronic Raman scattering for ω below $2\Delta_0$ corresponds to a photon induced breaking of Cooper pairs into Bogoliubov quasiparticles (bogolons). The Raman susceptibility in the superconducting phase is given by a polarization bubble with two Raman vertices, one of which is renormalized, and propagators for bogolons (2). The vertex renormalization must include the attractive pairing interactions and the repulsive Coulomb interaction. However, for magnitudes of the wavevector transfer \mathbf{q} small compared to both the inverse coherence length, ξ^{-1} , and the Fermi wavevector k_F , the vertex corrections due to the pairing interaction can be neglected. Thus for $q \ll \xi^{-1}, k_F$ the effective kernel, corresponding to $\Pi_{\mathbf{k}}(\omega)$ in equation 5 is the Tsuneto function (17), $\lambda_{\mathbf{k}}(\omega)$, which contains the temperature dependent gap function $\Delta_{\mathbf{k}}$

$$\lambda_{\mathbf{k}}(\omega) = \frac{|\Delta_{\mathbf{k}}|^2}{E_{\mathbf{k}}^2} \tanh\left(\frac{E_{\mathbf{k}}}{2kT}\right) \left(\frac{1}{2E_{\mathbf{k}} + \omega + i0} + \frac{1}{2E_{\mathbf{k}} - \omega - i0} \right). \quad (6)$$

In equation 6, $E_{\mathbf{k}}^2 = (\varepsilon_{\mathbf{k}} - \varepsilon_F)^2 + \Delta_{\mathbf{k}}^2$ gives the quasiparticle energy dispersion, ε_F is the Fermi energy. The Tsuneto function has poles at $\omega = \pm 2E_{\mathbf{k}}$, that is, at the threshold pair-breaking energy. Note that $\lambda_{\mathbf{k}}(\omega)$ is a response function and therefore a Kramers-Kronig-like dispersion relation holds between its real and imaginary part.

Within the above approximation, the Raman susceptibility in the superconducting state, χ_R^S , is given by

$$\chi_R^S(\mathbf{q} \rightarrow 0, \omega, T) = \langle \gamma_{\mathbf{k}}^2 \lambda_{\mathbf{k}}(\omega, T) \rangle_{BZ} - \frac{\langle \gamma_{\mathbf{k}} \lambda_{\mathbf{k}}(\omega, T) \rangle_{BZ}^2}{\langle \lambda_{\mathbf{k}}(\omega, T) \rangle_{BZ}}. \quad (7)$$

The first term of equation 7 gives the non-screened susceptibility and resembles that of equation 5, whereas the second one represents the Coulomb screening of the Raman polarization bubble. In the case of highly anisotropic gaps and Raman vertices one should take into account both the real and imaginary part of $\lambda_{\mathbf{k}}(\omega)$, in particular, if $\gamma_{\mathbf{k}}$ changes its sign near the FS (this implies a resonance). It is worth mentioning that the Raman susceptibility given by equation 7 corresponds to a *new* scattering channel that opens below T_c . Therefore, in principle, no relations like the “sum rule” for the infrared absorption are expected for the redistribution of the spectral weight from the normal to the superconducting state. Now we summarize the main theoretical results for the electronic Raman scattering from the superconducting phase.

(i) The expression for the scattering cross section contains only the square of the magnitude of the gap function, $|\Delta_{\mathbf{k}}|^2$ as seen from equations 6 and 7. This very important fact shows that the electronic Raman scattering is *not sensitive to the phase* of $\Delta_{\mathbf{k}}$.

(ii) Most of HTCS have a tetragonal crystal structure that possesses the D_{4h} point group. Within this group, both the trivial (constant) and the highly anisotropic $|d_{x^2-y^2}|$ s-wave gaps have A_{1g} symmetry, whereas the $d_{x^2-y^2}$ -wave gap is of B_{1g} symmetry. The Tsuneto function (equation 6) is fully symmetric, that is, it has A_{1g} symmetry because the corresponding $|\Delta_{\mathbf{k}}|^2$ does not change upon application of any symmetry operator of D_{4h} . In particular, this means that one cannot distinguish between $|d_{x^2-y^2}|$ and $d_{x^2-y^2}$ -like gaps. Impurities in the sample, however, may change the Raman response in a different way at very low frequencies: A gap in the Raman spectrum should appear for the $|d_{x^2-y^2}|$ symmetry gap while for $d_{x^2-y^2}$ there is a broadening of the zero gap region around the nodes. Unfortunately, the frequency range for these effects is experimentally difficult to access in a Raman experiment since it overlaps that of the quasi-elastic scattering and the elastic stray light.

(iii) The screening effect in equation 7 can be understood from simple symmetry considerations. The BZ average of any function with B_{1g} or B_{2g} symmetry vanishes but that of a function of A_{1g} symmetry does not. For the numerator in the second term in equation 7 one has $\langle B_{1g} \otimes A_{1g} = B_{1g} \rangle_{BZ}^2 = 0$, $\langle B_{2g} \otimes A_{1g} = B_{2g} \rangle_{BZ}^2 = 0$, and $\langle A_{1g} \otimes A_{1g} = A_{1g} \rangle_{BZ}^2 \neq 0$. Therefore, only the A_{1g} Raman response should be affected by the screening. This fact is most important for the HTCS with a single-sheet FS (one CuO_2 plane per unit cell). In these compounds there are only intraband mass

fluctuations which, presumably, are not strongly \mathbf{k} dependent and the scattering related to the average mass (A_{1g}) is completely screened (25). In multilayer systems, like Hg-1234 and (Cu,C)-1234 discussed here, interband fluctuations between the different sheets of the FS become important. These fluctuations give considerable amount of unscreened A_{1g} scattering (4,25).

(iv) The expression for the Raman susceptibility simplifies when averages over the FS instead of the BZ are performed. In this case, the unscreened part of χ_R^S in equation 7, at $T = 0$ K, can be written as

$$\text{Im } \chi_R^S(\omega) \propto \left\langle \gamma_{\mathbf{k}}^2 \frac{|\Delta_{\mathbf{k}}|^2 \Theta(\omega^2 - 4|\Delta_{\mathbf{k}}|^2)}{\omega \sqrt{\omega^2 - 4|\Delta_{\mathbf{k}}|^2}} \right\rangle_{FS}, \quad (8)$$

where Θ is the step function. This approximation is valid when $\gamma_{\mathbf{k}}$ and $\Delta_{\mathbf{k}}$ do not change significantly for small deviations of \mathbf{k} perpendicular to the FS. From equation 8 it follows that for a simple isotropic s-gap, $\Delta_{\mathbf{k}} = \Delta_0 = \text{const.}$, $\text{Im } \chi_R(\omega) = 0$ for $\omega < 2\Delta_0$, whereas for the $d_{x^2-y^2}$ gap (it has nodes!), or for one of $|d_{x^2-y^2}|$ type, the scattering continuum extends to zero Raman shift in absence of impurities. We conclude this paragraph with the theoretical predictions for the low frequency behavior of the electronic Raman scattering in superconductors. In clean tetragonal superconductors with a $d_{x^2-y^2}$ gap, which seems to be the relevant gap for most HTCS, the scattering efficiency varies with frequency as ω^3 for the B_{1g} and as ω for A_{1g} and B_{2g} spectra (3,4). The steeper dependence of the B_{1g} scattering on frequency comes from the fact that the nodes of both the Raman vertex and the gap function coincides. For HTCS with orthorhombic symmetry one must distinguish two cases: that of $\text{YBa}_2\text{Cu}_3\text{O}_7$, in which the orthorhombicity is determined by the chains along (010), and that of $\text{Bi}_2\text{Sr}_2\text{CaCu}_2\text{O}_8$ in which it is determined by a distortion (a superstructure) along (110). In the $\text{YBa}_2\text{Cu}_3\text{O}_7$ case the tetragonal B_{1g} symmetry is transformed into A_g (in the corresponding D_{2h} point group) and a linear appears in the ω -dependence of the B_{1g} scattering, while in $\text{Bi}_2\text{Sr}_2\text{CaCu}_2\text{O}_8$ the tetragonal B_{1g} symmetry remains B_{1g} of the D_{2h} point group and the ω^3 asymptotic behavior is preserved.

Raman scattering from phonons. HTCS are centrosymmetric materials and consequently only even parity optical phonons can be Raman active. The diagram for the scattering process is simple. The incoming laser light is coupled to the electrons in the sample which via electron-phonon-coupling transfer energy and crystal momentum from the light to the sample (Stokes) or vice versa (Antistokes) scattering. The Raman amplitude for one-phonon scattering, denoted here as T_p , is represented by a 3x3 matrix similar to $\gamma_{\mathbf{k}}$, but it is *not* \mathbf{k} dependent. The scattering efficiency is then proportional to $|T_p|^2$.

Phonon self-energy. The phonon self-energy describes the renormalization of a phonon due to its coupling to other excitations in the solids (here we will consider only electronic excitations). Note that the expressions for the electronic Raman susceptibility and the phonon-self energy $\Sigma(\omega)$ due to the same electronic excitations, are rather similar (18, 19). $\Sigma(\omega)$ can be calculated in the same way as $\chi_R(\omega)$ (see equations 5, 7, and 8) with the electron-phonon matrix element $g_{\mathbf{k}}(\mathbf{q})$ (\mathbf{q} is the phonon wavevector) substituted for the Raman vertex $\gamma_{\mathbf{k}}$. We note also here that the matrix element $g_{\mathbf{k}}(\mathbf{q})$ is a \mathbf{k} dependent *scalar*. Since the effect of the phonon self-energy is included in the linewidth and frequency of the phonons detected by Raman spectroscopy we make the following important remark: The phonon-self energy of the Raman-active phonons does *not* depend on the light polarization in a scattering experiment. $\Sigma(\omega)$ can be changed only by changing the \mathbf{q} of the phonon or the phonon branch. In a standard Raman experiment, however, one excites phonons with $\mathbf{q} \rightarrow 0$, i.e., even this effect can be neglected. An instructive example of *incorrect* treatments of the phonon self energy effect is given in (20).

The real part of the phonon self-energy, $\text{Re}\Sigma(\omega)$, gives the shift $\delta\omega_p$ of the phonon frequency, and $-\text{Im}\Sigma(\omega)$, the change $\delta\Gamma_p$ of the phonon linewidth, with respect to those of the “bare” phonon. In this connection it is tempting to make a parallel between the change of the phonon linewidth, $-\text{Im}\Sigma^S(\omega)$ due to the superconductivity and $\text{Im}\chi_R^S(\omega)$. Particularly worth noting is that $\text{Im}\Sigma^S(\omega)$ should be affected by the symmetry (of the phonon!) in that it should be screened for fully symmetric (A_g or A_{1g}) phonons as is the case of the corresponding (A_g , A_{1g}) electronic scattering. Similarly to the electronic Raman scattering, for multilayer superconductors, the screening should usually be reduced. This is supported by the experimental data presented below.

Fano effect. It turns out that in most HTCS, the electronic excitations responsible for the phonon renormalization (the phonon self-energy) are also Raman-active and contribute to the electronic Raman scattering. In this case, a quantum interference between the scattering amplitudes of the phonon (a discrete excitation) and the electronic continuum results in an asymmetric phonon lineshape. The spectral distribution of the phonon Raman intensity is given by the well known Fano expression, which is relatively simple for the case of isotropic vertices (23). The corresponding formula that accounts for \mathbf{k} -space anisotropy of the vertices, although more realistic for HTCS, is more complicated (Belitsky V. I.; Strohm T.; unpublished), and has not yet been used for quantitative analysis of data. Since we use the Fano formula for fitting the experimental data, we briefly present the physical quantities that are involved. For isotropic vertices $\gamma_{\mathbf{k}} = T_e$ and $g_{\mathbf{k}} = V$ we write for the Raman susceptibility

$$\left\langle \gamma_{\mathbf{k}}^2 \Pi_{\mathbf{k}}(\omega) \right\rangle_{BZ} = T_e^2 \left[R(\omega) - i\pi\rho(\omega) \right], \quad (9)$$

and for the phonon self-energy $\Sigma(\omega)$ in the limit $\mathbf{q} \rightarrow 0$

$$\Sigma(\omega) = \langle g_{\mathbf{k}}^2 \Pi_{\mathbf{k}}(\omega) \rangle_{BZ} = V^2 [R(\omega) - i\pi\rho(\omega)], \quad (10)$$

here $\rho(\omega)$ is the density of electronic excitations and $R(\omega)$ its Hilbert transform (23). We write the simplest form of the Fano expression for the Raman efficiency in terms of real and isotropic vertices (microscopic parameters)

$$I(\omega) \sim \pi T_e^2 \rho(\omega) \frac{(\omega - \omega_p^0 + T_p V / T_e)^2}{[\omega - \omega_p^0 - V^2 R(\omega)]^2 + [\pi V^2 \rho(\omega)]^2}. \quad (11)$$

Equation 11 is valid if the vertices T_e , V , and T_p are all independent of frequency and wavevector, i.e., they vary weakly around the “bare” phonon frequency ω_p^0 . In equation 11 we have neglected, for simplicity, other phonon renormalization processes (e.g., anharmonic interactions with two phonon excitations).

Experiment, experimental results and discussion

Samples and the experimental setup. In the Raman scattering experiment we used single crystalline grains present in a polycrystalline pellet (Cu,C)Ba₂Ca₃Cu₄O_x ($T_c=117$ K, from the field cooled magnetization data at 10 G) prepared by a high-pressure synthesis technique (24). The sample was kept in a flowing liquid helium cryostat which was used to vary its temperature from 3.8 to 300 K. We measured the Raman spectra of well oriented microcrystals in the pellet by means of a triple spectrometer equipped with a microscope. The 514.5 nm and 647.1 nm laser lines were used for exciting the spectra in an exact back-scattering configuration.

Experimental selection of scattering symmetry. The compound (Cu,C)-1234 crystallizes in the average tetragonal P4/mmm space group having four CuO₂ planes per primitive cell. Carbon atoms in (Cu,C)-1234 were found to form CO₃ molecule-like units which may introduce short range orthorhombic distortions in the lattice. The group-theoretical analysis at the Γ -point ($\mathbf{q} = 0$) predicts that $7A_{1g} + 2B_{1g} + 9E_g$ symmetry phonons are Raman allowed. In particular, we mention the two A_{1g} modes that showed the strongest superconductivity-induced effects. They involve mixed vibrations along the c -axis of oxygen in the CuO₂ planes and Ca moving in-phase and out-of-phase with the oxygen atoms.

We were able to choose crystals with exact crystallographic orientations by using the empirically established (partly by means of the Raman selection rules) connection between the external morphology of *tetragonal* HTCS crystals and the crystallographic axes. These are: (i) the HTCS crystals have a plate-like shape with the c axis perpendicular to the plate; (ii) under a microscope with a crossed polarization of the incident and reflected light, the color of the ab plane does not change upon rotation of the crystal around the direction of light, whereas it does for the ac or bc planes. We indicate the scattering configuration by means of Porto's notation. We denote by z a direction parallel to the c -axis of the crystal, x and y are

directed along $[100]$ and $[010]$ axes, respectively. We use the symbols x' and y' for two mutually orthogonal directions along $[110]$ and $[\bar{1}\bar{1}0]$. Thus $x(\bar{z}\bar{z})\bar{x}$, $z(x'x')\bar{z}$, $z(y'y')\bar{z}$, and $z(yx)\bar{z}$ select the A_{1g} , $A_{1g} + B_{2g}$, B_{1g} , and B_{2g} symmetry components of the Raman scattering efficiency, respectively.

Electronic Raman scattering. In Figure 1 we present polarized Raman spectra of well oriented (Cu,C)-1234 micro-crystals. The spectrum in Figure 1a is dominated by the A_{1g} vibration of the apex oxygen at around 500 cm^{-1} . The spectra in Figure 1b were recorded in the $z(y'y')\bar{z}$ scattering geometry that selects the B_{1g} , i.e., the $(x^2 - y^2)$ component of the Raman efficiency. The low frequency part ($\omega < 400\text{ cm}^{-1}$) of the flat electronic continuum in the normal state (120 K) reduces below T_c and a relatively broad electronic Raman peak emerges at 650 cm^{-1} . We measured a series of the B_{1g} spectra (not shown here), and found that the appearance of the peak correlates with the superconducting transition. Figure 1c shows the $A_{1g} + B_{2g}$ Raman spectra taken from the same microcrystal. In addition to the dramatic increase in intensity of the phonons at 235 and 360 cm^{-1} , a well pronounced broad peak at 490 cm^{-1} is also seen. We interpret it as being due to the pair breaking electronic excitations. The A_{1g} and B_{1g} electronic peaks shown in Figure 1 (the B_{2g} spectrum was very weak) illustrate also the main point of contention between the theory and the experiment. The first problem is the position of the peaks. Both types of calculations, one that involves a decomposition of the Raman vertex in the FS harmonics and FS integrations (3), and the other, based on the full 3D LDA-LMTO band structure (4) give nearly the same position of the A_{1g} and B_{1g} electronic peaks. In the case of (Cu,C)-1234, similarly to the other underdoped or optimally doped HTCS, the A_{1g} peak is shifted to lower frequency than the B_{1g} counterpart. HTCS with more than one CuO_2 plane have bonding and antibonding sheets of the FS. These two types of FS sheets may have different gaps. It has been suggested that this fact together with differences in the effective mass vertices may account for the positions of the peaks (25). The second, more serious problem is the relative intensity of the two peaks. Surprisingly, the A_{1g} peak that has to be screened appears much stronger than the completely unscreened B_{1g} peak. The screening terms to the B_{1g} electronic Raman response below T_c have been calculated in (26). However, an intensity ratio of the screened responses $I(A_{1g})/I(B_{1g}) \approx 10^{-2}$ is particularly small after the correction of the wrong mass vertex (27,28) used in equation 5 of (26).

The low frequency linear term of the A_{1g} scattering is rather pronounced. The ω^3 behavior of the B_{1g} peak, however, is not clearly seen because of the A_{1g} polarization leakage (see the A_{1g} phonon pattern) in combination with the weak B_{1g} spectrum and the orthorhombic distortions.

Superconductivity-induced phonon renormalization. The most remarkable feature of the spectra shown in Figure 1c is the development of strong phonon peaks in

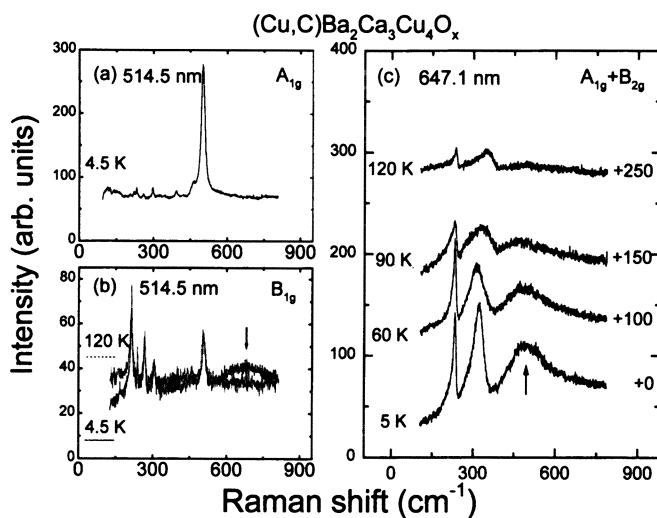


Figure 1. Polarized Raman spectra of (Cu,C)-1234 single crystals measured for $x(zz)\bar{x}$ (a), $z(y'x')\bar{z}$ (b) and $z(x'x')\bar{z}$ (c); in (b) and (c), the spectra are given for temperatures above and below $T_c = 117$ K. The spectra were corrected for the response of the Raman-scattering-measurement equipment.

going from the normal to the superconducting state. In the normal state, the 235 cm^{-1} and 360 cm^{-1} phonons have an asymmetric lineshape (Fano profile), an indication for a coupling of the phonons to the electronic continuum. In the superconducting state, the two lower frequency phonons show a significant change of their position, linewidth and especially the scattering intensity. We note the remarkable similarity in the phonon renormalization and intensity changes in both (Cu,C)-1234 and Hg-1234 (see, e.g., 11,12). The only common structural element in (Cu,C)-1234 and Hg-1234 is the stack of four CuO_2 planes per unit cell. This clearly indicates that the effect concerns only the superconducting CuO_2 layers in HTCS.

In order to quantify the experimental observations we fitted the spectra with the Fano function given by equation 11 plus electronic background $I_b(\omega)$ that simulates both the redistribution of the low frequency normal state continuum and the electronic peak below T_c . The results of the fitting procedure for the A_{1g} spectra of (Cu,C)-1234 are displayed in Figure 2. In our fit we used the renormalized frequency ω_p , the linewidth (HWHM) Γ_p that includes all the decay channels, the asymmetry parameter $q = [V T_p / T_e + V^2 R(\omega_p)] / \pi V^2 \rho(\omega_p)$, and the factor $I_c = \pi T_e^2 \rho(\omega_p)$ as fitting parameters. From equations 10 and 11 it follows that the phonon renormalization, $\delta\omega_p$ and $\delta\Gamma_p$, due to the coupling to the electronic excitations can be expressed as

$$\delta\omega_p = V^2 R(\omega_p) \quad \text{and} \quad \delta\Gamma_p = \pi V^2 \rho(\omega_p). \quad (12)$$

We note that the “bare” frequency, ω_p^0 , conceivable only as a frequency of a vibration in a harmonic lattice potential without free carriers, can not be determined from the experiment. It always includes, besides the electron-phonon self-energy, the real part of other phonon self-energy contributions, e.g., the phonon interaction with two-phonon excitations, the imaginary part of which is also responsible for the temperature dependent anharmonic broadening $\Gamma_{anh} \equiv \Gamma_{anh}^0 (1 + 2n_{\omega_p/2,T})$. The integrated phonon intensity given in Figure 2 was determined from equation:

$$I_p \equiv \pi I(\omega_p) \Gamma_p = \pi \rho(\omega_p) T_e^2 q^2 \Gamma_p. \quad (13)$$

Figure 2 clearly shows that the change of the frequency, linewidth and intensity of the phonons at 235 cm^{-1} and 360 cm^{-1} in (Cu,C)-1234 takes place when entering the superconducting state ($T_c = 117$ K). The corresponding phonons of Hg-1234 at 240 cm^{-1} and 390 cm^{-1} exhibit very similar temperature behavior (11,12). These A_{1g} phonons have frequencies below $2\Delta_0$ in both compounds. In addition to the softening of these phonons below T_c , they also *broaden*. From this fact we may conclude that the measured phonon self-energies are in favor of a gap allowing for pair breaking excitations below its maximum value Δ_0 . The calculation of the phonon renormalization yields a broadening for any phonon frequency lower than $2\Delta_0$ only for a gap function with nodes (7,8). Particularly interesting is the temperature dependence of the linewidth Γ_p . The phonon linewidth increases dramatically below

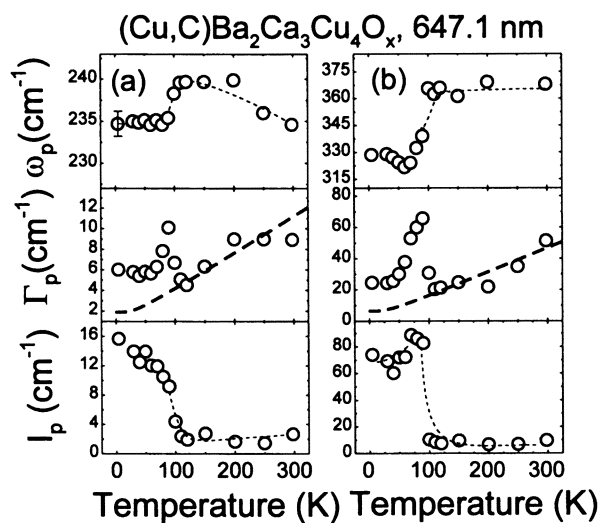


Figure 2. Temperature dependence of the fitted frequency ω_p , linewidth Γ_p and the phonon intensity I_p for the phonons at 235 cm^{-1} (a) and 360 cm^{-1} (b) in (Cu,C)-1234. Smooth dotted lines are given as a guide to the eye. The dashed lines in the linewidth panels represent a fit to the width found above T_c with the anharmonic broadening function $\Gamma_{anh} = \Gamma_{anh}^0 (1 + 2n_{\omega_p/2,T})$.

T_c , passing through a maximum slightly below T_c , and then decreases again. Nevertheless, at low temperatures, the phonon linewidths remain broader than those in the immediate vicinity of but above T_c . This behavior of Γ_p agrees with the model calculations for a d-wave superconductor given in (8). Immediately below T_c , the superconducting gap $2\Delta(T)$ opens and its magnitude increases with lowering the temperature. Thus the maximum gap sweeps over the phonons. The strength of the phonon renormalization is maximum when the phonon frequency coincides with the gap. At low temperatures, where $\Delta(T) = \Delta_0$, the renormalizations reach a temperature independent value as also seen in Figure 2.

Raman intensity of the A_{1g} phonons in the superconducting state. There are two main types of phonon self-energy effects. The first is the phonon renormalization which, for a phonon with given frequency and wave vector coupled to given excitations, does not depend on the way it is detected. In a Raman scattering experiment, however, if both the phonon and the electronic excitations are Raman active their hybridization leads to a mixture of their scattering amplitudes, i.e., to a mutual dependence of their Raman efficiencies. The increase of the phonon intensity in Figure 1c obviously correlates with the increase of the electronic peak intensity. The integrated phonon intensity I_p given in equation 13 can also be expressed as $I_p = \pi |T_p + T_e VR(\omega_p)|^2$. Therefore, one would expect the phonon Raman intensity to change with the real part of the phonon self-energy, $\delta\omega_p$.

We now introduce a simple relation that connects the Raman efficiency of the phonon with that of the electronic peak. First we notice the very weak Raman intensity of the phonons around 235 cm^{-1} and 360 cm^{-1} in the normal state (see Figure 1c). This implies that the phonon scattering amplitude is very small, a fact which allows us to set $T_p \approx 0$. The strong asymmetry of the phonon lineshape (related to the value of $q \approx 1$) then suggests $q \approx R(\omega_p) / [\pi\rho(\omega_p)]$ and $R \approx \rho$. Combining these expressions with equation 12 leads to $q\delta\Gamma_p = \delta\omega_p$. Under these conditions, we rewrite the phonon intensity I_p in equation 13 as

$$I_p = \pi T_e^2 R(\omega_p) \cdot \delta\omega_p. \quad (14)$$

The factor $\pi T_e^2 R(\omega_p)$ is the Kramers-Kronig transform of the electronic Raman continuum at $\omega = \omega_p$, $\pi T_e^2 \rho(\omega_p)$. Note also the difference in the units: $\pi T_e^2 \rho(\omega_p)$ is intensity per unit frequency, whereas πT_e^2 represents the integrated intensity. We further simplify equation 14 by approximating the electronic peak at $\omega = \omega_e$ as a δ -function, then $R(\omega_p) \sim (\omega_e - \omega_p)^{-1}$, and in suitable units, from the relation $\pi T_e^2 R(\omega_p) = I_e / (\omega_e - \omega_p)$ it follows

$$\frac{I_p}{I_e} = \frac{\delta\omega_p}{\omega_e - \omega_p}. \quad (15)$$

All the quantities in equation 15 can be determined from the experiment. It is interesting, however, to see to what extent equation 15 describes correctly the experimental results. We can compare, for example, the experimental phonon intensity, I_p^{exp} with the I_p^{calc} calculated from equation 15 using the experimental values for $I_e = \pi H_e \Gamma_e$ (H_e is the height of the electronic peak and Γ_e its linewidth, HWHM), $\delta\omega_p$, and $(\omega_e - \omega_p)$. The calculated intensities compare with the experimental ones as follows: $I_{235}^{\text{exp}} = 540 \text{ a.u.}$, $I_{235}^{\text{calc}} = 510 \text{ a.u.}$, and, $I_{360}^{\text{exp}} = 3250 \text{ a.u.}$, $I_{360}^{\text{calc}} = 2625 \text{ a.u.}$. The overall disagreement is not more than 40%, which is remarkably satisfactory considering the simple model used.

Electron-phonon coupling constant. We can estimate the electron-phonon matrix element V from the experimental data. For this purpose we use again a simple model. We denote, with N_e the number of states involved in the electronic peak around $\omega = \omega_e$ which is given by $N_e \approx \Delta_0 N_0$, i.e., all the states within the energy interval Δ_0 around the FS (N_0 is the two-spin density of states at the Fermi level) are redistributed and piled up at the position of the electronic pair breaking peak ω_e . We write the density of the electronic pair-breaking excitations as a δ -function, $\rho(\omega) = N_e \delta(\omega - \omega_e)$, then its Hilbert transform is $R(\omega) = N_e / (\omega_e - \omega)$ and from equation 10 we obtain

$$N_e V^2 = \delta\omega_p \cdot (\omega_p - \omega_e). \quad (16)$$

Equation 16 can be used to estimate $N_e V^2$ from the experimental data.

It is tempting to use these results to determine “experimentally” the electron-phonon coupling constant for a given phonon ν using McMillan’s expression (29) for the dimensionless electron-phonon coupling parameter λ (McMillan’s parameter)

$$\lambda \equiv 2 \int_0^\infty \frac{\alpha^2(\omega)F(\omega)}{\omega} d\omega, \quad (17)$$

$\alpha^2(\omega)F(\omega)$ is the electron-phonon spectral function (29). Using the expressions $N_e \approx \Delta_0 N_0$ and $\lambda = \sum_\nu \lambda_\nu$ we can write (11)

$$\lambda_\nu = \frac{1}{\Delta_0} \cdot \frac{N_e V_{p,\nu}^2}{\omega_{p,\nu}}. \quad (18)$$

Using equation 18 and the available experimental data, we estimated that in (Cu,C)-1234 the constants λ_ν for the two A_{1g} modes at 235 cm^{-1} and 360 cm^{-1} are $\lambda_{235} = 0.05$ and $\lambda_{360} = 0.07$. These values for the electron-phonon coupling constants are rather large when compared with $\lambda_{A_{1g}} = 0.01$ and $\lambda_{B_{1g}} = 0.02$ calculated for the plane oxygen modes at 440 cm^{-1} (A_{1g}) and 340 cm^{-1} (B_{1g}), respectively, in $\text{YBa}_2\text{Cu}_3\text{O}_{7-\delta}$ (30). Assuming $x \cong 10$, i.e., a total of 20 atoms per primitive cell, we would find a total $\lambda \cong 4$ if all phonons would couple to the superconducting carriers as much as those discussed above for $(\text{Cu,C})\text{Ba}_2\text{Ca}_3\text{Cu}_4\text{O}_x$. This would suffice to reach T_c 's of the order of 100 K.

Conclusions

The Raman scattering from (Cu,C)-1234 is similar to that found for Hg-1234 (11,12) and reveals rich superconductivity-related phenomena. The superconductivity-induced electronic Raman peaks and strong phonon self-energy effects are clearly seen in the Raman spectra of these compounds. The simple and physically transparent model presented here, in which the A_{1g} phonons couple to the quasiparticles created through pair breaking, accounts fairly well for the spectacular increase in the phonon Raman intensities below T_c . We obtained from the experimental data surprisingly high values of the electron-phonon coupling constants of the phonons under consideration.

Acknowledgments. This work was supported in part by NSF Grant DMR 95-10625, T. L. L. Temple Foundation, John J. and Rebecca Moores Endowment and the State of Texas through the Texas Center for Superconductivity at the University of Houston.

References

1. *Spectroscopic Studies of Superconductors*; Bozovic I., van der Marel D., Eds.; SPIE Proceedings; SPIE: Washington, 1996, Vol. 2696, Part A: Infrared and Raman Spectra.
2. Klein M. V.; Dierker S. B.; *Phys. Rev. B* **1984**, *29*, p. 4976.
3. Devereaux T. P.; Einzel D.; *Phys. Rev. B* **1995**, *51*, p. 16336.
4. Strohm T.; Cardona M.; *Phys. Rev. B* **1997**, *55*, p. 12 725.
5. Stauffer T.; Nemetschek R.; Hackl R.; Muller P.; Veith H.; *Phys. Rev. Lett.* **1992**, *68*, p.1069.
6. Zeyher R.; Zwignagl G.; *Z. Phys. B - Condensed Matter* **1990**, *78*, p. 175.
7. Nicol E. J.; Jiang C.; Carbotte J. P.; *Phys. Rev. B* **1993**, *47*, p. 8131.
8. Jiang C.; Carbotte J. P.; *Phys. Rev. B* **1994**, *50*, p. 9449.
9. Shapiro S. M.; Shirane G.; Axe J. D.; *Phys. Rev. B* **1975**, *12*, p. 4899.
10. Wittlin A.; Liu R.; Cardona M.; Genzel L.; Konig W.; Bauerhofer W.; Mattausch H.; Garcia-Alvarado F.; *Solid State Commun.* **1987**, *64*, p. 477.
11. Hadjiev V. G.; Zhou Xingjiang; Strohm T.; Cardona M.; Lin Q. M.; Chu C. W.; *Phys. Rev. B* **1998**, *58*, p. 1043.
12. Zhou Xingjiang; Hadjiev V. G.; Cardona M.; Lin Q. M.; Chu C. W.; *phys. stat. sol. (a)* **1997**, *202*, p. R7.
13. Hadjiev V. G.; Cardona M.; Du Z. L.; Xue Y. Y.; Chu C. W.; *phys. stat. sol. (b)* **1998**, *205*, p. R1.

14. Pickett W. E.; *Reviews of Modern Physics* **1989**, *61*, p. 433.
15. Krantz M. C.; Mazin I. I.; Leach D. H.; Lee W. Y.; Cardona M.; *Phys. Rev. B* **1995**, p. 5949.
16. Zawadowski A.; Cardona M.; *Phys. Rev. B* **1990**, *42*, p. 10732.
17. Tsuneto T.; *Phys. Rev.* **1960**, *118*, p. 1029.
18. Cardona M.; Ipatova I. P.; *Elementary excitations in Solids*, Birman J. L., Sebenne C., Wallis R. F.; Eds.; Elsevier, Amsterdam, 1992, p. 237.
19. Deveraux T. P.; *Phys. Rev. B* **1994**, *50*, p.10287.
20. Limonov M. F.; Rykov A. I.; Tajima S.; Yamanaka A.; *Phys. Rev. Lett.* **1998**, *80*, p. 825.
21. Strohm T.; Belitsky V. I.; Hadjiev V. G.; Cardona M.; *Phys. Rev. Lett.* **1998**, *81*, p. 2180.
22. Limonov M. F.; Rykov A. I.; Tajima S.; Yamanaka A.; *Phys. Rev. Lett.* **1998**, *81*, p. 2181.
23. Klein M. V.; *Light scattering in Solids I*, Cardona M.; Ed.; Springer, Berlin, 1983, pp.171f.
24. Gao Y.; Lin F. Y.; Du Z. L.; Chen F.; Xue Y. Y.; Chu C. W.; *Physica C* **1997**, *282-287*, p. 1243.
25. Krantz M.; Cardona M.; *J. Low Temp. Phys.* **1995**, *99*, p.205.
26. Manske D.; Rieck C. T.; Das Sharma R.; Bock A.; Fay D.; *Phys. Rev. B* **1997**, *56*, p. R2940.
27. Strohm T.; Muzar D.; Cardona M.; *Phys. Rev. B* **1997**, *58*, p. 8839.
28. Manske D.; Bock A.; Rieck C. T.; Fay D.; *Phys. Rev. B* **1997**, *58*, p. 8841.
29. McMillan W. L.; *Phys. Rev.* **1968**, *167*, pp. 331.
30. Thomsen C.; Cardona M.; Friedl B.; Rodriguez C. O.; Mazin I. I.; Andersen O. K.; *Solid State Commun.*, **1990**, *75*, p. 219.

Point Contact Spectroscopy of Organic Conductors

G. V. Kamarchuk¹, A. V. Khotkevich¹, V. M. Bagatsky¹,
and A. V. Kravchenko²

¹Institute for Low Temperature Physics and Engineering, Academy
of Sciences of Ukraine, 47, Lenin Avenue, 310164, Kharkov, Ukraine

²Kharkov State University, 310077, Kharkov, Ukraine

Homo- and heterocontacts of organic conductor β -(BEDT-TTF)₂I₃ and [(C₂H₅)₄N]_{0.5}[Ni(dmit)₂] were investigated at 4.2 K. The I-V characteristics of the contacts and their first dV/dI(V) and second derivatives d²V/dI² (V) (point-contact spectra) were measured in the voltage range 0-250mV. The experiments for contacts oriented in different crystallographic directions were carried out. The spectra measured on contacts with the current flow in the plane of the organic molecule layers display features caused by the interaction between the electrons and intramolecular vibrations. The spectra of the samples with the axis perpendicular to the BEDT-TTF layers have maxima reflecting the predominating contribution of the anion I₃ to the scattering of charge carriers in such point contacts. So, the interaction of electrons with intramolecular vibrations of organic conductors was demonstrated directly. Point-contact spectra of layered organic conductors were shown to be essentially anisotropic. The transition to heterojunctions with a superconducting inclusion is observed at T=4.2K with increasing confining force between the electrodes. The values of the energy gap for the organic superconductor and the excess current of the heterocontacts were calculated. The relation between the intensity of the electron-vibrational interaction and conducting properties of the materials under investigation was obtained. The criterion for the synthesis of new organic superconductor is discussed.

Introduction: Point-Contact Spectroscopy for Chemists.

Energy spectroscopy of metals takes one of the central places in modern solid state physics, since fundamental physical properties of conductors are essentially determined by the interaction of their electron and phonon systems.

The discovery of the point-contact spectroscopy method [1, 2] completed an arsenal of traditional means of spectroscopy investigations. It was shown that at low temperatures point-contact spectra (voltage dependencies of the second derivatives of point-contact current-voltage characteristics (IVC)) in normal state reflect both the electron-phonon interaction (EPI) function and an EPI anisotropy. The EPI function is relative to the function of density of phonon states. So in some cases we can obtain the unique information about energy spectra of metal systems, inaccessible for other experimental investigation methods. It should be mentioned that the point-contact spectroscopy method always has an advantage over tunneling spectroscopy in investigating new exotic conductors, because point contact is easier to produce than tunneling one.

The high technical level of experimental investigations (in particular, effective methods of obtaining samples - displacement technique [3] and "break junctions" [4]) and the development of the point contact theory allow to use this method for solving a number of actual metal physics problems.

Point-Contact Spectroscopy in Normal State. Real point contacts admit simple model description. An orifice with an effective diameter " d " in an infinite thin (but impenetrable for electrons) plane screen, dividing two metal semispaces, is one of the most fruitful theoretical models. Point-contact spectroscopy of EPI is realized in ballistic and diffusive regimes of current flow through the contact. These regimes correspond to pure and dirty limit conditions $d \ll l_i, l_e$ and $l_i \ll d^{1/2} \ll (l_i l_e)^{1/2}$, where l_i and l_e are electron mean free paths, corresponding momentum and energy relaxation. The analysis of contact IVC deviations arising as a result of phonon scattering of electrons, accelerated in electric field of the contact, is the basis of point contact spectroscopy. The frequency of phonons, generated by electrons just near the contact, is determined as $\omega = eV/\hbar$. It can reach easily its maximum (i.e. the maximum frequency of phonon spectrum ω_{max}) when increasing contact voltage. The contact IVC nonlinearities caused by inelastic scattering of electrons in the contact area, are connected with EPI spectrum by the principal correlation of the point-contact spectroscopy theory, such as

$$\frac{d^2 I}{dV^2}(V) = -\frac{\pi e^3}{\hbar} n(\varepsilon_F) \Omega \left[g_{pc}(\omega) + B(\omega) \right]$$

$\omega = eV/\hbar$

Here g_{pc} is the point-contact EPI function, $n(\varepsilon_F)$ is the density of electron states at Fermi level for one spin direction, Ω - is an effective volume of phonon generation in the contact. The background function $B(\omega)$ accounts the fact that experimentally determined second derivatives of the IVC differ from zero when $V > \hbar \omega_{max}/e$, while the EPI function is equal to zero beyond the phonon spectrum boundary. The function

$$g_{pc}(\omega) = \frac{(2\pi\hbar)^{-3}}{\oint dS/v} \langle K \rangle^{-1} \oint \frac{dS}{v} \oint \frac{dS'}{v'} \sum_{\nu} |M_{\bar{p}-\bar{p}',\nu}|^2 K(\bar{v},\bar{v}') \delta(\omega - \omega_{\bar{p}-\bar{p}',\nu}) \quad (1)$$

is one of the spectral EPI functions, belonging to the most detail characteristics of electron-phonon interaction. It is an anisotropic version of the thermodynamical EPI function $g(\omega)$ (Eliashberg function) and differs from $g(\omega)$ by the point-contact form-factor K , which depends on the geometry and purity of the contact. In (equation 1.) integration is made over the Fermi surface (FS) with the account of electron states with quasimomentums \mathbf{p}, \mathbf{p}' and velocities v, v' ; ν is a number of the branch of phonon spectrum; $|M_{\bar{p}-\bar{p}',\nu}|$ is the module of the EPI matrix element, defining a probability of a $\mathbf{p}-\mathbf{p}'$ transition when scattering on the phonon with energy $\hbar\omega_{q,\nu}$, $\mathbf{p}' = \mathbf{p} - \mathbf{q} + \mathbf{Q}$, where \mathbf{Q} is an inverse lattice vector; $\langle K \rangle$ is the point-contact form factor, averaged over the FS. The microscopic theory [5] relates the background $B(\omega)$ with nonequilibrium of the phonon distribution function in the contact and reabsorption of nonequilibrium phonons by electrons.

The experimental setup for researching contacts at low temperatures (point-contact spectrometer) includes the cryogenic equipment set, a magnet system and a complex of measurement devices. Usually the measurements of electric contact characteristics are carried out by four-probe method by scheme in which both a source of an electric bias and a source of modulating signal work in regime of current sources. If it is necessary the superconductivity of samples can be ruined by direct magnetic field.

The measured characteristics are the magnitude of a contact resistance R_0 in normal state at $V \rightarrow 0$, the IVC $I(V)$, and dependences of voltages of the first and second harmonics of the low-frequency modulating signal. This harmonics are proportional to the first and second IVC derivatives: $V_1(V) \sim dV/dI(I)$ and $V_2(V) \sim d^2V/dI^2(V)$.

Taking into consideration radiotechnical correlation among measured magnitudes, the principal expression of the point-contact theory can be rewritten as [6]

$$g_{pc}(\omega) + B(\omega) = C \tilde{V}_2 V_{1,0}^{-2} R_0^{1/2} \Big|_{V=\hbar\omega/e} \quad (2)$$

which is practically fit for the point-contact EPI function reconstruction. Here

$V_{1,0}$ is equal to V_1 at $V=0$, $C = -\frac{3}{8} \left(\frac{\hbar}{2\pi} \right)^{1/2} v_F k_F$, k_F is the Fermi wave vector.

In accordance to equation 2. $g_{pc}(\omega)$ function reconstruction includes transformation of experimental dependences $V_2(V) \sim d^2V/dI^2(V)$ to $\tilde{V}_2(V) \sim d^2I/dV^2(V)$ form and excluding background from $V_2(V)$. The software allows to get $g_{pc}(\omega)$ function, EPI constant λ_{pc} , mean $\langle \omega \rangle$ and root-mean-square $\langle \omega^2 \rangle^{1/2}$ phonon frequencies and some other characteristics.

The Superconductivity of Point Contacts. In normal state contacts have IV characteristics, representing Ohmic dependences with small nonlinearities caused by EPI. When one or both electrodes of the point contact are in superconducting state the IVCs of such systems are essentially different from considered above. The conductive properties of S-c-S (superconductor-superconductor) and S-c-N (superconductor-normal metal) contacts are essentially complicated by Josephson effects and reflection of charge carriers from NS boundary. These new conductivity effects widen an arsenal of methods of actual physical phenomena studies in metals with point-contact technique used.

Josephson Critical Current. Among the characteristic parameters that determine the properties of contacts in superconducting state, the superconducting coherence length ξ is of especial role. According to the microscopic theory of direct current Josephson effect in superconducting constrictions [7], characteristics of contacts less in size than ξ are independent of their specific geometry. In this case, a Josephson bridge may be considered as one with zero length and described in an orifice model. On condition that the orifice being monobinding only the area of the orifice not its shape matters as well as in contacts in normal state. The current through the contact was shown to be independent of l at $l \gg d$ for an arbitrary correlation between l and ξ both dirty $l \ll d \ll \xi$ and pure $d \ll (l, \xi)$ contacts. The theory testifies that Josephson critical current I_c of a point contact is always more than critical current value I_k of a tunneling one with such a resistance R_0 in normal state. At $T=0$

$$\frac{I_c}{I_k} = \begin{cases} 2 & , \quad l \gg d \\ 1.32 & , \quad l \ll d \end{cases} , \quad I_k = \frac{\pi \Delta}{2eR_0}$$

Δ is a half-width of energy gap of the superconductor. The expression for I_k is named Ambegaokar-Baratoff formula.

Energy Gap Spectroscopy of Superconductors. Point contacts allow to carry out measurements of gap in quasiparticle spectrum of superconductor. One way is connected with displaying subgap harmonics at electric characteristics of S-c-S contacts under contact voltages equaled to $2\Delta/en$, $n=1,2,3, \dots$. In another method energy gap can be defined from BKT theory using characteristics of S-c-N contacts (see, for example, [8]).

Excess Current. At high voltages $V \gg \Delta/e$ IVC of superconducting point contacts differs from that in normal state by excess current $I_{exc} = [I(V) - V/R_0(V)] \text{ sign} V$, where R_0 is the contact resistance at $V=0$ in normal state. Based on a basis of microscopic superconducting theory consideration [9] has shown that excess current effect in S-c-S and S-c-N contacts is connected with charge transport processes accompanied by electron-hole conversion of Andreev reflection type and differences between IVC of such contacts in the pure and dirty limit. At $V > 2\Delta$ the value of the $I_{exc}eR_0/\Delta$ for S-c-S contacts in the pure limit approaches $\pi^2/4 - 1 = 2.67$ - the result expected by the theory [9]. If

the shape of the contact deviates from an orifice then in the pure limit the product $I_{exc}eR_0/\Delta$ falls to $8/3=1.47$, predicted by the theory in the dirty limit. Excess current in S-c-N contacts is a half as that for S-c-S cases.

The Contribution of EPI Processes to IVC of Superconducting Contacts. The progress of experimental studies of EPI in pure S-c-N and S-c-S contacts [10, 11] is mainly related to the elaboration of the theory of inelastic electron-phonon scattering in these systems [12, 13]. According to the theory at $V \gg \Delta$ the IVC of such contacts is written as $I(V) = V/R_0 + I_{ph}^N(V) + I_{exc}(V)$. Here $I_{ph}^N(V)$ is an equation term, describing inelastic electron-phonon scattering for a contact in normal state and $I_{exc}(V)$ is excess current depending on voltages $I_{exc}(V) = I_{exc} + I_{ph}^s$. I_{exc} is defined as elastic component of excess current and a small inelastic correction $I_{ph}^s(V)$ is connected with EPI processes at electron-hole transitions. The most of the current through the contact in superconducting state is caused by the same scattering processes as those in normal state and the second derivative of the IVC is supposed to reflect the structure of the EPI function. A correlation between IVC second derivatives of contacts in normal and superconducting states allows to discover additional widening of Δ order predicted by the theory [11-13].

At low voltages the differences between of $V_2(V)$ dependences in normal and superconducting states are caused by appearing of the gap peculiarity in the IVC in superconducting state and by nonlinearity connected with a critical current of S-c-S contacts.

Elastic Spectroscopy of EPI. Another mechanism of nonlinear behaviour of the IVC of pure S-c-N point contacts [14] is also essential for strong pairing superconductors. This mechanism arises from electron-phonon renormalization of energy spectrum of superconductor and manifests itself in the elastic component of the current through the contact. Such an effect is observed [15] as maxima of the differential conductivity in the area of the character phonon energies of superconductor and may be used for EPI spectroscopy.

Experimental Results.

β -(BEDT-TTF)₂I₃. Homo- and heterojunctions of the organic conductor β -(BEDT-TTF)₂I₃ obtained by standard electrochemical techniques were studied. Single crystals in the form of plates with size up to $2 \times 2 \times 0,5 \text{ mm}^3$ were used as the counterelectrode in heterojunctions. The samples were prepared by displacement technique [3, 16]. The junction was formed at the contact between the edges of organic crystals in homojunctions or between a metal electrode and an organic crystal in the case of heterojunction (see insert to Figure 1). Owing to the contact geometry used for the electrodes, a situation favoring the formation of point contacts was realized so that their axis lie in the plane of the layer of organic molecules of the (BEDT-TTF)₂I₃ crystal, i.e., in the direction along which this compound has the highest conductivity.

The IVC of contacts and their second derivatives were measured in the voltage range 0-250mV. Measurements were made at 4,2K. For homojunctions, measurements could be made in most cases in the voltage range up to 100mV.

For $V > 100\text{mV}$, heating of contacts resulted in irreversible changes in their resistance or even their complete destruction. The situation was more favorable in the case of heterojunctions owing to the possibility of selecting counterelectrodes with high electrical and thermal conductivity. This circumstance made it possible to obtain samples exhibiting spectral properties over a wider range of voltages and to study the behavior of high-energy peculiarities on the second derivatives of the IVC. As a result, a sufficiently large body of statistical data has been accumulated for heterojunctions in the energy interval $0\text{--}250\text{meV}$.

The observed point-contact spectra can be divided into two groups. The first group includes a very large number of spectra and contains second derivatives of IVC having peculiarities over the entire investigated range of voltages. The second group includes the curves $d^2V/dI^2(V)$ with the limiting EPI energies of $27\text{--}30\text{meV}$.

Let us consider the point-contact spectra characterizing the first group (Figure 1). It is characteristic for the $\text{Cu-}\beta\text{-(BEDT-TTF)}_2\text{I}_3$ heterocontacts to have a low frequency peak on the second derivative of IVC in the region of $17\text{--}18\text{meV}$ (curve 1) corresponding to EPI in copper [17]. For higher energies, the vibrational spectra of the organic material display a number of peculiarities. The lowest frequency peculiarity of the spectrum was recorded earlier in [17]. A detailed investigation revealed that this peculiarity is resolved into two peaks at energies $54\text{--}55$ and 75meV .

Measurements show that the recorded curves may have quite different shapes. For example, inversion-type curves are also observed in addition to the ordinary point-contact spectra. This may be due to the following reason. The electron parameters of $\beta\text{-(BEDT-TTF)}_2\text{I}_3$ crystals are close to those of semimetals (e.g., the Fermi velocities for Sb [18] and an organic conductor [19] are nearly the same). This can affect the point-contact parameters of organic conductor. Hence the possibility of observing effects typical of semimetals like Sb cannot be ruled out [20]. For example, if a contact is contaminated then due to a decrease in the momentum mean free path, the ballistic flight condition for electrons is violated and electron states can be localized in the region of the constriction. Delocalization due to EPI will increase the conductivity and lead to the emergence of inversion spectra [20, 21]. Curve 3 in Figure 1 is an example of such a dependence for homojunctions. This point-contact spectrum has three clear peculiarities, viz., a low-frequency minimum at 14meV corresponding to the interaction of charge carriers with iodine anion vibrations, and two high-frequency peculiarities associated with vibrational modes of organic molecules at $54\text{--}55$ and 75meV . The $\text{Cu-}\beta\text{-(BEDT-TTF)}_2\text{I}_3$ junctions often display spectra intermediate between classical and inverse spectra, i.e., those containing ordinary peaks as well as singularities with the opposite sign. Curve 2 in Figure 1 is an example of such a spectrum. This dependence has region in which $d^2V/dI^2(V) < 0$ and contains minima whose positions correlate with the peaks at 55 and 75meV in curve 1 (see Figure 1).

In many cases, a change is observed in the relative height of peaks on the second derivatives of IVC. Such a variation of intensities of the same peaks in different point-contact spectra can be due to a change in the conditions of electron flight through the constriction and to the behavior of the background

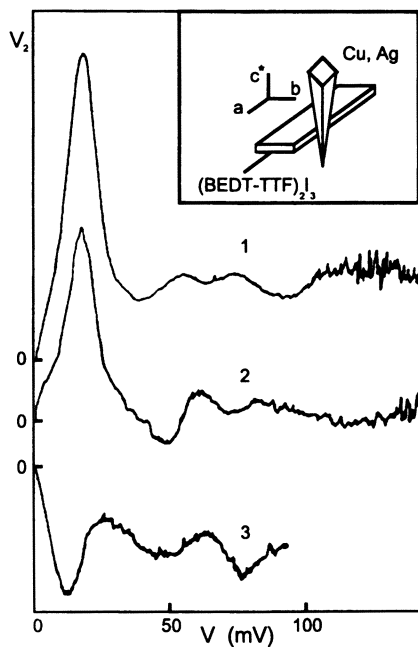


Figure 1. Point-contact spectra of an organic conductor belonging to the first group: 1, 2) heterojunctions Cu- β -(BEDT-TTF) $_2$ I $_3$, $R_0=420$ and 321Ω respectively; 3) homojunction with $R_0=186\Omega$.

function upon a transition from contact to contact, as well as a slight anisotropy of β -(BEDT-TTF)₂I₃ crystals in the *ab* plane which is manifested, in particular, in optical investigations [22].

We carried out a comparison with the data of optical investigation for curves recorded in a wider energy interval than for the dependences shown in Figure 1 and containing a number of additional peculiarities in the high-frequency region. One such curve is shown in Figure 2 (curve 1). In addition to the above-mentioned peculiarities, this point-contact spectrum also has peaks around 103, 134, 145, 170, and 200 meV corresponding to the organic metal. These singularities can be interpreted [23] easily by comparing the spectrum of reflection from the *ab* plane of the β -(BEDT-TTF)₂I₃ crystal in a polarization for which the vibrational transitions are manifested most clearly (e.g. along the direction $[1\bar{1}0]$). Such a spectrum, considered earlier in [24], is shown in Figure 2 (curve 2), which also contains the absorption spectrum (curve 3) of a monovalent insulating compound powder [25] (BEDT-TTF)I₃ composition, as determined by chemical analysis. This compound displays no electron transitions associated with free charge carriers and hence its vibrational structure can be observed very clearly.

A comparison of the point-contact and optical data reveals a good agreement of the positions of singularities. The difference in the shape and width of peaks on curve 1-3 can be due to thermal and modulation broadening of singularities on the point-contact spectra. A comparison of the curves shows that the transition at 54 meV correlates with the position of the doublet at 454 and 430 cm⁻¹, the peak at 103 meV practically coincides with the asymmetric band at 874 cm⁻¹, while the peak at 170 meV is close to the broad split band at 1300 cm⁻¹. High-intensity transitions at 1401, 1331, 490, and 476 cm⁻¹ are also clearly observed in the absorption spectrum of the insulating compound (BEDT-TTF)I₃ (see curve 3 in Figure 2). An analysis of the spectral properties of the monovalent salts (BEDT-TTF) [25] reveals that these bands have a vibronic origin and are manifested in the infrared spectrum of the dimerized structure as a result of interaction of completely symmetric vibrations ω_2 , ω_3 and ω_9 , ω_{10} with the charged localized on a molecule. These bands are not observed for neutral donor and become noticeable in the absorption spectrum of the complex due to the presence of open and partially overlapping electron shells in the molecules, as well as due to their dimerization. In this case, charge can be transferred between adjacent molecules in a dimer if they vibrate symmetrically and in antiphase. In the reflection spectra of conducting complexes, such bands are strongly broadened as a result of interaction with free charge carriers, and can be seen clearly against the background of high-intensity electron transitions. Apparently, these are the completely symmetric vibrations with the largest values of electron-vibrational interaction constants [25] that are manifested in point-contact spectra. In contrast to the intrinsic intramolecular vibrations (IMV) of the donor, the vibronic bands must be polarized along the direction of high conductivity of the crystal, i.e., parallel to the stacking axis in quasi-one-dimensional conductors, and in the *ab* plane in β -(BEDT-TTF)₂I₃ crystals on account of the anisotropy in the conducting properties characterising this plane.

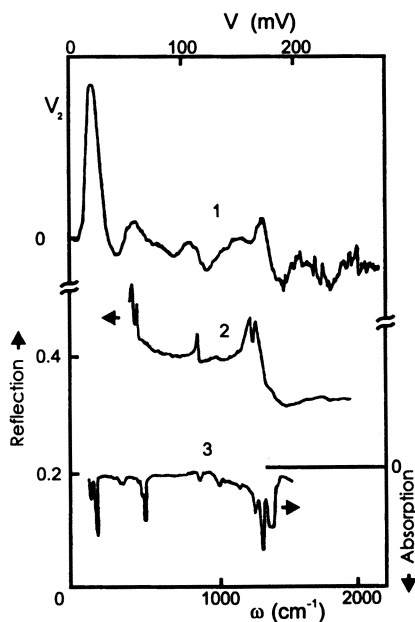


Figure 2. Comparison of point-contact and optical spectra: point-contact spectrum of the Cu- β -(BEDT-TTF) $_2$ I $_3$ heterojunction (curve 1) with $R_0=380\Omega$ at 4.2K; spectrum of reflection from the *ab* plane of the β -(BEDT-TTF) $_2$ I $_3$ crystal (curve 2 for light polarization corresponding to the direction of maximum conductivity ($T=295\text{K}$)); absorption spectrum of the (BEDT-TTF)I $_3$ powder in a pellet with KBr (curve 3) at $T=295\text{K}$.

The peak at 870cm^{-1} cannot be interpreted unambiguously. It may be of vibronic origin and be associated with the completely symmetric vibration ω_7 [25]. On the other hand, investigations carried out in [26] on the reflection spectra of conducting complexes based on the deuterioanalog of BEDT-TTF suggest that this singularity can be explained by antisymmetric vibration ω_{49} of the b_{2u} symmetry type. This vibration is found to be very intense due to the interaction of charge carriers with electron density oscillations between pairs of dimerized molecules.

The lower-intensity singularities in the point-contact spectra can apparently be due to the scattering of charge carriers by the IMV of the donor which interact weakly with the conduction electrons.

Figure 3 shows the dependences $d^2V/dI^2(V)$ characteristic of the second type of spectra. These dependences have peaks around 4 and 15meV, and do not contain the high-frequency singularities that are seen clearly in Figures 1 and 2. The spectral boundary lies in the region of 27-30meV. These curves are identical to the second derivatives of the IVC obtained in [27]. The peaks at 4 and 15meV in type II spectra can be explained, as in [27], by vibration at the anion, and correlate well with the position of bands in the Raman scattering spectrum of this compound at 30 and 120cm^{-1} [28]. These bands are due to the vibrational mode of Γ_3^- and the symmetric valence vibrations of the iodine atom respectively. It should also be remarked that the intense band at 139cm^{-1} and another weaker band near 110cm^{-1} were also observed in the absorption spectrum of the monovalent salt (see curve 3 in Figure 2). According to the conclusions drawn in [28], the former can be attributed to antisymmetric, and the latter to symmetric valent vibrations of atoms in Γ_3^- . However, the latter vibration is active in the Raman scattering spectrum and is manifested in IR measurements, probably due to deviation of the anion shape from linearity or symmetry. It is also possible that a dipole moment can emerge in this completely symmetric vibration as a result of a certain redistribution of the electron density between the donor and the acceptor due to displacement of Γ_3^- ions from their equilibrium positions.

A distinguishing feature of the point-contact spectra of the second type is the similarity of the second derivatives of IVC of homo- and heterocontacts (see Figure 3). That is due to the following reasons. In the ab plane of β -(BEDT-TTF) $_2\text{I}_3$, the electron Fermi velocity is $v_F \sim 10^7\text{cm/s}$ [19]. The sample conductivity in the direction normal to the ab plane is lower by 2-3 orders of magnitude. This leads to a much lower value of v_F at comparable relaxation times. Hence for heterojunctions oriented at right angles to the organic molecule layers, the intensity of peaks formed by EPI in the counterelectrode decreases considerably. Type II spectra of heterocontacts do not display such peculiarities. Hence the point-contact spectra of homo- and heterojunctions are found to be similar.

Taking into consideration an anisotropy of crystals and existence of two types of their spectra we have investigated characteristics of heterocontacts Cu- β -(BEDT-TTF) $_2\text{I}_3$ oriented along and perpendicular to the layers of organic molecules [29]. The experiments were carried out at the temperature of $T=4,2\text{K}$. The second derivatives of the I-V characteristics $d^2V/dI^2(V)$ were measured. The typical dependences are shown in Figure 4 for each contact orientation studied.

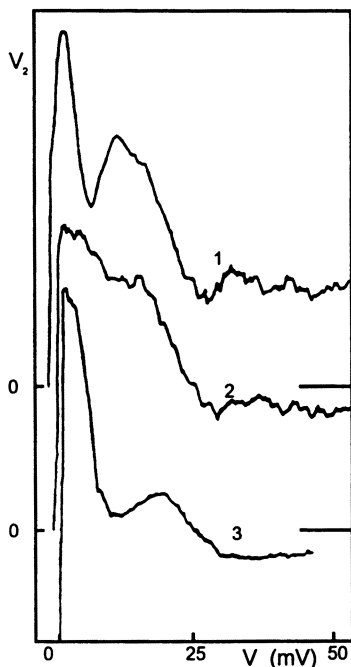


Figure 3. Point-contact spectra of organic conductors belonging to type II point contacts: 1) homojunction, $R_0=135\Omega$; 2) heterojunction $\text{Cu-}\beta\text{-(BEDT-TTF)}_2\text{I}_3$, $R_0=450\Omega$; 3) heterojunction $\text{Ag-}\beta\text{-(BEDT-TTF)}_2\text{I}_3$, $R_0=122\Omega$.

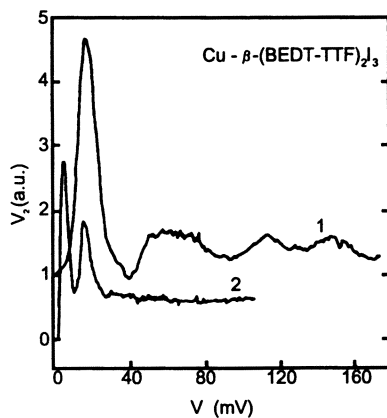


Figure 4. Point-contact spectra of the heterocontacts of an organic conductor $\beta\text{-(BEDT-TTF)}_2\text{I}_3$, typical of different orientations of contacts axis (a.u., arbitrary units): curve 1, contact axis in the plane of the layers of organic molecules; curve 2, contact axis perpendicular to the layers of organic molecules.

Curve 1 is for the samples with the current flow in the plane of the organic molecule layers. The spectra of the first type (curve 1) have features caused by the scattering processes both in copper and the organic metal. It is typical for the contacts discussed, to have a low-frequency maximum at 17 - 18 meV in the IVC second derivatives, which corresponds to the EPI in copper [17]. At higher energies some features of the vibrational spectrum of the organic metal are observed. The point-contact spectra of this type have maxima at 54-55, 103, 134 and 145meV (the measurements were carried out up to 150 - 160 meV). As comparison of point-contact data and optical reflection and absorption spectra shows, the above maxima are of the vibron nature and have the highest constants of electron-vibration interaction.

The contacts of the other type were formed by touching of β -(BEDT-TTF)₂I₃ plane with a copper needle point. Their preferential orientation was along the c^* axis of the organic crystal, i.e. perpendicular to the layers of organic molecules. The point-contact spectra of these samples differ considerably from the dependences of the first type. The point-contact spectra of the second type have maxima at 4 and 15meV. They do not show the high-frequency features pronounced in curve 1. The spectra boundaries are at about 27 to 30meV. The $d^2V/dI^2(V)$ dependencies for the contacts of this orientation are similar to those in Figure 3.

The absence of the components contributed by intramolecular vibrations of the donor in the point-contact spectra of the second type is quite reasonable assuming that the charge transfer direction in such samples is normal to the BEDT-TTF layers. Indeed, theory [30] does not anticipate the strong interaction between the molecule vibrations and the electron transition if they occur within the same plane. A much larger contribution is expected from the linear anions I₃⁻ nearly normal to BEDT-TTF, which was just observed in our experiment.

Thus, two types of point-contact spectra are observed in the organic metal crystal β -(BEDT-TTF)₂I₃. Point-contact spectra of the first type corresponding to the carriers transfer in the ab plane have pronounced features caused by the interaction between the current carriers and the intramolecular vibrations of the donor. Spectra of the second type, measured on the contact with axis perpendicular to the BEDT-TTF layers have maxima related to the anion I₃⁻ and no maxima which might be ascribed to the intramolecular vibrations of the donor.

The interesting peculiarity of the β -(BEDT-TTF)₂I₃ organic metal is that it is transformed under a certain pressure to a new crystalline state with a superconducting transition temperature of about 8K. Therefore, increasing the confining force between the contacting electrode, we can produce local stresses exceeding the threshold value and leading to the emergence of a region with higher values of critical parameters in the surface layer of the organic metal in the vicinity of the contact. As a result, we shall be able to observe a transition from the N-c-N type contact to the S-c-N type contact at 4,2K. We succeeded in realizing this situation by reducing the resistance of contacts to 1-5 Ω . An analysis of the characteristics of such contacts was carried out in the normal and superconducting states for different values of the magnetic field H .

An increase in the pressure between the electrodes leads to the emergence of contacts with the $d^2V/dI^2(V)$ dependences of the thermal type in the normal state (Figure 5, curve 1). The most probable reason of the emergence of such characteristics under given experimental conditions is plastic deformation of the material in the contact region. It is well known (see, for example, [31]) that the magnitude of the confinement force plays an important role in the formation of different types of point contacts. The forces below the elastic limit of the materials in contact are favorable to producing contacts corresponding to the spectral modes of current flow. The forces exceeding the elastic limit lead to plastic deformation and to an increase in the defect concentration in the contact region. Therefore, the conditions $d^{1/2} >> l_p (l_{l\epsilon})$ of the thermal model of current flow are realized, which affects the behavior of the second derivative of IVC. The following circumstance is also worth noting. During plastic deformation and recrystallization of metals, dislocations of the twinning plane type are formed. This can be regarded as an additional proof of the possibility of emergence of a superconducting region in a contact under investigation since an increase in the critical temperature of the organic metal is associated with twinning [24, 32].

The $I(V)$ and $d^2V/dI^2(V)$ dependences of such contacts in the superconducting state are similar to the characteristics of contacts with a superconducting inclusion of the N-S-c-N type, which was studied in [33]. It is shown in [34] that the minimum energy value for which a peak on the $dV/dI(V)$ dependence was observed determines the energy gap of peaks in the superconducting phase. Assuming that such a situation takes place in our case also, we can estimate the value of Δ and the ratio $2\Delta/kT_c$. The energy gap was determined from the midpoint of the distance between the positions of the s-shaped singularity on the $d^2V/dI^2(V)$ dependence (which correspond to the peak on the first derivative of IVC of the contact) in zero magnetic field. An increase in the magnetic field caused a displacement of this singularity and a decrease in the energy gap of the superconductor. For curve 2 in Figure 5, we have $\Delta=1.5meV$ and $2\Delta/kT_c=4.1$.

The IVC of such contacts in superconducting and normal states differ, as expected, by the excess current I_{exc} . For a dirty S-c-N contact, we have $I_{exc}eR_0/\Delta=0.73$ [35], where R_0 is the static resistance of the heterojunction in the normal state for $V=0$. For curve 3 in Figure 5, we have $I_{exc}eR_0/\Delta=0.06$. The small value of the excess current as compared to the theoretical value is due to the fact that only a fraction of the N-S boundary of a superconducting inclusion contributes to the point contact current because of a large distance from the centre of the contact.

[(C₂H₅)₄N]_{0.5}[Ni(dmit)₂]. One of the key problems of utmost importance for explaining superconductivity in organic compounds is associated with the role of intramolecular vibration (IMV) which are not observed in ordinary metals. Yamaji [36] proposed a superconductivity mechanism for organic metal involving an IMV donor. Subsequently, various methods were used [17,23,24] to obtain data indicating the possibility of operation of such a mechanism in BEDT-TTF salts. For example, a strong interaction between conduction electrons and IMV of an organic conductors was observed [17, 23]. These results lead to the conclusion that the IMV contribution to the formation of the superconducting

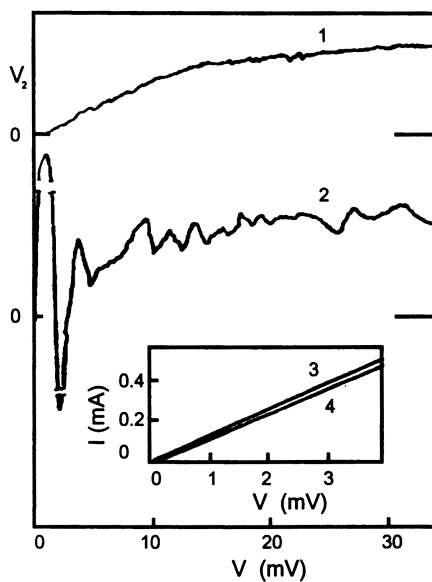


Figure 5. Dependences V_2 vs. $d^2V/dI^2(V)$ and $I(V)$ for the (BEDT-TTF)₂I₃-Cu contact; $R_0=4.1 \Omega$, $T=4.2 \text{ K}$: $V_2(V)$, $H\sim 6 \text{ kOe}$ (1); $V_2(V)$, $H=0$ (2); $I(V)$, $H=0$ (3); and $I(V)$, $H\sim 6 \text{ kOe}$ (4). Curves 1 and 2 are plotted to the same scale.

phase of such compounds can be significant. The variation of the intensity of such processes upon a transition from one compound to another and their correlation with the superconducting properties of the materials remain unclear. It is logical to assume that if the IMV contribution to the formation of the EPI in organic conductors is significant, the intensity of the electron-vibrational interaction (EVI) can correlate with the superconducting parameters of the material (in particular, the superconducting transition temperature T_c). In other words, materials with a higher T_c must display a higher intensity of interaction between conduction electrons and the IMV of the organic conductor, and *vice versa*. For this reason, it would be interesting to compare the results of measurements of EPI spectra with the values of T_c in different organic compounds. In order to simplify the problem, it is expedient to use first organic compounds with close compositions and structures, such as, for example, compounds belonging to families based on $[\text{BEDT-TTF}]^{n+}$ and $[\text{M}(\text{dmit})_2]^{n-}$ (M stands for metal and $\text{dmit}=\text{C}_3\text{S}_5$). Since the superconducting transition temperatures for such compounds are known as a rule, it is sufficient to study the EPI spectra of the objects under investigation. It should also be noted that the EPI data for organic compounds from the $\text{M}(\text{dmit})_2$ family are scarce or not available at all, and hence the measurement of EPI spectra for such materials forms an independent problem which is interesting itself.

We chose as objects of investigation the compound $\beta\text{-(BEDT-TTF)}_2\text{I}_3$ and one of organic conductors $[(\text{C}_2\text{H}_5)_4\text{N}]_{0.5}[\text{Ni}(\text{dmit})_2]$. Heterojunctions of $\text{Cu}-[(\text{C}_2\text{H}_5)_4\text{N}]_{0.5}[\text{Ni}(\text{dmit})_2]$ and $\text{Cu-(BEDT-TTF)}_2\text{I}_3$ were studied at $T=4.2\text{K}$. Contact axes were oriented along anionic planes in the case of $[(\text{C}_2\text{H}_5)_4]_{0.5}[\text{Ni}(\text{dmit})_2]$ and along cation planes in the case of $\beta\text{-(BEDT-TTF)}_2\text{I}_3$, i.e. in the direction corresponding to the highest conducting properties of the organic crystal. It was proved in [29, 37] that, for contacts with the axis in the plane of organic molecules the contribution from the transverse component has the minimum value in this case. For this reason, peculiarities associated with the scattering of charge carriers in a highly conducting plane of organic molecules are manifested with the highest probability and have the maximum intensity. Accordingly, the effect of EVI on the point-contact spectrum is the strongest in this case. Consequently, in order to analyze the manifestations of the IMV contribution to the point-contact spectrum and its correlation with the conducting properties of organic metals, it is sufficient to study the characteristic of junctions oriented along conducting layers.

Let us first consider the results obtained for the compound from family $\text{M}(\text{dmit})_2$. The point-contact spectra of $\text{Cu}-[(\text{C}_2\text{H}_5)_4]_{0.5}[\text{Ni}(\text{dmit})_2]$ junctions contain the superposition of contribution from copper and the organic metal. The contribution from copper has the form of a high-intensity low-energy peak at 17-18meV due to the interaction of conduction electrons with transverse acoustic phonons.

Singularities of the second derivatives of IVC of the contacts under investigation for an energy above 32meV (the boundary energy for the EPI spectrum of copper) correspond to the interaction of charge carriers with the vibrational modes of the organic conductor. The most clearly pronounced singularities are peaks corresponding to the energies 56-58, 70, 84, and 96meV. Singularities at higher frequencies could not be observed since the material

heating effects in the constriction region at voltages $V > 100 \text{ mV}$ led to the loss of stability of the junctions, changes in their resistance, or complete breakdown.

The shape of singularities of point-contact spectra for $\text{Cu}-[(\text{C}_2\text{H}_5)_4]_{0.5}[\text{Ni}(\text{dmit})_2]$ junctions depends on the condition of electron passage through the point-contact much more strongly than in the case of junctions between traditional conductors. As a matter of fact, the organic conductor $[(\text{C}_2\text{H}_5)_4]_{0.5}[\text{Ni}(\text{dmit})_2]$ as well as $\beta\text{-(BEDT-TTF)}_2\text{I}_3$ is close in electronic parameters to semimetals [38, 19]. As it was already mentioned above, a typical feature of such materials is the existence of point-contact spectra with opposite singularities, namely, along with ordinary ("direct") dependences, inverse spectra, i.e., the second derivatives of IVC of contacts with the opposite sign, can be observed in some cases [20, 23]. Inverse spectra are typical in the case of small inelastic mean free paths for electrons, as a result of which electron states can be localized in the region of constriction [21]. The EPI disturbs the localization of electrons and leads to an increase in the conductivity of the contact (accordingly, a decrease in its resistance), which is registered as a minimum on the second derivatives of IVC (in contrast to the peak in the case when the contact resistance increases). The accumulation of phonons in the constriction region upon an increase in voltage can also lead to a decrease in the mean free path in the contact region. In this case, the mode of the passage of electrons through the contact changes from the ballistic to diffusion mode for which weak localization effects play a significant role. This must naturally affect the behavior of singularities in the point-contact spectrum. As a result, point-contact spectra of an intermediate type appear (with inverse singularities at high voltages). Curve 3 in Figure 6 can serve as an example of a characteristic. It contains a number of minima corresponding to peaks at energies 56-58, 70, and 84 meV on curves 1 and 2 and being their mirror images relative to the abscissa axis. The small variation of the position of singularities on the curves can easily be explained. Curves of the type 3 are characterized by the background function which obviously differs from the background function in the case of a "direct" spectrum. The summation of the spectral function and the background function in the (opposite) cases under consideration will probably lead to different displacement of peaks on the EPI spectra, which called to a certain mismatching in the position of EPI peaks on different types of spectrum.

The experimental setup for $\text{Cu}-\beta\text{-(BEDT-TTF)}_2\text{I}_3$ junctions was similar to that used for the conductor $[(\text{C}_2\text{H}_5)_4]_{0.5}[\text{Ni}(\text{dmit})_2]$. Let us consider point-contact EPI function, obtained from the second derivatives of contacts of the materials under investigation. We selected for calculations five most intense (according to preliminary estimates) point-contact spectra of heterojunctions of organic conductors under investigation. Typical dependences of normalized point-contact EPI function for each material are shown in Figure 7. The values of mean $\langle \omega \rangle$ and root-mean-square $\langle \omega^2 \rangle^{1/2}$ frequencies of vibrations are 13.54, 17.803 and 15.86, 15.414 for the first and second curve respectively. The plots of the functions g_{pc} make it possible to estimate the contribution of the EVI to the point-contact spectrum. It can be seen from the figure that the intensity of high-frequency peaks corresponding to the interaction of electrons with IMV on curve 1 is much higher than the intensity of similar singularities on curve 2. This

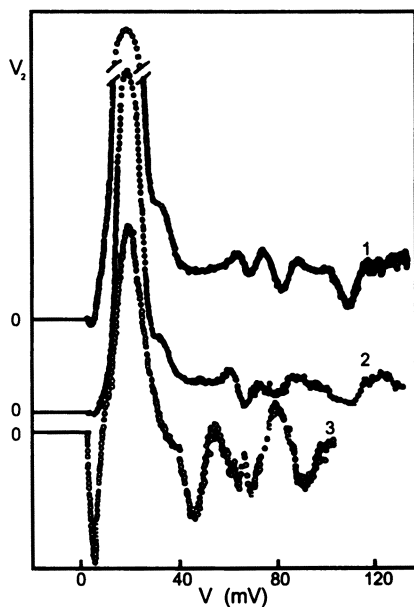


Figure 6. Point-contact spectra for $\text{Cu}-[(\text{C}_2\text{H}_5)_4]_{0.5}[\text{Ni}(\text{dmit})_2]$ heterojunction for R_0 , Ω : 48 (curve 1), 60 (curve 2), and 130 (curve 3).

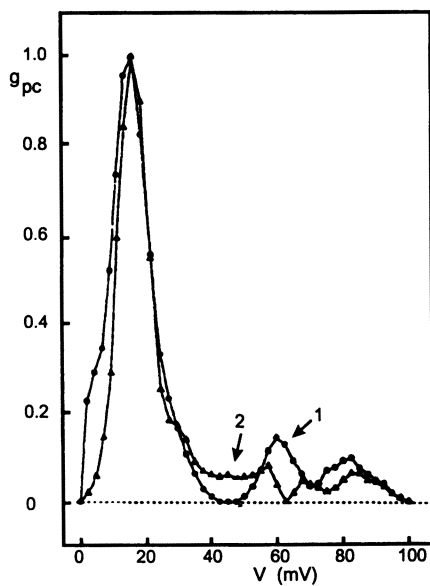


Figure 7. Point-contact function of electron-phonon interaction for heterojunction $\text{Cu}-(\text{BEDT-TTF})_2\text{I}_3$ (dark circles, curve 1) and $\text{Cu}-[(\text{C}_2\text{H}_5)_4]_{0.5}[\text{Ni}(\text{dmit})_2]$ (dark triangles, curve 2).

speaks in favor of a considerably larger contribution of the EVI to the point-contact spectrum for (BEDT-TTF)₂I₃ than in the case of [(C₂H₅)₄][Ni(dmit)₂].

Our results also correlate with the results of optical investigations [39] in which it was noted that the intensity of the peak at 1300cm⁻¹ in optical reflection spectra for M(dmit)₂ salts is much lower than the intensity of corresponding singularities in the salts (BEDT-TTF) with a charge transfer. This might indicate a lower EVI level in such materials. If we take into account the assumption that IMV make a certain contribution to the formation of the superconducting phase of such materials, it is not surprising that (BEDT-TTF) salts are superconducting, while most of M(dmit)₂ compounds are normal metals, and only some of them transit to the superconducting state under pressure [38]. Thus, a correlation is observed between EVI intensity and the superconducting transition temperature of the organic compounds under investigation.

Taking into account said above, it is natural to assume, in view of the correlation between the intensity of the point-contact spectra and the value of T_c, that the EVI level can serve as a criterion for the synthesis of new organic conductors. This is especially important for families of organic conductors for which superconducting properties are expected, but the values of T_c for whose known representatives are difficult to measure. Consequently, by measuring the EPI spectra for materials with a close composition and observing their variation in a series of analogous materials, we can predict the synthesis of new organic conductors belonging to this series. Since the search for new superconductors among organic materials is often carried out for analogs of a certain specific family, and the synthesis of each new compound takes quite a long time, the proposed criterion can help to reduce considerably the range of the search and hence to save the required time of investigation.

Literature Cited

1. Yanson I.K., *Zh. Eksp. Teor. Fiz.* **1974**, *66*, 1035; *Sov Phys. JETP* **1974**, *39*, 506.
2. Kulik I.O., Omelyanchouk A.N., and Shekhter R.I., *Fiz. Nizk. Temp.* **1977**, *3*, 1543; *Sov. J. Low Temp. Phys.* **1977**, *3*.
3. Bobrov N.L., Rybalchenko L.F., Khotkevich A.V., Chubov P.N., and Yanson I.K., USSR Inventors Certificate No.1631626, Bull. No.8, **1991**.
4. Muller C.J., van Ruitenbeek J.M., and de Jonge L.J., *Physica C* **1992**, *191*, 485.
5. Kulik I.O., *Fiz. Nizk. Temp.* **1985**, *11*, 937; *Sov. J. Low Temp. Phys.* **1985**, *11*, 516.
6. Khotkevich A.V., and Yanson I.K., *Atlas of point contact spectra of electron-phonon interactions in metals*. - Kluwer Academic Publishers: Boston/Dordrecht/London 1995 168 p.
7. Kulik I.O., and Omelyanchouk A.N., *Fiz. Nizk. Temp.* **1978**, *4*, 296; *Sov. J. Low Temp. Phys.* **1978**, *4*, 142.
8. Naidyuk Yu.G., von Lohneysen H., and Yanson I.K., *Phys. Rev. B* **1996**, *54*, 16077.

9. Zaitsev A.N., *Zh. Eksp. Teor. Fiz.* **1980**, 78, 221; *Sov. Phys. JETP* **1980**, 51, 111.
10. Yanson I.K., Kamarchuk G.V., and Khotkevich A.V., *Fiz. Nizk. Temp.* **1984**, 10, 415; *Sov. J. Low Temp. Phys.* **1984**, 10, 220.
11. Kamarchuk G.V., and Khotkevich A.V., *Fiz. Nizk. Temp.* **1987**, 13, 1275; *Sov. J. Low Temp. Phys.* **1987**, 13, 717.
12. Khlus V.A., *Fiz. Nizk. Temp.* **1983**, 9, 985; *Sov. J. Low Temp. Phys.* **1983**, 9, 510.
13. Khlus V.A., and Omelyanchouk A.N., *Fiz. Nizk. Temp.* **1983**, 9, 373; *Sov. J. Low Temp. Phys.* **1983**, 9, 189.
14. Omelyanchouk A.N., Beloborod'ko S.I., and Kulik I.O., *Fiz. Nizk. Temp.* **1988**, 14, 1142; *Sov. J. Low Temp. Phys.* **1988**, 14, 630.
15. Khotkevich A.V., Yanson I.K., Khotkevich V.V., and Kamarchuk G.V., *Fiz. Nizk. Temp.* **1990**, 16, 1199; *Sov. J. Low Temp. Phys.* **1983**, 16.
16. Chubov P.N., Yanson I.K., and Akimenko A.I., *Fiz. Nizk. Temp.* **1982**, 8, 64; *Sov. J. Low Temp. Phys.* **1982**, 8, 32.
17. Kamarchuk G.V., Pokhodnya K.I., Khotkevich A.V., and Yanson I.K., *Fiz. Nizk. Temp.* **1990**, 16, 711; *Sov. J. Low Temp. Phys.* **1990**, 16, 419.
18. Winamiller L.R., *Phys. Rev.* **1966**, 149, 472.
19. Bulaevskii L.N., *Adv. Phys.* **1988**, 37, 443.
20. Yanson I.K., Gribov N.N., and Shklyarevskii O.I., *Pis'ma Zh Eksp. Teor. Fiz.* **1985**, 42, 159; *JETP Lett.* **1985**, 42, 195.
21. Itskovich I.F., Kulik I.O., and Shekhter R.I., *Fiz. Nizk. Temp.* **1987**, 13, 1166; *Sov. J. Low Temp. Phys.* **1987**, 13, 659.
22. Kaplunov M.G., Yagubskii E.B., Rosenberg L.P., and Borodko Yu.G., *Phys. Stat. Sol. (a)*. **1985**.
23. Kamarchuk G.V., Khotkevich A.V., Kozlov M.E., and Pokhodnya K.I. *Fiz. Nizk. Temp.* **1992**, 18, 967; *Sov. J. Low Temp. Phys.* **1992**, 18, 679
24. Kozlov M.E., Baran N.P., and Pokhodnya K.I., *Fiz. Nizk. Temp.* **1989**, 15, 574; *Sov. J. Low Temp. Phys.* **1989**, 15, 323.
25. Kozlov M.E., Pokhodnya K.I., and Yurchenko A.A., *Spectrochim Acta* **1989**, A45, 437.
26. Kornelsen K., Eldridge J., Wang H.H., and Williams J.M., *Solid State Commun.* **1990**, 74, 501.
27. Nowack A., Poppe U., Weger M., Schweitzer D., and Schwenk H., *Z.Phys.B* **1987**, 68, 41.
28. Swietlik R., Schweitzer D., and Keller H.J., *Phys. Rev. B* **1987**, 36, 6881.
29. Kamarchuk G.V., Khotkevich A.V., Kolesnichenko Yu.A., Porhodnya K.I. and Tuluzov I.G., *J.Phys.:Condens. Matter* **1994**, 6, 3559.
30. Lipari N.O., Rice M.J., Duke C.B., Bozio R., Girlando A., and Pecile C., *Int. J. of Quantum Chem: Quantum Chem. Symp.* **1977**, 11, 583.
31. Yanson I.K., Kulik I.O., and Batrak A.G., *J.Low Temp. Phys.* **1981**, 42, 527.
32. Zvarykina A.V., Kartsovnik M.V., Laukhin V.N. et al., *Zh. Eksp. Teor. Fiz* **1988**, 94(9), 277; *Sov.Phys. JETP* **1988**, 67, 1891.
33. Shklyarevskii O.I., Gribov N.N., and Naidyuk Yu.G., *Fiz. Nizk. Temp.* **1983**, 9, 1068; *Sov. J. Low Temp. Phys.* **1983**, 9, 553.

34. Sh.klyarevskii O.I. Yanson I.K., and Gribov N.N., *Fiz. Nizk. Temp.* **1988**, *14*, 479; *Sov. J. Low Temp. Phys.* **1988**, *14*, 263.
35. Artemenko S.N., Volkov A.F., and Zaitsev A.V., *Zh. Eksp. Teor. Fiz* **1979**, *76*, 1816; *Sov. Phys. JETP* **1979**, *49*, 924.
36. Yamaji K., *Solid State Commun.* **1987**, *61*, 413.
37. Kolesnichenko Yu.A., Tuluzov I.G., and Khotkevich A.V., *Fiz. Nizk. Temp.* **1993**, *19*, 402; *Sov. J. Low Temp. Phys.* **1993**, *19*, 282.
38. Kajita K., Nishio Y., Moriyama S., Kato R., Kobayashi H., Sasaki W., Kobayashi A., Kim H. and Sasaki Y., *Solid State Commun.* **1988**, *65*, 361.
39. Tajima H., Naito T., Tamura M., Kobayashi A., Kuroda H., Kato R., Kobayashi H., Clark R.A., and Underhill A.E., *Solid State Commun.* **1991**, *79*, 337.

Chapter 15

Persistent Photoconductivity in High- T_c Superconductors

Axel Hoffmann¹, Z. F. Ren², J. Y. Lao², J. H. Wang², D. Girata³, W. Lopera⁴, P. Prieto⁴, and Ivan K. Schuller¹

¹Department of Physics, University of California at San Diego, 9500 Gilman Drive, La Jolla, CA 92093-0319

²State University of New York at Buffalo, Buffalo, NY 14260-3000

³Universidad de Antioquia, Medellin, Colombia

⁴Universidad del Valle, Cali, Colombia

Persistent photoconductivity is an interesting and unusual property of high T_c superconductors. Underdoped $\text{YBa}_2\text{Cu}_3\text{O}_{6+\delta}$ shows upon illumination a decrease of resistivity and an increase of T_c . These photo-induced changes are persistent at low temperatures and relax at room temperatures. A possible model for persistent photoconductivity in these materials is that electrons of photoinduced electron-hole pairs are trapped at localized states spatially separated from the conduction layer. We recently measured persistent photoconductivity in $\text{Tl}_2\text{Ba}_2\text{CuO}_{6+\delta}$ and Y-doped $\text{Bi}_2\text{Sr}_2\text{CaCu}_{8+\delta}$, which indicates that persistent photoconductivity might be a common phenomena in high- T_c superconductors.

One of the interesting features of the high- T_c cuprates is, that their superconducting and normal state properties can be changed by varying their carrier concentration. Typically this is accomplished by chemical doping, where either one cation is substituted by another one (e.g. Sr for La in $\text{La}_{2-x}\text{Sr}_x\text{CuO}_4$), or the oxygen-stoichiometry is varied (e.g. $\text{YBa}_2\text{Cu}_3\text{O}_{6+\delta}$). Furthermore it is possible to change the carrier concentration in some of the high- T_c superconductors by illumination, and thus “photodope” these materials. This persistent photoconductivity (1) and persistent photoinduced superconductivity (2) was first observed in $\text{RBa}_2\text{Cu}_3\text{O}_{6+\delta}$ (R = rare earth or yttrium), and recently also in cuprates without CuO chains, such as $\text{Tl}_2\text{Ba}_2\text{CuO}_{6+\delta}$ (3) and Y-doped $\text{Bi}_2\text{Sr}_2\text{CaCu}_{8+\delta}$.

This article will be structured as follows. First we will review the persistent photoconductivity and persistent photoinduced superconductivity as it is observed in $\text{RBa}_2\text{Cu}_3\text{O}_{6+\delta}$ and discuss theoretical models for this effect. Following we will present more recent data on similar effects in chainless cuprates and discuss the implications of these results.

Persistent Photoinduced Effects in $RBa_2Cu_3O_{7-\delta}$

Due to the finite penetration depth of light (typically 1000 Å) all photoconductivity measurements were made on thin films. *C*-axis oriented $RBa_2Cu_3O_{7-\delta}$ thin films were grown using magnetron sputtering on (100) MgO and (100) SrTiO₃ substrates (4). After growth these samples were fully oxygenated ($\delta \approx 0$). In order to prepare $RBa_2Cu_3O_{6+\delta}$ thin films with a specific oxygen content ($\delta > 0$), they were annealed at 500° C following pressure-temperature curves for a specific stoichiometry of the phase diagram (5). After annealing the oxygen content was determined by the *c*-axis parameter (δ) measured by high resolution X-ray diffraction and by T_c (7) for the superconducting films.

The resistivity measurements were done with a four probe technique, with the sample either directly immersed in liquid nitrogen, in a close cycle refrigerator, or in a He-flow cryostat, each equipped with optical quartz windows. For the illumination several different light sources were used. Most of the excitation measurements were done using a halogen lamp or an Ar laser ($\lambda = 514$ nm), with a typical power density at the sample surface of 1 Wcm⁻². For measuring spectral dependencies a 1000 W Hg-Xe arc lamp was used with an infrared water filter to protect the sample and the optics from excessive heating. Specific wavelengths in the range 250–900 nm were chosen with interference band-pass-filters having a bandwidth of 10 nm. Using this setup the power density of monochromatic light ranged between 0.04 and 5 mWcm⁻². After each light excitation the sample was relaxed at room temperature while monitoring the resistivity to determine when the sample was fully relaxed.

Basic Effect. The basic effect of illumination on the resistivity and T_c is shown in Figure 2 for an underdoped GdBa₂Cu₃O_{6.45} film. Before illumination the temperature dependence of the resistivity shows a minimum and an onset of superconductivity at roughly 20 K. After white light illumination for 8 h at 95 K, the lamp is turned off and the resistance is measured again as a function of temperature. The resistance changes such that the normal state resistance is metallic, decreases substantially and the T_c increases by more than 10 K. Notice that the change in resistivity and T_c is not due to heating, since the illumination is stopped during the measurement and heating would increase the resistivity and decrease the T_c . Furthermore this photoinduced change of T_c is remarkably different from the effect of illumination on a low T_c superconductor, which causes a deterioration of the superconducting properties due to pairbreaking (8).

Excitation and Relaxation. These photoinduced changes in $RBa_2Cu_3O_{6+\delta}$ thin films are persistent if the sample is kept at low temperatures (≤ 100 K), and relax if the sample is warmed up to room temperature. The time dependence of the excitation and of the relaxation is shown in Figure 1. For the excitation, the light source was switched on at $t = 0$, while the sample was kept at 95 K. For the relaxation, the temperature was raised from 95 to 300 K in about 12 min near $t = 0$. The time dependence of both the excitation and the relaxation follows a stretched exponential, which is given by (9):

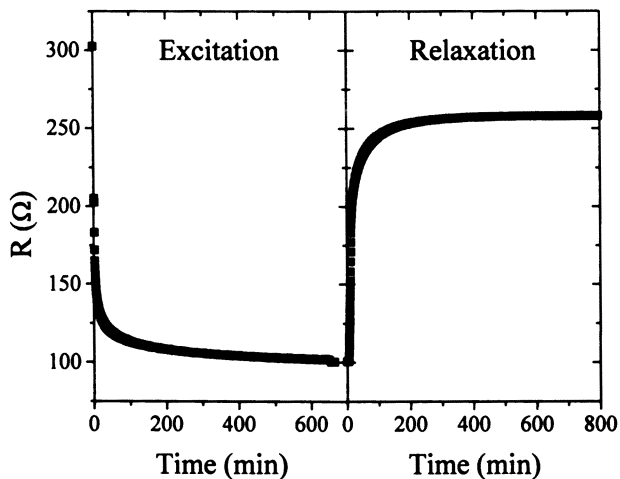


Figure 1. Time dependence of the excitation and relaxation of persistent photoconductivity in $\text{GdBa}_2\text{Cu}_3\text{O}_{6.4}$ film (Reproduced with permission from reference 10. Copyright 1995.)

$$\rho(t) = \rho(t = \infty) + \Delta\rho_{\max} \exp\left[-\left(t/\tau\right)^\beta\right]. \quad (1)$$

Here $\Delta\rho_{\max} = \rho(t=0) - \rho(t=\infty)$ is the difference between the initial and the saturation resistivity, τ is a characteristic excitation or relaxation time, and β is a dispersion parameter $0 < \beta < 1$. The relaxation shows a thermal activated behavior with an energy barrier of 0.9 ± 0.1 eV (9). Besides this thermal relaxation it is also possible to partially

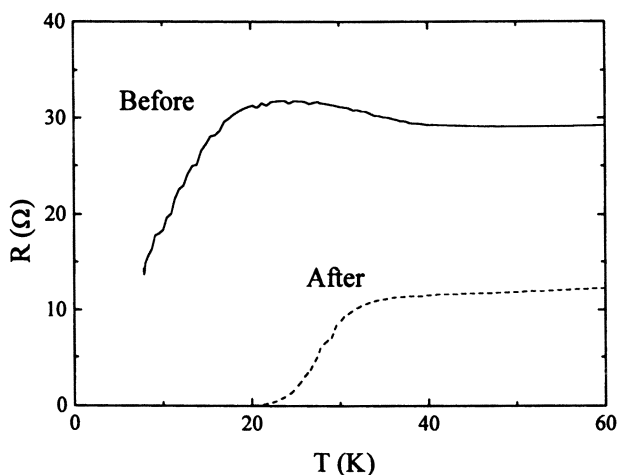


Figure 2. Temperature dependence of the resistance for a $\text{GdBa}_2\text{Cu}_3\text{O}_{6.45}$ film before (solid line) and after (dashed line) illumination (Reproduced with permission from reference 10. Copyright 1995.)

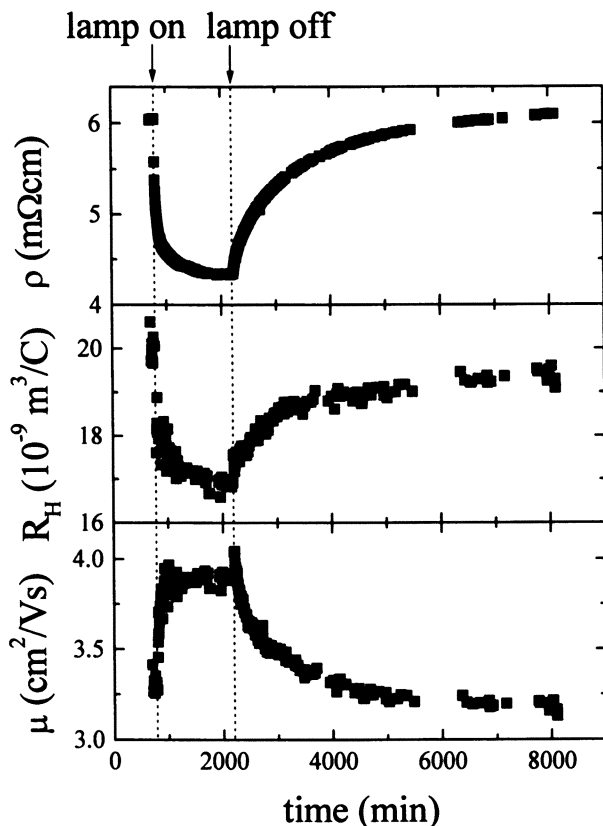


Figure 3. Time dependence of the resistivity ρ , Hall coefficient R_H , and Hall mobility $\mu = c(|R_H|/\rho)$ during excitation and relaxation in an $\text{YBa}_2\text{Cu}_3\text{O}_{6.5}$ film (Reproduced with permission from reference 12. Copyright 1992 American Physical Society.)

quench ($\approx 5\%$) the persistent photoconductivity using infrared light (0.8–1.3 eV) (11).

Other Photoinduced Changes. In addition to the decrease in the resistivity there are also photoinduced changes in the Hall coefficient R_H and the Hall mobility $\mu = c(|R_H|/\rho)$ (12). These changes are shown in Figure 3 for an $\text{YBa}_2\text{Cu}_3\text{O}_{6.5}$ film measured at room temperature. Clearly both R_H and μ have the same time dependence during excitation and relaxation as ρ . In a simple one band model, the Hall coefficient R_H is inversely proportional to the carrier density. Thus the data in Figure 3 suggest that the carrier density increases, which results in a decrease in resistivity. In addition the Hall mobility μ changes and contributes to the variation in the resistivity ρ (12). These variations in the transport properties are also accompanied by a change of the c -axis (13). Upon illumination the c -axis contracts, which is contrary to thermal expansion due to heating. Interestingly, all the observed photoinduced effects are similar to changes due to increased oxygen doping in $\text{R}\text{Ba}_2\text{Cu}_3\text{O}_{6+\delta}$ (14).

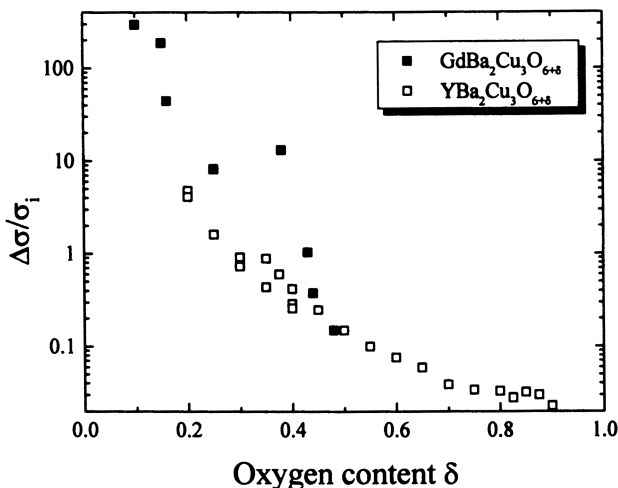


Figure 4. Relative change in conductivity $\Delta\sigma/\sigma_1$ as a function of oxygen content x of $RBa_2Cu_3O_{6+\delta}$. Solid symbols refer to $GdBa_2Cu_3O_{6+\delta}$, while open symbols refer to $YBa_2Cu_3O_{6+\delta}$ (Reproduced with permission from reference 15. Copyright 1995 American Physical Society.)

Doping Dependence. As shown above, the photoinduced effects in $RBa_2Cu_3O_{6+\delta}$ films are remarkably similar to oxygen doping effects. Also it has been shown that persistent photoconductivity only occurs in $RBa_2Cu_3O_{6+\delta}$ if there are oxygen vacancies in the CuO chains (13). Therefore it is interesting to take a look at the influence of oxygen stoichiometry on the persistent photoconductivity in these materials. In Figure 4 the saturation conductivity change after illumination at 95 K is shown as a function of oxygen content δ . The data is normalized to the conductivity before illumination σ_1 , since the conductivity decreases strongly with decreasing oxygen content δ . From Figure 4 it is clear that the photoinduced effect is strongly enhanced for fully deoxygenated $RBa_2Cu_3O_{6+\delta}$ (15).

Spectral Dependence. Early measurements of the spectral dependence of persistent photoconductivity in $RBa_2Cu_3O_{6+\delta}$ showed an onset at 1.6 eV (9,16). We extended the measurement of the spectral dependence into the UV region, which is shown in Figure 5. It has been shown that for a given wavelength, the magnitude of the photoinduced effects depends only on the incident photon dose

$$n = \frac{I \times t}{\hbar\omega}, \quad (2)$$

where I is the light intensity at the sample surface; t the measurement time, and $\hbar\omega$ the photon energy. The spectral efficiency in Figure 5 is given by $1/n'$, where n' is the photon dose necessary for a 2% reduction of the resistivity. Notice that $1/n'$ is proportional to the spectral efficiency η defined by Kudinov *et al.* (9):

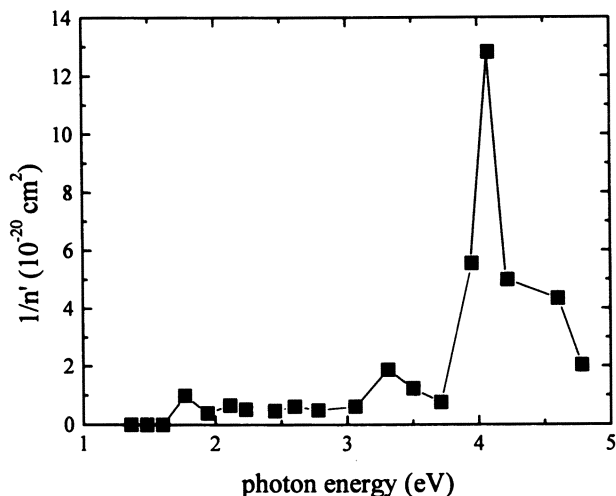


Figure 5. Spectral efficiency of the persistent photoconductivity for $\text{GdBa}_2\text{Cu}_3\text{O}_{6.3}$ (Reproduced with permission from reference 17. Copyright 1996 American Physical Society.)

$$\eta(\hbar\omega) = \frac{1}{R(0)} \left. \frac{\partial R(n)}{\partial n} \right|_{(n=0)} \quad (3)$$

It is worthwhile to mention, that there has been also observed an effect similar to persistent photoconductivity in $\text{YBa}_2\text{Cu}_3\text{O}_{6.0}$ upon irradiation with X-rays (18).

There are two features of the spectral dependence, which are remarkable. First the persistent photoconductivity shows an onset at 1.6 eV. Below 1.6 eV there is essentially no change of the resistivity upon illumination. This energy corresponds to the charge transfer gap in insulating $\text{YBa}_2\text{Cu}_3\text{O}_{6.1}$ as observed with optical absorption measurements (19). Interestingly this charge transfer gap vanishes in optical absorption measurements with increased doping (19), while it is still clearly resolved in photoconductivity measurements even for superconducting $\text{YBa}_2\text{Cu}_3\text{O}_{6+\delta}$ samples (9,16,20). This means that there are only localized states below 1.6 eV.

The second striking spectral feature is the peak of the spectral efficiency at 4.1 eV. This peak has been attributed to a $3d_{3z^2-1}$ to $4p_x$ electronic transition of Cu^{1+} atoms in an O-Cu-O dumbbell (21). These Cu^{1+} atoms are located in the CuO chains and have an oxygen vacancy on both sides. The enhancement observed for the persistent photoconductivity at 4.1 eV is much stronger, than what can be expected from the increased absorption at this energy alone (17). Thus this implies that the persistent photoconductivity is strongly enhanced as soon as an electron-hole pair is created in close proximity to an oxygen vacancy, which is also consistent with the observed doping dependence.

Theoretical Models

Since the oxygen vacancies in the CuO chains of $R\text{Ba}_2\text{Cu}_3\text{O}_{6+\delta}$ play an important role for the persistent photoconductivity (13,15,17), there were several models developed involving specifically the CuO chains in this material. The two main models are based on either photoassisted oxygen ordering (22) or trapping of photogenerated mobile carriers (9,15).

Photoassisted Oxygen Ordering. It has been shown, that $R\text{Ba}_2\text{Cu}_3\text{O}_{6+\delta}$ samples rapidly quenched from higher temperatures show transport and structural changes during room temperature annealing similar to persistent photoconductivity (23). This effect of room temperature annealing was explained by oxygen ordering in the CuO chains. Furthermore, the activation energy for the relaxation of the photoinduced effects is with 0.9 ± 0.1 eV (9) close to the oxygen diffusion activation energy of 1.3 eV (24). This suggests that the photoinduced effects could be due to photoassisted oxygen ordering (22).

There is an important difference between oxygen ordering in quenched samples and the photoinduced effects. While in quenched samples the oxygen in the CuO chains order during room temperature annealing, the oxygen has to disorder from a metastable ordered state in the photoexcited samples during room temperature relaxation. It has been shown, that the photoexcitation process is indeed independent from oxygen disorder induced by quenching (25). Furthermore, the oxygen ordering model implies, that persistent photoconductivity should vanish for completely deoxygenated ($\delta \approx 0$) $R\text{Ba}_2\text{Cu}_3\text{O}_{6+\delta}$ samples, contrary to the observed doping dependence (15). Therefore it is doubtful that the photoassisted oxygen ordering explains the persistent photoconductivity in $R\text{Ba}_2\text{Cu}_3\text{O}_{6+\delta}$.

Electron Trapping. In another model the incoming photons create electron-hole pairs (9,15). Subsequently, the electron is trapped at an oxygen vacancy in the CuO chain, while the hole is transferred to an extended state in the CuO_2 planes and thus enhances the conductivity. This model is consistent with all the observed data so far, in particular it can explain the doping dependence (15) and the spectral dependence (17) of the persistent photoconductivity. Furthermore this mechanism is also supported by measurements of the photoluminescence in $\text{YBa}_2\text{Cu}_3\text{O}_{6.4}$ (26).

The photoinduced structural changes (13) can be understood by a lattice distortion caused by the trapped electrons. This lattice distortion gives rise to an energy barrier, which inhibits the recombination of the trapped electrons with a hole (15). However, it is not presently clear how the proposed models can explain the photoinduced changes in the mobility (12). One possibility is that the photoinduced structural modification causes the change in the mobility.

Cuprates Without CuO Chains

The above shown measurements were all done on $R\text{Ba}_2\text{Cu}_3\text{O}_{6+\delta}$. One specific feature of this material that sets it apart from most other high T_c cuprates is that its structure contains CuO chains. Since early measurements did not show persistent photocon-

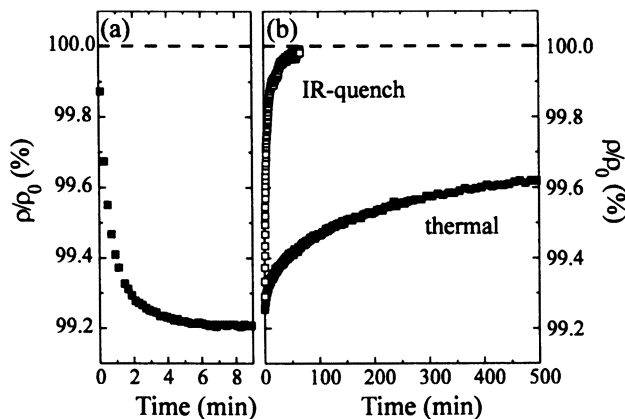


Figure 6. Excitation (a) and relaxation (b) of the persistent photoconductivity in $\text{Tl}_2\text{Ba}_2\text{CuO}_{6+\delta}$. In (b) solid symbols refer to thermal relaxation and open symbols refer to infrared quenching at 1100 nm. ρ_0 is the initial resistivity of the fully relaxed sample, which is also indicated by dashed lines (Reproduced with permission from reference 3. Copyright 1997 American Physical Society.)

ductivity in other cuprates besides $\text{RBA}_2\text{Cu}_3\text{O}_{6+\delta}$ (22), the theoretical models involved in one way or another specifically these CuO chains. We will now show measurements of persistent photoconductivity in cuprates *without* CuO chains (3). Thus, clearly persistent photoconductivity does not require the presence of CuO chains and might be a more common effect in these materials.

$\text{Tl}_2\text{Ba}_2\text{CuO}_{6+\delta}$. In contrast to $\text{RBA}_2\text{Cu}_3\text{O}_{6+\delta}$, $\text{Tl}_2\text{Ba}_2\text{CuO}_{6+\delta}$ has a rather simple structure with only one CuO_2 plane per unit cell sandwiched between TlO layers, and *no* CuO chains. By increasing in $\text{Tl}_2\text{Ba}_2\text{CuO}_{6+\delta}$ the oxygen concentration δ , it is possible to decrease the T_c from 85–0 K (27). Thus the $\text{Tl}_2\text{Ba}_2\text{CuO}_{6+\delta}$ films used for the persistent photoconductivity measurements are in the *overdoped* regime, meaning a decreasing T_c with increasing carrier density n ($\partial T_c / \partial n < 0$), while the $\text{RBA}_2\text{Cu}_3\text{O}_{6+\delta}$ films are in the *underdoped* regime ($\partial T_c / \partial n > 0$).

The $\text{Tl}_2\text{Ba}_2\text{CuO}_{6+\delta}$ films were grown by RF sputtering on SrTiO_3 substrates (28–31). The thicknesses of the films were 500–800 Å, so that the films were transparent and completely penetrated by the light used in the experiments. After growth, the T_c of the films was adjusted between 10 and 80 K by annealing in argon or air. The persistent photoconductivity measurements were performed in the same setup as for the $\text{RBA}_2\text{Cu}_3\text{O}_{6+\delta}$ films.

Basic Effect. The basic effect of illumination on the resistivity of $\text{Tl}_2\text{Ba}_2\text{CuO}_{6+\delta}$ is shown in Figure 7. Depending on the doping and the wavelength the normal state resistivity ρ and the T_c can either increase or decrease. The $\text{Tl}_2\text{Ba}_2\text{CuO}_{6+\delta}$ thin film with an initial T_c of 60 K (see Figure 7(a)) shows an increase in both T_c and ρ during illumination with 1000 nm light, while both T_c and ρ decrease during illumination with 400 nm light. In contrast, a higher doped $\text{Tl}_2\text{Ba}_2\text{CuO}_{6+\delta}$, with a T_c of 13 K,

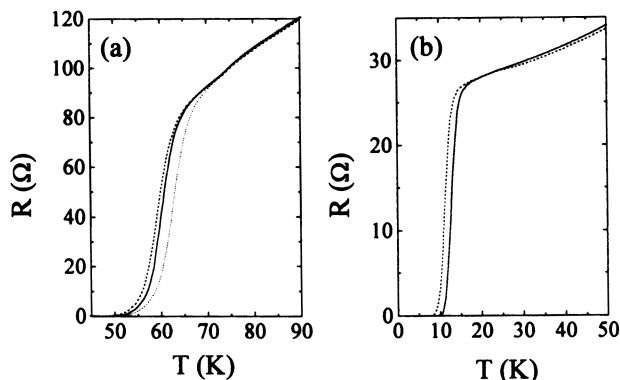


Figure 7. Resistance vs. temperature during (dashed or dotted line) and without (solid line) illumination for $\text{Tl}_2\text{Ba}_2\text{CuO}_{6+x}$ thin films with different doping. (a) Initial $R(T)$ (solid line) with $T_c = 670$ K and $R(T)$ during illumination with 1000 nm (dashed-dotted line) and 400 nm (dashed line) light. (b) Initial $R(T)$ with $T_c = 13$ K (solid line) and $R(T)$ during illumination with 440 nm (dashed line) light (Reproduced with permission from reference 3. Copyright 1997 American Physical Society.)

shows only a decrease of T_c and ρ , which is shown in Figure 7(b) for 440 nm light. Notice, that unlike in $\text{RBa}_2\text{Cu}_3\text{O}_{6+x}$, the change of T_c and ρ have always the same sign, which is due to the $\text{Tl}_2\text{Ba}_2\text{CuO}_{6+x}$ being overdoped. Also the photoinduced changes in T_c and ρ are smaller than the ones in underdoped $\text{RBa}_2\text{Cu}_3\text{O}_{6+x}$, but comparable to almost optimally doped $\text{RBa}_2\text{Cu}_3\text{O}_{6+x}$ (15, see also Figure 4).

One important difference between the measurements on $\text{Tl}_2\text{Ba}_2\text{CuO}_{6+x}$ (Figure 7) and $\text{RBa}_2\text{Cu}_3\text{O}_{6+x}$ (Figure 2) is the temperature dependence of the resistivity for $\text{Tl}_2\text{Ba}_2\text{CuO}_{6+x}$ was measured *during* illumination instead of with the light turned off. The reason for this is that in $\text{Tl}_2\text{Ba}_2\text{CuO}_{6+x}$ the persistent photoconductivity slowly relaxes even at low temperatures. However, any significant thermal heating due to the illumination can be ruled out, because of the very low power densities ($\approx 0.1 \text{ mWcm}^{-2}$) used during the measurements.

The time dependence of the excitation and the relaxation is shown in Figure 6 for the $\text{Tl}_2\text{Ba}_2\text{CuO}_{6+x}$ sample with a T_c of 13 K measured at 30 K. Obviously the time constant for the excitation is much faster than for $\text{RBa}_2\text{Cu}_3\text{O}_{6+x}$ (see Figure 1), and also there is still some thermal relaxation to the initial ρ even at 30 K, in contrast to $\text{RBa}_2\text{Cu}_3\text{O}_{6+x}$ where there is essentially no thermal relaxation at temperatures below approximately 100 K (9). This thermal relaxation in $\text{Tl}_2\text{Ba}_2\text{CuO}_{6+x}$ becomes faster at higher temperatures and takes only a few minutes above 100 K. Again both the excitation and the relaxation shows a stretched exponential behavior (see equation 1).

Also it is possible in the higher doped sample to quench the resistivity back to its initial value by illuminating the sample with 1100 nm light [see Figure 6(b)]. The original resistivity is this way recovered within one hour, unlike in $\text{RBa}_2\text{Cu}_3\text{O}_{6+x}$ where so far only a partial quenching of the persistent photoconductivity has been observed (11).

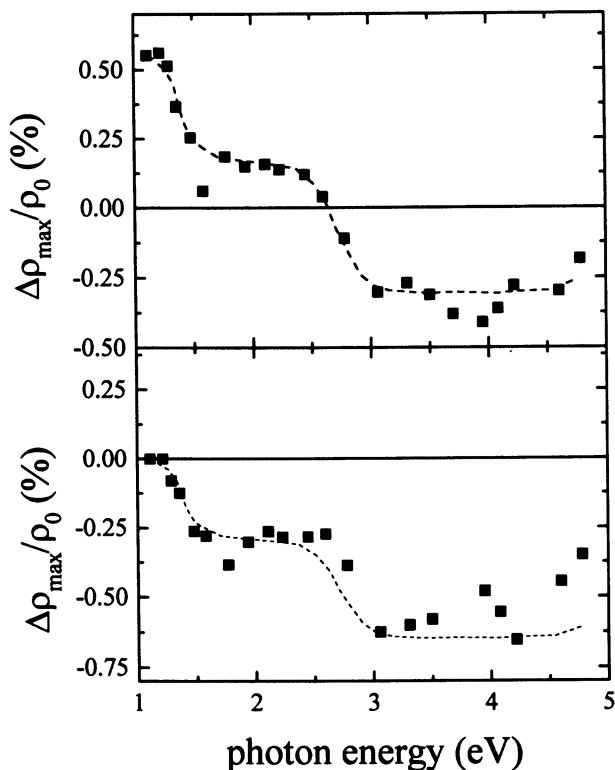


Figure 8. Spectral dependence of persistent photoconductivity in $\text{Tl}_2\text{Ba}_2\text{CuO}_{6+\delta}$ for the $T_c = 60$ K (a) and the $T_c = 13$ K (b) sample. The dashed lines are guides to the eye (Reproduced with permission from reference 3. Copyright 1997 American Physical Society.)

Spectral Dependence. The spectral dependence of the photoinduced resistivity changes at saturation $\Delta\rho_{\text{max}}$ normalized to the initial resistivity ρ_0 are shown in Figure 8, as they were measured at (a) 85 K and (b) 30 K for the $T_c = 60$ K and 13 K sample, respectively. Independent of doping there are three distinct energy regions, below 1.3 eV, 1.3–2.8 eV, and above 2.8 eV. In each of these energy regions $\Delta\rho_{\text{max}}$ is almost constant. For the lower doped $\text{Tl}_2\text{Ba}_2\text{CuO}_{6+\delta}$ sample ($T_c = 60$ K), the energy region with a photoinduced increase of ρ changes continuously into the region with a photoinduced decrease of ρ . On the other hand, the spectral efficiency $\eta(\hbar\omega)$ (see equation 3) is featureless from 1–4.8 eV. Interestingly, the onset of persistent photoconductivity for the higher doped $\text{Tl}_2\text{Ba}_2\text{CuO}_{6+\delta}$ ($T_c = 13$ K) sample is observed at a similar energy (1.3 eV) as it is for the underdoped $\text{RBA}_2\text{Cu}_3\text{O}_{6+\delta}$ (onset at 1.6 eV, see Figure 5).

This spectral dependence, with two plateaus, can be explained if one uses a similar purely electronic mechanism, as the one proposed for $\text{RBA}_2\text{Cu}_3\text{O}_{6+\delta}$ (1,3,15). This model proposes that in $\text{RBA}_2\text{Cu}_3\text{O}_{6+\delta}$ oxygen vacancies in the CuO chains trap photogenerated electrons. In $\text{Tl}_2\text{Ba}_2\text{CuO}_{6+\delta}$ there are two types of structural defects

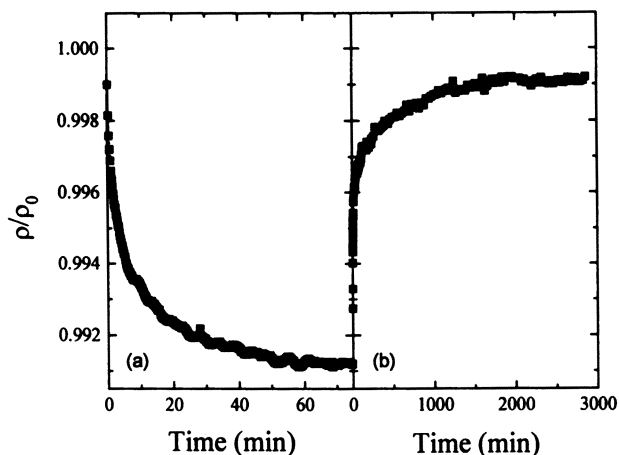


Figure 9. Time dependence of persistent photoconductivity in $\text{Bi}_2\text{Sr}_2\text{Ca}_{1-x}\text{Y}_x\text{Cu}_{8+\delta}$ during (a) excitation and (b) relaxation. (Reproduced with permission from reference 3. Copyright 1997 American Physical Society.)

(32), Cu for Tl substitution in the TlO layers and interstitial oxygen between the TlO layers, which might trap the photogenerated electrons. The presence of these two types of defects can explain the observed spectral dependence with two excited levels (see Figure 8). If this model is correct, then persistent photoconductivity should be present in most high- T_c cuprates, since all that it requires are localized electron states spatially separated from extended hole states in the conduction layers (CuO_2 planes).

On the other hand it is unlikely that the oxygen ordering model proposed for $\text{RBa}_2\text{Cu}_3\text{O}_{6+\delta}$ (22) can explain the observed persistent photoconductivity in $\text{Tl}_2\text{Ba}_2\text{CuO}_{6+\delta}$. It has been shown that structural ordering in $\text{Tl}_2\text{Ba}_2\text{CuO}_{6+\delta}$ always leads *only* to a decrease in resistivity and thus is clearly irreversible unless thermally relaxed (33). In contrast, the sign of the photoinduced resistivity changes depends on doping (see Figures 6 and 8) and is reversible (see Figure 6). In order for the structural ordering mechanism to be correct, this would imply the unlikely case that illumination with a single wavelength either *orders* or *disorders* oxygen, depending on doping or initial resistivity.

Y-doped $\text{Bi}_2\text{Sr}_2\text{CaCu}_2\text{O}_{8+\delta}$. As mentioned above the mechanism based on defect trapping of photogenerated electrons suggests that persistent photoconductivity should be a more general observed phenomenon in high- T_c cuprates. We also recently observed this effect in Y-doped $\text{Bi}_2\text{Sr}_2\text{CaCu}_2\text{O}_{8+\delta}$. These $\text{Bi}_2\text{Sr}_2\text{Ca}_{1-x}\text{Y}_x\text{Cu}_2\text{O}_{8+\delta}$ samples showed an insulating temperature dependence of the resistivity. The time dependence of the photoexcitation and thermal relaxation measured at 90 K is shown in Figure 9 and follows again a stretched exponential as in equation 1. For the photoexcitation we choose a wavelength of 470 nm, since this coincides with the resonance energy 2.6 eV observed in resonant Raman scattering (34).

This persistent photoconductivity in Y-doped $\text{Bi}_2\text{Sr}_2\text{CaCu}_2\text{O}_{8+\delta}$ is remarkably different from the photoinduced effects in pure $\text{Bi}_2\text{Sr}_2\text{CaCu}_2\text{O}_{8+\delta}$. In pure

$\text{Bi}_2\text{Sr}_2\text{CaCu}_2\text{O}_{8+\delta}$ there is upon illumination an *irreversible increase* of the resistivity (35), while in the Y-doped $\text{Bi}_2\text{Sr}_2\text{CaCu}_2\text{O}_{8+\delta}$ there is a *reversible decrease* of the resistivity. It is important to notice that the *irreversible increase* of resistivity was observed in oxygen annealed overdoped $\text{Bi}_2\text{Sr}_2\text{CaCu}_2\text{O}_{8+\delta}$, and that the irreversible increase is consistent with a simple loss of oxygen during illumination. Thus these irreversible changes are probably unrelated to the persistent photoconductivity observed in the other high- T_c cuprates. So far there have no reversible changes been observed in pure $\text{Bi}_2\text{Sr}_2\text{CaCu}_2\text{O}_{8+\delta}$.

The electron trapping mechanism used to explain the persistent photoconductivity in $\text{RBa}_2\text{Cu}_3\text{O}_{6+\delta}$ and $\text{Tl}_2\text{Ba}_2\text{CuO}_{6+\delta}$ can also be used for $\text{Bi}_2\text{Sr}_2\text{Ca}_{1-x}\text{Y}_x\text{Cu}_2\text{O}_{8+\delta}$. The substitution of Y for Ca might introduce localized defect states, which like in the other materials may trap photogenerated electrons. If this is the case then the persistent photoconductivity in $\text{Bi}_2\text{Sr}_2\text{Ca}_{1-x}\text{Y}_x\text{Cu}_2\text{O}_{8+\delta}$ should show a similar dependence with the Y content x as the doping dependence observed for $\text{RBa}_2\text{Cu}_3\text{O}_{6+\delta}$ (see Figure 4). This may also explain the absence of any reversible photoinduced changes in pure $\text{Bi}_2\text{Sr}_2\text{CaCu}_2\text{O}_{8+\delta}$.

Other Cuprates. Besides the cuprates discussed above ($\text{RBa}_2\text{Cu}_3\text{O}_{6+\delta}$, $\text{Tl}_2\text{Ba}_2\text{CuO}_{6+\delta}$, and $\text{Bi}_2\text{Sr}_2\text{Ca}_{1-x}\text{Y}_x\text{Cu}_2\text{O}_{8+\delta}$) there is to our knowledge no observation of persistent photoconductivity in other systems. But the recent results on cuprates without CuO chains suggest, that this effect is more widespread in this class of materials, as expected for the electron trapping mechanism. Indeed, we have preliminary results which suggest that persistent photoconductivity can also be observed in $\text{La}_{2-x}\text{Sr}_x\text{CuO}_4$. Furthermore, $\text{Tl}_2\text{Ba}_2\text{CaCu}_2\text{O}_8$ exhibits metastable photoinduced changes of its magnetic properties, which may be related to persistent photoconductivity (36).

These results may have important consequences for measurements using optical probes, e.g., Raman scattering or photoemission spectroscopy. The increased doping level during illumination, which leads to a reduced T_c , might have to be taken into account for the interpretation of the data. On the other hand the persistent photoconductivity can also be used as a tool to investigate doping effects. The reversible photodoping allows to measure in *one* sample the dependence of other physical properties on the carrier concentration in the high- T_c cuprates. Furthermore, persistent photoconductivity might exist in similar complex materials besides the high- T_c cuprates and allow to study doping dependencies, e.g. in the colossal magnetoresistive manganites, where one could expect a photoinduced transition from an insulating antiferromagnetic to a metallic ferromagnetic state (37).

Conclusion

In summary, we have shown persistent photoconductivity in a variety of different high- T_c cuprates ($\text{RBa}_2\text{Cu}_3\text{O}_{6+\delta}$, $\text{Tl}_2\text{Ba}_2\text{CuO}_{6+\delta}$, and $\text{Bi}_2\text{Sr}_2\text{Ca}_{1-x}\text{Y}_x\text{Cu}_2\text{O}_{8+\delta}$). The effect is characterized by a reversible change of the carrier concentration upon illumination. This photoinduced change of the carrier concentration is persistent with a long lifetime at low temperatures and relaxes thermally at elevated temperatures. The photoinduced changes in turn modify the resistivity (in most cases a decrease with illumination) and the T_c (increase or decrease depending on initial doping level). The observation of

persistent photoconductivity in $\text{Ti}_2\text{Ba}_2\text{CuO}_{6+\delta}$ and $\text{Bi}_2\text{Sr}_2\text{Ca}_{1-x}\text{Y}_x\text{Cu}_2\text{O}_{8+\delta}$ shows that this effect is not limited to cuprates with CuO chains.

The doping dependence in $\text{RBa}_2\text{Cu}_3\text{O}_{6+\delta}$ and the spectral dependence in $\text{RBa}_2\text{Cu}_3\text{O}_{6+\delta}$ and $\text{Ti}_2\text{Ba}_2\text{CuO}_{6+\delta}$ suggest that the persistent photoconductivity is due to an electron trapping mechanism. In this model the electron of a photogenerated electron hole pair is trapped at a localized state in the charge reservoir layer, while the remaining hole gets transferred to the conduction (CuO_2) layer. This model is in principle applicable to other cuprates as well, so that persistent photoconductivity might be a more common phenomenon in high- T_c materials.

The observed persistent photodoping effects might be important for measurements using optical probes. Furthermore these effects can also be used to study the doping dependence of other physical properties.

Acknowledgments

We gratefully acknowledge valuable discussions with D. Basov, G. Blumberg, Y. Bruynseraede, T. Endo, A. Gilbert, G. Güntherodt, J. Hasen, D. Lederman, P. Lemmens, J. Martín, D. Reznik, J. Santamaria, P. Seidel, M. Veléz, and J. Vicent. This work was supported by the NSF. Work at SUNY at Buffalo was sponsored by the New York State Energy Research and Development Authority (NYSERDA), and work at Universidad del Valle was sponsored by COLCIENCIAS. Prof. P. Prieto thanks the Guggenheim foundation for support of a sabbatical year at UCSD.

References

1. Kudinov, V. I.; Kirilyuk, A. I.; Kreines, N. M.; Laiho, R.; Lähderanta, E. *Phys. Lett. A* **1990**, *151*, 358.
2. Nieva, G.; Osquiguil, E.; Guimpel, J.; Maenhoudt, M.; Wuyts, B.; Bruynseraede, Y.; Maple, M. B.; Schuller, I. K. *Appl. Phys. Lett.* **1992**, *60*, 2159.
3. Hoffmann, A.; Schuller, I. K.; Ren, Z. F.; Lao, J. Y.; Wang, J. H. *Phys. Rev. B* **1997**, *56*, 13742.
4. Nakamura, O.; Fullerton, E. E.; Guimpel, J.; Schuller, I. K. *Appl. Phys. Lett.* **1992**, *60*, 120.
5. Osquiguil, E.; Maenhoudt, M.; Wuyts, B.; Bruynseraede, Y. *Appl. Phys. Lett.* **1992**, *60*, 1627.
6. Cava, R. J.; Batlogg, B.; Rabe, K. M.; Rietman, E. A.; Gallagher, P. K.; Rupp, L. W. *Physica C* **1988**, *156*, 523.
7. Tranquada, J. M.; Moudden, A. H.; Goldman, A. I.; Zolliker, P.; Cox, E. E.; Shirane, G.; Sinha, S. K.; Vakin, D.; Johnson, D. C.; Alvarez, M. S.; Jacobson, A. J.; Lewandowski, J. T.; Newsam, J. M. *Phys. Rev. B* **1988**, *38*, 2477.
8. *Nonequilibrium Superconductivity, Phonons, and Kapitza Boundaries*; Kenneth, E. G., Eds.; NATO Advanced Study Institute Series B: Physics; Plenum Press: New York, NY, 1981; Vol. 65.
9. Kudinov, V. I.; Chaplygin, I. L.; Kirilyuk, A. I.; Kreines, N. M.; Laiho, R.; Lähderanta, E.; Ayache, C. *Phys. Rev. B* **1993**, *47*, 9017.
10. Hasen, J. *Ph.D. Thesis*, University of California, San Diego, 1995.
11. Chew, D. C.; Federici, J. F.; Guitierrez-Solana, J.; Molina, G.; Savin, W.; Wilber, W. *Appl. Phys. Lett.* **1996**, *69*, 3260.
12. Nieva, G.; Osquiguil, E.; Guimpel, J.; Maenhoudt, M.; Wuyts, B.; Bruynseraede, Y.; Maple, M. B.; Schuller, I. K. *Phys. Rev. B* **1992**, *46*, 14249.

13. Lederman, D.; Moran, T. J.; Hasen, J.; Schuller, I. K. *Appl. Phys. Lett.* **1993**, *63*, 1276.
14. For a review, see: Markert, J. T.; Dunlap, B. D.; Maple, M. B. *MRS Bull. XIV* **1989**, *1*, 37.
15. Hasen, J.; Lederman, D.; Schuller, I. K.; Kudinov, V.; Maenhoudt, M.; Bruynseraede, Y. *Phys. Rev. B* **1995**, *51*, 1342.
16. Bud'ko, S. L.; Feng, H. H.; Davis, M. F.; Wolfe, J. C.; Hor, P. H. *Phys. Rev. B* **1993**, *48*, 16707.
17. Endo, T.; Hoffmann, A.; Santamaria, J.; Schuller, I. K. *Phys. Rev. B* **1996**, *54*, 3750.
18. Jiménez de Castro, M.; Alvarez Rivas, J. L. *Phys. Rev. B* **1996**, *53*, 8614.
19. Cooper, S. L.; Kotz, A. L.; Karlow, M. A.; Klein, M. V.; Lee, W. C.; Giapintzakis, J.; Ginsberg, D. M. *Phys. Rev. B* **1992**, *45*, 2549.
20. Markowitsch, W.; Stockinger, C.; Lang, W.; Kula, W.; Sobolewski, R. *Proceedings of the SPIE* **1996**, *2696*, 617.
21. Kelly, M. K.; Barboux, P.; Tarascon, J.-M.; Aspnes, D. E.; Bonner, W. A.; Morris, P. A. *Phys. Rev. B* **1988**, *38*, 870.
22. Osquiguil, E.; Maenhoudt, M.; Wuyts, B.; Bruynseraede, Y.; Lederman, D.; Schuller, I. K. *Phys. Rev. B* **1994**, *49*, 3675.
23. Veal, B. W.; You, H.; Paulikas, A. P.; Shi, H.; Fang, Y.; Downey, J. W. *Phys. Rev. B* **1990**, *42*, 4770.
24. Tolpygo, S. K.; Lin, J.-Y.; Gurvitch, M.; Hou, S. Y.; Phillips, J. M.; *Phys. Rev. B* **1996**, *53*, 12462.
25. Guimpel, J.; Maiorov, B.; Osquiguil, E.; Nieva, G.; Pardo, F. *Phys. Rev. B* **1997**, *56*, 3552.
26. Federici, J. F.; Chew, D.; Welker, B.; Savin, W.; Guitierrez-Solana, J.; Fink, T.; Wilber, W. *Phys. Rev. B* **1995**, *52*, 15592.
27. Kubo, Y.; Shimakawa, Y.; Manako, T.; Igarashi, H. *Phys. Rev. B* **1991**, *43*, 7875.
28. Wang, C. A.; Ren, Z. F.; Wang, J. H.; Petrov, D. K.; Naughton, M. J.; Yu, W. Y.; Petrou, A. *Physica C* **1996**, *262*, 98.
29. Ren, Z. F.; Wang, C. A.; Wang, J. H. In *Proceedings of the 10th Anniversary HTS Workshop on Physics, Materials & Applications*; Batlogg, B.; Chu, C. W.; Chu, W. K.; Gubser, D. U.; Muller, K. A., Ed.; World Scientific: Singapore, 1996; pp 199-200.
30. Ren, Z. F.; Wang, J. H.; Miller, D. J. *Appl. Phys. Lett.* **1996**, *69*, 1798.
31. Ren, Z. F.; Wang, J. H.; Miller, D. J. *Appl. Phys. Lett.* **1997**, *71*, 1706.
32. Wagner, J. L.; Chmaissem, O.; Radaelli, P. G.; Hunter, B. A.; Jorgensen, J. D.; Hinks, D. G.; Jensen, W. R. *Physica C* **1997**, *277*, 170.
33. Schilling, J. S.; Klehe, A.-H.; Looney, C.; Takahashi, H.; Mōri, N.; Shimakawa, Y.; Kubo, Y.; Manako, T.; Doyle, S.; Hermann, A. M. *Physica C* **1996**, *257*, 105.
34. Boekholt, M.; Moshalkov, V. V.; Güntherodt, G. *Physica C* **1992**, *192*, 191.
35. Tanabe, K.; Karimoto, S.; Kubo, S.; Tsuru, K.; Suzuki, M. *Phys. Rev. B* **1995**, *52*, 13152.
36. Szymczak, H.; Baran, M.; Gnatchanko, S. L.; Szymczak, R.; Chen, Y. F.; Ivanov, Z. G.; Johansson, L.-G. *Europhys. Lett.* **1996**, *35*, 452.
37. Kiryukhin, V.; Casa, D.; Hill, J. P.; Keimer, B.; Vigliante, A.; Tomioka, Y.; Tokura, Y. *Nature* **1997**, *386*, 813.

Chapter 16

Time-Resolved Optical Studies of Quasiparticle Dynamics in High-Temperature Superconductors: Experiments and Theory

D. Mihailovic and J. Demsar

Jozef Stefan Institute, Jamova 39, 1001 Ljubljana, Slovenia

Ultrafast time-resolved optical spectroscopy in high-temperature superconductors enables the direct real-time measurement of non-equilibrium quasiparticle recombination dynamics. In addition, it also gives detailed information about the symmetry of the superconducting gap and the “pseudogap”, their doping dependence and their temperature dependence. Experimental data, together with theoretical models on the photoinduced transmission amplitude and relaxation time as a function of temperature and doping in $\text{YBa}_2\text{Cu}_3\text{O}_{7.5}$ gives a consistent picture of the evolution of low-energy structure, where a temperature-independent gap is shown to exist in the underdoped state which evolves with doping into a two-component state near optimum doping, where the dominant response is from a T-dependent BCS-like superconducting gap.

The experimental study of non-equilibrium phenomena with real-time techniques has been used quite effectively in the past to investigate the quasiparticle (QP) relaxation dynamics in “conventional” non-cuprate superconductors (1). The main interest in the QP dynamics has been in superconducting junction devices, where the relaxation of carriers injected into a superconductor has been measured. The typical relaxation times in conventional superconductors are in the range 10^{-7} - 10^{-9} s and the quasiparticle relaxation processes could be experimentally measured by using fast electronics (2). In high temperature superconducting cuprates however, because T_c is higher and the superconducting gap is larger, the timescales are much shorter and electrical measurements become very difficult if not impossible with current state of the art electronics.

The availability of reliable ultrafast laser systems in the last decade has made possible the use of ultrafast optical investigations of QP relaxation and recombination phenomena with real-time resolution exceeding 20 fs. A number of time-resolved optical studies since the discovery of these materials have shown that potentially the technique could be a powerful new tool for the study of high-temperature superconductors (3-8). In particular, the separation of timescales enables quasiparticle relaxation processes to be distinguished from localized (possibly intra-gap) states (7). Rapid progress has been made particularly in the last few years, partly because of systematic measurements as a function of temperature and doping, and partly because of the development of theoretical models to describe the temperature dependence of the transient changes in optical constants and relaxation time in a superconductor (9). In this chapter we will describe the current state of the experiments and theory of ultrafast time-resolved laser spectroscopy as applied to high-temperature superconductors (HTS).

Optical spectroscopy, including infrared reflectivity and Raman spectroscopy has been very important in elucidating the low-frequency electronic excitation spectra of high temperature cuprate superconductors (10-13). However, because of the large number of ions in the unit cell the low-energy electronic structure becomes complicated, and it becomes difficult to distinguish between different overlapping spectral contributions. Because accurate identification of these different contributions - for example the Drude contribution from conduction electrons or the so-called mid-infrared contribution thought to come from polaron hopping - is crucial for the development of a theory of superconductivity, there has been a significant amount of controversy regarding the interpretation of the low-frequency spectra. The information provided by study of the QP recombination dynamics enables the identification of these different contributions on the basis of their lifetimes as well as the temperature dependences and doping systematics of photoinduced transmissivity or reflectivity data.

At this time there is an additional motivation for the study of non-equilibrium phenomena in these materials, because time-resolved experiments can give information about the gap structure of the superconductor, and consequently also about the nature of the carriers involved in superconductivity and consequently also about the pairing mechanism itself. For example, trapped, localized or polaronic states and correlated electrons are expected to have very different dynamics than charge carriers in extended band states.

Apart from the new information about the low-energy electronic structure, the study of non-equilibrium carrier dynamics gives us a thorough understanding of carrier relaxation dynamics, which is crucial also for the design and construction of non-equilibrium superconducting devices. Since the relaxation time in a superconductor essentially scales inversely with the magnitude of the superconducting gap (9), high temperature superconducting cuprates are likely to have much faster relaxation timescales than conventional superconductors, a consideration which is clearly important for high-speed electronics.

The Experimental Technique and Data Analysis

Time-resolved optical spectroscopy of superconductors involves measurement of the transient change of the optical transmission T through, or reflection R from a superconductor by a two step process. In the first step, the superconductor is excited by an ultrashort “pump” laser pulse and in the second, the change $\Delta R/R$ or $\Delta T/T$ of the weaker “probe” pulse is measured as a function of time delay after the photoexcitation. A typical experimental setup is shown schematically in Figure 1. A mode-locked laser (usually Ti:sapphire) is used to generate the laser pulses with pulselength τ_p ranging from 50-200 fs at around 800 nm (1.5 eV). The pulse energies are typically in the range 0.1-1 nJ.

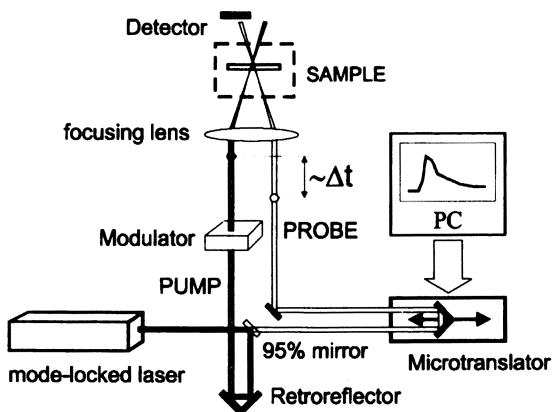


Figure 1. A typical time-resolved photoinduced transmission setup. A similar setup is also used for measuring the photoinduced reflection, except that the reflected probe beam is detected in this case.

The carrier density excited by the probe pulse is typically small compared to the normal state hole density in the cuprates, so the perturbation caused by the photoexcited carriers can be assumed to be small. The probe beam, which is usually (but not always) at the same wavelength as the pump beam, is suitably delayed in time with a Michelson interferometer and significantly attenuated, typically by a factor of 100. Usually the effect of additional photoexcitation by the probe beam can be neglected. Other laser systems have also been used in the past (14,15), for example the colliding-pulse mode-locked (CPM) dye laser, and amplified lasers, in the latter case the pump energies may be up to three orders of magnitude higher and can be as high as $1\mu\text{J}$. In this case the photoexcited carrier density can exceed the normal state carrier density.

The changes $\Delta R/R$ or $\Delta T/T$ in the case of weak photoexcitation are small (10^{-6} - 10^{-3}), so high-frequency lock-in detection at $\nu \sim 100$ kHz or more is usually used to reduce laser noise. It is usually sufficient to modulate only the pump beam and detect the probe light with a lock-in detector, but dual modulation techniques are

sometimes necessary when bad sample surface quality prevents pump scattered light from being sufficiently rejected.

The typical time-resolved photoinduced transmission signal on near optimally doped $\text{YBa}_2\text{Cu}_3\text{O}_{7.5}$ in the range from -6 ps to 13 ps (open squares) together with the fit (solid line) is presented in Figure 2. The signal is zero when the pump pulse is blocked (*A*), however there is a non-zero long lived component (*7,16*) present even at 12 ns after the pump pulse, seen as a signal at negative times, when the pump is unblocked (*B*). Besides the very slow component there's also a fast transient present, with a rise time of approximately 300 fs and a decay time of approximately 2 ps. From the temperature dependence of the time-resolved photoinduced transmission (reflection) spectra one can obtain the temperature dependence of the fast and slow component amplitude, indicated approximately by a difference between points *C* and *D* and points *D* and *B* respectively, together with the temperature dependence of typical relaxation time.

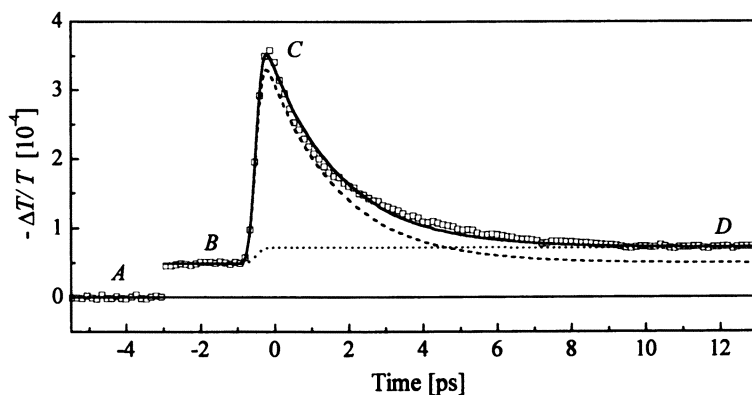


Figure 2: Typical shape of the time-resolved photoinduced transmission signal taken at the cryostat temperature 45 K on near optimally doped $\text{YBa}_2\text{Cu}_3\text{O}_{7.5}$ with $T_c = 90$ K (squares) using 200 fs Ti:sapphire laser pulses, together with the fit using a sum of the slow (dotted line) and fast (dashed line) component, with the effective rise time $\sigma \sim 300$ fs.

In the low repetition experiments using CPM laser, the slow component was found to be present even after $160 \mu\text{s}$ (*16*), therefore in the range of several 10 ps it can be considered as a constant and fitted by the Heaviside step function (zero at negative time delays and constant at $t > 0$). The fast component, on the other hand, was found to be reasonably well reproduced by single exponential decay with a characteristic relaxation time in the range $0.5 - 3$ ps depending on doping and temperature (*8,9*). The fit used in the Figure 2 is therefore a sum of the two (fast and slow) components. Since the rise time of the transient signal is pulse-width limited, in the case of single exponential decay the fast component of photoinduced transmission due to pump pulse is a solution of

$$\partial n / \partial t = -n / \tau_R + g(t); \quad n(t) \equiv \Delta T / T(t), \quad (1)$$

τ_R being the relaxation time, and $g(t) = A \exp(-2t^2/\tau_p^2)$ representing the photoexcitation with pump pulse width τ_p . Due to finite probe pulse width the resulting $n(t)$ should be convoluted with $g(t')$ to obtain the measured $n(t)$, however since it effects the rise time of the signal only, $n(t)$ can be approximated with the solution of the equation 1 with an *effective* pulse width $\tau_p' \approx \sqrt{2}\tau_p$

$$n(t) = C \exp[-t/\tau_R] \{1 - \text{Erf}[(4t\tau_R + \tau_p'^2)/(2\sqrt{2}\tau_p'\tau_R)]\} \quad (2)$$

As can be seen in Figure 2, the signal can be very well reproduced using a sum of a Heaviside step function and a single exponential decay both having a pulse width limited risetime.

A typical set of time-resolved photoinduced transmission traces in an underdoped $\text{YBa}_2\text{Cu}_3\text{O}_{7-\delta}$ sample with a $T_c = 53$ K and an optimally doped sample with $T_c = 90$ K obtained with a 200 fs Ti:sapphire setup are shown in Figure 3.

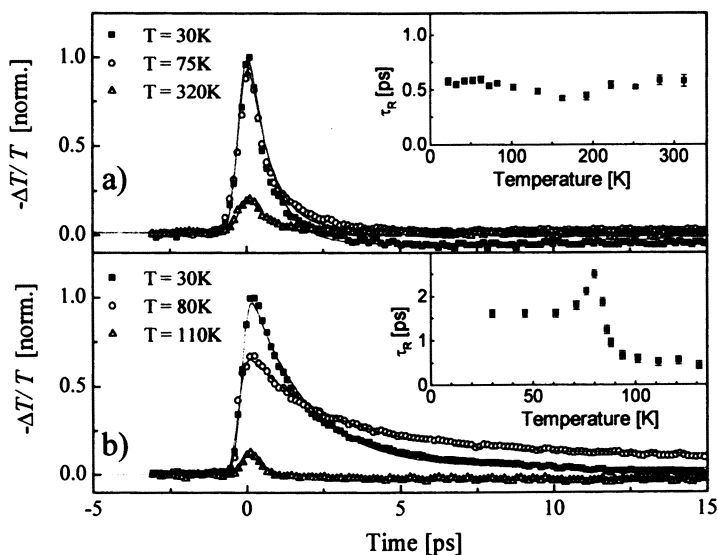


Figure 3: Typical set of time-resolved photoinduced transmission traces in a) underdoped ($\delta = 0.44$, $T_c = 53$ K) and b) near optimally doped ($\delta = 0.08$, $T_c = 90$ K) $\text{YBa}_2\text{Cu}_3\text{O}_{7-\delta}$ thin film on SrTiO substrate. The straight lines are fits to the data using single exponential decay with τ_R in the range 0.5 – 3 ps and a Heaviside step function representing the long-lived component (7,16). In the insets there are the temperature dependences of the relaxation time obtained using single exponential fit showing completely different behaviors in underdoped and near optimally doped state.

The data for a number of temperatures clearly show that both the lifetime of the decay and the amplitude of the signal are dependent on doping and temperature. A much longer decay time is seen below T_c in the sample with $T_c = 90$ K (inset to Figure 3b)), and a divergence below T_c , which is conspicuously absent in the underdoped sample (inset to Figure 3a)). The amplitude, on the other hand, increases with decreasing temperature in both cases.

Heating Effects. Laser heating of the sample is an important experimental problem in these experiments and has often been discussed in the literature (16-18). There are two effects to be considered. Firstly and more importantly the steady-state temperature of the probed volume increases due to the pump laser excitation. Since the thickness of the substrate or single crystal (~ 0.3 mm) is typically much bigger than the absorption length (~ 80 nm) one can calculate the temperature rise using a simple steady-state heat diffusion model (17), where the Gaussian laser beam with the average laser power P_L is focused into a spot of diameter d on a semi-infinite solid with reflectivity R , absorption coefficient α , and thermal conductivities κ_x , κ_y , κ_z . Choosing the center of the beam at the crystal surface as the origin of the coordinate system ($z=0$ at the surface and $z>0$ in the crystal), the boundary condition is that the temperature at $z = \infty$ is equal to the temperature of the cold finger. Since we are dealing with temperature rises of the order of 10 K, we can neglect the energy loss due to thermal radiation. Using this model we obtain the expression for the temperature rise

$$\Delta T(x, y, z) = \frac{\alpha(1-R)P_L^3 e^{-\alpha z}}{4\pi^2 d^2 \kappa_x \kappa_y \kappa_z} \times \int_0^{2\pi} d\varphi \int_0^\infty r \cdot dr \exp\left[-\left(\frac{x}{d} - \frac{r \cos \varphi}{k_x d}\right)^2 - \left(\frac{y}{d} - \frac{r \sin \varphi}{k_y d}\right)^2\right] \left[\int_{k_z z}^\infty \xi(u) du + \int_{-k_z z}^\infty \xi(u) du \right] \quad (3)$$

with $\xi(u) = e^{-\alpha u/k_z} / \sqrt{r^2 + u^2}$, $k_x^2 = \kappa_x \kappa_z / P_L^2$ and k_y , and k_z respectively and φ , r and u are the integration variables. In case of single crystals at 80K using $\alpha = 1.8 \times 10^7 \text{ m}^{-1}$ (19), $\kappa_x = \kappa_y = 8 \text{ W/mK}$, $\kappa_z = 2 \text{ W/mK}$ (20), $R \sim 0.1$, $d = 100 \mu\text{m}$ and $P_L = 10 \text{ mW}$ one obtains $\Delta T(0,0,0) = 12 \text{ K}$. In the case of experiments on thin films, since the film thickness is negligible in comparison with the substrate thickness. Therefore, using the value $\kappa_x = \kappa_y = \kappa_z \sim 18 \text{ W/mK}$ of SrTiO_3 at 80 K (21) one obtains $\Delta T(0,0,0) = 2.7 \text{ K}$.

Experimentally, CW heating can also be measured and accounted for quite accurately and is in agreement with the calculation. On thin film samples one can measure the effect of the laser heating with a four-point probe resistivity measurement of a thin microbridge made of the same superconductor film (Figure 4). Although this method works very well with thin films it is not applicable to single crystals. However, since the temperature dependence of the fast component in near optimally doped superconductors is strongly temperature dependent as shown in Figure 5, and it has been experimentally shown (9) that the amplitude at low

excitations is linearly dependent on pump fluence, one can often obtain ΔT quite accurately by scaling the temperature dependence of the fast component by normalizing the signal amplitude to the pump fluence and by adjusting the temperature scale due to heating.

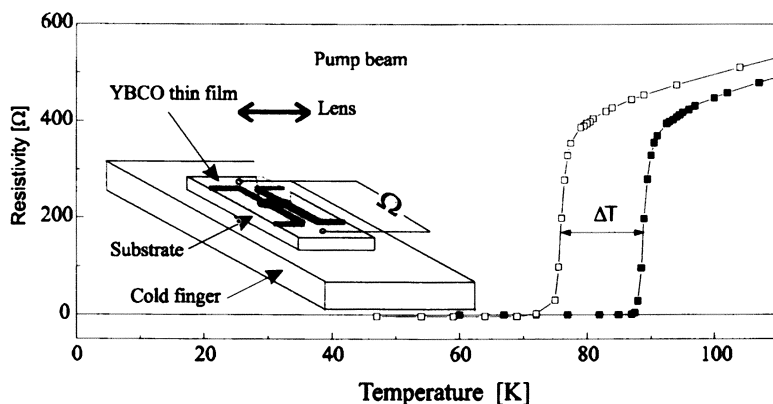


Figure 4: Experimental determination of ΔT at temperature close to T_C by measuring $R(T)$ of the illuminated microbridge (open squares) compared to the non-illuminated (solid squares). At $P_L = 40\text{mW}$, $d = 100\ \mu\text{m}$ one obtains $\Delta T(80\text{K}) \sim 13\ \text{K}$, which is consistent with the calculated result using equation 2 giving $\Delta T(80\text{K}) \sim 11\ \text{K}$.

In figure 5 there is a temperature dependence of the photoinduced transmission amplitude taken on the same thin film as used in figure 4 at three different laser fluences, where $\Delta T = 15\ \text{K}$ at $P_L = 40\ \text{mW}$ was determined, again comparable with the calculated temperature rise. When conducting the same analysis on single crystals using the temperature dependence of photoinduced reflectivity amplitude one obtains the result $\Delta T = 16 - 22\ \text{K}$ at $P_L = 10\ \text{mW}$, which is doping dependent.

Comparison with calculations made with a simple steady-state heat diffusion model give good quantitative agreement and as a result one can determine the temperature of the sample to within $\pm 2\ \text{K}$ in the temperature range 4 - 300K. It is important to note that because the thermal constants are very different for different superconductors (and substrates), different experimental configurations can give rise to heating effects which vary by more than one order of magnitude.

The second type of heating effect is non-equilibrium heating, where the temperature builds up during and after the pump laser excitation but dissipates before the next laser pulse. This effect can also be calculated accurately using the heat-diffusion model (16,18) with transient laser pulses including the anisotropy in thermal conductivity. The effect is smaller however, and typical values of the peak transient temperature increases in the low excitation experiments are $0.1-0.3\ \text{K/mW}$, so for most common experimental configurations it can be ignored. The effect is much more important if more intense laser pulses are used, from an amplified laser for example. In

such cases, the non-equilibrium heating effects need to be carefully considered in the analysis.

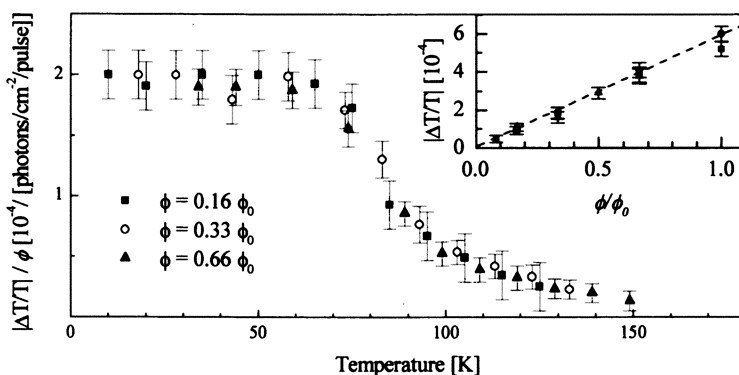


Figure 5: The T-dependence of the fast component amplitude, $|\Delta T/T|$, for a sample with $T_c = 89\text{K}$ using three different laser intensities. The data has been normalized with respect to the laser fluence, Φ . The insert shows low temperature $|\Delta T/T|$ vs. Φ , where $|\Delta T/T|$ scales linearly with Φ . $\Phi_0 = 5.5 \cdot 10^{13}$ photons/cm²/pulse.

Time-resolved Photoinduced Spectroscopy: Processes, Model and Experiment

Initial Hot Carrier Relaxation. An ultrashort laser pulse with an energy $E_L = 1\text{-}2\text{ eV}$ incident on a HTS results in the creation of an electron and a hole with a relative energy E_L (Figure 6a). For low and intermediate photoexcitation carrier densities (compared to the normal state carrier density), the process of energy relaxation can be described well by Allen's model (22). The model is applicable for intra-band relaxation in a metal or a semiconductor and has also been used successfully for determination of the electron-phonon coupling constant λ in conventional metallic superconductors using time-resolved experiments performed at room temperatures (23).

The photoexcited carriers first thermalize among themselves via intra-band scattering with a characteristic electron-electron ($e\text{-}e$) relaxation time of $\tau_{e\text{-}e} = \hbar E_F / 2\pi E^2 \approx 10\text{ fs}$, where E is the carrier energy measured from the Fermi energy E_F . This quasiparticle avalanche multiplication due to electron-electron collisions takes place as long as $\tau_{e\text{-}e}$ is less than the electron-phonon relaxation time $\tau_{e\text{-}ph}$. Further energy relaxation occurs by electron-phonon scattering which occurs on a timescale given by the electron-phonon relaxation time (22) $\tau_{e\text{-}ph} = T_c / 3\lambda \langle \omega^2 \rangle$, where T_c is initial carrier temperature, $T_c = E_l / C_e$, E_l is the energy density per unit volume deposited by the laser pulse, C_e is the electronic specific heat, and ω is the characteristic phonon frequency.

Electron-phonon relaxation time τ_{e-ph} and hence λ has been determined experimentally for the case of $\text{YBa}_2\text{Cu}_3\text{O}_{7-\delta}$ (14), as well as $\text{Bi}_2\text{Sr}_2\text{CaCu}_2\text{O}_8$ and $\text{Bi}_2\text{Sr}_2\text{Ca}_2\text{Cu}_3\text{O}_{10}$ (15) from relaxation time fits in time-resolved experiments using intense laser pulses. For $\text{YBa}_2\text{Cu}_3\text{O}_{7-\delta}$ τ_{e-ph} has been found to be $\tau_{e-ph} = T_c/3\lambda\langle\omega^2\rangle \approx 100\text{fs}$ for initial carrier temperatures $T_c = E_V/C_c$ in the range 3000 K (14). A different group found $\tau_{e-ph} \approx 60\text{fs}$ for $T_c \approx 410\text{K}$ (15) giving λ to be in the range $0.9 < \lambda < 1$. A similar λ was also found in $\text{Bi}_2\text{Sr}_2\text{CaCu}_2\text{O}_8$ (15). Thus in the absence of a gap in the low-frequency spectrum, for the range of typical photoexcitation densities E_I used in these experiments the relaxation process is complete within 10-100 fs. This is the usual case which occurs in metals (23).

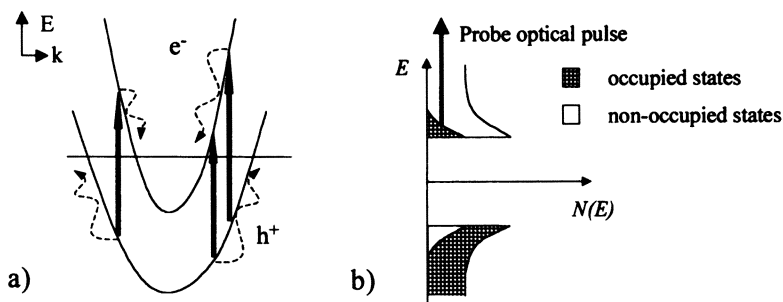


Figure 6: a) A scheme of the relaxation processes following the inter-band photoexcitation. If there is no gap (or "pseudogap") in the density of states near E_F the equilibrium at some slightly elevated lattice temperature would be achieved within 10-100fs. b) When the gap in the density of states is present, it creates the bottleneck for the quasiparticle relaxation. The photoexcited quasiparticles together with high-frequency phonons form a near steady state distribution with the relaxation time governed by anharmonic phonon decay (9). The variably delayed probe pulse therefore measures the temporal change in the photoexcited carrier density.

In a superconductor, however, the presence of a superconducting gap creates a relaxation bottleneck. The carriers therefore accumulate in quasiparticle states above the gap waiting to recombine into pairs. Their typical recombination time τ_R is 1-2 orders of magnitude longer than the initial intra-band Allen relaxation process (9) and can be probed by excited state absorption using a second probe laser pulse (Figure 6b).

It is the existence of this near-equilibrium QP population that gives us a powerful tool to investigate different aspects of the gap structure in high- T_c superconductors. Because the recombination dynamics depends on the density of electronic states at low energies, the time-resolved experiments give detailed information about the T -dependence, doping dependence and symmetry of the gap.

The Laser Probe Process. For probing the QP states it is quite important that the energy of the probe laser photons is above the plasma frequency of the material, because in this case we can make the simple assumption, that the probe absorption is due to an unscreened inter-band transition between the QP states and a band well above E_F (Figure 6b). The absorbance can then be approximated by the Fermi golden rule.

The *change* in the absorption probability is then given by $\delta r \propto \delta(-n_i \rho_f |M_{ij}|^2) \approx -\delta n_{pe} (\rho_f |M_{ij}|^2)$, where n_{pe} is the photoexcited quasiparticle density, ρ_f is the final density of unoccupied states and $M_{ij} = \langle \mathbf{p} \cdot \mathbf{A} \rangle$ is the dipole matrix element. The simplest case we can consider is to assume that the matrix element M_{ij} and the density of final states ρ_f are not changed by the photoexcitation process (the adiabatic approximation). Then the amplitude of the photoinduced absorption, $|\Delta A/A|$, is proportional to the photoinduced transmission amplitude, $|\Delta T/T|$ (and in the linear approximation also to $|\Delta R/R|$), which is in turn proportional to the change in the number of photoexcited quasiparticles $|\Delta A/A| \propto |\Delta T/T| \propto \delta r \approx -\delta n_{pe} (\rho_f |M_{ij}|^2)$.

In a complete description, the effects of the change in final states ρ_f and the matrix element M_{ij} (described by the Frank-Condon term $-n_i \delta(\rho_f |M_{ij}|^2)$) by the photoexcited particles need to be considered as well, since they can be important contributions, especially if polaronic lattice distortions occur around them. However, time-resolved spectroscopy enables these effects to be separated because they have very different dynamics (longer lifetimes).

When the Frank-Condon term is neglected, the probe signal is simply weighted by $\rho_f |M_{ij}|^2$. In the case of cuprates when $E_{probe} \approx 1.5$ eV, this corresponds closely to the O-Cu charge-transfer dipole transition, so the final state band in the probe process can also be identified (8).

Theoretical Model for the Temperature Dependence of the Photoinduced Reflection or Transmission. A theoretical description of the temperature dependence of the photoinduced transmission or reflection amplitude involves a calculation of the photoexcited carrier density n_{pe} as a function of temperature. Such a calculation was performed recently by Kabanov et al. (9).

The theoretical model for the photoinduced transmission amplitude, $|\Delta T/T|$, predicts very different temperature dependences, depending on the temperature dependence of the gap itself. In the case of a temperature-independent gap,

$$\left| \Delta T / T \right| \propto -\frac{1}{\Delta_0} \left[1 + \frac{2\nu}{N(0)\hbar\Omega} e^{-\Delta_0/k_B T} \right]^{-1}, \quad (4)$$

where Δ_0 is the energy gap, ν is the effective number of phonons per unit cell emitted in the QP recombination process, Ω is the typical phonon frequency and $N(0)$ is the density of states at E_F . The calculated T-dependence of the photoinduced transmission is shown in Figure 7. The predicted photoinduced transmission amplitude falls to zero asymptotically at high temperatures and one cannot easily identify a *temperature* associated with such a T-independent gap.

On the other hand, if the gap closes at a well defined temperature due to a

collective effect as in the BCS scenario, such that $\Delta(T) \rightarrow 0$ as $T \rightarrow T_c$, the relaxation bottleneck clearly disappears at this temperature and the formula for the temperature dependence of the photoinduced signal amplitude is somewhat modified:

$$|\Delta T/T| \propto \frac{1}{\Delta(T)+k_B T/2} \left[1 + \frac{2\nu}{N(0)\hbar\Omega} \sqrt{2k_B T/\pi\Delta(T)} \cdot e^{-\Delta(T)/k_B T} \right]^{-1}, \quad (5)$$

such that the photo-induced transmission amplitude drops to zero at T_c .

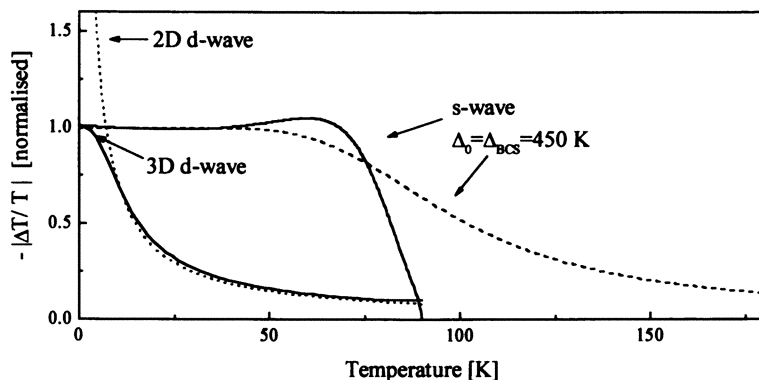


Figure 7: Theoretical predictions (9) for the amplitude of the photoinduced transmission as a function of temperature for the cases of temperature dependent BCS-like gap (“knee”-shaped upper solid line) and temperature independent s-wave gap (dashed line) with the same gap values, and for the 2D and 3D d-wave gap (dotted and solid line respectively).

It should be emphasized that the two cases are qualitatively different and can easily be experimentally distinguished. A T -dependent BCS-like collective gap, which closes at T_c , cannot be used to describe the asymptotic behavior at high temperatures, while in the T -independent gap model $|\Delta T/T|$ falls far too slowly at high T to be able to describe the data near optimum doping. Furthermore, in the case of a BCS-like T -dependent gap, there is also strong temperature dependence of the relaxation time which diverges close to T_c as $\tau_R \propto 1/\Delta(T)$ (3,8,9) since $\Delta(T) \rightarrow 0$ as $T \rightarrow T_c$ which is absent in the case of T -independent gap (see insert to Figure 3).

In the model calculations so far we considered the case of a T -independent gap and a BCS-like T -dependent gap. In both cases the gap was considered to be isotropic. We finish this section by considering the effect of a strongly anisotropy gap, applicable for example for the case of a pure d -wave superconductor. The effect of the finite density of states at low energies is that there is no real bottleneck in the QP relaxation and as a consequence we expect an increase in the photoinduced transmission only at the lowest temperatures, well below T_c . The calculated photoinduced transmission as a function of T is shown in Figure 4 for the case of a 2-dimensional DOS and a 3-dimensional d -wave DOS.

Comparison With the Data on $\text{YBa}_2\text{Cu}_3\text{O}_{7-\delta}$. The temperature dependence of photoinduced transmission and reflection for a large number of different oxygen concentrations have shown (8,9) that the behavior in underdoped samples with $\delta > 0.15$ is quite different than near optimum doping where $\delta < 0.15$. The data for three different samples with different doping δ are plotted as a function of temperature in Figure 8.

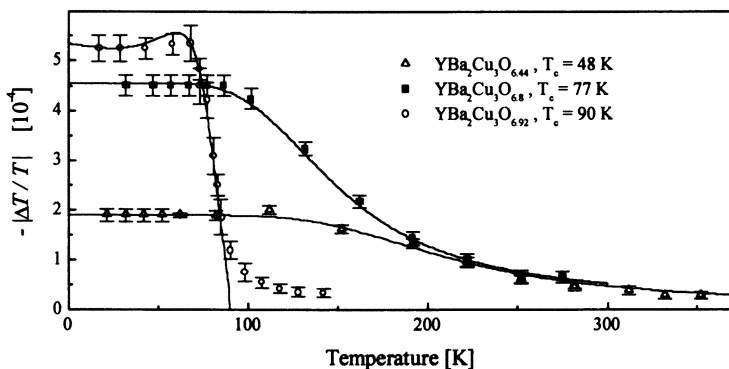


Figure 8: The temperature dependence of the photoinduced transmission amplitude for near-optimally doped sample and two underdoped samples. The solid lines are the fits to the data using equation 5 with a T-dependent BCS-like gap for near-optimally doped sample and the equation 4 with the T-independent pseudogap for the underdoped samples.

In the underdoped samples the photoinduced transmission amplitude, $|\Delta T/T|$, drops rather slowly with increasing temperature, while the data near optimum doping show an abrupt drop in the $|\Delta T/T|$, falling to near-zero close to T_c . Moreover, near optimum doping, a slight maximum is clearly observed in the data just below T_c as predicted by theoretical model (Figure 7). The calculated temperature-dependence of the photoinduced transmission is superimposed on the data in Figure 8. For $\delta > 0.15$, a T-independent gap fit was used, while for $\delta < 0.15$ the data is fitted by equation 5 for a T-dependent BCS gap, in both cases with excellent agreement with the data. The data on photoinduced transmission amplitude together with the relaxation time data thus provide clear evidence for the existence of a T-independent gap in the underdoped $\text{YBa}_2\text{Cu}_3\text{O}_{7-\delta}$ and a cross-over to a BCS-like gap near optimum doping. The temperature-dependence of the photoinduced transmission is actually a function of Δ/T in both cases, which means that the T-dependences of different samples can be scaled onto a single curve (9), provided the correct T-dependence of the gap is used. This enables us to define a criterion by which a temperature scale can be associated with the gap. In the BCS case when the gap closes at T_c , this scale is T_c itself. However, in the case of underdoped samples, where the fall-off at high temperatures is asymptotic, we chose the onset of a "pseudogap" at T^* where the amplitude of the signal falls to 10% of maximum. The main reason for choosing the 10% point and not

the mid-point for example is to enable comparison with the literature where the “onset” is the common criterion. A plot of the pseudogap temperature as a function of doping obtained in this way is plotted in Figure 9.

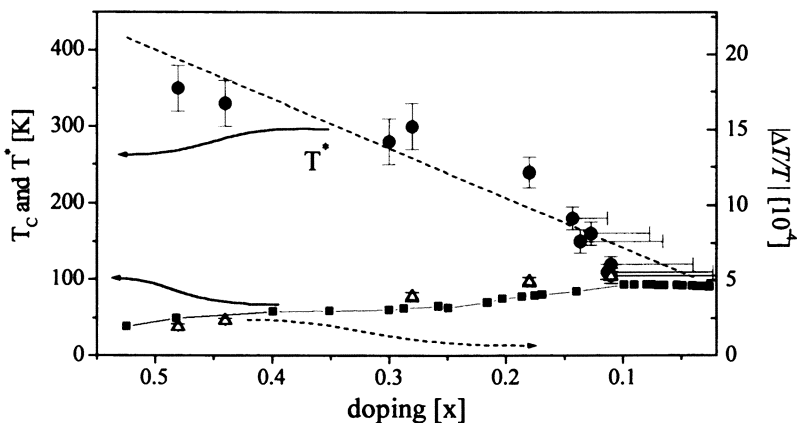


Figure 9: The pseudogap onset temperature (solid circles) for $\text{YBa}_2\text{Cu}_3\text{O}_{7-x}$ determined from time-resolved measurements together with the $\Delta T/T$ amplitude taken at series of samples of the same thickness and the same substrate in single experimental run.

Also shown in the plot is the magnitude of the photoinduced transmission signal at low temperature ($T \ll T_c$) as a function of doping x , which increases linearly with increasing hole concentration $n_h \propto (1 - x)$ in the CuO_2 planes. From equation 4, the amplitude of the photoinduced transmission is predicted to vary inversely with the magnitude of the $\Delta T/T$. From the linear relationship between $|\Delta T/T|$ and x one can deduce that the gap is inversely proportional to doping $\Delta_0 \propto 1/n_h$ in a large part of the phase diagram (24).

It is worth mentioning here that the cross-over between a T-independent gap and a T-dependent gap near optimum doping does not appear to be well defined, but there appears to be a small, but clearly visible non-zero signal in the $|\Delta T/T|$ above T_c (Figure 8). This is believed to be a result of the inhomogeneity of the hole density in the CuO_2 planes near optimum doping, where there appears to be a coexistence of regions with a collective gap and regions with a “local” T-independent gap. This observation would appear to be consistent with the two-component paradigm near optimum doping in $\text{YBa}_2\text{Cu}_3\text{O}_{7.8}$ (25).

Conclusion

In the present chapter we have described the time-resolved photoinduced absorption spectroscopy and its application in investigation of the low energy structure in high- T_c superconductors. Because time-domain spectroscopy enables the separation

of different spectral components in the low energy excitation spectrum by their lifetime, it can therefore resolve long-standing controversial issues regarding the origin of the different components in the low-energy spectra of the cuprates, which inevitably arise in the interpretation of frequency-domain spectroscopy data. This applies particularly to separation of quasiparticle states from localized states.

The recent theoretical model (9), has been used to explain the temperature dependences of photoinduced transmission or reflection in $\text{YBa}_2\text{Cu}_3\text{O}_{7-\delta}$. In spite of the fact that the model makes some simplifications, for example regarding the anisotropy of the gap and does not consider a realistic phonon density of states, the agreement with experiment appears to be sufficiently good to justify these simplifications.

We have presented the results of the measurements of the T-dependence of the photoinduced transmission over wide range of doping in $\text{YBa}_2\text{Cu}_3\text{O}_{7-\delta}$. The data have given the first direct experimental evidence for a cross-over from a T-independent gap in underdoped state to a T-dependent gap near optimal doping in the cuprates. Complementary data on the QP recombination time τ_R (3,8,9), which was not discussed in detail here, give additional support to the conclusions regarding the existence of a T-independent pseudogap and T-dependent collective gap made here on the basis of photoinduced transmission amplitude analysis. Particularly important is the observation of a divergence of τ_R at T_c in optimally doped $\text{YBa}_2\text{Cu}_3\text{O}_{7-\delta}$, which is a result of the fact that $\tau_R \sim 1/\Delta(T)$ (9) where $\Delta(T) \rightarrow 0$ at T_c . In the cross-over region the two gaps appear to coexist, suggesting a spatially inhomogeneous ground state configuration, in agreement with two-component models of the cuprates near optimum doping (25,26).

We conclude that the time-domain data on QP dynamics gives complementary information on the low-energy electronic structure of these materials, which cannot be obtained by more usual spectroscopic means and that the experimental method in conjunction with newly-developed theoretical models (9) is sufficiently general to be applicable also in other materials exhibiting gap in the low-energy excitation spectrum, such as charge-density wave systems or confined structures exhibiting a gap structure due to quantum size effects.

References

1. Non-equilibrium superconductivity, Langenberg, D.N.; Larkin, A.I., Eds.; Modern Problems in Condensed Matter Sciences, Volume 12, North Holland Physics Publishing: Amsterdam, The Netherlands, 1985.
2. Schuller, I. and Gray, K.E., *Phys.Rev.Lett.* **1976**, *36*, 429.
3. Han, S.G.; Vardeny, Z.V.; Wong, K.S.; Symco, O.G.; Koren, G., *Phys.Rev.Lett.* **1990**, *65*, 2708.
4. Easley, G.L.; Heremans, J.; Meyer, M.S.; Doll, G.L. and Liou, S.H., *Phys.Rev.Lett.* **1990**, *65*, 3445.
5. Chwalek, J.M.; Uher, C.; Whitaker, J.F.; Morou, G.A. and Agostinelli, J.A., *Appl.Phys.Lett.* **1991**, *58*, 980.

6. Albrecht, W.; Kruse, Th. and Kurz, H., *Phys.Rev.Lett.* **1992**, *69*, 1451.
7. Stevens, C.J.; Smith, D.; Chen, C.; Ryan, J.F.; Podobnik, B.; Mihailovic, D.; Wagner, G.A. and Evetts, J.E., *Phys.Rev.Lett* **1997**, *78*, 2212.
8. Mihailovic, D.; Podobnik, B.; Demsar, J.; Wagner, G. and Evetts, J., *J.Phys.Chem Sol.*, **1998**, *59*, 1937.
9. Kabanov, V.V.; Demsar, J.; Podobnik, B. and Mihailovic, D., *Phys.Rev.B*, **1999**, (Jan.1).
10. Timusk, T.; Tanner, D.B., in *Physical Properties of High-Temperature Superconductors III*; Ginsberg, D.M., Ed.; World Scientific: Singapore, **1992**; pp 363-470.
11. Timusk, T.; Tanner, D.B., in *Physical Properties of High-Temperature Superconductors I*; Ginsberg, D.M., Ed.; World Scientific: Singapore, **1989**; pp 339-399.
12. Thomsen, C; Cardona, M., in *Physical Properties of High-Temperature Superconductors I*; Ginsberg, D.M., Ed.; World Scientific: Singapore, **1989**; pp 409-508.
13. Blumberg, G.; Kang, Moonsoo; Klein, M. V. ; Kadowaki, K.; Kendziora, C., *Science* **1997**, *278*, 1427.
14. Chekalin, S.V.; Farztdinov, V.M.; Golovlyov, V.V.; Letokhov, V.S.; Lozovik, Yu.E.; Matveets, Yu.A.; Stepanov, A.G.; *Phys. Rev. Lett.*, **1991**, *67*, 3860.
15. Brorson, S.D.; Kazeroonian, A.; Face, D.W.; Cheng, T.K.; Doll, G.L.; Dresselhaus, M.S.; Dresselhaus, G.; Ippen, E.P.; Venkatesan, T.; Wu, X.D. and Inam, A., *Sol. Stat. Comm.* **1990**, *74*, 1305.
16. Thomas, T.N.; Stevens, C.J.; Choudary, A.J.S. ; Ryan, J.F. ; Mihailovic, D.; Mertelj, T.; Forro, L.; Wagner, G.; Evetts, J.E., *Phys Rev. B* **1996**, *53*, 12436
17. Carlslaw, H.S.;Jaeger,J.C., *Conduction of heat in Solids*, 2nd Ed., Oxford University Press, Oxford, UK, **1985**.
18. Bechtel, J.H., *J. Appl. Phys.* **1975**, *46*, 1585.
19. Kirchner, J.;Kelly, M.K.;Rashkeev, S.;Aoluani, M.; Fuchs, F.; Cardona, M., *Phys. Rev. B* **1991**, *44*, 217.
20. Hagen, S.J.; Wang, Z.Z.; Ong, N.P., *Phys.Rev.B*, **1989**, *40*, 9389.
21. Suemune, Y., *J.Phys.Soc.Japan*, **1965**, *20*, 174.
22. Allen, P.B., *Phys.Rev.Lett.*, **1987**, *59*, 1460.
23. Brorson, S.D.; Kazeroonian, A.; Moodera, J.S.; Face, D.W.; Cheng, T.K.; Ippen, E.P., Dresselhaus, M.S. and Dresselhaus, G., *Phys. Rev. Lett.*, **1990**, *64*, 2172.
24. Demsar, J.; Podobnik, B., Mihailovic, D., Wagner, G.A., Evetts, J.E., *Europhys. Lett.* **1998**, submitted.
25. Mihailovic, D., and Müller, K.A., *High-T_c Superconductivity 1996: Ten Years after the Discovery*; Kaldis, E. et al, Eds., Kluwer Academic Publishers, Amsterdam, Netherlands, **1997**, pp. 243-256.
26. Bianconi, A.; Missori, M., *Proceedings of the second international workshop on "Phase separation in Cuprate Superconductors"*; Sigmund, E; Müller, K.A., Ed., Springer Verlag, Berlin, **1994**, pp. 272-289.

Superconducting Plasma Phenomena in Josephson Coupled High T_c Superconductors

Kazuo Kadowaki^{1,2}, Itsuhiro Kakeya², Tetsu Wakabayashi²,
and Ryo Nakamura²

¹Institute of Materials Science, University of Tsukuba, 1-1-1, Ten-nodai,
Tsukuba, Ibaraki 305-8573, Japan

²CREST, Japan Science and Technology Corporation, 1-8, Honcho 4-chome,
Kawaguchi City, Saitama Pref. 332-0012, Japan

A comprehensive theoretical description of the superconducting plasma phenomena and the experimental justification are given for high T_c superconductors, which are considered to possess a characteristic property of intrinsic Josephson type of coupling along the c -axis because of highly two dimensional-like structure. There are two Josephson plasma modes: one is the longitudinal mode, which is known as the Nambu-Goldstone mode associated with the superconducting phase transition within the concept of spontaneously broken gauge symmetry and the other is the transverse mode, which is related to the occurrence of the Meissner effect due to the transverse currents. Although the theoretical frame of the superconducting phase transition using symmetry breaking concept has long been known well and it became even the model for the present unified field theories, the complete experimental proof in the case of superconductivity has been hindered for a long time, partly because there was no good testing examples in conventional superconductors, unfortunately. Since high T_c superconductors are known to have extremely low plasma energy ω_p as low as \approx meV in some cases such as in $\text{Bi}_2\text{Sr}_2\text{CaCu}_2\text{O}_{8+\delta}$ due to highly two dimensional superconducting nature with Josephson type of coupling along the c -axis, they lie even below the superconducting gap $2\Delta \simeq 80$ meV. Therefore, they are excellent candidates for examining the most interesting physical concept mentioned above, which results from the consequence of the spontaneously broken gauge symmetry. The gap formation of the Nambu-Goldstone mode (the longitudinal plasma mode) is known as the Anderson-Higgs-Kibble mechanism, which in fact has never been confirmed experimentally in the past. In the present study experimental identification has been made by separating the two modes by exciting independently one from the other using microwave resonance technique. A good agreement was obtained between the experimental results and the recent theoretical work, proving rigorously that the spontaneously broken symmetry works in the case of superconductivity very well. The recently discovered sharp temperature dependent phenomenon of the

Nambu-Goldstone mode near T_c can also be interpreted as a peculiar nature of the Josephson plasma within a category of the Josephson coupled system. Some implication of these results to high energy physics is made.

Superconducting Plasma Phenomena

In metallic substances superconducting phenomena are often observed below the critical temperature $T_c(I)$. The superconducting state can be treated as an ensemble of dense electrons whose electronic state is highly correlated due to electron-electron interactions in a degenerated Fermi sea, where the temperature concerning superconductivity is much lower than that of the Fermi temperature T_F . The strong correlation and the degeneracy are the direct consequence of the Fermi-Dirac statistics, which is the most fundamental requirement for electrons in quantum mechanics. Although in 1957 the basic concept of the mechanism of superconductivity has successfully been solved most elegantly by the theory of Bardeen, Cooper and Schrieffer (BCS theory)(2) introducing an idea of pairing of electrons that the ensemble of electron pairs undergoes a quantum mechanical phase transition into a macroscopic phase coherent state, it was not deeply understood until Anderson has pointed out the particular importance of the gauge invariance associated with their pairing theory to describe the superconducting phase transition correctly(3,4). Because an electron has a charge, the Coulomb interaction is inevitable and gives rise to the Coulomb gap in the low lying electronic excitation spectrum as high as the plasma energy, $\hbar\omega_p$, as in the normal electron system, where $\omega_p = \sqrt{4\pi ne^2/m}$. Here, n is the density of the electrons, e and m are the elementary charge and the mass of electron, respectively. This physical situation remains unchanged even in the superconducting state. As is widely known, the low lying collective excitation in a superconductor is nothing but the plasma mode(3,4). There are two independent plasma modes: the longitudinal and the transverse modes. The longitudinal mode is called as the Nambu-Goldstone mode associated with the superconducting phase transition(5,6). The Nambu-Goldstone mode in general should have zero gap in the excitation mode in the long wavelength limit ($k \rightarrow 0$). Historically, the gap formation of the low lying collective excitations was first argued by Anderson in terms of the Coulomb interaction among electrons (Anderson-Higgs mechanism)(7-9). Later, it has been understood from more fundamental and more general considerations on phase transitions on the basis of the concept of spontaneously broken symmetry of the electron system. According to this scenario, the longitudinal plasma in a superconductor as a Nambu-Goldstone mode can naturally be interpreted as a consequence of the spontaneously broken gauge symmetry(9-12).

The occurrence of superconductivity can be viewed as a kind of pure quantum mechanical phase transition in an electron system in a metal. This global and elegant understanding of the phase transition in general has been put forward early 1960's by Nambu(5) and others(6), who were triggered by the problem of violation of gauge invariance in the BCS theory(13-17). Soon later this approach has been applied to the elementary particle physics(18-20) and has resulted in a

great success which has never been seen before in the history of physics(12,21). Here, it is of great interest to note that all such approaches are fundamentally identical to the Ginzburg-Landau theory of superconductivity given by Ginzburg and Landau in 1950(22), which in fact is based on the theory of second-order phase transition first proposed by Landau as early as 1937(23).

The collective electronic excitation spectrum in metals may be given in the energy diagram as schematically shown in Fig. 1. In conventional metals, the plasma energy

$$E_p = \hbar\omega_p = \sqrt{\frac{4\pi\hbar^2 ne^2}{m}}, \quad (1)$$

lies as high as a few eV, which corresponds to the frequencies of 10^{15} cycles/sec., because of the high density of electrons. Note here that the frequency is simply determined by the density of electrons n . This situation remains unchanged even in the superconducting state, since this energy scale of the plasma $\sim E_p$ is much greater than the superconducting energy gap $2\Delta \sim \text{meV}$. Therefore, it was impossible to distinguish the plasma excitation modes in a superconducting state from the one in the normal state. Moreover, the plasma excitation modes have a wide spectrum because of the strong Landau damping mechanism existing in conventional metals.

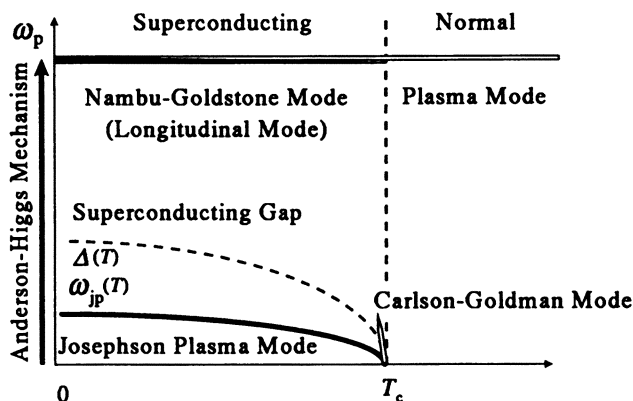


Figure 1: Energy diagram of collective excitations in metals

There have been several attempts to observe the superconducting plasma mode in the past(24-27). It was actually observed experimentally in the case of single

Josephson junction in combination with Josephson vortices(28). However, the plasma mode in this case was not the longitudinal one but the transverse mode. This is because the system with a single Josephson junction is essentially two dimensional. Therefore, it is clear that the observed mode was not the Nambu-Goldstone mode in a superconductor. To date the Nambu-Goldstone mode has never been found in a superconductor experimentally.

In high T_c superconductors such as $\text{Bi}_2\text{Sr}_2\text{CaCu}_2\text{O}_{8+\delta}$, which, for example, has a highly layered structure, the situation changes drastically. It is known from recent experimental results that the interlayer coupling in the superconducting state of these systems is of Josephson type (for example, 29-31). The strength of the coupling energy is described by the anisotropy parameter, γ , which is as high as 10^3 - 10^4 . Because of this the plasma frequency is reduced by the anisotropy factor and the plasma energy $\hbar\omega_p$ becomes even much smaller than the superconducting gap energy $\Delta \sim 40$ meV. Therefore, the plasma mode lies well below the superconducting gap and does not suffer from the Landau damping, resulting in a sharp excitation spectrum in the superconducting state (see, Fig. 1). Furthermore, it has been disclosed from the recent experimental studies that the Josephson plasma mode has a peculiar temperature dependence near T_c as is also schematically shown in Fig. 1. The fascinating feature here is that the energy of the plasma mode sharply decreases as the temperature approaches T_c . This behavior is in sharp contrast to the conventional superconducting plasma phenomena and cannot be expected in conventional superconductors. This is thought to be a peculiar effect of the Josephson coupled superconducting systems. Since this phenomenon is entirely new and very recent development in the field of superconductivity, a more detailed study is required for the full understanding.

Because of the experimental convenience most of experiments of plasma resonance have been performed by not varying frequencies but by varying magnetic field. Therefore, vortices are introduced in the sample and are involved in the plasma phenomena as long as it is not mentioned. It will be shown in both theoretically and experimentally that the plasma phenomena are modified dramatically in the presence of the vortices. In other words, the Josephson plasma resonance can be an excellent tool for studying the dynamical nature of vortices. However, this is not the aim of this review. Variety of interesting phenomena of the Josephson plasma in the vortex state in relation to the pinning state as well as the fascinating intimate interplay between plasma modes and vortices will separately be shown in detail in Part(II). The central purpose of this review is to study and understand a more fundamental nature of Josephson plasma phenomena in high T_c superconductors.

Longitudinal and Transverse Components of Electromagnetic Waves

Before discussing the Josephson plasma phenomenon concerning the longitudinal and transverse modes, we review some of interesting features of the electromagnetic waves within the classical electrodynamics, which is, perhaps, not widely known but is very useful. Furthermore, the subject described here has some similarity to the electrodynamics in plasma physics(32).

The electromagnetic waves in vacuum are known as the transverse waves so that one might not expect the existence of the longitudinal mode of the electromagnetic waves. In the following, however, we demonstrate the existence of the longitudinal mode in the electromagnetic waves, when they are in a medium with charges. This is exactly the case we are going to consider in this article. The Josephson plasma phenomena are nothing but the plasma waves (electromagnetic waves with charges) propagating in a superconducting electron system.

We begin with the most general form of the Maxwell's equation (in CGS Gaussian units) given as

$$\nabla \times \mathbf{E}(\mathbf{r}, t) = -\frac{1}{c} \frac{\partial \mathbf{B}(\mathbf{r}, t)}{\partial t} \quad (2)$$

$$\nabla \times \mathbf{H}(\mathbf{r}, t) = \frac{4\pi}{c} \mathbf{J}(\mathbf{r}, t) + \frac{1}{c} \frac{\partial \mathbf{D}(\mathbf{r}, t)}{\partial t} \quad (3)$$

$$\nabla \cdot \mathbf{D}(\mathbf{r}, t) = 4\pi \rho(\mathbf{r}, t) \quad (4)$$

$$\nabla \cdot \mathbf{B}(\mathbf{r}, t) = 0, \quad (5)$$

and the continuity equation

$$\frac{\partial \rho(\mathbf{r}, t)}{\partial t} + \nabla \cdot \mathbf{J}(\mathbf{r}, t) = 0. \quad (6)$$

Here, in the presence of substance, the dielectric displacement $\mathbf{D}(\mathbf{r}, t)$, the magnetic induction (the magnetic flux density) $\mathbf{B}(\mathbf{r}, t)$ and the current density $\mathbf{J}(\mathbf{r}, t)$ are related to the materials parameters such as the electric polarization $\mathbf{P}(\mathbf{r}, t)$, the magnetic polarization (the magnetization) $\mathbf{M}(\mathbf{r}, t)$ and the conductivity $\sigma(\mathbf{r}, t)$ through

$$\begin{cases} \mathbf{D}(\mathbf{r}, t) = \mathbf{E}(\mathbf{r}, t) + 4\pi \mathbf{P}(\mathbf{r}, t) \\ \mathbf{B}(\mathbf{r}, t) = \mathbf{H}(\mathbf{r}, t) + 4\pi \mathbf{M}(\mathbf{r}, t) \end{cases} \quad (7)$$

and

$$\mathbf{J}(\mathbf{r}, t) = \sigma \mathbf{E}(\mathbf{r}, t), \quad (8)$$

which are assumed to be a sufficiently good approximation.

We decompose an arbitrary vector field $\mathbf{V}(\mathbf{r}, t)$ to the longitudinal and the transverse components as

$$\mathbf{V}(\mathbf{r}, t) = \mathbf{V}_L(\mathbf{r}, t) + \mathbf{V}_T(\mathbf{r}, t). \quad (9)$$

Here, we define $\mathbf{V}_T(\mathbf{r}, t)$ and $\mathbf{V}_L(\mathbf{r}, t)$ to satisfy the following relations;

$$\nabla \cdot \mathbf{V}_T \equiv 0 \quad (10)$$

and

$$\nabla \times \mathbf{V}_L \equiv 0. \quad (11)$$

The subscripts T and L denote the transverse and the longitudinal components of the vector field $\mathbf{V}(\mathbf{r}, t)$. This decomposition is merely a mathematical treatment. Now, considering the physical meaning of $\nabla \cdot$ and $\nabla \times$, the vectors $\mathbf{V}_L(\mathbf{r}, t)$ and $\mathbf{V}_T(\mathbf{r}, t)$ mean the vector components, which directions are parallel to the direction that has a maximum slope of the vector field $\mathbf{V}(\mathbf{r}, t)$ and is perpendicular to the maximum slope of the vector field $\mathbf{V}(\mathbf{r}, t)$, respectively.

Applying this to the electric field $\mathbf{E}(\mathbf{r}, t)$ and the magnetic field $\mathbf{H}(\mathbf{r}, t)$, and the current $\mathbf{J}(\mathbf{r}, t)$ which are under concern, we obtain the following set of equations: for the electric field,

$$\mathbf{E}(\mathbf{r}, t) \equiv \mathbf{E}_T(\mathbf{r}, t) + \mathbf{E}_L(\mathbf{r}, t) \quad (12)$$

with

$$\begin{cases} \nabla \cdot \mathbf{E}_T(\mathbf{r}, t) \equiv 0 \\ \nabla \times \mathbf{E}_L(\mathbf{r}, t) \equiv 0, \end{cases} \quad (13)$$

and for magnetic induction,

$$\mathbf{B}(\mathbf{r}, t) \equiv \mathbf{B}_T(\mathbf{r}, t) + \mathbf{B}_L(\mathbf{r}, t) \quad (14)$$

$$\equiv \mathbf{B}_T(\mathbf{r}, t), \quad (15)$$

because

$$\nabla \cdot \mathbf{B}(\mathbf{r}, t) = 0. \quad (16)$$

For the current,

$$\mathbf{J}(\mathbf{r}, t) \equiv \mathbf{J}_T(\mathbf{r}, t) + \mathbf{J}_L(\mathbf{r}, t). \quad (17)$$

Integrating eq. (6), one obtain

$$\mathbf{J}(\mathbf{r}, t) = \mathbf{J}_T(\mathbf{r}, t) + \frac{1}{4\pi} \int_{-\infty}^{\infty} \nabla \left(\frac{1}{|\mathbf{r} - \mathbf{r}'|} \right) \frac{\partial \rho(\mathbf{r}', t)}{\partial t} d\mathbf{r}', \quad (18)$$

where $\mathbf{J}_T(\mathbf{r}, t)$ and $\mathbf{J}_L(\mathbf{r}, t)$ satisfy

$$\nabla \cdot \mathbf{J}_T \equiv 0 \quad (19)$$

and

$$\mathbf{J}_L(\mathbf{r}, t) \equiv \frac{1}{4\pi} \int_{-\infty}^{\infty} \nabla \left(\frac{1}{|\mathbf{r} - \mathbf{r}'|} \right) \frac{\partial \rho(\mathbf{r}', t)}{\partial t} d\mathbf{r}', \quad (20)$$

respectively. From the definition, $\nabla \times \mathbf{J}_L(\mathbf{r}, t) \equiv 0$. It is noted that the longitudinal current $\mathbf{J}_L(\mathbf{r}, t)$ satisfies the continuity equation as shown below:

$$\begin{aligned} \nabla \cdot \mathbf{J}_L(\mathbf{r}, t) &= \int_{-\infty}^{\infty} \nabla^2 \left(\frac{1}{|\mathbf{r} - \mathbf{r}'|} \right) \frac{\partial \rho(\mathbf{r}', t)}{\partial t} d\mathbf{r}' \\ &= - \int_{-\infty}^{\infty} \delta(\mathbf{r} - \mathbf{r}') \frac{\partial \rho(\mathbf{r}', t)}{\partial t} d\mathbf{r}' \\ &= - \frac{\partial \rho(\mathbf{r}, t)}{\partial t}. \end{aligned} \quad (21)$$

Considering the above mentioned properties we can rewrite the Maxwell's equation. For the electric field \mathbf{E} , it follows as

$$\nabla \cdot \mathbf{E}(\mathbf{r}, t) = 4\pi\rho(\mathbf{r}, t) \quad (22)$$

$$\longrightarrow \nabla \cdot \mathbf{E}_L(\mathbf{r}, t) = 4\pi\rho(\mathbf{r}, t) \quad (23)$$

and

$$\nabla \times \mathbf{E}(\mathbf{r}, t) = -\frac{1}{c} \frac{\partial \mathbf{B}(\mathbf{r}, t)}{\partial t} \quad (24)$$

$$\longrightarrow \nabla \times \mathbf{E}_T(\mathbf{r}, t) = -\frac{1}{c} \frac{\partial \mathbf{B}_T(\mathbf{r}, t)}{\partial t}. \quad (25)$$

In contrast to the electric field we need a calculation for the magnetic induction $\mathbf{B}(\mathbf{r}, t)$ such as

$$\nabla \times \mathbf{B}(\mathbf{r}, t) = \frac{4\pi}{c} \mathbf{J} + \frac{1}{c} \frac{\partial \mathbf{E}(\mathbf{r}, t)}{\partial t} \quad (26)$$

$$\begin{aligned} \longrightarrow \frac{4\pi}{c} \mathbf{J}_T(\mathbf{r}, t) + \frac{4\pi}{c} \int_{-\infty}^{\infty} \nabla \left(\frac{1}{|\mathbf{r} - \mathbf{r}'|} \right) \frac{\partial \rho(\mathbf{r}', t)}{\partial t} d\mathbf{r}' \\ + \frac{1}{c} \frac{\partial}{\partial t} (\mathbf{E}_T + \mathbf{E}_L). \end{aligned} \quad (27)$$

Integrating the equation $\nabla \cdot \mathbf{E}_L(\mathbf{r}, t) = 4\pi\rho(\mathbf{r}, t)$, one obtain

$$\mathbf{E}_L(\mathbf{r}, t) = - \int_{-\infty}^{\infty} \rho(\mathbf{r}', t) \nabla \left(\frac{1}{|\mathbf{r} - \mathbf{r}'|} \right) d\mathbf{r}'. \quad (28)$$

Substituting eq. (28) to eq. (27), one finally obtain an equation

$$\nabla \times \mathbf{B}_T(\mathbf{r}, t) = \frac{4\pi}{c} \mathbf{J}_T(\mathbf{r}, t) + \frac{1}{c} \frac{\partial \mathbf{E}_T(\mathbf{r}, t)}{\partial t}. \quad (29)$$

This means that the longitudinal component of the current $\mathbf{J}(\mathbf{r}, t)$ is canceled out by the time variation of the electric field $\mathbf{E}(\mathbf{r}, t)$. It is obvious from the last Maxwell's equation (eq. (5)) that

$$\nabla \cdot \mathbf{B}(\mathbf{r}, t) = 0 \quad (30)$$

$$\longrightarrow \nabla \cdot \mathbf{B}_T(\mathbf{r}, t) = 0. \quad (31)$$

Therefore, we succeeded in rewriting the Maxwell's equations by the longitudinal and the transverse components as

$$\nabla \times \mathbf{E}_T(\mathbf{r}, t) = -\frac{1}{c} \frac{\partial \mathbf{B}_T(\mathbf{r}, t)}{\partial t} \quad (32)$$

$$\nabla \times \mathbf{B}_T(\mathbf{r}, t) = \frac{4\pi}{c} \mathbf{J}_T(\mathbf{r}, t) + \frac{1}{c} \frac{\partial \mathbf{E}_T(\mathbf{r}, t)}{\partial t} \quad (33)$$

$$\nabla \cdot \mathbf{E}_L(\mathbf{r}, t) = 4\pi\rho(\mathbf{r}, t) \quad (34)$$

$$\nabla \cdot \mathbf{B}_T(\mathbf{r}, t) = 0. \quad (35)$$

It is interesting to note that, first, the longitudinal wave does exist only in the electric field $\mathbf{E}(\mathbf{r}, t)$ and does not exist in the magnetic induction $\mathbf{B}(\mathbf{r}, t)$. This means that the magnetic field component of the electromagnetic waves is always the transverse wave. It is interesting to further note that the longitudinal electric field originates from the merely charge density $\rho(\mathbf{r}, t)$. If the electric charge does exist, the Maxwell's equation can always be written by the transverse components of the electric field and the magnetic field only.

Second, the longitudinal and transverse waves are separated. This means that the longitudinal wave in the electric field is independent of the other transverse wave component of the fields. For example, if the elementary charge, e , is at rest at the origin, from eq. (28)

$$\begin{aligned} \mathbf{E}_L(\mathbf{r}, t) &= -\int_{-\infty}^{\infty} \nabla \left(\frac{1}{|\mathbf{r} - \mathbf{r}'|} \right) \rho(\mathbf{r}', t) d\mathbf{r}' \\ &= -\int_{-\infty}^{\infty} e\delta(\mathbf{r}') \nabla \left(\frac{1}{|\mathbf{r} - \mathbf{r}'|} \right) d\mathbf{r}' \\ &= -e\nabla \left(\frac{1}{|\mathbf{r}|} \right), \end{aligned} \quad (36)$$

because

$$\rho(\mathbf{r}, t) = e\delta(\mathbf{r}). \quad (37)$$

The electromagnetic waves propagating in a vacuum ($\rho(\mathbf{r}, t)=0$) have two degrees of freedom corresponding to the two polarizations of electric vector $\mathbf{E}(\mathbf{r}, t)$ and magnetic vector $\mathbf{H}(\mathbf{r}, t)$. This property is nothing but the consequence of the transverse waves with two transverse polarization components. The electromagnetic waves traveling through a system containing charged particles, however, have the third degree of freedom: the longitudinal waves. One may wonder why the third degree of freedom is created in the system containing of charged particles. As we already mentioned in deriving eq. (29) from the Maxwell's equation one may notice that the third mode is not newly created but it even exists in the electromagnetic waves propagating in vacuum, too. It does exist even in vacuum but it does not appear explicitly because it is exactly canceled out in vacuum.

Josephson Plasma in Single Josephson Junction

We begin by considering a single Josephson junction, which consists of two superconducting plates separated by a thin insulating layer as shown schematically in Fig. 2. Superconducting electron pairs can penetrate through such a thin layer quantum mechanically. This effect is called as Josephson effect. Josephson plasma is nothing but the plasma phenomenon in the superconducting electron pair system with the Josephson effect. When the insulating layer becomes infinitely thin, the Josephson plasma should become equivalent to the plasma in a bulk superconductor.

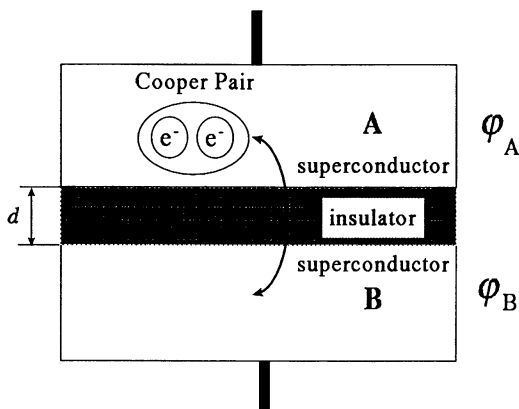


Figure 2: A schematic picture of a Josephson junction

The Josephson effect becomes significant, only when the superconducting pair tunneling current j_{pair} becomes nonlinear with spatial phase variation in-between two bulk superconductors A and B as shown in Fig. 2. The maximum current density through the barrier, j_c , can be expressed as

$$j_c = \frac{e\hbar n_s}{m_c d}, \quad (38)$$

where \hbar is the Plank constant, e the electric charge, n_s the superconducting electron density, m_c the c-axis effective mass and d the distance between two superconductors(33).

The penetration depth λ_c is given as

$$\lambda_c = \sqrt{\frac{c\phi_0}{8\pi^2 j_c d}}, \quad (39)$$

where ϕ_0 is the flux quanta and c the light velocity. The plasma frequency in this system can be given as

$$\omega_p = \frac{c}{\sqrt{\epsilon\lambda_c}}, \quad (40)$$

where ϵ denotes the dielectric constant of the junction.

The rigorous argument of the Josephson plasma in a single layer junction can be done as follows(24,25,34): Suppose that the Josephson junction of unit area

is made by sandwiching the thin insulating layer with a dielectric constant ϵ as shown in Fig. 2. When a Cooper pair moves from one superconducting electrode A to the other B, the phase difference $\varphi = \varphi_A - \varphi_B$ is created. The increase of the energy due to the phase difference, $\Delta E(\varphi)$ can be expressed as

$$\Delta E(\varphi) = E(1 - \cos \varphi) = \frac{\hbar j_c}{2e}(1 - \cos \varphi). \quad (41)$$

Since the transfer of a Cooper pair makes charge unbalance between two superconducting electrodes A and B, this causes an increase of static Coulomb energy $\Delta E(\delta n)$ as

$$\Delta E(\delta n) = \frac{(\delta Q)^2}{2C} = \frac{(2e\delta n)^2}{2C}, \quad (42)$$

where $C = \epsilon/4\pi d$ is the capacitance between two electrodes A and B, δQ and δn mean the net charge moved and the number of Cooper pairs moved from one electrode to another electrode, respectively. ϵ is the dielectric constant of the insulator between superconductors.

The Hamiltonian \mathcal{H} of this system, therefore, can be written as

$$\begin{aligned} \mathcal{H} &= \frac{(\delta Q)^2}{2C} + E(1 - \cos \varphi) \\ &= \frac{(2e\delta n)^2}{2C} + \frac{\hbar j_c}{2e}(1 - \cos \varphi). \end{aligned} \quad (43)$$

It is interesting to note that this Hamiltonian is equivalent to a pendulum where $[\delta n, \varphi] = 1$, so that δn plays the role of the momentum and φ that of the coordinate. When the variation of φ is small enough, eq. (43) is reduced to a harmonic oscillator with the eigen frequency ω_p to be

$$\hbar\omega_p = \sqrt{\frac{(2e)^2 E}{C}} = \sqrt{\frac{8\pi e d \hbar j_c}{\epsilon}}. \quad (44)$$

This equation can be rewritten as

$$\omega_p^2 = \frac{8\pi e d j_c}{\epsilon \hbar} = \left(\frac{c}{\lambda_J}\right)^2 \frac{1}{\epsilon}, \quad (45)$$

where

$$\lambda_J = \sqrt{\frac{\hbar c^2}{8\pi e j_c d}} = \sqrt{\frac{c\phi_0}{8\pi^2 j_c d}}. \quad (46)$$

This equation is equivalent to eq. (39).

Substituting the known material parameters for a typical high T_c superconductor $\text{Bi}_2\text{Sr}_2\text{CaCu}_2\text{O}_{8+\delta}$ to eq. (45), for example,

$$\begin{cases} \epsilon \approx 12.7 \\ d \approx 15 \text{ \AA} \\ j_c \approx 7.5 \times 10^{11} \text{ esu.A/cm}^2, \end{cases} \quad (47)$$

one may expect a value for the plasma frequency ω_p as

$$\omega_p = 2\pi f_p \approx 3.3 \times 10^{11} \text{ rad/sec.} \quad (48)$$

Therefore,

$$f_p \approx 53 \text{ GHz.} \quad (49)$$

This frequency lies just in a range of microwave region and the corresponding energy is approximately 0.2 meV, which is, in fact, much smaller than the superconducting energy gap $2\Delta \sim 80$ meV. This means that the plasma energy lies within the superconducting energy gap. In this condition it is expected that the quasiparticle damping is suppressed because of no Landau damping mechanism. As a consequence a sharp plasma resonance can be expected. Actually, such a sharp resonance was observed and was identified to be the Josephson plasma resonance in $\text{Bi}_2\text{Sr}_2\text{CaCu}_2\text{O}_{8+\delta}$ and other similar systems.

Although the essence of the Josephson plasma phenomena can be understood by a capacitor model as described above, one has to take into account additional two points to extend it to high T_c superconductors(35,36). First, one has to consider the charge unbalance in superconducting thin layers, since all high T_c superconductors are known to possess the layered structure, where an atomic scale thin layers of strong superconducting CuO_2 planes are stacked in series with a separation of each layers only by ~ 10 Å. This thin electrode effect requires a modification of the Josephson relation and will be discussed later in more detail. Second, the plasma excited in a single junction is restricted to the transverse plasma, because the system is essentially two dimensional. On the contrary to this a longitudinal plasma in a multistacked junction system can also be excited in addition to the two transverse plasma modes. This three dimensional effect leads us to a complete understanding of the plasma phenomena in a superconductor, which was missing in the previous studies.

Josephson Plasma in High T_c Superconductors

The study of Josephson plasma in high T_c superconductors was initiated by Fertig and Das Sarma(37,38) in their theoretical calculations of the collective excitation modes in the superconducting state in 1990. They showed that the superconducting plasma excitation energy lies well below the superconducting gap 2Δ at the long wave length limit, because of highly two dimensional character of the superconductivity. In 1991, Mishonov(39) has also arrived at the same conclusion independently, by knowing the infrared absorption data of Noh *et al.*(40), which for the first time suggest the existence of the collective excitations in high T_c superconductors at the infrared frequency range. Although their experimental results were obtained in powdered samples of $\text{La}_{2-x}\text{Sr}_x\text{CuO}_{4-y}$, $\text{Nd}_{1.85}\text{Ce}_{0.15}\text{CuO}_4$ and $\text{Bi}_4\text{Sr}_3\text{Ca}_3\text{Cu}_4\text{O}_z$ using sphere resonance technique, they clearly observed the plasma edges in the superconducting state, which lie well below the superconducting gaps in those compounds. Absence of the plasma edge in the normal state

as well as the shift of the edge by reducing the doping level were also noticeable observation in their work. They also reminded that such a sharp plasma edge was not found in $\text{YBa}_2\text{Cu}_3\text{O}_7$ compound. Soon after their report, Tamasaku *et al.*(41) confirmed their results by observing the sharp plasma edge for the *c*-axis in $\text{La}_{2-x}\text{Sr}_x\text{CuO}_4$ below T_c at about 50 cm^{-1} in the infrared spectrum. This result was interpreted as the plasma oscillation in the superconducting state along the *c*-axis, whose conductivity, in contrast, is highly incoherent in the normal state. Later, the occurrence of the superconducting coherent state from such a highly incoherent normal state has been thought of as the basic mechanism of high T_c superconductivity in the theory of interlayer coupling model proposed by Anerson(42,43).

Based on these experimental observation, Tachiki *et al.*(44) has formulated a theory of superconducting plasma in the system with highly layered structure. In their approach the underlying physical model has been a long debate, because the model explicitly includes a very striking physical situation that the high T_c superconductors are intrinsically inhomogeneous at the atomic scale in a unit cell of these materials. In this model the stronger superconducting order parameter lies at the CuO_2 layers which are separated only by 15 \AA in the case of $\text{Bi}_2\text{Sr}_2\text{CaCu}_2\text{O}_{8+\delta}$, for instance, and are coupled by the Josephson effect through rather insulating or semiconducting layers with the weaker order parameter. This means that the high T_c materials may be thought of as a system with many atomic scale Josephson junctions stacked in series along the *c*-axis.

In 1992, Kleiner *et al.*(29) for the first time showed the multiple branches of the $I - V$ characteristics for the *c*-axis in single crystalline $\text{Bi}_2\text{Sr}_2\text{CaCu}_2\text{O}_{8+\delta}$, whose separations in voltage are equal each other and whose number correspond to the number of the CuO_2 layers. They also showed the Fraunhofer pattern as well as the Shapiro step in microwave radiation(29,45). Independently, the similar results by Oya *et al.*(30), Kadowaki *et al.*(31), Régi *et al.*(46) and Yurgens *et al.*(47) have been reported. From these experimental results the idea of Josephson junction at the size of the unit cell scale stacked along the *c*-axis has been established by the end of 1994. This concept is now called as the intrinsic Josephson junction.

The electromagnetic absorption at microwave frequencies in these systems was first reported by Tsui *et al.*(48) in the course of study of the surface impedance measurement in $\text{Bi}_2\text{Sr}_2\text{CaCu}_2\text{O}_{8+\delta}$. They put a piece of the single crystal inside the microwave wave guide and measured the microwave surface impedance by sweeping magnetic field. They observed rather accidentally a broad peak, which was interpreted as an anomalous change of the surface impedance of the sample. They reported their experimental results with possible interpretations: (1) the surface impedance becomes anomalously dissipative when the external magnetic field is applied. This suggests that this anomalous dissipation may be due to a kind of resonance absorption such as electron spin resonance or cyclotron resonance. (2) However, the possibility of the cyclotron resonance was excluded by the fact that the frequency-magnetic field relation was anticyclotronic. (3) The anomalous absorption was considered to be a phenomenon strongly coupled with the vortex state, since the resonance field shows a maximum at the irreversibility line of this compound.

Soon after their report, Matsuda *et al.*(49) has reproduced their results by using the cavity resonator, which enables us to identify the origin of the absorption. They observed that the resonance takes place only when the microwave electric vector is applied parallel to the *c*-axis. Although it was shown later by more detailed experiments that the absorption was not only observed in this case but also with different conditions, this observation was sufficient to inspire Tachiki *et al.*(50) to identify this magnetoabsorption to be due to the Josephson plasma resonance.

According to Tachiki *et al.*(50-52), there exist two Josephson plasma modes: one is the longitudinal mode and the other is the transverse mode. In the experimental conditions by Tsui *et al.*(48) and Matsuda *et al.*(49) using microwave frequencies, it is evident that the mode observed must be only at $k \simeq 0$. Since two modes are degenerated at $k = 0$ it is not certain which mode is actually excited in the experiment. To answer this question, Kadowaki *et al.*(53-57) have performed the measurement of all possible configurations of the sample with respect to the microwave electric vector E_{rf} and magnetic vector H_{rf} in a cavity with TE₁₀₂ mode at 35 GHz frequency. From these experiments they were able to separate out two modes. The results were compared with the theoretical calculations(53,55-57) done by both Tachiki *et al.*(52) for the longitudinal mode and Takahashi *et al.*(58) for the transverse mode. As we will see below the experimental results are in excellent agreement with the theoretical predictions. This finally complete the distinction of two plasma modes experimentally, and therefore, confirms that the longitudinal plasma mode is the Nambu-Goldstone mode in a superconductor(59-61).

Josephson Plasma: (I) Longitudinal Plasma Mode

We consider a multi-stacked Josephson junction as a more realistic model of high T_c superconductors, which may be depicted in Fig. 3. Firstly we formulate the longitudinal plasma by following the method of Tachiki *et al.*(50-52) and Koyama and Tachiki(35). For simplicity we assume that the superconducting layers are so thin that the superconducting phase and the electromagnetic field do not vary inside layers. In this case the phase of superconducting order parameter $\varphi(\mathbf{r}, t)$ between ℓ -th layer and $\ell + 1$ -th layer must satisfy the gauge invariant relation

$$\varphi_{\ell+1,\ell}(\mathbf{r}, t) \equiv \varphi_{\ell+1}(\mathbf{r}, t) - \varphi_{\ell}(\mathbf{r}, t) - \frac{2\pi}{\phi_0} \int_{z_{\ell+s/2}}^{z_{\ell+1-s/2}} A_z(\mathbf{r}, t) dz, \quad (50)$$

where s and D are the thickness of the superconducting and insulating layers, respectively, and satisfy a relation $z_{\ell} = \ell(s + D)$. A is the vector potential.

When a uniform current $I(t)$ is fed from the electrode, a uniform current flow in the plane may be expected. Therefore, the total current must be uniform and be conserved. Let $\rho_{\ell}(t)$ be the charge density at the ℓ -th layer by ignoring the spatial dependence of $I(t)$ within the plane, therefore, by assuming current component only along the *c*-axis, $\mathbf{J}(\mathbf{r}, t) = (0, 0, J(t))$, then, a relation

$$J_{\ell+1,\ell}(t) = J_{\ell,\ell-1}(t) - s \frac{\partial \rho_{\ell}(t)}{\partial t} \quad (51)$$

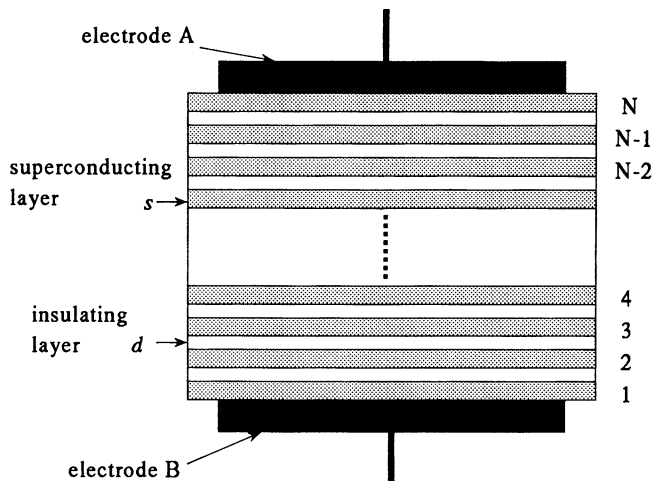


Figure 3: A schematic picture of a multistacked Josephson junction as a model of high T_c superconductors

can be obtained. From Maxwell's equation

$$\nabla \cdot \mathbf{D} = \nabla \cdot \varepsilon \mathbf{E} = 4\pi\rho \quad (52)$$

an equation

$$E_{l+1,l}(t) - E_{l,l-1}(t) = \frac{4\pi s}{\varepsilon} \rho_l(t) \quad (53)$$

is derived. Here ε is the dielectric constant at the insulating layer and only the c -axis components of \mathbf{E} and \mathbf{D} are considered. From eqs. (51) and (53), one obtain

$$J_{l+1,l}(t) + \frac{\varepsilon}{4\pi} \frac{\partial E_{l+1,l}(t)}{\partial t} = J_{l,l-1}(t) + \frac{\varepsilon}{4\pi} \frac{\partial E_{l,l-1}(t)}{\partial t}. \quad (54)$$

This equation means the current conservation law that the current including displacement current is conserved at each layer. The current $J_{l+1,l}$ is the tunneling current through superconducting ℓ -th and $\ell + 1$ -th layers and can be written as

$$J_{l+1,l}(t) = j_c \sin \varphi_{l+1,l}(t) + \sigma E_{l+1,l}(t). \quad (55)$$

Therefore, the total current $I(t)$ can be written as

$$I(t) = j_c \sin \varphi_{l+1,l}(t) + \sigma E_{l+1,l}(t) + \frac{\varepsilon}{4\pi} \frac{\partial E_{l+1,l}(t)}{\partial t}. \quad (56)$$

If one assumes the conventional Josephson relation as for the single junction, a relation between phase $\varphi_{i+1,l}(t)$ and voltage $V_{i+1,l}$ can be obtained by using the equation $V_{i+1,l}(t) = DE_{i+1,l}(t)$ as,

$$\frac{\partial \varphi_{i+1,l}(t)}{\partial t} = \frac{2e}{\hbar} V_{i+1,l}(t) = \frac{2\pi c}{\phi_0} DE_{i+1,l}(t). \quad (57)$$

When the superconducting layers are thick enough, the multi-stacked junctions can be considered as a series connection of n single junctions. In the case of high T_c superconductors, however, the layer thickness is very thin and comparable with the atomic distances. In such a case the conventional Josephson relation has to be modified by taking into account the Coulomb interaction between electrons. In order to include this effect correctly we differentiate eq. (50) with respect to t , then the following equation is obtained:

$$\begin{aligned} \frac{\phi_0}{2\pi c} \frac{\partial \varphi_{i+1,l}(t)}{\partial t} &= \left[A_0(z_{i+1}, t) + \frac{\phi_0}{2\pi c} \frac{\partial \varphi_{i+1}(t)}{\partial t} \right] \\ &\quad - \left[A_0(z_i, t) + \frac{\phi_0}{2\pi c} \frac{\partial \varphi_i(t)}{\partial t} \right] + V_{i+1,l}(t), \end{aligned} \quad (58)$$

where $A_0(z, t)$ is the scalar potential. If we assume a relation

$$\rho_l(t) = \frac{1}{4\pi\mu^2} \left[A_0(z_l, t) + \frac{\phi_0}{2\pi c} \frac{\partial \varphi_l(t)}{\partial t} \right], \quad (59)$$

where μ is the Debye screening length of the superconducting charges and inserting eq. (59) into eq. (58) using eq. (53), one obtain the modified Josephson relation as

$$\frac{\hbar}{2e} \frac{\partial \varphi_{i+1,l}(t)}{\partial t} = \frac{\varepsilon\mu^2}{sD} \left[-V_{i,l-1}(t) + \left(2 + \frac{sD}{\varepsilon\mu^2} \right) V_{i+1,l}(t) - V_{i+2,l+1}(t) \right]. \quad (60)$$

It is evident that when a parameter $\alpha = \varepsilon\mu^2/sD \ll 1$, eq. (60) can be reduced to the conventional Josephson relation (eq. (57)). Taking a set of parameters reasonable for high T_c superconductors, for example, $s=7 \text{ \AA}$, $D=6 \text{ \AA}$, $\mu=10 \text{ \AA}$ and $\varepsilon=10$, one can estimate to be $\alpha \sim 24 \gg 1$. This means that the thickness effect can not be neglected and one has to use the eq. (60) in high T_c superconductors. Using eqs. (56) and (60) one obtains an equation

$$\begin{aligned} \frac{\varepsilon}{c^2} \frac{\partial^2 \varphi_{i+1,l}(t)}{\partial t^2} &= \frac{\alpha}{\lambda_c^2} \left\{ \sin \varphi_{i+2,l+1}(t) - \left(2 + \frac{1}{\alpha} \right) \sin \varphi_{i+1,l}(t) \right. \\ &\quad \left. + \sin \varphi_{i,l-1}(t) + \beta \left[V_{i+2,l+1}(t) - \left(2 + \frac{1}{\alpha} \right) V_{i+1,l}(t) + V_{i,l-1}(t) \right] \right\} \\ &\quad + \frac{I(t)}{\lambda_c^2 j_c}, \end{aligned} \quad (61)$$

where $\beta = 4\pi\sigma\lambda_c/c\varepsilon^{1/2}$ and $\lambda_c = \{c\phi_0/8\pi^2 D j_c\}^{1/2}$. Putting $\sigma=0$ and $I(t)=0$, one obtain the dispersion relation for the longitudinal plasma mode as

$$\begin{aligned} \omega_L(k_x) &= \omega_p \sqrt{1 + 2\alpha [1 - \cos(k_x(s+D))]} \\ &\approx \omega_p \sqrt{1 + \varepsilon\mu^2 \frac{(s+D)^2}{sD} k_x^2}, \end{aligned} \quad (62)$$

where $\omega_p = c/\lambda_c \varepsilon^{1/2}$. As mentioned previously, $\mu \sim 10 \text{ \AA}$, it is obvious that the longitudinal plasma mode does not show strong dispersion as a function of k_x .

Josephson Plasma (II): Transverse Plasma Mode

From eq. (50) and the Maxwell's equations (eqs. (2), (3), (4) and (5)), one can obtain an equation of motion of the phase $\varphi_{l+1,l}(x, y, t)$ as

$$\begin{aligned} & \left(-\frac{\varepsilon}{c^2} + \frac{\partial^2}{\partial t^2} + \frac{\partial^2}{\partial x^2} + \frac{\partial^2}{\partial y^2} \right) \varphi_{l+1,l}(x, y, t) \\ &= \frac{8\pi^2 D j_c}{c \phi_0} \left[\frac{\lambda_c^2}{D^2} \sin \varphi_{l+2,l+1}(x, y, t) - \left(\frac{2\lambda_c^2}{D} + 1 \right) \sin \varphi_{l+1,l}(x, y, t) \right. \\ & \quad \left. + \frac{\lambda_c^2}{D^2} \sin \varphi_{l,l-1}(x, y, t) \right. \\ & \quad \left. - \frac{8\pi \lambda_c^2}{c \phi_0} \left(1 - \frac{\varepsilon \mu^2}{\lambda_c^2} \right) \left(\frac{\partial \rho_{l+1}(x, y, t)}{\partial t} - \frac{\partial \rho_l(x, y, t)}{\partial t} \right) \right]. \end{aligned} \quad (63)$$

If $\varphi_{l+1,l}(x, y, t) = \varphi(x, y, t)$, eq. (63) can be rewritten as

$$\left[-\frac{\varepsilon}{c^2} \frac{\partial^2}{\partial t^2} + \frac{\partial^2}{\partial x^2} + \frac{\partial^2}{\partial y^2} \right] \varphi(x, y, t) = \frac{\sin \varphi(x, y, t)}{\lambda_c^2}. \quad (64)$$

Taking an approximation $\sin \varphi(x, y, t) \sim \varphi(x, y, t)$, one can obtain an equation

$$\left[-\frac{\varepsilon}{c^2} \frac{\partial^2}{\partial t^2} + \frac{\partial^2}{\partial x^2} + \frac{\partial^2}{\partial y^2} - \frac{1}{\lambda_c^2} \right] \varphi(x, y, t) = 0. \quad (65)$$

This is the wave equation for the phase with the eigen frequency of $\omega_T(k)$

$$\omega_T(k) = \omega_p \sqrt{1 + \lambda_c^2 k^2}, \quad (66)$$

where $\omega_p = c/\lambda_c \varepsilon^{1/2}$ and $k = (k_x, k_y)$. For high temperature superconductors such as $\text{Bi}_2\text{Sr}_2\text{CaCu}_2\text{O}_{8+\delta}$, λ_c is very large, as large as 10^{-2} cm . This implies that $\lambda_c k = \lambda_c (\pi/L) (2n+1) \sim 0.3$, which can not be neglected. Here, $L \sim 1 \text{ mm}$ and is the dimension of the sample in the ab -plane, and $n \sim 0$ is assumed. This means that the transverse plasma has a strong dispersion with respect to k at $k \sim 0$. This also means that the transverse plasma mode exhibits strong sample size dependence.

The dispersion relations of both longitudinal and transverse plasma modes are shown in Fig. 4.

When $k=0$, both modes are degenerated at $\omega = \omega_p$. When $k \rightarrow \infty$, on the other hand, one may predict that $\omega_T \rightarrow ck/\varepsilon^{1/2}$. This is equivalent to the dispersion relation of light in superconductors. In summary, the transverse plasma is essentially the electromagnetic wave (transverse wave) propagating in a superconductor and is nothing but the collective transverse excitations of superconducting currents coupled with electromagnetic waves.

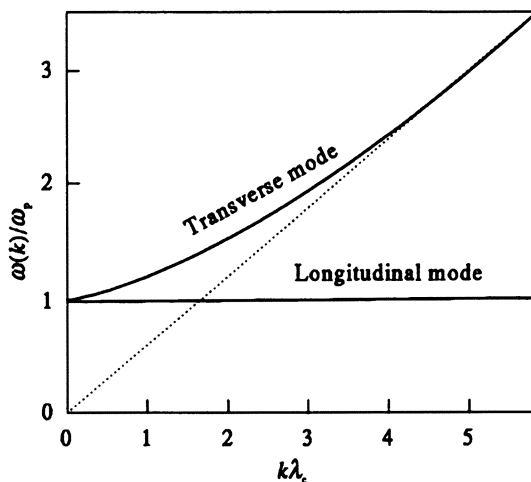


Figure 4: Dispersion relation of longitudinal and transverse plasma modes

Separation of Longitudinal and Transverse Plasma Modes

As mentioned above, Josephson plasma phenomena are the collective superconducting electron excitations induced by electromagnetic waves. We have already seen that there exist two plasma modes: the longitudinal and transverse modes, which have distinct proper dispersion relations. This difference originates from different physics. Therefore, it is interesting to distinguish two modes experimentally and investigate them in more detail, since to our knowledge, there has been no experimental studies to make distinction of these two modes. Perhaps, partly because there was no suitable systems with reasonable Josephson coupling strength, which brings down the working frequencies to a microwave region. High T_c superconductors such as $\text{Bi}_2\text{Sr}_2\text{CaCu}_2\text{O}_{8+\delta}$ are exception, in which all experimental conditions are matched and fulfilled nicely. In addition, it is impossible to overemphasize the importance of having high quality single crystals from experimental point of view.

The physical meaning of the two modes are different. The longitudinal mode is the Nambu-Goldstone mode appeared due to superconducting phase transition associated with the spontaneously broken gauge symmetry, whereas the transverse mode is related to the Meissner effect. Therefore, our interest in these significant differences of two modes in physical meaning strongly leads to a motivation to separate them experimentally and to investigate the nature of them.

We have successfully performed such experiments using high quality single crystal $\text{Bi}_2\text{Sr}_2\text{CaCu}_2\text{O}_{8+\delta}$ at 35 GHz microwave frequency(53-61). In the following, we first describe the experimental technique used to separate two modes in detail.

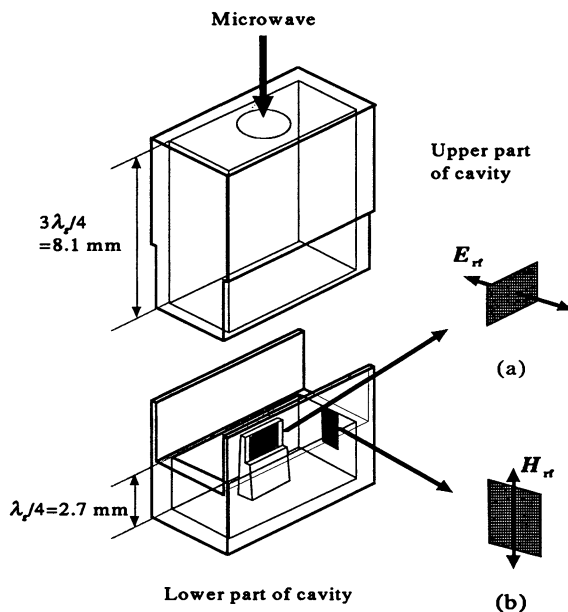


Figure 5: A cut view of the cavity resonator with TE_{102} mode used for the present study at 35 GHz. The sample location as well as the configuration between sample and microwave electric and magnetic fields are also displayed.

It is one of the characteristic properties of single crystalline $\text{Bi}_2\text{Sr}_2\text{CaCu}_2\text{O}_{8+\delta}$ samples that have always thin platelet shape because of the highly two dimensional property of the crystal. In this case it is very difficult to directly excite the transverse plasma by freely traveling microwaves. This was, however, the case of Tsui *et al.*(48), who first discovered anomalous absorption in high T_c superconductors. In their experiments the sample was set in a waveguide where microwaves are freely traveling. Since the microwave is traveling with time, it is not clear what actually is happening to cause the absorption. We have studied systematically the configurations of sample and microwave electric field E and magnetic field H by using cavity resonator. This is the only way to separate the effect of E and H . It was found by examining all possible configurations that for the longitudinal plasma excitation the microwave E vector is responsible for the excitation and has to be

applied perpendicular to the superconducting layers, while for transverse plasma excitation the microwave H vector has to be exerted parallel to the layers. This experimental configuration is summarized in Fig. 5. In this rectangular cavity the TE_{102} microwave mode is used for a practical reason. The cavity is cut into two pieces at the quarter position from the bottom in order to set the sample easily. The sample is attached by silicon grease either at the lower center of the cavity where the electric field is maximum and the magnetic field is minimum (see, Fig. 5(a)) or at the wall where the magnetic field is maximum and the electric field is minimum (see, Fig. 5(b)). Such detailed positions as well as the setting conditions of the sample is essential for this experiment. A piece of Teflon is used as a sample supporter, if it is necessary. The lower part of cavity after setting the sample it is mechanically slid in the rest of the upper cavity. The ESR signal of DPPH(α' -Diphenyl- β -Picryl Hydrazyl) is used for the magnetic field calibration.

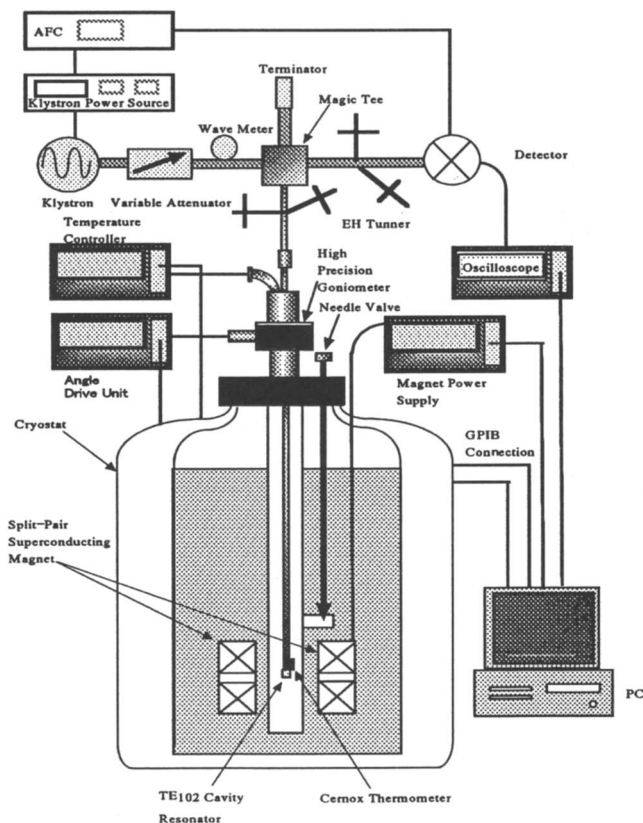


Figure 6: A block diagram of the experimental set up used for the preset Josephson plasma resonance

The microwave absorption is detected by the Schottky diode through the conventional microwave circuit using the magic tee bridge balance. The block diagram of the detection system used in the present study is shown in Fig. 6. The klystron (Okaya Denki Sangyo, Co. Ltd, Japan) is used for 35 GHz microwave generation. The microwave after the klystron is sent to the variable attenuator and the wave meter, then to the magic tee, where it is split equally to two branches. One of them is fed to the terminator and the other is fed to the cavity resonator. The reflected microwave returns to the magic tee, where the out put from it is adjusted so as to balance out and to minimize the detected power at the Schottky diode. When the absorption takes place, the reflected power is reduced by absorption. Therefore, the microwave power balance at the magic tee becomes uneven. This unbalanced power is detected as the absorption.

The cavity is inserted inside the variable temperature insert, where temperature is controlled by fine temperature controller (Neocera, LTC21, USA). The magnetic field is generated by the split superconducting coil up to 8 T with homogeneity of 10^{-4} .

The cavity and the whole transmission line of the microwave to the cavity are set on the precision goniometer, which can rotate within accuracy of 0.001° without backlash.

Experimental data are taken either by sweeping magnetic field at a fixed temperature or by sweeping temperature at a fixed magnetic field. All data are automatically stored on the personal computer through the original program software developed by ourselves.

We have already discussed the case for the transverse plasma previously. However, the mode calculated is in most general case, where there is no boundary condition of the sample. However, in practice the sample has a finite size so that it has to be taken into account (58). Hereafter, we concentrate on the case for the transverse plasma, where the boundary condition becomes very important.

Following the calculation developed by Takahashi *et al.* (58), we first set the experimental condition as shown in Fig. 7 and analyze the plasma mode excited in this condition. As seen in Fig. 7, the magnetic field H_{rf} of the microwave is applied parallel to the ab -plane. In this case, the current induced by H_{rf} flows in the ab -plane perpendicular to H_{rf} and circulates around the sample. At the edge of the sample this current flows along the c -axis and its direction is opposite at one end and the other. This situation is shown in Fig. 8.

This antisymmetric current induced by H_{rf} can excite the transverse plasma as shown in the following. The current induced can be described by the London equation as

$$\frac{4\pi}{c} \mathbf{j} = -\frac{1}{\lambda_c^2} \mathbf{A} \quad (67)$$

where

$$\begin{cases} \mathbf{j} = (0, 0, j_z) \\ \mathbf{A} = (0, 0, A_z). \end{cases} \quad (68)$$

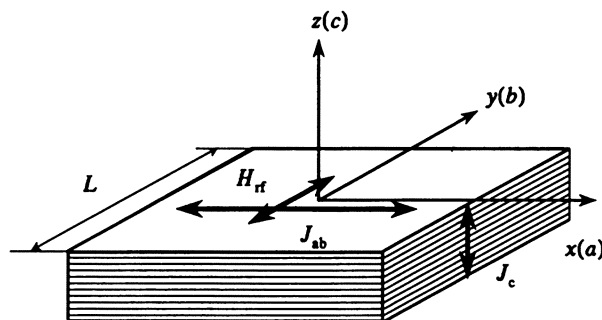


Figure 7: A schematic drawing of the geometry for the transverse plasma excitation

The Maxwell's equation can be written as

$$\begin{cases} \nabla \times \mathbf{B} = \frac{4\pi}{c} \mathbf{j} + \frac{4\pi}{c} \sigma \mathbf{E} + \frac{\varepsilon}{c} \frac{\partial \mathbf{E}}{\partial t} \\ \nabla \times \mathbf{E} = -\frac{1}{c} \frac{\partial \mathbf{B}}{\partial t}, \end{cases} \quad (69)$$

where $\mathbf{B}=(0, B_y, 0)$ and $\mathbf{E}=(0, 0, E_x)$. Operating $\nabla \times$ to the first equation of eq. (69), then solving it as B_y , one obtain

$$\left(-\frac{\partial^2}{\partial x^2} + \frac{1}{\lambda_c^2} + \frac{4\pi}{c^2} \sigma \frac{\partial}{\partial t} + \frac{\varepsilon}{c^2} \frac{\partial^2}{\partial t^2} \right) B_y = 0. \quad (70)$$

Putting $B_y \propto \exp i(kx - \omega t)$ to obtain the eigen modes, an equation

$$k^2 + \frac{1}{\lambda_c^2} - i \frac{4\pi}{c^2} \omega \sigma - \frac{\varepsilon}{c^2} \omega^2 = 0 \quad (71)$$

can be obtained. Introducing a complex wave number k as

$$k = k' + ik'' = \frac{\omega}{c} \sqrt{\varepsilon(\omega)}, \quad (72)$$

one can obtain a complex dielectric function $\varepsilon(\omega)$ as

$$\varepsilon(\omega) = \varepsilon \left(1 - \left(\frac{\omega_p}{\omega} \right)^2 \right) + 4\pi i \left(\frac{\sigma}{\omega} \right). \quad (73)$$

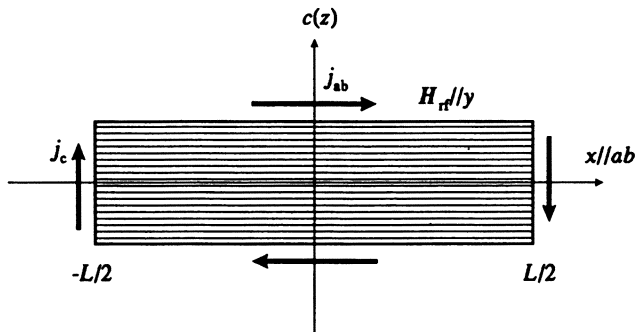


Figure 8: Induced current flow due to microwave H_{rf}

From the boundary condition that the magnetic field should be continuous at $x=\pm L/2$, i.e., $B_y(\pm L/2)=H_{rf}$, B_y can be expressed as

$$B_y = H_{rf} e^{-i\omega t} \left[\frac{e^{ikx} + e^{-ikx}}{e^{ikL/2} + e^{-ikL/2}} \right]. \quad (74)$$

Therefore, the electric field E_z generated by B_y can be written by the relation

$$\frac{\partial E_z}{\partial x} = \frac{1}{c} \frac{\partial B_y}{\partial t} = -i \frac{\omega}{c} B_y \quad (75)$$

as

$$E_z = - \left(\frac{\omega}{c} \right) H_{rf} e^{-i\omega t} \frac{1}{k} \left[\frac{e^{ikx} - e^{-ikx}}{e^{ikL/2} + e^{-ikL/2}} \right]. \quad (76)$$

It is obvious that this electric field E_z is antisymmetric, because it is an odd function with respect to x .

The energy absorbed by the resonance can generally be expressed as

$$\begin{aligned} P &= \int_{-L/2}^{L/2} \langle \text{Re}(\sigma E_z) \text{Re}(E_z) \rangle_t dx \\ &= \frac{1}{2} \int_{-L/2}^{L/2} \sigma |E_z|^2 dx. \end{aligned} \quad (77)$$

Performing the above integration, one finally obtain

$$P = \frac{d}{2} H_{\text{rf}}^2 \frac{\sigma}{|\varepsilon(\omega)|} \left(\frac{\frac{\sinh k''L}{k''L} - \frac{\sin k'L}{k'L}}{\cosh k''L + \cos k'L} \right), \quad (78)$$

where

$$\begin{cases} \varepsilon(\omega) = \varepsilon \left(1 - \frac{\omega_p^2}{\omega^2} \right) 4\pi i \frac{\sigma}{\omega} \\ k = k' + ik'' = \frac{\omega}{c} \sqrt{\varepsilon(\omega)}. \end{cases} \quad (79)$$

The resonance absorption can be obtained from the poles at either $\varepsilon(\omega)=0$ or $\cosh k''L + \cos k'L=0$. From the former condition one obtain $\omega=\omega_p$, while from the latter condition $k' = \frac{\omega}{c} \sqrt{\varepsilon(\omega)}$ and $k''=0$ can be obtained. From the latter condition an equation has to be fulfilled:

$$1 + \cos \left(\frac{\omega d}{c} \sqrt{\varepsilon(\omega)} \right) = 0. \quad (80)$$

Therefore, the following equation

$$\varepsilon \left(1 - \frac{\omega_p^2}{\omega^2} \right) = \left[\frac{(2n-1)\pi}{L \left(\frac{\omega}{c} \right)} \right]^2 \quad (81)$$

is required as a resonance condition. Here, n is a positive integer. Solving eq. (81) one finally obtains

$$\frac{\omega_n^2}{\omega_p^2} = \frac{1}{1 - \frac{1}{\varepsilon} \left[\frac{(2n-1)\pi}{L \left(\frac{\omega}{c} \right)} \right]^2}. \quad (82)$$

From experimental point of view, it is much easier to vary magnetic field than frequency. Therefore, we convert eq. (82) using an empirical relation $H_n/H_p = \omega_n^2/\omega_p^2$ to

$$\frac{H_n}{H_p} = \frac{1}{1 - \frac{1}{\varepsilon} \left[\frac{(2n-1)\pi}{L \left(\frac{\omega}{c} \right)} \right]^2}. \quad (83)$$

This means that many resonance peaks are expected corresponding to the various n values. This is one of the characteristic features of the transverse plasma mode. To find one resonance at least, one obtains a condition by taking $n=1$ as

$$1 - \frac{1}{\varepsilon} \left[\frac{\pi}{L \left(\frac{\omega}{c} \right)} \right]^2 > 0. \quad (84)$$

Therefore,

$$L \left(\frac{\omega}{c} \right) \geq \frac{\pi}{\sqrt{\varepsilon}}. \quad (85)$$

This means that the number of resonances depends on the sample size L , and at the smallest L ($L(\omega/c) < \pi/\varepsilon^{1/2}$), the transverse plasma mode should disappear. This is another significant feature and distinct difference of the transverse mode from the longitudinal one.

The number of resonances is expected as

$$n \leq \frac{1}{2} \left[1 + \frac{\sqrt{\varepsilon}}{\pi} \left(\frac{\omega L}{c} \right) \right], \quad (86)$$

as a function of L . For example, taking $\varepsilon \sim 10$ two resonances are expected for $L(\omega/c) = 3$ and three resonances are expected for $L(\omega/c) = 5$.

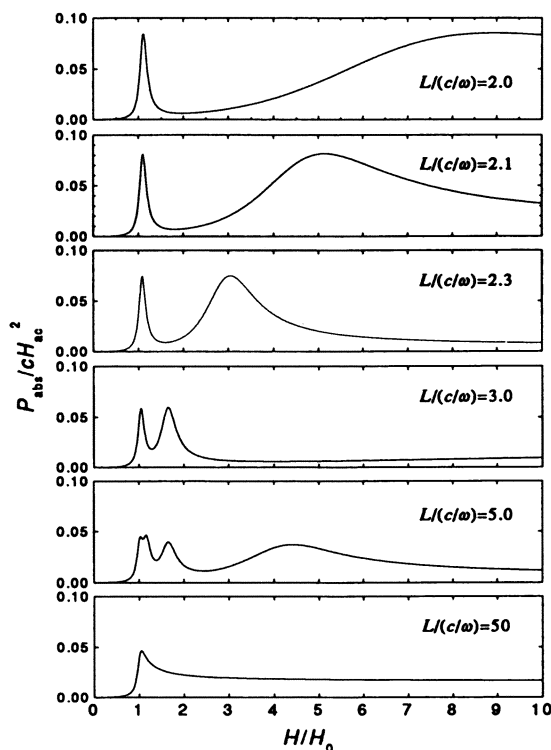


Figure 9: Numerical results calculated with various parameters of $L/(c/\omega)$

Figure 9 represents an example of the results of the numerical calculation of eq. (78) with parameters as indicated. The multiple absorption lines are clearly demonstrated and shift to the higher magnetic fields as a function of the parameter $L/(c/\omega)$.

In Fig. 10 the experimental results for single crystal $\text{Bi}_2\text{Sr}_2\text{CaCu}_2\text{O}_{8+\delta}$ are shown as a function of the sample size L at 35.0 GHz and 25 K (55,57). As is expected two resonance lines are observed in this range of L . As L is reduced from 2.5 mm, the higher field line shifts to higher fields and disappears. In our configuration of the cavity, the sample size for larger size is limited by the dimension of the cavity. By reducing the size of the sample the resonance disappears at a critical value of $L \leq 1.5$ mm, as seen in Fig. 10. This observed behavior is very similar to the result predicted theoretically as shown in Fig. 9. It is interesting to note that the resonance line width as well as the absorption intensity changes as a function of L , which are not considered here in detail.

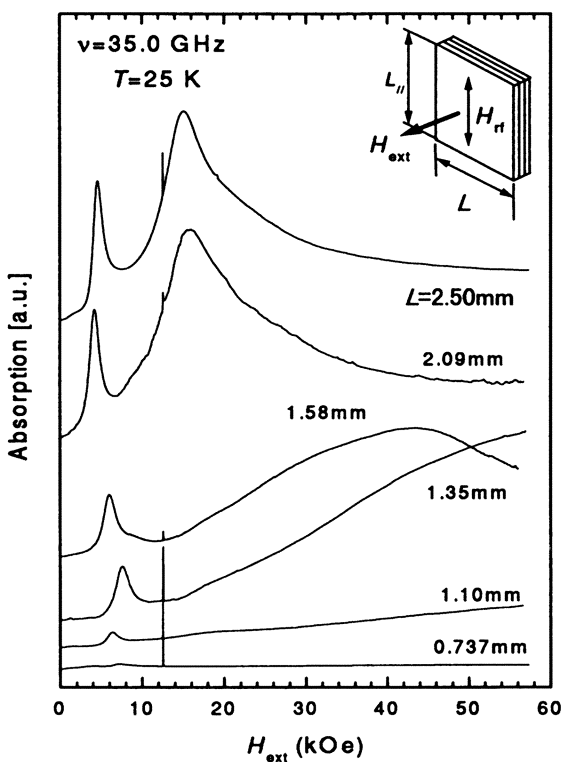


Figure 10: A set of resonance curves observed in $\text{Bi}_2\text{Sr}_2\text{CaCu}_2\text{O}_{8+\delta}$ as a function of the sample size L

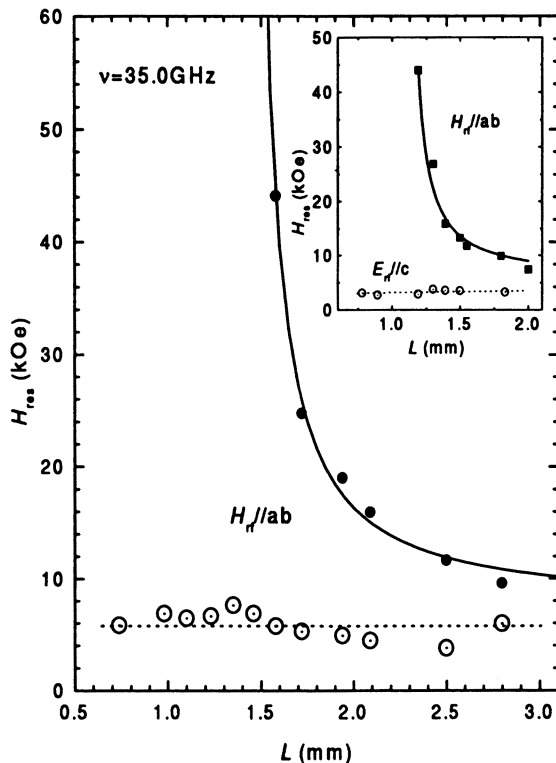


Figure 11: Josephson plasma resonance field plotted as a function of the sample length L for two cases

The results shown in Fig. 10 are plotted in Fig. 11. It is clearly observed that the resonance field is diverging as the sample size L approaches the critical value. Those are $L=1.51$ mm and 1.22 mm for two different samples. Such a behavior is not observed in the configuration of the longitudinal plasma resonance (E_{\parallel}/c), as seen in the inset of Fig. 11. Therefore, this proves that, first, the longitudinal plasma does exist, second, two plasma modes, the longitudinal and transverse modes, are experimentally separated.

The solid lines in Fig. 11 are the fitted curves with experimental results to eq. (83) using a fitting parameter of $\epsilon=12.7$.

Temperature Dependence of The Josephson Plasma Mode near T_c

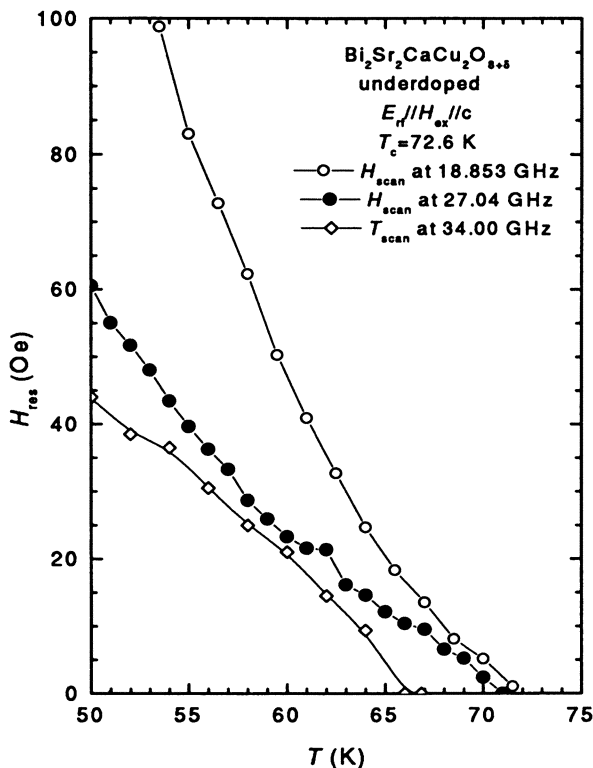


Figure 12: Temperature dependence of the Josephson plasma resonance line in underdoped Bi₂Sr₂CaCu₂O_{8+δ} at three different frequencies

Since the early stage of experimental study of the Josephson plasma in Bi₂Sr₂CaCu₂O_{8+δ}, it has been recognized that the resonance absorption shifts towards lower fields as temperature approaches T_c and it finally disappears at zero magnetic field just below T_c . Although a full experimental proof of such an anomalous behavior has been hindered until just recently because of experimental difficulties existing in the frequency scan measurements. This phenomenon has been attracted much attention from fundamental physics point of view, since such a behavior cannot be expected in conventional superconductors, where the

frequency of the plasma mode should be constant in all temperatures, as already shown schematically in Fig. 1. Since this phenomenon is so unusual and new that we will summarize some of the very recent development of our work only, which has not been completed yet at all. We remind the readers that at the present stage the answer is not still satisfactory and further experimental and theoretical study is required for the full understanding of this problem.

As noted before, it is common that for the Josephson plasma resonance in a microwave region the experiments have been carried out in magnetic fields simply because of experimental convenience. According to Bulaevskii *et al.*(62) this imposes an additional contribution to the resonance condition. Since the vortex pancakes in stead of vortex lines are introduced in highly layered superconductors such as $\text{Bi}_2\text{Sr}_2\text{CaCu}_2\text{O}_{8+\delta}$ in an applied magnetic field, the gauge invariant phase difference, $\varphi_{l,l+1}$, between l -th and $l+1$ -th CuO_2 layers is strongly affected, depending on the spatial arrangement of vortex pancakes in the adjacent CuO_2 layers. In this case the Josephson plasma resonance frequency $\omega_p(B)$ is given as

$$\omega_p^2(B) = \omega_p^2(0) \langle \cos \varphi_{l,l+1} \rangle, \quad (87)$$

where $\omega_p(0)$ means the plasma frequency at zero field and $\langle \dots \rangle$ denotes the thermal average.

When the temperature is raised towards T_c , the Josephson plasma resonance field in $\text{Bi}_2\text{Sr}_2\text{CaCu}_2\text{O}_{8+\delta}$ is known to decrease in the so-called vortex liquid phase according to the empirical relation(48,49);

$$\langle \cos \varphi_{l,l+1} \rangle \propto H^{-\alpha} T^{-\beta} \quad (88)$$

where $\alpha \approx 1$ and $\beta \approx 1$ are found experimentally. This relation is reproduced by the recent theory of Josephson plasma by Koshelev(63), who essentially calculated the phase correlation function of the pancake vortices using high temperature approximation. At a region very close to T_c , however, it is not at all obvious whether or not eq. (88) is valid, since it is apparent that such a high temperature approximation will be violated near T_c . Furthermore, it should be noted that the temperature dependent behavior of the Josephson plasma resonance is observed even though the magnetic field is absent. We do not exclude a possibility that there might be some possible effects of spontaneously created magnetic field near T_c due to superconducting fluctuations, since the magnetic field plays a role to reduce the Josephson coupling in the system.

In order to examine the behavior of the Josephson plasma mode as a function of temperature, it is ideal to measure the frequency dependence of the resonance at various temperature at zero field to avoid the effect of magnetic field. This is difficult to perform due solely to the experimental restriction. On the other hand, measurements in a fixed frequency either by scanning temperature in zero field or by scanning magnetic field at a fixed temperature are more practical. In Fig. 12, such an example of the experimental data is shown for underdoped $\text{Bi}_2\text{Sr}_2\text{CaCu}_2\text{O}_{8+\delta}$ with $T_c=72.6$ K. Three frequencies, 18.853 GHz, 27.04 GHz and 34.00 GHz were used in this experiment. It is clear that, first, the resonance fields at all three frequencies become zero as the temperature approach T_c in such

a way that the resonance line at higher frequencies meets zero field at a lower temperature. This clearly indicates that the resonance frequency has a sharp drop as temperature approach T_c . Second, the temperature dependence of the resonance field seems to change the character as a function of frequency, though it is not so clear because of considerable experimental errors in the measurement. Third, the resonance line shape (not shown here) changes the character below about 50 Oe to highly asymmetric shape and does not show broadening even very close to T_c . This is rather surprising in comparison with conventional superconductors, because the quasiparticle damping effect should increase significantly near T_c , resulting in much wider resonance line width.

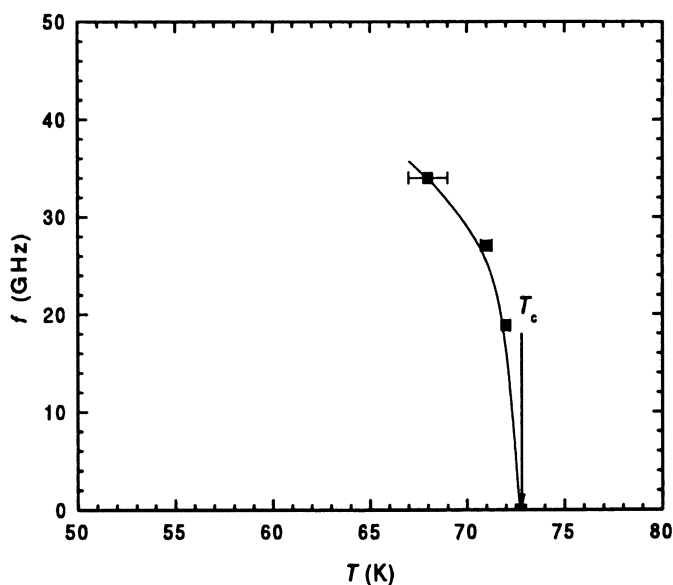


Figure 13: A frequency-temperature diagram of the Josephson plasma in underdoped $\text{Bi}_2\text{Sr}_2\text{CaCu}_2\text{O}_{8+\delta}$

Concerning the first point, the temperature dependence of the resonance frequency is shown much clearer by a plot in Fig. 13. This confirms that the plasma frequency is sharply falling towards zero energy at T_c (64). We note that neither absorption nor surface impedance anomaly was found above T_c at this frequency region.

Anomalous behavior shown above has been thought of the peculiar nature of the Josephson plasma mode. Very recently, Koyama(65) has developed a theory introducing the phason gauge, and were able to reproduce the observed temper-

ature dependence near T_c . However, it is still premature to lead any definite conclusions without much more detailed experimental as well as theoretical studies. It is finally remarked that the another phase excitation mode called as the Carlson-Goldman mode as was schematically shown in Fig. 1 has not been found in our measurement.

Concluding Remarks

We have described the superconducting plasma phenomena in detail with special emphasis on the Josephson nature of the coupling along the c -axis in high T_c superconductors. However, one might feel at a glance that the superconducting plasma phenomenon is insignificant, because it is similar in many respects to the plasma phenomena existing in the normal electron systems. However, one must recognize the important fact that the plasma mode in the superconducting state, especially the longitudinal plasma mode, which lies below the superconducting gap Δ , is of special importance, because it is the Nambu-Goldstone mode associated with the occurrence of the superconducting phase transition according to the concept of the spontaneously broken symmetry. The most important findings shown here are the proof of the validity of the spontaneously broken symmetry concept associated with the superconducting phase transition. In other words, the Anderson-Higgs-Kibble mechanism is proved in the case of superconductivity.

We confirmed the existence of the Nambu-Goldstone mode in the superconducting plasma, which has a finite gap. This gap nature is in turn associated with the mass of the plasmons in a superconductor. This can be estimated by the definition of the mass of particles $E = m_{\text{NG}}c^2$ as

$$m_{\text{NG}} = \frac{\hbar}{c\lambda\sqrt{\epsilon}} \quad (89)$$

$$\simeq 1.2 \times 10^{-36} \text{ (gram)}. \quad (90)$$

This mass is also compared with the bare electron mass $m_e = 9.1093897 \times 10^{-28}$ gram, which yields the ratio $m_{\text{NG}}/m_e \simeq 1.3 \times 10^{-9}$. Similarly, the mass of the Higgs boson can be estimated from the equation to be

$$m_{\text{Higgs}} = \frac{2\Delta}{c^2} \simeq 1.2 \times 10^{-34} \text{ (gram)}. \quad (91)$$

Therefore, the ratio between m_{NG} and m_{Higgs} is obtained to be $m_{\text{Higgs}}/m_{\text{NG}} \simeq 1 \times 10^2$.

It appears that the concept of the spontaneously broken symmetry works in fields from solid state physics where the energy scale ranges from meV to high energy physics where the relevant energy scale lies in TeV. It is very interesting to note that the initiation of this concept was triggered from the theory of superconductivity developed in the late 1950's. However, most remarkable success of this idea has been achieved in the field of particle physics and cosmology, where the approaches are out of our experimental capabilities. Because of this reason none of

these elegant theories has so far been tested rigorously by experiments. Although it is an continuous effort to accomplish the theory of Weinberg and Salam in the unified electroweak field theory(12,21), which may be the one of the nearest possible cases to be performed, the experimental energy is still thought to be insufficient to observe the Higgs bosons at the present status of the accelerator technology. Here, the observation of the Higgs bosons are crucial to complete the theory of Weinberg and Salam. It seems that the mass of the Higgs bosons are expected to be beyond the energies to be created using even the world biggest accelerators.

On the contrary to this the experiment of the superconducting plasma is much easier and can easily be done within our conventional solid state physics laboratory, where we are able to study an exactly identical concept used in the field theory in the Weinberg-Salam theory. Although the number of degree of freedom as well as the symmetry of the field are different, the superconducting phase transition can be described parallel to the field theory using the spontaneously broken symmetry. This is the fundamental importance to be stressed in this series of work concerning the superconducting plasma phenomena. As we have shown above the theoretical framework has been proved by making distinction of the two plasma modes experimentally, by which we finally confirmed that the Anderson-Higgs-Kibble mechanism works in the case of superconductivity.

Acknowledgements

The authors would like to thank their collaborators, who persistently and scrupulously carried out experiments which have not explicitly been described here. They are Mr. Kazuhiro Kimura, Mr. Naruki Kataoka and Mr. Daimon Sugawara. The authors is also deeply indebted to Prof. Masashi Tachiki, Dr. Tomio Koyama and Dr. Saburo Takahashi, Dr. Yoji Ohashi for their invaluable support concerning theoretical aspects of plasma phenomena in superconductors and symmetry breaking concept. The most of theoretical parts described here were taken from their publications which resulted from our fruitful collaborations. Chapter 7 "Separation of Longitudinal and Transverse Plasma Modes" was born also by stimulating collaboration with Prof. Koichi Kindo at the Research Center for Materials Science at Extreme Conditions, Osaka University as a part of Ph. D. thesis work of one of the authors Dr. Itsuhiro Kakeya.

This work has been supported in part by the University of Tsukuba Research Projects (category A) and in part by the Fund for the Venture Business Laboratory. CREST is the strategic fund for the science and technological development supported by the Science and Technology Agency of Japan under the Prime Minister's Office of Japanese government.

References

1. The first report of discovery of superconductivity was given in a series of publications: Kamerlingh Onnes, H. *Leiden Commun.* 1911, 120b, 122b, 124c

2. Bardeen, J; Cooper, L. N.; Schrieffer, J. R., *Phys. Rev.* **1957**, *108*, 1175.
3. Anderson, P. W., *Phys. Rev.* **1958** *110* 827.
4. Anderson, P. W., *Phys. Rev.* **1958** *112* 1900.
5. Nambu, Y., *Phys. Rev.* **1960** *117* 648.
6. Goldstone, J., *Nuovo Cimento* **1961** *19* 154.
7. Anderson, P. W., *Phys. Rev.* **1963** *130* 439.
8. Rickayzen, G., *Phys. Rev.* **1959** *115* 795.
9. Higgs, Peter W., *Phys. Rev.* **1966** *145* 1156.
10. Goldstone, J.; Salam, Abdus; Weinberg, Steven, *Phys. Rev.* **1962** *127* 965.
11. Kibble, T. W. B., *Phys. Rev.* **1967** *155* 1554.
12. More detailed description on the broken symmetry of superconductivity, refer to Weinberg, Steven, *The Quantum Theory of Fields*; Cambridge University Press: Cambridge, UK, 1998; Vol. 2, Chapter 21.6, Superconductivity, pp332-358.
13. Bardeen, J., *Nuovo Cimento* **1957** *5* 1766.
14. Bogoljubov, N. N., *Nuovo Cimento* **1958** *7* 794.
15. Pines, D.; Schrieffer, J. R., *Nuovo Cimento* **1958** *10* 3458.
16. Schafroth, M. R., *Phys. Rev.* **1958** *111* 72.
17. Rickayzen, G., *Phys. Rev.* **1958** *111* 817.
18. Nambu, Yoichiro, *Phys. Rev. Lett.* **1960** *4* 380.
19. Nambu, Y.; Jona-Lasinio, G., *Phys. Rev.* **1961** *textit122* 345.
20. Schwinger, Julian, *Phys. Rev.* **1962** *125* 397.
21. Moriyasu, K., *An Elementary Primer for Gauge Theory*; World Scientific Publishing Co. Ltd. 1983
22. Ginzburg, V. L.; Landau, L. D., *Zh. Eksp. i Theor. Fiz.* **1950** *20* 1064 (translation in *J.E.T.P.(USSR)* **1950** *20* 1064).
23. Landau, L. D., *Phys. Z. der Sowjet Union* **1937** *11* 26 (Translation in *J.E.T.P.(USSR)* **1937** *7* 19).
24. Anderson, P. W., *Lectures on The Many-Body Problems*; Caianiello, E. R., Ed.; Academic Press; New York, 1964 Vol. 2; pp113-135.
25. Lawrence, W. E.; Doniach, S., *Proceedings of the 12th International Conference on Low Temperature Physics* Kanda, E., Ed.; Shokabo; Tokyo, 1971; pp361-362.
26. Leubwohl, P; Stephen, M. J., *Phys. Rev.* **1967** *textit163* 376.
27. Fetter, Alexander L.; Stephen, Michael J., *Phys. rev.* **1968** *textit168* 475.
28. Dahm, A. J.; Denenstein, A.; Finnegan, T. F.; Langenberg, D. N.; Scalapino, D. J., *Phys. Rev. Lett.* **1968** *20* 859.
29. Kleiner, K.; Steinmeyer, F.; Kunkel, G.; Müller, P., *Phys. Rev. Lett.* **1992** *68* 2394.
30. Oya, G.; Aoyama, N.; Irie, A.; Kishida, S.; Tokutaka, H., *J. Appl. Phys.* **1992** *31* L829.
31. Kadowaki, K.; Mochiku, T., *Physica* **1994** *B194-196* 2239.
32. The readers should refer to text books, for example, such as Jackson, J. D., *Classical Electrodynamics*, Wiley, 1975, Chapter 10.
33. Tinkham, M., *Introduction to Superconductivity* McGraw-Hill Inc. 1996, 2nd edition, pp198.
34. Josephson, B. D., *Adv. Phys.* **1965** *14* 419.

35. Koyama, T.; Tachiki, M., *Phys. Rev.* **1996** *54* 16183.
36. Artemenko, S. N.; Kobelkov, A. G., *Phys. Rev. Lett.* **1977** *78* 3551.
37. Fertig, H. A.; Das Sarma, S., *Phys. Rev. Lett.* **1990** *65* 1482.
38. Fertig, H. A.; Das Sarma, S., *Phys. Rev.* **1991** *B44* 4480.
39. Mishonov, T. M., *Phys. Rev.* **1991** *B44* 12033.
40. Noh, T. W.; Kaplan, S. G.; Sievers, A. J., *Phys. Rev.* **1990** *B41* 307.
41. Tamasaku, K.; Nakamura, Y.; Uchida, S., *Phys. Rev. Lett.* **1992** *69* 1455.
42. Anderspn, P. W., *Science* **1995** *268* 1154.
43. Anderson, P. W., *Science* **1998** *279* 1196.
44. Tachiki, M.; Koyama, T.; Takahashi, S., *Phys. Rev.* **1994** *B50* 7065.
45. Kleiner, R.; Müller, P., *Phys. Rev.* **1994** *B49* 1327.
46. Régi, F. X.; Schneck, J.; Palmier, J. F.; Savary, H., *J. Appl. Phys.* **1994** *76* 4426.
47. Yurgens, A.; Winkler, D.; Zhang, Y. M.; Zavaritsky, N.; Claeson, T., *Physica* **1994** *C235-240* 3269.
48. Tsui, Ophelia K. C.; Ong, N. P.; Matsuda, Y.; Yan, Y. F.; Peterson, J. B., *Phys. Rev. Lett.* **1994** *73* 724.
49. Matsuda, Y.; Gaifullin, M. B.; Kumagai, K.; Kadowaki, K.; Mochiku, T., *Phys. Rev. Lett.* **1995** *75* 4512.
50. Tachiki, M.; Koyama, T.; Takahashi, S., *Coherence in Superconductors*, Deutscher, G; Revcodevschi, A., Eds.; World Scientific, 1996; pp371-392.
51. Tachiki, M.; Koyama, T.; Takahashi, S., *Physica* **1996** *C263* 1.
52. Tachiki, M.; Takahashi, S.; Kadowaki, K., *Physica* **1997** *C282-287* 2421.
53. Kadowaki, K.; Gaifullin, M. B.; Matsuda, Y.; Kumagai, K., Takahashi, S.; Tachiki, M., *Proceedings of the 8-th International Workshop on Critical Currents in Superconductors*, Matsushita, T.; Yamafuji, K., Eds.; 27-29, May, 1996, held in Kitakyusyu, Japan; pp235-238.
54. Kadowaki, K.; Gaifullin, M. B.; Mochiku, T.; Matsuda, Y.; Kumagai, K.; Takahashi, S.; Tachiki, M., *Czechoslovak J. Phys.* **1996** *46 Suppl. S3* 1625.
55. Kadowaki, K.; Kakeya, I.; Mochiku, T., *Physica* **1997** *B239* 123.
56. Kadowaki, K.; Kakeya, K.; Kindo, K.; Takahashi, S.; Koyama, T.; Tachiki, M., *Physica* **1997** *C293* 130.
57. Kakeya, I.; Kindo, K.; Kadowaki, K.; Takahashi, S.; Mochiku, T., *Phys. Rev.* **1998** *B57* 3108.
58. Takahashi, S.; Tachiki, M.; Kakeya, I.; Kindo, K.; Mochiku, T.; Kadowaki, K., *Physica* **1997** *C293* 64.
59. Kadowaki, K.; Kakeya, I.; Kindo, K.; Mochiku, T., *Physica* **1997** *C282-287* 2423.
60. Kadowaki, K.; Kakeya, K.; Gaifullin, M. B.; Mochiku, T.; Takahashi, S.; Koyama, T.; Tachiki, M., *Phys. Rev.* **1997** *56B* 5617.
61. Kadowaki, K.; Kakeya, I.; Kindo, K., *Europhys. Lett.* **1998** *42* 203.
62. Bulaevskii, L. N.; Maley, M. P.; Tachiki, M., *Phys. Rev. Lett.* **1995** *74* 801.
63. Koshelev, A. E., *Phys. Rev. Lett.* **1996** *77* 3901.
64. Kadowaki, K.; Kakeya, I.; Wakabayashi, T.; Nakamura, R., preprint.
65. Koyama, T., preprint and private communications.

Chapter 18

A Four Color Optical Sensor: Wavelength-Selective Dye/Superconductor Assemblies

Sara J. Eames¹, Steve M. Savoy¹, Cyndi A. Wells¹, Jianai Zhao¹,
John C. Warner², and John T. McDevitt^{1,3}

¹Department of Chemistry and Biochemistry, University of Texas at Austin,
Austin, TX 78712

²Department of Chemistry, University of Massachusetts at Boston,
100 Morrissey Boulevard, Boston, MA 02125-3393

Dye/superconductor assemblies have been prepared which can respond selectively to different wavelengths of visible light. Small changes in temperature caused by dye to superconductor energy transfer lead to measurable changes in resistance in the superconductor. The resulting signal is largest at wavelengths strongly absorbed by the dye layer. Several dyes with desirable wavelength-selective absorbance properties have been identified. The system has been further improved by the use of a polymeric matrix which spatially isolates the dye molecules, resulting in narrower absorption peaks. A four color sensor has been prepared with wavelength discrimination characteristics better than that of the cones in the human eye. Additionally, to understand energy transfer processes occurring within these assemblies, transient measurements have been performed on the assemblies using a sublimed dye. The information derived here has been used in conjunction with finite difference modeling studies to examine the thermal diffusivity of thin dye layers.

The detection and discrimination of different wavelengths of visible light by the human visual system has been a subject of interest for many years. In the human eye, color discrimination is achieved by the use of three cone cells based in the retina. These cone cells contain wavelength-selective chromophore units. Each chromophore contains one of three different receptor proteins, which tune the absorption peak of 11-*cis*-retinal to a specific wavelength range. The absorption of a photon by 11-*cis*-retinal activates a variety of sensing/signal transduction processes(1,2). In doing so, the chromophore behaves as a light-harvesting antenna.

Man-made optical detectors such as the semiconductor charge coupled device (CCD) have been designed to function over a broad range of wavelengths. In many color imaging and video applications, color selectivity has been achieved through the use of wavelength-selective filters. For the visible region, the highest detectivities are obtained with semiconductor based photovoltaic detectors. However, any given photovoltaic detector will have a practical range which is limited to a relatively narrow

³Corresponding author (mcdevitt@huckel.cm.utexas.edu).

wavelength band. In order to fully detect radiation throughout the UV-near IR-IR region either a series of photovoltaic detectors or a thermal based i.e. thermopile/pyroelectric detector is needed. A recent goal of the McDevitt group has been to develop wavelength selective detectors which operate in a much wider spectral range. Transition-edge bolometers with impressive sensitivities over this broad spectral region have been constructed from high-temperature superconductors such as $\text{YBa}_2\text{Cu}_3\text{O}_{7-\delta}$ (YBCO). In addition, these systems exhibit the highest detectivities yet reported for detectors which operate at 77K in the far-IR region, $\lambda \geq 20 \mu\text{m}$ (3).

Previously, our group has demonstrated that wavelength-selective single-color detectors can be constructed with molecular thin films as absorbing layers and YBCO as the transducing element(4-6). In these systems the highly sensitive bolometric properties of the superconductor element are coupled to a molecular dye. Small changes in temperature caused by dye to superconductor energy transfer events produce measurable resistance changes in the superconductor. Importantly, the response of the superconductor is magnified at wavelengths where the dye absorbs strongly. Therefore, the dye acts as an antenna in such composite structures.

In order to better understand the energy transfer processes occurring within these hybrid systems, their thermophysical properties must be well characterized. *In situ* monitoring of thermal properties of small dimension materials has become a subject of considerable focus. A number of techniques to measure thermophysical properties exist, including photoacoustic spectroscopy(7-9), photothermal deflection(10,11) and photopyroelectric spectroscopy(12). Our group has recently begun to study the thermophysical properties of thin dye layers deposited directly onto YBCO. The high temperature coefficient of resistance of YBCO around its critical temperature (T_C) and its very fast (subnanosecond) response times(13) are utilized in these measurements.

In this paper, we describe the preparation and characterization of wavelength-selective, color sensing assemblies created from a dye layer deposited on a high-temperature superconductor thin film. The dye modifies the broad-band sensing properties of YBCO, causing the system to have greater response to wavelengths of visible light that are absorbed by the dye layer. Several dyes with desirable wavelength-selective absorbance properties have been identified. Specifically, three dyes with absorption features that span the visible region have been used to prepare a three color sensor. With an aim to further improving the wavelength selectivity of the assembly, these dyes have been incorporated into a polymeric matrix. The matrix serves as a medium in which the individual dye molecules are spatially isolated, which results in a significant narrowing of the absorption peaks over those of a vapor deposited layer. To demonstrate the improved selectivity, a four color sensor has been prepared which exhibits excellent wavelength discrimination characteristics. In order to gain a deeper understanding of the energy transfer processes occurring within these systems, transient measurements of the YBCO voltage response have been carried out on the hybrid assemblies. Additionally, heat flow through the system has been modeled using a finite difference modeling method. The thermal diffusivity of a thin dye layer has been determined using information obtained from the transient studies.

Experimental

The hybrid sensors were fashioned using high quality thin films (1500 Å thick) of YBCO deposited onto polished MgO (100) substrates by the pulsed laser deposition method(14,15). A laser patterning technique was used to create microbridges with dimensions of 150 μm wide by 6.5 mm long. Gold contact pads were vapor deposited using an Edwards Auto 306 metal evaporator. Transition temperature and room temperature resistivity values obtained via four-point probe conductivity measurements were used to evaluate the quality of the YBCO films.

In selected cases, dye layers were deposited onto masked regions of the superconductor bridge by vacuum sublimation. The bridge was held at 77K to avoid degradation of the YBCO. Thicknesses of layers were determined from multiple scans of a Tencor Instruments (alpha step 100) profilometer. For a dye in polymer layer, a solution containing a cryogenic resin (Lakeshore GE-7031) and a dye was deposited by means of a microliter syringe. Typical concentrations of this solution were ~0.8g/L for the dye and ~100g/L for the polymer. Up to four different 0.5-0.3 μL drops were placed along the length of the microbridge. The polymer was deposited under low humidity conditions. The molecular dyes used in these studies were acridine orange base (AOB) [Aldrich], rhodamine 6G (Rh6G) [Aldrich], Oxazine 1 perchlorate (Ox1p) [Aldrich], and a squarylium-pyrylium dye (SqPy) (16,17). Each of the chromophores were chosen based upon their possession of a single, narrow absorption peak in the visible region and their ability to be thermally evaporated.

To optically characterize these assemblies, the sample was placed inside a closed-cycle helium cryostat and cooled to just below its transition temperature. A DC bias current of ~1 mA was directed through the bridge, and the in-phase photoinduced voltage which developed across the microbridge when exposed to a mechanically chopped light source was monitored by a lock-in amplifier (Stanford SR510). The optical response versus wavelength was probed using focused white light from a 300 W Oriel xenon arc-lamp which passed through a monochromator.

Measurement of the transient response of the dye-coated assemblies was carried out using the doubled line (532 nm) from a Continuum Surelite Nd:YAG pulsed laser with a 7 ns pulse width and a repetition rate of 10 Hz at peak operating voltage. Incident radiation of the surface was achieved by use of a 200 μm core multimode optical fiber which carried the light through the cryostat vacuum shroud. The incident power was controlled by varying the polarization angle of a waveplate placed in-line with a calcite polarization crystal before coupling to the fiber optic. The transient voltage was DC-coupled to a terminal 50 Ω input impedance of a Tectronix 540 TDS oscilloscope.

Three-dimensional finite difference modeling(18) was used to investigate the flow of heat through the hybrid assemblies. Orthogonal coordinate surfaces were superimposed on the modeled structure and nodes were defined by their intersection. The orthogonal surfaces were not evenly spaced, but placed at intervals that were close enough to allow smooth variations of spatial temperature with the least amount of computational time. The temperature distribution through the modeled structure was found by balancing the heat about each node. The heat balance equation for node i which has M_i neighbors is given by:

$$C_i \frac{T_i^{n+1} - T_i^n}{\Delta t} = P_i^n + \sum_{m=1}^{M_i} {}_i K_{a_m} (T_{a_m}^n - T_i^n) \quad (1)$$

where C_i is the heat capacitance associated with the i^{th} node, $T_{a_m}^n$ is the temperature of the m^{th} neighbor of the i^{th} node at time t_n , P_i^n is the heat generation rate, ${}_i K_{a_m}$ is the conductance between nodes i and m , and Δt is the time step of $t_{n+1} - t_n$. For internal nodes, M_i is six; nodes lying on the surface of the model will have fewer than six neighbors. The right side of the heat balance equation (1) was evaluated at $t_{n+1/2}$ using the Crank-Nicolson (CN) implicit procedure(19) because of the method's accuracy and time step stability which allows for efficient computation. For a structure containing N nodes, N equations and N unknowns are produced. The point-successive-overrelaxation method (SOR) was used to solve the resulting system of N equations(20).

The thermal parameter of diffusivity for Rh6G was varied to fit the theoretical temperature curves to that obtained experimentally through the transient voltage and resistivity curves. Laser illumination in the model was assumed to penetrate to a depth of 2100 Å into the dye. The thermophysical parameters of dye density as well as YBCO and MgO density and diffusivity needed for simulation were obtained both from the literature as well as experimentally. The density of the dye was found to be 1.24 g/cm³ by measuring the absorption of a solution prepared from a sublimed film of Rh6G. The thermophysical constants for MgO and YBCO at 80 K were obtained from Phelan and Hijikata(21) and references therein.

Results and Discussion

Figure 1 details the process of preparing a typical assembly. A high quality thin film of YBCO (Figure 1A) is patterned to form a microbridge (Figure 1B). Gold pads are evaporated on to the corners of the structure (Figure 1C) to minimize contact resistance. Dye layers are then deposited by vacuum sublimation or by casting dye loaded polymeric films directly on the surface of the superconductor. (Figure 1D).

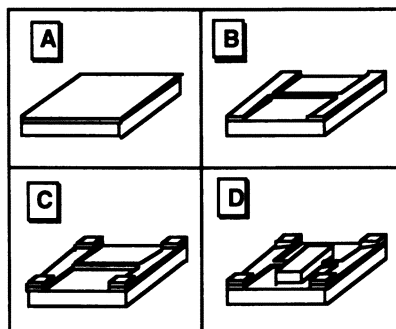


Figure 1. A schematic diagram of the steps needed for the construction of wavelength-selective high- T_C bolometers. (A) A 1500Å film of YBCO is deposited onto a MgO substrate. (B) The film is then patterned into a microbridge. (C) Next, Au contact pads are added at corners. (D) Finally, dye layer(s) are deposited across the microbridge.

The superconductor part of the composite sensor functions as a bolometer; that is, optical absorption leads to a change in temperature which causes a change in electrical resistance. Bolometers have been previously made from metals, which possess relatively small rates of change in resistance with respect to temperature. For a superconductor, the dR/dT is also quite small above the critical temperature (T_C). However, around T_C the dR/dT becomes very large as the resistance drops to zero over a few degrees (see Figure 2A). If a bridge is poised just below T_C , the bolometric response will be much greater. For optical measurements, the superconductor is patterned to form a microbridge to decrease the cross-sectional area available for current to bypass or 'short' around optically induced 'normal' state regions. Figure 2B shows the relationship between dR/dT and temperature and compares this to the steady-state optical response versus temperature characteristics of the same bridge. The peaks overlap nicely, indicating that the effect is bolometric in nature.

Optical response characteristics for a three color sublimed dye/superconductor structure are shown in Figure 3. The spectral response curves show the AOB-coated region responds selectively to blue light, whereas the Rh6G-coated region responds predominantly to green light, and the SqPy-coated region responds selectively to red

light. The absorbance spectra acquired for each of the dye films as deposited onto glass slides are also shown in Figure 3. These spectra have excellent agreement with the optical response recorded for the dye/superconductor assemblies. Each region of the superconductor exhibits maximum response at a wavelength in which the dye most strongly absorbs light. This behavior indicates that efficient energy transfer occurs between the dye and superconductor elements.

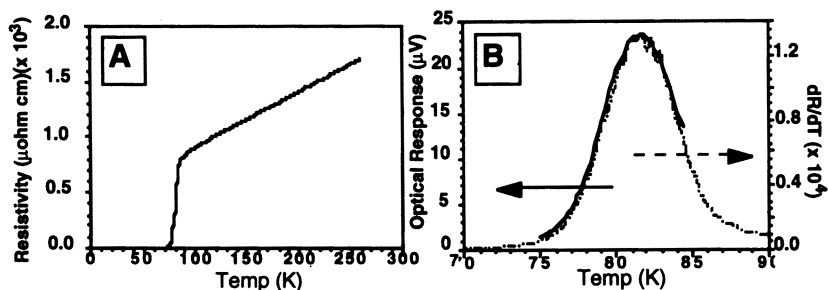


Figure 2. This illustration shows data sets acquired for a single 1500 Å thick YBCO film that was patterned into a microbridge structure. On the left, (A) shows the resistance versus temperature curve for the sample. On the right (B), the solid curve is the steady-state optical response measured upon illumination by a 1 mW He-Ne laser ($\lambda = 630\text{nm}$). For comparison, the dotted curve shows the dR/dT with respect to temperature as extracted from the data set for curve (A).

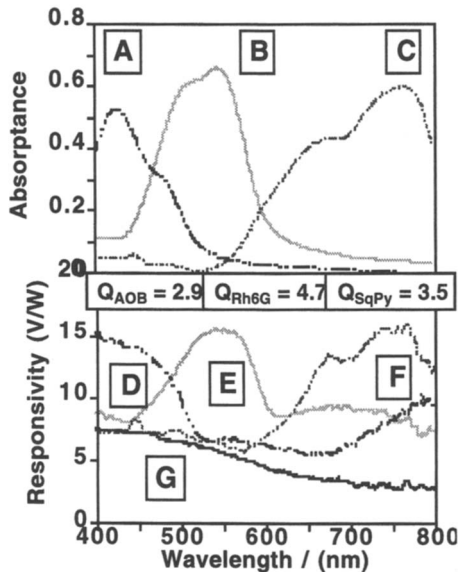


Figure 3. The absorbance spectra of the dyes (A) AOB; (B) Rh6G; (C) a Sq-Py dye are shown. The responsivity of a three-color sensor created by depositing these dyes onto YBCO are displayed in the lower half of this figure along with the Q-values [(D),(E),(F) respectively]. The responsivity of bare YBCO is also shown (G).

It should be emphasized that the dye functions as a light-harvesting antenna and not as a filter. As such, the devices respond to light in an intrinsically different manner to the usual semiconductor based detectors. The responsivity of the hybrid detector structure is directly proportional to the amount of light absorbed by the dye and not the amount of light transmitted by the dye. Figure 4 highlights the difference between the response of an antenna-based (A) and a filter-based (B) wavelength selective detector. If a cyan dye layer is used, the dye/superconductor system will have maximum response where this dye most strongly absorbs, i.e., in the red region of the spectrum (Figure 4A). Conversely, if the same dye layer is used as a filter in a typical silicon based system, the detector will respond to those wavelengths passed by the filter; namely blue and green (Figure 4B). Our system can be made to function in an analogous manner by placing a layer of the dye supported on a glass slide some distance above the superconductor. Figures 4C-E show the resulting optical response for an antenna (dye coated), bare microbridge and bare microbridge with a dye filter respectively.

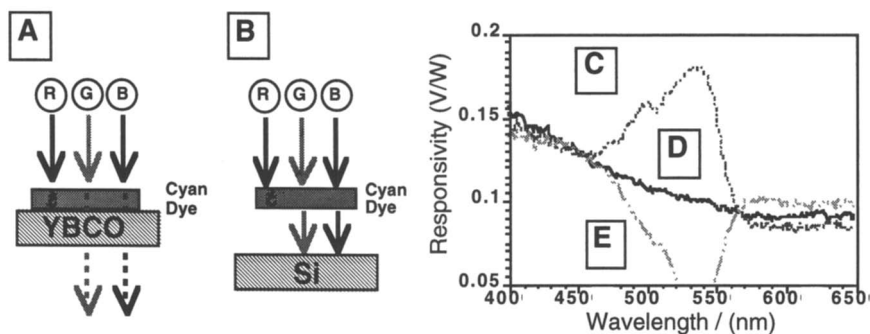


Figure 4. The response characteristics of an antenna-based (YBCO) and a filter based (silicon) detector are compared when a layer of cyan dye is utilized as the antenna or filter respectively. (A) For an antenna based detector; a layer of cyan dye amplifies its response to red light. (B) For a filter based detector, the same dye will cause the detector to respond to green and blue light. The effect can also be seen on a YBCO detector if the dye layer is spatially isolated from the detector. Trace (C) shows the response of a YBCO structure coated with Rh6G and compares it to (D) the response of a bare structure and (E) the response of the YBCO when using a separated Rh6G dye layer.

To evaluate the wavelength selectivity of this detector for comparison purposes, a figure of merit is needed. Several similarities exist between a radio-frequency (RF) antenna/tuned circuit and our dye-coated superconductor detector system. In a RF tuned circuit the quality-factor, Q , is used to quantify the frequency selectivity. This term can also be used for evaluation of the dye/YBCO structures:

$$Q = \frac{f_0}{\Delta f} \quad (2)$$

Here, f_0 is the center frequency and Δf is the bandwidth of the tuned circuit (full-width-half-maximum of the output power). A high Q -value indicates a high level of frequency selectivity. The antenna acts as both the absorbing and transducing element in the RF system, whereas the tuner circuit provides selectivity. In the hybrid dye/superconductor detector, the superconductor structure serves as the transducing element, while the dye layer functions as the absorbing and selective element. Although a dye may have

several resonance frequencies (i.e. absorption peaks), the spectral characteristics for a single absorption peak are nearly Gaussian in shape. Therefore, the selectivity of the detector structure in spectral regions where the dye possesses a single absorption band can be estimated using equation (2). Table I gives the Q-values for each dye used in the three color sensor. For comparison, the values for those of 11-*cis*-retinal in each of the cones of the human eye are also given. Although the Q-values for the three color sensor are not significantly different to those of the human eye, it should be noted from the λ_{\max} values that the separation of each peak is much greater in the three color sensor.

Table I. Q-values for dyes used in assemblies and the human eye

Dye / cone	λ_{\max} (nm)	Q value
acridine orange base, sublimed	463	2.9
rhodamine 6G, sublimed	535	4.7
squarylium-pyrylium dye, sublimed	711	3.5
blue cones, human eye	465	4.0
green cones, human eye	530	4.4
red cones, human eye	560	4.4
acridine orange base in polymer	501	7.8
rhodamine 6G in polymer	535	7.9
oxazine 1 perchlorate in polymer	655	6.4
squarylium-pyrylium dye in polymer	715	16.7

Improving Selectivity The original dyes used in our system were selected for their single narrow absorbance features in the visible region as determined from solution UV-visible spectra. However, the absorbance spectra of layers of sublimed dye show much broader peaks caused by the interaction of dye molecules in close proximity. Clearly, further improvement in the wavelength discrimination characteristics can be achieved with a matrix designed to minimize the dye-dye interactions. For our studies, a colorless polymer layer was chosen with due consideration of several issues which include chemical compatibility with all materials used, and low temperature adhesion. Firstly, the superconductor corrodes in air, water and acids, so water-based polymers, or those which contain or generate acid while setting cannot be used. Secondly, the dye and polymer must not chemically react and must be mutually soluble in a non aqueous solvent. Finally, the polymer must remain adhered to the superconductor at temperatures around 85 K.

The chosen polymer is soluble in a 50:50 toluene/ethanol mixture and is optically transparent above 300 nm. Figure 5 shows the absorption spectra of Rh6G sublimed on glass, in ethanol, and in a solid layer of the polymer. Interestingly, the polymer layer possesses almost identical spectral features to the solution sample. The effect is even more dramatic for the SqPy dye, where the absorption peak is much more severely broadened in the solid state.

To demonstrate the improved wavelength selective properties that can be achieved with the dye in polymer system, four color sensors have been prepared using the microliter drop technique described earlier. Four drops of polymer can be deposited along a single microbridge. Figure 6 shows the optical response characteristics of this sensor, and the Q-values of the dyes in the polymer matrix. The Q-values are now all greater than that of the human eye (see Table I) and again, the λ_{\max} are more widely spaced.

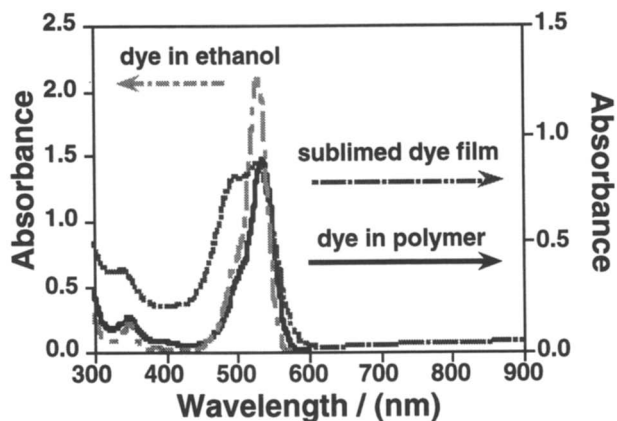


Figure 5. The effect of a matrix on the absorption characteristics of Rh6G. A solid layer of dye (A) possesses a very broad peak in comparison to that of the same dye dissolved in ethanol (B). By incorporating the dye into a polymer matrix, the dye molecules are spatially isolated and the resulting absorption peak (C) is of similar width to that of the dye in solution.

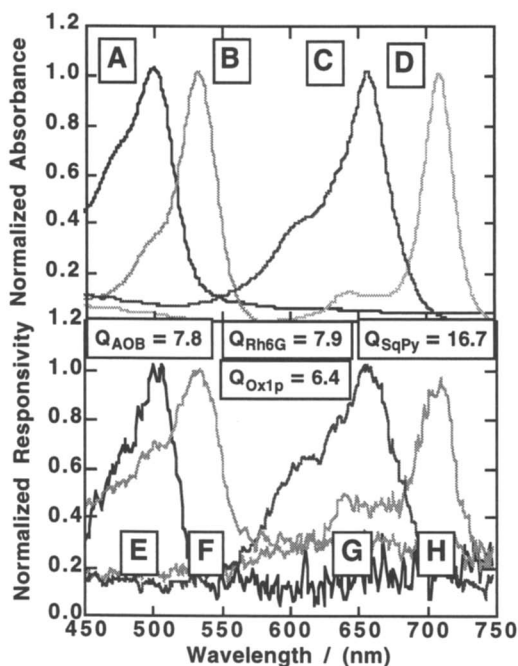


Figure 6. Here shown is the absorbance spectra of the following dyes incorporated into a polymer matrix: (A) AOB; (B) Rh6G; (C) Ox1p; (D) Sq-Py. In the lower half of the figure, the responsivity and Q-values of a four color sensor created by depositing these dyes is shown as curves (E),(F),(G) and (H) respectively.

Work is now in progress to improve the responsivity and signal to noise quality of these assemblies. To make the most efficient use of the incident light, it is desirable to understand the processes occurring within these structures at a much deeper level. The design of the assembly can then be further optimized. Specifically, information is needed concerning the signal development with time as the assembly is illuminated by pulsed optical radiation. Towards this goal, we have conducted transient voltage measurements and thermal modeling studies, which will be outlined in the next section.

Transient Voltage Measurements Since a YBCO microbridge is a highly sensitive transducer, it can be used to monitor the rate of thermal wave propagation through the dye layer following light absorption from a pulsed source. It has been previously determined that the transient response of granular high T_C thin films consists of two distinct mechanisms, namely a bolometric response(22,23) observed around T_C and a nonequilibrium response(24-27) observed at temperatures well below the transition temperature. For the dye-coated structures, the rear surface temperature profile is observed near T_C and is expected to be bolometric in nature.

Rh6G was chosen for this study due to its high extinction coefficient at the laser wavelength, ($\lambda = 532$ nm), its lower sublimation temperature, and its lack of morphological complications. Previous work with H_2OEP has shown that variations in the deposition temperature lead to differing morphologies of the dye films. Additionally, the films are of low density and large grain size which complicates reliable estimates of both thickness and density. As an alternative, Rh6G was deposited onto patterned films as described earlier, producing relatively smooth films with grain sizes on the order of $1 \mu\text{m}$. Electrical characterization of the YBCO microbridge before and after dye deposition showed that little damage occurred during the deposition.(28) The final structure consisted of two dye layers $\sim 2 \mu\text{m}$ wide deposited near the edge of a contact region with the center $2 \mu\text{m}$ of the microbridge left uncoated for a control response of the bridge.

Measurement of the transient response of the dye-coated assemblies was carried out using the doubled line (532 nm) from a Nd:YAG pulsed laser with a 7 ns pulse width and a repetition rate of 10 Hz. Figure 7 details the electrical configuration of the cryostat used in these studies, as well as the means by which the sample was illuminated. For the uncoated YBCO region, the input pulse width was too long to measure the true temporal bolometric rise time. As a result, the time required for the response to increase from 10% to 90% of the full rise time merely follows the laser pulse input. However, the delay in the transient rise time introduced by a dye layer was sufficiently long for layers greater than $\sim 2500 \text{ \AA}$ thick to be temporally separated from the laser profile. Figure 8 shows the normalized transient voltage as a function of time for selected thicknesses of Rh6G. Each of the thicknesses of dye displays a characteristic delay in the rise of the voltage (temperature) maximum that is for all practical purposes independent of the input optical power density and follows the square of the thickness. The time associated with one-half the voltage rise can be extracted from the transient profiles. A plot of the rise time as a function of the square of thickness gives a linear fit from which the diffusivity value of Rh6G at 80-82 K is found to be $\alpha_{Rh6G} = 1.4 \times 10^{-3} \text{ cm}^2/\text{s}$.

An important aspect of the determination of thermal diffusivity from these profiles is that the diffusion length be short compared to the optical penetration depth, i.e. a thermally thick film, where the optical penetration depth is defined by:

$$\mu_{Rh6G}(\lambda) = \frac{1}{\beta_{Rh6G}(\lambda)} \quad (3)$$

Here, $\beta_{\text{Rh6G}}(\lambda)$ is the solid state extinction coefficient at a particular wavelength. This requirement makes the simplification that the input pulse is confined to a small thickness. The optical penetration depth of Rh6G at the Nd:YAG laser wavelength used in the experiments ($\lambda = 532 \text{ nm}$) was determined from absorption measurements made on thin films deposited simultaneously on glass substrates during deposition onto the YBCO microbridge. From the absorption spectrum of the thin organic films, $\beta_{\text{Rh6G}}(532 \text{ nm}) = 4.7 \times 10^4 \text{ cm}^{-1}$ and so $\mu_{\text{Rh6G}}(532 \text{ nm}) = 2100 \text{ \AA}$. The assumption that the optical energy is absorbed uniformly at the surface of the dye layer is taken to be valid for thicknesses greater than 2500 \AA . Additional assumptions regarding solution to the one-dimensional heat flow from Kim *et. al.*(29) include:

- (1) The input pulse is treated as a point heat source
- (2) Thermal conductivity and heat capacity do not vary with temperature
- (3) No convective heat loss occurs in the dye layer
- (4) The dye film and YBCO are both homogenous materials
- (5) Rh6G/YBCO and YBCO/MgO thermal boundary layers are neglected
- (6) Heat flow is truly one-dimensional

Assumption (1) can be applied from previous arguments that the thermal diffusion length is small. At thicknesses $< 2100 \text{ \AA}$, a majority of the input pulse is absorbed by the dye before diffusion out of this 'skin' layer takes place. Thus, the onset of the flow of heat into the YBCO is completely isolated from the input pulse event. Assumption (2) and (3) can be neglected if the temperature is kept low, as is the case for 77 K operation. Assumption (4) and (5) are related to the materials properties of the structure. The morphology of Rh6G given by SEM suggests that the dye is smooth and does not possess different crystalline phases. X-ray powder diffraction (XRD) reveals that the substrate and YBCO are both of very high quality and void of macroscopic phase impurities. Measurement of the thermal boundary resistance at both the dye / YBCO and YBCO / MgO interfaces has not been accomplished and are assumed to be negligible in the present studies.

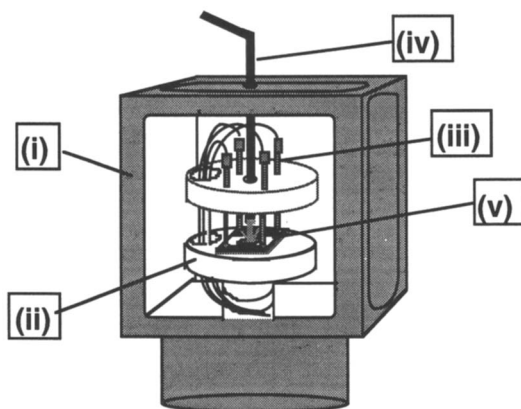


Figure 7. A detailed schematic of the optical delivery system used in transient voltage measurements is shown. Specifically, (i) the cryostat housing, (ii) the cold stage, (iii) current-voltage leads, (iv) the optical fiber which carries the light through the shroud and directs it at the dye/superconductor assembly (v).

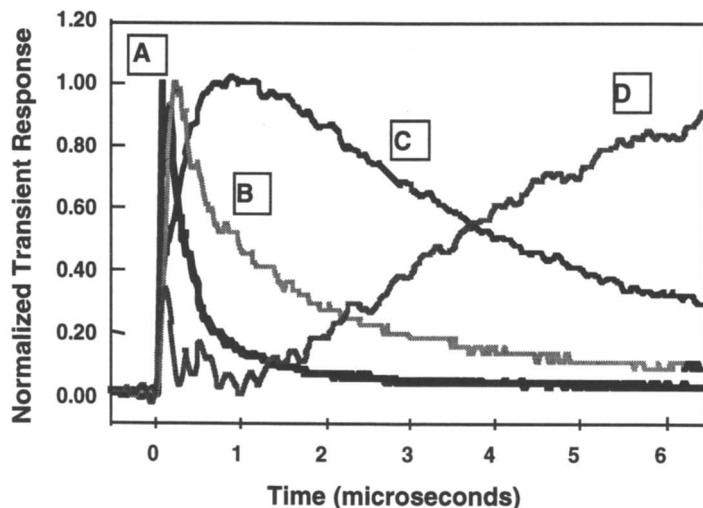


Figure 8. Transient optical response curves for YBCO microbridges coated with different thicknesses of Rh6G. Notice that the bare bridge (A) has a very fast response but that layers of dye of increasing thickness [(B) 3514Å, (C) 6950Å, (D) 24,071Å] have increasingly larger response times.

Thermal modeling In an effort to improve the response characteristics of the hybrid assemblies, future attempts to modify the structure of the sensor will be made. To aid in the design of these systems, we have initiated a computational program to predict the response features of these structures. Modeled in this study is a simple test bed structure which is analogous to the above described systems. A schematic of the modeled assembly having 7000 Å of Rh6G is shown in Figure 9. The best fit of modeled temperatures to the experimental temperatures for 7000 Å of Rh6G was found

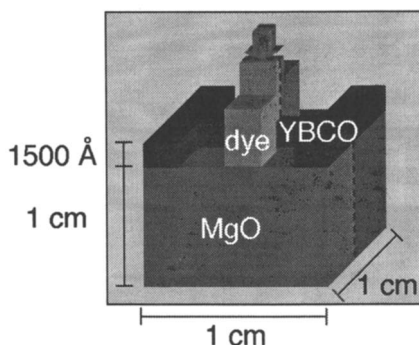


Figure 9. A schematic of the dye / superconductor assembly model used in three-dimensional finite difference analysis of heat flow through the assembly after laser illumination. The thicknesses of the layers were as follows: Rh6G 7000 Å, YBCO 1500 Å, and MgO 1 mm. The temperature distributions in the cross section shown were examined as a function of time.

for a diffusivity $\alpha_{\text{Rh6G}} = 1.4 \times 10^{-3} \text{ cm}^2/\text{s}$, a value in agreement with that obtained by the above described one-dimensional heat flow estimation. The temperature distributions through the assembly at a time when the peak temperatures are reached in the superconductor, as well as other selected times, is shown in Figure 10. Because heat disperses throughout the dye film as the thermal wave propagates toward the superconductor, the temperature change of the superconductor relative to the heat sink decreases with increased dye thickness. Thus, in order to maximize the sensitivity of wavelength-selective bolometers, the optimal dye thickness must be balanced between maximizing absorption and heat transfer characteristics.

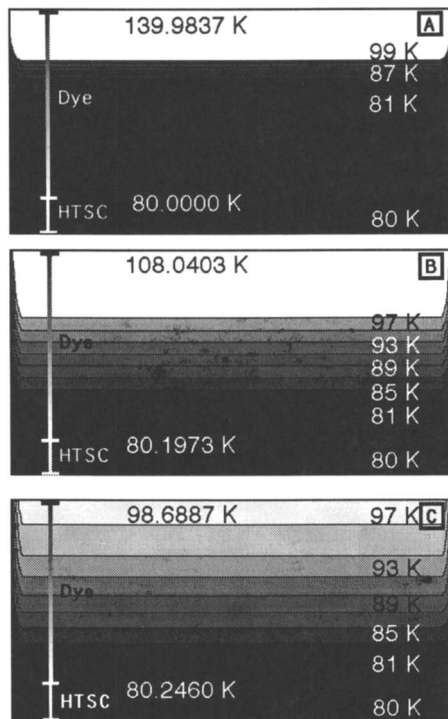


Figure 10. The temperature distributions in the illuminated assembly are shown for 40 ns, 450 ns, and 950 ns in (A), (B), and (C), respectively. The temperatures for the contour lines are shown on the right; the highest temperature in the dye and superconductor are shown on the left.

Summary

Molecular dye/high-temperature superconductor transition-edge bolometer assemblies capable of color selective optical response have been prepared. Initially, these systems utilized solid layers of the dyes deposited by sublimation. A three color sensor has been prepared with selectivity (Q -values) comparable to that of the human eye, but with better wavelength discrimination capabilities. Unlike prior semiconductor-based detectors where light transmission through filters evokes color separation in a subtractive mode, the dye/superconductor system functions through a light-harvesting method. The assembly displays an enhanced steady-state response to wavelengths

absorbed most strongly by the dye. However, the proximity (and therefore interaction) of the dye molecules in the solid layer causes the absorbance peaks to be significantly broadened. By incorporating the dye into a polymer, the molecules are sufficiently separated so that the peaks are as narrow as in solution. A four color sensor has now been prepared using dyes previously identified as suitable candidates for sublimation.

Moreover, the dye/superconductor assembly provides a convenient platform to study details of molecule/superconductor energy transfer processes. Because of the YBCO detector speed, thermophysical properties of sub-micron films of the dye layer can be determined provided that the extinction coefficient of the layer is high enough such that nonuniform heating effects are avoided. By comparing these results to those of three-dimensional finite difference modeling for the analysis of heat flow through the composite structures, it has been possible to estimate thermal diffusivity values for the dye. Knowledge of the thermophysical parameters of the absorbing layer is crucial for a complete understanding of the performance capabilities. Finally, it should be noted that superconductor sensors provide the capacity for detection of light over a much wider wavelength range than is currently available from semiconductor-based systems, and thus could be envisioned for use as a single component broadband detector of electromagnetic radiation.

Acknowledgments

JTM thanks the National Science Foundation (grant number: DMR-9631394) and the Texas Advanced Research Program for support of this work. JCW thanks members of Polaroid Media Research Division for useful discussions.

Literature Cited

- (1) T. Lamb and J. Bourriau *Colour: Art & Science*; Cambridge University Press: Cambridge, England, 1995 pp 237
- (2) K. N. Leibovic *Science of Vision*; Springer-Verlag: New York, 1990
- (3) S. J. Berkowitz, A. S. Hirahara and K. Char *App. Phys. Lett.* **1996**, *69*, pp 2125-2127.
- (4) J. Zhao, D. Jurbergs, B. Yamazi and J. T. McDevitt *J. Am. Chem. Soc.* **1992**, *114*, pp 2737-2738.
- (5) D. Jurbergs, R.-K. Lo, J. Zhao and J. T. McDevitt, *Dye-coated Superconductor Structures as Optical Sensors*: SPIE, 1994; Vol. 2159, pp 138-149.
- (6) D. C. Jurbergs, J. Zhao and J. T. McDevitt *App. Phys. Lett.* **1996**, *69*, pp 688-690.
- (7) A. Mandelis *In Principles and perspectives of photothermal and photoacoustic phenomena*; A. Mandelis, Ed.; Progress in photothermal and photoacoustic science and technology; Elsevier: Tokyo, 1992; Vol. 1.
- (8) M. J. Adams and G. F. Kirkbright *Analyst* **1977**, *102*, pp 281-292.
- (9) H. Vargas and L. C. M. Miranda *Phys. Rep.* **1988**, *161*, pp 43-101.
- (10) W. B. Jackson, N. M. Amer, A. C. Boccara and D. Fournier *App. Opt.* **1981**, *20*, pp 1333-1344.
- (11) H. K. Park, C. P. Grigoropoulos and A. C. Tam *Intl. J. Thermophys.* **1995**, *16*, pp 973-997.
- (12) C. Christofides *Crit. Rev. Sol. State Mat. Sci.* **1993**, *18*, pp 113-174.
- (13) S. M. Savoy, C. A. Wells, J. T. McDevitt and T. A. Rhodes *App. Phys. Lett.*, submitted.
- (14) D. Dijkkamp, T. Venkatesan, X. D. Wu, S. A. Shaheen, N. Jisrawi, Y. H. Min-Lee, W. L. McLean and M. Croft *App. Phys. Lett.* **1987**, *51*, pp 619.
- (15) P. Vase, S. Yueqiang and T. Freltoft *App. Surf. Sci.* **1990**, *46*, pp 61-66.
- (16) T. Santoh, C. Mihara and H. Sugata, U.S. Patent 5,190,849: , 1990.

- (17) D. J. Gravesteyn, C. Steenberg, J. Van der Veen and W. P. M. Nijssen, U.S. Patent 4,508,811, 1983.
- (18) K. W. Childs, HEATING, 7.2i, Radiation Shielding Information Center: Oak Ridge, 1994.
- (19) J. Crank and P. Nicolson *Proc. Camb. Phil. Soc.* **1947**, *43*, pp 50-67.
- (20) R. S. Varga *Matrix iterative analysis*; Prentice-Hall, Inc.: Englewood Cliffs, New Jersey, 1962.
- (21) P. E. Phelan and K. Hijikata *J. Electrochem. Soc.* **1994**, *141*, pp 810-815.
- (22) A. Frenkel, M. A. Saifi, T. Venkatesan, P. England, X. D. Wu and A. Inam *J. App. Phys.* **1990**, *67*, pp 3054-3068.
- (23) H. Kraus *Supercond. Sci. Tech.* **1996**, *9*, pp 827-842.
- (24) M. Hangyo, S. Tomozawa, Y. Murakami, M. Tonouchi, M. Tani, Z. Wang, K. Sakai and S. Nakashima *App. Phys. Lett.* **1996**, *69*, pp 2122-2124.
- (25) F. A. Hegmann and R. A. Hughes *App. Phys. Lett.* **1994**, *64*, pp 3172-3174.
- (26) M. Lindgren, W.-S. Zeng, M. Currie, C. Williams, T. Y. Hsiang, P. M. Fauchet, R. Sobolewski, S. H. Moffat, R. A. Hughes, J. S. Preston and F. A. Hegmann *OSA Ultrafast Electronics and Optoelectronics* **1996**.
- (27) M. Zorin, M. Lindgren, M. Danerud, B. Karasik, D. Winkler, G. Gol'tsman and E. Gershenson *J. Supercon.* **1995**, *8*, pp 11-15.
- (28) D. C. Jurbergs "Wavelength-Selective Optical Detectors Based On Molecular Material/High-Temperature Superconductor Structures," University of Texas at Austin, 1996.
- (29) S. W. Kim and R. E. Taylor *Intl. J. Thermophys.* **1993**, *14*, pp 135-147.

Author Index

- Ayache, Claude, 21
Bagatsky, V. M., 196
Browning, V. M., 78
Cardona, M., 180
Chechersky, Vladimir, 139
Chu, C. W., 180
Chu, Wei Kan, 41
de Wette, F. W., 95
Demsar, J., 230
Du, Z. L., 180
Eames, Sara J., 278
Faulques, Eric, 1, 21
Finger, L. W., 78
Fischer, A. K., 156
Girata, D., 216
Hadjiev, V. G., 180
Hoffmann, Axel, 216
Homonnay, Zoltan, 139
Hu, J. Z., 78
Iliev, Milko N., 107
Ivanov, Victor G., 120
Jumas, Jean-Claude, 21
Kadowaki, Kazuo, 245
Kakeya, Itsuhiro, 245
Kamarchuk, G. V., 196
Kanis, David R., 168
Khotkevich, A. V., 196
Kravchenko, A. V., 196
Lao, J. Y., 216
Leblanc, Annie, 21
Liu, Jiarui, 41
Lopera, W., 216
Maroni, V. A., 156
McDevitt, John T., 168, 278
Meyers, K. R., 78
Mihailovic, D., 230
Moliné, Philippe, 21
Nakamura, Ryo, 245
Nath, Amar, 139
Osofsky, M. S., 78
Ouili, Zeineddine, 21
Perry, Dale L., 66
Prieto, P., 216
Qadri, S. B., 78
Raphael, M., 78
Ren, Z. F., 216
Ritchie, Jason E., 168
Rumyantsev, V. V., 131
Savoy, Steve M., 278
Schuller, Ivan K., 216
Skelton, E. F., 78
Strohm, T., 180
Thilly, L., 78
Vertes, Attila, 139
Wakabayashi, Tetsu, 245
Wang, J. H., 216
Warner, C. J., 278
Wells, Cyndi A., 168, 278
Wu, K. T., 156
Xue, Y. Y., 180
Yampolskii, S. V., 131
Zhang, Zuhua, 41
Zhao, Jianai, 278

Subject Index

A

A-15 phases

- general properties, 22–23
- stoichiometric formula of A-15, 22
- superconducting properties versus composition and degree of atomic order, 22
- type structure at 300 K, space groups, 23*f*
- See also* Dissolution of A-15 phases in metallic dichalcogenides

Absorption measurements, pump–probe method, 17

Acridine orange base (AOB)

- absorbance spectra, 282*f*
- molecular dye, 280
- See also* Dye/superconductor assemblies

Alkali salts of C₆₀ (fullerene), unconventional, 3

Alkylamine adsorption to superconductors.

- See* Self-assembled monolayers (SAM) on YBa₂Cu₃O₇ (YBCO)

Antenna-based detectors

- versus filter-based, 283
- See also* Dye/superconductor assemblies

Apex oxygen sublattice in YBa₂Cu₃O_{7-x} single crystals

- combination scattering (CS) and infrared (IR) spectra for symmetrical (*g*-type) and antisymmetrical (*u*-type) displacements, 132–133

- differential characteristic of scattering (DCS) proportional to Fourier component of correlation function of ion displacements, 135
- evaluation of apex oxygen content, 135–137
- experimentally obtained DCS for defective film in comparison with DCS expression for free-defect film, 136
- explicit form of \hat{G} matrix within Debye model, 136
- imaginary part of \hat{G}^{-1} matrix proportional to correlation function, 136
- model, 132–133
- optical methods for study of quasi-two-dimensional and layered structures, 132
- polaritons in crystal due to interactions of phononic and electromagnetic modes, 135

- potential energy of oscillations of O(4) ion pair, 133

Raman light scattering, 133–135

Apical oxygen vibrations. *See* Ortho-II phase of YBa₂Cu₃O_x

Area density of element, measurement by Rutherford backscattering spectrometry (RBS), 43

Atomic displacement/thermal vibration anomaly, high-T_c superconductors (HTS), 53, 56

Auger and X-ray photoelectron spectroscopy (PES), electronic structure elucidation, 4

Auger spectroscopy

- Auger parameter for copper metal, 71*f*
- Auger parameters of elements in superconducting oxides, 70
- general considerations, 67–68
- studying high-temperature superconducting metal oxides, 68, 70
- X-ray photoelectron/Auger lines for studying superconducting metal oxides using Auger parameters, 72*f*
- See also* X-ray photoelectron and Auger spectroscopy

B

Backscattering spectrometry, Rutherford. *See* Rutherford backscattering spectrometry (RBS) application

Bardeen–Cooper–Schrieffer (BCS) theory basic concept of superconductivity mechanism, 246

- describing conventional superconductors, 2
- mechanism of superconductivity, 2

BEDT–TFF. *See* Bis(ethylenedithio)tetrathiafulvalene (BEDT–TTF); Organic superconductors; Point-contact spectroscopy (PCS)

Beer–Lambert law, yielding optical density and population dynamics of excited states, 17

Bi₂Sr₂Ca₂Cu₃O₁₀ and Bi₂Sr₂CaCu₂O₈ electron–phonon relaxation time and wavelength, 238

- See also* Time-resolved photoinduced spectroscopy

Bi₂Sr₂CaCu₂O_{8+d}

- candidates for examining spontaneously broken gauge symmetry, 245

- electron trapping mechanism, 227
 experimental results for single crystal as function of sample size, 269–270
 frequency–temperature diagram of Josephson plasma in underdoped sample, 273f
 persistent photoconductivity (PPC) in Y-doped, 226–227
 set of resonance curves as function of sample size, 269f
 temperature dependence of Josephson plasma resonance line in underdoped $\text{Bi}_2\text{Sr}_2\text{CaCu}_2\text{O}_{8+d}$ at three different frequencies, 271f
 time dependence of PPI during excitation and relaxation, 226f
See also Superconducting plasma phenomena
- Bi(ethylenedithio)tetrathiafulvalene (BEDT–TTF)**
 organic donor, 2–3
See also Organic superconductors; Point-contact spectroscopy (PCS)
- Bismuth-based ceramic superconductors**
 electric power applications, 156
See also Phase evolution in composite ceramic superconductors
- Bolometers.** *See* Dye/superconductor assemblies
- Bose statistics, electrons condensing as bosons, obeying, 2**
- Bosons, electron pair quasi-particles, 2**
- C**
- Carlson–Goldman mode**
 energy diagram of collective excitations in metals, 247f
See also Superconducting plasma phenomena
- Carriers, photoexcited.** *See* Photoexcited carriers
- Ceramic superconductors**
 bismuth-based materials, 156–157
See also Phase evolution in composite ceramic superconductors
- Channeling characterization**
 ion channeling technique, 53
 RBS of high-temperature superconductors (RBS), 48–53
 selective ^{18}O labeling and NRA/channeling analysis, 56, 61
See also Rutherford backscattering spectrometry (RBS) application
- Charge carriers.** *See* Photoexcited carriers
- Charge–density waves (CDWs)**
 decreasing critical temperature or inhibiting superconductivity, 21–22
See also Dissolution of A-15 phases in metallic dichalcogenides
- Colliding-pulse mode-locked (CPM) dye laser laser system from past, 232**
 low repetition experiments using CPM laser, 233
See also Time-resolved optical studies
- Composite ceramic superconductors.** *See* Phase evolution in composite ceramic superconductors
- Congestion of phases**
 imaging Raman microscopy (IRM) analysis, 162, 166
 IRM of region of $\text{CuO} + \text{Ca}_2\text{PbO}_4$ in Ag/Bi-2223 composite, 165f
See also Phase evolution in composite ceramic superconductors
- Conventional superconductors, leading to new selenides, 3**
- Cooper pairs, nature of pairing mechanism in high- T_c superconductors, 11, 13–15**
- Copper oxides compounds, unconventional, 3**
- Crank–Nicolson (CN) procedure, heat equation for dye/superconductor assemblies, 280**
 (Cu,C)Ba₂Ca₃Cu₄O_x ((Cu,C)-1234). *See* Raman scattering from superconducting phase
- Cuprates**
 changing carrier concentration by illumination, 216
 optical response of films grown by magnetron sputtering, 16
 photoinduced superconductivity, 16
 persistent photoconductivity (PPC) in, without CuO chains, 222–227
See also Persistent photoconductivity (PPC)
- Cuprate superconductors**
 characterization by Rutherford backscattering spectrometry (RBS), 42–47
d- or extended-*s*-wave (*s* + *id*) pairing possible, 2
 degradation pathways, 168
 efforts to comprehend self-energy effects, 10–11
 problem of structural defects, 4
 shell-model methods for phonon calculations, 4
 structures, analysis, and electronic states, 4
 unconventional, 3
See also Rutherford backscattering spectrometry (RBS) application
- Current–voltage characteristics (IVC), point-contact.** *See* Point-contact spectroscopy (PCS)
- D**
- Debye region, lattice specific heat, 102**
- Defects.** *See* Inhomogeneities
- Depth profiling**
 measurement by Rutherford backscattering spectrometry (RBS), 46, 47f
 RBS-channeling technique, 48

Dichalcogenides

- atomic, molecular, and misfit insertion, 27, 28f
- charge–density wave (CDW) transition of metallic diselenides (MSe₂), 24
- dependence of T_c on lattice instabilities, 24
- electron–phonon interaction as transition mechanism, 26–27
- general form for Se–M–Se slabs, 25f
- general properties, 23–27
- insertion of chemical species into van der Waals gap, 22
- lamellar structures of dichalcogenides, 23–24
- schematic inclusion of A-15 chains in 2H₁-MSe₂ with 2a × 2a superstructure, 29f
- structural and superconducting parameters of 1T-VSe₂, 2H₁-NbSe₂, and 2H₁-TaSe₂, 26t
- superconductivity competing and coexisting with CDW of different strength, 26
- See also Dissolution of A-15 phases in metallic dichalcogenides
- Displacement of apex oxygen ion, symmetrical (*g*-type) and antisymmetrical (*u*-type), 132–133
- Dissolution of A-15 phases in metallic dichalcogenides
- anisotropic ferromagnetism in metallic GaV₃Se₉, 35
- charge–density-wave (CDW) transition for metallic diselenides (MSe₂), 24
- comparison of superconducting parameters in crystal samples of 2H₁-NbSe₂, Nb₃Sn, and SnNb₃Se₉, 35t
- confirming dissolution of A-15 phase in diselenide matrix, 35, 38
- crystallographic and superconducting parameters for Nb₃Sn and V₃Ga phases, 23t
- dependence of T_c on lattice instabilities, 24
- evidence for CDW/ILD (incommensurate lattice distortion) on metallic transition metal diselenides, 24
- general form of Se–M–Se slabs, 25f
- intercalation process in MX₂ phases, 28f
- magnetization measurements at 4.5 K on oriented GaV₃Se₉ crystals, 27f
- new general emerging structure, 32
- new structures through dissolution process, 30, 32
- occurrence of superconductivity or magnetism in new phases, 32, 35
- Raman and Mössbauer characterization, 30, 32
- route to new insertion forms, 27
- schematic inclusion of A-15 chains in 2H₁-MSe₂ with 2a × 2a superstructure, 29f
- schematic representation of misfit compounds, 28f
- specific superconductivity of SnNb₃Se₉, 32, 35
- structural and compositional parameters of three new phases, 33t
- structural and superconducting parameters of 1T-VSe₂, 1H₁-NbSe₂, and 2H₁-TaSe₂, 26t
- structural characterization, 30, 31t, 33t
- superconductivity competing and coexisting with CDWs of different strength, 26
- susceptibility of powder samples versus temperature for SnNb₃Se₉ in zero field cooling, 34f
- susceptibility versus temperature for GaV₃Se₉ powder sample, 36f
- synthesis of powders and crystals, 30
- transition mechanism resulting from electron–phonon interaction in presence of quasi-2D nesting conditions, 26–27
- variation of critical fields versus temperature for oriented SnNb₃Se₉, 36f
- X-ray powder diffraction of 2H₁-NbSe₂, Nb₃Sn, and new phase Nb₃Sn/NbSe₂, 31t
- See also A-15 phases; Dichalcogenides
- Dye/superconductor assemblies
- absorbance spectra of various dyes in polymer matrix, 284, 285f
- assumptions regarding solution to one-dimensional heat flow, 287
- bolometer assemblies capable of color-selective optical response, 289–290
- difference between antenna-based and filter-based detector responses, 283
- dye layers by vacuum sublimation, 280
- effect of matrix on absorption characteristics of rhodamine 6G (Rh6G), 284, 285f
- evaluating wavelength selectivity of detector for comparison, 283–284
- experimental molecular dyes, 280
- experimental sensor preparation and testing, 279–281
- heat balance equation, 280
- hybrid sensors of YBa₂Cu₃O_{7-δ} (YBCO) thin films on MgO by pulsed laser deposition, 279
- improving selectivity by minimizing dye–dye interactions, 284–286
- optical characterization methods, 280
- optical penetration depth calculation, 286
- optical response characteristics for three color sublimed dye/superconductor structure, 281–282
- platform to study details of molecule/superconductor energy transfer processes, 290
- process of preparing typical assembly, 281
- quantifying frequency selectivity with quality-factor (Q), 283
- Q-values for dyes in assemblies and human eye, 284t
- resistance versus temperature curve, 281, 282f
- schematic diagram of steps for construction

- of wavelength-selective high- T_c bolometers, 281*f*
- schematic of model for three-dimensional finite difference analysis of heat flow through assembly after laser illumination, 288*f*
- schematic of optical delivery system in transient voltage measurements, 286, 287*f*
- solid-state extinction coefficient at particular wavelength, 287
- steady-state optical response versus temperature, 281, 282*f*
- studying thermophysical properties of thin dye layers on YBCO, 279
- techniques measuring thermophysical properties, 279
- temperature distributions in illuminated assembly, 289*f*
- thermal modeling to improve response characteristics, 288–289
- thermal parameter of diffusivity for Rh6G, 281
- three-dimensional finite difference modeling, 280
- transient optical response curves for YBCO microbridges coated with different Rh6G thicknesses, 286, 288*f*
- transient response measurement method, 280
- transient voltage measurements, 286–288
- wavelength-selective single-color detectors, 279

E

- Effective-mass approximation, applying to Raman vertex calculations, 182–183
- Elastic spectroscopy, electron–phonon interactions (EPI), 200
- Electrical resistivity
 - calculation of normal state of metal employing PDOS of compound, 102, 104
 - See also* Lattice dynamics
- Electromagnetic waves (EMWs)
 - application of Maxwell theory, 17–18
 - general form of Maxwell's equation, 249
 - longitudinal and transverse components, 248–252
 - propagating in vacuum, 252
 - set of equations for electric field, magnetic induction, and current, 250–251
 - See also* Superconducting plasma phenomena
- Electromigration
 - oxygen rearrangement in $\text{YBa}_2\text{Cu}_3\text{O}_x$ compounds, 115
 - See also* Oxygen reordering processes
- Electronic interband transitions, identification of electronic scattering continuum, 6, 9*f*, 10
- Electronic Raman scattering efficiency
 - intragand and interband transitions, 182
 - main theoretical results, 184–185
 - Raman susceptibility in superconducting state, 183–184
 - Raman vertex calculations, 182–183
 - scattering from solids theory, 181–185
 - Tsuneto function, 183
 - two-photon process, 182
- Electronic Raman scattering (ERS)
 - d*-wave pairing, 13–14
 - nature of pairing interaction, 11, 13–15
 - studying gaps and pseudo-gaps, 13–15
- Electron–phonon coupling constant, estimation from experimental data and model, 193–194
- Electron–phonon interaction (EPI). *See* Point-contact spectroscopy (PCS)
- Electron spectroscopy for chemical analysis (ESCA). *See* X-ray photoelectron and Auger spectroscopy
- Electron trapping
 - model for persistent photoconductivity (PPC), 222
 - See also* Persistent photoconductivity (PPC)
- Electron–vibrational interaction (EVI)
 - correlating with superconducting parameters, 210
 - criterion for synthesis of new organic conductors, 213
 - See also* Point-contact spectroscopy (PCS)
- Elements composition, by Rutherford backscattering spectrometry (RBS), 43, 46
- Emission Mössbauer studies
 - computer-analyzed components in two $\text{HoNi}_2(^{57}\text{Co})\text{B}_2\text{C}$ samples, 153*f*
 - configurations of ^{57}Co at Cu(1) site in $\text{YBa}_2\text{Cu}_3(^{57}\text{Co})\text{O}_{7-\delta}$, 142, 144*f*
 - Cu–O chains serving as charge reservoirs only, 142, 145
 - emission Mössbauer spectra of ^{57}Co -doped $\text{YBa}_2\text{Cu}_3\text{O}_{7-\delta}$, 143*f*
 - $\text{HoNi}_2\text{B}_2\text{C}$ system, 151–152
 - measuring absorption of gamma quanta emitted by ^{57}Co , 140
 - obtaining information on microscopic level, 139
 - oscillation of O(4) in Cu–O chain of $\text{YBa}_2\text{Cu}_3\text{O}_{7-\delta}$, 140–145
 - oxygen ions potentially moving in double-well potential, 142
 - praseodymium (Pr) substitution and metallicity of chain in $\text{YBa}_2\text{Cu}_3\text{O}_{7-\delta}$, 145
 - probing dynamics of Cu(1)–O(4) chain by ppm substitution of Cu(1) with ^{57}Co , 142
 - role of extraneous oxygen in superconductivity of
 - Nd–Ce–Cu–O system, 145–151
 - unit cell of $\text{YBa}_2\text{Cu}_3\text{O}_{7-\delta}$, 141*f*

- See also Nd-Ce-Cu-O system; $\text{YBa}_2\text{Cu}_3\text{O}_{7-d}$ (YBCO)
- Energy gap spectroscopy, superconductors, 199
- Exotic superconductors
alkali salts of C_{60} (fullerene), 3
copper oxide compounds, 3
dynamical spectra and interference effects, 4–11
high- T_c cuprates, 3
high- T_c cuprate structures, analysis, and electronic states, 4
important spectroscopies, 1–2
microwave resonance spectra, 17–18
nature of pairing interaction, 11, 13–15
new selenides from conventional superconductors, 3
optical devices, 18
organic superconductors, 2–3
photoexcited carriers and relaxation dynamics, 15–17
 SnNb_5Se_9 and $\text{Sn}(\text{Ta},\text{Nb})_5\text{Se}_9$ from $\text{Nb}_3\text{Sn}/\text{NbSe}_2$ and $\text{Nb}_3\text{Sn}/\text{TaSe}_2$, 3

F

- Fano interference effect
electronic Raman scattering, 186–187
examples at 162 cm^{-1} Raman band of SnNb_5Se_9 superconductor, 6, 7f
phonon line at 10 K Raman spectra of $\text{YBa}_2\text{Cu}_3\text{O}_7$, 6, 8f
Raman spectra of high- T_c cuprates, 6
- Fermi levels
four layers (sheets) of $\text{YBa}_2\text{Cu}_3\text{O}_7$, 6, 9f, 10
superconductors, 2
- Ferromagnetism
anisotropic ferromagnetism in metallic GaV_5Se_9 , 35, 36f
 GaV_5Se_9 from $\text{V}_3\text{Ga}/\text{VSe}_2$, 3
new selenides from conventional superconductors, 3
See also Dissolution of A-15 phases in metallic dichalcogenides
- Film thickness, by Rutherford backscattering spectrometry (RBS), 43, 44f
- Fullerene (C_{60}), alkali salts, unconventional, 3

G

- $\text{GdBa}_2\text{Cu}_3\text{O}_{6.45}$
basic effect of illumination on resistivity and T_c , 217, 218f
relative change in conductivity as function of oxygen content, 220
spectral efficiency of persistent photoconductivity (PPC), 221f
time dependence of excitation and relaxation of PPC, 217–219
See also Persistent photoconductivity (PPC)

- Green's function method, reproducing Raman spectra, 6, 10

H

- Hall coefficient
temperature dependence, 81–83
See also $\text{YBa}_2\text{Cu}_3\text{O}_{7-\delta}$ (YBCO)
- Hall effect
angular dependence of Hall resistivity in mixed state, 83
detwinned YBCO crystal below T_c , 83
See also $\text{YBa}_2\text{Cu}_3\text{O}_{7-\delta}$ (YBCO)
- Heterojunctions. See Point-contact spectroscopy (PCS)
- High- T_c bolometers. See Dye/superconductor assemblies
- High- T_c cuprates
structures, analysis, and electronic states, 4
unconventional, 3
See also Cuprates, high- T_c
- High- T_c superconductivity
application examples, 1
spectroscopies of interest, 1–2
- High-temperature superconductors (HTSs)
atomic displacement/thermal vibration anomaly, 53, 56
characterization by Rutherford backscattering spectrometry (RBS), 42–47
discovery and application interest, 78
early research history, 78–79
growing high-quality single crystals in abundant quantities, 79
importance of phonons, 95–96
lattice dynamical model, 96–97
need for processing methods capable of controlling interfacial properties, 168–169
overcoming difficult oxygen ratio determination, 46
phase diagrams and judging sample quality, 79
RBS-channeling characterization, 48–53
selective labeling by ^{18}O and NRA/channeling analysis, 56, 61
structural defects playing role in electrical properties, 50
technology allowing ultrathin crystalline film growth and periodic structures with controlled characteristics, 131
See also Lattice dynamics; Rutherford backscattering spectrometry (RBS) application; $\text{YBa}_2\text{Cu}_3\text{O}_{7-\delta}$ (YBCO)
- Homojunctions. See Point-contact spectroscopy (PCS)
- $\text{HoNi}_2\text{B}_2\text{C}$ system
computer-analyzed components in two $\text{HoNi}_2(^{57}\text{Co})\text{B}_2\text{C}$ samples, 153f
evidence of electronic phase inhomogeneity, 152
interplay of magnetism and superconductivity, 151–152

I

Imaging Raman microscopy. *See* Phase evolution in composite ceramic superconductors

Infrared spectroscopy

efficient technique of control of hybrid materials, 5–6

See also Self-assembled monolayers

(SAMs) on

YBa₂Cu₃O₇ (YBCO)

Inhomogeneities

c-axis lattice parameter measure of oxygen composition, 85

high-resolution X-ray-diffraction experiments, 85, 87

model relating slope and zero-temperature intercept to, 81

third and first harmonic ac susceptibility of T1 2201 crystal, 89, 90f

third harmonic ac susceptibility measurement of over-doped T1 2201 crystal, 89, 91f

See also YBa₂Cu₃O_{7- δ} (YBCO)

Intercalation process

atomic, molecular, and misfit insertion in dichalcogenides, 27, 28f

See also Dissolution of A-15 phases in metallic dichalcogenides

Interference effect

Fano, 6, 7f, 8f

See also Fano interference effect

Intramolecular vibration (IMV)

role in explaining superconductivity, 208, 210

See also Point-contact spectroscopy (PCS)

Ion channeling technique, studying displacement of atoms or lattice distortion, 53

Ion cluster beam bombardment

Ar-ion-cluster for smoothing thin film surfaces, 115f

oxygen rearrangement in YBa₂Cu₃O_x compounds, 115–116

See also Oxygen reordering processes

Ion displacements, symmetrical (*g*-type) and antisymmetrical (*u*-type), 132–133

J

Josephson critical current, role of superconducting coherence length, 199

Josephson effect

physics of superconductors, 17

plasma modes, 253

Josephson plasma modes

block diagram of experimental setup for preset Josephson plasma resonance, 263f

calculations for determining plasma frequency, 253–255

cavity resonator identifying origin or absorption, 257

electromagnetic absorption at microwave frequencies, 256–257

energy diagram of collective excitations in metals, 247f

equations for transverse plasma, 264–268

experimental technique for separating modes, 262–264

high-T_c superconductors, 255–257

Josephson effect, 253

longitudinal and transverse modes, 245

numerical results using indicated parameters, 268f

plasma resonance field as function of sample size for two cases, 270

schematic of Josephson junction, 253f

schematic of multistacked Josephson junction as model of high-T_c superconductors, 258f

set of resonance curves observed in Bi₂Sr₂CaCu₂O_{8+ δ} as function of sample size, 269f

single Josephson junction, 252–255

theory of superconducting plasma in system with highly layered structure, 256

See also Superconducting plasma phenomena

K

Kohlrusch's law

signature of dispersive scattering of charge carriers, 15

variation of photoconductivity versus time, 15

L

Laser annealing

monitoring oxygen reordering processes, 112–115

schematic of idea and results of Raman study of

isotopic substitution during laser annealing of

YBa₂Cu₃¹⁸O_{6.2} in air, 114f

variations of lineshape of *xx/yy* Raman spectra of

YBa₂Cu₃¹⁸O_{6.2} thin film during and after annealing steps in vacuum, 113f

See also Raman spectroscopy in YBCO type compounds

Laser probe process, time-resolved photoinduced spectroscopy, 239

Lattice dynamics

- Brillouin zone (BZ) of body-centered tetragonal structure, 100f
- calculated phonon densities of state (PDOS) of YBa₂Cu₃O₇, 101f
- characterization of optical phonons, 97
- determination of phonon specific heat and resistivity, 4–5
- electrical resistivity, 102, 104
- lattice specific heat, 102
- leading to dynamic stability of compounds, 97
- model, 96–97
- PDOS, 99
- phonon dispersion curves, 97, 99
- phonon dispersion curves of Nd₂CuO₄ along symmetry directions in BZ, 100f
- polarization diagrams of Raman A_{1g} modes of YBa₂Cu₃O₇, 97, 98f
- shell models based on interaction potentials between ion pairs, 104
- specific heat for YBa₂Cu₃O₇ in ranges 0–100 K and 0–10 K, 103f
- theoretical studies, and phonon-related properties, 95–96

Lattice specific heat measurements, 102

YBa₂Cu₃O₇ in ranges 0–100 K and 0–10 K, 103f

See also Lattice dynamics

Light-scattering processes. *See* Apex oxygen sublattice in YBa₂Cu₃O_{7-x} single crystals

Longitudinal plasma mode

dispersion relation of longitudinal and transverse plasma modes, 261f

Josephson plasma, 257–260

schematic picture of multistacked Josephson junction as model of high-T_c superconductors, 258f

separation of longitudinal and transverse plasma modes, 261–270

See also Josephson plasma modes; Nambu–Goldstone mode; Superconducting plasma phenomena

Low-dimensional synthetic metals

other ground states in competition with superconductivity, 21

See also Dissolution of A-15 phases in metallic dichalcogenides

M

Magnetotransport

mixed state properties of YBa₂Cu₃O_{7-δ}, 83–85

normal state properties of YBa₂Cu₃O_{7-δ}, 80–83

properties of YBa₂Cu₃O_{7-δ}, 80–85

structural defects, 4

See also YBa₂Cu₃O_{7-δ} (YBCO)

Maxwell theory

application to electromagnetic waves, 17–18

longitudinal and transverse plasma modes, 258, 260

physics of superconductors, 17–18

Meissner effect

superconductivity, 2

transverse plasma mode, 245, 261

Metal oxide superconductors

Auger parameters, 70, 71f

Auger spectroscopy, 68, 70

X-ray photoelectron/Auger lines for study using Auger parameters, 72t

Microprobe spectroscopy, application to superconductors, 1

Micro-Raman spectroscopy

lattice dynamical calculations for vibrational band assignment, 4–5

See also Raman microspectroscopy

Microwave resonance spectra, basic physics of superconductors, 17–18

Model

development for Ortho-II phase of YBa₂Cu₃O_x compounds, 123–127

lattice dynamics, 96–97

leading to dynamic stability of compounds, 97

studying apex oxygen sublattice in YBa₂Cu₃O_{7-x} single crystals, 132–133

See also Lattice dynamics

Monolayer assembly. *See* Self-assembled monolayers (SAMs) on YBa₂Cu₃O₇ (YBCO)

Mössbauer spectroscopy, emission

oxygen lattice in YBa₂Cu₃O_{7-δ}, 5

See also Emission Mössbauer studies

N

Nambu–Goldstone mode

confirming existence, 274

energy diagram of collective excitations in metals, 247f

gap formation known as Anderson–Higgs–Kibble mechanism, 245–246

longitudinal mode of superconducting phase transition, 245

physical meaning, 261

superconducting state, 18

See also Longitudinal plasma mode; Superconducting plasma phenomena

Nd–Ce–Cu–O system

bulk superconductor Nd_{1.84}Ce_{0.16}Cu(⁵⁷Co)O₄, 147, 151

Ce-poor bulk nonsuperconducting
 $\text{Nd}_{1.86}\text{Ce}_{0.14}\text{-Cu}^{(57)\text{Co}}\text{O}_4$ after deoxygenation, 147, 149f

Ce-rich bulk nonsuperconducting
 $\text{Nd}_{1.82}\text{Ce}_{0.18}\text{Cu}^{(57)\text{Co}}\text{O}_4$ after deoxygenation, 147, 150f

computer-analyzed components of $\text{Nd}_{2-x}\text{Ce}_x\text{-Cu}^{(57)\text{Co}}\text{O}_4$ at 80 K, 149f

electron density in 3d-band of CuO_2 planes by Mössbauer spectroscopy, 151

electron-doped system versus hole-doped analog
 $\text{La}_{2-x}\text{Sr}_x\text{CuO}_4$, 146

Mössbauer spectra of $\text{Nd}_{2-x}\text{Ce}_x\text{Cu}^{(57)\text{Co}}\text{O}_4$ ceramic samples at different temperatures, 148f

Mössbauer spectrum resolution into quadrupole split doublets corresponding to two species, 147, 148f

oxygenated and deoxygenated $\text{Nd}_{2-x}\text{Ce}_x\text{-CuO}_4$, 146

relative abundance of species B corresponding to superconducting volume fraction, 151

role of extraneous oxygen in superconductivity, 145–151

role of oxygen in manifestation of superconductivity in $\text{Nd}_{2-x}\text{Ce}_x\text{CuO}_4$, 146

species C (6-coordinate) only in oxygen-rich antiferromagnetically ordered “impurity” regions, 147

superparamagnetically relaxed spectrum consisting of quadrupole split doublet, 147, 148f

thermal treatment sequence of $\text{Nd}_{1.85}\text{Ce}_{0.15}\text{-Cu}^{(57)\text{Co}}\text{O}_4$ eliminating impurity phase, 151

O

Optical density, application of Beer–Lambert law, 17

Optical phonons
 calculation of, 97
 energies and polarizations of Raman A_{1g} modes of $\text{YBa}_2\text{Cu}_3\text{O}_7$, 98f
See also Lattice dynamics

Optical sensors
 application of dye/superconductor assemblies, 18
 detection and discrimination of wavelengths, 278–279
See also Dye/superconductor assemblies

Organic conductors. *See* Point-contact spectroscopy (PCS)

Organic superconductors
 convincing data evidencing self-energy effects, 11

donor bis(ethylenedithio)tetrathiafulvalene (BEDT–TTF), 2–3

donor tetramethyltetraselenafulvalene (TMTSF), 2–3

efforts in comprehension of self-energy effects in cuprates, 10–11

organic donors, 2–3

quasi-two-dimensional electronic character of β - and κ -phases, 10

stacking structures, 3

symmetry of order parameter from polarized electronic Raman spectra, 11, 12f

unconventional, 2–3

vibrational spectroscopy research areas, 10–11

Ortho-II phase of $\text{YBa}_2\text{Cu}_3\text{O}_x$
 Ag apical oxygen vibration in ZZ scattering configuration, 124
 assuming quasi-molecular species insulated from each other, 124
 clearly defined minimum in scattering efficiency correlating with shoulder of Ortho-I phase scattering efficiency, 127
 cosine of phase shift versus energy of exciting photons, 128f
 disputable assumption of polarizability of Cu–O chains in Ortho-II-like Ortho-I and Tetra phases, 124–125
 equation for absolute efficiency of Raman scattering, 123
 finite-size domains of Tetra, Ortho-II, and Ortho-I structures, 127, 129
 fractions of three phases in samples using calculated efficiencies, 127
 model development, 123–127
 phase characterizations, 120, 122
 physics problem, 122
 Raman for studying oxygen arrangement, 122
 Raman spectra of oxygen-deficient $\text{YBa}_2\text{Cu}_3\text{O}_x$ in ZZ scattering configuration at different wavelengths and decomposition into three Lorentzian components, 125, 126f
 relevant description based on relative abundance of different coexisting phases, 122–123
 scattering efficiency of apical oxygen vibrations in three phases, 125, 126f
 scattering efficiency of apical vibrations in Ortho-II, 123
 volume fraction phase determinations, 123
See also $\text{YBa}_2\text{Cu}_3\text{O}_x$ (YBCO)

Overdoped YBCO-type materials
 Raman spectroscopy, 116–117
See also Raman spectroscopy in YBCO type compounds

Oxazine 1 perchlorate
 molecular dye, 280
See also Dye/superconductor assemblies

Oxygen (apical) vibrations, scattering efficiency. *See* Ortho-II phase of $\text{YBa}_2\text{Cu}_3\text{O}_x$
 Oxygen reordering processes
 monitoring during laser annealing, 112–115
 other oxygen rearrangement processes by Raman spectroscopy, 115–116
See also Raman spectroscopy in YBCO type compounds
 Oxygen sensitivity limit, resonance method, 46

P

Pairing interactions

electronic Raman spectroscopy (ERS)
 studying gaps and pseudo-gaps, 13–15
 point-contact spectroscopy (PCS), 14
 studying nature of, 11, 13–15

Persistent photoconductivity (PPC)

basic effect of illumination on resistivity and T_c , 217, 218f
 basic effect of illumination on resistivity of $\text{Tl}_2\text{Ba}_2\text{CuO}_{6+\delta}$, 223, 224f
 cuprates without CuO chains, 222–227
 electron trapping model, 222
 Kohlrusch's law, 15
 persistent photoinduced effects in $\text{RBa}_2\text{Cu}_3\text{O}_{7-\delta}$, 217–221

photoassisted oxygen ordering model, 222
 photoinduced changes in resistivity, Hall coefficient, and Hall mobility during excitation and relaxation, 219

property common to several semiconductors, 15

reversible change of carrier concentration by illumination, 216, 227–228

saturation conductivity change as function of oxygen context, 220

spectral dependence in $\text{RBa}_2\text{Cu}_3\text{O}_{6+\delta}$, 220–221

spectral dependence in $\text{Tl}_2\text{Ba}_2\text{CuO}_{6+\delta}$, 225–226

spectral efficiency for $\text{GdBa}_2\text{Cu}_3\text{O}_{6.3}$, 221f
 theoretical models, 222

time dependence of excitation and relaxation, 217–219

time dependence of excitation and relaxation in $\text{Bi}_2\text{Sr}_2\text{Ca}_{1-x}\text{Y}_x\text{Cu}_{8+\delta}$, 226f

time dependence of excitation and relaxation in

$\text{Tl}_2\text{Ba}_2\text{CuO}_{6+\delta}$, 223f, 224

$\text{Tl}_2\text{Ba}_2\text{CuO}_{6+\delta}$, 223–226

Y-doped $\text{Bi}_2\text{Sr}_2\text{CaCu}_2\text{O}_{8+\delta}$, 226–227

Phase determination, oxygen-deficient $\text{YBa}_2\text{Cu}_3\text{O}_{6+\delta}$ and overdoped $\text{YSr}_2\text{Cu}_3\text{O}_{7.7}$ compounds, 5

Phase evolution in composite ceramic superconductors

heat treatment temperatures above and below liquidus onset temperatures, 158

insights into phase chemistry with Raman microspectroscopy (RMS) and imaging Raman microscopy (IRM), 157
 investigation of Ag/Tl-1223 composites with $\text{Tl} + \text{Bi} + \text{Pb} = 1.1$, 157–160
 IRM analysis of interior region of ceramic core in AG/Bi-2223 composite, 162, 164f
 IRM analysis of region of $\text{CuO} + \text{Ca}_2\text{PbO}_4$ congestion in Ag/Bi-2223 composite, 165f
 measurement methods, 157
 phase assemblages in fully processed Ag/Bi-2223 WIT composite, 160, 162
 possible links between Tl/Bi/Pb stoichiometry and phase chemistry, 160
 second phase congestion in OPIT-type Ag/Bi-2223 , 162, 166
 specimen preparation, 157
 spot-focused Raman spectra in vicinity of ceramic/silver interface in wire-in-tube Bi-2223 composite, 163f
 spot-focused Raman spectra of six phases in bismuth- and bismuth + lead-doped Ag/Tl-1223 samples after heat treatment, 159f
 summary of RMS results for $(\text{Tl,Bi,Pb})_{1.1}\text{Ba}_{0.4}\text{Sr}_{1.6}\text{Ca}_{2.0}\text{Cu}_{3.0}\text{O}_x$, 158f
 Tl-1223 wires appearing to disrupt connectivity of superconducting grains, 160, 161f

Phase separation

Raman evidences in $\text{YBa}_2\text{Cu}_3\text{O}_x$, 111–112
See also Raman spectroscopy in YBCO-type compounds

Phases. *See* Ortho-II phase of $\text{YBa}_2\text{Cu}_3\text{O}_x$

Phonon densities of state (PDOS)

calculated PDOS of $\text{YBa}_2\text{Cu}_3\text{O}_7$, 101f

PDOS for typical high-temperature superconductors (HTSs), 99

See also Lattice dynamics

Phonon dispersion curves

Brillouin zone (BZ) of body-centered tetragonal structure, 100f

measurements, 97, 99

Nd_2CuO_4 along symmetry directions in BZ, 100f

See also Lattice dynamics

Phonons

hardening (increase in frequency) below T_c , 11

Raman scattering from, 185

self-energy, 186

superconductivity-induced phonon renormalization, 188, 190–192

vibrational frequencies, 4–5

Phonons in high-temperature superconductors (HTSs)

theoretical studies of lattice dynamics, 95–96

See also Lattice dynamics

- Photoassisted oxygen ordering
 model for persistent photoconductivity (PPC), 222
See also Persistent photoconductivity (PPC)
- Photoconductivity
 evolution and relaxation of photogenerated charge carriers, 15
See also Persistent photoconductivity (PPC)
- Photodoping, definition, 15
- Photoelectron spectroscopy (PES)
 electronic structure elucidation, 4
See also X-ray photoelectron and Auger spectroscopy
- Photoexcited carriers
 dynamics of charge carriers, 16
 model of electron trapping at oxygen vacancies, 15–16
 rate equation for population decay of excited states, 17
 and relaxation dynamics, 15–17
 transient absorption or transmission measurements, 17
- Photoinduced reflection or transmission
 theoretical model for temperature dependence, 239–240
See also Time-resolved photoinduced spectroscopy
- Plasma phenomena. *See* Superconducting plasma phenomena
- Point-contact spectroscopy (PCS)
 basis of, 197
 central in modern solid-state physics, 196–197
 comparison of point-contact and optical data involving β -(BEDT-TTF) $_2$ I $_3$ (bis(ethylenedithio)tetrathiafulvalene (BEDT-TTF)), 203, 204f, 205
 contribution of EPI (electron-phonon interaction) processes to IVC (current-voltage characteristics) of superconducting contacts, 200
 correlation with optical investigations, 213
 dependences V^2 vs. d^2V/dI^2 (V) and $I(V)$ for (BEDT-TTF) $_2$ I $_3$ -Cu contact, 208, 209f
 elastic spectroscopy of EPI, 200
 electron-vibrational interaction (EVI) intensity correlating with superconducting parameters, 210
 energy gap spectroscopy of superconductors, 199
 EVI level as criterion for new organic conductor synthesis, 213
 excess current at high voltages, 199–200
 experimental setup for researching contacts at low temperatures, 198
 heterojunctions of Cu[(C $_2$ H $_5$) $_4$ N] $_{0.5}$ [Ni(dmit) $_2$] and Cu-(BEDT-TTF) $_2$ I $_3$ at 4.2 K, 210
 homo- and heterojunctions of organic conductor β -(BEDT-TTF) $_2$ I $_3$, 200–208
 intramolecular vibration (IMV) in explaining superconductivity, 208, 210
 Josephson critical current, 199
 normal state, 197–198
 organic conductor [(C $_2$ H $_5$) $_4$ N] $_{0.5}$ [Ni(dmit) $_2$], 208, 210–213
 peculiarity of β -(BEDT-TTF) $_2$ I $_3$ organic metal, 207
 point-contact EPI function, 197–198
 point-function EPI function for heterojunction Cu-(BEDT-TTF) $_2$ I $_3$ and Cu[(C $_2$ H $_5$) $_4$ N] $_{0.5}$ [Ni(dmit) $_2$], 211, 212f, 213
 principal expression of point-contact theory, 198
 reflecting EPI function and EPI anisotropy in normal state, 197
 shape of singularities of spectra for Cu[(C $_2$ H $_5$) $_4$ N] $_{0.5}$ -[Ni(dmit) $_2$], 211, 212f
 spectra characterizing hetero- and homo-junctions of Cu- β -(BEDT-TTF) $_2$ I $_3$, 201, 202f, 203
 spectra of heterocontacts Cu- β -(BEDT-TTF) $_2$ I $_3$ oriented along and perpendicular to layers of organic molecules, 205, 206f, 207
 spectra of organic conductors belonging to type II point contacts, 205, 206f
 superconductivity of point contacts, 199
 superposition of contribution from copper and organic metal in spectra of Cu-[(C $_2$ H $_5$) $_4$ N] $_{0.5}$ [Ni(dmit) $_2$] junctions, 210–211
 technique for studying nature of pairing, 14
 two types of point-contact spectra in organic metal crystal β -(BEDT-TTF) $_2$ I $_3$, 207
- Point-successive-overrelaxation method (SOR), solving equation for dye/superconductor assemblies, 280
- Polyparaphenylenevinylene (PPV), conducting polymer, 15
- Praseodymium (Pr), substitution for Y and metallicity of chain in YBa $_2$ Cu $_3$ O $_{7-\delta}$, 145
- ## Q
- Quality factor, Q
 quantifying frequency selectivity, 283
 values for dyes in assemblies and human eye, 284f
See also Dye/superconductor assemblies
- Quasiparticle (QP) relaxation dynamics
 real-time techniques for investigation, 20
See also Time-resolved optical studies

Quasi-two-dimensional crystalline structures
optical study methods, 132
See also Apex oxygen sublattice in $\text{YBa}_2\text{Cu}_3\text{O}_{7-x}$ single crystals

R

Radiation damage and regrowth, RBS-channeling characterization of high-temperature superconductors (HTS), 50

Raman light scattering

dynamical equations for O(4) ion oscillations in anharmonic approximation, 134
intensity of scattering light flux in zz -polarization, 134

mixing symmetrical (g -type) and antisymmetrical (u -type) phonon modes, 133–135

studying gaps and pseudo-gaps, 13–15

See also Raman scattering from superconducting phase

Raman microscopy. *See* Phase evolution in composite ceramic superconductors

Raman microspectroscopy

fabrication of wires and tapes, 5
hardening phonons (frequency increase) below T_c , 11

symmetry of order parameter from polarized electronic Raman spectra, 11, 12*f*

See also Phase evolution in composite ceramic superconductors; Raman spectroscopy

Raman scattering from superconducting phase

electronic Raman scattering efficiency theory, 181–185

electronic Raman scattering of well-oriented $(\text{Cu,C})\text{Ba}_2\text{Ca}_3\text{Cu}_4\text{O}_x$ ((Cu,C)-1234) microcrystals, 188, 189*f*

electron-phonon coupling constant, 193–194

experimental selection of scattering symmetry, 187–188

Fano effect, 186–187

fitting procedure results for A_{1g} spectra of (Cu,C)-1234, 191*f*

low-energy response of materials, 180

phonon self-energy, 186

Raman intensity of A_{1g} phonons in superconducting state, 192–193

Raman scattering from phonons theory, 185

samples and experimental setup, 187

superconductivity-induced phonon renormalization, 188, 190–192

temperature dependence of fitted frequency, linewidth, and phonon intensity for phonons in (Cu,C)-1234, 191*f*

theory of scattering from solids, 181–187
See also Electronic Raman scattering efficiency

Raman spectroscopy

investigation of structure of $\text{YBa}_2\text{Cu}_3\text{O}_{6.5}$ orthorhombic-II phase, 5

renormalization effects, 6

spectra for assessing nature of pairing mechanism of Cooper pairs in high- T_c superconductors, 11, 13–15

treatment of oscillations of apical O(4) atom in

$\text{YBa}_2\text{Cu}_3\text{O}_{7-\delta}$, 5

See also Raman microspectroscopy

Raman spectroscopy in YBCO-type compounds

Ar-ion-cluster bombardment for smoothing thin film surface, 115*f*

averaged tetragonal (T) phase, 110–111

coexisting oxygen ordering domains at microscopic level, 118

four phases for $\text{RBa}_2\text{Cu}_3\text{O}_x$ ($R = \text{Y}$), 108

local oxygen arrangements in basal planes of overdoped $\text{YBa}_2\text{Cu}_3\text{O}_x$ ($x > 7$) (YBCO), 116*f*

monitoring oxygen reordering processes during laser annealing, 112–115

Ortho-II ($x = 6.5$) phase, 110

Ortho-I ($x = 7$) and T ($x = 6$) phases of $\text{RBa}_2\text{Cu}_3\text{O}_x$, 109–110

overdoped YBCO-type materials, 116–117
oxygen rearrangement by electromigration and ion cluster beam bombardment, 115–116

phases differing by oxygen arrangement in basal planes, 108, 109*f*

phase separation evidences in $\text{YBa}_2\text{Cu}_3\text{O}_x$, 111–112

polarized Raman spectra of single $\text{YBa}_2\text{Cu}_3\text{O}_x$ crystal before (mainly Ortho-I) and after (mainly T-phase) annealing in vacuum, 110*f*

polarized Raman spectra of two different oxygen-deficient crystals of $\text{YBa}_2\text{Cu}_3\text{O}_x$, 110*f*

polarized Raman spectra of $\text{YBa}_2\text{Cu}_3\text{O}_{7.7}$ in several exact scattering configurations, 117*f*

Raman spectrum of $\text{RBa}_2\text{Cu}_3\text{O}_x$, superposition of coexisting microphases spectra, 108–109

schematic of idea and results of Raman study of isotopic substitution during laser annealing of $\text{YBa}_2\text{Cu}_3^{18}\text{O}_{6.2}$ in air, 114*f*
spectra of four stable phases in $\text{YBa}_2\text{Cu}_3\text{O}_x$, 108–111

variations of line shape and position of apex oxygen band (zz) with excitation phonon energy, 112*f*

- variations of lineshape of *xx/yy* Raman spectra of YBCO thin film during and after subsequent annealing steps in vacuum, 113*f*
- xx/zz* Raman spectra of two different YBCO thin films at low temperature, 112*f*
- zz* and *xx/yy* polarized spectra of $\text{YBa}_2\text{Cu}_3\text{O}_x$, before, during, and after two subsequent annealing steps in air, 111*f*
- Raman vertex calculations, 182–183
- RBS. See Rutherford backscattering spectrometry (RBS) application
- Reflection–absorption infrared spectroscopy (RAIRS)
- organization of spontaneously adsorbed monolayers, 169–170
- See also Self-assembled monolayers (SAMs) on $\text{YBa}_2\text{Cu}_3\text{O}_7$ (YBCO)
- Relaxation dynamics, photoexcited carriers, 15–17
- Reordering processes
- monitoring oxygen, during laser annealing, 112–115
- other oxygen rearrangements by Raman spectroscopy, 115–116
- oxygen-deficient $\text{YBa}_2\text{Cu}_3\text{O}_{6+\delta}$ and overdoped $\text{YSr}_2\text{Cu}_3\text{O}_{7.7}$ compounds, 5
- See also Raman spectroscopy in YBCO-type compounds
- Resistivity
- angular dependence of Hall resistivity in mixed state, 83
- electrical, 102, 104
- temperature dependence in twinned and untwinned samples, 80–81, 82*f*
- See also Lattice dynamics; Magnetotransport; $\text{YBa}_2\text{Cu}_3\text{O}_{7-\delta}$ (YBCO)
- Resonance (α, α) backscattering on oxygen, non-Rutherford scattering method, 46
- Rhodamine 6G (Rh6G)
- absorbance spectra, 282*f*
- molecular dye, 280
- See also Dye/superconductor assemblies
- Rutherford backscattering spectrometry (RBS) application
- advantages, 41–42
- aligned spectra for as-implanted, 650°C/1hr and 700°C/1hr annealed samples, 50, 51*f*
- area density for elements, 43
- Arrhenius plot for annealed samples from 650°C to 1000°C, 50, 51*f*
- atomic displacement/thermal vibration anomaly in HTS, 53, 56
- backscattering spectra of ultrathin YBCO ($\text{YBa}_2\text{Cu}_3\text{O}_{7-\delta}$) epi-film on SrTiO_3 and MgO substrates, 49*f*
- basis of technique, 41
- channeling characterization of high-temperature superconductors (HTSs), 48–53
- channeling dip of 1.8 MeV He ions through YBCO epi-film on MgO, 52*f*
- channeling dips at temperatures above and below T_c in YBCO single crystal, 55*f*
- channeling dips of {110} oriented YBCO film prepared with different parameters, 54*f*
- channeling dips using combined RBS signals from Cu, Ba, and Y sublattices, 56, 57*f*, 58*f*
- combining selective labeling with 3.05 MeV resonance scattering on ^{18}O and nuclear reaction analysis of ^{18}O , 61
- depth profiles of ^{18}O in 200 keV ^{18}O -implanted SrTiO_3 substrate single crystal, 61, 62*f*
- depth profiling, 46
- elements composition and stoichiometry, 43, 46
- energy analysis of α -particles for better depth resolution, 61, 62*f*
- energy spectrum on YBCO sample using He ion beam of resonance scattering energy at random incidence, 56, 59*f*
- film thickness measurement, 43
- high-resolution RBS-channeling study of initial growth stage of YBCO films, 48
- high-temperature superconductor (HTS) characterization, 42–47
- HTS thin films preparation and characterization, 42
- ion-channeling technique for studying atom displacement, 53
- phase transition manipulation by oxygen loss at specific crystallographic site in CuO chain, 56, 59*f*
- radiation damage and regrowth, 50
- RBS-channeling random and aligned spectra for as-implanted sample, 50, 51*f*
- RBS-channeling spectra at 3.045 MeV for thick $\text{YBa}_2\text{Cu}_3^{18}\text{O}_6^{18}\text{O}$ film, 56, 60*f*, 61
- RBS-channeling spectra for YBCO film implanted with Ar ions after annealing, 52*f*
- RBS-channeling technique studying structural displacement of atoms in HTS, 53, 56
- RBS spectrum of $\text{YBa}_2\text{Cu}_3\text{O}_{7-\delta}$ thick film on MgO substrate with SrTiO_3 buffer layer, 44*f*
- RBS spectrum of $\text{YBa}_2\text{Cu}_3\text{O}_{7-\delta}$ thin film on MgO substrate with SrTiO_3 buffer layer, 44*f*
- routine analysis for film preparation optimization, 42
- schematic drawing of unstrained YBCO film on MgO substrate, 52*f*
- schematics for {110} direction misorientation between YBCO film and SrTiO_3 substrate, 54*f*
- selective labeling by ^{18}O and NRA/channeling analysis, 56, 61

sensitivity limit of 2 MeV α -RBS for Y, Ba, and Cu in $\text{YBa}_2\text{Cu}_3\text{O}_{7-\delta}$ film, 45f
 strain relaxation in YBCO epi-film by RBS-channeling, 50, 53
 various ions for RBS analysis, 42
 $\text{YBa}_2\text{Cu}_3\text{O}_{7-\delta}$ film on MgO with and without buffer layer for depth profiling, 47f

S

Scattering efficiency of apical oxygen vibrations. *See* Ortho-II phase of $\text{YBa}_2\text{Cu}_3\text{O}_x$
 Selenides, new

from conventional superconductors, 3
 micro-Raman spectra of NbSe_2 , VSe_2 , and V_3Ga at 6 K, 10 K, and 300 K, 3, 7f
 micro-Raman spectra of SnNb_5Se_9 and GaV_5Se_9 at 10 K, 3, 7f

Mössbauer studies of SnNb_5Se_9 , 3

Self-assembled monolayers (SAMs) on $\text{YBa}_2\text{Cu}_3\text{O}_7$ (YBCO)

adsorption, thermal desorption, and readorption of various amine reagents, 177f
 adsorption of primary, secondary, and tertiary amines to YBCO, 176

alkylamine substitution pattern dependence on monolayer order, 176

atomic force microscopy (AFM) images and profilometry traces, 175f

characterization of monolayer order on smooth YBCO films, 170–174

comparison of antisymmetric methylene stretches and peak widths for a variety of substrates, monolayers, and substitution patterns, 172f

comparison of IR reflectivity of YBCO versus gold samples, 171f

difference in copper–copper spacing in oriented YBCO samples, 173–174

high degree of conformational order within monolayers on YBCO, 170

identification of important experimental variables, 178

information on organization of spontaneously adsorbed monolayers by reflection–absorption infrared spectroscopy (RAIRS), 169–170

molecular ordering characteristics for polycrystalline surfaces, 174–175

molecular tilt angle value by molecular mechanics energy calculations, 174

octadecylamine monolayer examination by RAIRS, 171f, 172–173

RAIRS data for octadecylamine, dioctylamine, and trioctylamine adsorbed on YBCO, 177f

symmetric methyl vibrational dipole and angle with respect to YBCO surface, 175f

thermal stability of monolayers, 176

unit cell of YBCO and copper-containing layers, 173f

Self-energy effects

convincing data evidencing in organic superconductors, 11

efforts in comprehension in cuprates, 10–11

Spectrometry techniques. *See* Rutherford backscattering spectrometry (RBS) application

Spin density-waves (SDW)

decreasing critical temperature or inhibiting superconductivity, 21–22

See also Dissolution of A-15 phases in metallic dichalcogenides

Squarylium–pyrylium dye (SqPy)

absorbance spectra, 282f

molecular dye, 280

See also Dye/superconductor assemblies

Stoichiometry, by Rutherford backscattering spectrometry (RBS), 43, 46

Structural properties

$\text{YBa}_2\text{Cu}_3\text{O}_{7-\delta}$, 85, 87–89

See also $\text{YBa}_2\text{Cu}_3\text{O}_{7-\delta}$ (YBCO)

Superconducting gap, Raman scattering for studying gaps and pseudo-gaps, 13–15

Superconducting plasma phenomena

Anderson–Higgs–Kibble mechanism, 245

attempts to observe superconducting plasma mode, 247–248

basic concept of superconductivity mechanism by Bardeen–Cooper–Schrieffer (BCS theory), 246

$\text{Bi}_2\text{Sr}_2\text{CaCu}_2\text{O}_{8+\delta}$ single crystal experimental results, 269–270

block diagram of experimental setup for preset Josephson plasma resonance, 263f
 cavity resonator (cut view) with TE_{102} mode for study at 35 GHz, 262f

concept of spontaneously broken symmetry in solid state physics to high-energy physics, 274–275

dispersion relation of longitudinal and transverse plasma modes, 261f

energy diagram of collective excitations in metals, 247

examining Josephson plasma mode behavior as function of temperature, 271f, 272–273

existence of Nambu–Goldstone mode, 274

experimental data collection, 264

experimental technique to separate two modes, 262–264

experimenting within conventional solid-state physics laboratory, 275

frequency–temperature diagram of Josephson plasma in underdoped

$\text{Bi}_2\text{Sr}_2\text{CaCu}_2\text{O}_{8+\delta}$, 273f

gap formation historically in terms of Coulomb interaction among electrons (Anderson–Higgs mechanism), 246

- high- T_c superconductors ($\text{Bi}_2\text{Sr}_2\text{CaCu}_2\text{O}_{8+\delta}$) of Josephson type, 248
- induced current flow due to magnetic field of microwave, 266*f*
- Josephson plasma
- high- T_c superconductors, 255–257
 - longitudinal plasma mode, 257–260
 - resonance decreasing as T raised to T_c in vortex liquid phase, 272
 - resonance field as function of sample size for two cases, 270*f*
 - single Josephson junction, 252–255
 - transverse plasma mode, 260
- longitudinal and transverse components of electromagnetic wave, 248–252
- Nambu–Goldstone mode, 245–246
- numerical results calculated with indicated parameters, 268*f*
- occurrence of superconductivity as kind of pure quantum mechanical phase transition in electron system of metal, 246–247
- physical meaning of two modes, 261
- plasma resonance experiments varying magnetic field, 248
- recognizing importance, 274
- schematic drawing of geometry for transverse plasma excitation, 265*f*
- schematic picture of Josephson junction, 253*f*
- schematic picture of multistacked Josephson junction as model of high- T_c superconductors, 258*f*
- separation of longitudinal and transverse plasma modes, 261–270
- set of resonance curves in $\text{Bi}_2\text{Sr}_2\text{CaCu}_2\text{O}_{8+\delta}$ as function of sample size, 269*f*
- temperature dependence of Josephson plasma mode near T_c , 271–274
- temperature dependence of Josephson plasma resonance line in underdoped $\text{Bi}_2\text{Sr}_2\text{CaCu}_2\text{O}_{8+\delta}$ at three different frequencies, 271*f*
- transverse mode and occurrence of Meissner effect, 245
- transverse plasma calculations, 264–268
- two Josephson plasma modes, 245–246
- Superconductive materials, conventional versus unconventional, 2
- Superconductivity
- Bardeen–Cooper–Schrieffer (BCS) mechanism, 2
 - definition, 2
 - Meissner effect, 2
 - point contacts, 199
- Superconductors, new. *See* Dissolution of A-15 phases in metallic dichalcogenides
- Superparamagnetism
- enhancing by partial removal of additional oxygen, 147
 - See also* Nd–Ce–Cu–O system
- Surface modification chemistry
- spontaneously adsorbed monolayer films for examining processes, 169
 - See also* Self-assembled monolayers (SAMs) on $\text{YBa}_2\text{Cu}_3\text{O}_7$ (YBCO)
- Susceptibility, ac
- third and first harmonic of T1 2201 crystal sample, 89, 90*f*
 - third harmonic ac susceptibility measurement of over-doped T1 2201 crystal, 91*f*
 - See also* Inhomogeneities
- Synchrotron-based X-ray photoelectron and Auger microscopy
- copper image from YBaCuO sample on PrBaCuO , 75*f*
 - high-temperature superconducting metal oxides, 72–73
 - schematic of beamline X1-SPeM-II at National Synchrotron Light Source, Brookhaven National Laboratory, 74*f*
 - strontium image from sample of $\text{Bi}_2\text{Ca}_2\text{SrCu}_2\text{O}_x$, 75*f*
 - See also* X-ray photoelectron and Auger spectroscopy
- T**
- Tetramethyltetraselenafulvalene (TMTSF), organic donor, 2–3
- Text overview, 1–2
- Thallium-based ceramic composites
- doped versions as composite wires, 156–157
 - See also* Phase evolution in composite ceramic superconductors
- Thermal modeling
- improving response characteristics of hybrid assemblies, 288–289
 - schematic of model in three-dimensional finite difference analysis, 288*f*
 - See also* Dye/superconductor assemblies
- Time-resolved optical studies
- availability of ultrafast laser systems, 231
 - colliding-pulse mode-locked (CPM) dye laser, 232
 - contribution identification for superconductivity theory development, 231
 - experimental determination of ΔT close to T_c by measuring resistivity of illuminated and nonilluminated microbridge, 235, 236*f*
 - experimental technique and data analysis, 232–237
 - laser heating of sample, 235–237
 - low repetition experiments using CPM laser, 233–234
 - nonequilibrium heating effect, 236–237
 - quasiparticle (QP) relaxation dynamics, 230
 - study of nonequilibrium carrier dynamics, 231

temperature dependence of fast component amplitude at three different laser intensities, 236, 237*f*
 typical set of time-resolved photoinduced transmission traces in underdoped and optimally doped $\text{YBa}_2\text{Cu}_3\text{O}_{7-\delta}$, 234–235
 typical time-resolved photoinduced transmission setup, 232*f*
 typical time-resolved photoinduced transmission signal on near optimally doped $\text{YBa}_2\text{Cu}_3\text{O}_{7-\delta}$, 223
See also Time-resolved photoinduced spectroscopy
 Time-resolved photoinduced spectroscopy
 comparison with data on $\text{YBa}_2\text{Cu}_3\text{O}_{7-\delta}$, 241–242
 cross-over between T-independent gap and T-dependent gap, 242
 information about T-dependence, doping dependence, and symmetry of gap, 237–238
 initial hot carrier relaxation, 237–238
 laser probe process, 239
 process of energy relaxation by Allen's model, 237–238
 pseudogap onset temperature for $\text{YBa}_2\text{Cu}_3\text{O}_{7-\delta}$, 242*f*
 separation of different spectral components in low-energy excitation spectrum, 242–243
 T-dependence over wide range of doping in $\text{YBa}_2\text{Cu}_3\text{O}_{7-\delta}$, 243
 T-independent gap and BCS-like (Bardeen, Cooper, and Schrieffer) T-dependent gap considerations, 239–240
 theoretical model for T-dependence of photoinduced reflection or transmission, 239–240
 theoretical predictions for amplitude of photoinduced transmission as function of temperature, 240*f*
 $\text{Tl}_2\text{Ba}_2\text{CuO}_{6+\delta}$
 proposed mechanism, 225–226
 resistance versus temperature during and without illumination, 223, 224*f*
 spectra dependence of persistent photoconductivity (PPC), 225–226
 time dependence of excitation and relaxation of PPC, 223*f*, 224
See also Persistent photoconductivity (PPC)
 Transmission measurements, pump-probe method, 17
 Transverse plasma mode
 dispersion relation of longitudinal and transverse plasma modes, 261*f*
 Josephson plasma, 260
 Meissner effect, 245, 261
 physical meaning, 261

separation of longitudinal and transverse plasma modes, 261–270
See also Josephson plasma modes; Superconducting plasma phenomena

U

Umklapp scattering, electrical resistivity calculations not including, 104
 Unconventional superconductors. *See* Exotic superconductors

V

van der Waals gap, insertion of chemical species into, of dichalcogenides, 22
 Vibrational frequencies
 increase below T_c of low-energy phonons, 11
 phonons, 4–5
 Vibrational spectroscopy
 focus on geometry and environment of anionic species, 10–11
 origin of vibrations, 10
 research areas for organic superconductors, 10–11
 self-energy effects, 11
 Vibration of apical oxygen, scattering efficiency. *See* Ortho-II phase of $\text{YBa}_2\text{Cu}_3\text{O}_x$
 Voltage measurements, transient dye-coated assemblies, 286–288
 schematic of optical delivery system, 287
See also Dye/superconductor assemblies
 Vortex liquid phase
 Josephson plasma resonance decreasing as T raised to T_c , 272
See also Superconducting plasma phenomena

W

Wavelength detection
 human eye, 278
 man-made optical detectors over broad wavelength range, 278–279
 wavelength-selective single-color detectors, 279
See also Dye/superconductor assemblies
 Wavelength-selective high- T_c bolometers. *See* Dye/superconductor assemblies
 Weinberg–Salam theory, analogy to Nambu–Goldstone and longitudinal plasma mode, 18

X

X-ray photoelectron and Auger spectroscopy
 application to superconducting materials, 68, 70

combination with microscopy for spectromicroscopy, 70, 72
 complementary to Auger spectroscopy, 67
 copper image from sample of YBaCuO deposited on PrBaCuO, 75f
 electronic and bonding phenomena for study, 66–67
 general considerations, 67–68
 overlayer thin films of YBa₂Cu₃O_{6.9}, 69f
 schematic of beamline X1-SPEM-II at National Synchrotron Light Source, Brookhaven National Laboratory, 74f
 spectra of metal cuprate high-temperature superconductors, 69f
 strontium image from Bi₂Ca₂SrCu₂O_x sample, 75f
 studying films and interfaces involving superconductors, 68
 synchrotron-based X-ray photoelectron and Auger microscopy, 72–73
 two-fold purpose, 66
 X-ray photoelectron/Auger lines for studying superconducting metal oxides using Auger parameters, 72f
See also Auger spectroscopy

Y

YBa₂Cu₃O_{6.5}

electron-trapping model, 222
 relative change in conductivity as function of oxygen content, 220
 time dependence of resistivity, Hall coefficient, and Hall mobility, 219–220
See also Persistent photoconductivity (PPC)

YBa₂Cu₃O_{7-δ} (YBCO)

angular dependence of Hall resistivity in mixed state, 83
c-axis lattice parameter as measure of oxygen composition for bulk samples, 85
 configurations of ⁵⁷Co at Cu(1) site, 142, 144f
 electron–phonon relaxation time and wavelength from time-resolved experiments, 238
 emission Mössbauer spectra of ⁵⁷Co-doped YBCO at different temperatures, 143f
 field dependence of ρ_{xy} along *a*-axis of detwinned YBCO crystal below *T_c* as function of applied field, 84f
 Hall effect in detwinned YBCO crystal below *T_c*, 83
 high-energy X-rays probing interior of crystal, 87, 89
 high-resolution specular scan of (006) reflection for YBCO crystal, 88f
 high-resolution X-ray-diffraction measurements, 85, 87
 inhomogeneities affecting properties, 85

linear temperature dependence of resistivity, 80–81
 magnetoresistance along *a*- and *b*-axes for detwinned crystal in mixed state, 85, 86f
 magnetotransport properties, 80–85
 mixed state properties, 83–85
 model relating slope and zero-temperature intercept to sample inhomogeneities, 81
 nature and impact of structural inhomogeneities, 89, 92
 normal state properties, 80–83
 oscillation of O(4) in Cu–O chain, 140–145
 praseodymium (Pr) substitution for Y and metallicity of chain, 145
 pseudogap onset temperature from time-resolved measurements, 242f
 relationship between oxygen content and *c*-axis length, 87
 resistivity versus temperature for twinned YBCO crystal, 82f
 rocking curve of (006) diffraction peak of YBCO crystal sample, 88f
 rocking curves for quality of individual grains or domains, 87
 sensor preparation and testing of thin YBCO layers on MgO, 279–281
 structural studies, 85, 87–89
 temperature dependence of Hall coefficient along *a*- and *b*- axes of detwinned YBCO crystal, 82f
 temperature dependence of photoinduced transmission and reflection, 241–242
 temperature-dependent Hall coefficient, 81, 83
 temperature-dependent magnetoresistivity of detwinned crystals of YBCO, 83, 85
 temperature-dependent resistivity of twinned and untwinned samples, 81
 third harmonic ac susceptibility measurements of over-doped T1 2201 single-crystal sample, 89, 91f
 third harmonic and first harmonic ac susceptibility measurements of inhomogeneous T1 2201 crystal sample, 89, 90f
 three-dimension plot of (7- δ) versus *y* and *z* for twinned YBCO crystal showing variations in oxygen content, 89, 90f
 transition-edge bolometers with impressive sensitivities, 279
 typical time-resolved photoinduced transmission signal near optimally doped YBa₂Cu₃O_{7- δ} , 233
 typical time-resolved photoinduced transmission traces in underdoped and optimally doped YBa₂Cu₃O_{7- δ} , 234f
 unit cell, 141f
See also Dye/superconductor assemblies; Emission Mössbauer studies; Raman spectroscopy in YBCO-type compounds; Time-resolved photoinduced spectroscopy

- YBa₂Cu₃O₇ (YBCO)**
nonsuperconductive corrosion products, 169
See also Self-assembled monolayers (SAMs) on YBa₂Cu₃O₇ (YBCO)
- YBa₂Cu₃O_x (YBCO)**
discovery of RBa₂Cu₃O_x compounds (R = Y), 107–108
oxygen atom arrangement types in basal planes, 121f
oxygen content dependence on normal-state or superconducting properties, 120
Raman evidences for phase separation, 111–112
- Raman spectra of four stable phases, 108–111
Raman spectroscopy of overdoped YBCO-type materials, 116–117
Raman spectroscopy powerful for studying oxygen arrangement, 122
stable and metastable ordered phases predictable by Monte Carlo simulations, 108
See also Apex oxygen sublattice in YBa₂Cu₃O_{7-x} single crystals; Ortho-II phase of YBa₂Cu₃O_x; Raman spectroscopy in YBCO-type compounds